SOFT X-RAY MICROANALYSIS AND MICROSCOPY: A UNIQUE PROBE OF THE ORGANIC CHEMISTRY OF HETEROGENEOUS SOLIDS

G. D. Cody, R. E. Botto, H. Ade,[†] S. Wirick,[‡] A. Davis,[§] and G. Mitchell[§]
Chemistry Division, Argonne National Laboratory, Argonne IL 60439
[†]Department of Physics, North Carolina State University, Raleigh, NC 27695
[‡]Department of Physics, SUNY at Stony Brook, NY 11794
[§]Coal and Organic Petrology Labs., Pennsylvania State University, University Park, PA 16802

Keywords: X-ray microscopy, carbon, coke

INTRODUCTION

Many problems in fuel chemistry relate directly to the heterogeneous nature of materials such as coals and cokes. Recent advances in X-ray micro-focusing techniques coupled with synchrotron light sources have resulted in a scanning transmission X-ray microscope (STXM) located at the National Synchrotron Light Source at Brookhaven National Laboratory. Carbon's 1s near absorption edge region is rich with fine structure associated with photo-excited transitions to various low lying, unoccupied molecular orbitals. Preliminary carbon near edge absorption micro-spectroscopy (C-NEXAFS) and microscopy on complex organic solids such as coal has been performed using the scanning transmission microscope on the X1A beamline at NSLS. In many cases, spectacular chemical heterogeneity was observed down to the submicron level using the intensity of the prominent absorption fine structure on carbon's absorption edge for contrast.[1-3] STXM/C-NEXAFS has also been applied to biological specimen[4-6] and heterogeneous polymers.[7]

In the present paper, the STXM and C-NEXAFS microanalysis will be used to analyze the microchemistry of cokes and highly carbonaceous materials. The issue of molecular orientation will be addressed by using the intrinsic polarization of the X-ray beam at X1A.

EXPERIMENTAL

Sample: Two samples of carbonized materials were selected for STXM analysis. The first is a naturally coked coal from western Pennsylvania. The other is a laboratory derived sample of carbonized (1000 °C) pyrene.

Sample Preparation: A crucial aspect of STXM and C-NEXAFS is the necessity of preparing extremely thin specimens. The relatively high molar absorption coefficient of carbon at these wavelengths, $\mu = 1 \times 10^4\ cm^2/g$, and the high bulk density of carbon in coal requires that sample thicknesses be less than 800 nm. There are a variety of methods available to obtain specimens of this thicknesses, however, ultra-microtoming was found to yield the most favorable results. Thicknesses in the range of 100 to 200 nm were readily produced. Artifacts associated with the technique, for example, scoring marks paralleling the cutting direction of the diamond knife and chatter marks perpendicular to the cutting direction, were readily identifiable.

Scanning Transmission X-ray Microscopy: The microscope, a scanning transmission X-ray microscope (STXM), is located at the terminus of the X1A beam line at the National Synchrotron Light Source (NSLS). The elements of the STXM relevant to this paper are described as follows. At the head of the instrument, soft X-rays are generated using an undulator which resides on the 2.5 GeV electron storage ring. Energy selectivity (0.3 eV resolution) is controlled with a tunable spherical monochromator. X-ray micro-focusing is managed with near field optics, i.e., a Fresnel phase zone plate and an order sorting aperture.[8] Currently, the STXM has a resolution limit of 55 nm, however, in the future, the resolution down to 10 nm may be possible.[9] X-ray transmission is detected using a gas-filled proportional counter. Details on the instrument's specifications have been reported elsewhere.[8]

C-NEXAFS: The physics of NEXAFS is similar to valence shell electronic state spectroscopy, with one important distinction, the initial state of the photo-ionized electron is in an atomic, not molecular, orbital. Herein lies the major advantage of inner shell over valence shell spectroscopy, the photo-ionized core hole is highly localized, thus, the initial orbital is more readily identified and, in principle, specific information on functional groups may be obtained. Absorption of X-rays occurs through the interaction of an X-ray photon with an electron in an atomic core resulting in the promotion of the inner shell electron to a relatively low-lying unoccupied molecular orbital (LUMO). Molecules containing π orbitals generally have their lowest energy inner shell transition to the first unoccupied, or antibonding, π^* orbital.

In alkanes, a relatively intense absorption band is observed which correspond to the transition from carbon's 1s to a 3p Rydberg-like orbital which overlaps with a C-H σ^* transition. These transitions are referred to as 1s - 3p/σ^* transitions.[10]

The intensity of a given electronic transition is a function of its dipole moment. Given some preferred orientation in a molecular assemblage, linear dichroic effects are expected and can be measured. For aromatic systems, the 1s - π^* transitions are naturally polarized in the direction of the $2p_z$ orbitals, i.e., out of the ring. The 1s - σ^* transitions are polarized parallel with the $2p_{x,y}$ plane, i.e., opposite that of the 1s - π^* transitions. Degrees of preferred orientation can be calculated from the change in intensity with orientation via the relationship,

$$I_0/I_{90} = \cot^2\alpha \qquad (1)$$

where α is the angular degree of preferred orientation, i.e., $\alpha = 45$ is completely random, while $\alpha = 0$ is perfectly aligned.

RESULTS AND DISCUSSION

Figure 1 presents a reasonably high resolution image of the naturally coked coal acquired with the monochromator tuned to the 1s - π^* transition of aromatic carbon. Clearly there is considerable microstructure which may be related to either chemistry or molecular orientation. Figure 2 presents the laboratory carbonized material. In this sample, there is also considerable microheterogeneity, with a domain scale somewhat finer than the coke (Figure 1).

The C-NEXAFS spectra of light and dark regions in Figure 1 are presented in Figure 3. At the low energy end, enormous differences in intensity of the 1s - π^* transitions are clearly evident. At the high energy end of the near edge region, the 1s - σ^* transitions also exhibit significant differences in intensity. The fact that the two types of transition exhibit a contrast reversal indicates that the differences in absorption are related to molecular orientation. Using Equation 1, we calculate an preferred orientation of 20 degrees off of completely random.

The C-NEXAFS spectra of the laboratory coke is presented in Figure 4. In this case, there are also significant differences in absorption; however, there is no contrast reversal between the 1s - π^* and 1s - σ^* transitions. This indicates that the contrast evident in Figure 2 is related to variation in the chemistry and density, but not to variations in molecular orientation.

ACKNOWLEDGMENTS

This work was performed at the National Synchrotron Light Source (NSLS) which is supported by the U.S. Department of Energy. GDC gratefully acknowledges the Chemistry Division of Argonne National Laboratory for support granted through the award of the Enrico Fermi Scholarship. GDC and REB acknowledge support from the Office of Basic Energy Sciences, Division of Chemical Sciences, U.S. Department of Energy, under contract number W-31-109-ENG-38. SW and the STXM Facility are supported by the U.S. Department of Energy, under contract number 89ER60858.

REFERENCES

1. Botto, R. E.; Cody, G. D.; Ade, H.; Behal, S.; Disko, M.; Wirick, S. *Energy Fuels*, **1994**, *8*, 152.
2. Cody, G. D.; Botto, R. E.; Ade, H.; Behal, S.; Disko, M.; Wirick, S. *Energy Fuels*, **1995a**, *9*, 75.
3. Cody, G. D.; Botto, R. E.; Ade, H.; Behal, S.; Disko, M.; Wirick, S. *Energy Fuels*, **1995b**, in press.
4. Williams, S.; Zhang, X.; Jacobsen, C.; Kirz, J.; Lindass, S.; Hof, J. V.; Lamm, S. S. *J. Microsc.*, **1993**, *170*, 155.
5. Zhang, X.; Ade, H.; Jacobsen, C.; Kirz, J.; Lindass, S.; Williams, S.; Wirick, S. *Nucl. Instr. Meth. In Phys. Res.*, **1994**, *A 347*, 431.
6. Buckley, C. J. *Bone*, **1992**, *13*, 100.
7. Ade, H.; Zhang, X.; Cameron, S.; Costello, C.; Kirz, J.; Williams, S. *Science*, **1992**, *258*, 972.
8. Jacobsen, C.; Williams, S.; Anderson, E.; Browne, M. T.; Buckley, C. J.; Kern, D.; Kirz, J.; Rivers, M.; Zhang, X. *Opt. Commun.*, **1991**, *86*, 351.
9. Ade, H. *Synchrotron Radiation News*, **1994**, *7*, 11.

10. Hitchcock, A. P.; Newbury, D. C.; Ishii, I.; Stohr, J.; Horsley, J. A.; Redwing, R. D.; Johnson, A. L.; Sette, F. *J. Chem. Phys.*, **1986**, *85*, 4849.

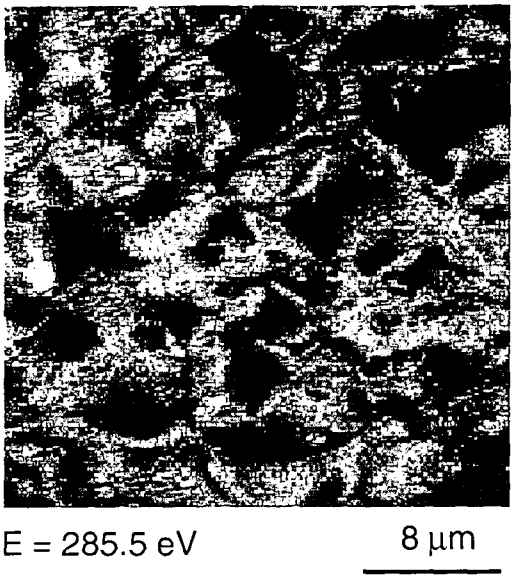

Figure 1. X-ray image of the naturally coked coal. Monochromator tuned to the aromatic 1s-pi* electronic transition.

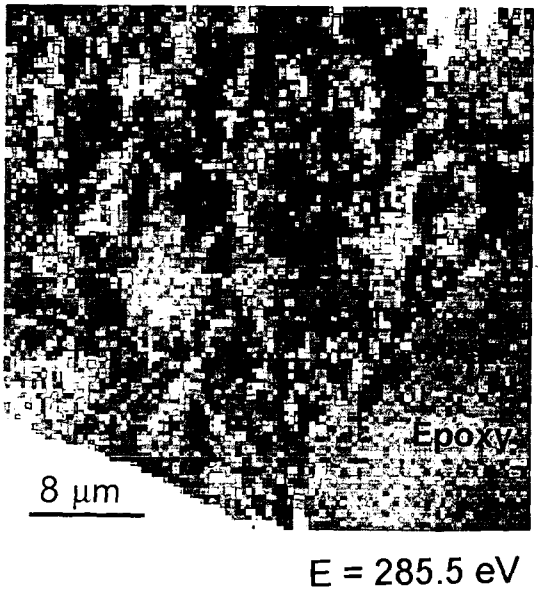

Figure 2. X-ray image of the carbonized pyrene sample. Monochromator tuned to the aromatic 1s-pi* electronic transition.

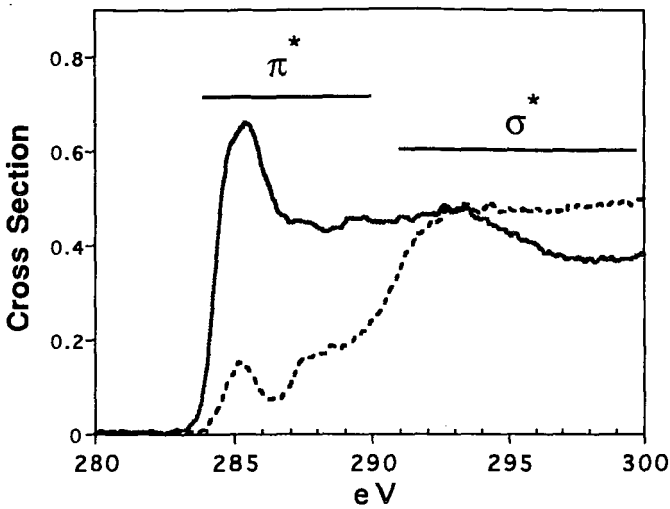

Figure 3. The C-NEXAFS spectra of light and dark regions in Figure 1.

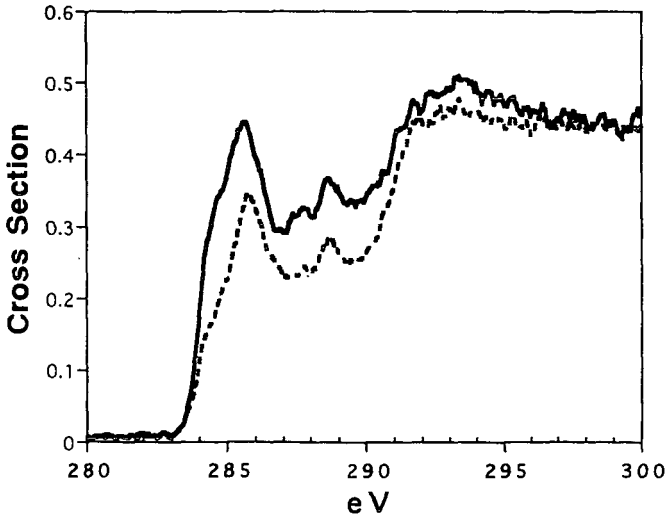

Figure 4. The C-NEXAFS spectra of the laboratory coke.

THE DEVELOPMENT OF POROSITY IN PITTSBURGH #8 AND WYODAK CHARS AS STUDIED USING CONTRAST MATCHING SMALL ANGLE NEUTRON SCATTERING

Peter J. Hall and M. Mirari Antxustegi
Department of Pure and Applied Chemistry, University of Strathclyde
295 Cathedral Street, Glasgow G1 1XL, SCOTLAND

Joseph M. Calo
Division of Engineering, Box D, Brown University, Providence, RI, USA

Keywords: Contrast Matching Small Angle Neutron Scattering, Interparticle Scattering, Porosity.

INTRODUCTION

The development of porosity in coal chars is important in both combustion and gasification processes and there have been a large number of investigations and techniques applied to the subject[1]. A persistent problem in understanding the development of porosity is the existence of closed porosity, which cannot be accessed from the external surface. Intrusive techniques, such as mercury porosimetry[2], or adsorbative techniques[3] cannot, by definition, give information about such porosity. On the other hand, small angle x-ray scattering (saxs)[4] and small angle neutron scattering (sans)[5] techniques monitor scattering from both open and closed porosity and consequently cannot distinguish them. Additionally, saxs data may be complicated by interparticle scattering.

Recently, progress has been made in the understanding of closed and open porosity by using contrast-matching small angle neutron scattering (sans) to investigate the development of porosity[6,7]. In Hall *et al.*[6], sans was first performed on dry powdered phenolic resin char (prc). As with saxs, scattering is off open and closed porosity, as well as some interparticle scattering. Sans was then performed on phenolic resin char saturated with deuterated toluene. Following ultrasonication of the toluene/char mixture, the deuterated solvent fills any accessible porosity and interparticle voids. Hall *et al.*[6] showed that deuterated toluene has the same neutron scattering density as typical polycrystalline carbon ($\sim 5.6\ 10^{10}$ cm^{-2}) and therefore contrast matches the carbon very closely. With respect to neutrons there is no scattering contrast between the carbon and deuterated toluene in the pores and therefore no coherent scattering. Open porosity is therefore becomes "invisible" to the neutrons. Neutron scattering from the deuterated toluene/char mixture was therefore due to carbon and any porosity that could not be accessed by the deuterated toluene. Hall *et al.*[6] showed that there was significant residual scattering in the contrast matched sample which was due to a well developed closed pore system. The difference between the dry and contrast matched samples was therefore due to scattering in open pores and interparticle scattering from the external surfaces of the packed prc particles.

Pittsburgh #8 coal is a coking coal and following slow pyrolysis (heating rates ~ 10 $Kmin^{-1}$) under nitrogen it goes through a fluid phase[8] before the onset of significant carbonization. The resulting chars have low surface areas and are highly graphitic[9]. From investigation of the desorption of oxygen complexes, Hall and Calo[9] have speculated that Pittsburgh #8 char has very low levels of microporosity and that gasification proceeds by the creation of new pores. This thesis has not been explicitly tested.

Conversely, Wyodak is a Subbituminous coal and forms a char of high surface area.

The objective of the present work is to use a technique to investigate the development of Pittsburgh #8 and Wyodak coal chars: contrast matching sans.

EXPERIMENTAL

BET surface areas were obtained from adsorption of nitrogen at 77K using a Quantasorb apparatus over the range $0.01<P/P_o<0.95$.

The sans was performed at the Intense Pulsed Neutron Source (IPNS) at the Argonne National Laboratory at the small angle diffractometer (SAD)[10]. The sample holders were made of Suprasil with a path length of 0.2 cm. The scattering data were corrected for the scattering from the sample holder and other instrumental backgrounds. Normalization for the sample thickness and transmission were made and the data were scaled to yield absolute calibration.

Pittsburgh # 8 and Wyodak coals were selected from the Argonne Premium Coal sample programme. Great care was taken to avoid contact with air during the pyrolysis procedure. The coal was heated under a slight positive pressure of nitrogen at 10 K min^{-1} to 1273K with a heat soak time of 1 hour. The resulting char was ground to between 60 and 100 Tyler mesh. For sans on the contrast matched samples, the chars were mixed with excess deuterated toluene and placed in an ultrasonic bath for 4 hours. Activation of the chars was by air in a tube fumace at 673K.

RESULTS AND DISCUSSION

Pittsburgh #8 char: 77K nitrogen adsorption isotherms were made for Pittsburgh #8. The surface area of the ungasified char was 8 m^2g^{-1}, which suggests no significant open porosity. This has been previously observed by Hall and Calo and is typical of chars from coking coals. The isotherm is of Type 2 according to the BDDT[11] classification, which is typical for non-porous materials or materials which have pore systems with significant amounts of meso- or macro- porosity. As discussed, the gas adsorption gives no indication as to the possible existence of closed porosity or whether porosity development proceeds by opening porosity or developing new porosity.

Small angle neutron scattering for the ungasified char is shown in Figure 1. To summarize, the dry curve represents coherent scattering from open and closed porosity as well as interparticle scattering. The contrast matched curve represents scattering from closed porosity and the difference curve represents scattering from open porosity and interparticle scattering.

From the dry curve it can be seen that there is no significant scattering for $q>0.15$ $Å^{-1}$. This suggests the absence of scatterers of size less than ~40 Å and the absence of well developed microporosity. There is therefore consistency between the isotherm and sans data. The scattering data increases monotonically over the q range studies which suggests that the size of the largest scatterer cannot be resolved. This may be either due to interparticle scattering or scattering from a small number of large pores.

From Figure 1 it can be seen that the effect of contrast matching by the addition of deuterated toluene reduced significantly the scattered intensity at all q-values. To illustrate this more graphically, the scattering is shown on a linear scale as an insert in Figure 1. The integral under the "dry" scattering curve is 2.19 (arbitrary units) and the integral under the contrast matched curve is 0.10 (arbitrary units). Therefore scattering has been reduced by a factor of 22. Therefore, 4.8% of the total scattering is due to closed porosity. This compares to 59.9% for the ungasified phenolic resin char of Hall *et al.*[6] and shows clear differences between the pore structures of prc and Pittsburgh #8 coal char. Figure 1 also shows that there is no significant scattering for $q>0.078$ Å, for the contrast matched sample, which suggests the absence of porosity less than ~75Å. It is probable therefore that scattering is due to a small number of large pores.

Gasification to 0.8% burn-off increases the surface area to 80 m^2g^{-1}, which suggests the development of porosity. Analysis of the BET isotherm curve shows a BDDT Type 2 adsorption isotherm for this char although the knee is more clearly defined than for the ungasified char. This may suggest the development of significant levels of microporosity. The sans data for the 0.8% burn-off char are shown in Figure 2. The results are qualitatively the same as for the ungasified char. Contrast matching reduces the scattered intensity very significantly, which

suggests that there is very little porosity. The scattering integral for the dry sample is 3.33 (arbitrary units) and this reduces to 0.15 for the contrast matched sample. Therefore 4.8% of the total scattering is due to closed porosity, which is similar to the ungasified char. The scattering data suggests that deuterated toluene can access all of the porosity developed during gasification.

Comparison of the scattering from the contrast matched samples in Figures 2 and 3 (shown as an insert in Figure 2) shows that they are very similar. Invariance of scattering from contrast matched samples has previously been observed by Hall *et al.*[6] for phenolic resin. This constitutes evidence that the scattering is indeed from closed porosity which is unaffected by gasification. The scattering data from the 0% and 0.8% samples therefore show that gasification proceeds by the creation of new porosity, rather than the opening of closed porosity as is the case for phenolic resin char[6].

The dry scattering curve in Figure 2 is typical for a material with a well developed micropore system. For convenience, the scattering behaviour for Porod type of behaviour is also shown in Figure 2. The upward deviation from this is due to the presence of micropores formed during gasification. Since the ungasified char has a low surface area, and the adsorption isotherm for the ungasified char is typical for a non-porous material, the scattering in the "difference" curve of Figure 1 is therefore dominated by interparticle effects, i.e. scattering determined by the external surface of the particles and the packing of the char particles. Again, this effect has been observed by Hall *et al*[6] for phenolic resin char. The form of the scattering curve for the ungasified sample approximates to Porod behaviour, which suggests that it is due to the presence of relatively large scale scatterers. Since the surface area of the 0.8% gasified char suggests the development of open porosity then the difference curve of Figure 2 must therefore contain information about interparticle scattering as well as the additional porosity. The difference curves are compared in Figure 3. The curves converge at low-q, which suggests that the nature of the background scattering has not changed significantly. The difference between the two difference curves ($0.8\%_{diff}$-$0\%_{diff}$ in Figure 3) is therefore due to scattering from any additional pores created during the gasification process. Using the technique of subtracting interparticle scattering effects, the development of porosity in Pittsburgh #8 coal char can be studied in detail.

BET surface areas increase with gasification. The surface area at 13.5% burn-off is 252 m^2g^{-1}. The isotherms are all of type 2, although the "knee" seems to be more clearly defined for the 0.8% and 4.5% gasified chars. Sans for the gasified chars are shown in Figure 4. The data are difference scattering curves that have been corrected for interparticle scattering by further subtraction of the "difference" scattering curve of Figure 1. The scattering curves therefore give information about pores that have been developed during gasification. The Guinier analysis[12] for the 0.8% gasified char shows a linear section with a radius of gyration, R_g=16.3Å. Therefore, the early stage of gasification appears to produce microporosity. The scattering curve for the 4.5% gasified char in Figure 4 is also typical for a microporous network and the Guinier plot is also linear with R_g=13.5Å. The conclusion is that further microporosity is being produced. In contrast, the scattering curve for the the 13.5% gasified char is typical for a pore system with a wide range of pore sizes. The Guinier plot confirms this by showing curvature over the entire q-range. The log-log plot is linear over the range 0.0058Å<q<0.054Å and the slope of the line is -3.8. This deviates slightly from the Porod ideal and is probably due to fractal roughening of the pore surfaces. The fractal dimension is 2.2, which agrees with other fractal investigations of the surfaces of gasified carbon surfaces. Therefore in the burn-off range 4.5%-13.5% micropores appear to being opened to produce a pore system with a wide size range.

Wyodak Char: In this case, the picture is quite different. It is not possible to define the amount of interparticle scattering as in the case of Pittsburgh #8 because in the case of ungasified wyodak char, there is some initial opened and closed porosity. As before, the extent of scattering due to closed porosity can be obtained by examining the scattering from the contrast matched sample. But after substracting the scattering due to closed porosity, the difference curve will tell about the interparticle scattering at the same time as the open porosity. Another input in the scattering curve could be scattering of the mineral matter in the coal char. This may have much more importance than in the case of Pittsburgh #8 because in the results presented here the

gasification is taken to much later stages. At 70% weight loss, the ash content of the sample is high. It is observed that there is a bump in the scattering curve between $0.03Å^{-1}<q<0.09Å^{-1}$ that remains invariant with gasification. The origin of this feature could be scattering from ash particles, but further work is needed to test this.

The contrast matched curve for the ungasifyed Wyodak char in Figure 5 shows considerable scattering. This suggest the presence of closed porosity in the sample. Other experiments show that the extent of closed porosity diminishes as gasification increases to 58% weight loss where it can be seen that the scattering from the closed pore is almost nil (Figure 6). After this stage, around 68% weight loss, the extent of closed porosity seems to increase. The explanation for this could be associated with the scattering of ash particles. The BET surface area decreases from $397m^2g^{-1}$ for 58% weight loss char to $267m^2g^{-1}$ for 68% weight loss char.

The results show that scattering from open porosity increases faster than the decrease of scattering from closed porosity. This may suggest that during the gasification process, both pore opening and pore creation take place simultaneously.

CONCLUSIONS

Contrast matching has been shown to be a very powerful technique for investigating the development of porosity in carbons both in terms of understanding the effects of closed porosity and the elimination of interparticle scattering. Contrast matching sans shows that Pittsburgh #8 char has very little closed porosity and consequently that pore development during gasification proceeds by the creation of new pores. In the early stages of gasification (<4.5% burn-off) a pore system with significant microporosity is produced. In later stages of gasification (4.5%-13.5% burn-off) the tendency is to open these micropores, producing a pore system with a broad size distribution. Ungasified Wyodak coal char has a significant amount of closed porosity that opens as gasification proceeds, giving a minimum of closed porosity around 58% weight loss. It is also shown that the increase of surface area during gasification is due to pore opening and creation.

ACKNOWLEDGEMENTS

The work was supported by a British Coal extra mural grant and MMA acknowledges support of a University of Strathclyde scholarship. Travel funding for MMA was from the Bellahouston Trust.

REFERENCES

1. Lowell, S. and Shields *Powder Surface Area and Porosity*, Chapman and Hall, London, 1984.
2. Bale, H.D. and Schmidt, P.W. *Phys Rev Lett*, 53, 596, (1984).
3. Hall, P.J. *Chemical Physics Letters*, 124, 467-469, (1986).
4. Porod, G. in Small Angle X-ray Scattering, edited by Glatter, O. and Kratky O., Academic Press, N.Y., 1982, pp: 17-52.
5. Kostortz, G. in Treatise on Material Science and Technology, Vol 15-- Neutron Scattering, edited by Kostortz, G., Academic Press, N.Y., 1979, pp: 227-290.
6. Hall, P.J., Antxustegi, M.M. and Calo, J.M. *Proc. Int Conf. Carbon '94*, Granada, Spain, 1994
7. Gethner, J.S., Journal of Applied Physics, 59 (4), 15 February 1986, pp: 1068-1085.
8. Mahajan O.P. in Coal Structure, edited by Meyers, R.A., Academic Press, N.Y., 1982, pp: 51-86.
9. Hall P.J. and Calo, J.M., Abstracts of Papers of ACS 1990, vol 35, no 3, Washington DC, pp: 705-712.
10. Epperson, J.E., Thiyagarajan, P. and Klippert, T.E., SAD Manual, IPNS, Argonne National Laboratory, Argonne, IL 60439.
11. Brunauer, S., Deming, L.S., Deming, W.S. and Teller, E. (1940), J. Amer. Chem. Soc., 62, pp: 1723.
12. Guinier, A. and Fournet, G.,in Small Angle Neutron Scattering (translated by Walker, C.B., Kudowitch, K.L., Edited by Wiley, N.Y., 1955, pp: 19-23.

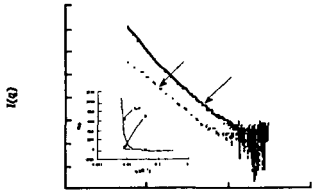

Figure 1. Small angle neutron scattering from unactivated Pittsburgh #8 coal char dry (a), contrast matched by mixing with deuterated toluene (b) and the difference (c) between scattering curves (a) and (b).

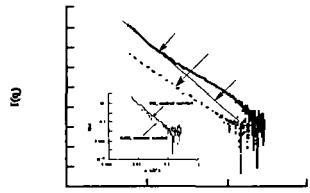

Figure 2. Small angle neutron scattering from Pittsburgh #8 coal char gasified to 0.8% weight loss in air at 673K dry (a), contrast matched by mixing with deuterated toluene (b) and the difference between scattering curves (a) and (b). A comparison of the scattering from the contrast matched ungasified and 0.8% gasified Pittsburgh #8 coal chars is sbown as an insert.

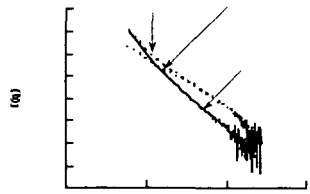

Figure 3. The method for correcting the "difference" scattering curve (curve (c) in Figure 3) by subtraction of the interparticle scattering (curve (c) in Figure 1) to show scattering from pores produced during gasification ($0.8\%_{diff}$-$0\%_{diff}$) for Pittsburgh #8 coal char gasified to 0.8% burn-off in air at 673K.

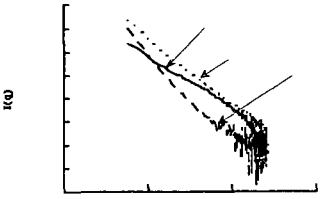

Figure 4. "Difference" scattering curves corrected for interparticle scattering to show small angle neutron scattering from pores produced during gasification for Pittsburgh #8 coal char gasified to different levels of burn-off in air at 673K.

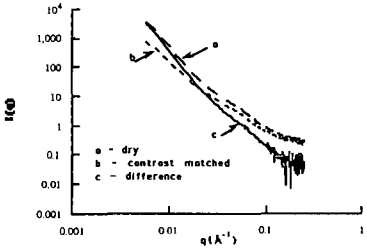

Figure 5: Small angle neutron scattering from ungasified Wyodak coal char dry (a), contrast matched by mixing with deuterated toluene(b) and the difference (c) between scattering curves (a) and (b).

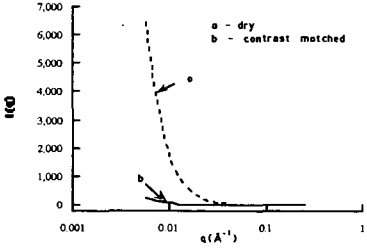

Figure 6: Small angle neutron scattering from Wyodak coal char gasified to 58% weight loss dry (a) and contrastmatched by mixing with duterated toluene (b). The intensity is shown in linear scale to show how the scattering of the contrast matched almost disappears.

SMALL ANGLE NEUTRON SCATTERING APPLICATIONS IN FUEL SCIENCE

P. Thiyagarajan
IPNS Division
George D. Cody, Jerry E. Hunt and Randall E. Winans
Chemistry Division
Argonne National Laboratory
Argonne, IL 60439.

Keywords: SANS Asphaltenes Coal

INTRODUCTION

Small angle neutron scattering (SANS) is a versatile technique[1], extensively used in condensed matter research, spanning the scientific fields including polymer science, metallic alloys, magnetic materials, porous materials, ceramics, composites, structural biology and colloidal systems of industrial and technological importance. SANS is useful to study both solid and liquid systems to obtain the size, morphology, molecular weight, particle size distribution in a size range of 10 to 1000 Å, as well as to study the phenomena such as phase separation, crystallization etc. In the presence of inter-particle interactions (e.g. ionic micelles) this will yield information on the surface potentials (e.g. surface charge density) of the colloids[2].

Three properties of neutrons make SANS to be unique and the information complementary to other techniques. The scattering cross-sections of the elements do not depend on their atomic number, but vary between the isotopes[3]; e.g., b_H=-0.3740x10^{-12}cm and b_D=0.6674X10^{-12}cm. This permits investigations of systems containing hydrogen (polymers, biological macromolecules, micelles, coals, asphaltenes) and multicomponent systems (clay-polymer composites, virus, microemulsions, coals). The high penetration of cold neutrons is valuable for the study of bulk materials under a variety of conditions, such as a wide range of temperature, magnetic field, pressure, shear etc. The magnetic moment of neutrons permits them as a powerful probe for the study of magnetic materials.

The SANS experiments can be carried out at either reactor facilities (e.g. ORNL, NIST, ILL-France), or at Pulsed Neutron Sources (e.g. ANL, ISIS-Great Britain). The neutron beams, usually, have circular cross-section with a diameter of 8-12mm, and the sample thicknesses are typically 1-5mm, depending on the chemical composition of the sample. Majority of SANS experiments require data in a wide q ($q=4\pi.\sin\theta/\lambda$, where θ is the half the scattering angle and λ is the wavelength of the neutrons) range, in order to carry out analysis on morphology, fractal dimension, particle size distribution, phase separation etc. To measure data in a wide q range at the SANS instruments at reactors, one has to repeat the experiments 2 to 3 times by changing the sample-to-detector distance or the wavelength of the neutrons or both. The SANS instruments at the pulsed neutron sources, on the other hand, yield data in a wide q range in a single measurement, by using neutrons with a wide range of wavelengths which are determined by time-of-flight techniques. This may serve as an advantage for studying systems which cannot be exactly reproduced for the repetitive measurements. In this paper we discuss briefly a few fundamental principles of SANS and demonstrate the technique with a few examples.

BASIC PRINCIPLES

A number of reviews[4,5,6] describe the basic principles of small angle scattering and hence we only give relevant formulae useful for obtaining the structural information. Briefly, the intensity of the scattered neutrons, I(q), in the low q region is determined by the number density of particles, n, the distance correlations due to time-averaged position vectors of the atoms within a particle [intra-particle structure factor, P(q)] and those due to the distribution of particles [inter-particle structure factor, S(q)] within the sample volume.

$$I(q) = n\,P(q)\,S(q) \qquad (1)$$

In dilute systems S(q) tend to oscillate around 1.0 in the low q region and the measured I(q) is determined essentially by P(q). Analysis of the measured I(q) for dilute systems will yield direct information on the structural properties of the particles, in terms of size and shape. If the data is calibrated to be on an absolute scale, additional infomation such as molecular weight and volume can also be obtained. In the absence of inter-particle interactions the differential scattering cross-section can be written as

$$I(q) = k\,\left|\int(\rho_s-\rho_m)\,e^{iqr}\,d^3r\right|^2 \qquad (2)$$

where ρ_s and ρ_m are the scattering length densities (scattering length per unit volume) for the particle and the matrix, and the k includes all the constants to place the data on an absolute scale. Table I contains scattering length densities ($\rho=\sum b.N_A.d/M$, where b is the scattering length[3], N_A.is the Avogadro's number, d is the physical density and M is the molecular weight) for a number of normal and per-deuteriated solvents. At low q region, equation 2 reduces to a simple form, Guinier equation[4],

$$I(q) = I(0)\exp(-q^2 R_g^2/3) \quad (3)$$

$$I(0) = n\, v^2(\rho_s-\rho_m)^2 \quad (4)$$

In eq. 3, R_g is known as the radius of gyration of the particle and v in eq. 4 is the volume of the solvent excluded by the particles. This is defined as the root-mean square value of all the pair-wise distances from the centroid of the scattering volume and this parameter does not specify the shape. In the case of monodisperse system, R_g can be used to determine the dimensions of the particles, provided the shape is known. In the case of spherical particles $R_g = \sqrt{(3/5)}$. radius. A plot of Ln.I(q) vs. q^2 (Guinier plot) will yield a straight line in the q region where $q.R_g \leq 1.0$. The absolute slope of the straight line can be used to determine the R_g and the y-intercept yields I(0) which can be used to determine the molecular weight of the particle. In the case of polydisperse systems the measured R_g is the z-avearaged value given by $R_g^2 = \Sigma N_i.M_i^2.R_{g^2i} / \Sigma N_i.M_i^2$ and the molecular weight from I(0) is the weight-averaged value. It can be seen from eq. 4 that the magnitude of I(0) can be manipulated by changing either the scattering length density of the solute, ρ_s, or the solvent, ρ_m, and can be made zero by exactly matching these two parameters. This method is called contrast varation[7] which can be done by changing the deuteration levels of either the solute or solvent. In the case of binary system the contrast variation method can be used to determine I(0) at different ρ_m values and a plot of $\sqrt{I(0)}$ vs ρ_m will give a straight line whose slope is proportional to the solvent excluded volume, v (see eq. 4) and the x-intercept gives ρ_s value. The value in turn can be used to determine the partial specific volume of the particle provided the chemical composition of the constituents is known. The contrast matching technique has been used to advantage in the case of coals. The composition and the density of the coals is such that its scattering length density is similar to the scattering length density of perdeuteriated toluene (see Table I). If coal is imbibed in the perdeuteriated toluene then for neutrons the particulate region of the coal and the solvent filling the accessible pores resemble as a system of uniform scattering length density. Hence the scattering from the pores accessible to the solvent will be negligible. However if there exists pores inaccessible to the solvent then they will produce SANS signals. Thus SANS can be used to characterize the closed pores in coals as well as other porous materials[8]. Such manipulation has also been done to see the effects of confined space on the phase separation in binary solvents[9] and micellization.

As mentioned earlier, the low q region gives the size parameter, R_g, but delineation of the shape information requires data in a wide q region. The log(I).vs.log(q) plots yield important information on the probable shapes. In the case of infinitely long particles the scattering signal in the low q region is convoluted by a powerlaw of q^{-1}. In the case of sheet like particles the scattering signal in the low q region is convoluted by a powerlaw of q^{-2}. Thus the measured differential scattering cross-sections for the rod and a sheet, respectively, are given by

$$I(q) = q^{-1}.\exp(-q^2.R_c^2/2) \quad (5)$$

$$I(q) = q^{-2}.\exp(-q^2.R_t^2) \quad (6)$$

These equations can be used to obtain the cross-sectional radius of gyration, R_c, of the rod-like particle from a modified Guinier plot[5] for a rod, Ln.[q.I(q)] vs. q2 and the thickness factor, R_t, of the lamellar particle can be obtained from a modified Guinier plot for a sheet, Ln.[q2.I(q)]. vs. q^2. The radius of the rod can be obtained by multiplying R_c by $\sqrt{2}$, and the thickness of the sheet can be obtained by multiplying the R_t by $\sqrt{12}$. The y-intercepts in these plots can be used to obtain the mass per unit length and mass per unit area respectively.

For obtaining information on the morphology of the particles, the data in the whole q region can be modelled by using the form factors for shapes such as sphere, ellipsoid, cylinder, random coil etc., and obtain the size parameters best describing the scattering signal. Form factors for several known geometries are available in Guinier and Fournet (1955)[4]

In the case of self-similar aggregates the scattering signals exhibit powerlaw behavior in a wide q region. The log(I) vs log(q) plots can be fitted in the linear regions and the absolute values of the slope can be used to describe the system in terms of fractal dimensions[10-12]. If the absolute value of the slope is a fraction in the region of 1-3, then the system is a mass fractal and the magnitude tells about the packing density of the fractal objects. If the fractal objects are formed through aggregation then it is possible to delineate the kinetics of aggregation. For example if the absolute value of the slope is around 1.7 then the cluster-cluster aggregation model may explain the aggregation mechanism, and if it is around 2.5 then it could be due to diffusion limited aggregation. If the absolute value of the slope is between 3-4 then the system is quite large and the system may be a surface fractal. A value close to 4 corresponds to a smooth surface and that close to 3 implies a particles with a rough surface.

The scattering signal in the case of polydisperse systems cannot easily be fitted with either the form factor of known geometrical objects or at times it may not exhibit linear curves in the Guinier plot [Ln I(q) vs q2]. If the measured scattering data contains data in the q region where $q.R_g \leq 1.0$ such that R_g is the largest particle size then unique information on the particle size distribution can be obtained by using maximum entopy technique. If the particles are too large and the data cannot be measured to very low q values fulfilling the relationship $q.R_g \leq 1.0$, then it may not be possible to get the correct particle size distribution. The pore size distribution in coals is quite wide and the pores are quite large and hence the scattering techniques cannot give the correct pore size distribution for coals.

EXPERIMENTAL

We have conductued a number of SANS experiments on coals, coal macromolecules and asphaltenes at the Small Angle Diffractometer (SAD) at the Intense Pulsed Neutron Source of Argonne National Laboratory. This instrument uses neutrons produced in pulses by spallation due to the deposition of 450 MeV protons on a depleted uranium target, followed by a solid methane moderator (22 K) yielding a wavelength range of 1 to 14 Å . Detection of scattered neutrons was accomplished with an area sensitive, gas-filled proportional counter, and the wavelength of the scattered neutrons was determined by their times-of-flight. The accessible q range using SAD is from 0.005 to 0.25 $Å^{-1}$ in a single measurement. The samples at ambient to 100 C were measured in Suprasil cells, while the high temperature measurements were done in a stainless steel cell

EXAMPLES

Coals are complex materials and a variety of techniques have been applied to understand their chemical and physical structures. Scattering studies on coals have brought out the fractal nature of the network structure[12] and the structural modifications occurring due to solvents such as pyridine. SANS showed that Pittsburgh #8 in C_5D_5N swelling is due to the breaking of the hydrogen bonded network of coal structure[13]. In order to gain a better understanding of the coal structure we took an an approach to study the pyridine-extracted species[14] in deuteriopyridine as well as the extracts with their acidic groups methylated. The scattering behavior of both neat and O-methylated extracts of APCS #3 (5 wt.% in C_5D_5N) is shown in Fig. 1a and the Guinier plot for the neat sample is shown in Fig. 1b. The slope of the fitted line in Fig. 1b gives an R_g of 41±3Å and I(0)=0.01 $cm^2.mg^{-1}$ which corresponds to a molecular weight of 6365 daltons and a solvent excluded volume of 9000 $Å^3$. This clearly shows that the macromolecule is not a solid sphere, rather a random coil. The data thus can be fitted well with the form factor for a random coil and the fit is also shown in Fig.1 for the neat sample. The R_g value from the fit is consistent with that from Guinier analysis. The O-methylated macromolecules exhibit a powerlaw behavior in the low q region with an absolute slope of -1.7 (Fig. 1a). However the scattering behavior is similar in the q region above 0.03 $Å^{-1}$. This indicates that the particles are similar in both neat and O-methylated samples, however they aggregate further in the O-methylated sample. The blocking of the hydrogen bonding interactions between the macromolecular surface and deuteropyridine leads to large net work structures resembling a system aggregated due to cluster-cluster aggregation. The size of the smallerst cluster is around 70 Å. We obeserved that the differences between the neat and O-methylated cases decreases with decreasing in rank of the coals, however the net work strctures seem to be more dense than seen in the case of APCS #3 in C_5D_5N.

Another system in the fuel chemstry which is quite complex and widely studied is the asphaltenes. We carried out SANS studies on heptane precipitated asphaltenes[15] form Maya vacuum resids in deuteriated 1-methylnaphthalene (d10-1MN) in a wide temperature range of 20 to 400 C. This study showed that a 5 wt.% asphaltenes solution in d10-1MN at ambient temperatures form large colloidal systems, but they break down with increasing temperature. To compare the behavior of extracted coal macromolecules and asphaltene colloids we have shown the temperature effect on R_g and I(0) values in Figs. 2a and 2b respectively. It can be seen that at 20C the size and I(0) for the asphaltene colloids in d10-1MN are larger than those for the pyridine extracted coal macromolecules in C_5D_5N. With increase in temperature the asphaltene colloids become smaller than the coal macromolecules (Fig.2a). However the I(0) values, which are directly proportional to the solvent excluded volume of the particles and the contrast, continue to be larger than the coal macromolecules. The larger I(0) values for the asphaltenes (smaller size) suggest that the asphaltene colloids may be more densely packed than the coal macromolecules in C_5D_5N. This can be confirmed with contrast variation studies on asphaltenes in organic solvents and such studies are in progress. Our studies on asphaltenes[15] showed that they have a rod shape with a radius around 18A, but with varying lengths depending on the temperature. We used modified Guinier analysis (Fig.3a) to obtain the cross-sectional radius of the particle and MaxEnt analysis for the polydispersity (Fig.3b).

CONCLUSIONS

In the field of fuel chemistry we encounter several systems which are quite complex as well as multicomponent in nature (crude oil). A wide range of physical and chemical methods have

been used to understand these systems and we are still far from complete understanding. For example coals have been studied in pure solid to chemically modified states. Since chemical modification and/or solvent extraction result in a number of different systems, it would be very important to understand the products in terms of thier colloidal properties as a function of the type of solvent used to disperse them, as well as other physical conditions. Such knowledge will be helpful in the design of processing techniques. Another area of research where SANS can be useful is in the characterization of synthetic and modified clays[16,17] which are being developed for processing in the petroleum industry. The major limitations for performing SANS experiments are the nonavalilability/high cost of certain deuteriated solvents and the paucity of beam time at the neutron scattering centers.

ACKNOWLEDGEMENT
This work benefited from the use of the Intense Pulsed Neutron Source, ANL funded by the Office of Basic Energy Sciences, Division of Materials Science, U.S. Department of Energy under contract # W-31-109-ENG-38. This work was done under the auspices of U.S. DOE, BES-Division of Chemical Sciences under the same contract.

REFERENCES:
1) L.A. Feigin & D. I. Svergun (1987) Structure Analysis by Small Angle X-ray and Neutron Scattering, Plenum Press, New York.
2) S. H. Chen, E. Y. Sheu, J. Kalus & H. Hoffmann (1988) J. Appl. Cryst. 21, 751-769.
3) V. F. Sears,Neutron Scattering Lengths and Cross sections. In K.Skold & D. L. Price (ed) Neutron Scattering Methods of experimental Physics, R. Celotta & J. Levine (Series ed) 23A, 521-549) Academic Press, Inc, New York.
4) A. Guinier & G. Fournet (1955) Small Angle Scattering, Wiley, New York.
5) O. Glatter & O. Kratky (1982) Small Angle X-ray Scattering, Academic Press, New York.
6) G. D. Wignall, (1987) In Encyclopedia of Polymer Science and Engineering, 2nd ed. Vol.10 112-184, Wiley, New York.
7) H.B. Stuhrmann & A. Miller (1978) Small ANgle Scattering of Biological Molecules, J. Appl. Cryst. 11, 325-345.
8) P.J. Hall, M.M. Antxustegi & J.M. Calo (1994) (Private Communication to P. Thiyagarajan)
9) M.Y. Lin, S.K. Sinha, J.M. Drake, X.-I. Wu, P. Thiyagarajan & H.B. Stanley (1994) Phys Rev Letters, 72, 2207-2210.
10) J. Feder (1988) *Fractals*, Plenum Press, New York.
11) T. Freltoft, J. K. Kjems & S.K. Sinha (1986)*Physical Rev. B*, **33**, 269
12) H.D. Bale & P.W. Schmidt (1984) *Phys. Rev. Lett.*, **53**, 596.
13) R.E. Winans & P. Thiyagarajan (1988) *Energy & Fuels* **2**, 356
14) G.D. Cody, P. Thiyagarajan, R. E. Botto, J. E. Hunt & R.E. Winans (1994) Energy and Fuels 8, 1370-78.
15) P. Thiyagarajan, J.E. Hunt, R.E. Winans, K.B. Anderson & J.T. Miller (1995) Energy and Fuels (In Press)
16) K.A. Carrado, P. Thiyagarajan, R.E. Winans & R.E. Botto (1991) Inorganic Chemistry, 30, 794-799.
17) A. Moini, T.J. Pinnavaia, P. Thiyagarajan & J.W. White (1988) J. Appl. Cryst 21, 840-842.

TABLE I
Neutron Scattering Length Densities (ρ)

System	Chemical formula	Density(g/cm^3)	ρ(10^{10}cm^{-2})
Benzene	C_6H_6	0.8786	1.18
Benzene-d6	C_6D_6	0.950	5.43
Cyclohexane	C_6H_{12}	0.7786	-0.277
Cyclohexane-d12	C_6D_{12}	0.89	6.678
Methanol	CH_3OH	0.7914	-0.373
Metanol-d4	CD_3OD	0.89	5.81
1-methylnaphthalene	$C_{11}H_{10}$	1.02	1.54
1-methylnaphthalene-d10	$C_{11}D_{10}$	1.1	6.08
Pyridine	C_5H_5N	0.9819	1.79
Pyridine-d5	C_5D_5N	1.05	5.71
Toluene	$C_6H_5CH_3$	0.8669	0.94
Toluene-d8	$C_6D_5CD_3$	0.94	5.64
Water	H_2O	1.0	-0.56
Water-d2	D_2O	1.105	6.358
polycrystalline carbon		1.4	5.6

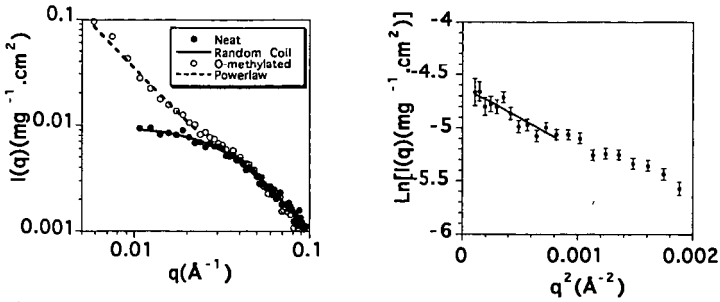

Fig.1a: SANS of APCS #3 in C_5D_5N (●), solid line is the fit for a random coil. Data for O-methylated extracts (o), dotted line is the powerlaw fit. Fig. 1b: Guinier plot fot the pyridine extracts from APCS #3 in C_5D_5N. The size of error bars is smaller than the size of the symbols.

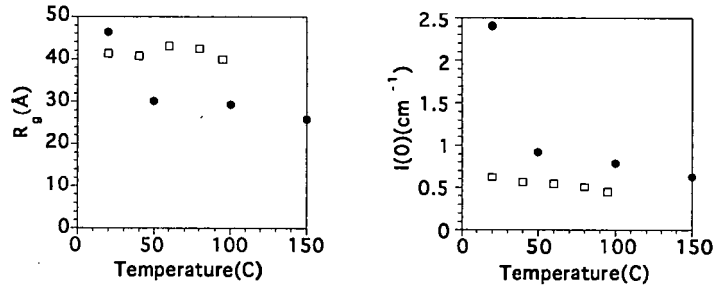

Fig.2a: Temperature effect on the Rg of the 5 wt% APCS #3 macromolecules in C_5D_5N (square) and 5 wt.% asphaltenes in $C_{11}D_{10}$ (filled o). Fig 2b: Temperature effect on the I(0) of the APCS #3 pyridine extracts in C_5D_5N (square) and 5 wt.% asphaltenes in $C_{11}D_{10}$ (o). The size of error bars is smaller than the size of the symbols.

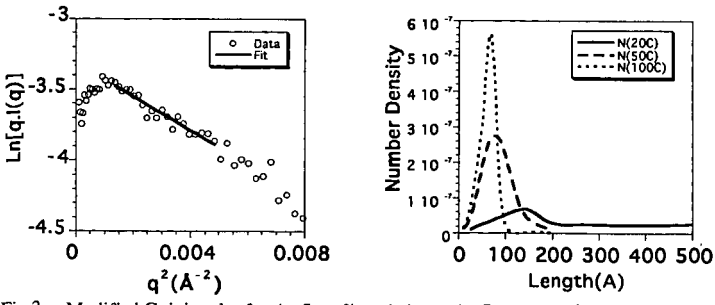

Fig.3a: Modified Guinier plot for the 5 wt.% asphaltenes in $C_{11}D_{10}$ at 20C. The size of error bars is smaller than the size of the symbols. Fig. 3b: Length distribution for the 5 wt.% asphaltenes in $C_{11}D_{10}$ as a funtion of temperature (radius of the rods is 18Å). 20C (solid line), 50C (dashed line), 100C (dotted line).

CHLORINE IN FIVE ILLINOIS COALS AND THREE BRITISH COALS: AN X-RAY ABSORPTION NEAR-EDGE STRUCTURE (XANES) SPECTROSCOPY INVESTIGATION.

M.-I.M. Chou, J.M. Lytle, and Y.C. Li
Illinois State Geological Survey
615 E. Peabody Drive
Champaign, IL 61820

F.E. Huggins and G.P. Huffman
University of Kentucky

Ken K. Ho, Illinois Clean Coal Institute

KEYWORDS: chlorine, coal, x-ray

ABSTRACT

The chlorine x-ray absorption near-edge structure (XANES) spectra of five Illinois coals and three British coals, and two series of char samples were examined. The char samples were prepared by stepwise heating one Illinois and one British coal in air at temperatures from 200 to 650°C. The chlorine XANES spectra for all the coals are similar and chloride anion was determined to be the predominant form of chlorine. The identity of the positive counter ions with which the chlorine anions are associated in the coals could not be unambiguously determined from XANES spectra. Nevertheless, the XANES spectra of the raw coal and its partially combusted char samples show significant changes in the form (and concentration) of chlorine with increasing char preparation temperature. The appearance of NaCl was observed in the chars from the British sample between 200 to 350°C but was not observed in the chars from the Illinois sample. The appearance of sodium chloride in British chars and not Illinois chars may indicate an isolated incidence due to dehydration and to the high sodium content of these coals, but it could also imply that in the British coal sodium cations are paired with chloride anions and this sodium could be associated with the sodium sulfate mechanism of boiler corrosion.

INTRODUCTION AND BACKGROUND

The total Cl content in coal has been used in Great Britain to predict the boiler corrosivity of a coal. It has been reported that British coals with more than 0.3% Cl are not recommended for pulverized-coal-fired boilers.[1,2] However, a recent survey conducted through a joint effort of the Electric Power Research Institute and the Illinois Clean Coal Institute indicates that many midwestern United States utilities have decades of experience burning high-Cl Illinois coals in a large variety of boiler equipment with no reported Cl-related fireside corrosion problems.[3] This suggests that the extent of boiler corrosion may not be directly related to the amount of Cl in the coal but to how the Cl occurs in the coal or to other factors such as the alkali and sulfur content of the coal, the type of boiler in which the coals were burned, and boiler operating parameters.[4]

If the nature of the Cl in coals with different corrosion potentials varies, then determination of how the Cl occurs in coals may provide a method to assess a coal's boiler corrosion potential. The current American Society for Testing and Materials (ASTM) standard method can determine the total chlorine content, but not the forms of chlorine in coal[5]. In many previous attempts at determining the forms of chlorine in coals, indirect methods were used, and some mixed results were reported. For example, Hamling and Kaegi[6] stated that chlorine in coal samples from one of the high-chlorine Illinois mines was predominantly in the form of organic chloride(s), and the organically associated chlorine does not apparently contribute to boiler corrosion and fouling problems. Chou[7] suggested that chlorine in coals occurs in two major forms: chloride anions dissolved in the pore water of coal, and chloride anions adsorbed on the inner surfaces of the micropores in macerals (organic fraction of the coal). It is clearly desirable to generate representative data with a more direct method of determination. Huggins and Huffman[8] recently used K-edge X-ray absorption fine structures (XAFS) spectroscopy to examine the occurrence of chlorine in coals from various locations worldwide. This nondestructive technique was applied in this study to directly examine five Illinois coals and three British coals and chars produced from the coals by stepwise heating under air.

EXPERIMENTAL PROCEDURES

Samples - Five Illinois coals, representing five specific geological locations[9] in Illinois, and three coals previously obtained from Great Britain were analyzed for chlorine by XANES. Data on chlorine and ash composition of the coals are listed in Table 1. Illinois coals have

much higher moisture contents than the British coals. Two of the three British coals have high ash contents. Among these coals, the two high ash content British coals also contain the highest sodium and potassium content.

Char preparation - Partially combusted coal samples (chars) were prepared from two coals, an Illinois coal (C-32795) and a British coal (C-32500). The coal sample was placed in a constant temperature zone of a Lindberg tube furnace. Under a flow of air, the furnace temperature was increased from room temperature to 200°C and remained at 200°C for 30 minutes before the first sample was collected. After the first sample was taken out, the temperature was increased to 250°C and held at 250°C for 30 minutes in order for the second sample to be collected. This stepwise heating was continued and a sample was collected at each 50°C interval until the final temperature of 1000°C was reached. These partially combusted samples were submitted to the University of Kentucky for XANES analysis.

XANES analysis - Chlorine XAFS spectra were obtained at beam-line X19A of the National Synchrotron Light Source (NSLS), Brookhaven National Laboratory. The spectra were obtained from the samples as-received by suspending them in the monochromatic X-ray beam in ultrathin (6 μm) polypropylene baggies. The chlorine XAFS spectra were collected in fluorescence geometry using a Lytle-type fluorescent detector with nitrogen as the ionization gas and helium in the sample chamber. The beam-line was operated in the focussed spot mode, although the spot was de-focussed somewhat in order to obtain a better sampling of the coal and char samples. Each spectrum consisted of about 500 points collected at energies between about 50 eV below the chlorine edge (2825 eV) to about 300 eV above the edge. Dilute samples of sodium chloride in boric acid were used as the primary standard for the chlorine edges. The principal peak position of the derivative XANES spectrum of NaCl was defined as the zero point of energy for the purpose of calibrating the chlorine XANES spectra. All spectra were collected and stored in a MicroVAX computer at NSLS and were transferred electronically to a similar computer at the University of Kentucky for analysis.

The chlorine spectra were first calibrated with respect to the primary standard (NaCl), then normalized to the edge step, corrected for background slope above and below the edge, and finally divided into separate XANES and extended X-ray absorption fine structure (EXAFS) regions. Analysis of the EXAFS regions of these spectra is generally not very informative, so that the data reported here comes from only the XANES region, that is, the structure within ±50 eV of the chlorine K absorption edge.

RESULTS AND DISCUSSIONS

Variation of forms of chlorine in coals - Based on the XANES spectra of standard compounds[8], a strong broad peak at about 1 eV followed by a much weaker, broad peak at about 20 eV is indicative of an ionic form of chlorine. The chlorine XANES spectra of the Illinois coals and the British coals are shown in Figures 1 and 2, respectively. The spectra of the Illinois coals and those of the British coals show a predominant form of chlorine as chloride anions. These anions may be in solution and have significant interaction with maceral surfaces presumably via ionic functional groups, such as quaternary amines or oxygen functional groups anchored via cations. The identity of these positive counter ions with which the chlorine anions are associated in the coals could not be unambiguously determined from XANES spectra. Nevertheless, the appearance of a sharp peak at 12.5 eV is indicative of the crystalline form of NaCl which is observed only in the spectrum of a British coal (C-33499). The ash composition of the coals indicated that this British coal is one of the coals which have high ash and high sodium contents.

Variation of forms and concentration of chlorine during stepwise heating under air - A procedure for the quantification of different forms of chlorine, similar to that done for sulfur[10], has not been established because most coals appear to have only one major form of chlorine, chloride anion. In this study, a separate set of experiment, using stepwise heating of one British coal (C-32500) and one Illinois coal (C-32795) under air, was conducted to attempt to remove the more volatile chlorine step by step from the less volatile chlorine and examine the residues by XANES. The XANES analysis on the changes, if any, of the forms of chlorine in chars during stepwise heating may help in understanding the nature of chlorine in these coals. The XANES spectra of the Illinois and the British coal and their partially combusted char samples were compared, as shown in Figure 3. The XANES spectra show significant changes in the form of chlorine (and concentration) with increasing char preparation temperature. In addition, there are differences between the variation of chlorine in the British coal compared to that in the

Illinois coal. A small peak at about 12.5 eV, diagnostic of the presence of NaCl, is apparent in the spectra of the chars formed at 200 to 350°C from the British coal. This feature is absent from the spectra of chars from the Illinois coal. The ash composition of these coal indicated that the British coal (C-32500) used has high ash and high sodium contents.

Above 350°C, the spectra of chars from both coals show a prominent sharp peak at about -1 eV that dominates the spectra in the range 400 - 600°C. Above 600°C, the spectra degrade in quality, as virtually all of the chlorine has been evolved from the samples. The peak position and shape of the spectra for the chars prepared at 400°C are similar to those noted for chlorine in organic (aromatic) compounds[8]. However, other less similar chlorine forms (hypochlorite, e.g. NaOCl) could be possible. The possible presence of organic chlorine in these chars raises some interesting speculations as to its possible origin. Alternative possibilities are: (i) it was present in the coal originally, but at such a low level (<10% of the total chlorine) that it did not register in the Cl XANES spectrum of the coal until the more volatile forms of chlorine had been evolved during low-temperature char preparation; or (ii) it was formed by reaction between the char and HCl evolved during char preparation. This phenomenon, the appearance of "organic" chloride, was not seen in a previous investigation[8], which was done by *in situ* heating under helium followed by XANES Cl analysis. In that study, however, the heating temperature was low, reaching only 350°C.

The chlorine content in the chars was estimated using a parameter known as step-height in the analysis of the chlorine XANES spectra. The results (Figure 4) showed that both coals experienced a large decrease in chlorine content at early stages of heating over the temperature range 250 to 400°C. The decrease of the remaining chlorine content in chars during further heating from 400°C to 600°C was very limited. In comparison with a previous study by Liu[11] in which chlorine evolution was based on HCl gas analysis, this study measured the chlorine content of the chars. In that study, the differences in chlorine evolution as a function of temperature between Illinois and British coals when heated under air were observed using a temperature-programmed thermogravimetric analyzer equipped with Fourier transform infrared spectrometry (TGA-FTIR). When comparing these two results, it should be noted the experiments in the two studies were conducted under different conditions. For example, the samples in this study during stepwise heating were heated much more slowly and at a longer residence time, which may have allowed more chlorine in the Illinois coals to be evolved at lower temperatures as compared with the TGA-FTIR analysis.

SUMMARY AND CONCLUSIONS

The data based on X-ray absorption near edge spectrum (XANES) analysis indicate that, in general, chlorine in coal mainly occurs in an ionic form. To balance the negative charge of these chloride anions, the occurrence of sodium and other cations, such as amino functional group, in the pore water of the coal are important. The identity of the positive counter ions with which the chlorine anions are associated in the coals could not be unambiguously determined from XANES spectra. Nevertheless, the current XANES data clearly indicated the appearance of NaCl in a British coal and in chars formed at 200 to 350°C from another British coal. The appearance of sodium chloride in the British char and not in the Illinois char may indicate an isolated incidence due to the dehydration of the coal sample and to the high sodium concentration of the coal samples, but it could also imply that in the British coal sodium cations are paired with chloride anions and this sodium could be associated with the sodium sulfate mechanism of boiler corrosion during coal combustion. Further investigation using *in situ* techniques to determine volatile alkali metals and chlorine-containing compounds produced during coal combustion may shed light on this speculation.

ACKNOWLEDGEMENT & DISCLAIMER

This report was prepared by M.-I. M. Chou and the ISGS with support, in part, by grants made possible by the U.S. Department of Energy (DOE) Cooperative Agreement Number DE-FC22-PC92521 and the Illinois Coal Development Board (ICDB) and the Illinois Clean Coal Institute (ICCI). Neither authors nor any of the subcontractors nor the U.S. DOE, ISGS, ICDB, ICCI, nor any person acting on behalf of either assumes any liabilities with respect to the use of, or for damages resulting from the use of, any information disclosed in this report. Technical assistance by J.B. Bruinius and J. Zhao is acknowledged.

REFERENCES

1. Bettelheim, J.; Halstead, W.D.; Les, D.J.; Mortimer, D. Combustion problems associated with high chlorine coals: Erdol and Kohle-Erdgas *Petrochemie*, v. 33, p. 436, 1980.

2. Raask, E. *Mineral Impurities in Coal Combustion: Behavior, Problems and Remedial Measures*, Hemisphere Publishing Corporation, New York, 1985.
3. Wright, I.G.; Ho, K.K.; Mehta, A.K. Survey of the effects of coal chlorine on fireside corrosion in pulverized coal-fired boilers, in Proceedings of EPRI Symposium The Effects of Coal Quality on Power Plants: Fourth International Conference" August 17-19, 1994 Charleston, SC.
4. Meadowcroft, D.B.; Manning, M.I.(editors) Corrosion Resistant Materials for Coal Conversion Systems, Applied Science Publishers, New York, 1983.
5. American Society for Testing Materials, 1991, Annual Book of ASTM Standards, D-2492, p. 289-294.
6. Hamling, J.W. and D.D. Kaegi, Characterization and Removal of Chlorides in Illinois Coal, Proceeding of the First Annual Pittsburgh Coal Conference, 849-855, September 17-24, 1984.
7. Chou, C.-L. 1991 Distribution and forms of chlorine in Illinois Basin coals. In: Stringer, J. and Banerjee, D.D. (eds), Coal Science and Technology 17: Chlorine in Coal, Elsevier Science Publishing Co., New York, p 11-29.
8. Huggins F.E. and G.P. Huffman, Chlorine in Coal: A XAFS Spectroscopic Investigation, Fuel, 1995, 74, 556-569.
9. I. Demir, R.R. Ruch, J. Steele, and S. Kahn, Washabiltiy of Trace Elements in Product (Marketed) Coals from Illinois, ISGS Open File Series in press 1995.
10. Huffman, G.P., N. Shan, F.E. Huggins,L.M. Stock, K. Chatterjee, J.J. Kilbane, M.-I.M. Chou, and D.H. Buchanan. Sulfur speciation of desulfurized coals by XANES spectroscopy, Fuel, 1995, 74, 549-555.
11. Liu, J., Behavior of Chlorine in Illinois Coals Comparing with that in British Coals During Combustion and Pyrolysis, A Master's Degree thesis presented to the faculty of the Department of Chemistry, Western Kentucky University, Bowling Green, Kentucky, 1994.
11. Chou, M.-I., W.P. Pan, F.E. Huggins, J.M. Lytle, L. Liu, and K.K. Ho. 1994. Chlorine in coal and boiler corrosion. proceedings of the 11th International Pittsburgh Coal Conference. Pittsburgh, PA. September 12 - 16, 1994. pp. 359-364.

Table 1. Ash composition and chlorine content in coals

Coal sample	Moisture	*Ash	*Na_2O	*K_2O	*Cl
Illinois coals					
C-32783	15.22	12.86	0.20	0.21	0.16
C-32779	12.62	9.63	0.14	0.20	0.08
C-32795	9.42	5.76	0.14	0.14	0.45
C-32661	6.79	8.17	0.07	0.20	0.26
C-32662	7.99	7.00	0.08	0.21	0.35
British coals					
C-33499	4.55	14.79	0.31	0.48	0.61
C-33500	4.16	22.24	0.31	0.89	0.43
C-33502	3.21	3.13	0.10	0.02	0.81

* % moisture free basis; Data on Illinois coals were provided by Dr. Ilham Demir of the ISGS.

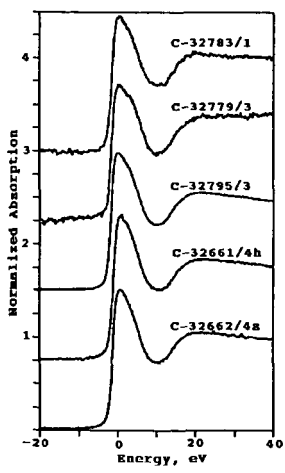

Figure 1: XANES spectra of the five Illinois coals and their specific geographic locations.

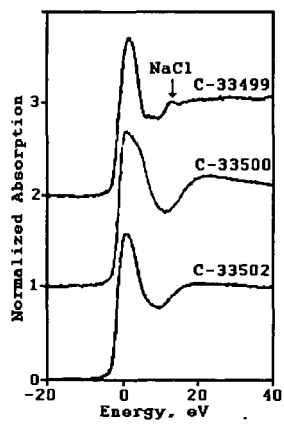

Figure 2: XANES spectra of the British coals.

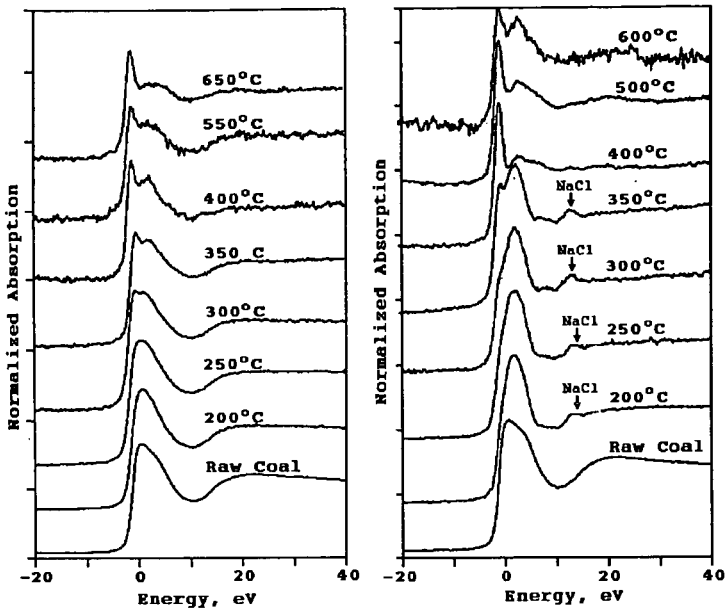

Figure 3: XANES spectra of one Illinois (C-32795, left) and one British (C-33500, right) coal and chars from step-wise heating under air.

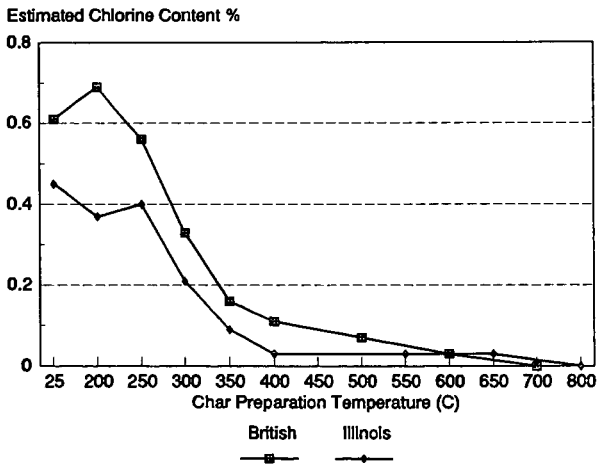

Figure 4: Comparing chlorine content in chars produced from stepwise heating of a British coal (C-32500) and an Illinois coal (C-32795) under air.

CONCURRENT CHANGES IN AGGREGATION AND SWELLING OF COAL PARTICLES IN SOLVENTS

Masaharu Nishioka

Nihon Rikagaku Laboratories,
2-5-601 Ohara-cho, Ashiya 659 Japan

Keywords: Solvent Swelling, Laser Scattering, Coal Association

INTRODUCTION

The behavior of solvent(-induced) swelling of coal without complete dissolution in any solvents has been used as evidence for the three-dimensionally cross-linked macromolecular network model of coal structure. Sanada and Honda[1] applied the statistical theory of rubber elasticity to coal swelling. Since then coal swelling has been used to characterize the macromolecular nature of coal by many workers[2-10]. Four major methods have been used: the volumetric method using glass tubes[1,7-13], the gravimetric method[1,3,4], the method requiring a piston type of apparatus[10,14,15], and direct observation using a microscope[6,16-18]. The easiest and most commonly used one is probably the volumetric method.

The conventional volumetric technique with glass tubes was selected to investigate the physical structure of coal in this author's recent papers[19-22]. Some steps in the method were modified. Coal samples and solvents were weighed, and each initial height before swelling was calculated from the mass and bulk density of the samples. This was necessary to obtain reproducible results, particularly at low coal (slurry) concentration. In the previous paper[20], coal/solvent mass ratios (*C/S*) were used as an index of *concentration*. From this study, it was found that coal swelling is strongly dependent on C/S[20]. The high dependence of C/S on coal swelling is very important, because changes in swelling with C/S is not thermodynamically allowed for the three-dimensionally cross-linked network model.

The results showed that swelling ratios, Q, did not change in the common range of C/S = 10-20 % which is generally used for the conventional volumetric swelling method, but significantly increased at < C/S = 5 %[20]. At the low C/S, the dependence of coal concentration on Q is given by

$$Q = [Q]/(C/S)^n \quad (1)$$

where

$$[Q] = \lim_{\log(C/S)\to 0} Q \quad (2)$$

and n is a constant. $[Q]$ is defined as the intrinsic swelling ratio, which is independent of C/S. The $[Q]$ values were consistently more than two times larger than those conventionally observed. Therefore, conventionally observed swelling ratios are apparent values. It is thought that intra- and intermolecular (secondary) interactions are solvated more at a lower C/S value and coal swells more. The process of attaining associative equilibria is presumably very difficult when using the volumetric method. The dependence of C/S on coal swelling means that swelling changes depending on uniformity of coal and solvent. Coal and solvent are usually mixed only at the initial time with a thin rod. It is not practical to continuously mix coal and solvent for a long time, because it may take more than 24 h to reach its equilibrium value[21,22]. These strongly suggest that coal swelling should be measured at a very *low* coal concentration with *continuous mixing* for a given period to avoid the effect of these unknown factors. Furthermore, measurements of volumetric swelling at low C/S values are difficult. Therefore, an apparatus specifically designed for these factors is necessary.

The objective of this paper was to observe coal swelling in solvents at *low coal concentration with continuous mixing*. It can be thought that coal swelling is given by the difference of particle sizes between poor and good solvents. The measurement of particle sizes in solvents by a laser scattering method is applied to the system. The swelling ratio measurement by a particle size distribution was probably first suggested by Turpin *et al.*[17], but the details were not reported. The observation of coal swelling under the conditions is very important to better understanding of coal structure and also the behavior of coal particles in coal/oil systems in various processes.

EXPERIMENTAL

Blind Canyon (DECS-16) and Illinois No. 6 (DECS-2) coals (-20 mesh) were obtained from the DOE Coal Bank at Pennsylvania State University. These pyridine extracted coals (PI) were prepared by Soxhlet extraction for 3 days. Pyridine extracts (PS) were also used. PI and PS were dried under vacuum at 95°C overnight. All samples were ground with a agate set to arbitrary particle sizes (-100 mesh). The same lots of samples were used for particle size measurements. Standard polyvinylpyrrolidone with average molecular mass of 10,000 and cross-linked polyvinylpyrrolidone were obtained from Aldrich Chemical Co. These polymers as received were used for particle size measurements.

For a new method of swelling, Model LAB-TEC 1000 particle size analyzer (LASENTEC, Bellevue. WA) was used. This analyzer is a scanning laser type of apparatus[23]. When the focal spot intercepts a particle, some light is scattered back to the probe and converted into an electronic pulse, which is converted to size by the relationship:

$$d = v/t \quad (3)$$

The duration of the pulse represents the time (t) the focal spot illuminated the particle. Since the velocity

(v) of the focal spot is known, the distance (d) for the focal spot scanned across the particle can be determined. This distance represents the length of a chord of the particle. Pulses representing the chord lengths are classified by counting circuits, then transferred to a computer for processing and presentation on a display or a printer. The LAB-TEC 1000 classifies particles into 29 channels, ranging from 0.2 to 250 μm. The distribution is presented in two ways in this study. Scanned count is the uncorrected random chord frequency distribution. Volume diameters are the distribution of volume, derived from the scanned count data, when particles are assumed to be spherical. The mean volume diameter and the mean diameter with scanned counts are shown as Dv and Dc, respectively. LASENTEC® measuring beakers (100 ml) were used for a sample container. Samples were agitated with a magnetic stirrer during measurement.

RESULTS AND DISCUSSION

Attempt of swelling ratios by particle size distribution

The reproducibility of measurements using this particle size analyzer was confirmed with a standard powder sample provided by the manufacturer before every measurement. The critical factor to obtain reliable results was to adjust a focal point of laser to the inner wall of the measuring beaker. Once the focal point is carefully tuned, measurements of the particle size distributions were reproducible.

The particle size distribution of the PI sample from Blind Canyon (DECS-16) coal ground to arbitrary was measured in methanol and pyridine. The coal concentration was 0.25 g/100 ml (coal/solvent). Since the evaluation method using glass tubes can be used only down to the value of C/S = 2-3 %, this coal concentration was relatively low for the swelling measurement. In addition to low coal concentration, coal particles were observed with continuous mixing. Laser was continuously scanned for several hours, and the distributions averaged every 20 scans were monitored several times. This was repeated for one week after preparation of samples. Any significant change in the distributions was not observed for these measurements.

Figure 1 shows the particle size distributions of this sample with volume diameters in (a) methanol and (b) pyridine. The distribution in methanol did not significantly change with time, while that in pyridine changed from time to time. The change in the distribution in pyridine was not dependent on time but apparently reversible from time to time. Two typical distributions in pyridine are shown here. The Dv value in methanol was 120 μm, while pyridine values were (b-1) 130 μm and (b-2) 60 μm. Methanol is a very poor solvent for coal, while pyridine is one of the best. The particle size distributions in pyridine were, however, approximately the same or smaller than that in methanol. This is surprising, because swelling ratios of high-volatile bituminous coals can be estimated to be more than 3 at this concentration range by the conventional volumetric method[20]. The above measurements were also evaluated using PI from Illinois No. 6 (DECS-2) coal. General results obtained from the DECS-16 coal were again similar for this sample.

Particle size distribution of standard polymers

To confirm the above proposed mechanism, the particle size distribution of standard polymers was evaluated under the same conditions. Fine powders of polyvinylpyrrolidone (average molecular mass; 10,000) and cross-linked polyvinylpyrrolidone as received were used. Polyvinylpyrrolidone readily dissolves in methanol and water, but does not dissolve in n-hexane and toluene. Toluene is a slightly better solvent than n-hexane. The distribution in toluene changed from time to time, and two representative distributions are shown. Mean volume diameters determined were 14 μm in n-hexane and 18 and 31 μm in toluene, respectively. The difference between these distributions is small, but the change in particle sizes with larger diameters is seen in toluene. The change was apparently reversible.

The particle size distribution of cross-linked polyvinylpyrrolidone was evaluated next in methanol and n-hexane. *Figure 2* compares these distributions with scanned counts at a concentration of 0.50 g/100 ml (polymer/solvent). As a significant portion of particle volume diameters exceeded 250 μm, the distributions with scanned counts are presented. The specific swelling ratio (Q^{20}) of this sample in methanol and n-hexane were 4.0 and 3.0, respectively. This suggests that methanol is a better solvent than n-hexane and swells the polymer. Therefore, the particle size of this polymer in a good solvent (methanol) was expected to be larger due to swelling. The results, however, shows that particle sizes in methanol (Dc=34 μm) are actually smaller than those measured in n-hexane (Dc=53 μm). One interpretation is that this cross-linked polymer is initially swollen in methanol but concurrently disaggregates. The overall particle size distribution may reflect these adverse effects.

It was notable that particle sizes of pyridine extracted DECS-2 and -16 coals observed in pyridine and methanol were nearly equal, considering the volumetric swelling in pyridine was much larger than in methanol. Apparent reversible changes in the particle size distribution of coal were observed in pyridine. The results obtained from standard polymers are consistent with these results.

Change in numbers of coal particles in solvents

From the above results, the following behavior of coal particles in solvents is suggested: Coal particles are highly aggregated even at the relatively low C/S values. Coal particles are swollen, but interparticle disaggregation also occurs in good solvents. This may lead to apparent small coal swelling in good solvents observed by particle size distributions. If this interpretation is correct, numbers of coal particles should be different between poor and good solvents. Numbers of coal particles can be measured as numbers of light scattered back to the probe by this apparatus.

The numbers of particles of the PI from DECS-2 coal were evaluated in methanol, toluene, chloroform and pyridine at concentrations of 0.1 - 0.5 g/100 ml. *Figure 3* shows the accumulated channel % for ≤ 1.3 μm. Obviously, coal particles with small diameters increased in the order of better solvents for coal; methanol, toluene, chloroform and pyridine at all concentrations tested.

Effect of coal concentration on the particle size distribution

Volumetric swelling increases at low coal concentration[20]. The evaluation method using glass tubes was used down to the value of C/S = 2-3 %. The particle size distribution was investigated to evaluate the effect of coal concentration at further low values. Volume diameter distributions for the DECS-16 coal were measured in coal concentration from 1 g to 0.1 g per 100 ml pyridine. Since the dependence of coal concentration on volumetric swelling was remarkable below C/S = 2-3 %, a notable increase in the particle size would be expected at the concentrations of 1 to 0.1 g/100 ml. No significant increase in the particle size with a decrease in coal concentration was found, but a decrease in the particle size is noted at lower coal concentrations. These results again demonstrate the significant variance in coal swelling observed by two different procedures; the volumetric swelling and the particle size distribution methods. The results can be interpreted on the bases of the proposed mechanism. Coal particles may swell at low coal concentration to large extent, but interparticle disaggregation due to a decrease in coal concentration seems to control the overall particle size distribution.

CONCLUSIONS

A new method of coal swelling has been developed under the condition of low coal concentrations with continuous mixing of coal and solvent. The change in particle size distributions by a laser scattering procedure was used for the evaluation of coal swelling. Particle size distributions in good and poor solvents were nearly equal, but reversibly changed in good solvents from time to time. It was concluded that aggregated coal particles disaggregate in good solvents, and that an increase in the particle size distribution due to swelling in good solvents are compensated by a decrease in the particle size due to disaggregation. Therefore, the behavior of coal particles in solvents is controlled by aggregation in addition to coal swelling. This implies that an increase in the particle size due to coal swelling in actual processes is not so large as expected by the results obtained from the conventional coal swelling methods.

ACKNOWLEDGEMENT

This work was partly supported by the U.S. Department of Energy under Contract No. DE-AC22-92PC91047 when this author was at Viking Systems International.

REFERENCES

1 Sanada, Y. and Honda, H. *Fuel* 1966, **45**, 295
2 Larsen, J. W. and Kovac, J. in 'Organic Chemistry of Coal' (Ed. J. W. Larsen), American Chemical Society, Washington, DC, 1978, Ch. 2
3 Lucht, L. M. and Peppas, N. A. in 'New Approaches in Coal Chemistry' (Eds. B. D. Blaustein, B. C. Bockrath and S. Friedman), American Chemical Society, Washington, DC, 1981, Ch. 3
4 Nelson, J. R. *Fuel* 1983, **62**, 112
5 Szeliga, J. and Marzec, A. *Fuel* 1983, **62**, 1229
6 Brenner, D. *Fuel* 1984, **63**, 1324
7 Matturro, M., Liotta, R. and Isaacs, J. J. *J. Org. Chem.* 1985, **50**, 5560
8 Hsieh, S. T. and Duda, J. L. *Fuel* 1987, **66**, 170
9 Painter, P. C., Park, Y. and Coleman, M. M. *Energy & Fuels* 1988, **2**, 693
10 Hall, P. J., Marsh, H. and Thomas, K. M. *Fuel* 1988, **67**, 863
11 Liotta, R., Brown, G. and Issacs, J. *Fuel* 1983, **62**, 781
12 Green T. K., Kovac, J. and Larsen, J. W. *Fuel* 1984, **63**, 935
13 Otake, Y. and Suuberg, E. M. *Fuel* 1989, **68**, 1609
14 Aida, T. and Squires, T. G. *Am. Chem. Soc. Div. Fuel Chem. Prepr.* 1985, **30**(1), 95
15 Eser, S., Jenkins, R. G., Wei, G., Schobert, H. H. and Joseph, J. T. *Fuel* 1991, **70**, 1445
16 Brenner, D. *Fuel* 1985, **64**, 167
17 Turpin, M., Ellis, B. and Rand, B. in 'International Conference on Coal Science' (Eds. J. A. Moulijin, K. A. Nater and H. A. and G. Chrmin), Elsevier, New York, 1987, p. 85
18 Cody, G. D. Jr, Larsen, J. W. and Siskin, M. *Energy & Fuels* 1988, **2**, 340
19 Nishioka, M. *Fuel* 1993, **72**, 997
20 Nishioka, M. *Fuel* 1993, **72**, 1001
21 Nishioka, M. *Fuel* 1993, **72**, 1719
22 Nishioka, M. *Fuel* 1993, **72**, 1725
23 LAB-TEC 1000 User's Manual

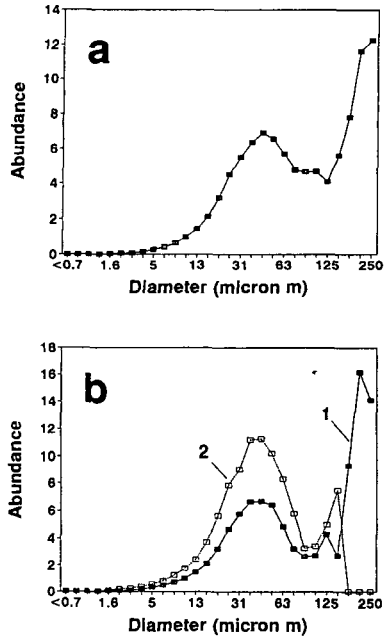

Figure 1 Particle size distribution with volume diameters of the pyridine extracted DECS-16 coal at coal/solvent = 0.25 g/100 ml, (a) in methanol (*Dv*; 120 μm), (b-1) in pyridine (*Dv*; 130 μm) and (b-2) in pyridine at another scanning (*Dv*; 60 μm) (average of 20 cycles)

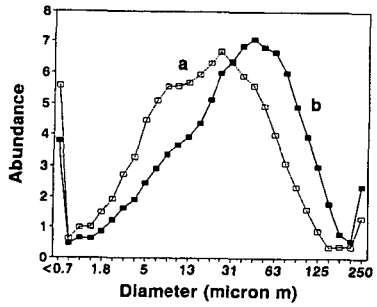

Figure 2 Comparison of particle size distributions with scanned counts of cross-linked polyvinylpyrrolidone at sample/solvent = 0.50 g/100 ml, (a) in methanol (*Dc*; 34 μm) and (b) *n*-hexane (*Dc*; 53 μm) (average of 20 cycles)

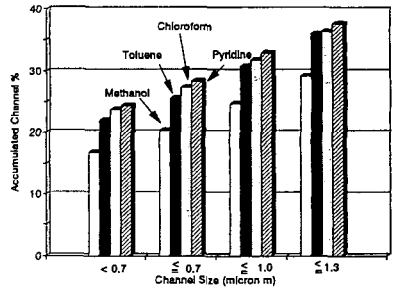

Figure 3 Accumulated channel % for channel sizes of ≤ 1.3 μm for the PI sample from DECS-2 coal

Applications of the ^{13}C NMR Magic Angle Turning Experiment to Coal Studies

R. J. Pugmire[a], W. Wang[b], M. S. Solum[b], D. M. Grant[b], and J. Z. Hu

Departments of Chemical and Fuels Engineering[a] and Chemistry[b]
University of Utah, Salt Lake City, Utah 84112, USA
and Wuhan Institute of Physics., Chinese Academy of Science, Wuhan, The People's Republic of China

Keywords: ^{13}C NMR, Two Dimensional Spectroscopy, Coal Structure

INTRODUCTION

One of the important contributions of high resolution ^{13}C CP/MAS to coal science is the measurement of the structural parameters of coal.[1-2] It has been demonstrated[3-5] that the structural parameters directly derived from ^{13}C CP/MAS experiments can be utilized to predict the details of coal devolatilization and char formation processes. One of the advantages of spinning a solid sample at the magic angle is the reduction of the line broadening contributions due to the chemical shift anisotropy (CSA). The chemical shift anisotropy is proportional to the strength of the external magnetic field and the CSA of aromatic carbons (200-240 ppm) is greater than that of the aliphatic carbons (20-100 ppm). When the sample is spun at the magic angle the CSA induced powder patterns break up into spinning sidebands and, in order to obtain a ^{13}C CP/MAS spectrum in which the aromatic carbon sidebands do not overlap the aliphatic carbon signals, it is necessary to spin the sample at approximately 4 KHz at a magnetic field of 2.35 Tesla. At a higher magnetic field strength a greater spinning rate is required. High speed magic angle spinning not only reduces the contributions of the spinning side bands but it also destroys very useful information on the local electronic environment that is embedded in the principal values of the CSA tensors.

The CSA exhibits three frequency components for each carbon in a powdered sample, the principal values, and spinning the sample at the magic angle averages these three values to the isotropic chemical shift of each nucleus. Hence, elimination of the CSA contribution increases the spectral resolution in conventional CP/MAS experiments but also throws away two thirds of the available data for each carbon. Thus, a major dilemma exists between spectral resolution and the richness of the data that is contained in powdered samples such as coal. Fortunately, the recently developed two-dimensional (2D) magic angle turning (MAT) experiments, (the triple echo-MAT[6] and PHORMAT[7]) when applied at an extremely slow rotation rate, can provide both types of information without serious penalty. In the MAT experiments, a sideband free isotropic chemical shift spectrum which has resolution in the isotropic shift dimension comparable to the standard CP/MAS spectrum is obtained by projecting the 2D data onto the evolution frequency axis. Concurrently, an essentially static powder pattern is projected onto the acquisition frequency axis and the powder pattern for each individual isotropic chemical shift is obtained by simply taking a spectral slice at the specified isotropic chemical shift value in the acquisition dimension.[6-8] In this paper, the power of the MAT experiments is further explored in a study of coals at a magnetic field strength of 9.4 Tesla.

EXPERIMENTAL

The experiments were performed on a Chemagnetics CMX-400 spectrometer with a ^{13}C frequency of 100.6 MHz. The probe used was a Chemagnetics pencil rotor design and samples were spun at *ca.* 30 Hz in a 9.5 mm rotor with a specially built low speed drive tip. The proton decoupling field strength on this probe is 50 KHz. The spinning speed was maintained within 0.25 Hz with a Chemagnetics speed control unit and the pulse sequences used are described elsewhere.[6-8]

Results and Discussion

The usefulness of the MAT experiments can best be described by examining the data obtained from a model compound with a diversity of carbon types. The PHORMAT pulse sequence[7] was used to generate the composite data in Figure 1 in which the two-dimensional (2D) contour plot of p-ethoxyphenylacetic acid is displayed. All ten carbons are clearly resolved in the contour plot. The isotropic chemical shifts of these carbons are projected onto the evolution axis while the composite powder pattern data are projected onto the axis representing the acquisition dimension. As previously described,[6-8] the principal values of the CSA tensors of each carbon can be found by examining the powder patterns taken at the individual isotropic chemical shift frequencies. Figure 3 displays a stacked plot of the powder patterns at the isotropic chemical shift frequency of each carbon. In this case none of the carbons overlap and, hence, no ambiguity is encountered in identifying the types of carbons associated with each powder pattern. Orendt, et. al.[2] have described the general shapes of powder patterns associated with different types of aromatic carbon functional groups, e.g., protonated, alkyl substituted, aryl ethers, and bridgehead carbons. The powder

patterns for the methyl, CH_2-, and CH_2O- groups in p-ethoxyphenylacetic acid also exhibit characteristic shapes which can be used to identify overlapping carbon signals. The analysis of overlapping powder patterns in carbons with accidental degeneracy of the chemical shifts has been described by Hu, et. al.[6], and Wang, et. al.[9] for model compounds and for coals.[8]

The application of the triple-echo version of the MAT experiment to coal samples has been previously reported.[6,8] The PHORMAT version of the MAT experiment does not require spectral shearing, as in the triple-echo MAT experiments, which simplifies the extraction of the principal values. The 2D PHORMAT data for Pocahontas #3 coal is presented in Figure 2. At first glance, one could assume that the useful information obtainable from the data is no greater than that of the standard CP/MAS experiment. However, by examining the spectral slices obtained at different isotropic chemical shifts, one can readily recognize the contributions from different types of carbon atoms. Figure 4 exhibits spectral slices taken at selected isotropic chemical shift values in the aromatic region from the data portrayed in Figure 3. One can easily recognize the characteristic line shapes of powder patters due to substituted, bridgehead, and substituted aromatic carbons. One can also identify the features of composite patterns derived from overlapping signals from different structural types of carbons, i. e., protonated/bridgehead (slices at 120, 125, and 130 ppm), bridgehead/substituted (slices at 130 and 135 ppm), and substituted (slices at 135, 140, and 145 ppm). In Figure 4 the heavy vertical lines represent the frequency for the δ_{22} components of the protonated, bridgehead, and substituted carbons.

2D data set on experimental data of this type in model compounds. Versions of these tools have been used for analysis of the spectral slices in coals and efforts are under way to expand these capabilities to include the entire 2D data set. It is interesting to note that the MAT experiments can also be used on polymer systems to refine the structural analysis and assess crystalline and non-crystalline components.

Acknowledgments

Support for this work was made available by the National Science Foundation through the Advanced Combustion Engineering Research Center, the U. S. Department of Energy Pittsburgh Energy Technology Center through the Consortium for Fossil Fuel Liquefaction Science (Contract No. DE-FCC22-93PC93053), and by Basic Energy Sciences, Office of Energy Research, U. S. Department of Energy (Contract No. DE03-94ER14452).

REFERENCES

1. M. S. Solum, R. J. Pugmire and D. M. Grant, Energy & Fuels, 3 (2), 187-193 (1989).
2. A. M. Orendt, M. S. Solum, N. K. Sethi, R. J. Pugmire and D. M. Grant, " Advances in Coal Spectroscopy" Edited by Henk L. C. Meuzelaar, Plenum Press · New York and London, 1992, Page 215-223.
3. T. H. Fletcher, A. R. Kerstein, R. J. Pugmire, M. S. Solum and D. M. Grant, Energy Fuels, 6 (4), 414-431 (1992).
4. T. H. Fletcher, M. S. Solum, D. M. Grant, and R. J. Pugmire, Energy Fuels, 1992, 643-650.
5. D. M. Grant, R. J. Pugmire, T. H. Fletcher and A. R. Kerstein, Energy Fuels, 3 (2), 175-186 (1989).
6. J . Z. Hu, A. M. Orendt, D. W. Alderman, R. J. Pugmire, C. Ye and D. M. Grant, Solid State NMR, 1994, 3, 298.
7. J. Z. Hu, W. Wang, F. Liu, M. S. Solum, D. W. Alderman, R. J. Pugmire, and D. M. Grant, J. Magn. Reson., 1995, A113 (in press).
8. J. Z. Hu, M. S. Solum, R. J. Pugmire, C. Ye, and D. M. Grant, Energy & Fuels, 1995 (in press).
9. W. Wang, J. Z. Hu, D. W. Alderman, R. J. Pugmire, and D. M. Grant, Solid State NMR, 1995, 4 (in press).

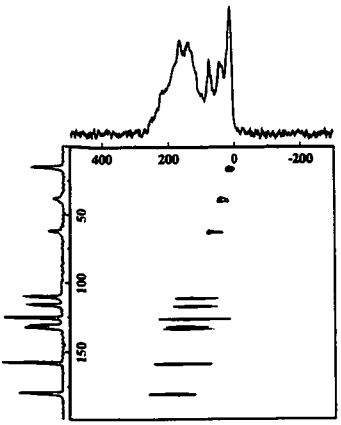

Figure 1. Two dimensional MAT data for p-ethoxyphenylacetic acid. The isotropic chemical shifts are projected on the evolution dimension while the powder patterns are projected on the acquisition dimension.

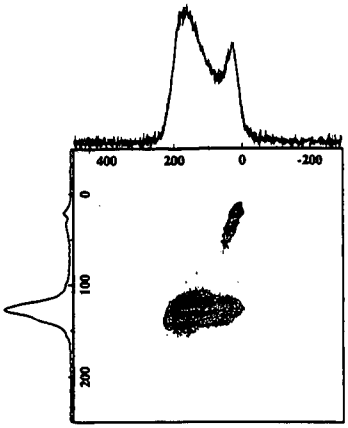

Figure 2. Two dimensional MAT data for Pocahontas #3 coal from the Argonne Premium Coal Sample Bank.

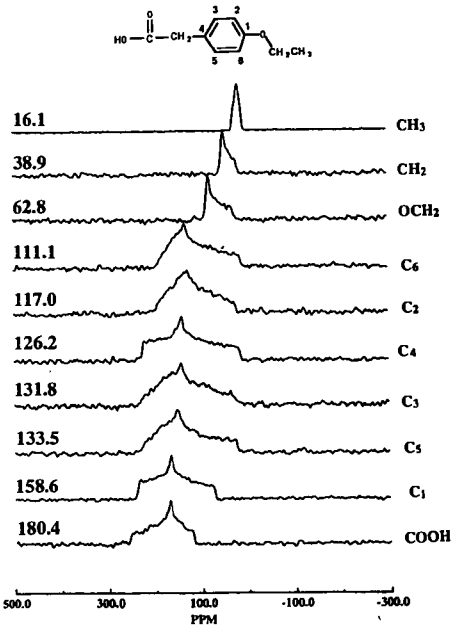

Figure 3. Powder patterns obtained from spectral slices taken from Figure 1.

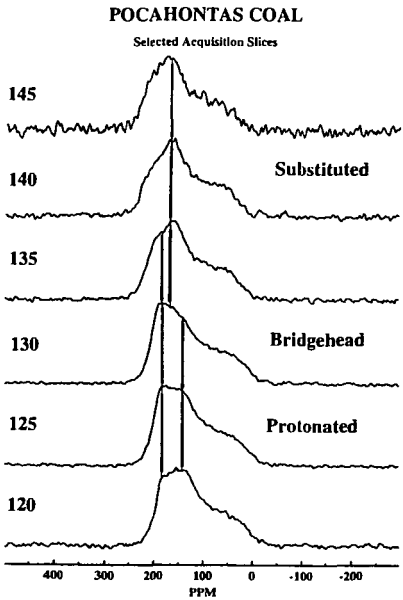

Figure 4. Powder patterns taken from Figure 2 at selected spectral slices illustrating composite patterns that still have features which can be attributed to protonated, bridgehead, and substituted aromatic carbons. The heavy vertical lines represent the approximate frequencies of the δ_{22} component of the principal values of the chemical shielding tensor for the different types of aromatic carbons.

APPLICATIONS OF TOROIDS IN HIGH-PRESSURE NMR SPECTROSCOPY

R. J. Klingler, J. W. Rathke, Klaus Woelk, Kurt W. Kramarz, and Rex Gerald
Chemical Technology Division
Argonne National Laboratory
Argonne, Illinois, 60439.

Keywords: high-pressure NMR, supercritical fluids, hydroformylation, NMR-imaging

Abstract

Toroid detectors have distinct NMR sensitivity and imaging advantages. The magnetic field lines are nearly completely contained within the active volume element of a toroid. This results in high NMR signal sensitivity. In addition, the toroid detector may be placed next to the metallic walls of a containment vessel with minimal signal loss due to magnetic coupling with the metal container. Thus, the toroid detector is ideal for static high pressure or continuous flow monitoring systems. Toroid NMR detectors have been used to follow the hydroformylation of olefins in supercritical fluids under industrial process conditions. Supercritical fluids are potentially ideal media for conducting catalytic reactions that involve gaseous reactants, including H_2, CO, and CO_2. The presence of a single homogeneous reaction phase eliminates the gas-liquid mixing problem of alternative two-phase systems, which can limit process rates and adversely affect hydroformylation product selectivities. A second advantage of toroid NMR detectors is that they exhibit a well-defined gradient in the rf field. This magnetic field gradient can be used for NMR imaging applications. Distance resolutions of 20 μ have been obtained.

Introduction

The vitality of the industrial process arena is strongly influenced by the development of new instrumental techniques. This work focuses on a special type of NMR detector whose unique properties make it an ideal choice for *in situ* NMR spectroscopic analysis of synthesis gas reactions. In addition, the same toroid NMR detectors are useful for imaging applications. In contrast to conventional NMR imaging techniques, the new toroid cavity NMR-imaging method retains all chemical shift and coupling constant information.

High-pressure NMR spectroscopy

One of the key properties of toroids for NMR applications is that the magnetic field lines are nearly completely contained within the windings of the coil. This contrast with the Helmholtz and solenoid coils that are typically used in commercial NMR spectrometers. In the latter type of coils, the magnetic field lines are more diffuse and extend well outside the coil windings, see Figure 1. The result is a signal-to-noise advantage of 3-5 for toroids compared with Helmholtz detectors [1-3]. More significantly for high pressure work, a toroid detector may be operated near the walls of a metallic containment vessel. Thus, in the cell design [4] of Figure 2, there is minimal dead volume. Furthermore, the small internal reactor volume of only 8 ml minimizes the amount of hazardous materials required for the experiments. The reactor in Figure 2 is routinely operated at 250 °C and 300 atm pressure. Typical *in situ* spectroscopic results obtained during the hydroformylation of propylene [5,6] are presented in Figures 3 and 4.

Special emphasis has been placed on exploring the use of supercritical fluids as homogeneous reaction media for catalytic synthesis gas transformations. Supercritical fluids consisting of carbon dioxide or water are environmentally benign solvents. Furthermore, separations of products may be accomplished by facile pressure alterations [7] instead of energy intensive distillations. In addition, mixing is not required for supercritical fluids. The oxo process is an important industrial reaction that is sensitive to gas-liquid mixing conditions [8]. Interestingly, we have found that the reaction exhibits improved straight chain aldehyde product selectivity [5,6] when the reaction is conduced in supercritical carbon dioxide as indicated in the last row of Table 1.

Supercritical fluids also have advantages for fundamental mechanistic analyses. Thus, the low viscosity of supercritical fluids results in NMR linewidths that are up to an order of magnitude sharper than those found in conventional organic solvents [5,9]. Thus, in benzene solvent where the ^{59}Co NMR linewidths are broader than those in Figure 4 by a factor of six,it would be difficult to resolve $HCo(CO)_4$ and $Co_2(CO)_8$. Furthermore, the acyl intermediate would not be detectable. The oxo process was investigated by a combination of

^1H, ^{13}C, and ^{59}Co spectroscopy under industrial process conditions. It was found that the high temperature reaction chemistry is dominated by mechanistically significant $\cdot Co(CO)_4$ radical concentrations which are formed by homolysis of the Co-Co bond in $Co_2(CO)_8$. The Co-Co bond dissociation enthalpy in $Co_2(CO)_8$ has been measured, $\Delta H^o = 19 \pm 2$ kcal/mole and $\Delta S^o = 29 \pm 4$ cal/(K·mol), by NMR magnetic susceptibility measurements over the temperature range of 120 to 225°C and from the contact chemical shift of the carbon monoxide ligand in the ^{13}C NMR spectra, $\Delta H^o = 19 \pm 2$ kcal/mole. The $\cdot Co(CO)_4$ radical induces a complex manifold of facile hydrogen atom transfer reactions that may be quantitated by ^1H and ^{59}Co NMR line shape analysis [10].

NMR-Imaging

Toroid cavity detectors may be used for rotating frame spectroscopic imaging [11]. The well-defined rf field gradient that is produced within a toroid cavity [12] minimizes the problems that were encountered in early applications of the rotating frame imaging technique using surface coils [13]. The salient feature of the rotating frame imaging technique is that the high-resolution NMR spectral information is not lost as is the case in conventional magnetic resonance imaging (MRI). As an example, five capillaries containing different solvents were placed at a spacing of 0.8 mm outward from the center of the cavity. The result in Figure 5 demonstrates that in a single experiment, the toroid cavity imaging technique can chemically distinguish between water and acetone, in addition to identifying the location of these samples along the distance axis. The chemical shift resolution of this technique is equivalent to that of a normal NMR spectrum. Alternatively, the ultimate resolution with respect to distance for the toroid cavity detector is under study. The data in Figure 6 demonstrates the distance resolution by ^{19}F NMR spectroscopy of two Teflon layers that were placed around the central conductor of the toroid cavity resonator. The measured thickness of the Teflon layers, as well as their 20 μm separation, is accurately reproduced by the imaging data. This distance resolution is already better than that which can be attained for solid samples using conventional MRI techniques. This toroid cavity imaging technique could find a wide range of applications in the characterization of surface layers and in the production of advanced materials. Potential areas of application include *in situ* NMR monitoring of growth sites during ceramic formation processes, analysis of the oxygen annealing step for wires coated with high-temperature superconductors, investigation of the reaction chemistry as a function of distance within the diffusion layer for electrochemical processes.

Acknowledgement

Support for this work was provided by the office of Basic Energy Sciences, Division of Chemical Sciences, U.S. Department of Energy.

References

1. D. W. Alderman and D. M. Grant, 21st Experimental NMR Conference, Tallahassee, Florida, 1980.
2. T. E. Glass and H. C. Dorn, *J. Magn. Reson.* **52**, 518 (1983).
3. J. W. Rathke, *J. Magn. Reson.* **85**, 150 (1989).
4. J. W. Rathke, U. S. Patent 5,045,793 issued Sept. 3 (1991).
5. J. W. Rathke, R. J. Klingler, and T. R. Krause, *Organometallics*, **10**, 1350 (1991).
6. J. W. Rathke and R. J. Klingler, U. S. Patent 5,198,589 issued Mar. 30 (1993).
7. M. McHugh, U. Krukonis, *Supercritical Fluid Extraction*; Butterworths: Stoneham, MA, 1986.
8. R. L. Pruett, In *Advances in Organometallic Chemistry*; F. G. A. Stone and R. West, Eds.; Academic Press: New York, 1079; Vol. 17, pp 1-60.
9. J. M. Robert and R. F. Evilia, *J. Am. Chem. Soc.* **107**, 3733 (1985).
10. R. J. Klingler and J. W. Rathke, *J. Am Chem. Soc.* **116**, 4772 (1994).
11. K. Woelk, J. W. Rathke, and R. J. Klingler, *J. Magn. Reson.* **105**, 113 (1994).
12. K. Woelk, J. W. Rathke, and R. J. Klingler, *J. Magn. Reson.* **109**, 137 (1994).
13. D. I. Hoult, *J. Magn. Reson.* **33**, 183 (1979).
14. P. Pino, F. Piacenti, and M. Bianchi, In *Organic Syntheses via Metal Carbonyls*: I. Wender, P. Pino, Eds.; Wiley: New York, 1977; Vol. 2, pp 98.
15. I. Kisshenbaum and E. J. Inchalik, "Oxo Process," In Encyclopedia of Chemical Technology, 3rd ed., Vol. 16, John Wiley & Sons, New York, pp637-653 (1981).

Table 1. Selectivity in the Hydroformylation of Propylene

Solvent	n/i-Butyraldehydes
2,2,4 - Trimethylpentane[a]	4.6
Benzene[a]	4.5
Toluene[a]	4.4
Diethyl ether[a]	4.4
Ethyl alcohol, 95%[a]	3.8
Acetone[a]	3.6
Commercial plants[b]	3.0 - 4.1
CO_2 (0.5 g/ml)[c]	7.2

[a] T = 108 °C, P(CO) = 140 atm, $P(H_2)$ = 100 atm, ref 14.
[b] T = 140-180 °C, P(CO) = 100-150 atm, $P(H_2)$ = 100-150 atm, ref 15.
[c] T = 80 °C, P(CO) = 56.1 atm, $P(H_2)$ = 56.1 atm, ref 5,6.

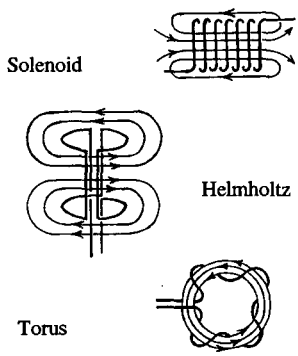

Figure 1. NMR detector coils.

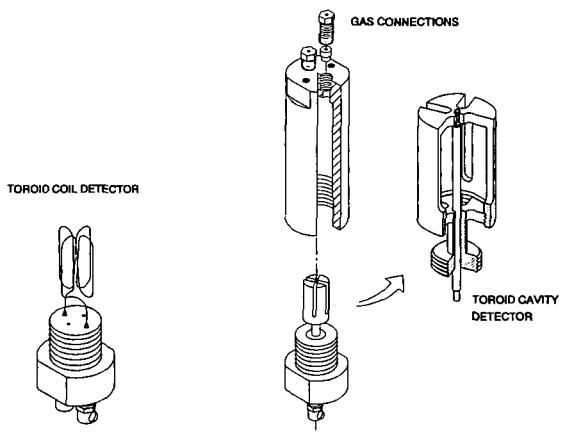

Figure 2. High-pressure NMR cell with toroid coil or cavity detector.

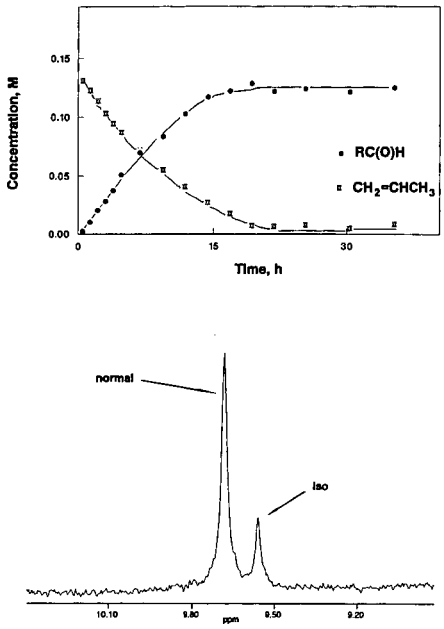

Figure 3. Butryaldehyde product mixture based on *in situ* ^{1}H NMR spectra during the hydroformylation of propylene in supercritical carbon dioxide at 80 °C.

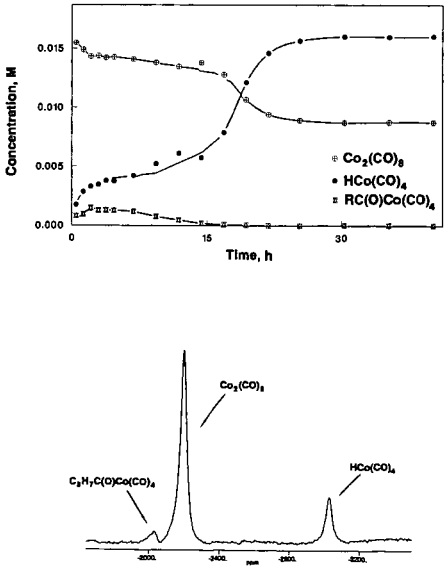

Figure 4. Organocobalt intermediates based on ^{59}Co NMR spectra during the hydroformylation of propylene in supercritical carbon dioxide at 80 °C.

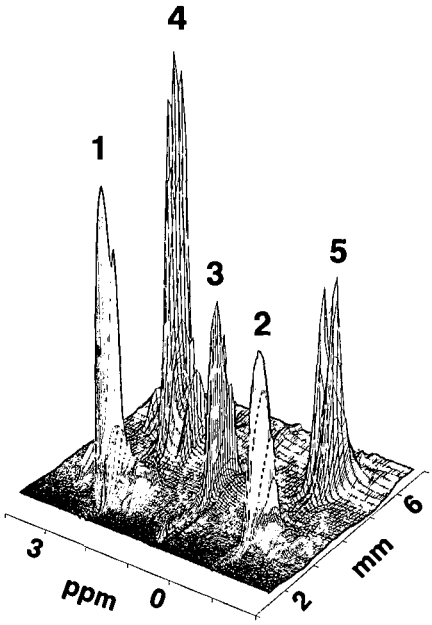

Figure 5. Simultaneous resolution of NMR chemical shift and radial displacement for five capillary tubes containing: 1, water; 2, isopropanol; 3, acetone; 4, water; and 5, isopropanol.

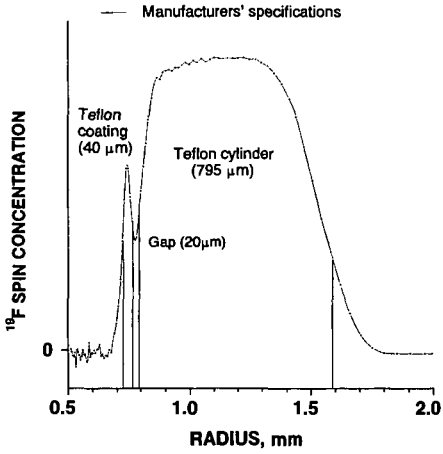

Figure 6. Plot of teflon concentration versus radial displacement based on ^{19}F NMR imaging.

VERY HIGH FREQUENCY EPR OF SULFUR COMPOUNDS IN COAL

R. B. Clarkson, R. L. Belford, P. Ceroke, W. Wang, W. Shi, K. Motsegood,
A. Smirnov, T. Smirnova, M. J. Nilges
Illinois EPR Research Center
University of Illinois, Urbana, IL 61801

Keywords: Aromatic sulfur, EPR, quantitative measurement

INTRODUCTION

The overall goal of our work during the last five years has been the non-destructive elucidation of molecular structure in coal and coal-derived materials [1]. Special emphasis has been placed on determining the concentration and molecular forms of organic sulfur in coal. Our approach has been to use the naturally occurring unpaired electrons in coal as reporters of their environment, making use of electron magnetic resonance (EMR) spectroscopy to develop a detailed picture of the types and arrangements of atoms "seen" by the electrons. During this period, we constructed the first 95 GHz (W-band) EMR spectrometer in the USA (and the second in the world). With this advanced spectrometer, we were the first to discover that the aromatic sulfur in coal produced a unique EMR signature. Extensive experimental and theoretical work on model aromatic sulfur compounds in the thiophene series (thiophene, benzothiophene, dibenzothiophene, etc.) has enabled us to develop a detailed understanding of the relationships between the molecular and electronic structure of these compounds and their EMR spectra. This new basic scientific knowledge in turn allowed us accurately to analyze the W-band EMR spectra from coal, desulfurized coal, and a variety of coal derived materials. We developed an automated computer program (based on spin quantum mechanics) which can analyze the EMR spectra and which reports the aromatic sulfur content of the coal as well as key spectral parameters. This analysis method has been tested on coal blends of know sulfur content as well as on a variety of coals from the IBCSP and elsewhere. The precision of the method is conservatively ± 0.1% of the aromatic sulfur in the sample. Identical samples measured both by EMR and XANES gave nearly identical results. The EMR technique has the twin advantages of simplicity and absolute concentration readout; an analysis takes less than five minutes to perform. Applications of the EMR technique include the determination of aromatic sulfur in coal, evaluation of the effectiveness of desulfurization technologies, and the evaluation of the effects of desulfurization on the rest of the molecular forms in coal.

EXPERIMENTAL PROCEDURES

A. Coal Sample Preparation

Significant progress has been made in the development of a standard protocol for coal sample preparation. Following the same protocol for all the samples allows the direct comparison of results from various types of coals. The development of a standard method also allows the calibration of the precision of the techniques and calculation of error limits. The techniques developed must allow for the sensitivity of coal samples to oxygen.

Since the EPR lineshape changes when samples are exposed to oxygen, preparation of coal samples for EPR analysis is done in a nitrogen atmosphere glove bag. All the necessary items needed for coal sample preparation, including the coal samples are exposed to nitrogen environment for two to three days. The oxygen concentration inside the bag is monitored continuously by keeping an oxygen sensitive electrode in the glove bag. The oxygen meter used is manufactured by "Yellow Springs Instrument Company" Yellow Springs, Ohio. The electrode utilizes a membrane with a KCl solution on the inside. The membrane must be kept wet so the electrode is stored in a beaker of distilled water. This meter gives oxygen concentration directly in ppm. EPR sample tubes are prepared at the oxygen level ~4-6 ppm. The EPR sample tubes (.7 mm O.D. quartz tube) are sealed at one end before being placed inside the glovebag. After the tubes are filled, a high quality vacuum grease is applied on the open end and tubes were carefully transferred in small labeled plastic vials. The vials are removed from the glovebag only when EPR spectroscopy is done.

B. W- Band EPR Spectroscopy

The key to our work plan is the W-band spectrometer. This unique instrument has been built over the last three years, and now incorporates several important technical innovations that make it well-suited for the present research work [2]. All spectroscopy at W-band (ca. 95 GHz) is done on the instrument constructed in our laboratory. Routine spectra were taken under nitrogen gas flow to avoid any possible oxygen sensitive changes. Lower power (15 db) is used to avoid saturation effects. Different modulation amplitudes were tried and finally a best compromise was achieved between the S/N ratio and the resolution of the spectrum. Data is acquired by a computer, which also controls the magnetic field sweep of the experiment.

C. Model Compounds

A 1000:1 mole ratio mixture of powdered boric acid (Aldrich) and the selected member of the thiophene series (thiophene, benzothiophene, dibenzothiophene, benznaphthothiophene, dinaphthothiophene, thianthrene) is heated to the melting point of boric acid (190°C). The molten mass is vortexed to maximize the dispersion of the selected thiophene in the molten solution and then allowed to cool to a glass. The glass is crushed into fine powder and loaded into a quartz sample tube. The tube is placed in a Ray-O-Net irradiation unit and subjected to UV irradiation at 254 nm for 20 to 30 minutes. The sample tube is then removed from the UV light and sealed for analysis. Degassing before and after the irradiation shows no effect on the EPR spectra. This method is a convenient way to produce matrix-isolated ionic radicals at room temperature. Their disordered state closely approximates the environment of similar compounds found in coal. Data on the model compounds is summarized in Table I [3].

We have used four microwave frequencies, S-band (2-4 GHz), X-band (9.5 GHz), Q-band (35 GHz), and W-band (95 GHz) to study the radicals produced by this method. CW saturation behavior of the organic radicals has been studied. Modulation amplitude profiles of the sample are routinely probed to achieve the best compromise between the S/N and resolution of possible hyperfine structure. Wide magnetic field scans have been performed for the sample at X-band to make sure all signals are accounted for. Low temperature experiments at liquid nitrogen temperature (77 K) were also performed for the sample at 9.5 GHz; no discernible difference in EPR parameters (g and linewidth) were observed, suggesting that the radical is a rigid structure at room temperature. Care has also been taken to avoid distortion of the signal by RC filters.

X-band and Q-band spectra were obtained from Varian E-line EPR spectrometers outfitted with a tracking Varian NMR gaussmeter and a HP frequency divider with a Fluke frequency counter. W-band EPR is performed using the spectrometer system built in our laboratory. All g-value measurements are based on direct field and frequency measurements. A statistical treatment of the g-matrix measured from seven independently prepared samples of DBT in BAG shows that experimental errors are very small (max. standard deviation, $\sigma_{n-1}=11\times10^{-5}$). S-band ESEEM is done on a locally-built Electron Spin Echo (ESE) spectrometer.

A computer-assisted analysis using an EPR powder spectrum simulation program and the spectral parameter optimization routine based on the SIMPLEX algorithm are performed to: 1) confirm the direct measurements of principal g values, 2) extract possible hyperfine interaction, and 3) accurately assess the linewidths and lineshapes. The calculation of principal values of the g matrix is based on Stone's theory (ref Stone) with certain modifications. The SCF-MO wave function and orbital energies are obtained from the semi-empirical method PM3 in MOPAC (ref QCPE 455) All calculations employ an IBM R6000 workstation.

RESULTS AND DISCUSSION

The anisotropic g matrix is one of the most important and fundamental EPR parameters. It is generally viewed as characteristic of the electronic structure of the molecule that contains one or more unpaired electrons. But for most organic radicals, the elements of the g matrices are very close to the free-electron value ($g_0 = 2.00232$). Experimentally resolving such small differences was difficult using conventional 9.5 GHz EPR, and this greatly limited the usefulness of g matrix as a structure indicator. The development of very high frequency EPR (VHF-EPR) has overcome this problem. From the simple resonance condition one can see easily that the difference in resonance fields for two slightly different g factors is proportional to the product of the microwave frequency and the difference between the two g factors.

$$\Delta B = B_1 - B_2 = \frac{2\pi\hbar\nu}{\beta}\left(\frac{1}{g_2} - \frac{1}{g_1}\right) = \left(2\pi\frac{\hbar}{\beta}\right)\left(\frac{\Delta g}{g_1 g_2}\right)\nu$$

Therefore the g resolution will be enhanced by a factor of 10 on going from X-band (9.5 GHz) to W-band (95 GHz) providing the line does not broaden substantially with microwave frequency.

At a sufficiently high field, the electronic Zeeman interaction will dominate the electron-nuclear hyperfine interaction, and both the electron and nuclear spins will be quantized along the external field. Under favorable conditions, the anisotropic hyperfine coupling matrix, A, can be resolved or partially resolved along the canonical directions of g matrix, yielding additional valuable information about molecular structure and other properties related to the ground electronic state of a molecule. Indeed, we have observed the anisotropic A matrix in the continuous wave VHF-EPR spectra of a series of thiophenic radicals. In addition, an auxiliary experiment using a low frequency pulsed spectrometer at S-band (2-4 GHz) also reveals the anisotropic hyperfine interactions between the

electron spin and the ring protons.

The multifrequency approach has resulted in a unified set of magnetic parameters (g and A matrices), from which it is possible to identify and characterize the radical species in terms of properties related to its molecular orbital structure. The total spin energy Hamiltonian for an electron with spin S is written:

$$\mathcal{H}_{spin} = \mathcal{H}_{ez} + \mathcal{H}_{so} = \beta_e \, B \cdot (L + g_e \, S) + \lambda \, L \cdot S$$

The shift due to organic heteroatoms (O and S) results from a change in resonance energies caused by anisotropy in g_e and the spin-orbit constant λ, coupling the spin and orbital angular momenta (L). The larger the field shift ΔB, the more sensitive our experiment will be to the presence of sulfur. It is for this reason that we observed the shift due to sulfur at higher spectrometer frequencies. Since XANES results from Illinois coals shows that thiophenic sulfur is the aromatic form in which the majority of organic sulfur is found in these coals, the connection between molecular and electronic structure found in the series of model thiophènes can be used as a basis for the analysis of VHF-EPR spectra from coal.

Several experiments have been performed to test the accuracy of the VHF-EPR method for aromatic sulfur analysis in coal. The first of these tests was suggested by Dr. Ken Ho, ICCI project monitor, and consisted of of making blends of two coals of known sulfur composition. VHF-EPR analyses of these blends then could be checked against the *known sulfur content*. Accordingly, a vitrinite (organic sulfur 2.9% dmf) and a sporinite (organic sulfur 4.25%) were blended, and the sulfur content of these blends measured by VHF-EPR was compared to the known composition. Figure 1 shows the results of this test. The VHF-EPR results agree with the known values to better than ± 0.1%.

The second type of test which was performed to evaluate the method was the direct analysis of organic sulfur content in a variety of coals of widely differing character, spanning the range of sulfur content from less than 0.5% to more than 11%. These coals were selected because each had been carefully analyzed for organic sulfur content by other chemical and physical methods. Figure 2 shows the excellent correlation between VHF-EPR analyses and the published organic sulfur content of these coals.

The third type of test which we performed to validate the VHF-EPR method was a direct comparison of results from the method and those obtained by XANES on identical samples. Sets of samples prepared by Dr. Steve Palmer, Southern Illinois University-Carbondale, were sent to Prof. G. Huffman, University of Kentucky, for analysis by XANES, as well as to us for analysis by VHF-EPR. Figure 3. shows the comparison of the two methods on four IBCSP coals. Nearly perfect agreement is seen in IBC 101, 102, and 106, while a considerable disagreement is seen in values for IBC 109. Figure 4 shows a similar comparison between VHF-EPR and IBCSP published values for *organic sulfur* in these coals. A comparison of Figures 3 and 4 show that the VHF-EPR determination of aromatic sulfur is at variance with both XANES and proximate analytical data in the case of IBC 109, and that a much better correlation exists for the XANES data than for the proximate analytical data. The reasons for disagreement in the case of IBC 109 are currently being investigated.

CONCLUSIONS

This research and development project has demonstrated a new analytical method for determining the aromatic sulfur content of coals and coal-related materials. It is based on VHF-EPR technology, and is non-destructive, quick, and precise. The method requires only a few tenths of a milligram of sample. The precision of this measurement seems less sensitive to sample oxidation than does XANES, although a much more detailed comparison of the two methods clearly is in order. VHF-EPR analysis for aromatic sulfur seems a good choice for routine coal characterization. It also should be very useful in the evaluation of various desulfurization technologies, and as a monitor of the extent of desulfurization. Several scientific questions remain for future work. These include: (a) the effects of spin exchange in modifying observed g-values in coals; (b) the effects of oxygen and sample oxidation; and (c) the advantages of working at magnetic fields *higher than 3.4 T*. Additional instrument development and fundamental research on items (a) - (c) could extend the technique into the analysis of heteroatomic oxygen as well as sulfur.

This work was prepared with the support, in part by grants made possible by the Illinois Department of Energy and Natural Resources through its Coal Development Board and Illinois Clean Coal Institute (K. Ho, project manager), and by the U. S. Department of Energy (DE-FC22-92PC-92521). However, any opinions, findings, conclusions, or recommendations expressed herein are those of the authors, and do not necessarily reflect the views of IDENR, ICCI, and the DOE.

REFERENCES

1. "Electron Magnetic Resonance of Standard Coal Samples at Multiple Microwave Frequencies," R. B. Clarkson, W. Wang, D. L. Brown, H. C. Crookham, and R. L. Belford, in Techniques in Magnetic Resonance for Carbonaceous Solids, R. Botto and Y. Sanada, eds., ACS Advances in Chemistry Series **229**, American Chemical Society, Washington, 1993, 507 - 528.

"Multi-Frequency Electron Magnetic Resonance," R. L. Belford and R. B. Clarkson, in Techniques in Magnetic Resonance for Carbonaceous Solids, R. Botto and Y. Sanada, eds., ACS Advances in Chemistry Series **229**, American Chemical Society, Washington, 1993, 107 - 138.

2. "Very High Frequency EPR - 94 GHz Instrument and Applications to Primary Reaction Centers from Photosynthetic Red Bacteria and Other Disordered Systems," W. Wang, R. L. Belford, R. B. Clarkson, P. H. Davis, J. Forrer, M. J. Nilges, M. D. Timken, T. Walczak, M. C. Thurnauer, J. R. Norris, A. L. Morris, and Y. Zhang, *Appl. Magn. Reson.*, **6**, 195 - 215 (1994).

3. "Electron Magnetic Resonance of Aromatic Radicals on Metal Oxide Surfaces," R. B. Clarkson, K. Mattson, W. Shi, W. Wang, and R. L. Belford, *Mol. Engineering*, **4**, 89 - 117 (1994).

Table I.
Summary of g-matrix values for selected thiophene radicals on alumina

Species	g_1	g_2	g_3
THI	2.00506±.00050	2.00506±.00050	2.00234±.00010
BTH	2.00642±.00038	2.00451±.00012	2.00226±.00013
DBT	2.01130±.00026	2.00624±.00015	2.00236±.00010
BNT	2.00583±.00012	2.00495±.00012	2.00224±.00011
DNT	2.00518±.00052	2.00326±.00047	2.00224±.00051

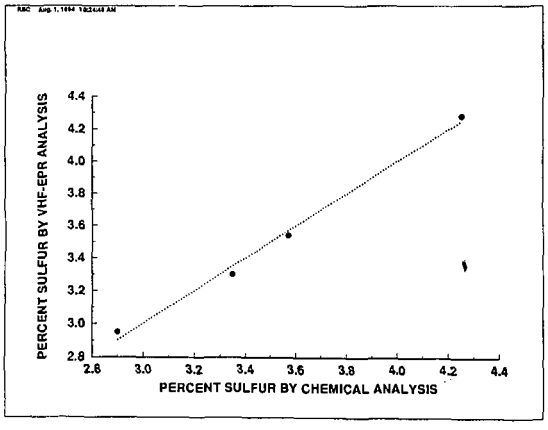

Figure 1. VHF-EPR sulfur analysis test on vitrinite/sporinite blends

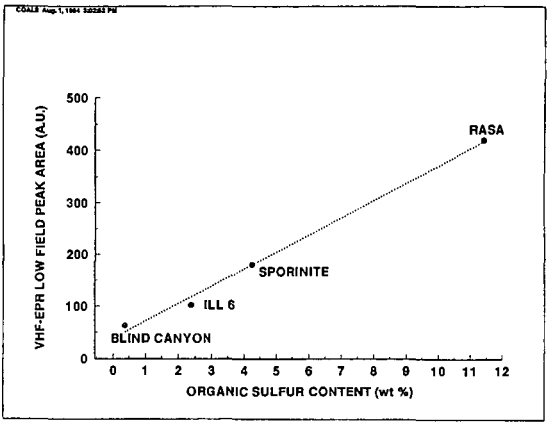

Figure 2. Correlation between VHF-EPR and other analytical methods for organic sulfur in a series of coals with widely differing sulfur contents.

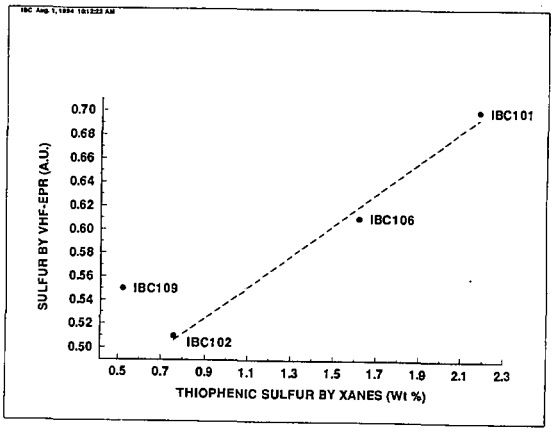

Figure 3. Comparison of VHF-EPR and XANES analyses on four IBCSP coals. The XANES figures are for thiophenic sulfur.

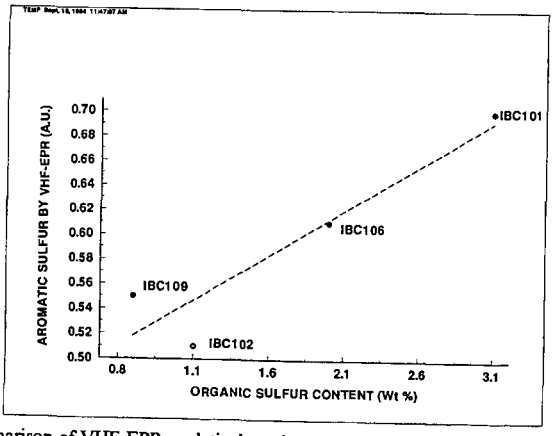

Figure 4. Comparison of VHF-EPR analytical results and IBCSP values for organic sulfur in four coals.

SWELLING BEHAVIOR OF O-ALKYLATED APCS COALS AS EXAMINED BY THE EPR SPIN PROBE METHOD

Ruisong Ding, David Tucker and Lowell D. Kispert
Department of Chemistry, Box 870336
The University of Alabama
Tuscaloosa, AL 35487-0336

KEYWORDS: O-Alkylated Coal, EPR Spin Probe, Hydrogen Bonding

ABSTRACT

Known O-alkylation procedures have been used to derivatize the carboxyl and hydroxyl groups in the APCS coals Lewiston-Stockton, Wyodak-Anderson, Beulah-Zap, Illinois #6, Upper Freeport, and Pittsburgh #8. In general the resulting decrease in hydrogen bonding reduced the cyclical variation in nitroxide spin probe retention observed for nonalkylated coals when small amounts (<1%) of pyridine are present in the toluene swelling solvent. An increase in spin probe retention by the O-alkylated coals relative to the underivatized coals indicates a more open arrangement in the coal due to a decrease in attractive forces, confirming that microporosity increases with increasing rank.

INTRODUCTION

A recent study of Tucker,[1] using an EPR spin probe method we have developed, and an earlier study by Green and Larsen[2] showed that an unexpectedly large number of guest molecules could be included in the swelled macromolecular structure of coal by spiking a "poor" swelling solvent such as toluene (or chlorobenzene) with as little as 100 ppm of a strong swelling solvent such as pyridine. The specific amount of included guest material depends on the rank of the coal undergoing swelling, but all ranks showed reproducible fluctuations in the number of trapped guest molecules as the pyridine content was increased by increments of 100 ppm. This oscillatory uptake behavior was explained as follows. At low ppm pyridine, weak hydrogen bonds which isolate interconnected micropore systems are disrupted. As the concentration of pyridine increases, disruption of weak hydrogen bonds which protect individual micropores will occur, followed at 1-5% pyridine by disruption of stronger hydrogen bonds within the macromolecular structure resulting in an opening of the structure. The cartoon given in Figure 1 emphasizes the active sites that can hydrogen bond (OH) with guest molecules, the interconnected micropore system, the hydrogen bonds of individual micropores and the stronger hydrogen bonds within the macromolecular structure.

In an effort to examine the integrity of the proposed swelling model for the action of binary solvents composed of less than 1% strong swelling solute in a poor swelling solvent, the Argonne Premium Coal Samples (APCS)[3,4] of Lewiston-Stockton (LS), Wyodak-Anderson (WA), Beulah-Zap (BZ), Illinois #6 (I6), Upper Freeport (UF) and Pittsburgh #8 (P8) were O-alkylated by a published procedure.[5] Due to space limitations, only the results for BZ, WA and LS coals will be presented here. The O-alkylated coal differs from the underivatized coal because interactions involving the acidic protons of the hydroxyl and carboxylic groups are no longer possible. Helium density and mercury porosimetry measurements revealed that the secondary structure (intermolecular associations) of the O-alkylated coals is significantly altered.[5] Furthermore, it is known that lower rank coals have lower microporosity (pores smaller than 18 Å) and largely consist of macropores, while higher rank coals have higher microporosity. Microporosity is a measure of the short-range intermolecular forces which contribute to the secondary structure of coal. Upon O-methylation the total porosity (<2200 Å) increases, and the increase is more pronounced for the higher ranked coals. The dramatic increase in the microporosity of O-methylated coals indicates a more open arrangement in the regions where short-range attractive molecular interactions are affective.[4] Since higher rank coals lack the very polar carboxylic acid functionalities and also have a low total concentration of polar functional groups, relative to subbituminous rank coals, microporosity increases with rank.

EPR SPIN PROBE METHOD

Electron paramagnetic resonance (EPR) techniques have been used previously to follow the inclusion of molecular probes in the micropore structure of coal in order to determine the changes in pore size, shape characteristics, pore wall chemistry, and hydrogen bonding which occur during the swelling process.[6]

The most common molecular probes are stable cyclic nitroxyl free radicals (depicted in Figure 2) which contain a ring nitrogen that is also singly bonded to oxygen and flanked by four methyl groups which sterically stabilize the radical. The unpaired electron density is distributed over both the nitrogen (40%) and the oxygen (60%) atoms. Reactive substituents (R) on the ring allow for chemical reactions to be studied, and varying the size and shape of a non-reactive substituent, allows evaluation of the effect on shape or size of the structural features of coal. The spin probe technique has been described in detail.[6] Briefly the coal sample is swelled in a mM nitroxide spin probe solution for approximately 18 h until equilibrium is reached. The coal slurry is then filtered and the solid is vacuum dried to remove the swelling solvent. The samples are then washed with cyclohexane, a non-swelling solvent, to remove any spin probes not trapped in the coal structure. The samples are again vacuum dried and then sealed in evacuated EPR tubes for subsequent measurement of the concentration of the nitroxide radicals trapped in the coal structure.

EXPERIMENTAL

Spin probe VII (Tempamine) was obtained from Aldrich and used as received. This probe contains an amino group which can react with acidic sites in the coal, or in the absence of such sites, it can be trapped in small pores. Ca. 4 g of APCS coal samples, obtained from the Argonne Premium Coal Sample program,[3,4] were O-alkylated according to a literature method,[5] although the work-up procedure was modified as follows. Warm water (100 mL) was added to the reaction mixture and the pH was adjusted to 7. Volatiles were removed by distillation under vacuum for 2 h at 22°C and then at 40°C for 3 h. The residue was treated with hot water (500 mL) to dissolve ammonium salts. The mixture was left to stand overnight; the aqueous layer was decanted, and the procedure was repeated 5 times. The product was isolated by filtration and washed with hot water (4-6 L) until the washings were devoid of halide ions. The alkylated coal was first dried over $CaCl_2$ under N_2, then under vacuum for 2 days and finally at 110°C for 3 days. The alkylated coal was sealed underN_2. Infrared analysis was used to follow the decrease in adsorption in the 3300-3600 cm^{-1} region (loss of hydroxyl groups) and the adsorption increase in the 1730 cm^{-1} region (esterification of the carboxylic acids).

RESULTS AND DISCUSSION

The retention of spin probe VII in BZ APCS lignite is given in Figure 3 as a function of percent pyridine present in toluene swelling solvent. The important feature to note is that large variations occur in the spin probe retention. In the absence of pyridine 1.2×10^{18} spins/g of probe VII is retained in the BZ lignite. When very small amounts of pyridine are present the spin probe retention drops to 0.8×10^{18} and then increases to 1.8×10^{18} with 0.1% pyridine. A decreasing variation in the amount of spin probe retained occurs as the percent pyridine in toluene is increased, becoming more or less constant near 0.4×10^{18} spins/g .

Totally different behavior, shown in Figure 4, of spin probe VII retention as the percent pyridine is increased occurs with O-alkylated BZ. The highest spin probe retention (4.1×10^{18} spins/g) is obtained in the absence of pyridine and this then decreases without any evidence of oscillation to ca. 2.4×10^{18} spins/g with a pyridine content of $\geq 0.5\%$.

Similar plots for Wyodak-Anderson coal and alkylated Wyodak-Anderson coal are given in Figures 5 and 6, respectively. As the percent pyridine increases from 0% to 0.01% (Figure 5) the retained spin probe concentration in units of 10^{18} spins/g drops from 6.1 to 4.8, then rises to 5.5 at 0.02%, drops to 3.6 at 0.08%, rises to 4.9 at 0.1%, drops to 3.2 at 0.2%, rises to 5.5 at 0.6%, and drops to 3.1 at 1%. Further variation is observed as the pyridine content increases to 5%. Above 5% the retained spin concentration equals approximately 3.7±.5. For the alkylated coal (Figure 6), the spin concentration is nearly constant at $9.0 \pm 0.2 \times 10^{18}$ spins/g with the variation close to the relative error of ±0.1.

Figures 7 and 8 show the results of a similar study for Lewiston-Stockton and alkylated Lewiston-Stockton coal, respectively. The spin probe concentration in units of 10^{18} spin/g (Figure 7) varies from 2.2 at 0% pyridine to 1.8 at 0.06%, increases to 2.1 at 0.08%, decreases to 1.7 at 0.4%, increases to 2.0 at 0.6%, and then decreases to 1.6 at 1%, 1.4 at 2% and 1.2 at 4%. In contrast, the spin probe retention in the alkylated coal (Figure 8) decreases from 7.6 at 0% pyridine to 6.9 at 0.2% and then gradually increases to 7.4 at 2%.

In all three coals, the absolute value of the spin probe concentration increased upon alkylation (a factor of 4 for Beulah-Zap, lignite; 2.5 for Wyodak-Anderson subbituminous and 5.4 for Lewiston-Stockton high volatile bituminous coal). Previous porosity measurements[5] indicated that an increase in microporosity occurs upon alkylation and that this increase is more pronounced in high ranked coals than in the lower ranked coal. This is confirmed by this study. It is also clear that upon alkylation the cyclical variation is nearly eliminated, confirming the role of the hydrogen-bonding scheme outlined in the introduction. The largest variation in spin concentration with % pyridine occurred for Wyodak-Anderson coal suggesting more extensive changes in local structure with pyridine at less than 1% than for the high ranked Lewiston-Stockton coal. Beulah-Zap, which loses water upon exposure to air, has a lower tendency to retain the spin probe than the high rank Lewiston-Stockton coal.

ACKNOWLEDGMENT

This work was supported by the U. S. Department of Energy, University Coal Grant program, Grant no. DE-FG22-93PC 93202.

REFERENCES

1. Tucker, D. Ph.D. dissertation, University of Alabama, 1994 Entitled. "The Use of the EPR Spin Probe Method to Study Structural Changes in Solvent Swelled, Weathered Coal."

2. Green, T. K.; Larsen, J. W. *Fuel* 1984, *63*, 1538.

3. Vorres, K. S. "User's Handbook for the Argonne Premium Coal Sample Program," 1989, ANL/PCSP-89/1.

4. Vorres, K. S. *Energy and Fuels* 1990, *4*, 420.

5. Liotta, R.; Rose, K.; Hippo, E. *J. Org. Chem.* 1981, *46*, 277.

6. Kispert, L. D.; Tucker, D.; Sady, W. *Prepr. Pap. Am. Chem. Soc., Div. Fuel Chem.* 1994, *39*, 54 and references cited therein.

Figure 1
A cartoon depicting a possible pore structure with the location of (OH) sites that can hydrogen bond with guest molecules and localized hydrogen bonding (~~).

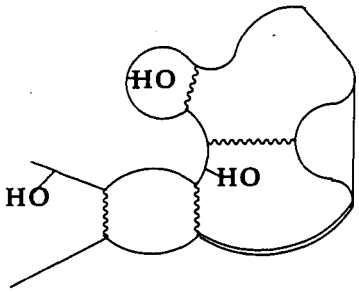

Figure 2
(a) General structure of a nitroxide spin probe,
(b) Structure of spin probe VII (TEMPAMINE)

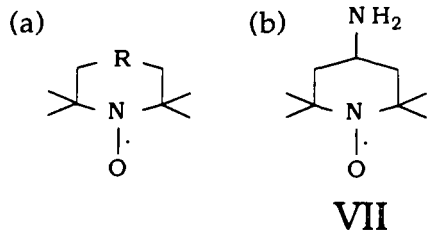

Figure 3
Retention of spin probe VII in Beulah-Zap APCS lignite after swelling with toluene spiked with pyridine.

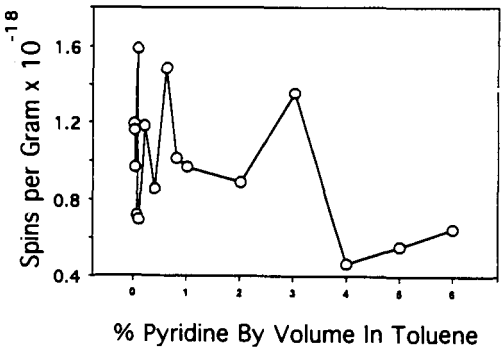

Figure 4
Retention of spin probe VII in O-alkylated Beulah-ZAP APCS lignite after swelling with toluene spiked with pyridine.

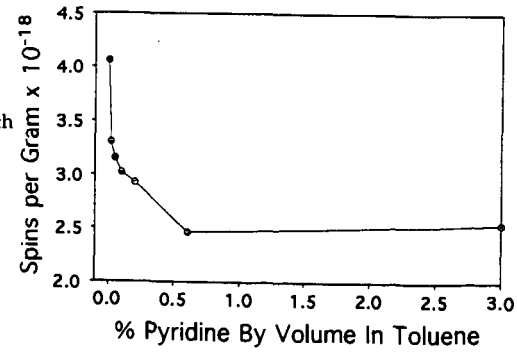

Figure 5
Retention of spin probe VII in Wyodak-Anderson sub-bituminous APCS coal after swelling with toluene spiked with pyridine.

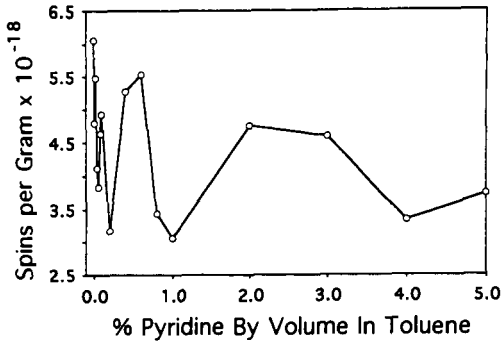

Figure 6
Same as Figure 5 except with O-alkylated Wyodak-Anderson coal.

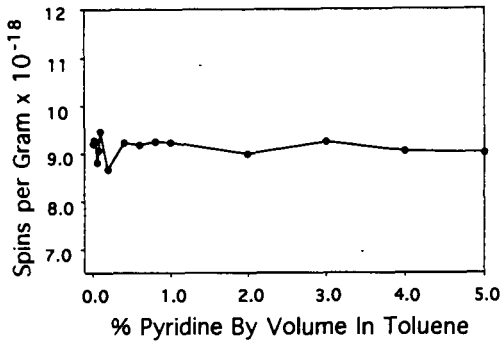

Figure 7
Same as Figure 5 except with Lewiston-Stockton high volatile bituminous APCS coal.

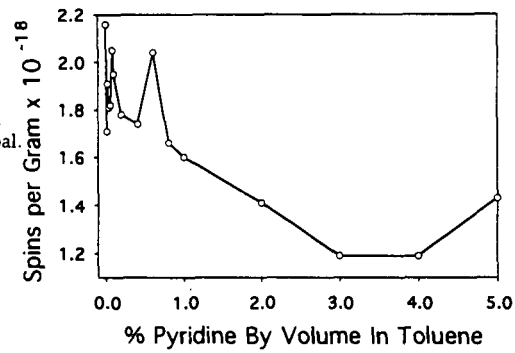

Figure 8
Same as Figure 5 except with O-alkylated Lewiston-Stockton coal.

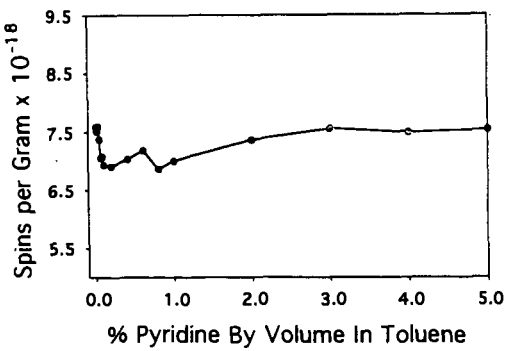

THE CHARACTERIZATION OF FLUORINATED GRAPHITE

Edward W. Hagaman, Andrei A. Gakh and Brian K. Annis

Chemical and Analytical Sciences Division
Oak Ridge National Laboratory
P.O. Box 2008
Oak Ridge, Tennessee, 37831-6201

Keywords: Fluorine, X-ray photoelectron spectroscopy, atomic force microscopy

INTRODUCTION

The characterization of solid fossil fuels by chemical and spectroscopic methods requires extensive modelling in less complex systems for chemical proof of principle and technique development. In previous work coal was fluorinated with dilute, elemental fluorine under conditions that were expected to lead to materials that contain only fluoromethine moieties. The solid state, cross polarization/magic angle spinning (CP/MAS) ^{13}C NMR spectra of the fluorinated coal are complex, indicating more chemical modification than originally anticipated.

Our goal in the coal derivatization was to sequentially increase the severity of the fluorination and observe by ^{19}F and ^{13}C NMR the type and concentration of fluorine functional groups created in the coal milieu. This requires the ability to discriminate between C, CF, CF_2, and CF_3 moieties in the coal matrix. The task can be accomplished by implementing the spectral editing technique of Wu and Zilm[1] which distinguishes different kinds of carbon resonances, especially CH and CH_2 resonances. These experiments utilize cross polarization (CP) and polarization inversion (PI) to effect the discrimination. Our version of this experiment is a triple resonance experiment that incorporates ^{19}F-^{13}C CP, PI, and simultaneous ^{1}H and ^{19}F dipolar decoupling.

In order to evaluate the elemental fluorine chemistry in a matrix simpler than coal, fluorinated graphite was prepared. X-ray photoelectron spectroscopy (XPS) was used to characterize the surface species, i.e., count CF, CF_2 and CF_3 species. These well-characterized samples are the models we will use to test the NMR editing experiments. The XPS and atomic force microscopy (AFM) data on the first fluorinated graphites we have prepared are reported in this paper.

EXPERIMENTAL

Fluorination of Graphite. Highly oriented pyrolytic graphite (HOPG), 0.7 g, was ground in a ceramic mortar and placed in a 19 mm quartz tube. The tube was placed in an oven and the powder was dried in a flow of nitrogen (2-3 cm^3/min) at 250 °C for 2 h. The flow of nitrogen was replaced by pure fluorine (2 cm^3/min) over 30 min and fluorination was continued for an additional 20 h at 250-260 °C. At the end of the fluorination the fluorine gas stream was replaced with nitrogen and the sample was cooled. The nitrogen purge was continued for 2 h at room temperature. The sample was then transferred to a glass vial under nitrogen and flushed for an additional 2 min to displace traces of air and moisture. The visual appearance of the sample did not change significantly during the fluorination.

A second sample of HOPG, a single platelet with dimensions of 0.4 x 0.8 x 0.05 mm, was subjected to the fluorination under similar conditions for 21 h. The isolated platelet was stored under nitrogen in a glass vial. No change in the visual appearance of the sample was found and the weight loss of the sample during the fluorination was lass than 0.1%.

Atomic Force Microscopy (AFM). The atomic force microscope used in this investigation was a Digital Instruments Inc., Nanoscope II which uses a Si_3N_4 tip attached to cantilever to scan the surface. Tip motion is monitored by light deflected from the cantilever.

X-ray Photoelectron Spectroscopy (XPS). The XPS data were acquired on a Kratos Ltd. spectrometer The energy analysis chamber is a Kratos Axis system designed for general purpose XPS using a small spot lens. In this instrument the standard orientation of the detector is orthogonal to the sample surface. The data reported in Table 1. are from experiments performed in this configuration. The spectrum of the HOPG platelet was also recorded after tilting the platelet 35° from its normal orientation to the detector. The x-ray source used in this work was an Al Kα monochromator (15 kV, 60 ma maximum). A UV flood lamp was used to charge

neutralize the fluorinated HOPG powder sample. The pass energy of the HOPG platelet was 20 eV. The pass energy of the HOPG powder was 40 eV. The instrument was calibrated to Au 4f at 84.0 eV. The graphitic component of the C 1s peak was observed at 284.5 eV for the conductive HOPG platelet, as expected. The graphitic component of the powdered, nonconductive HOPG was assigned this same value.

RESULTS AND DISCUSSION

Figure 1 compares the AFM image of the surface of a platelet of HOPG prior to fluorination (a) with the surface after fluorination (b). The images depict a 250 x 250 nm surface area (note the expanded z scale). At the resolution used for these measurements the graphite surface is flat. The surface after fluorination exhibits random rutted or channeled features with dimensions on the order of tens of nm. Features are etched into the surface to a depth of ca 1 nm. Since the XPS results discussed below are compatible with the surface functionality being CF_x moieties, the surface features shown in Fig. 1b likely represent fluoridation of the surface with loss of surface carbon extending to a depth equal to several graphite layers.

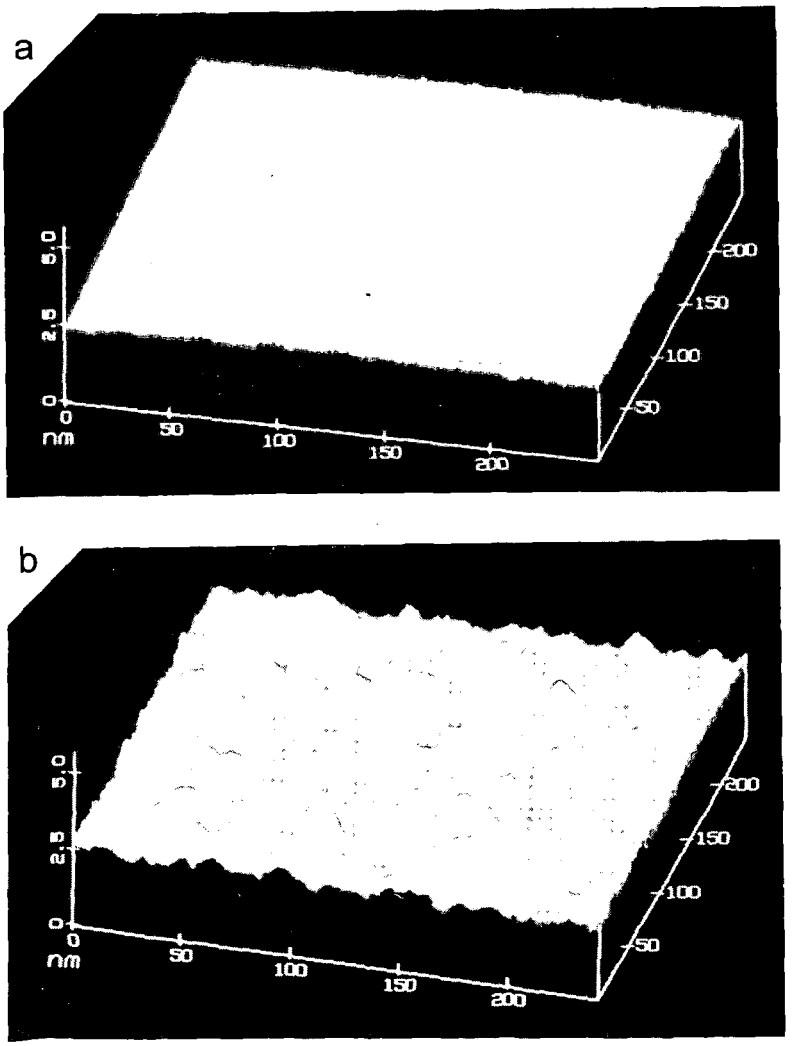

Figure 1. Atomic Force Microscopy Images of a: HOPG and b: Fluorinated HOPG

Two fluorinated samples were analyzed by XPS: the first is the sample of HOPG used for the AFM measurements shown in Fig. 1b; the second was a fluorinated graphite powder described in the experimental. Qualitative XPS survey scans showed only carbon, fluorine and oxygen on both surfaces. Figures 2 and 3 show the C 1s, F 1s and O 1s spectra of the platelet and powder sample, respectively. The powder had to be charge neutralized, which may account for some of the increase in peak width. Each spectrum has been band fitted, showing the different components which comprise the spectrum. Table 1. lists the atomic concentrations, peak position and width of each component.

Table 1. XPS Data for Fluorinated Platelet and Powdered HOPG

Platelet HOPG			
XPS Peak	Binding Energy eV	Peak Width, eV	Atomic Conc., %
C 1s 1	284.5	0.6	49.8
C 1s 2	285.7	1.42	6.7
C 1s 3	287.0	2.03	4.4
C 1s 4	289.8	1.55	13.0
C 1s 5	291.8	1.70	5.0
C 1s 6	294.1	2.49	2.6
F 1s 1	688.6	1.50	15.7
O 1s 1	532.1	2.28	0.9
O 1s 2	535.1	1.45	2.0
Powdered HOPG			
C 1s 1	284.5	2.17	33.2
C 1s 2	285.7	1.93	0.6
C 1s 3	287.0	1.48	3.5
C 1s 4	289.2	2.37	24.4
C 1s 5	292.0	2.30	1.8
C 1s 6	293.9	2.65	0.2
F 1s 1	686.1	3.05	5.5
F 1s 2	688.1	2.49	24.6
O 1s 1	532.9	3.95	5.2
O 1s 2	534.8	1.51	0.9

The C 1s peak at 284.5 eV is from pure graphite. Bonding an electronegative atom to carbon shifts the C 1s peak to higher binding energy. The second major carbon peak at 289 eV represents CF and a shift at approximately 292 eV represents CF_2. The C 1s peak at 294 eV is attributed to CF_3.[2] The CF_2 moiety has an F 1s peak at ca 690 eV; the CF F 1s peak shifts to approximately 689 eV. The assignments of chemical shifts to bonding type indicated here are from XPS data bases.[3]

The spectra indicate that the surface of both materials has been fluorinated. The dominant peak in the carbon spectrum for both samples is at 284.5 eV and is due to graphitic carbon. The majority of the fluorine is in the form of CF. Both the C 1s and the F 1s peaks corresponding to CF are approximately equal in both samples, supporting these assignments. There are minor components in the C 1s spectrum which indicate CF_2 and CF_3. The XPS analysis was repeated for the platelet sample of fluorinated HOPG after tilting the platelet 35°. This orientation biases the sensitivity of the analysis to the surface layer relative to the underlayers. An increase in the F 1s and the C 1s of the CF component relative to the graphitic C 1s peak is observed, showing fluorine to be concentrated on the surface.

The fluorinated HOPG platelet has a 2.6:1 ratio of $CF:CF_2$. The ratio in the powder is 13.6:1. The platelet has more comparable concentrations of CF_2 and CF functional groups (desirable in an NMR test sample) but a low absolute concentration of all CF species that may make the NMR analysis difficult. The XPS correlation between the fluorinated platelet and powder reveals the same qualitative chemistry occurs in both materials. Attempts to increase the CF_2 component in the powder are in progress.

ACKNOWLEDGEMENTS

This research was sponsored by the Division of Chemical Sciences and the Division of Material Sciences, Office of Basic Energy Sciences, U.S. Department of Energy, under Contract No. DE-AC05-840R21400 with Martin Marietta Energy Systems, Inc.

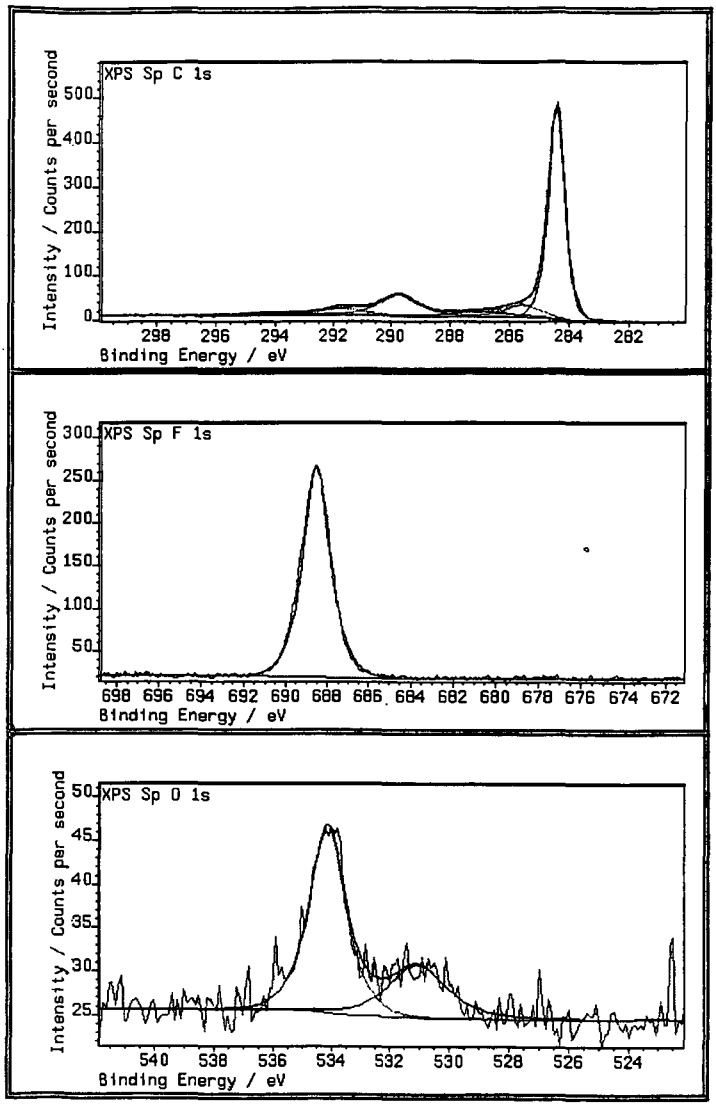

Figure 2. Carbon, Fluorine, and Oxygen X-ray Photoelectron Spectra of a Fluorinated HOPG Platelet.

REFERENCES

1. Wu, X.; Zilm, K. W. *J. Magn. Reson. Ser. A*, **1993**, *102*, 205.

2. Cox, D. M.; Cameron, S. D.; Tuinman, A.; Gakh, A.; Adcock, J. L.; Compton, R. N.; Hagaman, E. W.; Kniaz, K.; Fischer, J. E.; Strongin, R. M.; Cichy, M. A.; Smith III, A. B. *J. Am. Chem Soc.*, **1994**, *116*, 1115.

3. (a) Moulder, J. F.; Stickle, W. F.; Sobol, P. E.; Bomben, K. D. "Handbook of X-ray Photoelectron Spectroscopy" Jill Chastain, Ed., Perkin Elmer Corp. 1992. (b) "NIST Standard Reference Database 20" entitled "NIST X-ray Photoelectron Spectroscopy Database" ver. 1.0, compiled by C. D. Wagner, Surfex Co., Program written by D. M. Bickman, copyright 1989.

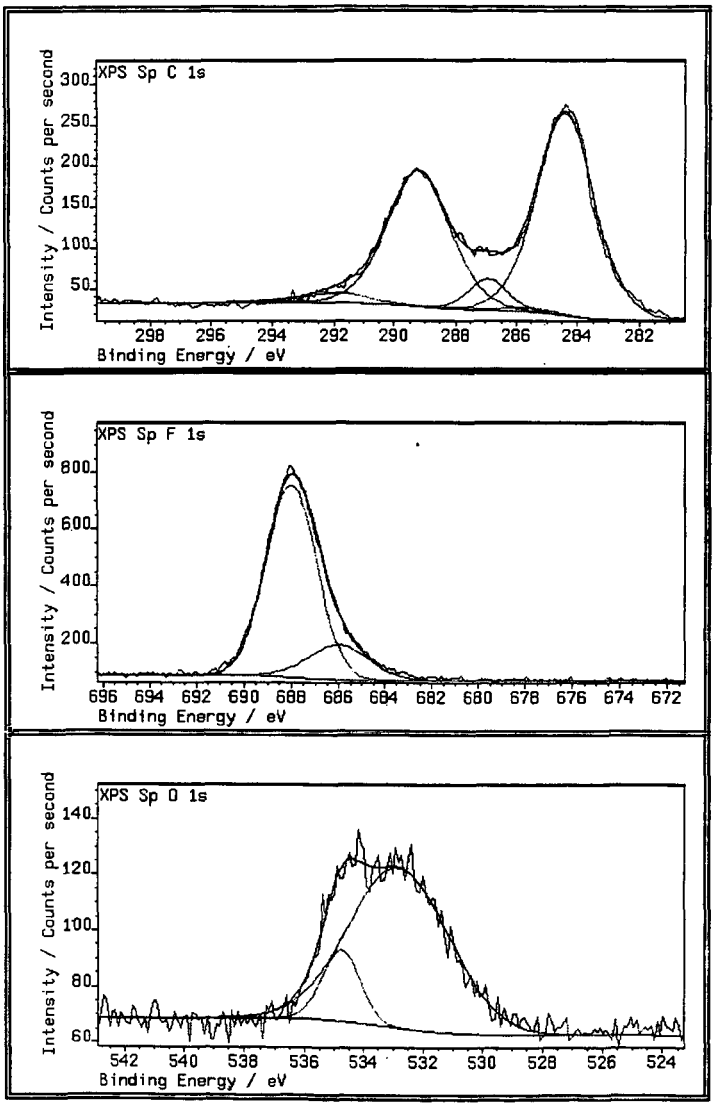

Figure 3. Carbon, Fluorine and Oxygen X-ray Photoelectron Spectra of a Fluorinated HOPG Powder.

CHARACTERIZATION OF CARBON MATERIALS USING QUANTITATIVE OPTICAL MICROSCOPY

J. C. Crelling and D. Bensley

Geology Department, Southern Illinois University
Carbondale, IL 62901

Keywords: reflectance, density gradient centrifugation, carbon density

INTRODUCTION

Research which was directed towards the characterization of ultra-fine coal has been utilized in the analysis of vitrinite and high-temperature carbon materials. Equipment and procedures have been developed which permit full reflectance characterization on particles as small as 1.5 micrometers diameter using rotational polarization techniques. Microstructural characterization using optical methods in conjunction with density gradient centrifugation (DGC) have been employed to assess carbon density within its spacial context. Using reflectance mapping techniques with apparent density data obtained from DGC processing, reflectance "images" recorded on the sample can be correlated to reflectance data obtained from DGC fractions. By comparing reflectance values associated with specific density fractions to reflectance values obtained from specific areas within the mapped reflectance image the spacial distribution of reflectance and density can be determined for a complex heterogeneous material.

PROCEDURES

Samples are processed for both petrographic examination and DGC processing. Petrographic samples are processed using standard metalurigical mounting and polishing techniques used for vertical white-light observation. Reflectance data is obtained using a Leitz MPVIII compact microscope modified for rotational polarization reflectance. The modified optical configuration uses the same components that are employed in conventional reflectance. The only variance with convention is the adaptation of the polarizer to permit rotation through 360 degrees, instead of the standard fixed 45 degree orientation, and the use of a fixed stage position during analysis. All polarizer rotation, data acquisition and data processing functions are computer controlled using a 80386/20 mHz computer. Microscope interfacing is made via a gear coupled polarizer and stepping stage, stepping stage controller and IEEE bus. A separate A/D converter controls data acquisition. Optical correction is made on all measurements to remove the effect of residual polarization within the vertical illuminator and transmission optics. Without this correction a pronounced anisotropic signal, induced by rotating one polarizer against a "stationary polarizer" within the light path, would be recorded. This "stationary polarizer" should not be confused with an actual optical component but represents the optical effect caused by residual polarization within the vertical illuminator. Sequential measurements are made across samples with both the maximum reflectance and the spacial orientation of the point stored within a data file.

DGC processing requires samples to be crushed to a particle size $>15\mu m$. The sample is then dispersed in a brig 35 solution to obtain a uniform suspension. The suspension is applied to the top of a vessel filled with an aqueous sodium polytungstate gradient ranging from 1.0 to 2.2 g/mL. The vessel is centrifuged forcing particles to their appropriate density level. After centrifugation the vessel is fractionated by pumping, filtering and weighing the resulting density layers from the density gradient. The resulting density profile accurately represents the density composition of the samples constituents.

DISCUSSION

Figures 1 and 2 illustrate the results obtained from sequential reflectance measurements. The area boxed out with squares represent the point locations where individual reflectance measurements were made. Figure 1 illustrates the results obtained from a vitrinite maceral in coal while figure 2 illustrates reflectance mapping of a C-C composite sample. Figures 3 and 4 represent DGC profiles of the coal sample and C-C composite sample respectively. The indicated points on the DGC profile indicate measured fractions with the average fraction density and reflectance values indicated. Figures 5 and 6 illustrate the spacial density relationships calculated for the "mapped" telocollinite and C-C composite samples respectively.

Figures 1 and 5 illustrate the level of heterogeneity present in vitrinite macerals in both reflectance and density properties. Figures 2 and 6 show the effects of "stress" graphitization in graphitized phenolic pitch. In both cases heterogeneity of the carbon can be quantitatively evaluated using combined DGC/Ro mapping techniques.

CONCLUSIONS

Both reflectance mapping and DGC analysis can be used to quantitatively assess carbon heterogeneity. By combining these analysis the spacial distribution of reflectance and density can be determined enabling assessment of physical properties within a morphological context.

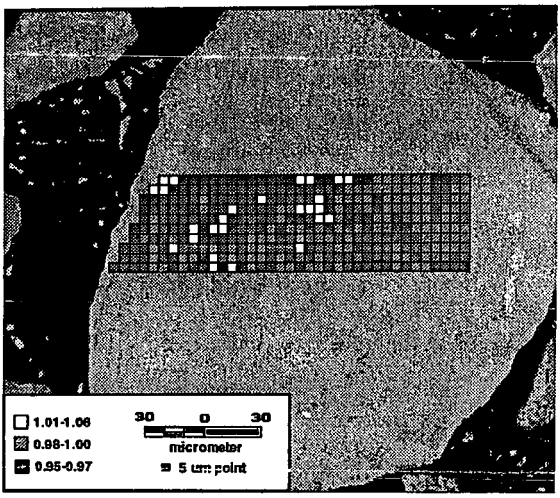

Figure 1: Reflectance distribution as measured on a apparently homogeneous vitrinite maceral.

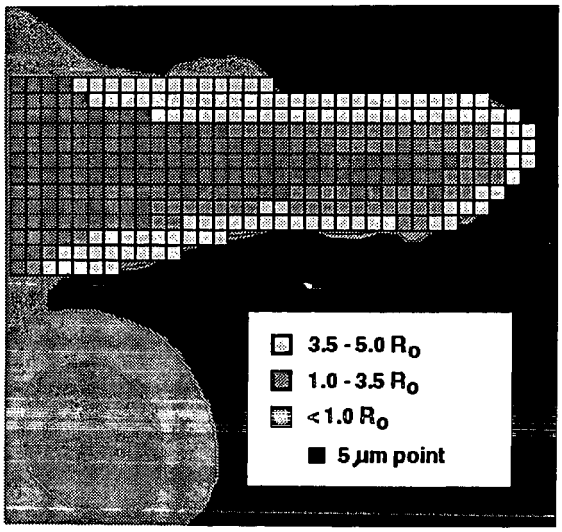

Figure 2: Reflectance distributions measured on a C-C composite sample.

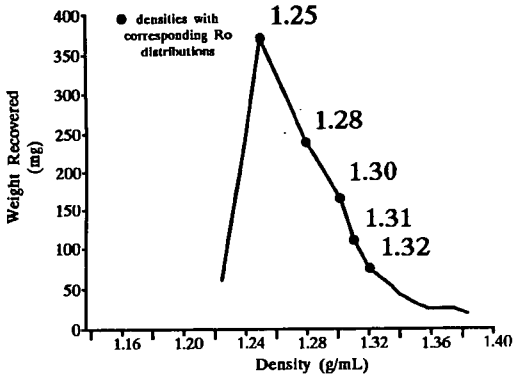

Figure 3: DGC profile of coal sample from which a single vitrinite maceral was mapped (figure 1).

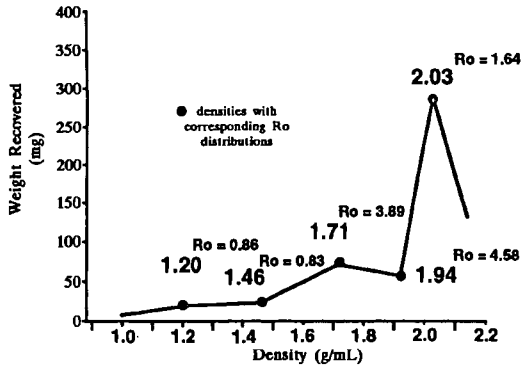

Figure 4: DGC profile of a C-C composite sample from which a single area was mapped (figure 2).

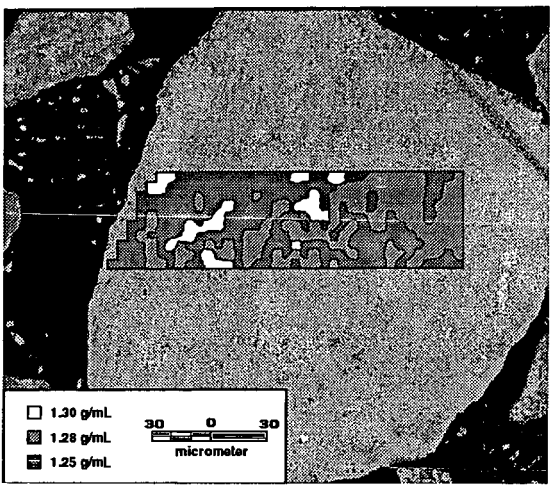

Figure 5: Density correlations made on the mapped vitrinite maceral using combined reflectance mapping/DGC techniques.

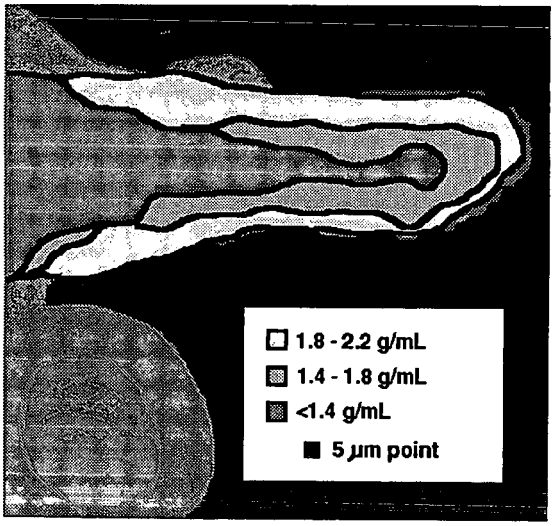

Figure 6: Density correlations made on the mapped C-C composite area using combined reflectance mapping/DGC techniques.

COUPLED LC-GC TECHNIQUES FOR THE CHARACTERISATION OF PAC IN FUEL AND ENVIRONMENTAL SAMPLES

Alastair C Lewis[1], Stuart C. Mitchell[1], Robert E Robinson[2] and Keith D Bartle[1]

[1]School of Chemistry, University of Leeds, Leeds, UK LS2 9JT.
[2]On leave from Triton Analytics Corp., Houston, Texas 77084.

Keywords: Polycyclic aromatic compounds, Coupled liquid chromatography - gas chromatography, mass spectrometry, atomic emission detection.

INTRODUCTION

Exposure to polycyclic aromatic hydrocarbons has long been identified as of considerable environmental concern[1]. Originating from both natural and anthropogenic sources, many PAC exhibit significant carcinogenic and mutagenic[2,3] properties which are critically dependent on structure. Although PAC occur naturally in fossil fuels, the predominant contributions to environmental pollution are caused by the combustion of organic fuels. Recent studies have identified characteristic source fingerprints for coke ovens, diesel and gasoline engines, road tunnels and wood combustion emissions[4]. However, despite the wealth of literature on the identification of parent polycyclic aromatic hydrocarbons[5,6] and polycyclic aromatic heterocycles[7,8], little is known about the composition and concentration of the many substituted and heteroatom-containing PAC that are produced either by combustion processes or as products of atmospheric reactions[9] and are potentially more of a health risk than parent PAH or are simply unknown[3,10]. Due to the complexity of fuel and environmental samples which contain many hundreds of aliphatic, aromatic and polar compounds, multidimensional chromatographic methods which provide separation by virtue of chemical class (group-type) or by molecular mass can greatly simplify the identification of individual PAC. LC-GC has been used previously for quantitative analysis of PAH in diesel exhaust emission extracts[11,12] urban air particulates[13,14] and other fuel related applications[15]. In this study, on-line coupled LC-GC techniques have been investigated for the identification of trace level PAC in a range of fuel feedstocks, combustion products and urban air particulate extracts. Positive identification of individual PAC was obtained by direct coupling of LC-GC to mass spectrometry and atomic emission detection.

EXPERIMENTAL

Samples: An urban air particulate sample was collected by high volume air sampler (Graseby Anderson, UK) drawing air at a rate of $0.4m^3$ through a quartz microfibre filter (Whatman UK), using a previously described method[14]. The filter was placed in an extraction vessel at 110°C and was extracted with CO_2 and 10% toluene at 400 atm, for 90 minutes using an ISCO SFX 2-10 extractor with Model 100D and 260D syringe pumps. Pressure was maintained within the cell using a 25 mm i.d. x 10 cm length of fused silica capillary tubing. The extract was collected in 3 ml of dichloromethane, which was subsequently reduced to dryness and re-dissolved in *ca.* 2 ml *n*-hexane, for compatibility with the subsequent normal phase LC step. Previous extractions of standard dust samples (NIST SRM-1649) have showed that Soxhlet equivalent or better recoveries were obtained for all certified PAH; the results have been reported earlier[14]. A typical UK diesel sample was used for a preliminary investiagtion by LC-GC-AED.

LC-GC-MS Analysis: A Carlo-Erba Dualchrom 3000 Series LC-GC instrument (Fisons, Italy), consisting of two HPLC syringe pumps, a UV detector, on-column interface, early solvent vapour exit and GC was coupled via a heated transfer line to a Finnigan Mat ion trap detector mass spectrometer (ITD/MS)[10,13]. HPLC separation was performed using a 100 mm x 2 mm i.d. column containing 5 µm 'Spherisorb' silica (Phase Separations, UK) packing. Pentane and dichloromethane were used as the mobile phase, with a stepped polarity gradient. Sample injection was via a 20 µl loop injector. LC separation was monitored by UV detection (254 nm), and was recorded by chart recorder. From the detector the eluent passed into the on-column interface which in stand-by position routed the flow through to waste. On transfer a pneumatically actuated valve was used to switch the flow through a fused silica capillary column which transfers the sample onto the retaining pre-column. GC separation was performed on a 25 m x 0.32 mm i.d. fused silica capillary column coated with a 0.33 µm film of dimethyl siloxane (BPX-5 SGE, UK). The column inlet was connected by means of a press-fit connector to a 4 m section of the separation column which was used as a retaining pre column. The pre-column was connected to 10 m x 0.53 mm i.d. uncoated fused silica retention gap, deactivated by phenyldimethyl silylation. This connection also includes an early solvent vapour exit for the evaporation of mobile phase. The exit has a twofold advantage; firstly reducing the time required

to evaporate the mobile phase and, more importantly minimising the amount of mobile phase entering the detector(s). The partially concurrent solvent evaporation rate at 65°C for a 50:50 *n*-pentane : dichloromethane (%v/v) mobile phase using the solvent vapour exit was determined to be 100 µL/min at an inlet carrier gas pressure of 120 kPa. With an LC solvent flow rate of 100 µL/min, the helium carrier gas was essentially free of solvent contamination prior to the ion trap detector (ITD). On completion of the sample transfer via on column interface, the fused silica capillary column was removed from the GC inlet, to eliminate possible vaporisation of the polyamide coating and subsequent bleed into the carrier gas at high oven temperatures. Transfer of eluent from the GC oven to the ITD/MS for detection was via a heated transfer line at 250°C. Mass scans were performed at 1 scan/sec with a mass range of 50-350 amu.

LC-GC-AED Analysis: Normal phase HPLC was performed using an in-house built LC system[12]; a Brownlee Micro gradient dual syringe HPLC pump (Brownlee Labs, Santa Clara, USA), a Rheodyne 7040 injection valve (Berkley, USA) with a 20 ml sample loop and a 100 mm x 2 mm i.d. column packed with 5mm 'Spherisorb' silica (Phase Separations, UK). Detection was by means of a Uvikon 735LC UV detector (Kontron Instruments, UK) equipped with a 1 ml flow cell and operated at a wavelength of 254 nm. Eluate passes from the UV detector entering a ten-port valve fitted with a pneumatically activated valve interface (Valco Instruments Co., Inc., Houston, Texas, USA). Selected fractions were transferred to a Hewlett Packard 5890 Series II GC via a 350 µl loop interface and a short length of deactivated silica capillary. The speed of concurrent solvent evaporation optimised by venting through an early solvent vapour exit prior to the pre-column and analytical column. Following solvent evaporation the solvent exit was closed. A Hewlett Packard 5921A Atomic Emission Detector (AED) was used for multi-element detection. Transfer of the eluate from the GC was via a heated transfer line (320°C) into the cavity of the AED, which houses a microwave induced helium plasma (MIP).

RESULTS AND DISCUSSION

The LC solvent program developed, provided the initial elution of essentially all polycyclic aromatic hydrocarbons as a single unresolved peak 4 mins into the analysis. Polarity differences appear to be the major basis for class separation between the other classes of PAC present in the samples. Alkylated PAH species such as methyl chrysenes elute with the parent PAH compounds and require a less polar mobile phase to separate them from the bulk of components, therefore using a LC mobile phase of 15% DCM and 85% pentane, the parent and alkylated PAH species could be separated into distinct ring size fractions, and the ring size fractions produced can then be transferred directly to MS. Whilst the LC stage provides much improved PAC type selectivity the separation into particular groups eg parent, heterocycles, nitrated, oxygenated etc, is not totally complete since there is some polartity overlap of species in different groups. For example, large parent PAH compounds such as coronene, have similar retention characteristics as 2 ring nitro-PAC species.

Separation /Identification of Alkylated Polycyclic Aromatic Hydrocarbons: For the urban air particulate extract using LC-GC-MS, alkylated pyrene and chrysene compounds were found to make up the majority of alkylated substituted PAH in the air particulate, in the form of methyl/dimethyl/ethyl compounds. Using a 15% DCM and 85% pentane a ring size fraction of parent and alkylated PAH corresponding to the benz[a]anthracene/chrysene group was transferred to the MS. This separation is of particular interest in view of the marked difference in carcinogenic activity of methyl chrysenes.

Separation/Identification of Nitro-Polycyclic Aromatic Compounds: Most nitro-PAC produce an abundant molecular ion peak (M^+) and several characteristic fragments: $(M\text{-}NO)^+$ and $(M\text{-}NO_2)^+$. The fractions analysed were examined for the presence of mononitro-, dinitro-, methyl-nitro, and dimethyl-nitro PAC. 9-nitroanthracene (mass 223) and 1-nitropyrene (mass 247) were identified by comparison with GC retention times and mass chromatograms of reference compounds. An isomer of nitroanthracene was also identified. Derivatives of nitrated PAC (eg. alkyl or hydroxyl) are more difficult to identify via mass spectrometry, since they fragment differently from the mono-substituted nitro-PAC compound. No compounds of this type were identified have been identified to date by this technique, however attempts are continuing to develop a LC-GC-MS procedure for this analysis. Nitrated PAC are considered to be the most carcinogenic group of PAC[3], and their formation and atmospheric reactions are little understood, although there is some evidence that some are formed as artifacts of sampling by reaction with atmospheric OH followed by NO_2 attack[16,17].

Separation/Identification of Oxy-Polycyclic Aromatic Compounds: Oxygenated PAC are considered to be as carcinogenic as many of the parent PAH due to their similarity in structure and properties to the products of the PAH metabolic process. The metabolites formed can

decompose via triol intermediates which form adducts with DNA which then cause carcinogenic or mutagenic effects[3]. Detection of oxy-PACs was greatly simplified by their separation as a class from the nitro PACs. The identification of 9-anthraldehyde, 9-phenanthraldehyde and 9-fluorenone was confirmed by co-injection of standards. 9,10-anthracenedione (anthraquinone), plus its mono and di-substituted methyl derivatives which were all identified as being present in an urban air particulate extracts. A summary of the separation of urban air particulate extract by HPLC is shown in Table 1. Quinone-PAC are thought to be formed in the atmosphere from parent PAH by reaction with singlet molecular oxygen[18,19], formed either via a sensitization mechanism[20], or via ozonolysis[21].

Separation/Identification of Polycyclic Aromatic Heterocycles: The coupling of LC-GC separation with the Hewlett Packard atomic emission detector has vastly improved the ability of the instrument to speciate trace level heterocyclic PAC in complex hydrocarbon samples. Fractionation by LC enables interference from co-eluting hydrocarbons and more polar species to be eliminated, thus allowing sulphur (181 nm), nitrogen (174 nm) and oxygen (777 nm) PAC rich fractions to be transferred directly to the GC. For a typical diesel a series of substituted dibenzothiophenes, carbazoles and quinones were readily identified from the transfer of discrete LC fractions. For each element, the response was significantly enhanced due to increased sample concentration and the reduction in the formation of molecular species in the plasma. Indeed, the improved sensitivity of the detector operating within the LC-GC system, particularly for nitrogen has increased the reliability of elemental formulation.

CONCLUSIONS

Both LC-GC techniques provide an excellent technique for the rapid and much improved separation and identification of polycyclic aromatic compounds in fuel and environmental samples. Furthermore, the combination of elemental and compositional information from AED with molecular and structural information from MS offer a powerful approach to speciation of complex sample matrices. The increased compound-type selectivity in the primary separation improves the detection of very level species, by coupling on-line advantages with reduced sample complexity at the final separation stage. The limitations of systems are the individual detection capabilities of the mass spectrometer and atomic emission detector and the solubility of some of the most polar PACs in a solvent compatible with normal phase HPLC. However, both techniques so far have provided valuable insight into the source, formation and distribution of such compounds pre- and post combustion.

REFERENCES

(1) United States National Academy of Sciences. *Particulate Polycyclic Organic Matter.* Committee on the Biological Effects of Atmospheric Pollution, National Research Council, National Academy Press, Washington DC, USA.,1972.

(2) Bridford K, J Finklea, J.Wagoner, J.Moran, P.Coplan (Eds.). Human exposure to polynuclear aromatic hydrocarbons. In: R Freudental and P.Jones (Eds.), *Polynuclear Aromatic Hydrocarbons:Chemistry, Metabolism and Carcinogenesis.* Rave Press, New York, 1976, Vol. I., 319-324.

(3) Merschundermann V., Mochayedi S., Kevekordes, S., Kern, S., Wintermann F. *Anticancer Res.*1993, **13**, 2037-2043.

(4) Khalili, N.R., Scheff, P.A., Holsen, T.M., *Atmospheric Environment*, 1995, **29**, 4, 533-542.

(5) Lee M.L., Novotny N.V., Bartle K.D., *Anal. Chem.*, 1976, **48**,1566-1572.

(6) Grimmer G., in *Handbook of Polycyclic Aromatic Hydrocarbons*, A.Bjorseth (Ed.) Marcel Dekker, Inc New York. 1983, **Vol.1**, 154-156.

(7) Palmer, S.R., Kruge, M.A., Hippo, E.J., Crelling, J.C., *Fuel*, 1994, **73**, 1167-1172.

(8) Xiaoling, M., Sakinishi, K., Mochida, I., *Ind. Eng. Chem. Res.*, 1994, **33**, 218-222.

(9) Broddin G., Cautreels W., Cauwenberghe K.A., *Atmos. Environ.* 1980, **14**, 895-910.

(10) Lee M.L., Novotny N.V., Bartle K.D., *Analytical chemistry of polycyclic aromatic compounds.* Academic Press (London) Ltd 1981, 441-451.

(11) Davies I.L., Raynor M.W., Williams P.T., Andrews G.E., Bartle K.D. *Anal. Chem.* 1987, **59**, 2579-2583.

(12) Kelly G.W., Bartle K.D., Clifford A.A., Robinson R.E., *J. High Resol. Chromatogr.* 1992, **15**, 526-530.

(13) Kelly G.W., Bartle K.D., Clifford A.A., Scammells D., *J. Chromatogr. Sci.* 1993, **31**, 73-76.

(14) Lewis A.C., Kupiszewska D., Bartle K.D., Pilling M.J., *Atmos. Environ.* 1995 **29**, .

(15) Kelly G.W, Bartle K.D., *J. High Res. Chrom.* 1994, **17**, 390-397.

(16) Later D.W. *The handbook of polycyclic aromatic hydrocarbons.* 1985 **Vol. 2**. pp 265-349. Bjorseth A and Ramdahl T (Eds) Marcel Dekker Inc. New York.

(17) Atkinson R., Lloyd A.C., Darnall K.R., Winer A.M., Pitts J.N., *Advances in Photochemistry* 1980 **Vol. 11**. Pitts J.N, Hammond G.S, Gollnick K. (Eds), Wiley, New York.
(18) Konig J., Balfanz E., Funcke, W., Romanowski, T., *Polynuclear aromatic Hydrocarbons: Mechanisms, Methods and Metabolism* 1985 pp 739-740 M. Cooke and A.J. Dennis (Eds), Battelle Press, Columbus, Ohio.
(19) Lane D.A., Katz, M., *Environ. Sci. Technol.* 1977, **8**, 137-154.
(20) Van Cauwenberghe K.A., *The handbook of polycyclic aromatic hydrocarbons.* 1985 **Vol. 2**. pp 351-384. Bjorseth, A., and Ramdahl, T., (Eds) Marcel Dekker Inc. New York.
(21) DeMore, W.B., Raper O.W., *J. Phys. Chem.* 1966, **44**, 1780-1785.

Table 1. Separation of Urban Air Particulate Extract by HPLC.

Time Interval / min	Isolated Class / Compound(s)[a]
0 - 2.7	Solvent[b] Aliphatic compounds[b]
2.7 - 3.7	Polycyclic aromatic hydrocarbons[b] Alkylated PAH[b]
3.7 - 5.5	9-Nitroanthracene[b] Nitroanthracene isomer[b] 1-and 2-Nitronaphthalene 1-Nitropyrene[b]
5.5 - 6.5	2-Nitrofluorene[b]
11.5 - 14.0	9-Anthraldehyde[b] 9-Phenanthraldehyde[b] 2-Naphthaldehyde 9-Fluorenone[b]
14.0 - 17.0	9,10-Anthracenedione[b] Benzanthrone[b] 7,8 Benzoquinoline[b] benz[a]anthracene 7,12-dione[b] 2-Methyl-9,10-anthracenedione[b] 2-Fluorenealdehyde[b] 2-Nitro-9-fluorenone[b,c] 9-Anthracenone[b]
17.0 - 19.0	2-Methyl-1,4-naphthoquinone
19.0 - 21.0	1,4- Naphthoquinone[b]
24.0 - 25.0	Acenaphthenequinone[c]

[a]LC elution order based on reference standards
[b]Compounds identified in Leeds urban air particulate extract
[c]Compound only partially soluble in *n*-hexane.

$\delta^{13}C$ GC-IRMS CHARACTERISATION OF EXTRACTABLE AND COVALENTLY-BOUND ALIPHATIC HYDROCARBONS IN PETROLEUM SOURCE ROCKS TO REVEAL COMPOSITIONAL FRACTIONATION EFFECTS.

Gordon D. Love(1), Colin E. Snape(1), Anthony E. Fallick(2) and Christopher Taylor(2).
(1) University of Strathclyde, Dept. of Pure & Applied Chemistry, Thomas Graham Building, 295 Cathedral St., Glasgow G1 1XL, UK.
(2) Scottish Universities Research & Reactor Centre (SURRC), East Kilbride, Glasgow G75 OQU, UK.

Keywords : stable isotope geochemistry, kerogen formation, selective preservation .

INTRODUCTION

The structural elucidation of sedimentary fossil organic matter at a molecular level remains a challenging task, on account of its heterogeneous, largely insoluble nature. An elaborate sequential extraction/degradation scheme to differentiate between molecular alkanes (both easily extractable, and those physically-trapped or clathrated within the macromolecular structure) and alkyl moieties covalently bound within the kerogen network, was recently devised by the Strathclyde group. Briefly, the scheme incorporates exhaustive solvent extraction with dichloromethane (DCM) followed by pyridine to remove physically trapped material and then a mild batch hydrogenation step is performed to cleave weak heteroatomic bonds (principally ester, thioether and possibly ether linkages). The key and final stage in this procedure to release strongly-bound hydrocarbons is pyrolysis at high hydrogen pressures (up to 15 MPa, about 150 atmospheres) which is known as hydropyrolysis. Thermolysis in a high hydrogen pressure (reducing) environment eliminates the problem of low yields often associated with the use of sterically-bulky chemical reagents and limits the extent of retogressive, char-forming chemistry. Hydropyrolysis gives rise to overall carbon conversions approaching 100% for Type I and Type II kerogens (these have higher H/C ratios than coals, which are classified as Type III kerogens on the basis of elemental composition) with low hydrocarbon gas yields.

The attractiveness of the scheme lies in the fact that it recognises that the structure of sedimentary organic matter is three dimensional, comprising an organic macromolecular network (kerogen) in which material is trapped with differing degrees of mobility. The increase in severity of the reaction conditions as the sequence proceeds, produces a series of soluble products whose constitution is determined by the strength of association of structural units. The differences in the yield and distribution of selected classes of aliphatic hydrocarbons (such as biomarkers) produced from sequential degradation of a series of vitrinite concentrates [1] and petroleum source rocks [2] are reported elsewhere.

The carbon isotopic signature of the bulk organic matter and individual molecules can be helpful in determining the types of organisms contributing to sediments. Stable carbon isotopic analysis of whole oils, source rock kerogens and bulk hydrocarbon fractions has been used for several years to aid source-oil and oil-oil correlations.[3] However, since kerogens are usually composed of components derived from different biological sources, bulk carbon measurements by conventional isotope mass spectrometry (following combustion) yields only a composite value. Thus, the complexity of fractionation processes and the information they can convey may be hidden within the bulk isotopic measurements. In order to resolve these separate contributions, the isotopic compositions of individual molecular constituents must be determined. Compound-specific carbon isotope measurements became practical with the recent development of reliable computer controlled gas chromatography-isotope ratio mass spectrometry (GC-IRMS).[4, 5] In this technique, a gas chromatograph is coupled to a combustion furnace and the resultant CO_2 is subsequently continuously analysed by a stable isotope mass spectrometer. The isotopic composition of a specific compound is determined by integrating and ratioing the ion currents of masses 45 ($^{13}CO_2$) and 44 ($^{12}CO_2$) measured during the time that the compound of interest is eluting through the mass spectrometer. Similar isotopic compositions for a series of compounds often implies that they have originated from the same biological sources. Differences in isotopic composition of carbon-bearing substances are usually expressed in terms of the conventional δ-notation giving the permil deviation of the isotope ratio of a sample (sa) relative to that of a standard (st), i.e.

$$\delta^{13}C_{sa} = \left[\frac{(^{13}C/^{12}C)_{sa}}{(^{13}C/^{12}C)_{st}} - 1 \right] \times 10^3 \quad (‰, \text{PDB}) \qquad 4.1$$

The standard commonly used is Peedee belemnite (PDB), a Cretaceous marine carbonate sample, whose $\delta^{13}C$-value defines 0‰ on the δ-scale.

Biological (autotrophic) carbon fixation proceeds by a limited number of assimilatory pathways that transfer carbon dioxide (CO_2), bicarbonate ions (HCO_3^-) and carbon monoxide (CO) from the inorganic carbon reservoir to the biosphere. All pathways of autotrophic carbon fixation entail isotope fractionations of varying magnitude, which, in sum, discriminate against ^{13}C and thus lead to preferential incorporation of isotopically light carbon into cell material. C_3 plants which rely exclusively on the C_3 pathway and constitute the bulk of higher plants, range from about -23 to -34‰ with a mean close to -27‰. Higher plants and some bacteria

utilising the C_4 dicarboxylic pathway are isotopically heavier, displayng average $\delta^{13}C$-values between -12 and -14‰ and a total spread from -6 to -23‰. Compounds derived from methanotrophic bacteria exhibit an unusually light isotopic signature, typically lighter than -50‰. The isotopic signature of eukaryotic algal-derived hydrocarbons are often extremely variable from sample to sample (-8 to -35‰) despite the fact that the C_3 path operates in most algal species and are sensitive to the conditions prevailing in the aquatic environment, such as pH.[6]

In ancient sedimentary systems, the structure and stable isotope ($\delta^{13}C$) content of lipid components may still be (partially) preserved and are often diagnostic of their biological source. GC-IRMS, used in conjunction with the sequential degradation scheme, offers an attractive route to probe compositional fractionation effects that might occur in sedimentary fossil organic matter, due to differences in the mode and extent of incorporation of the different initial biological inputs. As an example, the interesting preliminary results from the sequential degradation of an immature type I oil shale (Göynük) are presented and the implications of these findings, in terms of our present understanding of kerogen formation, are discussed. Göynük oil shale (Oligocene, lacustrine, NW Turkey) represents an important world deposit, with reserves estimated at 10^9 tons, occurring in 100-150 m thick seams underlain by lignites.

EXPERIMENTAL

The bulk geochemical data for the Göynük oil shale[2] and the experimental procedure for the sequential extraction/degradation scheme[1] are reported elsewhere. The Göynük sample used in this study was highly aliphatic (liptinite rich, principally alginite) and was especially organic-rich (ash content < 25%). The aliphatic fractions produced from sequential degradation were analysed by GC-FID using a Varian 3400 gas chromatograph. Separation was achieved with a WCOT 25m fused silica capillary column (0.39mm i.d.) coated with CP-Sil 5CB (0.12µm thickness). Helium was employed as the carrier gas and a temperature program of 50°C (4 mins) to 320°C (12 mins) at 4°C min^{-1} was used. The injection and detection temperatures were both set at 320°C. Compound specific $\delta^{13}C$ measurements were carried out on aliphatic fractions using a VG Isochrom II GC-IRMS instrument. Chromatographic conditions were similar to that used for GC-FID. Urea adduction was employed to separate the straight chain aliphatic components from co-eluting branched/cyclic alkane components, prior to analysis. In general , the reproducibilitiy of multiple analyses for n-alkanes and n-alkenes was excellent (± 0.5‰), after urea adduction had been performed. $\delta^{13}C$ of bulk kerogens (carbonate-free) were also determined by conventional isotope mass spectrometry to provide a suitable reference. All delta values are reported relative to the PDB standard.

RESULTS AND DISCUSSION

DCM extraction of Göynük oil shale released 4.1% w/w of total extract (dry, ash-free basis) of which only a small amount (0.1% w/w) consisted of aliphatic hydrocarbons. The GC-FID trace of the total aliphatic fraction is shown in Figure 1 and it can be seen that the major constituents present were C_{21}, C_{23}, C_{25}, C_{27}, C_{29} and C_{31} n-alkanes (max. C_{23}). An odd carbon predominance of n-alkanes is usually associated with a continental higher plant input; although this is generally in the range n-C_{25} to n-C_{31}. The distribution observed in the case of Göynük may be explained by bacterial reworking of higher plant material during early diagenesis. This can result in the reduction of the chain length of n-alkane components while preserving a noticeable odd over even carbon number predominance. One cannot, however, rule out an input from aquatic organisms. This highlights the speculative nature of interpreting the compound distribution in geological samples. Hopanes were also visible in the GC trace. Monitoring of the m/z 191 fragmentogram by gas chromatography-mass spectrometry (GC-MS) showed that these were hopanes (C_{27} and C_{29}-C_{32}) whose biological configurations had been preserved [17β(H)- for C_{27}; 17β(H), 21β(H)- for C_{29}-C_{32}] indicating a contribution from bacteria. The preservation of the original stereochemistries reflects the immaturity of the sample.

The results of the GC-IRMS analysis for the solvent-extractable n-alkanes isolated from Göynük, as displayed in Figure 3, provided definitive evidence the that n-C_{21}-n-C_{31} alkanes in the bitumen phase of Göynük were not derived from the same parent organisms. The C_{21} and C_{23} n-alkanes had the heaviest isotopic signatures (ca -20‰) and appeared to be derived solely from freshwater algae. The C_{30} and C_{31} members were relatively depleted in ^{13}C (-26.5 and -28.1‰, respectively) indicating an origin from allochthonous higher plant matter. This is consistent with the negative (-7 to -9‰) isotopic fractionation which prevails in the assimilation of atmospheric or dissolved CO_2 in comparison with the assimilation of dissolved HCO_3^- inorganic species by aquatic organisms. The intermediate n-alkanes had isotopic ratios from -22 to -24‰ indicating these chain lengths could be derived from both sources. Thus, analysis of the solvent-extractable alkanes implied an input from diverse sources, including algae, higher plants and bacteria.

Sequential catalytic hydropyrolysis of Göynük (following exhaustive solvent extraction with DCM then pyridine, followed by low temperature catalytic hydrogenation) produced a high yield of aliphatic products from the residual kerogen (approx. 23% w/w on a dry, ash-free basis) and a high overall conversion (over 90% w/w). A bimodal distribution of n-alkanes/n-alk-1-enes (maximum C_{20} and submaximum C_{28}) was produced, with the n-alk-1-enes

paralleling the distribution of their saturated analogues. The GC profile of aliphatics produced from sequential hydropyrolysis are shown in Figure 2 and in each case the n-alk-1-enes elute immediately before the n-alkanes. Interestingly, GC-IRMS indicated that the $\delta^{13}C$ values for the n-alkanes and n-alk-1-enes products were identical within the limits of experimental reproducibility (± 0.5‰) and therefore, were almost certainly derived from the same biological source. These findings are in contrast with the generally accepted rationale that alkyl moieties in the molecular weight range (n-C_{12}-n-C_{20}) are derived principally from phytoplankton while longer-chain n-alkanes (principally n-C_{25}-n-C_{33}) are products of the defuctionalisation of the cuticular waxes of continental higher plants. Thus, a bimodal distribution of aliphatics found in a crude oil or produced from pyrolysis of a sediment may either indicate an input from a single class of organism or may be the result of an input from two or more sources. The observation of isotopic uniformity in the major aliphatic pyrolysis products from a number of kerogens was recently reported[7] and appears to support an origin of the long alkyl chains in these kerogens from aliphatic macromolecular networks derived from the selective preservation of highly resistant aliphatic biopolymers. Non-hydrolysable highly aliphatic biomolecules have been identified in leaf cuticles, sporopollenins and algal cell walls may be a possible source of long-chain n-alkanes (>C_{20}) in sediments and high wax crude oils[8], as well as of shorter chain homologues. The heavy values of $\delta^{13}C$ (ca. -19‰) obtained for n-alkanes produced by sequential hydropyrolysis were typical of those found in some eukaryotic algal species.[9]

It is therefore proposed that Göynük oil shale was largely derived from the highly aliphatic resistant biomacromolecules occurring in the outer cell walls of freshwater green algae, termed *algaenans*. The results for Göynük support the view that kerogens may be composed almost exclusively from selectively preserved or partly altered resistant biomacromolecules rather from random polymerisation and condensation of the remnants from microbial degradation of the initial biomass. This mechanism of kerogen formation is often termed the *Selective Preservation* pathway.

Another point which should be noted from the data displayed in Figure 3 is the fact that the aliphatics produced from sequential hydropyrolysis (ca. -19‰) were distinctly isotopically heavier than the bulk organic carbon of the oil shale (-23.8‰). Even allowing for the presence of vitrinite (around 30% vol), an isotopic balance indicates that liptinite other than lamalginite, with a lighter isotopic signature than the bulk oil shale, must be present. Small quantities of higher plant liptinite can be identified from petrographic analysis of Göynük. GC-IRMS analysis of the n-alkanes (approx. 1.5% w/w on a dry, ash-free basis) released by mild catalytic hydrogenation (320°C, 7.0 MPa H_2) prior to hydropyrolysis, indicated that these were largely derived from higher plant sources (-26 to -28‰ for n-alkanes >C_{22}). Whether this reflects the isotopic composition of the whole hydrogenation product requires further investigation. However, it was observed that with increasing conversion (at higher temperatures) and consequently with higher yields of aliphatic products, the isotopic composition of n-alkanes released by hydrogenation and fixed-bed pyrolysis assumed a less negative (heavier) isotopic composition (approaching the algal isotopic signature). Thus, it was proposed that the more thermally labile n-alkyl components of the kerogen structure were derived largely from allochthonous higher plant material (isotopically light) while the additional n-alkanes released by higher conversion regimes originated from an autochthonous (algal) source (isotopically heavy). As a check, non-sequential hydropyrolysis was conducted on a pyridine-extracted GOS sample. The isotopic signatures of the n-alkanes produced (ca. -24.0‰) were similar to the $\delta^{13}C$ value determined for the bulk carbon of the Göynük kerogen (-23.8‰). Thus, the compositional fractionation effect observed was real and not produced by a kinetic isotope effect associated with hydropyrolysis. The heavy isotopic values of algal-derived aliphatics was likely to reflect low concentrations of dissolved CO_2 in the environment of carbon fixation for Göynük. In such circumstances, many carbon-fixing organisms utilise special pathways (such as assimilation of HCO_3^-) for accumulation of inorganic carbon. The isotopic fractionation effects associated with such pathways are small in comparison to those produced by the regular C_3 pathway, and the resultant organic carbon is relatively enriched in ^{13}C. A thermally-resistant algal backbone for Göynük is consistent with petrographic analysis, which showed alginite (and in particular, lamalginite) to be the dominant maceral.

Additionally, the sequential degradation procedure was applied to the Dunnet torbanite (Type I, Scotland) and a Kimmeridge clay from Dorset (Type II, SW England). Both samples were immature source rocks (< 0.4% R_o) and thus offered a good comparison with Göynük Oil Shale. A lack of any noticeable compositional fractionation for either sample was reflected in the GC-IRMS data for the aliphatic fractions produced (Figures 4 and 5). It was observed that the $\delta^{13}C$ values of aliphatic products from low temperature DCM extraction, mild catalytic hydrogenation and hydropyrolysis were very similar in magnitude, although in the case of Dunnet, the bitumen phase (DCM-extractable) aliphatics were slightly isotopically lighter. A relative lightness of solvent-extractable lipids (usually ca. 2-4‰) relative to the $\delta^{13}C$ value for the bulk kerogen has been widely observed however.[5] The only report of compositional fraction that has appeared in the geochemical literature to date, that parallels that of Göynük, is that of the Messel oil shale (type I, Western Germany). Robinson *et al.*[10] concluded from a study of the extractable lipids that the major sources of organic matter in the Messel oil shale were dinoflagellates and bacteria, especially cyanobacteria. Compound-specific carbon ($\delta^{13}C$) isotope measurements showed that the aliphatic components of the bitumen phase were derived

from diverse sources, including methanotrophic bacteria.[5] However, the analytical pyrolysis products from this oil shale showed a striking similarity to those of algaenans isolated from cultured *Tetraedron Minimum* algae.[11] Scanning electron microscopy (SEM) confirmed that the bulk of the organic matter of Messel oil shale was composed of a *Tetraedron*-type fossilised algal species. While these results for Messel at first seem at variance, it should be recognised that the extractable organic matter of the Messel shale, like that of Göynük, represented at best a few percent of the total organic matter, whilst the kerogen represented 95% or more. In such cases, conclusions based on analyses of solvent extracts probably suffer from a severe bias. Thus, the interpretation of biomarker data with respect to major sources of organic matter should be performed with great caution as it may lead to false interpretations being made.

In the case of Dunnet shale, the similarity in the distribution of aliphatics released at each stage in the degradation scheme (not shown here) together with the observance of isotopic uniformity in the n-alkane/n-alkene products from sequential hydropyrolysis, supported an origin of the aliphatic constituents of this torbanite as being derived almost exclusively from fresh- to brackish-water alga, *Botryococcus*.. A mechanism of selective preservation of resistant aliphatic biopolymers in algal cell walls, as with Göynük, can explain the formation of torbanite. Largeau and co-workers demonstrated the presence of highly resistant biopolymers, termed PRB (Polymère Resistant de *Botryococcus*), in cell walls of Botryococcus.[12,13] Structural and morphological similarities between PRB A and immature Torbanite demonstrated that the resistant polymer was selectively preserved and thus afforded a major contribution to Torbanite formation.[14] Unlike the algal precursor of ultralaminae-type alginite, *Botryococcus* appears to impart a molecular fingerprint (the characteristic n-alkane distribution observed for DS) to the bitumen phase at low maturities. This might be explained by the fact that Botryococcus is anomolously hydrocarbon-rich and can contain up to 76 percent of its dry cell weight as extractable lipids .[15]

CONCLUSIONS

The application of a sequential degradation scheme to an immature oil shale (Göynük), in conjunction with compound specific carbon ($\delta^{13}C$) measurements, highlighted the fact that significant compositional fractionation effects may exist between aliphatic constituents of the free molecular (bitumen) phase and those covalently bound to the insoluble kerogen network. It thus appears, particularly for immature type I source rocks, that the bitumen phase is not necessarily a low molecular weight indicator of the constituents of the bulk kerogen. The isotopic uniformity of the aliphatics released by the high-conversion hydropyrolysis step lends further support to the theory that selective preservation is an important mechanism in kerogen formation.

REFERENCES

1. Love, G.D., Snape, C.E. and Carr, A.D. *Prep. Am. Chem. Soc. Div. Fuel Chem.* **1993**, 38(4), 1281-12 and *Energy & Fuels*, submitted.
2. Love, G.D., Snape, C.E., Carr, A.D. and Houghton, R.C. *Org. Geochem.*, submitted.
3. Schoell, M. In *Advances in Petroleum Geochemistry, Volume 1.* (Eds. J. Brooks and D.H. Welte) pp. 215-245. Academic Press, London, 1984
4. Bjorøy, M., Hall, K. and Jumeau, J. *Trends in Analytical Chemistry* **1990**, 9(10), 331-336.
5. Freeman, K.H., Hayes, J.M., Trendel, J.-M. and Albrecht, P. *Nature* **1990**, 343, 254-256.
6. Schidlowski, M. In *Biological Markers in the Sedimentary Record* (Ed. R.B. Johns) pp. 347-361. Elsevier, Amsterdam, 1986.
7. Eglinton, T.I. *Org. Geochem.* **1994**, 21, 721-736.
8. Tegelaar, E.W., Matthezing, R.M., Jansen, J.B.H., Horsfield, B. and de Leeuw, J.W. *Nature* **1989**, 342, 529-531.
9. Hayes, J.M., Takigiku, R., Ocampo, R., Callot, H.J. and Albrecht, P. *Nature* **1987**, 329, 48-51.
10. Robinson, N., Eglinton, G. and Cranwell P.A. *Chem. Geol.* **1989**, 76,153-173.
11. Goth, K., de Leeuw, J.W., Püttman, W. and Tegelaar, E.W. *Nature* **1988**, 336, 759-761.
12. Largeau, C., Derenne, S., Casadevall, E., Kadouri, A. and Sellier, N. In *Advances in Organic Geochemistry 1985* (Eds. D. Leythaeuser and J. Rullkotter) pp. 1023-1032. Pergamon Press, Oxford, 1986.
13. Berkaloff, C., Casadevall, E., Largeau, C., Metzger, P., Peracca, S. and Virlet, J. *Phytochemistry* **1983**, 22, 389-397.
14. Rohmer, M., Dastillung, M. and Ourisson, G. *Naturwissenschaften* **1980**, 67, 456-458.
15. Maxwell, J.R., Douglas, A.G., Eglinton, G. and McCormick, A. *Phyochemistry* **1968**, 7, 2157-2171.

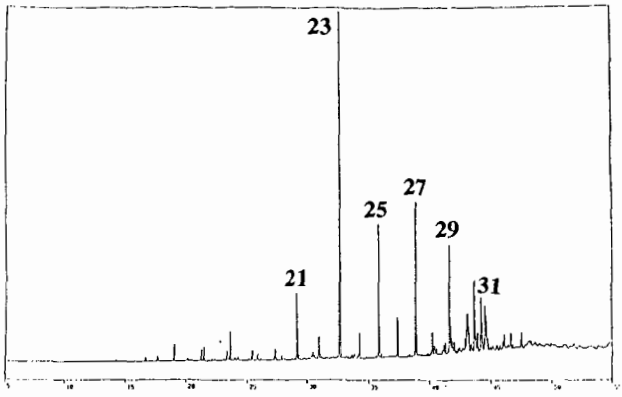

Figure 1. GC-FID trace of the free aliphatic hydrocarbons released by dichloromethane extraction of Göynük Oil Shale.

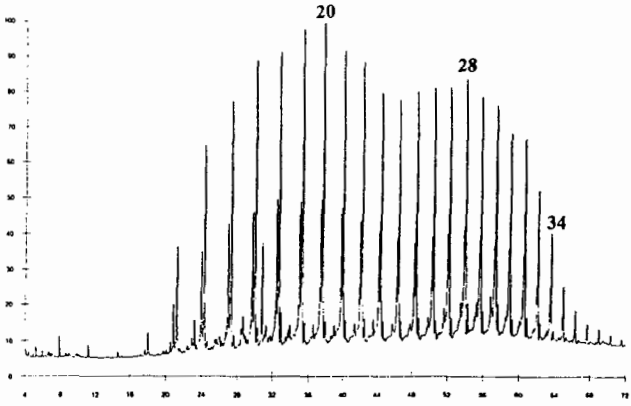

Figure 2. GC-FID trace of the aliphatic hydrocarbons produced from sequential hydropyrolysis of Göynük Oil Shale.

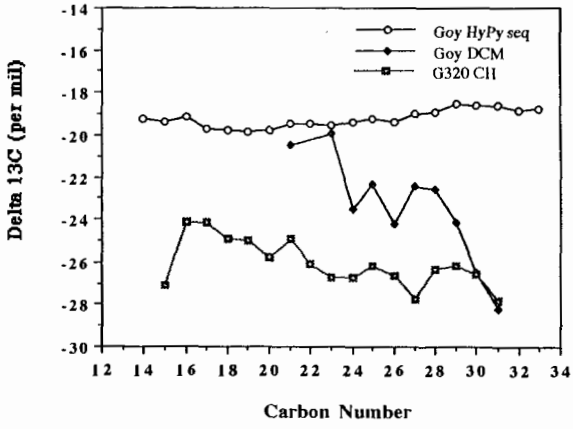

Figure 3. GC-IRMS analysis of n-alkanes produced from sequential degradation of Göynük Oil Shale.

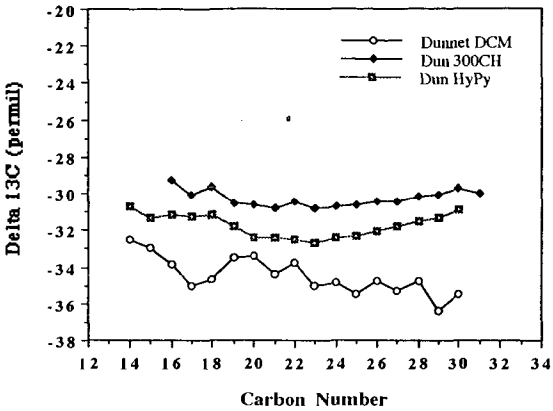

Figure 4. GC-IRMS analysis of n-alkanes produced from degradation of Dunnet torbanite. ($\delta^{13}C$ of bulk TOC = -29.2‰)

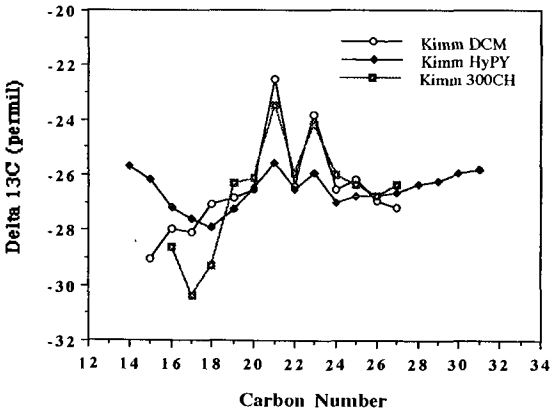

Figure 5. GC-IRMS analysis of n-alkanes produced from degradation of Kimmeridge clay. ($\delta^{13}C$ of bulk TOC = -23.8‰)

FOSSIL FUEL CHARACTERIZATION USING LASER DESORPTION MASS SPECTROMETRY: APPLICATIONS AND LIMITATIONS

Jerry E. Hunt and Randall E. Winans
Argonne National Laboratory, Chemistry Division
Argonne, IL 60439 USA

Keywords: Argonne Premium Coals, laser desorption, matrix-assisted laser desorption

INTRODUCTION

High molecular weight compounds (>600 amu) in fossil fuels have been overlooked in the past principally because of inappropriate analytical techniques. Most of the techniques have accessed only the easily volatilizable fraction. Mass spectrometry characterization of any presumed heavy components has mostly depended on pyrolysis to break up the larger molecules prior to analysis, especially by pyrolysis gas chromatography mass spectrometry. The material that is outside of the volatilizable fractions has received little attention. However, laser desorption mass spectrometry (LDMS) and matrix-assisted laser desorption/ionization mass spectrometry (MALDI) are particularly applicable to those molecules which resist intact ionization by traditional gas-phase methods. The application and limitations of these techniques to model compounds and fossil-derived materials is discussed in this study.

LD and MALDI mass spectrometry are increasingly used to detect intact molecular species, such as proteins with masses from 1000 to 100,000 amu and beyond.[1] MALDI is also being used for a few high molecular weight polymers.[2] A good example, related to coal-type systems, is the report on lignin mass spectrometry by MALDI.[3] Here the mass spectrum shows a wide molecular distribution of several hundred to larger than 16000, with the center of gravity of the distribution around 2600. The results are interpreted in terms of oligomeric lignin molecules. Thus, if there are indeed large molecular species in a polymeric content in fossil fuel extracts, MALDI is an attractive technique.

We have previously reported laser desorption of coal extracts that show only low molecular weight ions (<2000 amu).[4-6] We compare LD with fast atom bombardment and desorption chemical ionization mass spectrometry, two other soft ionization techniques. All of these techniques produce similar data that differ only in minor details. We have used our two TOF mass spectrometers for coal analysis by MALDI, have carefully analyzed our data and the instrumental conditions and conclude that the bulk of coal material produces only low molecular weight ions (up to 2000 amu). In agreement with these reports, Hanley showed LD and MALDI data of pyridine extracts which produced a distribution of ions between 150 and 1500.[7] In addition, field ionization mass spectrometry has found similar pattern in the low mass region.[8] Recently, Herod et. al[9-12] have interpreted their LD and MALDI data in terms of high mass species being desorbed. We have presented alternate interpretations for these results.[6]

In our hands, LD or MALDI of coals and extracts do not show any reproducible ion intensity over mass 2000. The conditions whereby large molecular ions can be desorbed intact are very specialized. This paper will describe the scope and limitations of laser desorption and matrix-assisted laser desorption in time-of-flight mass spectrometers as applied to high molecular weight molecules, such as proteins and polymer systems.

EXPERIMENTAL

The coals used in this study are the Argonne Premium Coal Samples. The procedures for the pyridine extract of the Argonne Premium Coals have been reported previously.[5] The laser desorption mass spectra and matrix-assisted laser desorption mass spectra were recorded on a linear time-of-flight mass spectrometer constructed at Argonne and a Kratos Kompact MALDI III linear/reflectron time-of-flight mass spectrometer. The spectra were produced by exposing the samples distributed as thin layer on a stainless steel sample holder to laser pulses from either a Nd:YAG or a

nitrogen laser. The laser is operated close to the ionization threshold to minimize possible fragmentation of the desorbing material and to optimize resolution.

The matrices used were dihydroxybenzoic acid, sinapinic acid, indoleacrylic acid and 2-(4-hydroxyphenylazo)-benzoic acid (HABA) purchased from Aldrich. The polyethylene sample were purchased from Petrolite. The polyethylene glycol was purchased from Aldrich.

RESULTS

Coals

Coals are a unique sample for LD and MALDI. They are chemically very complex, heterogeneous, and most likely polydisperse in mass. Figure 1 shows a positive ion LD mass spectrum of the pyridine extract of APCS 1 mv bituminous coal produced using 337 nm laser pulses, displaying a distribution of ions between roughly 200 and tailing to 2000 amu. The major ion series seen are alkyl-pyrenes (-fluoranthenes), -chrysenes, -benzopyrenes, -phenlypyrenes (-pyreneobenzofurans), -carbazoles, and -benzoperylenes. Laser desorption favors the aromatic compounds. Laser desorption with the Nd:YAG fundamental wavelength of 1064 nm, 532 nm (frequency doubled), and 266 nm (frequency quadrupled) show similar spectra.

The MALDI spectrum of the same sample from sinapinic acid is shown in figure 2. The matrix/laser combination is sinapinic acid with 337 nm laser light. At first glance the data indicate a continuum of high mass peaks, but the observed "signal" is actually a result of chemical noise from the matrix and ion saturation of the detector creating a false signal at the detector which is not correlated with the laser blast or sample. In an attempt to see higher mass ions, we have deflected the low mass ions using time-gated pulsed deflection, so that these intense ions do not impact the detector. The results show no high mass ions. Matrix-assisted laser desorption/ionization using 2,5-hydroxybenzoic acid, HABA, nicotinic acid, sinapinic acid, 3-hydroxypicolinic acid, silver nitrate, silver acetate, silver picolinate and indole acrylic acid, have been attempted on the pyridine extracts of Argonne coals. No higher mass or other ions are observed in the MALDI experiments beyond those of the matrix and those seen in the neat coal extracts.

The Nature of the MALDI Event

In order to assess the characteristics of the MALDI mass spectrum, we present a protein mass spectrum. The inset in the figure 2 shows the MALDI of a protein in the sinapinic acid matrix. Here the molecular ion is easily observed above the background without detector saturation. A feature of MALDI in time-of-flight instruments is that at higher masses the resolving power decrease. The peak with for each of the two protein ions using this matrix is about 4000 mass units a the baseline. An important aspect of MALDI is the low resolution, especially at higher masses. In the case of two single proteins the mass resolution in ~150 $m/\Delta m$ full width at half maximum. This means that a distribution of molecules, for example from 10000 to 200000 amu, would appear only as a broad unresolved hump in the mass spectrum. In fact, MALDI for polymers above 10,000 amu the resolution for a linear time-of-flight mass spectrometer is insufficient to identify individual oligomers. Sharp peaks are not be observed. The amount of available charge in the MALDI event to span such a large mass region is also questionable.

The MALDI mass spectrum (HABA matrix) of polyethylene glycol 3000 is shown in figure 3. The distribution of oligomers is clearly observed. In the case of more nonpolar species, such as polyethylene, we have found that common organic matrices do not result in mass spectra. Silver nitrate or other silver salt must be added to polyethylene to produce mass spectra of silver cationized oligomers. We have easily observed polyethylene up to 2500MW with this method.

CONCLUSIONS

LDMS and MALDI time-of-flight instruments are easy to operate, fast, and are suitable for quantitative measurement of molecular weight distributions of certain coal components. LD, in particular, is better suited to mixture analysis than MALDI.

Although matrix-assisted laser desorption time-of-flight analysis has been touted as a universal molecular weight distribution tool, it is hardly that. The successful application of the MALDI is greatly dependent on the chemical structure of the system under investigation. Different chemical structures may require significantly different sample preparation. The sample preparation step is perhaps the most important component of a MALDI experiment. First, nonpolar compounds (e.g., polyethylenes) have not been successfully analyzed by any organic matrix-assisted technique that the authors are aware. Second, ion intensities from mixtures of compounds rarely show true abundances. Third, in mixed systems the lowest concentration species may be not observed at all because of the high background noise levels that are a feature of matrix-assisted laser desorption. The fact that spectra are easy to obtain should not overshadow the fact that sample preparation is the critical factor in successful analyses. Furthermore, the conditions useful for one system may not be useful for others. The conditions and matrices presently used for coal in MALDI are most appropriate for proteins. Thus, there is a strong possibility that any observed high mass ions may be from contaminant proteins contained in the coal.

However, the fact remains that LDMS and MALDI are capable of producing intact, unfragmented molecular ions from biopolymers, macroscopic molecules based on aromatic building blocks, and polymers. MALDI can provide values for the molecular weight as well as shows the entire distributions of polymer species. The question arises, if there were high mass material in coals and extracts, would they be detected by this technique. First, optimal matrices must be found. There is good reason to believe that good miscibility of matrix and the coal in the condensed form is the prerequisite for a good matrix, as has been found to be true for protein desorption. Matrices working well for polar biopolymers will not be optimal for coals. Most of the protein matrices actively exclude ionic components, which are needed for cationizaton. Second, if the mass distribution is extremely polydisperse it may be difficult to detect the high mass material above background as the contribution at any mass may be low even if the contribution to the total mass over a wide range is high. Finally, the mass spectrum is sensitive to the number average molecular weight; a low value, however, does not preclude the presence of high molecular weight species.

ACKNOWLEDGMENT
This work was performed under the auspices of the Office of Basic Energy Sciences, Division of Chemical Sciences, U.S. Department of Energy, under contract number W-31-109-ENG-38.

REFERENCES

1. R. C. Beavis, *Org. Mass Spectrom.* **27**, 653-659 (1992).
2. J. E. Campana, L.-S. Sheng, S. L. Shew, B. E. Winger, *trends in analytical chemistry* **13**, 239-247 (1994).
3. J. O. Metzger, et al., *Angw. Chem. Int. Ed. Eng.* **31**, 762-764 (1992).
4. J. E. Hunt, K. R. Lykke, R. E. Winans, *Preprints Am. Chem. Soc., Div. Fuel Chem.* **36**, 1325-1328 (1991).
5. R. E. Winans, R. L. McBeth, J. E. Hunt, P. E. Melnikov, Monomers in Coal Macromolecules, 1991 International Conference on Coal Science, University of Newcastle upon Tyne, UK, September 16-20, (1991).
6. J. E. Hunt, R. E. Winans, *Preprints Am. Chem. Soc., Div. Fuel Chem.* **39**, 831-934 (1994).
7. J. A. Burroughs, B. M. Cadre, L. Hanley, presented at American Society for Mass Spectrometry Meeting, San Francisco, CA, (1993).
8. A. A. Herod, B. J. Stokes, H.-R. Schulten, *FUEL* **72**, 31-43 (1993).
9. A. A. Herod, et al., *Rap. Commun. Mass Spectrom.* **8**, 815-822 (1994).
10. A. A. Herod, et al., *Rap. Commun. Mass Spectrom.* **8**, 808-814 (1994).
11. A. A. Herod, et al., *J. Chem. Soc., Chem. Commun.*, 767-769 (1993).
12. A. A. Herod and R. Kandiyoti, *FUEL* **74**. 784-786 (1995).

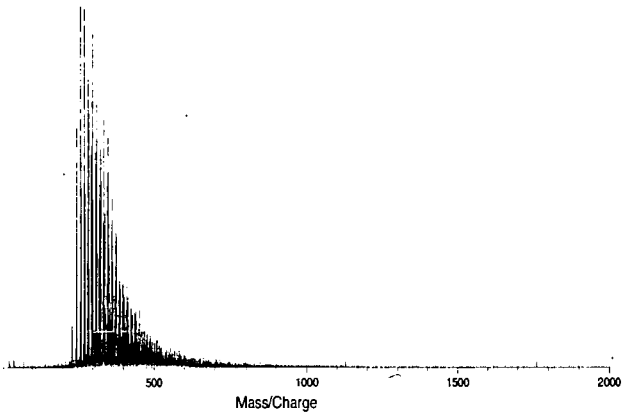

Figure 1. LD mass spectrum of the demineralized pyridine soluble fraction of APCS 1 (Upper Freeport).

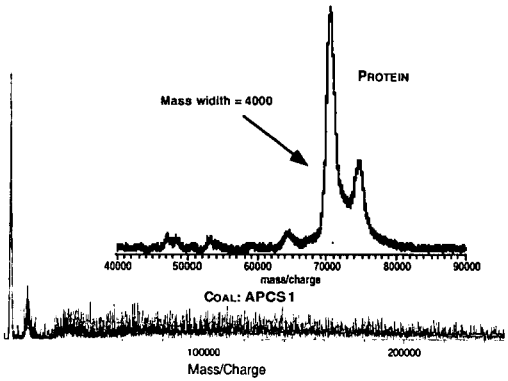

Figure 2. MALDI linear mass spectrum of APCS 1 (Upper Freeport) using sinapinic acid as matrix showing the effect of detector saturation. The inset is the MALDI of two proteins, synapsin IA, IB, in sinapinic acid.

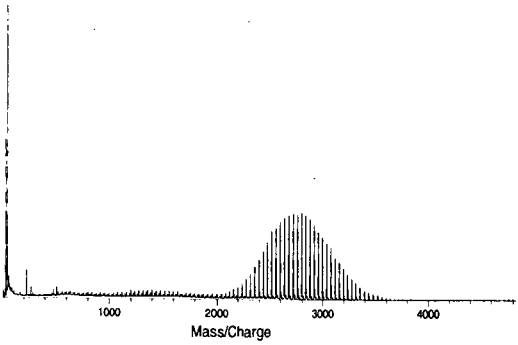

Figure 3. MALDI reflectron spectrum of polyethylene glycol showing intact cationized molecular ion formation.

HIGH RESOLUTION MASS SPECTROMETRY FOR THE CHARACTERIZATION OF COMPLEX, FOSSIL ORGANIC MIXTURES

Randall E. Winans, George W. Haas, Yeonhee L. Kim, and Jerry E. Hunt
Chemistry Division
Argonne National Laboratory
Argonne, IL 60439

Keywords: Argonne Premium Coals, Desorption Chemical Ionization High Resolution Mass Spectrometry (DCIHRMS)

INTRODUCTION

The nature of molecules with heteroatom functionality in the pyridine extracts of the Argonne Premium Coal Samples is being explored using high resolution mass spectrometry (HRMS), with desorption chemical ionization (DCI). Structural information is obtained from tandem MS experiments using high resolution to select the ions to fragment. The first DCIHRMS spectra of complex mixtures are shown. Molecular weight distribution determined by DCI are similar to those determined by laser desorption and field ionization mass spectrometry with very little ion intensity observed at greater than 1000 Daltons. Results are correlated with other techniques such as NMR, XPS, and XANES.

PyMS has been used extensively to examine coals and separated macerals. Results from electron impact (EI) in high resolution mode have demonstrated the importance of not only single heteroatom containing molecules in coals, but also multiple heteroatom containing molecules.[1] Both PyGCMS and PyMS have been used to analyze the more volatile pyrolysis components. Thermogravimetric MS techniques yield quantitative data with rather slow heating rates.[2] Also, a standard technique now used to provide molecular weight distribution of volatile tars is field ionization MS (FIMS).[3] FIMS results are published for all eight Argonne coals,[4] while Meuzelaar, Schulten and co-workers have correlated the results from PyFIMS, low voltage EI and TGAMS on the same coal.[5] They found similar patterns in the low mass regions. FABMS has been applied to coal pyrolysis products yielding data similar to FIMS.[6] Finally, the first DCIMS results have been discussed[7] and will be expanded in this paper with the addition of high resolution data.

EXPERIMENTAL

The Argonne Premium Coal samples used in this study have been described[8] and further information is available on World Wide Web - http://www.anl.gov/PCS/pcshome.html. Pyridine extracts[7] were thermalized directly in the source of a Kratos MS50 TA using a desorption chemical ionization probe heated from 200 to 700 °C @ 100 °C/min. The spectrometer was operated at a dynamic resolution of 10,000 and scanned at 10 s/decade of mass. Isobutane was used as the CI gas and poly(dimethylsiloxane) (PDMS) was used as the internal mass calibrant. For group analysis, all scans with ions above background are averaged and only those which occur a minimum of four times are saved. Formulae which fit within ±3.5 millimass units are assigned for each averaged ion peak. The formula are then sorted by hydrogen deficiency and heteroatom content.

RESULTS AND DISCUSSION

In general, the data from DCIHRMS are similar to those found by field ionization (FIMS).[4] A major problem is finding an internal mass calibrant because perfluorokerosene (pfk), which is used in electron impact, does not ionize in isobutane CI. PDMS is an effective calibrant,[9] but the measurements are not consistently as good as with pfk because the reference peaks are spaced at larger increments of mass. Therefore, we are looking at some alternative reference materials. Recently, a resolving power of 80,000 was achieved by the source used in this study.

Samples of averaged spectra are shown for four of the Argonne coals in Figure 1. The spectra typically show ion intensity out to $m/z \approx 700$ and useful information ends at the low mass end of 90, due to the isobutane. Normally $[M+H]^+$ ions are observed under these conditions.

The subbituminous coal (Figure 1a) gave a distribution similar to bituminous coals, except for a series of fatty acids C_{25}, C_{27}, C_{29}, C_{31} (major) and C_{26}, C_{28}, C_{30} (minor). Also, pyrolysis fragments of lignin remnants are observed at m/z = 111, 125, 139, 153, which correspond to the series $Ph(OH)_2(CH_2)_xH$, x = 0-3. The acids were also observed in the lignite coal by DCIMS. With FIMS,

they were only observed in the lignite, but the lignin fragments are observed in both low rank coals.[4] It is interesting to note that these are not the major species seen by PyGCMS of low rank coals.

In the Illinois No. 6 coal (Figure 2b), the fatty acids are absent and the lignin derived pyrolysis fragments are alkylated C_0-C_4 monohydroxybenzenes. However, the molecular size distribution is very similar to the low rank subbituminous coal. Another difference is the large number of sulfur containing ions in the Illinois coal as one would expect.[1]

The hvA bituminous Pittsburgh seam coal gave a higher molecular size distribution of the ions. However, alkylated hydroxybenzene species are still observed, but their overall contribution to the total ion current found is significantly less than with the low rank coals.

The Blind Canyon coal (APCS 6) (Figure 1d) is unusual in that it contains significant amounts of resinite and sporinite macerals. Ions at m/z = 320 ($C_{25}H_{20}$), 321, 324 ($C_{25}H_{24}$), 325 (100), 342 ($C_{26}H_{30}$), 343 correspond to triterpenoid hydrocarbons from resinite, which has also been observed in Curie point pyrolysis MS[10] and by GCMS in benzene-methanol extract.[11]

All of the total ion response curves are bimodal such as is seen in Figure 2a for the Lewiston-Stockton hvA bituminous coal (APCS 7). This effect has also been seen in the temperature programmed thermolysis of whole coals. For the whole coal, the first peaks had been thought to be small molecules such as those that are solvent extractable. The extract also contains larger molecules which are released as pyrolysis temperatures where weak bond cleavage is occurring. No evidence is found for very large polycyclic aromatics volatilizing at the higher temperatures.

The change in the ion mass distribution with temperature for APCS 7 is shown in Figure 2b. The ions at m/z = 157 and 111 are artifacts from the extraction solvent, pyridine, representing the dimer of pyridine and an oxygenated alkyl pyridine molecule, respectively. At increasing desorption temperature, the size of the ions increases from scan 9 to scan 12. Around scan 18, pyrolysis begins and distribution shifts to small ions and finally the mass distribution shifts higher in scan 21. It is interesting to note that the distributions are similar in scan 12 and 21 even though the temperatures differ by 220 °C. In addition, over the entire temperature range, a series of distinct peaks are observed between 470 and 600. Exact mass measurements suggest that they are alkylated aromatic hydrocarbons with 4 rings. This was confirmed by tandem MS experiments and are possibly greatly modified biomarkers. They were not observed by FDMS, but have been seen in both FAB and EI MS experiments.[6,7]

Finally, from the exact mass measurement, formulae can be calculated resulting in information on ring size and heteroatom distribution. An example is shown in Figure 3 for the Pocahontas lv bituminous coal (APCS 5). The ring size varies from 4 to 7 with the most abundant being six (rings + double bonds = 18, 19). Even though the heteroatom content combined is lower than all the other coals, from statistical viewpoint every polycyclic aromatic with 6 rings should have a heteroatom in it. This is what we are observing in the extract. Some preliminary MSMS results suggest that annelated furans are the likely form of the single oxygen molecules, which agrees with NMR experiments.[12] XPS results indicate that over 60% of nitrogen exist in pyrrole type structures which is analogous to furan for oxygen and thiophene for sulfur.[13] These structures are probably important in determining the tertiary structure of high rank coals.

CONCLUSIONS

High resolution CIMS data further support the notion that the size of the stable aromatic clusters is not large in coals except the very high rank coals and inertinite macerals. The DCI spectra appear to be very representative of the sample with little discrimination for molecular types such as aliphatics.

ACKNOWLEDGMENT

This work was performed under the auspices of the Office of Basic Energy Sciences, Division of Chemical Sciences, U.S. Department of Energy, under contract number W-31-109-ENG-38.

REFERENCES

1. Winans, R. E. and Neill, P. H. In Geochemistry of Sulfur in Fossil Fuels, W. L. Orr and C. M. White, Eds., ACS Symposium Series 429, ACS, Washington, D.C., 1990, Ch. 15, p. 249-259.
2. Szabo, P.; Varhegyi, G.; Till, F.; and Szekely, T. *Thermochimica Acta*, **1990**, *170*, 167-177.

3. Schulten, H.-R. and Marzec, A. *Fuel*, **1986**, *65*, 855-860.
4. Solomon, P. R.; Serio, M. A.; Despanda, G. V.; and Kroo, E. *Energy Fuels*, **1990**, *4*, 42-54.
5. Yun, Y.; Meuzelaar, H. L. C.; Simmleit, N.; and Schulten, H.-R. *Energy Fuels*, **1991**, *5*, 22-29.
6. Winans, R. E. *J. Anal. & Appl. Pyrolysis*, **1991**, *20*, 1-13.
7. Winans, R. E.; McBeth, R. L.; Hunt, J. E.; and Melnikov, P. E. *Proceedings, 6th International Conference on Coal Science*, University of Newcastle-upon-Tyne, England, September 16-20, 1991, pp. 44-47.
8. Vorres, K. S. *Energy Fuels*, **1990**, *4*, 420-425.
9. McCamish, M.; Allan, A. R.; and Roboz, J. *Rapid Comm. Mass Spectrom.*, **1988**, *1*, 124-125.
10. Meuzelaar, H. L. C.; Huai, H.; Lo, R.; and Dworzanski, J. *Fuel Proc. Tech.*, **1991**, *28*, 119-134.
11. Hayatsu, R.; McBeth, R. L.; Neill, P. H.; Xia, Y.; and Winans, R. E. *Energy Fuels*, **1990**, *4*, 456-463.
12. Winans, R. E.; McBeth, R. L.; Melnikov, P. E.; and Botto, R. E. *Proceedings, 7th International Conference on Coal Science*, Banff, Canada, September 12-17, 1993, pp. 515-518.
13. Kelemen, S. R.; Gorbaty, M. L.; and Kwiatek, P. J. *Energy Fuels*, **1994**, *8*, 896.

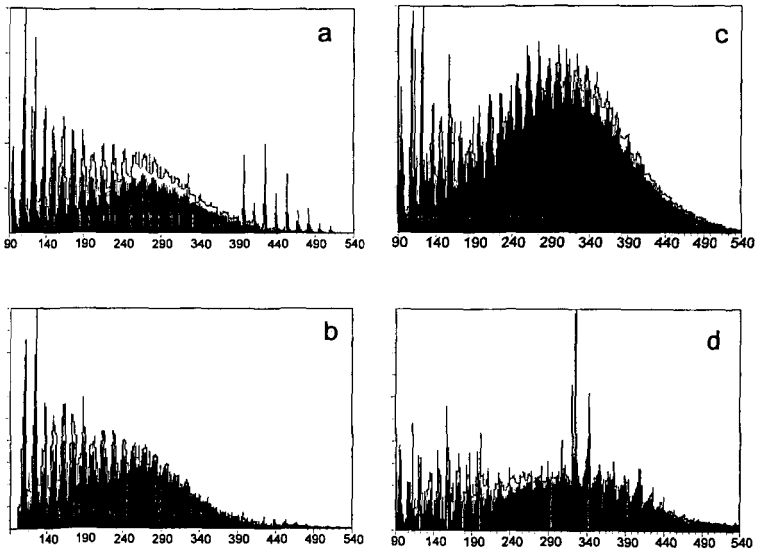

Figure 1. DCI mass spectra of selected Argonne coals. Data are derived from averaging over the total heating range. (a) Subbituminous coal (APCS 2); (b) Illinois No. 6 hvC (APCS 3); (c) Pittsburgh seam (APCS 4); and (d) Blind Canyon (APCS 6).

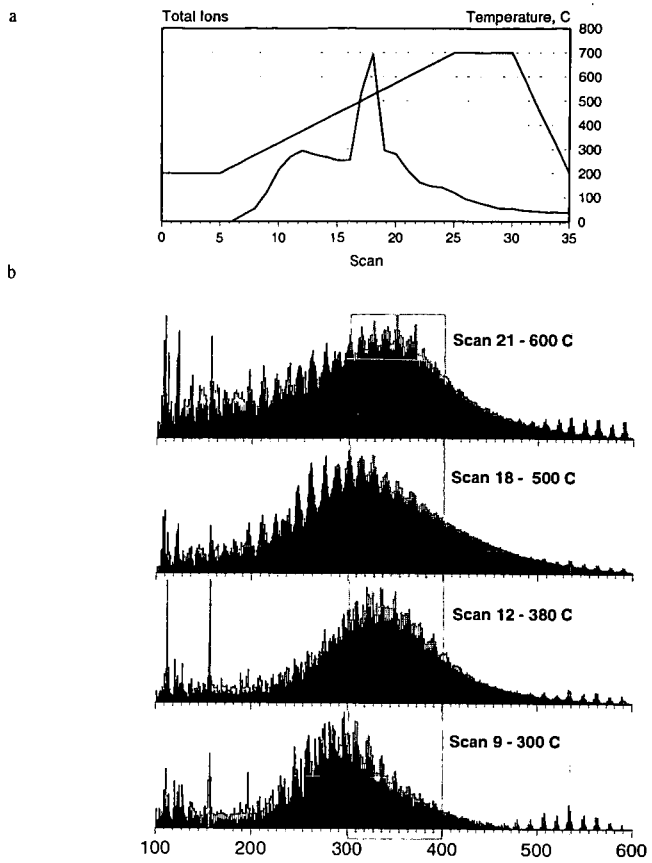

Figure 2. Data from Lewiston-Stockton bituminous coal(APCS 7). (a) Total ion response. (b) Selected scans labelled with scan numbers from Figure 2(a).

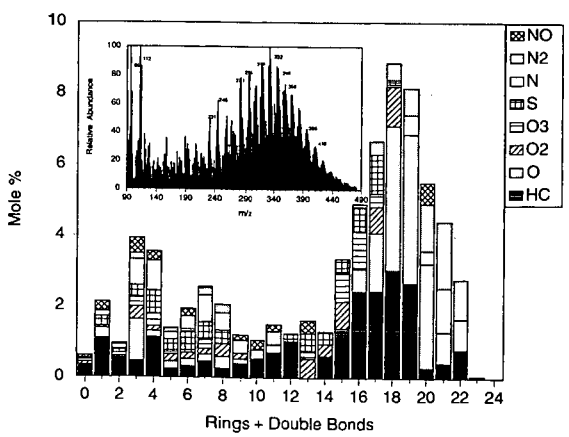

Figure 3. Group analysis of DCIHRMS data from Pocahontas extract(APCS 5). The inset is the averaged spectrum used to calculate the distributions.

IMPROVED SIZE EXCLUSION CHROMATOGRAPHY OF COAL DERIVED MATERIALS USING N-METHYL-2-PYRROLIDINONE AS MOBILE PHASE

Barry R. Johnson, Keith D. Bartle, Alan A. Herod* & Rafael Kandiyoti*
School of Chemistry, University of Leeds, Leeds LS2 9JT, UK
*Department of Chemical Engineering, Imperial College, London SW7 2BY,UK

Keywords Size exclusion chromatography, molecular mass distribution, coal derived materials

INTRODUCTION

A detailed knowledge of the molecular mass distribution (MMD) in coal and its derived products is essential for a fundamental understanding of coal structure, and of the processes occurring during pyrolysis, liquefaction and combustion. Indeed with increased economic and environmental pressure to use natural resources more effectively such knowledge can be applied to gaining more from finite coal reserves. Of the methods available for determining MMDs size exclusion chromatography (SEC) is perhaps the most routinely employed. In SEC tetrahydrofuran (THF) is the most commonly employed mobile phase. However THF has limited solvating power for coal derived materials and consequently a significant proportion of such materials goes undetected. In addition the interpretation of chromatograms with reference to calibration of the column with polystyrene standards is flawed[1]. By comparison, N-methyl-2-pyrrolidinone (NMP) is capable of solvating more of the coal sample and therefore gives the opportunity to determine an improved MMD. In this contribution the extended capabilities of NMP as the mobile phase are demonstrated primarily through the analysis of a coal tar pitch. Both NMP and THF are used as mobile phases for SEC using a number of detection techniques, allowing comparison and evaluation of different chromatographic systems to the analysis of coal derived materials.

EXPERIMENTAL

The principle coal product used in these investigations was a high temperature coal tar pitch, with observations confirmed by similar experiments on a Point of Ayr Pilot Plant extract of Point of Ayr (PoA) coal, and a synthetic pitch. Neither pitch sample was wholly soluble in THF, unlike the PoA sample. The systems developed were then applied to the examination of char material from the British Coal, Coal Technology Development Division (CTDD) Gasification Pilot Plant (Stoke Orchard). The gasifier feed stock was power station grade Daw Mill coal. Char samples were derived from experiments at atmospheric pressure and 960°C. Organic material was extracted from the char using three different techniques. Supercritical fluid extraction, carbon dioxide with toluene modifier (400atm, 200°C), and liquid solvent extraction (1:1 NMP:CS_2 and sonication) both produced greater yields than the more conventional soxhlet extraction. However, in each case the yield was low indicating destruction of potential tar forming materials within the gasifier.

The chromatographic analyses and separations were performed on three systems:

For the THF based analytical system two Jordi gel (5µm, polydivinylbenzene packing) analytical SEC columns (250 x 10 mm, 500 & 100-A^{o}), with guard column, were operated at room temperature with a THF flow rate of 1.0ml/min. Detection was through fixed wavelength (254 or 280 nm) uv absorption and evaporative light scattering detection (ELSD).
Fractionation of the coal tar pitch was performed on two PL Gel (10 µm, styrene-divinylbenzene copolymer packing) preparative scale (600 x 25 mm, 500 & 100-A^{o}) columns. 40 mg of the pitch, in THF, was injected onto the columns with a THF flow rate of 10 mL/min and uv absorption detection used at 254 nm. Using this apparatus the pitch eluted over a volume range of some 40mL. A continuous series of aliquots of the column effluent were collected for each of 22 separate injections. The fractions from the same collection times were then combined and dried in a vacuum oven to remove the solvent.
The NMP based apparatus consisted of a single PL gel (3µm, styrene-divinylbenzene copolymer packing) SEC column (250 x 10 mm, Mixed Bed E) with guard column connected in series to a variable wavelength uv absorption detector (260-700 nm) and a uv/vis fluorescence detector (280-750 nm). Columns were operated at a temperature of 80°C, with an NMP flow rate of 0.5 mL/min.
All SEC apparatus were calibrated using narrow polystyrene standards (162 - 410,000 g/mol, Polymer Labs Ltd). Injection volumes were 20-µl of a 1-10 mg/mL solution for the analytical systems, and 2ml for the preparative scale experiments.

RESULTS AND DISCUSSION

The THF-SEC chromatograms, from both uv absorption and ELSD, of the THF soluble portion of the soft pitch are shown in Figure 1. The range of the calibration with polystyrenes is marked on the figure. This clearly illustrates the difficulties being addressed in the present work[1,2]. However before these are examined two other interesting features are revealed in this figure. The two monitoring wavelengths employed give very similar profiles, and so are detecting similar material. The ELSD chromatogram shows material eluting over the same time range, but gives a different profile, and therefore more

information, at the shorter elution times. This ELSD detection method produces excellent results for the heaviest material within the sample, a portion often underestimated by other detectors.

Returning to the main point of Figure 1. The pitch sample elutes over a much greater time range than the calibrants. In fact the majority of the pitch sample elutes at retention volumes greater than the smallest calibrant. Obviously this 'late' material is not of very small mass, but is interacting with the column packing material, and so the separation occurring is through both adsorption and size exclusion mechanisms. This multimode separation phenomena is well documented[1,2] and means that a MMD cannot confidently be assigned to the sample.

The application of NMP as a mobile phase for analysing such material was investigated next. The dried THF extract of the coal tar pitch was redissolved in NMP, and appeared to be completely soluble. This was analysed on the NMP-SEC apparatus together with the NMP extract of the pitch. The resulting chromatograms are presented in Figure 2. The polystyrene calibration for this apparatus gave an exclusion limit at ~550s and a total permeation limit (peak of toluene elution) at ~1365s. The NMP extract shows two unresolved maxima in the chromatogram. The first is at the exclusion limit indicating large molecular material, with the second within the columns resolving range. The important feature to note here is that there is no material eluting after the total permeation limit. This observation is repeated in the fluorescence detected chromatogram. In the case of the THF extract of the soft pitch, again there are two maxima, one at the exclusion limit and one within the columns resolving range. However, here the two peaks are baseline resolved. Again there is no material eluting after the total permeation limit.

These chromatograms indicate that the molecular material solvated by NMP has a continuous mass range limited only by the exclusion limit of the columns (~30,000 polystyrene equivalent mass units, p.e.m.u. - manufacturers figures). Indeed, by consideration of the intensity of the excluded peak a large proportion of the pitch has a high molecular mass. The majority of the THF soluble material has a much smaller mass, < 5000 p.e.m.u. The presence of the excluded material in this sample may be due to processes occurring during drying and removal of the original THF. A similar effect has been reported during experiments to measure molecular mass by vapour pressure osmometry, where accurate weighing of solvent free sample is essential.

The examinations in Figures 1 & 2 raise an important question about the mechanism of separation occurring in the THF and NMP systems[2,3]. Clearly there is adsorption chromatography occurring within the THF system, so what effect is this having on the size separation mechanism of the porous column packing? Figure 3 presents some results from an investigation of the order of elution of coal derived material with NMP or THF as the mobile phase. The preparative scale separation of the coal tar pitch produced narrow retention volume defined fractions with known elution order, confirmed on the analytical THF system. These fractions were dissolved in NMP and injected on to the NMP-SEC system. Figure 3 illustrates the finding that the elution order remains largely the same. There is however a greater peak broadness in this NMP system for each individual fraction.

These observations indicate that the non-size exclusion contribution to the separation mechanism is much less when NMP is the chromatographic mobile phase. This may well be due to both the greater solublising powers of NMP and the higher temperatures at which the NMP columns are operated. This is supported by the fact that no thermally treated coal derived material has been found to elute after the retention time of toluene.

We now turn to an examination of material extracted from the gasifier char. The supercritical fluid extraction, Figure 4, yields material which is generally of low molecular weight. There is no excluded peak. This is consistent with previous SFE of coal and environmental materials[4]. Also illustrated is the extension of extraction to larger molecules as more modifier is used. It is interesting to note that SFE produces material up to the total permeation limit of the column.

Chromatograms produced from the analysis of the mixed solvent extract are shown in Figure 5. This is a powerful technique capable of solvating 60% of some raw coals[5]. This increased extraction power over SFE is seen by the presence of a large peak in the chromatogram corresponding to excluded material. Indeed there appears to be more excluded than retained material. The lowest molecular weight material indicated by Figure 4 to be present in the original char may well be lost from the material examined in Figure 5 by the processes used to remove CS_2 from the extract filtrate. This last figure also illustrates that the excluded material is absorbing significant amounts of uv light at 500nm. The corresponding fluorescence chromatograms show very little fluorescence at any wavelength. This supports the assumption that this excluded material consists of larger molecular structures and not aggregated low molecular weight compounds which generally have strong fluorescence spectra.

CONCLUSIONS

From the results reported here it is clear that NMP surpasses THF as a mobile phase for SEC of coal derived materials. It offers the opportunity to analyse more of the sample, and has shown much reduced adsorption effects. Investigation has shown that this technique can be applied to materials of industrial relevance. Polystyrene calibration for these materials remains a source of error particularly for higher mass materials, but is probably less inaccurate for low masses with NMP-SEC. The combination of

NMP-SEC and new MS techniques (LIMA, MALDI), might provide a possible route to the manufacture of relevant coal calibrants and thus accurate MMDs.

ACKNOWLEDGEMENTS

The authors gratefully acknowledge the permission given by CTDD allowing collection and analysis of the gasifier samples and supply of the PoA liquefaction extract, in particular Drs Nigel Patterson and Sam Moore. We would also like to thank the EPSRC and ETSU for funding this work.

REFERENCES

1. K. D. Bartle, M. J. Mulligan, N. Taylor, T. G. M. & C. E. Snape, Fuel 63 (1984) 1556.
2. A. L. Lafleur & M. J. Wornat, Analytical Chemistry 60 (1988) 1096.
3. A. L. Lafleur & Y. Nakagawa, Fuel 68 (1989) 741.
4. S. B. Hawthorne & D. J. Miller, Anal Chem 66 (1994) 4005
5. M. Iino, T. Takanohashi, H. Ohsuga & K. Toda, Fuel 67 (1988) 1639

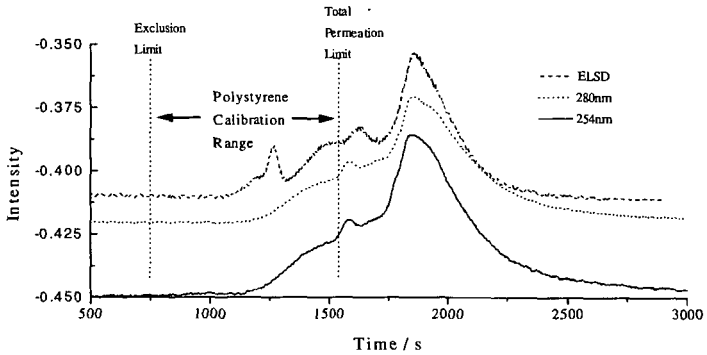

Figure 1 Size exclusion chromatographic analysis of coal tar pitch using multiple detectors with tetrahydrofuran as the mobile phase.

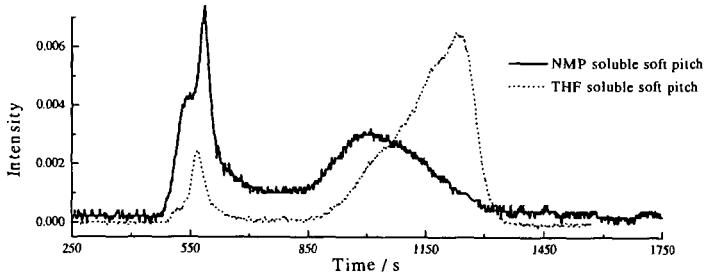

Figure 2 SEC chromatograms of solvent separated coal tar pitch fractions using uv absorption detection at 280nm and N-methyl-2-pyrrolidinone as the mobile phase.

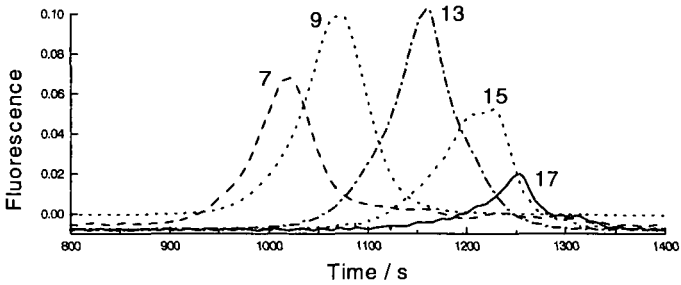

Figure 3 NMP-SEC chromatograms of pitch fractions from preparative scale THF-SEC.

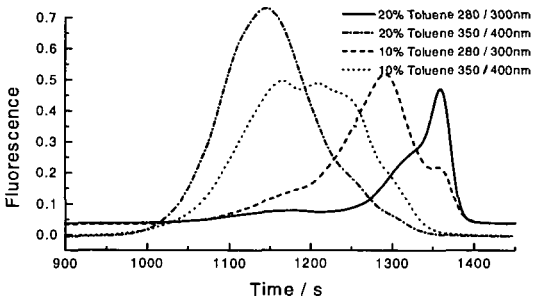

Figure 4 Chromatograms of supercritical fluid extracts from gasifier char.

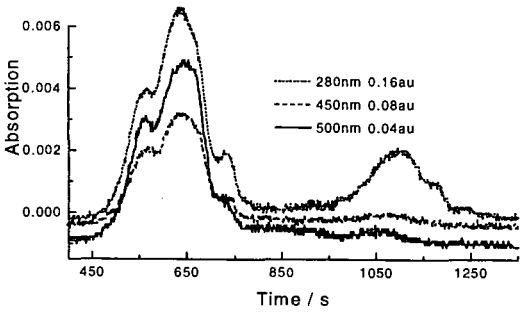

Figure 5 Chromatograms of mixed solvent extract from gasifier char.

DETERMINATION OF ORGANIC SULFUR FORMS IN SOME COALS AND KEROGENS BY ATMOSFERIC PRESSURE TEMPERATURE PROGRAMMED REDUCTION (AP-TPR).

J. Yperman[a], I. I Maes[a], D. Franco[a], C. E. Snape[b], S. C. Mitchell[c], S. R. Palmer[d], J. Mullens[a] and L.C. Van Poucke[a]

a) Laboratory of Inorganic and Physical Chemistry, Limburgs Universitair Centrum, B-3590 Diepenbeek, Belgium
b) Department of Pure and Applied Chemistry, University of Strathclyde, 295 Cathedral Street, Glasgow G1 1XQ, United Kingdom
c) School of Chemistry, University of Leeds, Leeds LS2 9JT, United Kingdom
d) Mechanical Engineering and Energy Processes, Southern Illinois University at Carbondale, Carbondale, IL 62901, U. S. A.

ABSTRACT

The following samples have been investigated as examples for the applicability of the atmospheric pressure temperature programmed reduction (AP-TPR) technique : Indiana #5, Herrin #6, and Upper-Freeport (Argonne Premium coal, USA), Kimmeridge Dorset-Cuddle (Type II kerogen, UK) and Mequinenza (lignite, Spain). The Mequinenza lignite has been treated with diluted nitric acid in order to remove pyrite while for the Upper Freeport and the Kimmeridge the pyrite was removed by a $LiAlH_4$ treatment. The Indiana #5 and Herrin #6 were treated with a peroxy-acetic acid solution at room temperature in order to remove beside pyrite also other sulfur groups. The AP-TPR profiles of the treated and untreated samples are discussed and compared with each other. It is demonstrated that $LiAlH_4$ as the peroxide treatment not only removes pyrite, but also changes and removes other sulfur functionalities. The AP-TPR technique proved that the pyrite signal is clearly resolved and that possible retrogressive reactions might be hidden under other sulfur functionalities, which has no important influence on the interpretation of the AP-TPR profile after pyrite reduction.

INTRODUCTION

As often discussed, the presence of sulfur is undesirable in metallurgical coke, as well as in the production of smokeless and formed fuels. Therefore a prior desulfurization is recommended. While inorganic sulfur can mostly be removed by simple physical methods, the removal of organic-bound sulfur always needs a chemical treatment. Herefore, it is necessary to know which sulfur forms occur in the coal in order to choose a suitable method of desulfurization and to estimate the extent of desulfurization as well as the kind of sulfur functionalities that have been removed. At the moment a number of chemical and instrumentation methods are used for the determination of these different sulfur functionalities in coal [1]. AP-TPR[2-5] proved to be a powerful technique to gain more insight into the sulfur form distribution in the raw as well as in the treated coal.

EXPERIMENTAL

Samples : the treatments and the analyses of the coals and kerogens have been described previously[6-7] and are listed in table I and II.
Apparatus : the atmospheric pressure TPR setup has been described previously[3-5].
Samples were heated from 20° to 1000°C, at a rate of 5°C/min. Experiments were always recorded in a pure H_2-atmosphere.

RESULTS AND DISCUSSION

a) Mequinenza Lignite

In figure 1 the AP-TPR-results are shown for the Mequinenza lignite as received (a) and treated (b) with diluted nitric acid. Based on model compound work[5], it is possible to assign the regions in the AP-TPR profiles to specific organic sulfur groups. For the raw Mequinenza lignite figure 1 curve (a), the first peak at 395°C must be attributed to alifatic sulfide as well as to mixed aryl-alkyl sulfides. The quite pronounced shoulder around 500°C can be attributed to pyritic sulfur. The second peak at 605°C represents the di-aryl sulfides. Above 700°C, simple thiophenes are visible. Above 800°C, even more complex thiophenic structures can be observed. The total amount of sulfur detected by the AP-TPR-technique is 6.0%, or an overall 76% sulfur recovery.

Looking at the HNO_3-treated Mequinenza lignite AP-TPR profile [figure 1 curve (b)] and comparing it with curve (a) of the native coal, pyrite as well as alifatic sulfides have been mostly removed. This results in a less pronounced first signal still demonstrating the presence of aryl-alkyl sulfides. But also aryl sulfides are present as shown by the peak at 645°C. A well pronounced signal at 730°C refers to the presence of simple thiophenes. It is believed that due to the effect of the HNO_3 treatment also a better accessibility of the coal towards the reduction proces is established. The sulfur yield of this AP-TPR-experiment is 4.6%, i.e. a 53% sulfur recovery of the total amount of sulfur present in the coal sample.

b) Kimmeridge Kerogen

In figure 2 the Kimmeridge Dorset-Cuddle AP-TPR-profiles are shown. The sulfur recovery is quite high for the native kerogen (a) as for the $LiAlH_4$-treated (b). The changes in the AP-TPR-profiles [see curve (a) vs. (b)] are spectacular. This was also the case for the HP-TPR plots[6]. The pyrite peak is not visible in the raw material kinetogram. The first main peak for the kerogen can be attributed to aryl-alkyl sulfur forms (T_{max} at 410°C). The second corresponds with di-aryl sulfur functionalities. The onset of the first peak starts later suggesting the absence of pure alifatic sulfur forms in Kimmeridge Kerogen. The AP-TPR results show some differences with the HP-TPR findings, probably due to the disturbing role

of pyrite.
Looking at figure 2 curve (b), the $LiAlH_4$ treatment not only removes pyrite, but obviously has also a drastic influence on the other sulfur groups. Beside pyrite aliphatic sulfur forms as well as certain amounts of aryl-alkyl sulfides are also removed. The signal starting at 175°C, indicates that beside some desulfurization also some new, easy to reduce, sulfur compounds are formed, in this case thiols. The main peak (T_{max} at 630°C) in figure 2 curve (b) is much more narrow than the corresponding one in figure 2 curve (a) with a maximum at 600°C. This indicates that the $LiAlH_4$ treatment also partly removes or changes di-aryl sulfides. It is quite clear that the $LiAlH_4$ treatment disturbs the other sulfur forms in the kerogen as well during the desulfurization by breaking certain sulfur bonds and creating others.

c) Bituminous coal

Figure 3 gives the AP-TPR-spectra of the raw and $LiAlH_4$-treated Upper Freeport samples (both with almost a 100% sulfur recovery). The peak at 530°C is believed to be the pyrite signal. The shoulders at lower and higher temperatures must be assigned to alifatic sulfides and aryl-alkyl sulfides, and pure aryl sulfides (T_{max} at 585°C), respectively.
Because of the high amount of pyrite, the $LiAlH_4$ treatment is quite effective. .This is shown by the AP-TPR-profile in figure 3 curve (b). Only simple thiophenic structures are detected, but only in very small amounts. These findings are in agreement with the one of the HP-TPR experiment. It is clear that according to the coal type, the $LiAlH_4$-treatment can cause different effects during the desulfurization process.

d) Argonne Premium coals

In figure 4 the AP-TPR profiles of Indiana #5 as received [curve (a)] and after treatment with peroxy-acetic acid for 6 hours [curve (b)] and 24 hours [curve (c)] are shown. The sulfur amount in wt % detected by the set-up is 2.9%, 1.1% and 0.73%, respectively. Using the model compound work[5], the signal at 460°C can be attributed to alifatic sulfides and aryl-alkyl sulfides. The shoulder around 540°C is attributed to pyrite and the peak at 595°C refers to di-aryl sulfur compounds. The feature at higher temperature is caused by simple thiophenes.
Comparing figure 4 curve (a) with curves (b) and (c), it is clear that beside the removal of pyrite [minimum in both profiles (b) and (c) at 540°C] the other non-thiophenic compounds are also partly removed by the peroxy-acetic acid treatment. The longer the treatment is performed, the less non-thiophenic sulfur is found. One can conclude that the peroxide method is an overall desulfurization method as many sulfur forms are affected by this oxidation. In how far condensed or complex thiophenic sulfur is attacked by this treatment is not clear at the moment. At the moment AP-TPR is not capable to reduce these sulfur functionalities effectively.
In figure 5 the AP-TPR results are shown for the Herrin #6. The profile for the raw material is given by figure 6 curve (a). The peak at 425°C corresponds with alifatic sulfides. The one at 485°C refers to aryl-alkyl sulfur functionalities. In this case the pyrite peak is not visible because of its low presence. The 485°C signal and the huge signal with a maximum at 605°C refer to aryl sulfur compounds and even some simple thiophenic structures. For the oxidised samples, the AP-TPR profiles in figure 5 curves (b) and (c) show the same trends as for the Indiana #5, i.e. all sulfur forms present in the raw coal are attacked by the peroxide treatment. The longer the experiment is performed the more sulfur forms of all kind are removed. The sulfur recoveries in wt% for the AP-TPR experiments in figure 5 are again quite high: 3.4%, 2.0% and 1.3%, for curves (a), (b) and (c) respectively.

CONCLUSIONS

It is demonstrated that AP-TPR provides differentiated profiles which can be explained in terms of different organic sulfur functionalities. The pyrite signal can be distinguished very easily from the organic sulfur peaks. It is shown by the AP-TPR technique that different desulfurization treatments not only removed the specific sulfur group, but also affect other sulfur forms present in the coal as well. This is also found by other treated coal samples using the same or other methods.

ACKNOWLEDGEMENT

The authors like to thank mrs. M. Vanhamel and Mr. J. Kaelen for their technical assistance with the TPR experiments. I. I. Maes is supported by a specialisation grant from the "Vlaams Instituut voor de bevordering van het wetenschappelijk-technologisch onderzoek in de industrie (IWT)".

REFERENCES

1. Davidson, R., Organic Sulfur in Coal, IEA Coal Research, London, 1993.
2. Majchrowicz, B.B., Franco, D.V., Yperman, J. , Reggers, G., Gelan, J., Martens, H., Mullens, J. and Van Poucke, L.C., Fuel, 1991, **70**, 434.
3. Majchrowicz, B.B.,Yperman, J., Mullens, J. and Van Poucke, L.C. , Anal. Chem., 1991, **63**, 60.
4. Yperman, J., Franco, D., Mullens, J., Reggers, G., D'Olieslaeger, M., Van Poucke, L.C. and Marinov, S.P. in *Composition, Geochemistry and Conversion of Oil shales*, C. Snape (ed.), Kluwer academic Publishers, 1995, 449.
5. Ismaïl, K., Mitchell, S.C., Brown, S.D., Snape, C.E., Buchanan III, A.C., Britt, P.F., Franco, D.V., Maes, I.I. and Yperman, J., Energy & Fuel, in press.
6. Mitchell, S.C., Snape, C.E., Garcia, R., Ismaïl, K. and Bartle, K.D., Fuel, 1994, **73**, 159.
7. Palmer, S.R., Kruge, M.A., Hippo, E.J. and Crelling, J.C., Fuel, 1994, **73(7)**, 1167.

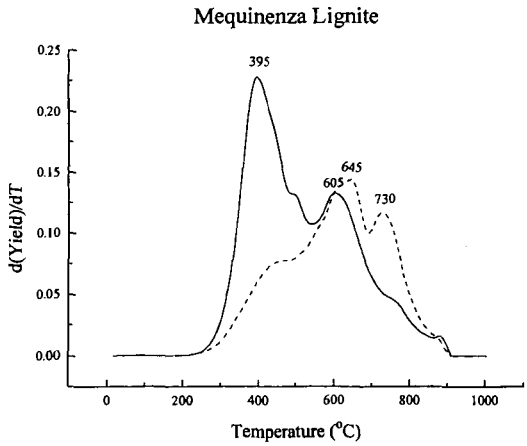

Figure 1: TPR-profiles of a Mequinenza Lignite as received (a) and after HNO_3 treatment (b).

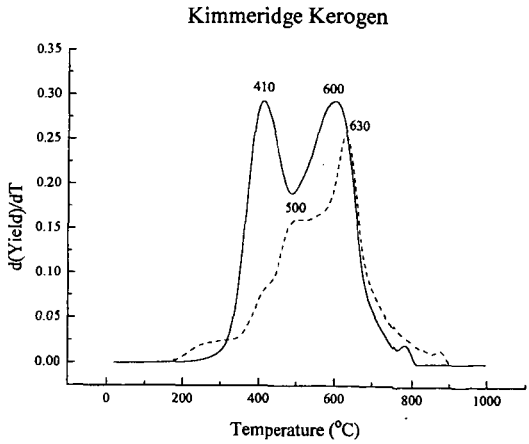

Figure 2 : TPR-profiles of Kimmeridge Kerogen as received (a) and after $LiAlH_4$-treatment (b).

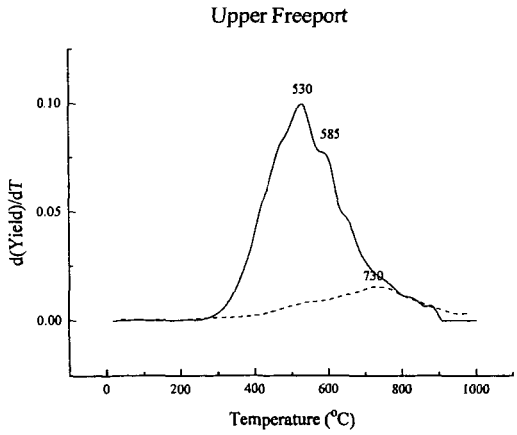

Figure 3 : TPR-profiles of Upper Freeport as received (a) and after $LiAlH_4$-treatment (b).

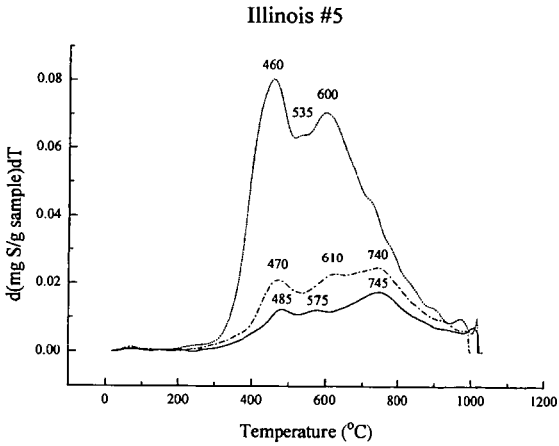

Figure 4 : TPR-profiles of Indiana #5 as received (a) and after 6 hours (b) and 24 hours (c) oxidation.

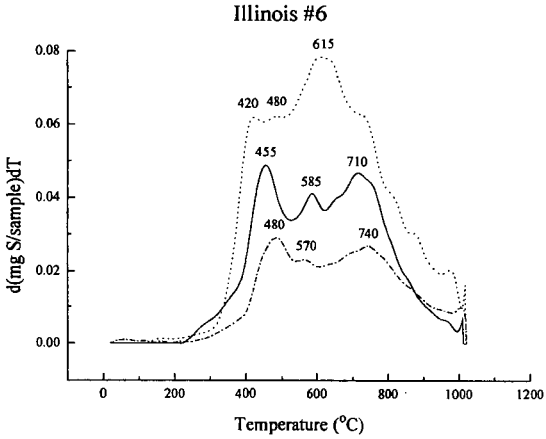

Figure 5 : TPR-profiles of Herrin #6 as received (a) and after 6 hours (b) and 24 hours (c) oxidation.

Table I

sample (wt % dmmf)		Mequinenza	Kimmeridge	Upper Freeport
	C	66.4	55.5	88.0
	H	5.8	6.2	4.8
	N	1.6	2.1	1.6
Sulfur (wt % db)	Total	9.0	8.3	2.32
	pyritic	0.5	n.d.	1.77
	sulfatic	0.5	n.d.	0.01
	organic	8.0	n.d.	0.54
after treatment Sulfur (wt % db)	Total	8.6	5.8	0.48

Table II

sample (wt % db)		Herrin #6	Indiana #5
	C	69.1	72.1
	H	5.1	5.1
	N	4.4	1.5
	O	9.5	8.4
Sulfur (wt % db)	Total	4.4	3.8
	pyritic	1.2	1.8
	sulfatic	0.1	0.0
	organic	3.1	2.0
After 6 hours ox. total sulfur (wt % db)		3.1	2.2
After 24 hours ox. total sulfur (wt % db)		1.9	2.0

DETERMINATION OF COAL RANK BY THERMOGRAVIMETRIC ANALYSIS

He Huang, Keyu Wang, M. T. Klein and W.H. Calkins*
Department of Chemical Engineering
University of Delaware, Newark, Delaware 19716

Key words: thermogravimetric analysis, coal rank, coal pyrolysis

INTRODUCTION

The thermogravimetric analysis patterns of coals and their residues reveal subtle differences between coals and changes which occur during the processing. It is the purpose of this paper to call attention to some of the various processes occurring during the TG analysis, and to show how these patterns can be interpreted in terms of changes or differences in coal structure. It is also our purpose to show how manipulation of the various TGA parameters, i.e., heating rate program, purge gas type, and the way in which the TG data are treated, can be used to reveal important aspects of the coal structure. Finally, the use of TGA as an objective criterion for determining coal rank is discussed.

EXPERIMENTAL

Apparatus. A horizontal thermogravimetric analyzer (TGA), TA Instruments model 51 (New Castle, Delaware), was employed. An approximately 30 mg sample of the coal or coal residue was loaded in a quartz pan and mounted in the instrument. The program of manipulation of the TG variables were determined by the objectives of the particular experiment.

RESULTS AND DISCUSSION

A representative TG scan on Illinois #6 coal from the Argonne Premium Coal Sample program dried in a vacuum oven with a nitrogen purge at 105 °C for 48 hours is shown in Figure 1. The weight loss resulting from heating at a ramp rate of 10 °C/min to 950 °C in nitrogen at 100 cm^3/min defines the amount of Volatile Matter (VM) in the coal. Further weight loss occurred at 950 °C after the introduction of oxygen, which was caused by the combustion of the organic material remaining. This defines the Fixed Carbon content (FC). The residue represents the ash content, which is in agreement with ash content determined by ASTM D3174.

The differential of the weight loss (DTG) curve highlights the various TG processes more clearly. The DTG curve for Illinois #6 shows a pattern which is more complex than the other Argonne coals. This becomes even more distinct and complex if the heating rate is slowed down to about 1 °C/min. The curve shown in Figure 2 has been smoothed by a rigorous mathematical treatment (1) of the numerous data points obtained in the analysis. There is a low temperature peak representing the loss of residual moisture below 200 °C. The main Volatile Matter peak starts at 350-400 °C and actually consists of three or perhaps four individual weight loss processes. The large peak is broad and probably consists of a number of pyrolysis processes. The well defined peak at 571 °C is tentatively identified as due to pyrite decomposition to pyrrhotite and sulfur because this peak is absent in coals containing little or no pyrite. Also, the decomposition temperature corresponds closely to that reported for pyrite (2). Two other small peaks are not yet identified but are fairly broad. They disappear gradually during coal liquefaction.

The DTG curves of the Illinois #6 coal in nitrogen and in hydrogen given in Figure 3 show similar patterns. However, all three peak temperatures in hydrogen, especially the highest temperature peak, are shifted to lower temperatures than those run in nitrogen. This might be due to the quenching by hydrogen of free radicals generated in the pyrolysis process to form more volatile products. The difference in the effect of the different gases is particularly apparent when the Volatile Matter produced is compared. Figure 4 shows the Volatile Matter produced in hydrogen and in nitrogen over a wide range of heating rates. The Volatile Matter yields are consistently higher, and therefore the Fixed Carbon yields are lower, in hydrogen than in nitrogen.

The heating rate also has a strong effect on the yields of Volatile Matter in either hydrogen or nitrogen (Figures 4a, 4b, and 4c). In hydrogen, the Volatile Matter yields decrease somewhat as the heating rate increases. This may be because, at the higher heating rates, the pyrolysis times are shorter, providing less time for reaction with the molecular hydrogen to form more volatile products. However, in nitrogen, the Volatile Matter yields increase with heating rate. At the low heating rates, the unquenched free radicals react to form more retrograde products (fixed carbon). This is in agreement with

the well known observation of the increase in yield of flash pyrolysis products compared with that of slow pyrolysis. This is shown by experiments on three coals of differing rank.

TGA of Coal Liquefaction Residues. When the Illinois #6 coal is reacted in tetralin (8:1 tetralin to coal by weight) at 400 °C, the fine structure of the DTG profile of the partially reacted coal residue gradually disappears. This is shown in Figure 5, which suggests that liquefaction promotes the removal of the materials producing the fine structure peaks.

It is interesting that the changes in Volatile Matter of the residue during liquefaction are insensitive to whether the liquefaction is run in nitrogen or hydrogen, or in the presence of catalyst and hydrogen (Figure 6). This is not true, however, for the formation of Fixed Carbon. In general, more Fixed Carbon is formed as the liquefaction proceeds. However, the amount formed is greatly diminished when the liquefaction is carried out in the presence of hydrogen and a hydrogenation catalyst (Figure 7).

TGA of Coals of Various Ranks. DTG curves for all eight Argonne Premium Coals, dried at 105 °C for 48 hours and run at 10 °C/min with a nitrogen gas purge rate of 100 cm^3/min, are shown in Figure 8. This clearly shows the gradual shift of peak temperature as the coal rank increases from Lignite to low volatile bituminous coal. At the same time, the peak height increases to a maximum and then decreases again as the rank increases. This trend is more clearly evident in the plot of peak temperature vs carbon content (in wt%) shown in Figure 9. If peak height is plotted against carbon content, a volcano type curve is obtained. This is shown in Figure 10. While there are a number of measures of coal rank (3 - 12), this provides an independent and objective measure of coal rank which can be useful particularly in borderline cases.

SUMMARY AND CONCLUSIONS

1). Thermogravimetric Analysis (TGA) provides sensitive, rapid and reproducible results concerning the various weight loss processes that can be a reflection of the physical and chemical structure of coals. Additional information can be obtained by variation of TG variables, such as heating rate and purge gas type.

2). TGA also reveals changes in the physical and chemical structure of coal as it undergoes coal liquefaction. This technique also is capable of revealing the onset and rate of the retrograde reactions occurring during the liquefaction process.

3). TGA provides an independent measure of coal rank.

ACKNOWLEDGEMENTS

The support of this work by the Department of Energy under DE22-93PC93205 is gratefully acknowledged. The use of Argonne Premium Coal Samples provided by Dr Karl Vorres is also acknowledged. Additional funds for purchase of thermal analysis equipment was provided by the University of Delaware.

REFERENCES

1. Wang, Keyu; Huang, He; Wang, Shaojie; Klein, M.T.; Calkins, W.H. 'A novel smoothing technique for thermogravimetric analysis data', to be submitted in *Anal. Chem.*
2. Luganov, V.A.; Schebalin, V.I. Can. Metall. Q. *Fuel*, 1982, **21**, 157.
3. Krevelen, D.W. van 'Coal Typology, Physics, Chemistry, Constitution' 3rd ed., Elsevier Publishers (1994).
4. 'Classification of Coals by Rank' *ASTM D388*, 1966 (Reapproved 1972).
5. 'Gross Calorific Value of Solid Fuel by the Adiabatic Bomb Calorimeter' *ASTM D2015*, 1966 (reapproved 1972).
6. 'Preparing Coal Samples for Microscopical Analysis by Reflected Light' *ASTM D2797*, 1972.
7. 'Microscopical Determination of the Reflectance of the Organic Components in a Polished Specimen of Coal' *ASTM 1798*, 1972.
8. 'Proximate Analysis of Coal and Coke' *ASTM D3172*, 1973.
9. 'Volatile Matter in the Analysis Sample of Coal and Coke' *ASTM D3175*, 1973.
10. 'Ultimate Analysis of Coal and Coke' *ASTM D3176*, 1974.
11. 'Carbon and Hydrogen in the Analysis Sample of Coal and Coke' *ASTM D3178*, 1973.
12. 'Gross Calorific Value of Solid Fuel by the Isothermal-Jacket Bomb Calorimeter' *ASTM 3286*, 1973.

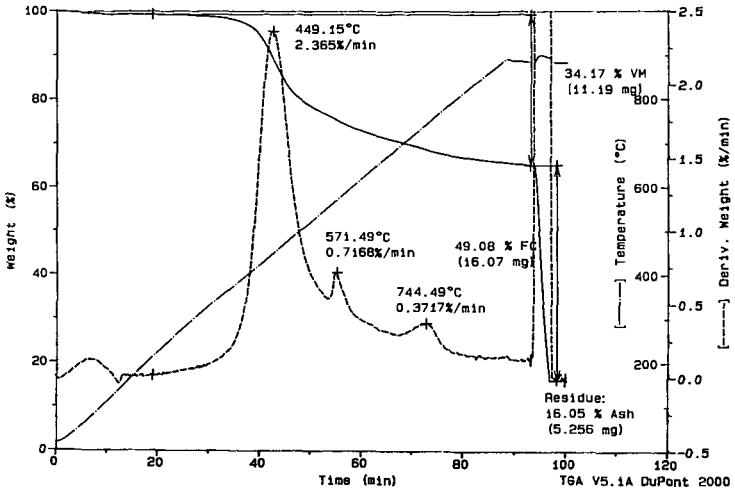

Figure 1 A TG scan on the Illinois #6 coal at 10 °C/min

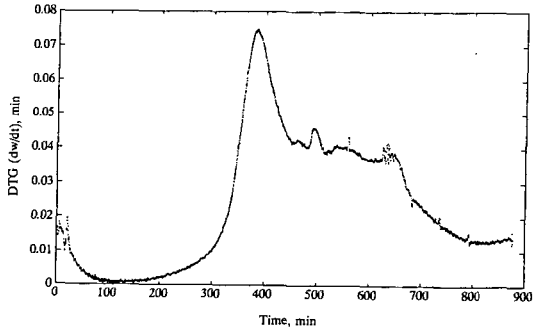

Figure 2 A TG scan on the Illinois #6 coal at 1 °C/min

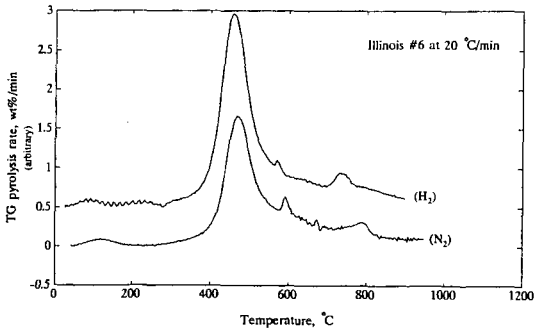

Figure 3 - Effect of gas atmospher on DTG of the Illinois #6 coal pyrolysis

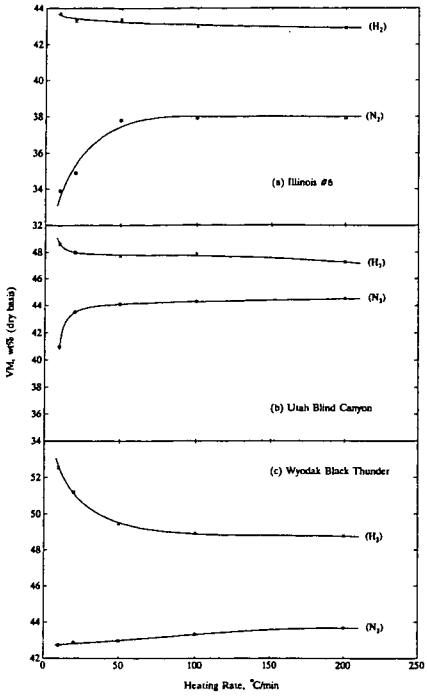

Figure 4 Effect of heating rate on the VM yields determined by TG pyrolysis in N_2 and H_2 of a). Illinois #6, b). Utah Blind Canyon, and c). Wyodak Black Thunder

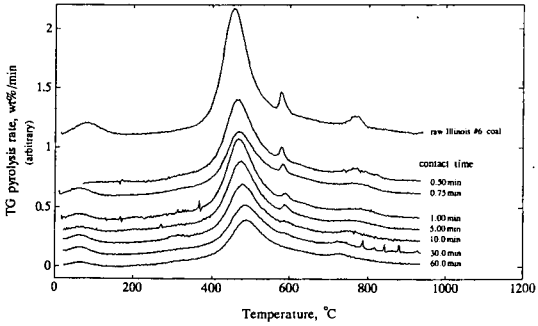

Figure 5 DTG profiles for residues of the Illinois #6 coal after liquefaction in tetralin at the selected contact times (TG scan at 10 °C/min; Liquefaction run at 390 °C under 1000 psig N_2)

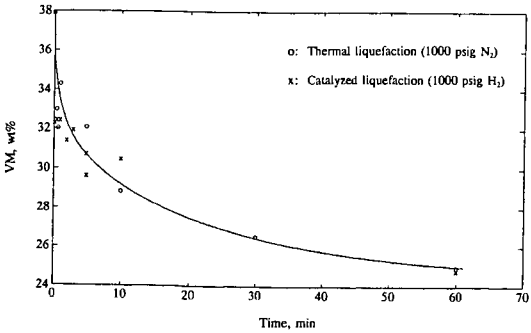

Figure 6 VM (volatile matter) in the liquefaction residues determined by TGA

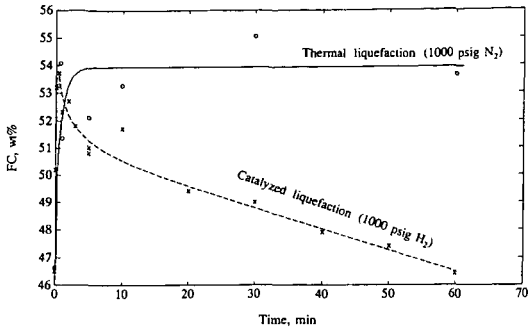

Figure 7 FC (fixed carbon) in the liquefaction residues determined by TGA (Liquefaction run: T:C = 8:1; 390 °C; TG scan: 100 cm^3(STP)/min N_2; 100 °C/min)

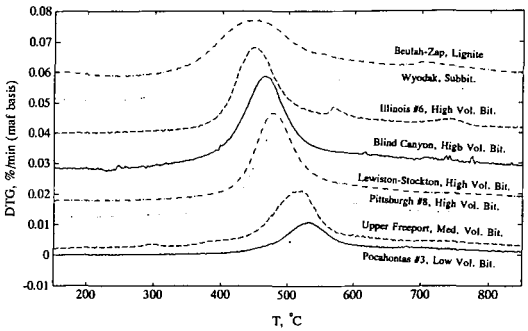

Figure 8 Pyrolysis DTG profiles of the Argonne Premium Coal samples

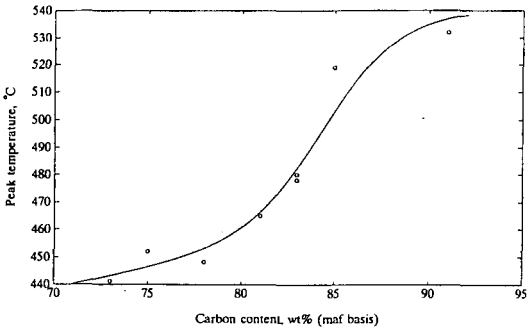

Figure 9 Peak temperature vs. carbon content of the Argonne Premium Coal samples

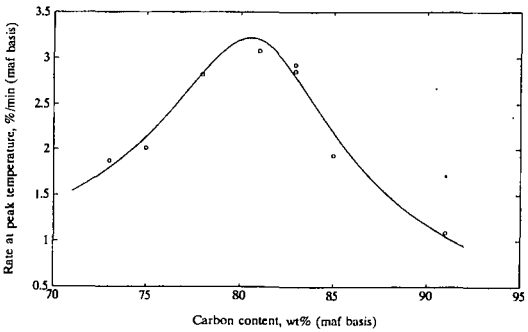

Figure 10 Rate at peak temperature vs. carbon content of the Argonne Premium Coal samples

A THERMOGRAVIMETRIC ANALYSIS OF CATALYTIC HYDROPROCESSING OF A COAL-DERIVED LIQUID

X. Song[1], S. Lu[2], H. Fu[2] and I.G. Dalla Lana[2]
[1]Corresponding author, Department of Chemical Engineering, Laval University
Ste-Foy, Quebec, Canada G1K 7P4
[2]Department of Chemical Engineering, University of Alberta
Edmonton, Alberta, Canada T6G 2G6

Keywords: Thermogravimetric analysis, coal-derived liquids, hydroprocessing.

INTRODUCTION

Thermogravimetric analysis (TGA) has normally been used to study thermal behaviours of solid materials. The extension of this technique to materials in fluid phases is less common. So far there have been very few reports dealing with the application of TGA to solid-catalyzed gas-phase reaction system. Massoth and Cowley [1] described the use of a stirred flow microbalance in studying the catalytic hydrogenation of 1-butene under steady-state reaction conditions. More recently, TGA was combined with techniques such as online MS or GC analysis to study catalytic reactions [2,3]. However, the use of TGA in studying a solid-catalyzed gas-liquid reaction, especially when the liquid is a relatively non-volatile complex feedstock, is very limited.

Laboratory-scale experiments on the hydroprocessing of complex feedstocks such as coal-derived liquids (CDLs) involve considerable preparation and time as well as chemical analysis to obtain useful information. The application of TGA to studies of such a complex reaction system appears appealing because of its small sample size requirement, short running period, simple operation and thus low running expense. In the present work, an attempt was made to explore the usefulness of TGA to catalytic hydroprocessing of a CDL. A programmed heating of an organic complex such as a CDL usually involves vaporization and chemical reactions such as thermal cracking, coking, etc., depending on temperature and operation conditions. If the system contains an active solid catalyst, the process will be more complicated. We found that many operating parameters have significant effects on the TGA data of CDL-catalyst mixture samples. For such a complex system, it is essential to set-up standardized operating conditions. The effects of various operating parameters on TGA curves were investigated in order to establish a reliable procedure. This paper reports TGA results of catalytic hydroprocessing of a CDL, the influence of TGA atmosphere (carrier gas) on CDL weight loss, and the comparison of performances of different catalysts in TGA of CDL.

EXPERIMENTAL

TGA experiments were carried out using a Perkin Elmer TGS-2 Thermogravimetric Analyzer. In most runs, the amount of CDL in a CDL-catalyst mixture sample was about 20 mg. H_2 or N_2 was used as a carrier gas (100 ml/min, atmospheric pressure). Temperature was programmed from 50 °C to 450 °C at a heating rate of 5 °C/min. The weight loss of a catalyst itself due to removal of moisture was obtained under these conditions, and was usually less than 5%. The weight loss of CDL in contact with the catalyst was obtained by subtracting the weight loss of the catalyst from total weight loss of the mixed sample.

RESULTS AND DISCUSSION

In our preliminary experiments, we found that many TGA operating conditions such as heating rate, sample weight, pan material and carrier gas flow rate significantly influenced TGA data. Efforts were therefore made to find reasonable conditions, and the following were chosen: heating rate = 5 °C/min; CDL sample weight = 20 mg; pan material = quartz; carrier gas flow-rate = 100 ml/min.

Effect of catalyst particle size What occur in the samples under our operating conditions involve gas-liquid-solid heterogeneous reactions, such as thermal/catalytic cracking, hydrogenation, coking, etc. Weight loss percentage and weight loss rate can be considered as measurements of overall conversion and conversion rate, respectively. Conversion is strongly dependent on the contact among gas (carrier gas), liquid (CDL) and solid (catalyst). In the present work, the mixed samples of CDL and catalyst were made by simply immersing a catalyst into CDL. Particle size of the catalyst will influence the contact among the three phases, and thus conversion. Fig. 1 shows the influence of catalyst ($Ni\text{-}Mo/Al_2O_3$) particle size on weight loss of CDL, where the weight of CDL in the mixed samples (catalyst content 50 wt%) was 20 mg and hydrogen was used as the carrier gas. It can be noted that the presence of the catalyst has a significant effect on CDL weight loss. Compared to the data obtained in the absence of the catalyst, CDL in contact with the catalyst has an increased weight loss at lower temperatures and a decreased weight loss at higher temperatures. The finer the catalyst particles, the greater the CDL weight loss (Fig. 1a). In addition, the presence of catalyst brings about a lower temperature at which maximum CDL weight loss rate occurs (maximum weight loss rate temperature). The finer the catalyst particles, the greater the maximum of CDL weight loss rate (Fig. 1b).

In order to examine whether the difference between the curve for pure CDL and the curves for CDL in contact with the catalyst resulted from the catalysis (a chemical factor) or from the better contact between CDL and atmosphere (H_2) provided by CDL dispersion on fine solid catalyst

particles (a physical factor), a mixture of fine glass beads (0.10 - 0.12 mm) with CDL was subjected to TGA. It was found that TGA curves with and without glass beads almost overlapped, indicating that inert materials such as glass beads cannot result in substantial change in TGA curve of CDL. In other words, the increased CDL weight loss at lower temperatures and the decreased at higher temperatures in the presence of a catalyst is mostly caused by the interaction between CDL and active sites on the catalyst surface, not by a larger exterior area exposing to hydrogen. Finer catalyst particles resulted in a greater CDL weight loss and a greater weight loss rate. This is because there are more accessible catalytic sites for CDL to reach on smaller catalyst particles.

An anomalous observation is that, at relatively high temperatures the presence of catalyst always suppresses CDL weight loss. The coke formation on catalyst surface at higher temperature is the most probable reason for the phenomenon. To examine this speculation, following calcination was carried out. A residue in a sample pan was calcined at 600 °C in air in a muffle furnace for 30 minutes after TGA. The residue was weighed before and after the calcination respectively. The weight loss of the residue during the calcination accounts for the coke formed during the TGA run. CDL weight loss was obtained by subtracting catalyst weight loss from total weight loss of the sample. The results listed in Table 1 indicates that coking on catalyst surface does occur at higher temperatures. This may result from the high content of aromatics in the CDL. In subsequent runs, the catalyst particles finer than 0.12 mm were used.

Influence of the catalyst content in CDL-catalyst mixture Fig. 2 shows the influence of catalyst content in a mixture sample on CDL weight loss. Hydrogen was used as a carrier gas. CDL weight in the sample was 20 mg. The important point is that the presence of a catalyst in the feedstock resulted in an increased CDL weight loss at low temperatures. This increased weight loss is shown in Fig. 3, which was obtained by subtracting CDL weight loss observed in the absence of the catalyst from that in the presence of the catalyst. It is seen from Fig. 3 that a high catalyst content (> 50%) or a low one (< 40%) is not favourable for CDL weight loss. The fact that too high a catalyst content suppresses weight loss suggests that the weight loss is affected not only by catalytic effects but also by adsorption of CDL on the catalyst surface. When the catalyst content is increased to a certain extent (> 50%), enhanced adsorption causes somewhat stabilized adsorbed species on the catalyst surface. On the other hand, when catalyst content is too low (< 40%), it is difficult to make a uniformly mixed CDL-catalyst sample. Therefore, an intermediate catalyst content is suggested in order to obtain reliable data. In subsequent runs, a catalyst content of 40% or 50% is used.

Reproducibility of TGA results The above discussions indicate that the TGA data of CDL strongly depend on the operating conditions. Strictly controlled operating conditions are essential because of the small sample size and high sensitivity of the TGA system. Several operating parameters have been chosen. Using these standardized parameters, tests of TGA reproducibility for CDL without and with a catalyst were carried out, and the maximum deviation in CDL weight loss observed among three independent runs is 0.7% for pure CDL sample and 1.2% for CDL-catalyst mixture sample, respectively.

Effect of gas atmosphere This series of runs was carried out with Ni-Mo/Al_2O_3 catalyst. CDL weight and the catalyst content in the feedstock were 20 mg and 40 wt% respectively. Fig. 4a shows that CDL weight loss is higher when the sample is heated in hydrogen than in nitrogen. This observation is in agreement with that of Kordulis et al. [4] for Safaniya asphaltene. A lower maximum weight loss rate was also observed in an inert atmosphere (Fig. 4b). The same tendency was observed in the presence of a catalyst. In both hydrogen and nitrogen, the effect of the catalyst was displayed at lower temperatures (< 300°C), as evidenced by the higher weight loss and the lower temperature for maximum weight loss rate. At temperatures above 300 °C, weight loss was suppressed by the catalyst because of coke formation as discussed earlier. The fact that a hydrogen atmosphere is conducive to weight loss suggests that contacting the CDL plus catalyst with H_2 suppresses the formation of coke on the catalyst to some extent. Comparison between curves 2 and 4 indicates that, for CDL feedstock which is of high aromaticity, catalytic *hydroprocessing* is much more effective than catalytic processing without the participation of hydrogen.

Comparison between different catalysts Fig. 5 summarizes the results obtained from CDL with three different catalysts at identical TGA conditions. A comparable run with pure CDL is also included. All the experiments were run in hydrogen (100 ml/min). Mixed samples contained 20 mg of CDL and 40 wt% of catalyst. Compared to the curve for pure CDL (Fig. 5, curve 1), all three curves for catalyst presence show a similar tendency, i.e., below 300 °C, the presence of catalysts has a positive effect on CDL weight loss, while above 300 °C, it suppresses CDL weight loss. Three residues from these runs were subjected to calcination using the same method as described earlier, and the results are shown in Table 2.

It is indicated in Fig. 5 and Table 2 that the interactions between three catalysts and CDL are different. The retention of CDL on the catalysts while being heated is likely to be caused by the combination of two factors, i.e., (1) surface adsorption affinity for the components present in CDL and (2) the condensation of aromatic compounds. The former predominates at lower temperatures while the latter does at higher temperatures. The additional weight loss of CDL in

the presence of catalysts may be attributed to catalytic (hydrogenation/hydrocracking) activity of the catalysts, which may occur over the whole temperature range tested. The differences between the TGA curves for different catalysts likely represent different catalytic selectivities for competing reactions such as thermal and catalytic cracking, hydrocracking, hydrogenation and coking. Coking is favoured at higher temperatures with a deficiency of H_2. Among the three commercial catalysts tested, Co-Mo/Al_2O_3 exhibits the maximum retention of CDL mass over the entire programmed temperature range. One may deduce that there is a stronger interaction between CDL and Co-Mo/Al_2O_3, which brings about somewhat stabilized adsorbed species. Because of the stable adsorption, on the one hand, it becomes more difficult for volatile components to evaporate and for reactive heavier species to be converted into lighter ones, and on the other hand, it becomes easier for aromatic species to condense on active sites of the catalyst.

If the catalyst which exhibits the minimum retention of CDL mass during the temperature-programmed heating to 450 °C is considered to be the superior one, the Ni-Mo/Al_2O_3 appears to be the best for hydroprocessing of CDL. The TGA curves have shown a different extent of CDL weight loss for each catalyst. These real differences in weight loss suggest that TGA may be useful as a tool for a quick but rough evaluation of hydrocracking catalysts.

A comparison between hydrocracking catalyst test results using the TGA method and from high-pressure batch tests To evaluate the ability of TGA to indicate the relative activities of catalysts for hydroprocessing CDL, additional runs at 13.9 MPa and 400 °C were carried out in a catalytic stirred tank reactor operated in a closed (batch) mode [5]. The following comparisons were obtained from analysis of the product liquid:

Hydrodesulfurization activity:	Ni-Mo/Al_2O_3 > Ni-W/Al_2O_3 > Co-Mo/Al_2O_3
Hydrodenitrogenation activity:	Ni-Mo/Al_2O_3 > Ni-W/Al_2O_3 > Co-Mo/Al_2O_3
Hydrodeoxygenation activity:	Co-Mo/Al_2O_3 > Ni-Mo/Al_2O_3 > Ni-W/Al_2O_3
Aromaticity-reducing ability:	Ni-Mo/Al_2O_3 > Ni-W/Al_2O_3 > Co-Mo/Al_2O_3
H/C ratio of the product liquid:	Ni-W/Al_2O_3 > Ni-Mo/Al_2O_3 > Co-Mo/Al_2O_3
Conversion to gas-oil (343-524 °C):	Ni-Mo/Al_2O_3 > Ni-W/Al_2O_3 > Co-Mo/Al_2O_3

While some of the above differences may be small, these results suggest that the Ni-Mo/Al_2O_3 catalyst provided the best overall performance. The TGA results yielded the weight loss in the following sequence (see Fig. 5):

$$\text{Ni-Mo/Al}_2\text{O}_3 > \text{Ni-W/Al}_2\text{O}_3 > \text{Co-Mo/Al}_2\text{O}_3.$$

Thus there may be some qualitative relation between overall catalyst performance and weight loss during a temperature-programmed TGA experiment.

SUMMARY

Because of small sample size and high sensitivity of TGA, its results will be significantly affected by operation conditions, especially when the sample involves a complicated system like the mixture of a relatively non-volatile CDL and a solid catalyst. In order to ensure reproducibility and to make valuable comparisons of experimental data, strictly standardized procedures need to be pre-defined in applications such as catalytic hydroprocessing (gas-liquid-solid systems).

TGA can provide useful information about solid-catalyzed relatively non-volatile liquid phase reaction systems. Such an application to hydroprocessing of a CDL was demonstrated in the present work. The weight loss of CDL as a function of increasing temperature is increased at lower temperatures and lowered at higher temperatures when a catalyst is present, irrespective of whether the atmosphere is H_2 or N_2. Preliminary results suggest that the catalyst most active for hydroprocessing of the CDL tested is the catalyst producing the greatest weight loss.

Our experimental results suggest that many of the molecular fragments are strongly absorbed on the surface of the catalyst. In a batch-type experiment such as in a TGA weighing pan, this adsorption may persist over the entire range of temperature tested and its magnitude may vary with the type of catalyst tested. At higher temperatures (>300 °C), the reactions involving coking increasingly dominate.

What occurs during TGA of CDL in H_2 atmosphere in the presence of a catalyst is so complicated that some ambiguities in TGA results exist. So far it is not yet possible to comment in depth about the chemistry involved because TGA only provided a mass-temperature record of the process. Additional work using TGA combined with some means of identifying the chemical character of the evolved gases seems to be valuable. Recent designs of TGA equipment available enable mass changes as large as ten grams to be monitored. Access to such equipment would enable chemical analysis of the residue as well as the evolved gases to be determined.

REFERENCES

[1] F.E. Massoth and S.E. Cowly, Ind. Eng. Chem. Fund., 15 (1976) 218.
[2] J.W. Dean and D.B. Dadyburjor, Ind. Eng. Chem. Res., 27 (1988) 1754.
[3] D.E. Rogers and L.M. Parker, Appl. Catal., 51 (1989) 181.
[4] C. Kordulis, F.M. Faus and B. Delmon, Appl. Catal., 23 (1986) 367.
[5] I.G. Dalla Lana, "Hydroprocessing of Coal-Derived Liquids", Final Report to Alberta Office of Coal Research and Technology, (1990).

Table 1 Coke formation from pure CDL and from CDL-catalyst mixture

Sample for TGA	Weight loss after TGA (wt%)	Weight loss after calcination (wt%)	Coke formed during TGA (wt%)
pure CDL	82.38	98.80	16.42
CDL-catalyst mixture	77.47	98.79	21.32

Table 2 Coke formation on three commercial catalysts

Mixture samples for TGA	$Ni\text{-}Mo/Al_2O_3$ & CDL	$Co\text{-}Mo/Al_2O_3$ & CDL	$Ni\text{-}W/Al_2O_3$ & CDL
Weight loss of CDL after TGA (%)	77.47	74.08	75.44
Weight loss of CDL after calcination (%)	98.79	98.82	98.78
Coke formed during TGA (%)	21.32	24.74	23.34

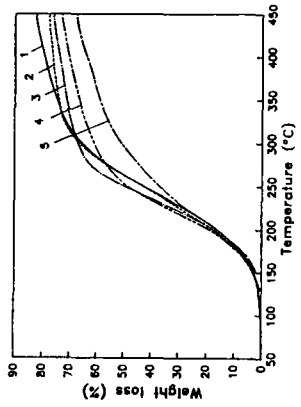

Fig. 2 Influence of catalyst content (wt%) in mixture sample: (1) 0%; (2) 25%; (3) 40%; (4) 50%; (5) 60%. Carrier gas = H_2.

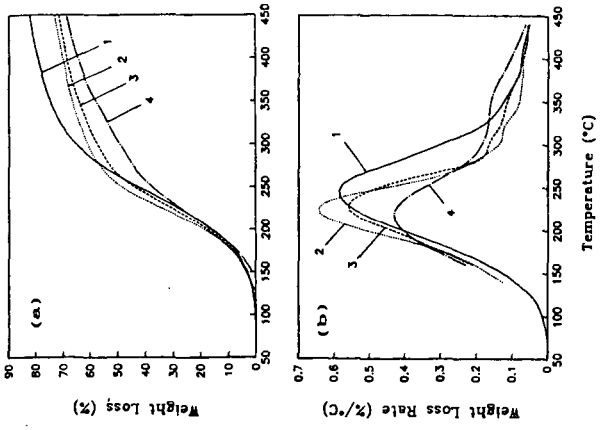

Fig. 1 Effect of catalyst particle size on TGA curve of CDL: (1) no catalyst; (2) <0.12 mm; (3) 1.59 mm; (4) 3.18 mm. Catalyst content = 50 wt%; carrier gas = H_2.

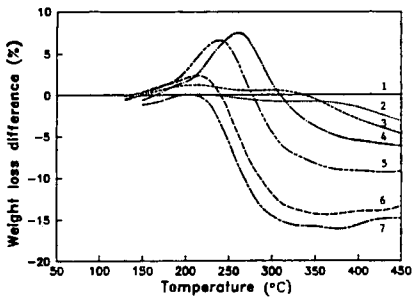

Fig. 3 The difference between CDL weight losses in the present of the catalyst and that in the absence of the catalyst. Catalyst content: (1) 0; (2) 10%; (3) 25%; (4) 40%; (5) 50%; (6) 57%; (7) 60%.

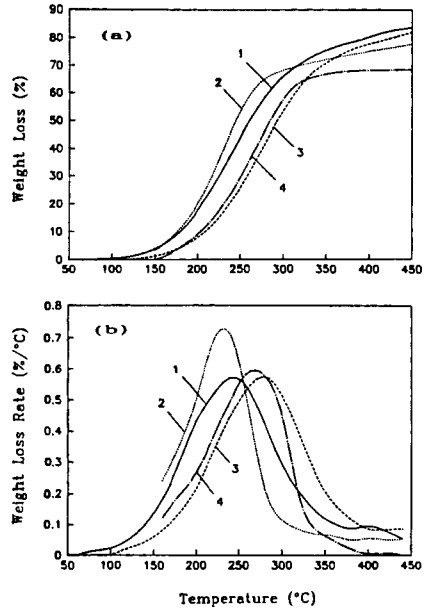

Fig. 4 Effect of atmosphere on TGA curve of CDL with and without the catalyst: (1) H_2, without catalyst; (2) H_2, with catalyst; (3) N_2, without catalyst; (4) N_2, with catalyst. Catalyst content = 40%.

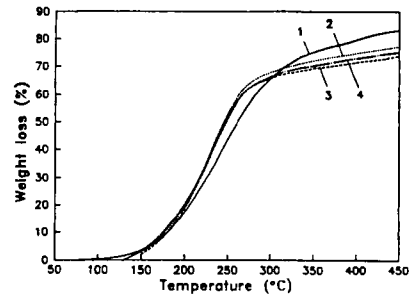

Fig. 5 TGA curves of CDL in the presence of different commercial catalysts: (1) no catalyst; (2) Ni-Mo/Al_2O_3; (3) Co-Mo/Al_2O_3; (4) Ni-W/Al_2O_3. Carrier gas = H_2.

ANALYSIS OF ORGANIC / INORGANIC ANALYTES IN ENVIRONMENTAL SAMPLES BY PACKED CAPILLARY CHROMATOGRAPHY

Mark D. Burford[1], Neil G. Smart[2], Mark M. Robson[1], Stuart C. Mitchell[1], Keith D. Bartle[1] and Antony A. Clifford[1]

[1] School of Chemistry, University of Leeds, Leeds LS2 9JT, UK

[2] British Nuclear Fuels plc, Springfield Works, Salwick, Preston PR4 OXJ, UK.

Keywords: Packed capillary columns, organic and inorganic analytes, metals.

INTRODUCTION

Recent progress in the development of techniques for packing of high efficiency capillary columns has enabled the concept of unified chromatography to be realised [1]. Packed capillary columns offer the advantages of both packed column (high loading capacity, wide range of stationary phases) and capillary column (speed of analysis, high resolution) techniques to produce a versatile and efficient analytical procedure. For the detailed investigation of fossil fuel and environmental samples the rapid growth of packed capillary chromatography offers the unique opportunity to analyse both organic and inorganic components as the column can be operated in both gas chromatography (GC) and supercritical fluid chromatography (SFC) modes. In this study, the use of packing capillary columns, prepared in-house, is investigated for both high pressure GC and SFC using helium and CO_2 as the mobile phase respectively. Several spiked and real world samples have been used to demonstrate the potential of packed capillary columns in the analysis of organic and inorganic analytes in fuel and environmental samples.

EXPERIMENTAL

Column packing procedure

A number of fused silica capillary columns, of varying length, were packed using supercritical CO_2 at 300 bar. The fused silica tubing was connected to a packing reservoir, cleaned with methanol and dried. The packing material was then placed in the reservoir. The end of the reservoir was connected to a high pressure valve which facilitated the introduction of the mobile phase. The end of the column was connected, via a Valco union containing a metal screen (2 µm), to a linear restrictor (12 µm i.d. x 30 cm fused silica tubing). The column tubing and restrictor were then immersed in an ultrasonic bath (~60-70°C). Liquid CO_2 was introduced into the system by opening both valves. The column was continuously sonicated at constant pressure throughout the packing procedure. On completion, sonication was stopped whilst the pressure was maintained for a further 30 minutes approximately, prior to depressurisation. The depressurisation step was performed slowly to avoid backflushing and possible deformation of the packed bed. At a pressure of 70-80 bar, both valves were closed and the system vented. The column was then ready for use.

High pressure gas chromatography

Two different packed capillary stationary phases were evaluated for the analysis of light hydrocarbons. The fused silica columns, i.d. of 250 µm, were packed with either 5 µm ODSII (C_{18}) or 5 µm hexyl (C_6) (Phase Separations, Deeside, UK). Three different column lengths (10, 20 and 30 cm) were installed in a Lee Scientific 600 Series SFC oven fitted with a Valco AC14LTWP injection valve and an FID. All samples were injected neat by varying the injection time. The system was evaluated using high pressure helium (20-100 bar) and carbon dioxide (40-65 bar).

Supercritical fluid chromatography (SFC)

The chromatographic system comprised an RPT 9400 (RPT Inc., San Jose, California) micro SFC pump, Lee Scientific 600 Series SFC oven, Lee Scientific micro UV detector and a Merck-Hitachi D2500 integrator. A valco AC14LTWP injection valve with an injection volume of 200 ηl was used. The various components were connected via silica capillary. A 12 µm linear restrictor was located after the UV-VIS detector and heated to 350°C to avoid blockages. The system was operated manually.

RESULTS AND DISCUSSION

High pressure gas chromatography

Microcolumns packed with conventional gas GC packings have previously been investigated at high pressures by Giddings and coworkers [2]. However, only recently has the use of LC packings been explored in high pressure packed capillary GC by Liu and Yang [3]. Conventional packing techniques introduce the stationary phase as a slurry but a new packing technique using supercritical CO_2 have been shown to provide a significant improvement in packing and column efficiency [1]. In the present study, to evaluate column performance helium

was used as the mobile phase in the analysis of low molecular weight hydrocarbons. Figure 1 shows the chromatogram obtained from the analysis of a 12 component synthetic mixture of C_5-C_8 hydrocarbons using a 20 cm x 250 µm i.d. column packed with 5 µm octadecylsilica (ODS-C_{18}). At 120 bar helium pressure, complete separation of all 12 compounds was achieved within 20 minutes. The resolution obtained from the analysis of the mixture containing six C6 isomers and four C8 isomers demonstrates the high efficiency provided by high pressure packed capillary GC for the separation of light hydrocqrbon geometrical isomers. The separation is comparable to that acheived using open tubular capillary columns but with a considerably reduced analysis time. Furthermore, due to the higher sample loading of the pacvked column, it is possible to inject the sample directly thus avoiding any possible discrimination effects normally associated with split-splitless injection when using open tubular capillary columns. The full range of the ODS column with helium as the mobile phase is shown in Figure 2 for the analysis of a light naphtha standard (Supelco 4-8265) conducted under the same conditions as above. From the chromatogram it is clear that the low molecular weight compounds are well-resolved but as the molecular weight increases the resolutin tails off indicating the current limit of the technique. Analysis of the standard by an open tubular chromatography confirmed this observation, with separation of the higher molecular weight compounds reduced considerably. However, the overall analysis time was also reduced by approximately one third.

Supercritical fluid chromatography (SFC)

The chromatographic analysis of the organic and metallic components recovered from fuel and oil related environmental samples generally involves two specific separation techniques due to the distinctive chemical and physical characteristics of both types of analytes. The organic components of interest such as polycyclic aromatic hydrocarbons (PAHs), polychlorinated biphenyls (PCBs) and petroleum hydrocarbons are sufficiently volatile to be amenable to capillary gas chromatography (GC). However, the organometallic and inorganic species, which in general cannot be volatilized or are thermally unstable at GC operating temperatures are chromatographically separated using ion-exchange or high performance liquid chromatography (HPLC) [4].

The use of supercritical fluid chromatography (SFC) has proved to be a suitable technique for the analysis of a wide range of organic compounds. For example, the separation and identification of the EPA priority PAHs in a coal tar oil can be achieved using a 30 cm x 250 µm i.d. capillary column packed with 5 µm ODS1 stationary phase (See Figure 3). The use of this short column which contained a tailor made PAH stationary phase (Phase Separations, Deeside, UK) eluted the 16 priority PAHs within 30 minutes. Whilst the elution of organic components by supercritical fluids is readily attainable, the elution of metal ions is considerably more difficult due to the charge neutralisation required to solvate ions in the mobile phase [5]. Furthermore, previous studies have demonstrated that ionic organometallic compounds result in poor peak shapes due to their chemical reactivity with the stationary phase [6]. However, by chelating the metal ion with a ligand to form a neutral metal complex the solubility and hence the chromatography of the metal species can be significantly improved [7].

Initial SFC investigations of common metal complexes such as metal dialkyldithiocarbamates (DDC) used packed columns with an organically modified carbon dioxide (CO_2/MeOH) mobile phase. More recently, capillary GC with pure carbon dioxide has offered improved resolution [8], but the technique requires that the metal DDC complex be sufficiently soluble in the mobile phase to avoid broad peak shapes and poor reproducibility [7]. Packed capillary chromatography offers the advantages of both a packed column (e.g. high loading capacity and a wide range of stationary phases) and a capillary column (e.g., speed of analysis and high resolution) and therefore metal DDC complexes with relatively low solubility can be adequately resolved using just pure CO_2. Figure 4 shows the chromatogram of an organic extract containing the DDC ligand and the metal complexes $Fe(DDC)_3$ (7 µg) and $Ni(DDC)_2$ (14 µg).

Organometallic compounds can also be separated using the same 20 cm packed capillary ODS1 column (Figure 5) with pressure programming. Both ionic (triphenyltin chloride) and non-ionic (tetraphenyltin, triphenylarsenic and ferrocene) species were detected with good chromatographic peak shapes. Earlier studies have found that the presence of an anionic functional group increases the polarity and chemical reactivity of the organometallic compounds, which consequently results in poor peak shapes [6] and/or incomplete recovery of injected samples [9]. Thus the elution of the ionic components has previously required an organic modifier to avoid peak tailing [6], however this addition step was not necessary with the packed capillary system.

The wide range of metal complexes and organometallic species that are amenable to SFC should also be amenable to supercritical fluid extraction (SFE), and several researchers have adequately demonstrated this application [5,10]. For example, the diethyldithiocarbamate (DDC) metal complexes analysed by packed capillary are generally poorly soluble in low pressure (150 atm) and low temperature (50°) carbon dioxide [5], with solubility values in the region of 10^{-7} - 10^{-6} mol/L. Consequently, the complexes are difficult to elute from the packed capillary column without high pressures (350 atm) (See Figure 5). Thus, if the temperature and pressure of the supercritical fluid is substantially increased the solubility of the metal DDC complexes will also increase, as shown in Table 1.

Table 1. Solubility of cadmium (II) diethyldithiocarbamate in CO_2.

CO_2 conditions	Solubility (mol/L)
250 atm, 50°C	3.6×10^{-6}
250 atm, 100°C	1.6×10^{-5}
350 atm, 50°C	5.3×10^{-6}
350 atm, 100°C	6.5×10^{-5}

Using high pressure carbon dioxide (400 atm) to solvate the DDC ligand it was possible to recover between 50 and 70% of spiked Pb^{2+} and Cd^{2+} from filter paper. It is envisaged that further extractions of the metal ions with fresh complexing agent at this rigorous extraction condition could potentially achieve quantitative SFE recoveries.

REFERENCES

[1] D. Tong, K.D. Bartle and A.A. Clifford, *J. Microcol. Sep.*, 6 (1994) 249.
[2] M.N. Myers and J.C. Giddings, Anal. Chem, 38 (1966) 29.
[3] Y. Liu and F.J. Yang, J. Microcolumn Separations, 3 (1991) 251.
[4] B.R. Willeford and H. Veening, *J. Chromatogr.*, 251 (1982) 61.
[5] C.M. Wai, Y Lin, R. Brauer, S. Wang and W.F. Beckert, *Talanta*, 40 (1993) 1325.
[6] J.W. Oudsema and C.F. Poole, *Fresenius J. Anal. Chem.*, 344 (1992) 426.
[7] K.E. Laintz, J.-J. Yu and C.M. Wai, *Anal. Chem.*, 64 (1992) 311.
[8] P. Manninen and M-L. Riekkola, *J. High Resolut. Chromatogr.*, 14 (1991) 210.
[9] E. Blake, M.W. Raynor and D. Cornell, *J. Chromatogr.*, 683 (1994) 223.
[10] J. Wang and W.D. Marshall, *Anal. Chem.*, 66 (1994) 3900.

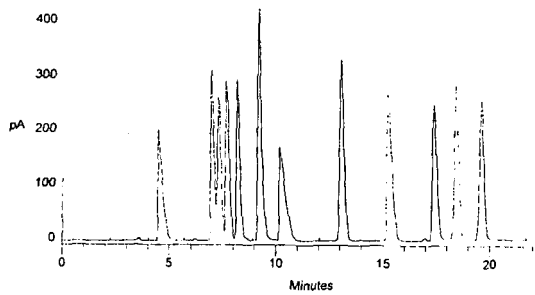

Figure 1
High pressure gas chromatogram of a mixture of: 1 Pentene, 2 Methyl Pentene, 3 Methyl Pentane, 2 Methyl Pentane, 2, 3 Dimethyl Butane, Methyl Cyclopentane, Cyclohexane, 3 Methyl Hexane, 3 Methyl Heptane, Octane, 2, 2, 4 Trimethyl Pentane, 2, 2, 4 Trimethyl Pentane.
Conditions: 20 cm, 250 μm ID, octadecylsilica column (Phase-Separations, Deeside, UK), Helium mobile phase at 120 bar, with the following temperature program: 4 minutes isothermal at 40 C, 5° C per minute ramp to 220 °C

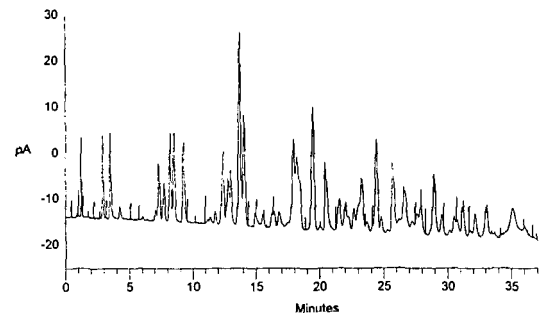

Figure 2
High pressure gas chromatogram of a light naphtha standard (Supelco 4-8265)
Conditions: 20 cm, 250 μm ID, octadecylsilica column (Phase-Separations, Deeside, UK), Helium mobile phase at 120 bar, with the following temperature program: 4 minutes isothermal at 40 C, 5° C per minute ramp to 220 °C

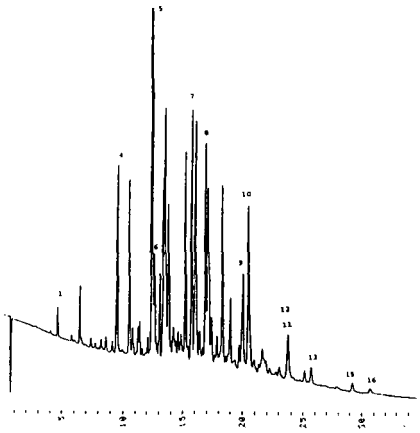

Figure 3
Supercritical fluid chromatogram of base coal tar oil analysed using the following conditions:
Column: PAH 5 μm (Phase-Separations, Deeside, UK), 30 cm column, 250 μm ID, column oven temperature 100°C, detector wavelength 254, with the following gradient 100 to 300 bar CO_2 and 0.10 to 1.00 μL/min methanol over 30 minutes.
Peak identification; 1 naphthalene; 2 acenaphthene; 3 acenaphthylene, 4 fluorene; 5 phenanthrene; 6 anthracene; 7 fluoranthene; 8 pyrene; 9 benzo[*a*]anthracene; 10 chrysene; 11 benzo[*b*]fluoranthene; 12 benzo[*k*]fluoranthene; 13 benzo[*a*]pyrene; 14 dibenzo[*a,h*]anthracene; 15 benzo[*ghi*]perylene; 16 indeno[1,2,3-*cd*]pyrene.

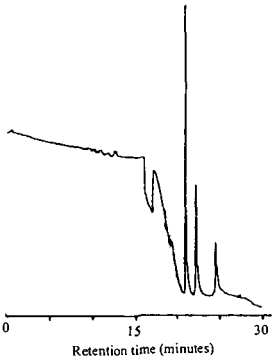

Figure 4. SFC separation of a mixture of DDC, $Fe(DDC)_3$ and $Ni(DDC)_2$ using a 20 cm x 250 μm I.D. capillary column packed with 5μm ODS1 stationary phase. Separation obtained with carbon dioxide pressure programme starting at 100 atm and increasing the pressure at 16 atm/min to 350 atm, then holding the pressure at 350 atm for 15 minutes. UV detection at 220 nm.

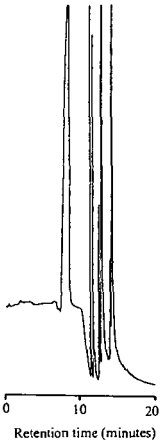

Figure 5. SFC separation of organotin, organoarsenic and ferrocene compounds using a 20 cm x 250 μm I.D. capillary column packed with 5μm PAH stationary phase. Separation obtained with carbon dioxide pressure programme starting at 100 atm and increasing the pressure at 16 atm/min to 350 atm, then holding the pressure at 350 atm for 15 minutes. UV detection at 220 nm.

INVESTIGATION OF JET FUEL THERMAL STABILITY USING PHOTON CORRELATION SPECTROSCOPY AND A QUARTZ CRYSTAL MICROBALANCE

Wayne M. Trott
Energetic and Multiphase Processes Department 1512
Sandia National Laboratories
P. O. Box 5800
Albuquerque, New Mexico 87185-0834

Keywords: Jet Fuels, Particle Size Distribution, Mass Deposition

INTRODUCTION

The thermal stability of aviation fuels is an important concern in designs for enhanced aircraft performance. In addition to its primary use as a propellant, jet fuel serves as a coolant for the environmental control system, engine lubrication, avionics, etc. in present military applications. Thermal loads on the fuel are anticipated to increase concurrently with the demands of advanced aircraft. Unfortunately, elevated temperatures in hydrocarbon-based fuels lead to oxidative degradation, producing insoluble products in the bulk liquid as well as deposits on contacting surfaces.[1] These processes reduce heat exchanger efficiencies and can result in obstructions of critical components, including valves, filters, and injection nozzles.

Efforts to develop highly stable jet fuels and thereby mitigate loss of heat-transfer efficiency and fouling problems in flight systems would certainly benefit from a predictive model that adequately accounts for the global physics and chemistry leading to insoluble particle formation and solids deposition. Recent experiments by Jones and Balster[2,3] have illustrated the complexity of these processes. In particular, their studies of Jet-A, POSF-2827 fuel[3] have demonstrated that observed insolubles are early products of autoxidation chemistry and that the "yield" of these products is directly correlated with O_2 availability. Their results also suggest that surface deposits arise from a precursor material formed in the bulk fuel in one of several independent reaction channels leading to the formation of various degradation products. Additional experimental work incorporating sensitive, real-time diagnostic methods for monitoring incipient particle formation as well as mass deposition on surfaces is clearly needed. To address this need, an experimental assembly designed for simultaneous application of photon correlation spectroscopy (PCS) and a quartz crystal microbalance (QCM) has been assembled and tested. The main aspects of this assembly and preliminary results obtained from integrated PCS and QCM measurements are described in this paper.

EXPERIMENTAL

PCS is a well established and widely used dynamic light scattering technique for quantitative measurement of particle size distributions in liquid samples. Briefly summarized, this technique monitors fluctuations in the intensity of scattered light due to Brownian motion of particles in a laser-illuminated volume. The scattered light is viewed by a photomultiplier, converted into pulse trains by an amplifier/discriminator and processed by a digital correlator, which performs an autocorrelation of the time-dependent intensity signal. For a monodisperse suspension of particles, the autocorrelation exhibits an exponential decay rate $G(\tau) \propto e^{-2\Gamma\tau}$. The decay constant, Γ, is related to the translational diffusion coefficient, D, of the scattering particles and to the geometry of the experiment through the relations

$$\Gamma = q^2 D;\ q = \frac{4\pi n \sin(\theta/2)}{\lambda}$$

where q represents the magnitude of the scattering wave vector which can be determined from the refractive index of the liquid (n), the scattering angle, (θ), and the wavelength of the incident light (λ). For spherical particles, the particle size can be determined from the Stokes-Einstein equation

$$D = \frac{kT}{3\pi\eta d}$$

where k is the Boltzmann constant, T the absolute temperature, η the fluid viscosity, and d the particle diameter. Detailed discussions of PCS instrumentation and data reduction methods are available elsewhere.[4,5] Under favorable circumstances, PCS can be used for accurate, noninvasive sizing of particles over a diameter range of a few nm to several microns. Successful application of this technique to real-time, *in situ* measurements of particle formation in heated jet fuels has been reported previously.[6] Under isothermal conditions, thermally stressed fuels appear to generate simple, monomodal particle size distributions that exhibit a systematic increase in mean particle diameter as a function of time at elevated temperature.

The QCM provides a sensitive, compact system for complementary measurements of surface deposition. This device is a bulk-wave resonator, consisting of a piezoelectric quartz wafer with metal

electrodes on each face, that can be electrically excited into resonance. When the crystal is excited in this manner, it undergoes a shear deformation with displacement maxima at the crystal faces. Mass accumulated on the crystal faces moves synchronously with the oscillating surfaces, resulting in a shift of the resonant frequency. The QCM is typically incorporated in an oscillator circuit, where the oscillation frequency decreases with mass accumulation. The theory that relates measured frequency changes to mass deposition has been presented in detail elsewhere.[7] Under conditions of constant fluid density and viscosity, the surface mass density (mass/area), ρ_s, is related to the measured decrease in frequency, $\Delta\nu$, as follows:

$$\rho_s = \left(-2.21 \times 10^5 \frac{g}{cm^2 s}\right) \frac{\Delta\nu}{\nu_0^2}$$

where ν_0 is the unperturbed resonant frequency of the device (~5 MHz). The QCM permits quantitative measurements at very low deposition rates; a typical system can easily achieve a resolution of ~0.1-0.2 $\mu g\text{-}cm^{-2}$. The utility of QCM instrumentation in jet fuel thermal stability studies was demonstrated by Klavetter et al.[8] Most of these initial tests were performed under conditions of abundant oxygen availability. Recently, Zabarnick and co-workers have used QCM systems to investigate the thermal stability of various jet fuels at relatively low oxygen availability[9] and to evaluate the effect of several jet fuel additives.[10]

A schematic diagram of the jet fuel test system designed for integrated PCS and QCM measurements is shown in Figure 1. The stainless steel pressure vessel (300 ml. capacity, Parr Instruments) provided optical access for the PCS source laser (typically a HeNe laser, 35 mW peak power) as well as a viewing port for the PCS collection optics at a 90° angle to the incident light. The lid of the vessel was modified to accommodate a mounting clamp for the QCM sensor and a hermetic, rf feedthrough assembly, as described previously.[8] The QCM was mounted vertically in the fuel in order to mitigate gravitational effects on deposition. Gas inlet and outlet ports were also located on the fixture lid, permitting fuel exposure to an oxidative or inert atmosphere at variable pressure, as desired. In order to reduce the time required to attain the target temperature and to optimize temperature uniformity in the cell, heating was supplied by band heaters attached to the window "arms" in combination with the heating mantle provided with the vessel. Temperatures were monitored by thermocouples positioned in the fuel sample and at several points on the outside of the vessel. The desired stress temperature was maintained by using one of the thermocouples as a feedback device for a programmable temperature controller (Eurotherm Model 818).

In all tests described in this paper, samples were prepared by filtering the fuel through a 0.2-μm PTFE filter, sealing the vessel, and then sparging with the desired gas (oxygen or nitrogen) for ~45 minutes. Typically, the vessel was filled to within 0.75" of the lid. For some tests, a 50 psig atmosphere of O_2 or N_2 was imposed prior to heating. In other experiments, the fuel was heated under ambient pressure conditions. Data acquisition included the frequency and dc voltage output of the QCM oscillator circuit as well as the output of the digital correlator (Langley-Ford, Model 1096). Intensities of transmitted and scattered laser light were monitored by a laser power meter (located at the output port of the test vessel) and a frequency counter (coupled to the amplifier/discriminator), respectively. In reducing the PCS data, several available algorithms were utilized, including a discrete exponential fitting program and two Laplace inversion routines.[11]

RESULTS AND DISCUSSION

Previous investigations[6,8] of jet fuel thermal stability have shown that the rates of both particle growth and mass deposition are sensitive to the temperature of the sample. Hence, reasonable uniformity of the temperature field in the test vessel is required for facile, quantitative interpretation of PCS and QCM data. Evaluation and optimization of temperature conditions in the assembly described above has been achieved by conducting heating tests employing an array of thermocouples. The results of one test are given in Figure 2. In this case, five thermocouples were placed in the fluid. Measurements were obtained near the bottom (TC1), center (TC4), and top (TC5) of the fluid volume, as well as along the side of the vessel (TC3) and within one of the three arms containing window ports (TC2). Another device (TC6) was used to monitor the outside wall temperature. The target temperature for this test was 150 C. Both fairly rapid heating and acceptable temperature uniformity in the fuel were achieved. At the target point, temperatures throughout the main body of the cell were uniform to within 0.8 C. The temperature in the extension arms was slightly hotter (~2 C). Similar results have been obtained in tests with other target temperatures.

Thus far, integrated PCS and QCM tests have been performed on Jet A 91-POSF-2827, a non-hydrotreated fuel that is known to resist oxidation but produce surface deposits in appreciable quantities at elevated temperatures, and Jet A-1 POSF-2747, a hydrotreated fuel that is highly stable with regard to surface deposition even though it consumes O_2 rapidly.[9] Results on the first substance are more developed and will be described here. Jet A 91-POSF-2827 contains a relatively high level (up to 0.1 mass percent) of sulfur compounds; these components are thought to play a significant role in both inhibition of oxidation and deposit formation.[3] A summary of mass

deposition results from QCM measurements in this fuel is provided in Table 1. Figures 3 and 4 illustrate selected QCM data in graphical form; relevant particle growth curves (as determined by PCS) and transmitted/scattered light intensity plots are shown in Figures 5 and 6, respectively.

The data obtained in this work are generally consistent with results of previous jet fuel thermal stability tests performed under similar conditions. The critical role of dissolved oxygen has been emphasized in earlier studies[3,8,9] and is again demonstrated by the tests conducted near 150 C using O_2 and N_2, respectively, as the sparge and confining gas (cf. Table 1). With abundant oxygen, the QCM system registered a mass deposition rate of 0.88 $\mu g\text{-}cm^{-2}\text{-}hr^{-1}$. A substantially lower rate was obtained when oxygen was effectively purged from the system. In fuel sparged with nitrogen and heated to 148 C under 50 psig N_2 confinement, the observed rate was only 0.13 $\mu g\text{-}cm^{-2}\text{-}hr^{-1}$. This low value compares favorably with previous QCM results acquired under oxygen-depleted conditions.[8,9] Similarly, particle formation in the fluid was very heavy with abundant oxygen but largely suppressed when the fuel was stressed with severely limited oxygen availability. In the latter case, the PCS technique was unable to provide meaningful correlations at any time during testing at elevated temperature; however, some hints of particle generation were seen in the raw data and, after the fuel cooled to room temperature, a small concentration of particles with mean diameter near 200 nm was observed. Processes leading to the generation of bulk and surface insolubles in the absence of O_2 are evidently minor but not negligible.

The remaining tests have also addressed the role of oxygen availability. For example, Figure 3 shows QCM results for a Jet A 91-POSF-2827 sample sparged with O_2 and heated to 139 C under ambient pressure. A plot of temperature measured by a thermocouple positioned in the fuel is also included in this figure for comparison. After the sample attained a constant temperature, mass accumulation closely corresponding to a linear deposition rate of 0.23 $\mu g\text{-}cm^{-2}\text{-}hr^{-1}$ was registered. The rate determined in this test compares favorably to the results of Zabarnick[9] which indicate similar deposition behavior (accumulation of 3.6 $\mu g\text{-}cm^{-2}$ at a nearly linear rate in 15 hours) for Jet A POSF-2827 sparged with air and heated to 140 C under ambient pressure. The most significant difference in experimental conditions for these two tests was the choice of oxygen vs. air for the sparging gas. The similarity in recorded mass accumulation rates suggests that the additional oxygen availability has a negligible effect on surface deposition at this temperature. In this case, added oxygen in the confining atmosphere should also play a minor role. The slightly higher deposition rate of 0.27 $\mu g\text{-}cm^{-2}\text{-}hr^{-1}$ seen in Jet A 91-POSF-2827 heated to 138 C under 50 psig O_2 (cf. Table 1) supports this expectation. Similarly, Klavetter et al.[8] reported nearly identical rates for the same fuel sparged with O_2 and heated to 160 C under 50 psig O_2 and N_2 overpressures (1.18 vs. 1.23 $\mu g\text{-}cm^{-2}\text{-}hr^{-1}$, respectively). These results all appear to be linked to this fuel's tendency to consume oxygen relatively slowly.

An additional comparison can be made with deposition rates determined by Klavetter et al.[8] for Jet A 91-POSF-2827 (confining pressure of 50 psig O_2) over a temperature range of 160-200 C. The QCM results acquired in the present work expand this range down to 133 C. Figure 4 shows an Arrhenius plot with data from three relevant tests (1, 3, and 4; cf. Table 1) added to the earlier results obtained at higher temperature. The Arrhenius "line" derived from a linear least-squares fit to the data implies an activation energy of 20 kcal/mol for the global deposition process. This value is somewhat lower than the 26 kcal/mol activation energy calculated for this fuel in Ref. 8; however, it is consistent with the behavior of other fuels examined in that study.

The simultaneous PCS and light intensity measurements provide added insight. In all tests where *some* oxygen was supplied in the sparge gas and confining pressure, large concentrations of particles formed in the fluid within several hours. Consistent with previous PCS measurements,[6] particles were detected earlier and the mean particle diameter increased more rapidly with increasing stress temperature. The influence of added oxygen at a given temperature is illustrated by the PCS results in Figure 5. At 133 C, significant particle formation was observed earlier in the presence of abundant oxygen; however, the initial rate of increase in particle size was approximately the same in the both cases. Dissimilar behavior was observed at later times. At ambient pressure, the mean particle size inferred from the PCS data increased steadily throughout the test whereas, under 50 psig O_2 confinement, the particle size appeared to level off near 300 nm. This phenomenon is probably an artifact arising from multiple scattering effects that can occur when particles are present in high concentration. The scattered light intensity data are consistent with this interpretation. Figure 6 demonstrates the complex behavior of the scattered light intensity vs. time for the test performed under 50 psig O_2. The intensity increased rapidly during the first two hours of this test, reaching a maximum value at approximately 150 minutes. This time period corresponds to the initial phase of particle formation and growth (cf. Figure 5). Thereafter, the intensity fell to roughly half the peak value at about 300 minutes and then recovered slightly. This period coincides with the observed "saturation" in particle diameter. The fuel exhibited a very "cloudy" appearance at these times, a further indication that particle formation had occurred to such an extent that the laser intensity reaching the PCS measurement volume (i.e., center of the cell) was

severely attenuated by particle absorption and scattering. In contrast, the scattered light intensity was observed to be still slowly increasing after five hours of heating Jet A 91-POSF-2827 at 133 C under ambient pressure and the fuel appeared to be only slightly "cloudy" at this point.

Figure 6 also provides results of laser power measurements taken at the exit optical port of the test vessel during the test under 50 psig O_2 confinement. The maximum in scattered light intensity accompanied a steep decline in the transmitted laser power, illustrating the important role of particle scattering and absorption at this point in the experiment. The late-time recovery of both signals shown in Figure 6 may be due in part to particle settling as the mean size increased. Also, Mie theory predicts a complex dependence of scattering cross section vs. particle diameter at sizes > 400 nm. Estimates of the relative mass involved in particle formation under an O_2 overpressure vs. ambient pressure were calculated from Mie intensity parameters in combination with the light intensities. A Beer's Law-type relationship was used to infer the laser power reaching the center of the cell from power measurements incident on and transmitted by the sample. Attenuation of the scattered light intensity by particles in the sample was accounted for in a similar fashion. These calculations suggest that the mass associated with particle formation in the fuel heated under 50 psig O_2 is 3-5 times higher (for a given time during the test) than in fuel heated at ambient pressure. For Jet A 91-POSF-2827 under these conditions, excess oxygen clearly affects the generation of bulk insolubles more substantially than it accelerates surface deposition.

CLOSURE

An experimental setup for simultaneous, real-time investigation of particle formation and surface deposition in heated jet fuels has been assembled and tested. The design permits integrated PCS and QCM measurements in a nearly isothermal environment. Data obtained from integrated measurements on Jet A 91-POSF-2827 are generally consistent with earlier results from tests performed with the individual techniques. With this fuel, oxygen availability is a factor in both particle formation and mass accumulation on surfaces. In particular, excess oxygen (at a given temperature) leads to substantially larger concentrations of particles in the bulk liquid. Integrated PCS and QCM measurements should find application in thermal stability tests of a wide range of fuel types and should permit detailed evaluation of various additives, including antioxidants, dispersants, etc. Under some conditions leading to extensive generation of bulk insolubles, quantitative particle sizing using PCS may be limited by multiple scattering effects.

ACKNOWLEDGMENTS

This work was jointly supported by the U. S. Air Force, Aero Propulsion and Power Directorate of Wright Laboratory, Wright-Patterson AFB, and the U. S. Department of Energy, Pittsburgh Energy Technology Center (PETC) through Sandia National Laboratories under contract DE-AC04-94AL85000. The support of W. E. Harrison III and Dr. W. M. Roquemore of Wright Laboratory as well as S. Rogers of the U. S. DOE PETC is gratefully acknowledged. The excellent technical assistance of Jaime Castañeda is greatly appreciated.

REFERENCES

1. R. N. Hazlett, *Thermal Oxidation Stability of Aviation Turbine Fuels*, ASTM Monograph 1 (American Society for Testing and Materials, Philadelphia, PA, 1991).
2. E. G. Jones and W. J. Balster, "Application of a Sulphur-Doped Alkane System to the Study of Thermal Oxidation of Jet Fuels," ASME Paper 92-GT-122 (American Society of Mechanical Engineers, New York, 1992).
3. E. G. Jones and W. J. Balster, "Phenomenological Study of the Formation of Insolubles in a Jet-A Fuel," *Energy & Fuels* 7, 968 (1993).
4. B. B. Weiner, "Particle Sizing Using Photon Correlation Spectroscopy," in *Modern Methods of Particle Size Analysis*, H. G. Barth, Ed. (Wiley, New York, 1984), pp. 93-116.
5. B. J. Berne and R. Pecora, *Dynamic Light Scattering with Applications to Chemistry, Biology and Physics*, (Wiley, New York, 1976).
6. E. A. Klavetter, S. J. Martin, W. M. Trott, and T. J. O'Hern, "Advanced Thermally Stable, Coal-Derived, Jet Fuels Development Program Annual Report: Experiment System and Model Development," Wright Laboratory Report, WL-TR-94-2003, December 1993.
7. S. J. Martin, V. E. Granstaff, and G. C. Frye, "Characterization of a Quartz Crystal Microbalance with Simultaneous Mass and Liquid Loading," *Anal. Chem.* **63**, 2272 (1991).
8. E. A. Klavetter, S. J. Martin, and K. O. Wessendorf, "Monitoring Jet Fuel Thermal Stability Using a Quartz Crystal Microbalance," *Energy & Fuels* 7, 582 (1993).
9. S. Zabarnick, "Studies of Jet Fuel Thermal Stability and Oxidation Using a Quartz Crystal Microbalance and Pressure Measurements," *Ind. Eng. Chem. Res.* **33**, 1348 (1994).
10. S. Zabarnick and R. R. Grinstead, "Studies of Jet Fuel Additives Using the Quartz Crystal Microbalance and Pressure Monitoring at 140 °C," *Ind. Eng. Chem. Res.* **33**, 2771 (1994).
11. P. Russo, K. Guo, and L. Delong, "A New Look at Distribution Analysis of Dynamic Light Scattering Data, Using Only a Microcomputer," Society of Plastics Engineers, 46th Annual Technical Conference Proceedings, 1988, pp. 983-985.

Table 1: QCM Results in Jet A 91-POSF-2827

Test #	Sparge Gas	Confining Pressure	Temp. (C)	Deposition Rate ($\mu g\text{-}cm^{-2}\text{-}hr^{-1}$)
1	O_2	50 psig O_2	151	0.88
2	N_2	50 psig N_2	148	0.13
3	O_2	50 psig O_2	138	0.27
4	O_2	50 psig O_2	133	0.39
5	O_2	Ambient	133	0.63 (early) 0.15 (late)
6	O_2	Ambient	139	0.23

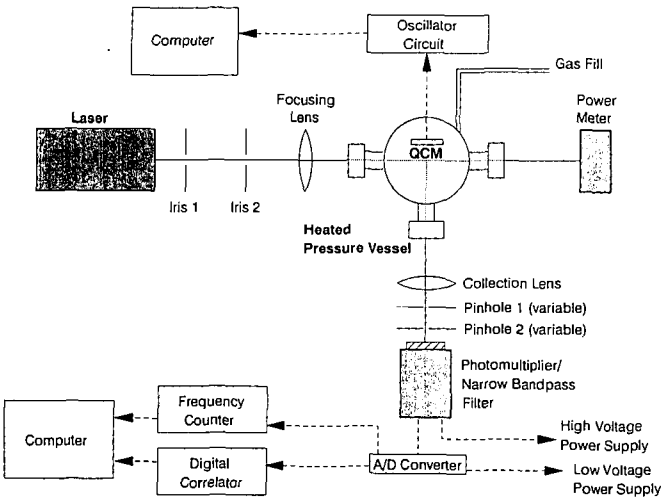

Figure 1. Schematic representation of integrated PCS/QCM system for studies of heated jet fuels.

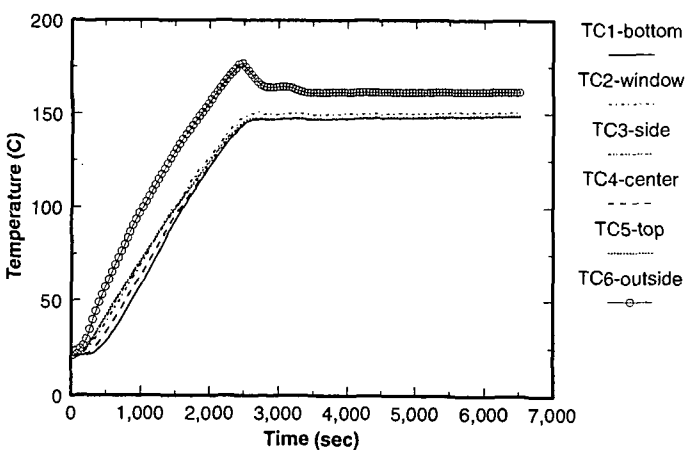

Figure 2. Temperature measurements at various points in the pressure vessel during heating of Jet A fuel. Target temperature was 150 C. Thermocouple locations are noted on legend.

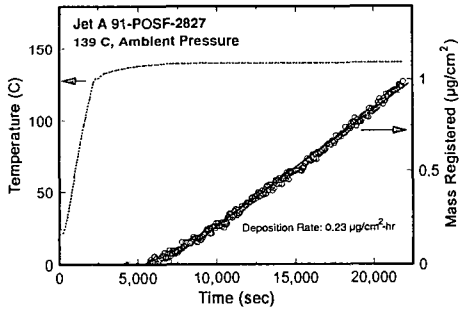

Figure 3. Mass deposition recorded by QCM in Jet A 91-POSF-2827 heated to 139 C. Test performed at ambient pressure. Temperature history in fuel is also shown.

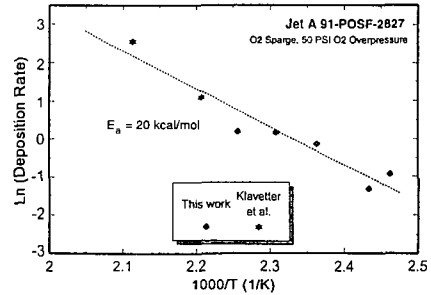

Figure 4. Arrhenius plot for Jet A 91-POSF-2827 tested at temperatures in the range 133-200 C.

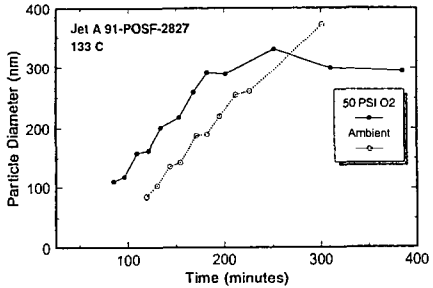

Figure 5. Particle growth measured by PCS for Jet A 91-POSF-2827 heated to 133 C. Tests conducted at two different pressure conditions.

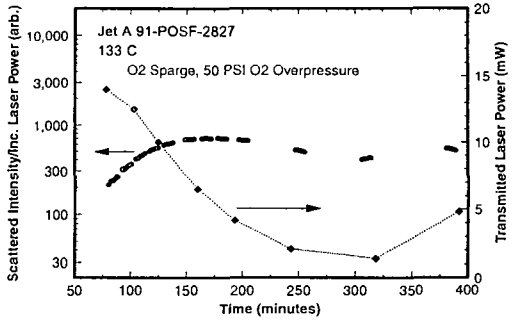

Figure 6. Normalized scattered light intensity (logarithmic scale) and transmitted laser power (linear scale) for Jet A 91-POSF-2827 heated to 133 C.

A NOVEL METHOD FOR THE DETERMINATION OF THE BOILING RANGE OF LIQUID FUELS BY THERMOGRAVIMETRIC ANALYSIS

He Huang, Keyu Wang, Shaojie Wang, M.T. Klein, and W.H. Calkins*
Center for Catalytic Science and Technology, Department of Chemical Engineering
University of Delaware, Newark, Delaware 19716

Key words: boiling range, liquid fuels, SimDis TGA

INTRODUCTION

The most widely used separation technique in the petroleum industry as well as in much of the chemical industry is distillation. This is particularly true of all liquid fuel production processes, including coal-derived liquid fuels, and shale oil as well as petroleum. To design and operate a suitable distillation column system requires a knowledge of the boiling point distribution of the materials to be separated. In recognition of this need, the ASTM developed the classical distillation procedures of ASTM D86, D216, D447, D850, and D1078. Since these methods required a relatively large sample and are not particularly precise, the widely used simulated distillation analysis based on gas chromatography (ASTM D3710-83) was introduced. This method requires only a small sample size and is reasonably rapid. However, it is limited to materials boiling below about 350°C. Above that temperature the column packing becomes unstable and the materials being analyzed tend to crack. Also the results measured by the SimDis GC method are determined by the interactions between the tested sample and the selected column packing. Therefore the GC method is not fundamentally a determination of the boiling range of the sample mixture but rather a measure of the range of interactions of the sample with the packing.

To avoid the limitation in the higher boiling range of the tested material in the SimDis GC method, Schwartz et al developed a capillary supercritical fluid chromatography (SFC) method (1). When the SFC is properly calibrated, it has been shown to be a suitable simulated distillation method, even for materials having atmospheric equivalent boiling points as high as 760 °C or 1400 °F. However this does not eliminate the problem of interactions of the sample with the packing material.

In their work, Schwartz et al also used both atmospheric "flow"thermogravimetric analysis (FTGA) and vacuum thermogravimetric analysis (VTGA) methods to distinguish between evaporation and thermal decomposition. They have observed a bimodal distribution of DTG (the rate of weight loss) on Arabian heavy atmospheric residue in both FTGA and VTGA runs. The first peak in the VTGA (about 0.2-0.5torr) profile is shifted towards lower temperature as compared with the FTGA profile since the sample vaporization was enhanced by a reduced pressure. However, the reduced pressure had no effect on the position of the second peak in the VTGA curve since the thermal decomposition or pyrolysis rate was not significantly affected by the reduced pressure. Therefore, the low temperature peak in each DTG curve is interpreted as the sample vaporization profile and the high temperature peak as the thermal decomposition or pyrolysis reactions.

In the investigation of the hydrocracking of high boiling coal derived vacuum resids, it became important to measure the degree to which the resids had been broken down to lower boiling products. This plus the importance of a simple, rapid, and accurate analytical distillation technique mentioned above motivated the development of an analytical TGA method for boiling range measurement, i.e. atmospheric equivalent boiling point (AEBP) curve, of a variety of samples. While supercritical chromatography was an alternative, the use of thermogravimetric analysis to determine the AEBP curve was an attractive approach. Such a SimDis TGA method would not be affected by interactions with column packing and not limited by sample boiling point range. Development of this novel SimDis TGA method and the preliminary results on a variety of samples are presented in this paper.

EXPERIMENTAL

TGA Apparatus. A horizontal thermogravimetric analyzer (TGA), TA Instruments model 51 (New Castle, Delaware), was used. In this particular instrument, dual thermocouples were used for the system temperature control. One is a furnace thermocouple and the other is a sample thermocouple, which is located very close to the test sample. The sample thermocouple is always used for the temperature measurements. Only the furnace thermocouple is used for control in the ramp method (constant heating rate). However, either the furnace thermocouple or the sample thermocouple can be used for isothermal control, depending on the purpose. If the "Isothermal" mode is selected, the

furnace thermocouple is used. On the other hand, if the "Isotrack" mode is selected, the sample thermocouple is used. The isotrack mode gives much better temperature control, for example, ± 0.01 to ± 0.05 °C for the range of 60 to 280 °C,compared to the Isothermal mode.

Nitrogen was used as an inert carrier gas at 100 ml/min volumetric flow rate. Vacuum TGA (VTGA) was carried out by attachment of the thermogravimetric analyzer to a vacuum pump. A vacuum gauge from 0-760 mmHg (0-1 atm.) range was used to monitor the pressure. After a sample was loaded onto the sample pan, the vacuum metering valve (shown in Figure 1) was gradually opened, and the pressure was adjusted to a predetermined value (down to 30 mmHg or 0.0395 atm). By this control and use of a ballast tank (buffer), the pressure (or vacuum) of the TGA chamber was found to be very stable during the VTGA analysis.

TGA Sample Pan. The SimDis TGA method requires a change in the conventional TGA sample pan because the rate of weight loss in the open pan system is controlled not only by the vapor pressure of the test sample but also by mass transfer. The TGA sample characteristics in the pan as well as the diffusion out constantly change with the sample amount as the TG analysis proceeds. For those reasons, a new sample pan configuration with a small aperture at the top, as shown in Figure 2, was devised. The objective of this change is to make the rate of the weight loss from the sample pan primarily determined by the partial pressure of the sample molecules. This partial pressure has been shown from thermodynamic considerations and experimentation to be essentially equal to the vapor pressure of the sample. Three cylindrical quartz TGA sample pans with different sizes of circular aperture at the top were fabricated. The diameters of the apertures were 0.615, 0.974,and 1.538 mm. In each TGA test, about 80 mg of liquid sample was injected into the sample pan by a syringe before the TG analysis.

SimDis TGA Methods. Analytical variables, such as carrier gas flow rate, pressure, and temperature or heating rate, were held constant during a TG analysis. Two methods, i.e.,a ramp method and an isotrack method, have been used in the SimDis TGA technique. In the ramp method, a constant heating rate was used and the rate of the weight loss determined versus temperature. In the isotrack method, the temperature of the sample is very rapidly heated to a predetermined temperature within 2 minutes, and precisely controlled at this preset temperature within 0.01 to 0.05 °C after 5 minutes. The weight change and the DTG (the differential of the weight loss curve) decay are determined as a function of time.

Materials Studied. A light paraffinic vacuum distillate from Amoco and a converted resid liquid were used to test the SimDis TGA technique.

SimDis TGA Calibration. A SimDis TGA system can be calibrated by either a synthetic mixture which contains compounds of known boiling range or a 'standard' mixture for which distillation curves are available. In either case, the calibration sample should be similar to the sample for which the boiling range is to be determined. For the synthetic mixture, the paraffins, especially n-alkanes, provide a wide range of boiling components for calibration purposes. For the 'standard' mixture, any petroleum sample with known boiling range distribution could be selected. Some variation between samples of the same boiling point but different chemical structure are to be expected due to variation in molecular characteristics (such as molecular weight and shape) and heats and entropies of vaporization of the samples.

n-Alkane standards, C-10 to C-32, were purchased from Aldrich Chemical Co (Milwaukee, NJ). The SimDIS TGA was calibrated with a synthetic mixture of these n-alkane standards shown in Table 1.

SimDis TGA Data Processing. The smoothed and noise-free DTG curves were acquired by an 11 point smoothing technique (2).

RESULTS AND DISCUSSION

Strategies for Selection of the Optimum Method for Determining Boiling Point Range of an Unknown Sample. The analytical variables of the SimDis TGA technique include: 1). time-temperature profile: ramp method or isotrack method; 2). pressure: atmospheric pressure or under vacuum (down to 0.03 atm.); 3). size of the aperture at the top of the pan; and 4). carrier gas type and flow rate.

For a pure compound, SimDis TGA can be run using either the ramp or isotrack method. For an unknown mixture, the ramp method provides information concerning the vaporization range of the sample. If run under at least two pressures (vacuum), it can distinguish quantitatively between the material boiling so high that pyrolysis will occur and that fraction volatilizing under distillation conditions.

To accurately obtain the boiling range curve for a mixture, the isotrack method is the preferred technique. This method translates the decay of the rate of weight loss into the boiling point distribution. Therefore, the optimum conditions to run a simulated distillation by TGA are those conditions which give the highest sensitivity and stable decay curve. To accomplish this, the optimum conditions for a SimDis TGA run is dependent on the boiling range of the test sample. For example, for light samples, it is better to run the SimDis TGA at a low isotrack temperature, small hole size of pan, and atmospheric pressure. For very high boiling mixtures, SimDis TGA should be run at a higher isotrack temperature, larger hole size of pan, and high vacuum (for example, 30 mmHg). For a mixture containing a very broad boiling range, the test can be run at either more than one temperature or more than one pressure (vacuum) or both to detect the very volatile fraction as well as the higher boiling components.

The recommended general steps to run an unknown sample using the SimDis TGA technique are:

1). ramp at 1 to 5 °C/min to 600 °C at 1 atm and/or under vacuum (down to ca. 0.03 atm.) at 100 cm^3/min N_2. Oxygen is then introduced to burn off the combustible material remaining (if any). In this run, IBP (Initial Boiling Point), FBP (Final Boiling Point) and/or PT (Pyrolysis Temperature), the boiling range and volatile fraction, and ash fraction (if any) are determined.

2). based on the results obtained from Step 1, select the optimum conditions of aperture size of pan, isotrack temperature, pressure, etc. to run a SimDis TGA.

SimDis TGA by the Ramp Method. Typical DTG curves from SimDis TGA runs using the ramp method at two pressures on a light paraffinic vacuum distillate from Amoco are shown in Figure 3. The rate-of-weight-loss curves show a distinct shift to lower temperatures as the pressure is reduced. No pyrolysis is evident in this determination since the DTG curve is entirely shifted under vacuum. The volatilization range for this sample at atmospheric pressure is between about 200°C and 470 °C. Under the vacuum of 0.238 atm., it is shifted to between about 180°C and 420 °C. The volatilization ranges are somewhat lower than the actual boiling range because of the nitrogen gas sweep and controlled diffusion.

SimDis TGA Calibration. Temperature-time plot for a calibration run using a synthetic mixture of hydrocarbons of C_{10} to C_{32} is shown in Figure 4. The predetermined isotrack temperature was 280 °C. The DTG decay curve for this calibration is shown in Figure 5. Although the temperature of the sample reached the predetermined temperature of 280 °C within 2 minutes, the loss of the light fractions in the synthetic mixture, such as C_{10} and C_{15}, occurred before the temperature became stable. In other words, the light fractions in the synthetic mixture of C_{10} and C_{15} were evolved from the sample pan within this initial 2-5 minutes. This is clearly illustrated in Figures 6 and 7, the plot of wt% of sample in the pan vs. temperature and wt% of sample in the pan vs. DTG decay, respectively. From the concentrations of the C_{10}-C_{32} components in the synthetic mixture given in Table 1, we can find the rates of weight loss at which the components were evolved from the pan. The plot which describes a linear relationship of log (rate of weight loss) vs $1/T_b$ (T_b, the boiling point of C_{20}-C_{32}) is shown in Figure 8, in accordance with the Clausius-Clapeyron equation. This shows that the DTG decay determined by TGA technique is indeed measuring the vapor pressure and therefore boiling range.

SimDis TGA Test. For a mixture containing a wide range of boiling materials, such as the light paraffinic vacuum distillate from Amoco, the DTG decay determined under the same conditions of running the calibration mixture can be translated into a boiling range distribution using the equation of

$$T_b = \frac{B}{\ln(r) - A} \qquad (1)$$

where r is the decay rate of the test sample and A and B are parameters determined by calibration (for this case, A = -21.06 and B = 12778).

Temperature-time plot for the test sample of the light paraffinic vacuum distillate is similar to that as shown in Figure 4. The DTG decay curve is shown in Figure 9. Although the temperature of the sample reached the predetermined temperature of 280 °C within 2 minutes, the 10 wt% of light fractions in the vacuum distillate were lost before the temperature became stable, i.e.,the 10 wt% of light fractions in the vacuum distillate were evolved from the pan within this initial 2-5 minutes. This is clearly illustrated in Figure 10, the plot of wt% of sample in the pan vs. temperature. The simulated distillation curve for this vacuum distillate is shown in Figure 11.

A simulated distillation run by the isotrack method has been made on a sample of Wilsonville # 258 resid converted using sulfided molybdenum naphthenate at 403°C for 60 minutes. The boiling range curve derived from the DTG decay of this sample is shown in Figure 12. The fraction of material in which the product boiled below 850 °F (the cut-off point for resid) was 93.8 wt% (including tetralin fraction).

Advantages of the SimDis TGA Method. The most significant advantages to using the TGA technique for simulated distillation are:

1). SimDis TGA is run at much lower temperature than other techniques, especially if combined with vacuum.
2). there is no limitation to the sample type. The sample can be very light or very heavy. Even a sample with a very wide range of boiling materials can be tested by this technique.
3). Highly reproducible results can be obtained. The experimental cycle for one run can be 1 to 12 hrs, depending on sample and purpose. No cleaning is required as would be necessary in a distillation column.
4). Very small amounts of sample (30-80 mg) are required for each SimDis TGA run;
5). The SimDis TGA method measures the true boiling characteristics of the sample and is not affected by interactions between the test sample and packing, as is the case with the chromatographic methods.

SUMMARY AND CONCLUSIONS

1. Two analytical methods (a ramp and an isotrack method) have been developed for determining the boiling range of an unknown sample based on the use of thermogravimetric analysis.

2. These methods require the use of a special cylindrical sample pan with a small hole in the top to control the rate of weight loss (diffusion of the sample vapors exiting the pan). Under these conditions, the diffusion rate is proportional to the vapor pressure of the sample at the particular temperature of the analysis.

3. For screening an unknown sample, the "ramp method" is used in which the temperature of the sample is increased at a predetermined rate while holding the purge gas flow rate constant. The temperature range of volatilization is measured. If high boiling material is present which involves pyrolysis of the sample rather than only volatilization, a similar "ramp method" is run under vacuum. This indicates which portion of the sample is volatilized and what portion is pyrolyzed under the conditions of the test.

4. For more precise determination of the boiling range of a sample, the isotrack method is used. In this method, the sample is rapidly heated to a predetermined temperature and then held constant while the rate of weight loss (DTG) is measured. When the system is properly calibrated with a known sample, the rate of weight loss (DTG decay) can be translated by a computer program into an actual boiling range.

ACKNOWLEDGEMENTS

The support of this work by the subcontract from CONSOL under DOE Contract DE-AC22-94PC93054 and by the Department of Energy under DE22-93PC93205 is acknowledged. Helpful discussions with F.P. Burke, R.A. Winschel, and S.D. Brandes are gratefully acknowledged. Additional funds for purchase of thermal analysis equipment was provided by the University of Delaware.

REFERENCES

1. Schwartz, H.E.; Brownlee, R.G.; Boducszynski, M.; Su, F. *Anal. Chem.* 1987, 59, 1393.
2. Wang, Keyu; Huang, H.; Wang, S.; Klein, M.T.; Calkins, W.H.* "A Novel Smoothing Technique for Thermogravimetric Analysis Data", to be submitted to *Anal. Chem.*

Table 1 Concentrations and properties of the C_{10}-C_{32} components in the synthetic mixture

No. of Carbon	Name	MW	b.p.,°C	m.p.,°C	W, g	C, wt%
10	Decane	142.28	174.1	-29.7	1.2298	18.26%
15	Pentadecane	212.41	270.6	10.0	1.2068	17.92%
20	Eicosane	282.54	343.0	36.8	1.1238	16.69%
25	Pentacosane	352.67	401.9	55.0	1.0716	15.91%
30	Triacontane	422.80	449.7	65.8	1.0402	15.45%
32	Dotriacontane	450.85	467.0	69.7	1.0618	15.77%

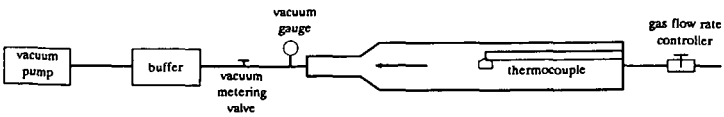

Figure 1 Instrumentation of vacuum thermogravimetric analyzer (VTGA)

Figure 2 A SimDis TGA sample pan

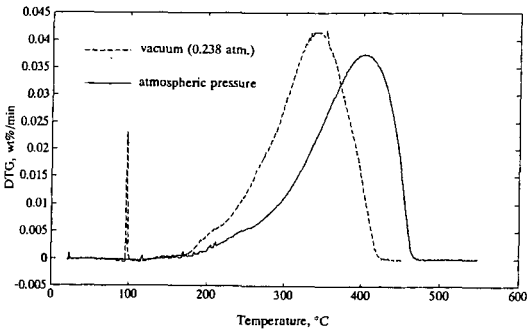

Figure 3 DTG curves from SimDis TGA runs using the ramp method at two pressures on a light paraffinic vacuum distillate from Amoco

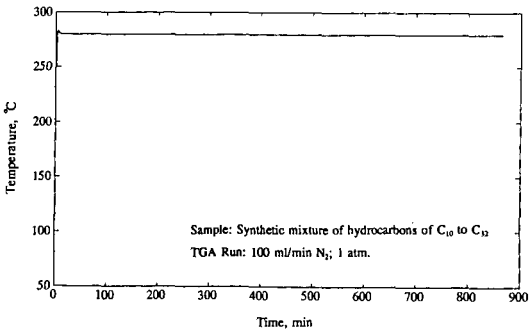

Figure 4 Temperature-time plot for the calibration sample of a synthetic mixture of n-alkanes

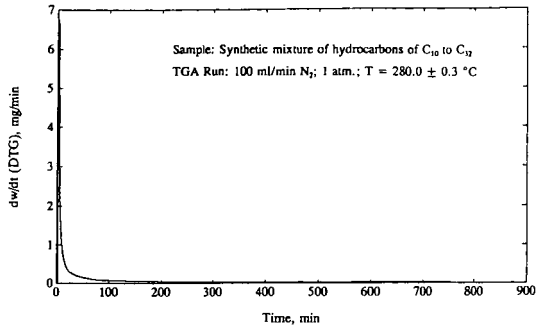

Figure 5 DTG decay curve for the calibration run

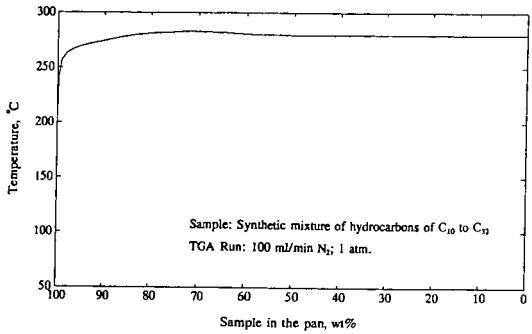

Figure 6 Plot of wt% sample in the pan vs. temperature for the calibration run

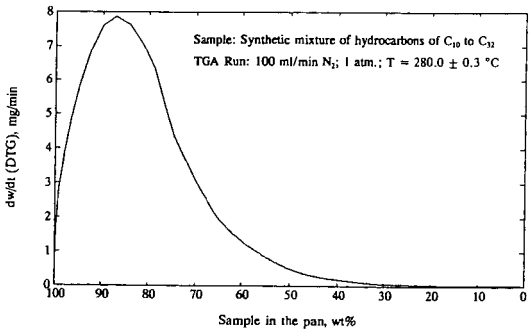

Figure 7 Plot of wt% sample in the pan vs. DTG decay for the calibration run

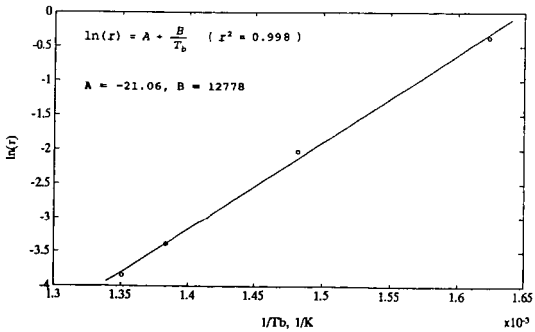

Figure 8 ln(r) vs. $1/T_b$ (r: rate of weight loss; T_b: boiling point of C_{20}-C_{32})

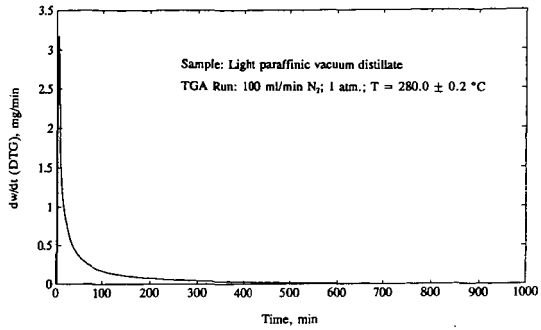

Figure 9 DTG decay curve for the light paraffinic vacuum distillate

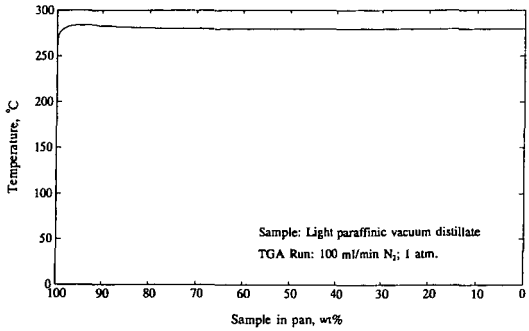

Figure 10 Plot of wt% sample in the pan vs. temperature for the light paraffinic vacuum distillate

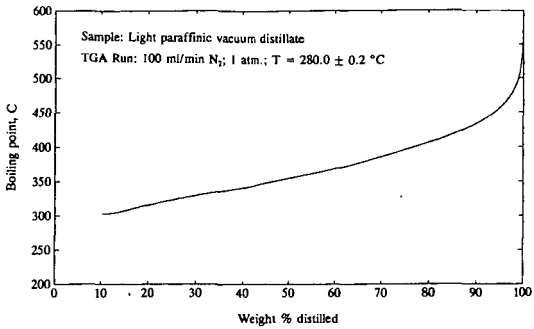

Figure 11 Simulated distillation curve (AEBP) for the light paraffinic vacuum distillate

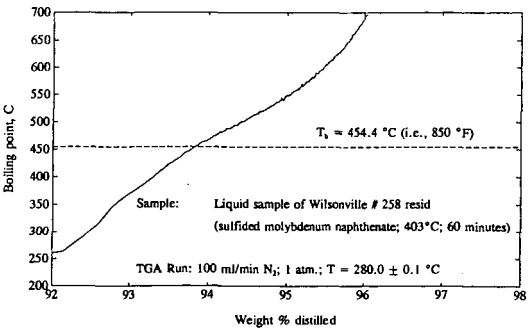

Figure 12 Simulated distillation curve (AEBP) for the liquid sample of a resid conversion run under 1500 psig H_2

Cloud Point Determination Using a Thickness Shear Mode Resonator

James J. Spates[1], Stephen J. Martin[2], Arthur J. Mansure[2], and Jeffrey W. Germer[3]

[1]Ktech Corporation, Albuquerque, NM 87110
[2]Sandia National Laboratories, Albuquerque, NM 87185
[3]Petrolite Corporation, St. Louis, MO 63119

Keywords: cloud point, thickness shear mode resonator, viscosity

Introduction

Crude oils and crude oil products contain substantial amounts of petroleum waxes, consisting of a distribution of high molecular weight hydrocarbons. These waxes or paraffins have limited solubility in oil and tend to precipitate out at a temperature determined by the concentration and constituents of the wax. Precipitation and deposition of wax results in narrowing of pipelines, making crude oil recovery difficult.

A parameter of practical importance is the wax precipitation temperature, traditionally known as the *cloud point*, at which visible crystallization occurs. Deposition problems arise in oil field operations at or below this temperature. Several techniques can be used to determine the cloud point [1]: (1) visual observation, (2) viscosity measurement, (3) differential thermal analysis, and (4) pulsed nuclear magnetic resonance.

In this paper we describe a new technique for measuring cloud point based on measuring properties of the fluid and accumulated deposit using a quartz resonator. The thickness shear mode (TSM) resonator consists of a thin, highly polished disk of AT-cut quartz with circular electrodes on both sides (Figure 1). Applying an RF signal to the electrodes causes the piezoelectric quartz crystal to be excited into a shear mode of vibration in which crystal faces undergo in-plane displacement.

The TSM resonator is instrumented as a sensor by incorporating it as the frequency-control element of an oscillator circuit. Wessendorf [2] has described an oscillator circuit capable of exciting the crystal in liquid media. This oscillator tracks the resonant frequency of the crystal and has level-control circuitry to measure the amplitude of the oscillation voltage; it provides a feedback voltage to maintain this at constant level. The level control compensates for changes in resonator damping caused by (1) changes in the viscosity of the contacting fluid and/or (2) deposits that form on the crystal. Since both of these changes occur with oil at the cloud point, the feedback voltage is a good indicator of the cloud point.

When a TSM resonator operates in contact with a fluid, the shear motion of the surface radiates a critically damped shear wave into the contacting fluid (Fig. 2). This mechanical coupling causes both a change in stored and dissipated energy in the crystal, leading to a change in resonant frequency and crystal damping (oscillator feedback voltage). Kanawaza and Gordon showed that resonant frequency decreases proportionally with $(\rho\eta)^{1/2}$, where ρ and η are liquid density and viscosity, respectively [3]. The change in crystal damping or feedback voltage due to liquid contact is also proportional to $(\rho\eta)^{1/2}$ [4].

A rigid film deposited onto the resonator surface moves synchronously with the oscillating surface. This causes a change in the stored (kinetic) energy of the resonator. This results in a decrease in resonant frequency proportional to the areal mass density (density times thickness) contributed by the layer [5]. Since moving the rigid layer does not result in dissipation of energy, however, there is no change in crystal damping or oscillator feedback voltage.

A compliant film deposited on the resonator surface behaves differently than a rigid one. While the lower film surface moves synchronously with the resonator surface, the upper film region may lag behind [6]. This induces a shear strain in the film. Since compliant films are typically viscoelastic, i.e., having both elastic and viscous character, strain in the film leads to both energy storage and dissipation. As the thickness of the compliant film increases, it initially leads to a decrease in resonant frequency; at larger

thicknesses, however, the film causes an increase in frequency [6]. Thus, frequency alone is not a good indicator of deposit thickness. Initially, the feedback voltage increases with film thickness; at larger thicknesses, voltage tends to saturate. At the cloud point, the precipitation of wax results in both a change in the viscosity of the fluid, as well as formation of a viscoelastic deposit on the resonator surface. Since both effects lead to an increase in crystal damping, this parameter is a good indicator of the cloud point.

System Description

Figure 3 is a block diagram describing the cloud point detector system. The system consists of a test cell and peripheral equipment for temperature control and data acquisition. The temperature controller allows sample temperature to be easily varied to determine the cloud point of the test fluid. The data acquisition system is made up of a voltmeter (HP 3478A), frequency counter (HP 5384A), and scanning thermometer (Keithley 740). A personal computer acquires data from these instruments.

The test cell, shown in Fig. 4, has two parts: the cell body and the cell head. The cell body holds a glass sample cup with a volume of 25 cm^3. The body, made of stainless steel, has thermoelectric coolers on each of the four vertical surfaces. Heat sinks are attached to the coolers so that waste heat can be efficiently transferred to the room air, facilitated by a fan. The thermoelectric units heat and cool samples over the range of 5°C to 85°C. A stir bar is inserted in the sample cup to maintain sample uniformity; this is driven magnetically from below. The cell body also contains an o-ring seal on the surface that maintains pressure and prevents the loss of the more volatile sample constituents. Overpressurization is prevented by a 100 psi pressure-relief valve.

The cell head includes the sensor, oscillator, a thermocouple, and electrical connectors to output the oscillator frequency and feedback voltage. The electrical connector that holds the sensor was designed to allow rapid sensor changeout.

Experimental Section

A clean and dry TSM resonator was installed in the cell head and reference measurements were made of the resonant frequency and oscillator feedback voltage. A crude oil simulant, consisting of Shell wax 300 and kerosene, was then placed in the test cell at room temperature. The lid, with sensor attached, was bolted onto the cell, sealing the test volume. At the start of a test, the cell temperature was elevated to 80°C. After the temperature stabilized, the controller was set for a certain cooling rate and final temperature; data acquisition was initiated.

The cloud point of the sample was also determined by visual observation. This was done by placing a mirror beneath the sample cup and observing a change in clarity as the sample was cooled. The sample was initially heated to 80°C and then cooled to 40 °C with the lid on to contain volatile components. The lid was removed at 40°C so that the cloud point could be observed.

Figure 5 shows the change in oscillator feedback voltage and resonant frequency vs. temperature for two different cooling rates for a wax/kerosene sample. A dashed line indicates the visually-determined cloud point at an intermediate cooling rate of 1°C/min. The oscillator damping voltage, in particular, shows an abrupt increase at the visually-observed cloud point due to the onset of wax precipitation. This is due to increased resonator damping from a combination of increased fluid viscosity and wax depositing on the resonator. The resonant frequency also shows an abrupt change at the cloud point. It is clear that the best indication of cloud point (i.e., agreement with visual observation) obtained from the resonator measurement is the point at which the damping voltage first changes slope during cooling.

The cloud point determined from resonator measurements is slightly higher for the lower cooling rate. This is to be expected since the lower rate provides more time for the nucleation of wax crystals to occur. Below the cloud point, the responses are quite dependent upon the cooling rate. This may be due to a dependence of the crystal properties on the cooling rate. Graham [7] has noted that slower cooling rates lead to crystals that are larger, more irregularly-shaped, and more aggregated.

Figure 6 shows the change in oscillator feedback voltage and resonant frequency vs.

temperature for two wax concentrations. The samples are both cooled at a rate of 1°C/min. The "original" sample shows a cloud point of 34.4°C, while the sample with added wax shows a cloud point of 36.6°C. As expected, the higher concentration of wax precipitates out at a higher temperature. The oscillator voltage clearly indicates the onset of wax precipitation in each case. The oscillation frequency shows a more complicated behavior, resulting from the fact that oscillation frequency initially decreases with accumulated layer thickness, then increases.

Conclusion

The resonator exhibits large responses in both oscillator feedback voltage and resonant frequency at the cloud point. The temperature at which the feedback voltage first changes slope during the cooling process is an indication of cloud point that is consistent with visual determination. This technique is less subjective and operator dependent than visual means and works equally well with opaque samples. Moreover, since the resonator operates at extremely low shear rates, it perturbs the sample less than a rotating-cup viscometer.

Acknowledgements

The authors are grateful for assistance from J. E. Miller, R. S. Sandoval, R. W. Cernosek, K. O. Wessendorf, and T. W. Schneider of Sandia National Laboratories. This work was performed at Sandia National Laboratories, supported by the U.S. Department of Energy under contract No. DE-AC04-94AL85000.

References

[1] Newberry, M. D., *SPE Production Engineering* (SPE#11561), 151.

[2] Wessendorf, K. O. *Proc. 1993 Frequency Control Symp.* (IEEE, New York, 1993) pp. 711-717.

[3] Kanazawa, K. K.; Gordon II, J. G. *Anal. Chem.* **1985**, *57*, 1770-1771.

[4] Martin, S. J.; Frye, G. C.; Wessendorf, K. O. *Sensors and Actuators A* **1994**, *44*, 209-218.

[5] Sauerbrey, G. *Z. Phys.* **1959**, *155*, 206-222.

[6] Martin, S. J.; Frye, G. C. *Proc. 1991 Ultrasonics Symposium*, (IEEE, New York, 1991), 393-398.

[7] Graham, D. E.; Stockwell, A.; Thompson, D. G. *Chemicals in the Oil Industry* (Royal Society of Chemistry, 1983) Special Publication no. 45.

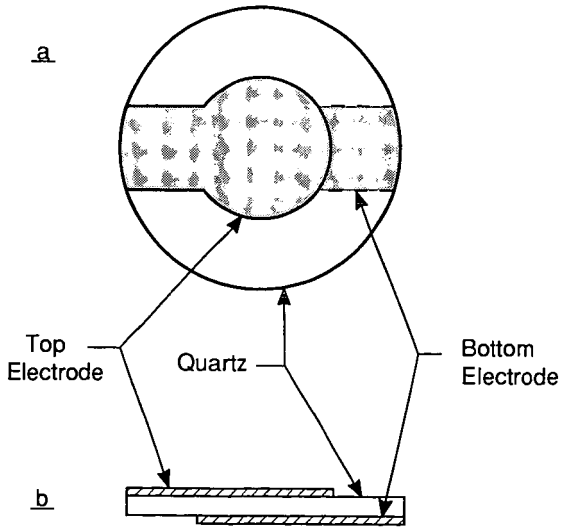

Fig. 1. *Top (a) and side (b) views of a quartz thickness shear mode (TSM) resonator.*

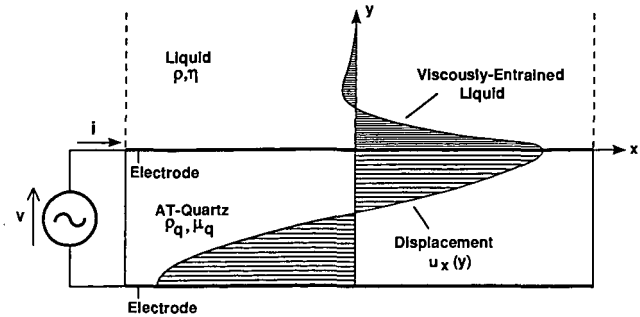

Fig. 2. *Cross-sectional view of a smooth TSM resonator with the upper surface contacted by a liquid. Shear motion of the smooth surface causes a thin layer of the contacting liquid to be vicously entrained.*

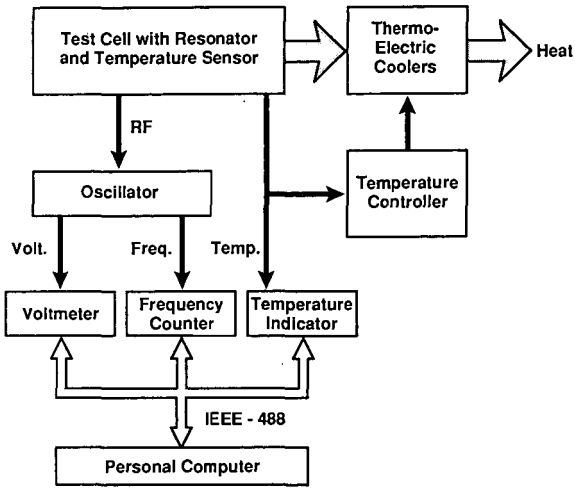

Fig. 3. *Block diagram of the cloud point detector system used for TSM resonator and visual cloud point determinations.*

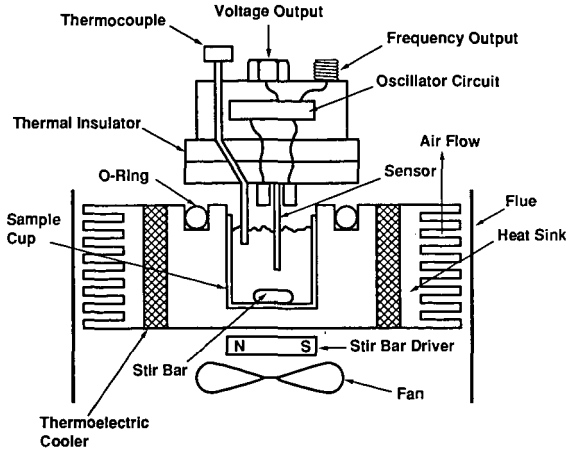

Fig. 4. *Cloud point detector test cell with TSM resonator (sensor), oscillator circuit, thermocouple, sample cup, stir bar with driver, thermoelectric coolers, heat sinks and fan.*

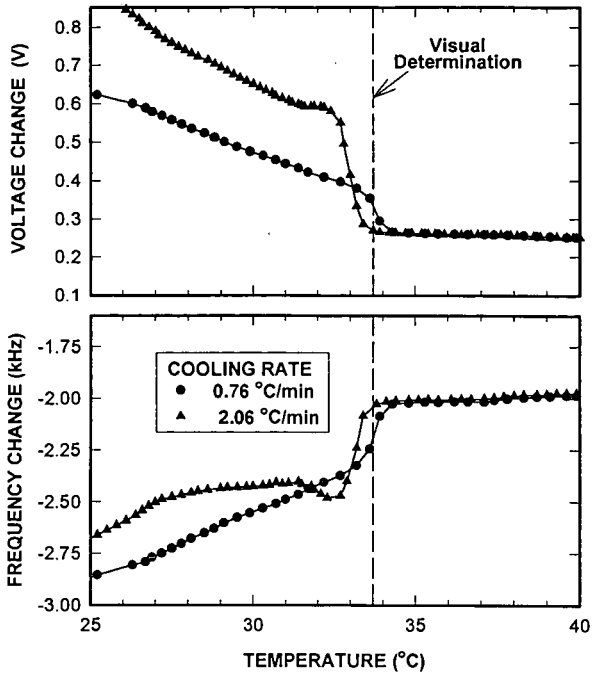

Fig. 5. *Voltage change and frequency change measurements of TSM resonator vs.temperature for a Shell wax 300/kerosene mixture cooled at two rates. Dashed line indicates the visually determined cloud point.*

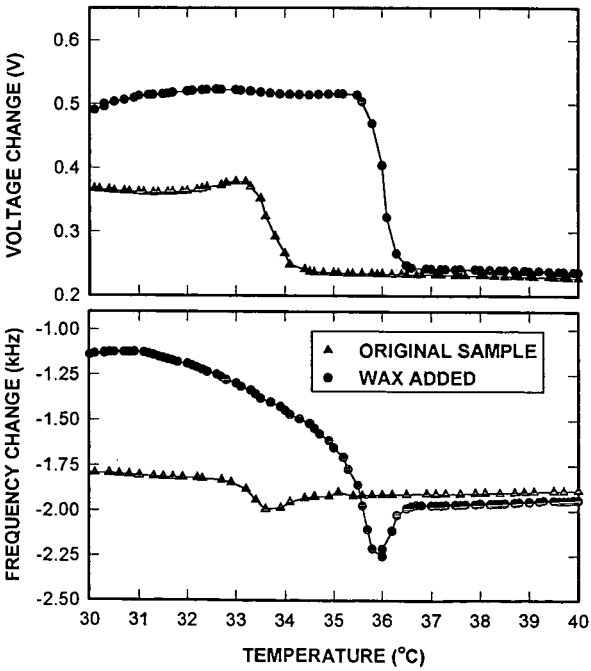

Fig. 6. *Voltage change and frequency change measurements of TSM resonantor for two different Shell wax 300/kerosene concentrations cooled at the same rate.*

CHARACTERIZATION OF PETROLEUM RESID COMPONENTS FRACTIONATED BY HIGH VACUUM SHORT-PATH DISTILLATION AND GEL PERMEATION CHROMATOGRAPHY

Frank Sen-Chun Lee
Department of Chemistry
Hong Kong Baptist University
Kowloon, Hong Kong

Keywords: petroleum resids; heavy oils; hydrocarbon type analysis

INTRODUCTION

The traditional cut point between distillable oils and resids by vacuum distillation is 1000°C. The recent advent of high vacuum, short-path distillation (DISTACT molecular still) makes it possible to cut deeper into resid components (see references cited in ref 1). By varying the wall temperature and pressure of the DISTACT unit, the 1000+°F resid components can be further cut into narrow boiling fractions up to an atmospheric equivalent end point of about 1350°F. In this study, this additional resid components distillable between 1000 and 1350°F was fractionated and characterized. Furthermore, the asphaltenes in the bottom material were separated into molecular weight cuts by GPC (Gel permeation Chromatography). Such fractionation scheme allows us to compare systematically the composition and properties of the full range petroleum resid components as a function of AEBP (Atmospheric Equivalent Boiling Point) or molecular weight.

EXPERIEMNTAL

The two feedstocks used in this study were both high sulfur 1000+°F petroleum vacuum resids originated from different crude blends. The two are similar in general properties as shown in Table 1. The DISTACT fractionation scheme is illustrated in Figure 1, which lists the different temperature and pressure combinations used to cut the different boiling fractions. The AEBPs of the fractions were measured by GC simulated distillation. The GPC separation was carried out on a Waters GPC system using a set of Water Styregel columns arranging in the order of 60, 100, 100 and 500 A pore sizes. The dimensions of each of the columns were 7 mm i.d. and 100 cm long. The elution solvent was tetrahydrofuran and the flow rate was 5 ml/min. Multiple runs were made in order to collect sufficient material for characterization. The VPO (Vapor Pressure Osmometry) measurement were made in nitrobenzene solvent at 120°C, using infinite dilution method.

Three LC (Liquid Chromatographic) procedures were used for compound type separation. The IX (Ion Exchange) separation used two sequentially connected columns each packed with anion (MP 1 resin for trapping acids) or cation (MP 50 resin for trapping bases) exchange resins obtained from Biorad. The neutrals were eluted by toluene from the column sequence while the acidic and basic material were desorbed from their respective columns by isopropanol/toluene solvent mixed with minor amounts of formic acids or isopropylamine, respectively. The ABN (Acid/Base/Neutral) separation by alumina LC was carried out on two sequentially connected columns packed with acidic (for trapping bases) and basic (for trapping acids and pyrrolics) alumina, respectively. The neutrals were eluted from the column sequence by cyclohexane (neutral I) and toluene (Neutral II). Afterwards, the two columns were disconnected and the pyrrolics in the basic alumina column was first eluted by dichloromethane. Finally, a mixture of dichloromethane and methanol was used to elute the acids and bases from their respective columns. In ORA separation, the asphaltenes and maltenes were first separated by hexane dissolution. The maltenes were then separated by Silica Gel LC into oil and resin fractions.

The NMR hydrocarbon analysis was based on data from combined H-1 and C-13 solution NMR analysis using the Brown-Lader model (2).

RESULTS AND DISCUSSION

1. Properties of DISTACT fractions: The boiling curves of the fractions from GC simulated distillation are shown in Figure 2. In Table 2, the wt % yield and the boiling ranges are listed. The BP data show a progressive increase in boiling range from the lighter to the heavier fractions, indicating the validity of the DISTACT distillation technique in terms of BP separation. The four distillable fractions from O3 through O6 account for 61% of the total resid material, with their T50 temperature (temperature at which 50 wt% is distillable) increases regularly from 840, 980, 1080 to 1090°F. The end points of the two bottom cuts, R1 and R2, are both above 1400°F. Their T50 points are in the 1320-1350°F range. Overall, about 80 wt% of the total 1000+°F resid mass is DISTACT distillables.

The ORA yield and elemental composition in Tables 3 and 4 indicate that as the BP of the fractions increases, the H/C ratio decreases and the concentrations of asphaltenes, Rams carbon and heteroatoms increase regularly. On a resid feed basis, the four distillate fractions account for 16% of the Ramscarbon, 29% N, 43% S and 10-12% Ni/V. Thus, while the higher cut point of the DISTACT technique significant increases the distillable yield, it also allows the carryover of significant amounts of catalyst poisons.

The MW data for the DISTACT fractions are listed in Table 8 along with the NMR results to be discussed later. The number average MWs of the fractions obtained by GPC and VPO agree very well. The MW increases regularly from 400 for fraction O6 to 8-900 for O3 and 14-1500 for the bottom fraction R1, in the same direction as the BP.

2. Compound Type Separation: The compound type distribution of the DISTACT distillables was studied by IX and Alumina ABN separation using resid B as the sample. In both cases, a "normal" and a "reversed" column separation procedures were carried out. The yield distribution and the elemental composition of the fractions from the two separations are summarized in Tables 5 (IX) and 6 (Alumina). In IX separation, the total mass recovery is 98% in the normal sequence and only 93.7 % in the reversed one, indicating small material losses due to irreversible adsorption by IX resins, especially the cation IX resin. The mass recovery in the alumina separation is essentially quantitative irrespective of the column sequence. The yield of the total polar material (acids plus bases) in alumina separation is lower than those of IX (12-13 vs 18-20%). Furthermore, the alumina LC gives similar acid/base yield distributions after column switching whereas different results were obtained in the IX case. It is likely that the IX resins adsorb significant amounts of extra high MW polyaromatics in addition to the N/O containing polar species because of their high adsorptivities. This extra material can locate themselves in either the acid or base fractions depending on the order of the columns.

Based on the more consistent alumina ABN separation, the neutral material amounts to about 88-90% of the total distillables. The three polar fractions--pyrrolics, acids and bases--account for only 10-12% of the total mass but 98-99% of the total N and metals. The S is more evenly distributed (IX results). The low H/C ratios of the polar fractions (1.0-1.3) indicate their highly aromatic nature. The MWs of the ABN fractions differ only slightly: 570 for neutrals compared to 580-600 for acids and bases. The order is consistent with the BP curves as shown on the right of Figure 2.

The highly functionalized structure of the three polar fractions are evidenced from their FTIR spectra shown in Figure 3. The pyrrolic fraction shows a strong band around 3500 cm^{-1}, indicative of N-H absorption. The acids show a series of bands from 3400-3650 cm^{-1}, indicative of phenolic O-H with varying extent of H bondings. All three polar fractions distinguish themselves from the two neutral fractions by their prominent carbonyl absorption bands around 1650-1750 cm^{-1}. The pyrrolics and the bases also show the aromatic C-C and C-N bands around 1550-1620 cm^{-1}, suggesting the presence of N in the ring systems. On the other hand, the spectra of the two neutral fractions show only typical hydrocarbon structure free of any heteroatom functionalities.

In Table 7, the MW, % aromatic C, MW and ABN yield distribution between the gas oils and the DISTACT distillates are compared.

3. NMR Average Structure: The polyaromatic structure of the DISTACT fractions were determined by combined C-13 and H-1 NMR analyses using the improved Brown-Lader model (2). The model assumes that all the molecules being analyzed are aromatic with the aliphatics present only as side chains on the polyaromatic core. Thus, before NMR analysis, the aliphatics in the ABN neutrals of the DISTACT fractions were further separated by Silica Gel LC. Such separation showed that the DISTACT bottom fractions (R1 and R2) contain only 0.04-0.05 wt% of pure aliphatic components. In the distillate portion, the aliphatics in the four lighter fractions O4 through O6 is less than 5%, but as much as 41% was found in the heaviest fraction O3.

Table 8 lists the NMR-derived average molecular structural parameters for the DISTACT fractions of resid A. The C_A increases smoothly from 21.4 to 36.9% with increasing boiling range of the fractions. The cluster ring number (number of aromatic rings in the polyaromatic core) also increases with boiling range from an average of 1.6 rings for O6 to 5.4 rings for the heaviest fraction R1. The cluster weights of the average molecule in the fractions are compared with their

corresponding MWs measured by VPO and GPC. For the four distillate fractions O3 through O6, the cluster weight and the MW for each fraction is fairly close. Within the uncertainties of the average structure determinations, the data suggest that the molecules in the distillates on the average contain only one cluster. This is opposed to the residue fraction R1 where the MW is about twice that of the cluster weight. Thus, the average molecule in R1 contains about 2 clusters.

4. Asphaltenes: Asphaltenes represent the heaviest component in resids. As shown earlier, nearly all the asphaltenes are in the DISTACT bottom material. The asphaltenes in the DISTACT bottom of resid B was fractionated by GPC into seven MW fractions. Essentially quantitative mass recovery was observed in GPC separations.

The MW of the separated fractions were further determined by both VPO and analytical GPC. The yield distribution, elemental composition, MW and NMR derived structural parameters of the GPC fractions are summarized in Table 9. The data show that the major differences among the different fractions are MW and NMR structure parameters, while the elemental and metal concentrations are grossly similar. The MW increases smoothly from less than 620 for the lightest cut 7 to 50-5100 for the two heaviest cuts 1 and 2.

The NMR data show that about 55 wt% of the asphaltenes (sum of cuts 4 through 7) has an average cluster size of 4-6 rings. The total of cuts 2 and 3, which account for 35% of the asphaltenes, has about 6-7 rings. The heaviest asphaltenes (cut 1), which accounts for 10 wt% of the total asphaltenes and 1.2 wt% of the resid mass, has an average of 14 rings. Comparing the cluster weight with the MW of the fractions, it is seen that all but fraction 6 have multiple clusters per average molecule. The number of clusters per molecule increases with the MW of the fractions from 3-4 clusters for fractions 4 and 5 to 6-10 clusters for fractions 2 and 3. The heaviest fraction 1 has the highest number of rings per cluster (14) but only 5 clusters per average molecule.

SUMMARY

The composition and properties of resid components as a function of increasing BP or MW are compared in Table 10. Results show satisfactory BP separation of the maltenes by DISTACT and MW separation of the asphaltenes by GPC. A comparison among the properties of gas oils, DISTACT fractions and GPC MW cuts show that there is a continuous and smooth increase of aromaticity, polarity and NMR derived polyaromatic cluster size with BP or MW. The same compound types exist in different boiling fractions but the relative amounts of the different types change with BP. The commonly suggested "structural discontinuity" between asphaltenes and other heavy oil components is not apparent except for the heaviest asphaltene fractions, which account for about 1.2 wt% of the total resid mass. However, the analytical data for this fractions of heavy and highly polar material remain questionable because of their reactive nature.

REFERENCES

1. Boduszynski, M.M., Energy and Fuels (1988) 2, 597-613; (1987) 1, 2-11 and the references therein.
2. Hasan, M.A., M.F. Ali and A. Bulchar (1983) Fuel, 62, 518 and the references therein.

ACKNOWLEDGEMENT

The experimental work of this paper was carried out when the author was working at Amoco Research Center of Amoco Corporation in Naperville, IL. The author would like to express his sincere appreciation to Amoco for supporting this research, and the many capable colleagues who helped me on this project including in particular Mr. Al Hensley, Dr. L. J. Duffy, Mr. Wayland Chan, Dr. Om Mahajan, Dr. Naresh Sethi, Mr. D. Maciejewski and Dr. R. L. Ollendorff.

Figure 1. DISTACT Fractionation Scheme

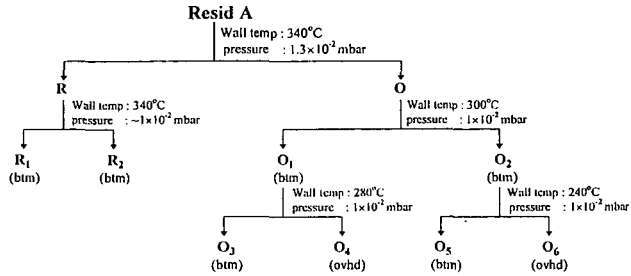

Figure 2. GC Simulated Distribution of DISTACT Fractions

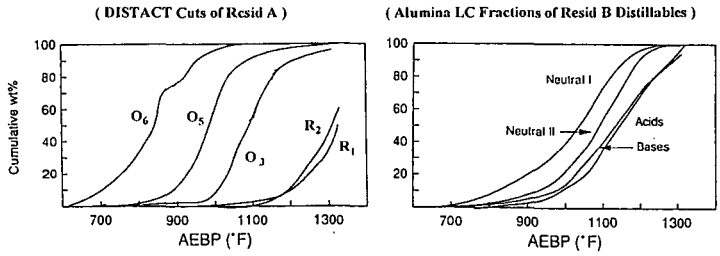

Figure 3. FITR Spectra of Alumina LC Fractions (Resid B DISTACT Distillables)

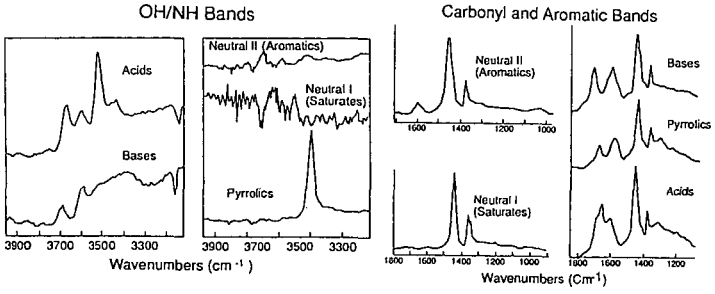

TABLE 1

RESID FEED PROPERTIES

Properties	Virgin High-S Resid A	Virgin Resid B
Wt% C	84.10	84.72
Wt% H	10.29	10.35
Wt% S	4.64	3.75
Wt% N	0.51	0.52
PPM, Ni	50	56
PPM, V	228	222
H/C	1.46	1.47
% C_A	30.0	32.6
Wt% Rams	17.1	20.0
Wt% 1000-°F	18	0
ORA (Wt%) :		
Oil	30.0	40.9
Resin	58.2	46.2
Asphaltene	9.6	12.9

TABLE 2

DISTACT FRACTION YIELD AND BOILING RANGE BY GC SIMULATED DISTILLATION (RESID A)

	Boiling Range			
Fraction Code	Wt%	IBP	T50	T90
R_1	37.4	900	1350	> 1400
R_2	6.6	1000	1320	> 1400
O_3	5.6	700	1080	1250
O_4	23.0	700	1090	1220
O_5	12.3	700	980	1090
O_6	15.0	600	840	960

IBP = Initial Boiling Point; T50 and T90 = °C when 50 and 90 wt%, respectively, of materials are distillable.

TABLE 3 ORA AND RAMSCARBON YIELDS OF DISTACT FRACTIONS (RESID A)

Fraction	Oil	Resin	Asphaltenes	Total	Rams C
	Wt%				
R_1	5.7	68.5	22.7	96.9	32.9
R_2	7.5	69.3	21.3	98.1	33.1
O_3	28.5	66.8	4.0	99.3	12.8
O_4	39.6	58.9	1.2	99.7	7.4
O_5	53.4	46.6	0.2	100.2	2.2
O_6	65.2	34.4	0.1	99.7	0.3
Weighted Sum of Above Fractions	29.7	58.4	10.5	98.6	17.2
Feed by Direct Analysis	30.0	58.2	9.6	97.8	–

TABLE 4 ELEMENTAL COMPOSITION OF DISTACT CUTS (RESID A)

Fraction	C	H	N	O (by difference)	S	Total Metals	H/C
	Wt%						
R_1	83.50	9.09	0.70	0.49	6.16	0.06	1.31
R_2	83.77	9.39	0.69	0.03	6.07	0.05	1.35
O_3	83.98	10.61	0.37	0.74	4.28	0.02	1.51
O_4	84.54	11.07	0.27	0.22	3.89	0.01	1.57
O_5	85.13	11.26	0.21	0.24	3.61	< 0.01	1.59
O_6	85.28	11.69	0.12	0.05	2.86	< 0.01	1.64

TABLE 5

ELEMENTAL COMPOSITION OF COMPOUND-TYPE FRACTIONS SEPARATED BY ION-EXCHANGE LC (Resid B; DISTACT distillate)*

	Original Sample* (Direct Measurement)	Reversed Column Sequence (Cation + Anion Resins)				Normal Column Sequence (Anion + Cation Resins) †			
		Neutrals	Acids	Bases	Calculated Sum of Fractions	Neutrals	Acids	Bases	Calculated Sum of Fractions
Wt% Yield	= 100	80.4	8.0	9.9	98.3	74.0	14.1	5.6	93.7
Wt% C	85.31	84.87	82.56	82.29	84.43	85.09	83.45	81.55	84.63
Wt% H	11.17	11.54	9.28	8.51	11.05	11.59	8.87	8.94	11.02
Wt% N	0.28	< 0.01	1.66	1.45	0.28	< 0.01	1.79	0.81	0.30
Wt% S	3.06	2.18	3.81	2.93	2.39	2.15	3.5	2.12	2.35
Wt% Total Metals	–	< 0.01	0.05	0.07	–	< 0.01	0.07	< 0.01	< 0.01
Elemental Sum : Wt%	96.8	98.8	97.3	95.3	98.2	98.9	97.1	93.4	98.3
PPM Ni	9	0.4	102	15	10	0.4	85	< 5	12
PPM V	68	0	151	153	27	0.2	430	< 2	60
H/C	1.57	1.63	1.35	1.22	1.57	1.63	1.28	1.32	1.56

*The fraction has an ORA distribution of 65.1% oil, 34.6% resin, and 0.3% asphaltenes.

† In ion exchange separation, two columns, one packed with cation resin and the others packed with anion resins, are connected in series. The basic material is trapped on the cation resins whereas the acidic material is trapped on the anion resins. The reverse sequence has the cation column in front of the anion column, whereas the reverse is true in the normal sequence.

TABLE 6

ELEMENT COMPOSITION OF COMPOUND-TYPE FRACTIONS SEPARATED BY ALUMINA LC (Resid B; DISTACT distillate)

Fraction	Normal LC Sequence (Basic + Acidic Alumina, Acid Material First)					Reversed LC Sequence (Acidic + Basic Alumina, Basic Materials First)				
	Yield	C	H	N	H/C	Yield	C	H	N	H/C
	wt %									
	(Standard As-Received Alumina, 2% H_2O)									
Neutral I (Cyclohexane Elution)	35.6	86.21	13.34	(2 ppm)	1.86	56.4	85.38	12.69	(6 ppm)	1.78
Neutral II (Toluene Elution)	53.5	84.35	9.95	(128 ppm)	1.42	34.0	84.91	9.00	(270 ppm)	1.27
Total Neutrals (I and II)	88.1	85.09	11.30	(78 ppm)	1.59	89-90	85.20	11.30	(103 ppm)	1.59
Pyrrolics	3.36	83.75	8.29	1.93	1.19	2-3	–	–	2.0	–
Bases	7.52	70.87	7.25	1.51	1.01	8.26	–	–	1.65	–
Acids	2.74	82.20	9.13	1.31	1.33	1.39	–	–	1.60	–
Sum of Fractions	101.7	–	–	0.22	–	100-102	–	–	0.23	–

TABLE 7

COMPARISON OF PROPERTIES BETWEEN GAS OILS AND DISTACT DISTILLABLES

	Heavy Vac Gas Oil A	Heavy Vac Gas Oil B	Resid B DISTACT distillate
% C_A (by C-13 NMR)	21.8	24.9	25.0
Total N (ppm)	1540	2820	2700
Avg MW	400 ± 30 (by MS)	350 ± 30 (by MS)	570 (VPO)
Alumina ABN Yield (wt%, normalized)			
1. Neutrals	93	90	87
2. Pyrrolics	0.49	0.88	3.3
3. Acids	3.5	5.0	2.6
4. Bases	3.0	4.0	7.3
5. Total polars (2 + 3 + 4)	7.0	9.9	13
N Concentration in ABN Fractions (Wt% observed) :			
1. Neutrals	0.013	0.024	0.008
2. Pyrrolics	3.0	3.2	1.9
3. Acids	2.3	3.2	1.4
4. Bases	1.3	0.82	1.6

TABLE 8

CALCULATED AVERAGE MOLECULAR STRUCTURAL PARAMETERS OF RESID A DISTACT FRACTIONS

1. Calculated Structural Parameter				
Sample	# Condensed Aromatic Rings	NMR Cluster Wt	VPO MW	GPC MW
R_1	5.4	749	1380	1500
O_3	4.3	918	800	900
O_4	3.4	838	500	500
O_5	2.5	701	470	–
O_6	1.6	526	400	450

2. Experimental Data							
Sample	H/C	C_A	Ha	H_{alpha}	$H_{methylenes}$	H_{methyl}	C_{methyl}
R_1	1.35	36.9	8.0	15.3	59.4	17.3	9.7
O_3	1.51	26.8	5.5	11.2	63.3	20.0	11.6
O_4	1.57	25.0	5.7	10.3	63.7	20.3	10.1
O_5	1.59	23.4	5.3	11.2	62.0	21.5	9.4
O_6	1.64	21.4	5.4	11.6	59.5	23.5	13.5

TABLE 9 PROPERTIES OF GPC CUTS OF RESID B ASPHALTENES

GPC Cut Number	1	2	3	4	5	6	7
H/C	1.09	1.09	–	1.14	1.13	1.07	–
GPC Number Avg. MW	5160	5020	3720	2410	1330	620	–
VPO Number Avg. MW	–	6830	–	2460	1370	–	–
Yield (wt%)	9.7	14.3	20.5	17.4	17.1	12.4	8.5
Elemental Composition (wt%) :							
C	83.72	84.23	–	84.30	84.16	84.08	–
H	7.60	7.66	–	8.00	7.90	7.52	–
N	1.13	1.11	–	1.01	1.02	1.16	–
S	6.37	6.49	–	6.18	6.09	5.96	–
O (by difference)	1.2	0.5	–	0.5	0	1.3	–
Metal Concentration (ppm) :							
Fe	134	29	34	87	35	320	–
Ni	228	130	122	127	144	450	–
V	590	490	490	530	490	1230	–
Ca	101	141	44	64	50	344	–
Zn	66	34	21	43	29	82	–
Total Metals	1120	830	711	850	750	2430	–
NMR Parameters							
C_A (by C_{13}-NMR)	51	48	–	47	47	53	–
Number of condensed aromatic rings	14	7.0	–	5.7	4.4	5.1	6.4
Cluster weight	1004	654	–	595	501	490	470

TABLE 10

SUMMARY OF PROPERTIES OF HEAVY OIL COMPONENTS AS A FUNCTION OF BP

Chemical Properties	Vacuum Gas Oil (FHD-756)	1000+ Resid								
		DISTACT Distillables				DISTACT Bottom		Asphaltenes		
T90 BP (°F)	850	960	1090	1220	1250	Total	Asphaltene Removed	> 1300°F		
Ave. MW	400	400	470	500	800	1380	800	500-600	1300-2400	4000-5000
% C_A by NMR	22	21	23	25	27	37	32	53	47	48
Number of Condensed Aromatic Rings	1.5	1.6	2.5	3.4	4.3	5	5	5	4-6	7
Atomic H/C Ratio	1.7	1.64	1.59	1.57	1.51	1.31	1.4	1.07	1.13	1.09
Wt% S in fraction	–	2.9	3.6	3.9	4.3	6.2	6	6.0	6.1	6.5
Wt ppm Ni + V	< 1	1	12	80	130	490	410	1700	620	620
Wt% N in fraction	0.15	0.12	0.21	0.27	0.37	0.7	0.6	1.16	1.01	1.11
ABN Separation by Alumina LC										
Neutral Material :										
Wt% Aromatics	47	82				50-70		20-30		
Wt% Saturates	45	6				0.1		< 0.1		
Ave. MW	400	570				–		–		
Polar Materials (Acids Plus Bases) :										
Wt%	8	10-13				30-40		70-80		
Ave. MW	400	580-600				–		2000		

SPECTROSCOPIC CHARACTERIZATION OF VISBREAKING TARS

R. Scotti, M. Clericuzio, C. Pirovano

Eniricerche S.p.A., via Maritano, 26 - 20097 San Donato Milanese (MI) - Italy

Keywords: Fluorescence spectroscopy, NIR spectroscopy, Visbreaking tar.

INTRODUCTION

Visbreaking (VB) is a thermal cracking process, widely used in the refineries of Western Europe to obtain distillates (gasoil, naphtha) from a petroleum residue (feedstock). The visbroken residue (tar) is used to produce fuel oil, after addition of the appropriate amounts of cutter-stock.

Even if the highest conversion of feedstock would be desirable, the severity of the VB process is limited by the stability of the resulting VB tars. The stability index (SI) here employed is:

$SI = 1 + V_{cet}$, where V_{cet} is the maximum amount of *n*-cetane, expressed as *ml* of cetane for *g* of sample, that can be added before the flocculation of asphaltenes starts. VB tars having SI<1.1 are considered to be unstable and cannot be used in the preparation of fuel oils with the appropriate specifications.

Several papers can be found in the literature dealing with the molecular changes occuring during the VB process [1-3]. The present paper is aimed at verifying the amount of information that can be extracted from optical spectroscopies and, in particular, the possibility of directly monitoring the physico-chemical modifications caused by VB process. To this purpose a series of VB tars, produced from a single feedstock at different severities, were investigated by a number of spectroscopic techniques, viz.: NIR; UV-Vis; Fluorescence; ^1H and ^{13}C NMR; EPR.

EXPERIMENTAL

The lab visbreaking apparatus has already been described in detail elsewhere [4]. VB experiments were carried out in a continuous bench-scale unit under isothermal conditions (442 °C); the severity of the process was therefore determined only by residence times, varying from 3.5 to 9 minutes. The feedstock employed in the VB experiments was a 500°C + vacuum residue (VR) produced from a mixture of different crudes. VB tars were produced after distillation at 350 °C (350+, atmospheric pressure) or at 500 °C (500+, under vacuum). Asphaltenes were separated according to the IP 143 method. Deasphalted oil (DAO) was fractionated into saturate, aromatic and polar components via liquid chromatography according to a partially modified ASTM D 2549 method, using n-hexane, n-hexane/toluene, clorophorm/diethylether/ethanol as eluents. The feedstocks was also characterized in terms of elemental analysis (ASTM D5291), total sulphur (ASTM D1552), Conradson Carbon Residue (CCR, ASTM D5430), specific gravity (ASTM D4052) and viscosity, measured at 50 and 100 °C by a RMS 800-Rheometrics.

Near-Infrared spectra were collected on a Guided Waves model 260, UV-Vis spectra on a diode-array Hewlett-Packard 8452A spectrophotometer.

Fluorescence spectra (corrected both in excitation and in emission using the standard Perkin-Elmer procedure of the instrument) were recorded on a Perkin-Elmer MPF-66 spectrofluorimeter.

^1H and ^{13}C NMR spectra were recorded on a Bruker AMX-300, operating at 300.130 MHz for proton and 75.470 MHz for carbon. ^{13}C quantitative spectra were obtained using an Inverse Gate decoupling technique. $CDCl_3$ was used as solvent.

EPR spectra were recorded on a Bruker ESP 300 E operating at X-band (9.5 GHz). Strong pitch (3×10^{15} spin/cm ± 15%) was used as quantitative reference.

RESULTS AND DISCUSSION

The physico-chemical properties of feedstock, VB tars, and the fractions obtained from 350+ tars are reported in tabs. 1, 2 and 3, respectively.

The molar ratio of aromatic carbon (F_{ar}) and the main lengths of side chains (*n*) were calculated by NMR analysis, according to Dickinson [5,6].

A general increase of F_{ar} and of asphaltene content with increasing VB severity is evident (tabs. 2-3). From the analysis of tar fractions (tab. 3) it turns out that the increase in F_{ar} and the decrease in *n* mainly occurs in asphaltenes. This is in agreement with previous studies of the molecular effects of VB [2]: at relatively low severity asphaltene dealkylation occurs via breaking of aliphatic side chains, dehydrogenation and ring-opening of naphthenic moieties occurs, leading to more aromatic structures.

The relative amount of radicals (from EPR) increases with VB severity (tab. 2). *g* factors are not significantly affected by thermal treatment within each series. These radicals are associated with non-localized π systems stabilized by resonance over polyaromatic centers [7]. The slight difference between 350+ and 500+ tars ($g_{350+} = 2.0026 \pm 0.0001$; $g_{500+} = 2.0029 \pm 0.0001$) could be assigned to the different content in heteroatoms of the two series.

The electronic absorption spectrum of a typical VB tar shows a broad and unstructured band spanning the UV and visible regions of the spectrum, with absorption maxima around 260-270 nm (data not shown). For each sample the extinction coefficient $\varepsilon_w = A/cl$ (c expressed as w/v) was calculated as the slope of the straight line fitting the absorbances at 0.1, 0.05, 0.025, 0.0125 mg/ml in CCl_4. The use of w/v concentrations, rather than molar, is justified by the critical values of average molecular weights in heavy petroleum derivatives, owing to association phenomena [8]. ε_w, obtained at 280 and 320 nm, increases with increasing VB residence time within each of the two series, 350+ and 500+ (fig.1, only 500+ shown).This is in agreement with the increase of aromatic chromophores.

Fluorescence spectra were recorded both in THF and CCl_4 solutions (0.0125 mg/ml).

The excitation spectra show, in both solvents, two main maxima, centered at about 330 and 390 nm (data not shown). Emission spectra were recorded with excitation centered at 394 nm: in THF a maximum in emission is observed at 453 nm (fig. 2, top). In fig. 3 emission intensities at 453 nm (in THF) are plotted for the eight samples: they show an increase with increasing VB severity in both series, which is related to the increase in aromaticity.

Spectra recorded in CCl_4 are markedly different (fig. 2, bottom). The overall intensity is approximately 4-fold smaller in CCl_4 than in THF, and maxima in emission are red-shifted about 25 nm . This clearly shows that in CCl_4 VB tars are much more aggregated: in fact, formation of molecular complexes is expected to lead to fluorescence quenching and red-shifted emissions. Molecular association is a well-known phenomenon in the chemistry of asphaltenes, even at very low concentrations [8-9]. Our explanation is that the polar THF is more effective in disrupting the aggregation state of VB tars.

An interesting phenomenon is observed when fluorescence spectra are recorded in CCl_4. Immediately after the solution is prepared, the intensity of the spectrum decreases gradually with time until a plateau is reached, generally within one hour (fig. 4). The phenomenon is partially reversible after stirring the solution, and is much less evident in THF. Slow diffusion phenomena in solution, or a simple sedimentation effect might be responsible for this. NMR-Imaging studies are in progress to have more information.

An analogous phenomenon is observed in the NIR spectrum. The freshly prepared solution in CCl_4 (10 mg/ml) shows an increase of baseline with time (fig. 5), probably due to Rayleigh scattering. It is likely that rather large particles are formed.

To avoid changes in baseline, NIR spectra were recorded under stirring, using optical fibers.

The spectra show a broad continuum with increasing absorption at higher energy, which is attributed to electronic transitions of large aromatic ring systems [10], and a second region at lower energies, which is attributed to vibrational overtones and combination bands of predominantly saturated hydrocarbons [10]. The ratio between I_{1200} (electronic transitions) and I_{2300} (C-H stretch plus bend) increases with severity (fig. 6).

CONCLUSIONS

1) Our data suggest that it is possible to monitor the severity of VB by means of optical spectroscopies (potentially also on-line). In fact UV and NIR absorption intensities, as well as fluorescence emission intensities, are all sensitive to the molecular changes occurring during the VB process.

2) The solvent has a marked effect on the solution structure of VB tars; in particular in CCl_4, as compared to THF:

- a) solute molecules are in a higher aggregation state;
- b) the equilibrium structure is reached rather slowly, and is at least partially reversible by stirring;
- c) rather large particles are probably formed.

Care should therefore be taken in analytical applications when using CCl_4 as solvent, otherwise the reproducibility of measures will be strongly affected.

REFERENCES

1) Singh I.D., Kothiyal V., Kapoor M.P., Ramaswamy V. and Aloopwan M.K.S. - *Fuel* **72**, 751, 1993.

2) Tatsumi T. J., Nakasuga A., Yoshida H., Suhara S., and Tominaga H. - *J. Japan Pet. Inst.* **28**, 318, 1985.

3) T. Zerlia and G. Pinelli - *Fuel* **72**, 1109, 1993.

4) Del Bianco A., Garuti G., Pirovano C. and Russo R. - *ACS Preprints, Division of Petroleum Chemistry* 408, 1994.

5) Dickinson E.M. - *Fuel* **59**, 290, 1980.

6) Calemma V., Iwanski P., Nali M., Scotti R. and Montanari L. - *Energy Fuels* **9**, 225, 1995.

7) Yen T.F., Erdman J.G. and Saraceno A.J. - *Fuel* **34**, 694, 1962.

8) Speight J.G., Wernick D.L, Gould K.A., Overfield R.E., Rao B.M.L. and Savage D.W. - *Revue de l'Institut Francais du Petrole* **40**, 51, 1985.

9) Sheu E.Y., De Tar M.M., Storm D.A. and De Canio, S.J. - *Fuel* **71**, 299, 1992.

10) Mullins O.C. - *Anal. Chem.* **62**, 508, 1990.

Table 1: Physico-chemical properties of feedstock

Specific gravity 15°C	0.9896	CCR wt%	14.3	*Dist. fractions*	°C
Viscosity 50 °C [cSt]	30,800	SI	6.3		
Viscosity 100°C [cSt]	660			Initial Boiling Point	306
H wt%	10.9			5 wt%	434
C wt%	86.3	C7-Asphaltenes wt%	5.8	10 wt%	478
N wt%	0.8	*DAO composition*:		30 wt%	563
S wt%	1.4	Saturates wt%	25.4	50 wt%	618
V [ppm]	79	Aromatics wt%	46.2	70 wt%	680
Ni [ppm]	58	Polars wt%	22.6	90 wt%	756

Table 2: Physico-chemical properties of 350°C+ and 500°C+ VB-tars

Time [min]	SI	Sp.Gr.	V. 50 [cSt]	V. 100 [cSt]	H/C	N %wt	S %wt	Coke %wt	F_{ar}	N_r x10^{16}
350 °C +										
3.5	1.8	1.000	26,700	400	1.42	1.1	1.3	0.03	0.26	5.5
5	1.5	1.004	30,100	450	1.40	1.1	1.3	0.04	0.29	6.8
7	1.2	1.006	30,200	440	1.36	1.2	1.3	0.22	0.30	8.0
9	1.1	1.008	31,200	470	1.36	1.2	1.3	0.40	0.32	8.5
500 °C +										
3.5	1.9	1.011	259,750	1,600	1.35	1.5	1.3	0.04	-	6.5
5	1.6	1.013	429,700	2,250	1.33	1.5	1.3	0.06	-	6.7
7	1.3	1.025	1,155,400	3,750	1.30	1.4	1.3	0.28	-	10.8
9	1.2	1.032	1,862,500	6,050	1.27	1.4	1.4	0.53	-	12.9

Time: residence time; SI: stability index; Sp.Gr: specific gravity at 15°C; V.50, V.100: viscosity at 50 and 100°C; F_{ar} : molar ratio of aromatic C by NMR; N_r : spin density [spin/g] by ESR.

Table 3: Composition of VB-tars 350 °C +

Time [min]	SI	Satur.	Aromatics			Polars			Asphaltenes		
		wt %	wt%	F_{ar}	*n*	wt%	F_{ar}	*n*	wt%	F_{ar}	*n*
3.5	1.8	25.4	41.5	-	-	22.2	-	-	10.9	0.56	-
5	1.5	25.7	40.3	0.35	6.1	22.4	0.42	5.3	11.6	0.62	4.7
7	1.2	24.2	36.6	0.33	5.9	26.4	0.45	5.5	12.8	0.67	4.2
9	1.1	24.0	36.9	0.34	6.2	25.5	0.44	5.3	13.6	0.68	3.7

Time: residence time; SI: stability index; F_{ar} : molar ratio of aromatic C by NMR; *n*: main length of side chains.

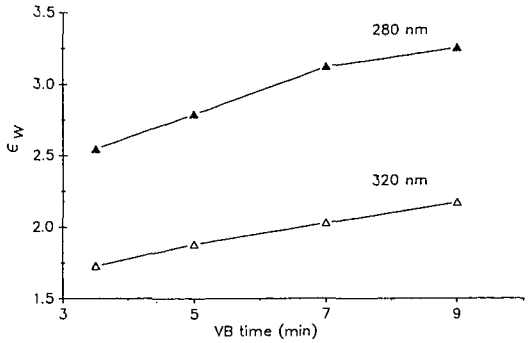

Fig. 1 - Extinction coefficients of 500+ tars (per gram) vs. VB severity.

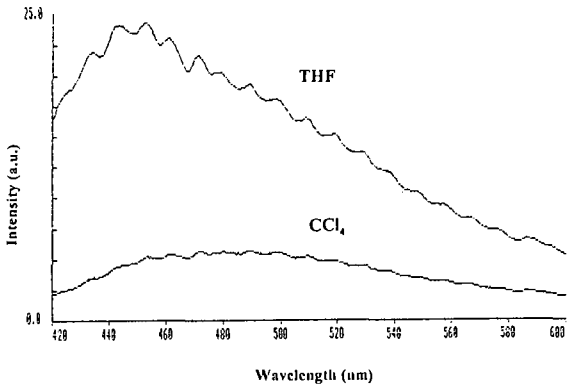

Fig. 2 - Fluorescence emission spectra of a selected VB tar. Excitation: 394 nm.

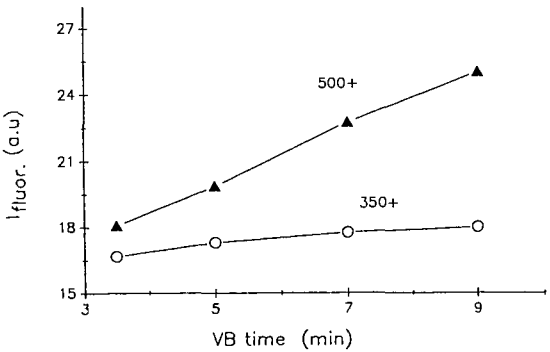

Fig. 3 - Intensity of fluorescence emission at 500 nm (exc. 394 nm) vs. VB severity. Solvent: THF.

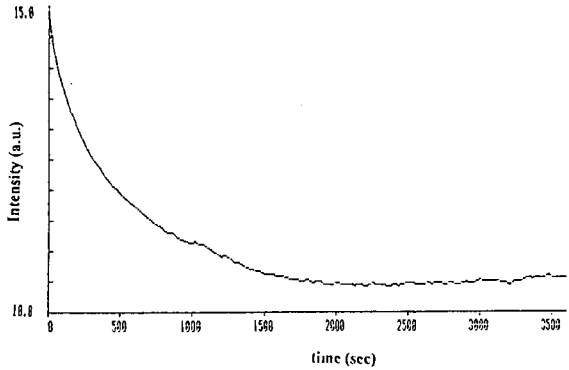

Fig. 4 - Time evolution of the intensity of fluorescence emission at 500 nm (exc. 394 nm). The solution is prepared by 1:100 dilution of an initial sol. in CCl_4.

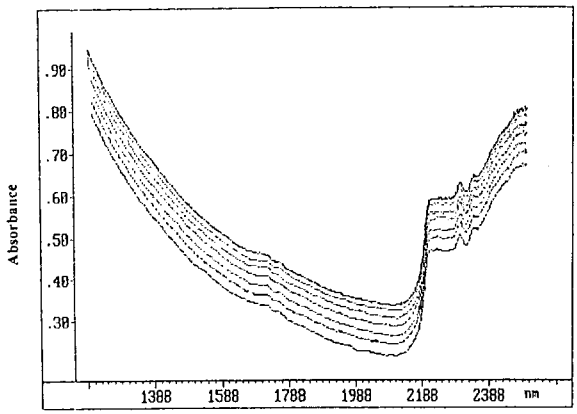

Fig. 5 - NIR spectra of a selected VB tar in $\dot{C}Cl_4$. Spectra were recorded every 8 minutes from 0 (bottom trace) to 48 min. (top trace).

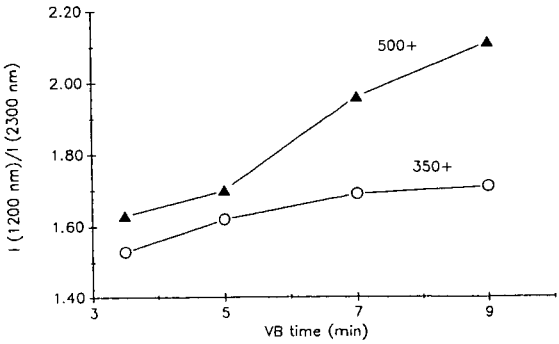

Fig. 6 - NIR intensity ratio between the bands at 1200 and 2300 nm vs. VB severity. Solvent: CCl_4.

THE STUDY OF COAL-DERIVED PYRITE USING ATMOSPHERIC PRESSURE TEMPERATURE PROGRAMMED REDUCTION (AP-TPR) AND TGA

Inge I. Maes, Jan Yperman, Dirk V. Franco, Jules Mullens and Lucien C. Van Poucke
Laboratory of Inorganic and Physical Chemistry
Limburgs Universitair Centrum
B-3590 Diepenbeek, Belgium

Grazyna Gryglewicz and Piotr Wilk
Institute of Chemistry and Technology of Petroleum and Coal,
Technical University of Wroclaw
50-344 Wroclaw, Poland

Keywords: pyrite, coal, AP-TPR

ABSTRACT

It is possible with AP-TPR to determine qualitatively as well as quantitatively the different organic sulfur forms in coal. The presence of pyrite might disturb an accurate sulfur determination by AP-TPR as is the case in other thermal techniques. Therefore it is important to have an insight into the behaviour of pyrite under the reducing experimental conditions. This study presents an explanation for the behaviour of pyrite subjected to a linear temperature increase up to 1000°C in an inert (TGA) as well as reducing (AP-TPR) atmosphere. Two pyrite samples were extracted from coal of the Halemba and Jastrzebie mine. As an example of the consequences of the presence of pyrite in coal, a discussion of the AP-TPR kinetogram of the Siersza coal of high pyritic sulfur content is included.

INTRODUCTION

Pyritic and organic sulfur are the two major sulfur forms in coal. Pyritic sulfur occurs mainly as iron sulfide, FeS_2. There are two naturally occurring forms of FeS_2, pyrite and marcasite of which pyrite is a major contributor to the total sulfur content of coals.

The AP-TPR technique is used to determine the organic sulfur functionalities in coal-derived materials. It is recommended to record pyrite free samples in order to overcome interference and to have an accurate view of the organic sulfur functionalities present in the raw coal. In the past, extraction with diluted nitric acid was commonly used to obtain pyrite free coal samples. Nevertheless, using this method, a complete removal is not always achieved when the pyrite is highly disseminated and present in particles of < 5 μm [1]. In addition, it has been demonstrated that the nitric acid treatment may have an influence on the coal structure and consequently some other organic sulfur functionalities might be changed [2]. More and more this treatment has been replaced by the lithium aluminium hydride procedure [3,4]. At the moment, $LiAlH_4$ is thought to cause selective desulfurization of the pyrite, although there is still a possibility that cleavage of di- and polysulfide linkages can occur. Moreover, a reduction of other organic sulfur compounds is not excluded.

The AP-TPR technique proved to be very promising for monitoring the consequences of different types of selective chemical treatments on coal [5]. In those cases, the ability in distinguishing pyritic sulfur from organically-bound sulfur is very desirable. The AP-TPR analysis has appeared to be useful in following the changes in the organic sulfur functionalities induced by heat treatment of coal as well [6].

The purpose of this paper is to present results of our study on the conversion of coal pyrite during the AP-TPR experiment. For this purpose coal pyrite was chosen to avoid a discrepancy which could be arised from the use of mineral pyrite. Moreover, coal-derived pyrite can be enriched in trace elements which can affect on its reactivity [7].

EXPERIMENTAL

a) Samples

The two pyrite samples studied in this paper are extracted from the Halemba and Jastrzebie coal. The pyrite concentrates are firstly cleaned by means of gravity separation and consequently by magnetic separation. The obtained coal-derived pyrites show a high degree of purity, which is determined by X-ray diffraction analysis.

The subbituminous coal sample originates from the Siersza mine (Poland) and is chosen for its high pyritic sulfur content of 4.17 wt%.

b) Used Techniques

Powder X-ray diffraction (XRD) with Mo K_α radiation was used for identification and purity control of the extracted pyrite samples.

Atmospheric Pressure-Temperature Programmed Reduction (AP-TPR) experiments are recorded

according to the procedure mentioned in previous papers [5,8,9]. A further optimization is performed by using a MKS flow controller (Model 2476). This set-up guarantees a flow of 50 cm^3 min^{-1} H_2-gas through the reactor during the entire AP-TPR experiment. All experiments are recorded with a heating rate of 5 °C min^{-1} and without the use of a reducing mixture. In this study the experimental AP-TPR data are smoothed by a more narrow 11 point Savitsky-Golay-Gorry filtering algoritm [10,11]. This change results in sharper signals and more detailed AP-TPR profiles. All samples were grounded before analysis to a particle size of less than 147 µm.
The Thermographical Analysis (TGA) experiments are performed with a TA Instruments (formerly Du Pont) Model 2000-951 apparatus. The samples (20-30 mg) are heated up to 1000°C at a heating rate of 5 °C min^{-1} in a pure argon gas stream of 50 cm^3 min^{-1}. The TGA data manipulation was performed using a 13 point smoothing filter of the Savitsky-Golay procedure.

RESULTS AND DISCUSSION

In Figure 1 the AP-TPR kinetogram of the Halemba pyrite sample is presented. The profile consists of two well separated maxima. The first temperature maximum is found at approximately 570 °C and the second at 690 °C. From this point it is clear that the pyrite (FeS_2) is not reduced in one step, but in two. The difference in shape between the two peaks also suggests a difference in reducing conditions. For the pyrite extracted from the Jastrzebie coal, the AP-TPR profile is comparable, as can be seen in Figure 1. In this kinetogram the maximum reducing temperatures are at 575 °C and 675 °C. Here the difference between the two reducing step mechanisms is even more obvious. Relatively, the first reducing peak has gained in intensity and the second peak has broadened even more in comparison to the Halemba pyrite curve.
In order to understand better the reason for this phenomenon, a TGA experiment is carried out under an argon atmosphere on the Halemba pyrite sample. The TGA plot is shown in Figure 2. Undoubtly, there is only one sharp peak at 600 °C visible. Calculations have proven that the mass decrease of 27.73 % during the experiment corresponds with a loss of 0.19 mmol sulfur for an amount of 0.18 mmol pyrite which was originally present in the examined sample. Taking into account the experimental error, this calculation illustrates that indeed only one sulfur is liberated for each FeS_2 molecule. Consequently, the signal in Figure 2 has to result from the thermal decomposition of pyrite into troilite (FeS) and elemental sulfur. The corresponding chemical reaction can be written as follows:

$$FeS_2\,(s) \xrightarrow{T\nearrow,\ Ar} FeS\,(s) + S\,(g)$$

In an inert atmosphere this reaction takes place at approximately 600 °C. The first Halemba pyrite maximum reduction temperature of the AP-TPR kinetogram in Figure 1 is found at 570 °C. From non-isothermal kinetic studies it is known that the removal of sulfur from pyrite under hydrogen is more favorable than under an inert atmosphere [12,13]. This can explain the 30 °C temperature difference between the thermal decomposition under argon and the AP-TPR reduction under H_2 atmosphere. Consequently, this means that probably the first reduction step of pyrite takes place after thermal liberation of the elemental sulfur. In the gaseous phase this sulfur will then react with the H_2-gas forming H_2S and is as such detected. This gas phase reaction proceeds rapidly, which is translated in a corresponding sharp, high peak in the AP-TPR kinetogram. The same profile characteristics can be seen in the Jastrzebie pyrite kinetogram in Figure 1. It also seems that the first reduction peak of both pyrite samples is at almost the same temperature.
The TGA experiment shows that the troilite does not decompose thermally at temperatures up to 1000 °C. In consequence, the second reduction peak in both pyrite AP-TPR kinetograms can thus be attributed to the direct reduction of FeS. In contrast with the first reduction peak, this reaction occurs between the H_2-gas and FeS in the solid phase according to:

$$FeS\,(s) + H_2\,(g) \xrightarrow{T\nearrow} Fe\,(s) + H_2S\,(g)$$

This solid phase mechanism causes the broadening of the second pyrite reduction peak. The H_2-gas reacts with the surface of the solid troilite which causes a slower reduction and consequently a broader reduction peak in comparison to the former gas-gas reaction. Consequently, the second reduction peak of the Halemba and Jastrzebie kinetograms are not so similar as the first. The peaks do not have the same maximum reduction temperatures, nor the same shape. Assumed is that this reduction in the solid phase is strongly dependent on the morphology. Minor physical differences of the troilite surface can affect the course of the reduction process. In consequence, the AP-TPR kinetogram can look a little different for each experiment if the troilite particles originating from the thermal decomposition of pyrite have a different particle size or different surface characteristics. Because of the nature of the solid-gas reduction, the peaks exhibit a broad contour. Depending on the relative concentrations, this band can usually be seen as a background on which possible reducing peaks of other sulfur groups present in for instance coal are superimposed.

As an example, the kinetograms of two AP-TPR experiments of the same Siersza coal sample are shown in Figure 3 and 4. Both profiles exhibit one sharp, intense peak that can easily be recognised as the first reduction peak of pyrite: the reduction of elemental sulfur in the gaseous phase. The Siersza coal was chosen for its high pyrite content (4.17 wt%) which explains the rather stupendous appearance of the first pyrite reduction peak in the kinetogram. As predicted, the second reduction peak is not so reproducible. This does not disturb the organic sulfur reduction peak characterization at 750-760 °C. The coal sample kinetograms prove that a qualitative analysis can be possible, even though the troilite reduction peaks are not exactly reproducible and the reduction conditions are hard to control. Also, it can be stressed upon that these experiments also suggest that most of the elemental sulfur, thermally liberated from pyrite, is reduced by the H_2-gas under AP-TPR conditions. However, still a smaller amount of elemental sulfur could have reacted with the organic matrix to form organic sulfur groups which will be reduced at higher temperatures. The extend of this taking place is not known at this point, but will be the subject of further investigations. If the objective of the AP-TPR analysis is to study the organic sulfur distribution in coal, than it may be opportune to remove the pyrite in advance. In this way, no elemental sulfur can react with the organic matrix and the troilite reduction peak can not interfere with the organic sulfur reduction peaks.

CONCLUSIONS

In this study the mechanism of pyrite reduction is explained. It is demonstrated that in the first reduction step sulfur is thermally liberated from FeS_2. In the AP-TPR experiment this S-gas is then reduced into H_2S at approximately 570 °C. Around 680 °C, the solid FeS is transformed under a reducing atmosphere into Fe and H_2S.

The kinetogram of a pyrite sample exhibits at first a sharp reduction peak followed by a broader and less intense reduction band. Because of the characteristic reduction peak at approximately 570 °C, pyrite can easily be recognised in the AP-TPR kinetogram of most coal samples. The troilite reduction peak at approximately 680 °C is in most cases too broad to be of great disturbance for the AP-TPR analysis of coal. The organic sulfur group reduction peaks will only be superimposed upon the FeS band.

ACKNOWLEDGEMENTS

The authors would like to thank Mrs. M. Vanhamel and Mr. J. Kaelen for their technical assistance with the AP-TPR experiments. I. I. Maes is supported by a specialisation grant from the "Vlaams Instituut voor de bevordering van het Wetenschappelijk-Technologisch onderzoek in de industrie".

REFERENCES

1. Davidson, R. *Organic Sulphur in Coal*, IEA Coal Research, London, 1993
2. Calkins, W. H. *Fuel* **1994**, 73, 475
3. Gryglewicz, G.; Jasienko, S. *Fuel* **1992**, 71, 1225
4. Lawlor, D. L.; Fester, J. I.; Robinson, W. E. *Fuel* **1963**, 42, 239
5. Yperman, J.; Franco, D. V.; Mullens, J.; Reggers, G.; D'Olieslaeger, M.; Van Poucke, L. C.; Marinov, S. P. *Nato ASI, "Composition, Geochemistry and Conversion of Oil Shales, Ackay", Series C, Vol. 455*, Kluwer, Dordrecht, The Netherlands,1995, pp 449
6. Yperman, J.; Franco, D.; Mullens, J.; Van Poucke, L.C.; Gryglewicz, G.; Jasienko, S. *Fuel* (in press)
7. Spears, D. A.; Martinez Tarazona, M. R.; Lee, S. *Fuel* **1994**, 73,1051
8. Mullens, J.; Yperman, J.; Carleer, R.; Franco, D. V.; Van Poucke, L. C.; Van Der Biest, J. *Applied Clay Science* **1993**, 8, 91
9. Ismail, K.; Mitchell, S. C.; Brown, S. D.; Snape, C. E.; Buchanan III, A. C.; Britt, P. F.; Franco, D. V.; Maes, I. I.; Yperman, J. *Energy & Fuels* **1995**, accepted
10. Savitsky, A.; Golay, M. J. E. *Analytical Chemistry* **1964**, 36, 1627
11. Gorry, P. *Analytical Chemistry* **1990**, 62, 570
12. Tsai,C.S. *Fundamentals of Coal Beneficiation and Utilization,Coal Science and Technology 2*, Elsevier, Amsterdam, 1982, pp 235
13. Sugawara,T.; Sugawara,K.; Ohashi,H. *Fuel* **1988**,67,1263

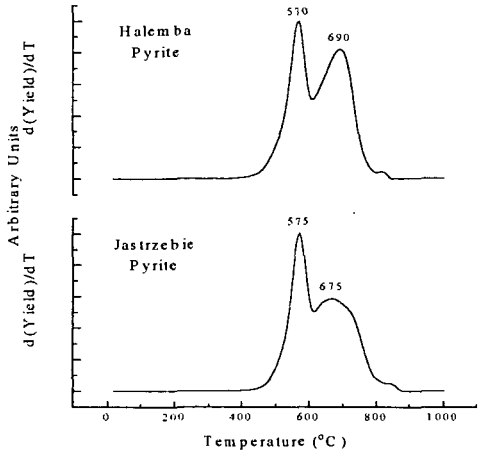

Figure 1 : AP-TPR kinetograms of the Halemba and Jastrzebie pyrite sample

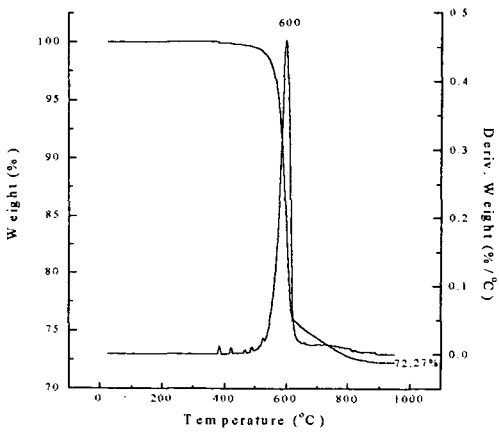

Figure 2 : TGA spectrum of the Halemba pyrite sample

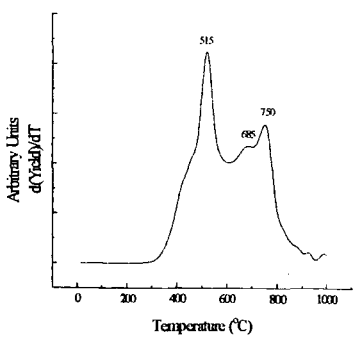

Figure 3 : AP-TPR kinetogram of the Siersza coal sample - I

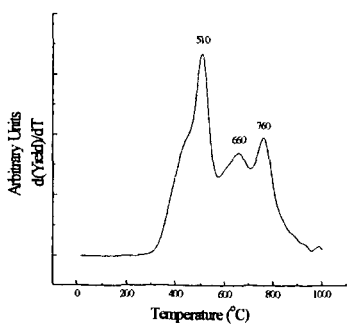

Figure 4 : AP-TPR kinetogram of the Siersza coal sample - II

RATIONALE FOR CONTINUING R&D IN DIRECT COAL CONVERSION TO PRODUCE HIGH QUALITY TRANSPORTATION FUELS

R.D. Srivastava and H.G. McIlvried
Burns and Roe Services Corporation
Pittsburgh Energy Technology Center
P.O. Box 18288
Pittsburgh, PA 15236
D. Gray and G.C. Tomlinson
The Mitre Corporation
McLean, VA 22102
E.B. Klunder
Pittsburgh Energy Technology Center
Pittsburgh, PA 15236

ABSTRACT
For the foreseeable future, liquid hydrocarbon fuels will play a significant role in the transportation sector of both the United States and the world. Factors favoring these fuels include convenience, high energy density, and the vast existing infrastructure for their production and use. At present the U.S. consumes about 26% of the world supply of petroleum, but this situation is expected to change because of declining domestic production and increasing competition for imports from countries with developing economies. A scenario and time frame are developed in which declining world resources will generate a shortfall in petroleum supply that can be alleviated in part by utilizing the abundant domestic coal resource base. One option is direct coal conversion to liquid transportation fuels. Continued R&D in coal conversion technology will result in improved technical readiness that can significantly reduce costs so that synfuels can compete economically in a time frame to address the shortfall.

BACKGROUND
The United States continues to rely heavily on liquid fuels for transportation, and, in spite of the strong interest in using alternative fuels, hydrocarbon liquids will continue to play a significant role in our energy future. This is primarily because of their convenience, high energy density, and the enormous infrastructure in place for their production, distribution, and end-use. Currently, the U.S. consumes about 17.5 million barrels per day (BPD) of oil (about 35 quads/yr - 1 quad/yr equals approximately 500,000 BPD). Of this, 75% is used by the transportation sector.

Current domestic crude production is 6.6 million BPD, having steadily declined from 9 million BPD ten years ago at a decline rate of about 3%/yr. Currently, the U.S. imports over 50% of its petroleum, and the Energy Information Administration (EIA)[1] predicts that this will increase to 68% by the year 2010.
The U.S. currently uses 26% of the world's total petroleum production. Even if this percentage were to remain constant, a significant shortfall in the petroleum supply in the U.S. is likely to occur because of declining domestic production. Because of competition from rapid economic development worldwide, the U.S. may not be able to import sufficient oil to meet future demand.

Coal resources in the U.S. are enormous. EIA estimates total reserves at 1.7 trillion short tons. Coal represents an inexpensive, domestic resource that can be used as a feedstock to produce clean, high-quality transportation fuels in an environmentally sound manner.

The Department of Energy (DOE) Fossil Fuel Energy's R&D program has been largely responsible for technological improvements in coal liquefaction in the U.S. The goal of the DOE program is to develop and demonstrate coal liquefaction technology that is competitive with crude oil at $25-30/bbl in 1993 dollars. The purpose of this program is to reduce vulnerability to energy supply disruptions, to create new high wage jobs, and to do this while respecting the environment.

THE WORLD ENERGY PICTURE

At the last World Energy Congress meeting in 1992[2], MITRE presented a world energy demand model that was used to estimate total commercial world energy demand to the year 2100. If energy use efficiency does not improve, estimated world demand will reach 2,090 quads by 2100. If energy conversion and end-use efficiencies continue to improve, the world's commercial energy demand will be reduced from 2,090 quads in the no-efficiency-improvement case to about 1,050 quads in 2100. However, even with efficiency improvements, world energy demand will still increase three-fold over the present level of 350 quads per year.

The question is whether this demand can be satisfied with known energy resources. To answer this, the world resources of oil and natural gas must be determined. The United States Geological Survey[3] estimates the world's ultimate resource of conventional oil as 1.7 trillion barrels (about 10,000 quads). Estimates for natural gas are less certain; therefore, a range was assumed: 10,000-20,000 trillion cubic feet[4] (TCF) (10,000-20,000 quads).

Figure 1 shows resource depletion curves. By 2100 oil will be essentially depleted, and natural gas will either be depleted or in rapid decline. Although not shown on the figure, coal availability worldwide is enormous. Estimates range from 45,000 quads[5] for proved reserves to 240,000 quads[6] for the total resource, between 500 and 2000 years supply at current usage rates.

The estimated conventional fossil energy resource and the postulated world energy demand scenario can be combined to produce a world energy demand/supply scenario as shown in Figure 2. In this scenario, it is assumed that oil, gas, and present day nuclear use follow the depletion curves shown, coal use remains constant at the present level, and hydroelectric power supply triples between now and the year 2100. The area designated as "21st Century" represents the energy shortfall. In this constant coal use scenario, the shortfall will have to be supplied by advanced nuclear energy technologies and renewable or sustainable energy technologies.

Figure 2 shows that before the year 2030, and perhaps as early as 2010, the demand on world oil is such that supply cannot keep pace, and the world oil supply starts to decline. This scenario is optimistic, since it assumes that world oil use is essentially constant from the present to 2030. However, world oil use is actually increasing, so that the imbalance of oil supply and demand will occur before 2030. If the world energy demand scenario presented above is credible, then the world may have less than 30 years before a significant shortfall in conventional liquid fuel supplies occurs.

THE UNITED STATES ENERGY PERSPECTIVE

Let us now concentrate on the situation in the U.S. The U.S. annually produces about 17 quads of domestic crude oil and natural gas liquids (NGL), and this production is declining. Figure 3 shows a resource depletion scenario from the present to the year 2100 for oil, natural gas, and power from current nuclear plants (nuclear energy from current technologies is assumed to phase out over the time period shown). It is evident from Figure 3 that the declining domestic energy supply, especially liquid fuels, must be made up by expanding petroleum imports or by increasing the use of our domestic coal reserves.

The ability of the U.S. to import oil may be limited. Two import scenarios which may be applied to the U.S. energy situation from now until 2050 are (1) the U.S. will continue to consume 26% of total world petroleum and (2) the U.S. will import a fraction of the world's oil that is proportional to the U.S. GDP compared to the world GDP. In both cases, the supply of oil to the U.S. declines early in the next century.

Two U.S. demand scenarios may be considered. The higher demand scenario is from the EIA, and the essentially constant demand scenario is from the MITRE energy model. Depending on which

scenario is selected, a shortfall in petroleum supply (domestic production plus imports) begins somewhere in the 2005-2015 time period and becomes significant by 2010-2030. The probable shortfall is between 1 and 3.5 million BPD in 2030. This is illustrated in Figure 4.

MEETING THE SUPPLY SHORTFALL

One alternative to meet this supply shortfall is to produce liquid fuels from coal. In direct liquefaction, coal reacts with hydrogen in a hydrogen donor solvent vehicle to produce a distillate product that can be refined into liquid transportation fuels. The product from direct coal liquefaction is easy to refine because it is an all-distillate, low sulfur and nitrogen liquid. Transportation fuels that meet the strict environmental regulations expected to be in force in the next century can be made from domestic coals.

If coal conversion is to play a significant role in alleviating the liquid fuel supply problem before the year 2030, then the liquefaction technologies must be in a state of readiness for commercial deployment about 15 years earlier, because lead times for the introduction of new energy technologies are on the order of 10 to 15 years, even after the technologies are technically ready for commercial deployment. Although direct liquefaction technology has undergone very significant improvements over the past decade and achieved a high level of technical readiness, it is still not cost competitive. Therefore, continuing R&D is needed to reduce costs to meet the target of 2015 for the start of commercial deployment. Further R&D can achieve additional process improvements to permit earlier introduction of coal-derived transportation fuels into the marketplace.

Current liquefaction program activities cover all aspects of technology development from basic and exploratory research through bench-scale operations to proof-of-concept (POC) demonstration. The four integrated elements of the direct liquefaction program are development of the catalytic two-stage direct liquefaction process, coprocessing development, advanced liquefaction concepts development, and POC (3 ton/day) testing of promising technologies.

To help identify the high-cost elements of direct coal liquefaction, DOE contracted with Bechtel[7] to develop a conceptual commercial design of a direct coal liquefaction facility to produce hydrotreated distillate products from either bituminous or subbituminous coal. The Bechtel design, which represents the current state of the art for direct liquefaction, yielded a cost of about $34/bbl of crude oil equivalent (COE). Although higher than the present world oil price (WOP) of about $17/bbl, this cost is significantly lower than earlier estimates of $40-50/bbl because of process improvements from the R&D undertaken over the last decade. Because direct liquefaction technology is still evolving and additional process improvements are expected, costs will decrease further as improvements are incorporated.

THE IMPACT OF CONTINUING R&D ON DIRECT COAL LIQUEFACTION COSTS

Table 1 shows the elements of cost for the baseline direct liquefaction conceptual commercial plant and the estimated reduction in cost that can be achieved by further R&D. Areas of most importance in reducing costs include decreasing capital investment, improving product yields, and reducing catalyst cost.

Several opportunities are available for reducing capital investment, such as increasing space velocity to reduce the number of liquefaction reactor trains and improving H_2 production. Replacing the current ebullated bed reactors with slurry reactors decreases the COE cost by about $1-2/bbl. By employing advanced technologies now under development, the capital cost of H_2 production can be decreased by an estimated 12% with a resulting decrease in the COE cost of about $1/bbl.

Product quality improvement is equally important. One way to do this is to increase the yield of products boiling below 850°F. An increase of 10% in these products will decrease the COE cost by

about $3/bbl. Catalyst costs are a significant contributor to product costs. If 90% of the catalyst can be recovered and reused, the COE cost will be reduced by about $2/bbl.

The high probability of achieving the improvements discussed above suggests that a $6/bbl decrease in the COE price to about $28/bbl is readily achievable. The R&D strategy is to concentrate efforts over the next few years in the high potential areas listed above. With no further R&D, direct coal liquids will remain at the Bechtel baseline cost of about $34/bbl of COE, and coal liquids would not be competitive with petroleum until 2030. With continued R&D, the cost of direct liquids will be reduced to about $28/bbl ($0.67/gal) and be competitive in 2017, 13 years earlier.

STRATEGY FOR DEVELOPING A COMMERCIAL COAL LIQUEFACTION INDUSTRY
Once cost competitiveness is achieved, the next step is to achieve commercialization. Initial pioneering production of coal-derived transportation fuels will require a capital expenditure of $3.8 to $4.6 billion for each plant to produce about 70,000 BPD of liquid fuels; it may require five to seven years to achieve full production. Because of the costs involved, coal-derived liquid fuels will probably not make a major contribution to the nation's transportation fuel needs until a significant imbalance between crude oil supply and demand occurs, expected sometime between 2015 and 2030.

The liquefaction plants to produce coal-derived fuels will be designed to meet the highest standards for environmental compliance. The transportation fuels produced by coal liquefaction technologies will be environmentally superior to their petroleum-derived counterparts and will be capable of meeting all requirements of the 1990 Clean Air Act Amendments. Coal liquefaction technologies can also be utilized to co-convert wastes, such as plastics, to environmentally acceptable fuels.

The key to commercialization will be integration with the existing petroleum refining/distribution infrastructure. In achieving commercialization, two intermediate technologies are important. The first is coprocessing of petroleum-derived wastes (plastics, tires, waste oil) with coal. Development of this technology is being driven by dwindling landfill availability and increases in tipping fees. These additional incentives may permit early implementation of this technology. The second technology is coprocessing of coal with heavy petroleum resids or oils. This technology is seen as being commercially feasible as a mid-term option and is likely to account for the first production of coal-based transportation fuels in existing petroleum refineries.

THE CONTRIBUTION OF DIRECT COAL LIQUEFACTION TO THE U.S. ECONOMY
If construction of coal liquefaction plants can be initiated in the year 2012, one million BPD capacity could be in place by 2030. Although direct coal liquefaction would only provide a portion of the energy mix needed to address the U.S. shortfall, production of high quality transportation fuels from U.S. coal will constitute a new and growing domestic industry that will employ engineering and construction personnel, plant operators, coal miners, and related workers. An estimated 333,000 jobs would be created by a one million BPD industry.

Demonstrating the ability to produce coal-derived transportation fuels at $28/bbl by the year 2010 could have the effect of moderating the world oil price at $28/bbl from 2017 onwards with consequent savings to the U.S. economy of up to $200 billion (1993 dollars) between 2015 and 2030. An R&D program that can reduce dependence on oil imports, help in providing national energy security, provide domestic jobs, and save $200 billion in balance of payments is a sound investment in the nation's future.

CARBON DIOXIDE EMISSIONS
Concern has been expressed that increased coal use will result in excessive emissions of carbon dioxide into the atmosphere, thereby exacerbating the potential for global warming. Figure 5 shows the

energy mix that will result in no further increase in annual carbon dioxide emissions in the U.S. over the present. This figure shows that, because of the decrease in oil and gas, coal use can be increased substantially after 2015 with no net increase in annual carbon dioxide emissions. Coal use can be increased by about 7 quads over present consumption by 2030 with no further increase in carbon dioxide emissions. If this amount of coal were used for production of liquid fuels, about two million BPD of coal-derived fuels could be produced.

CONCLUSION

Because of the long-term nature of the market opportunity and the consequent long wait for return on investment, without government participation, private industry is unlikely to fund these activities. Therefore, continued government support for laboratory, bench, and POC activities is essential to continue the development of transportation fuels from coal.

The analysis presented in this paper clearly shows that the world will need substantial amounts of "new" energy to continue economic progress in the next century. The U.S. has the opportunity to develop coal liquids technology that will help ensure our continued economic prosperity by creating a new industry with highly skilled jobs and providing opportunity for export of U.S. technology on the world market without compromising environmental quality.

References

1. Energy Information Administration, "Annual Energy Outlook 1995," January 1995.
2. Gouse, S.W., D.Gray, G.C. Tomlinson, D.L. Morrison, "Potential World Development through 2100: The Impacts on Energy Demand, Resources, and the Environment," World Energy Council Journal, December 1992.
3. USGS, 14th World Petroleum Congress, Norway, May 1994.
4. Masters, C.D., "Oil and Gas - Where in the World and Why?" 8th V.E. McKelvey Forum on Mineral and Energy Resources, Houston, TX, February 1992.
5. World Resources Institute, "People and the Environment," Oxford University Press, 1994.
6. Institute of Gas Technology, "World Reserves Survey 1987," 1989.
7. Bechtel and Amoco, "Direct Coal Liquefaction Baseline Design and System Analysis," report prepared for DOE under Contract DE-AC22-90PC89857, March 1993.

Table 1. Estimated Cost Impact of Continued R&D on Direct Liquefaction

Cost Elements, $MM	Baseline 28,776 tpd	Increased Space Velocity	Improvement in Yield	Catalyst Recovery & Recycle	Improvement in Hydrogen Production
Coal Handling	222	222	226	226	226
Liquefaction	941	762	762	822	822
Gas Cleanup/Byprd Rec.	297	297	297	297	297
Product Hydrotreating	107	107	113	113	113
ROSE Unit	46	46	43	43	43
Gasification	334	334	342	342	302
Air Separation	244	244	250	250	220
ISBL Field Cost	2192	2013	2034	2094	2024
OSBL Field Cost	978	978	981	978	968
Total Field Cost	3170	2991	3015	3072	2992
Total Capital	3889	3669	3699	3768	3670
Refined Product Cost, $/bbl					
Capital*	23.61	22.25	20.37	20.77	20.23
Coal	7.84	7.85	7.51	7.51	7.51
Catalyst	2.57	2.58	2.33	0.23	0.23
Natural Gas	3.59	3.45	2.90	2.74	2.69
Labor	1.66	1.67	1.51	1.51	1.51
Other O&M	0.33	0.33	0.29	0.29	0.30
By-Product Credits	(4.18)	(4.05)	(3.43)	(3.29)	(3.25)
RSP	35.42	34.08	31.48	29.76	29.22
Quality Premium	(1.19)	(1.19)	(1.19)	(1.19)	(1.19)
COE	34.23	32.89	30.29	28.57	28.03
Plant Output, million bbl/yr	24.16	24.16	26.58	26.58	26.58

*Includes maintenance materials, taxes, and insurance.

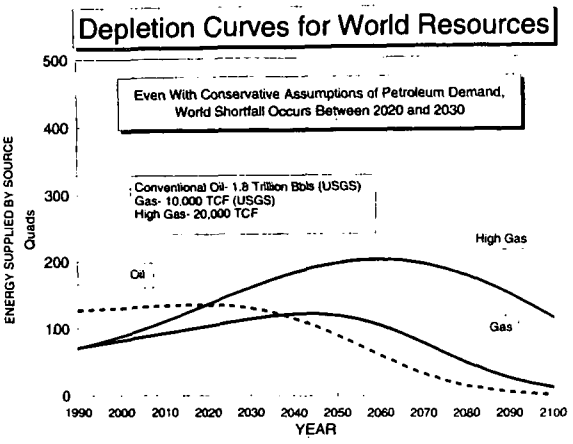

Figure 1

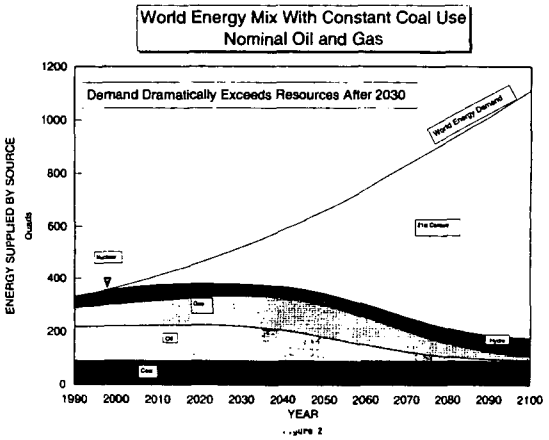

Figure 2

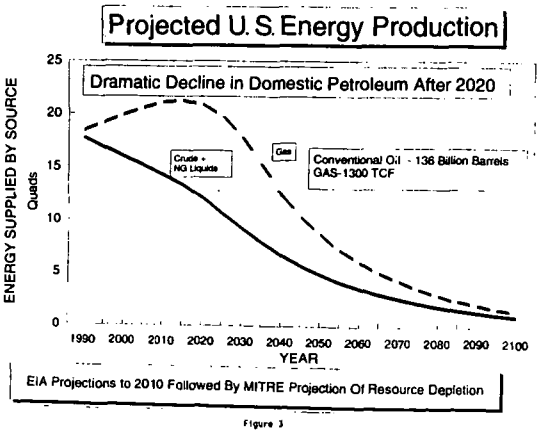

Figure 3

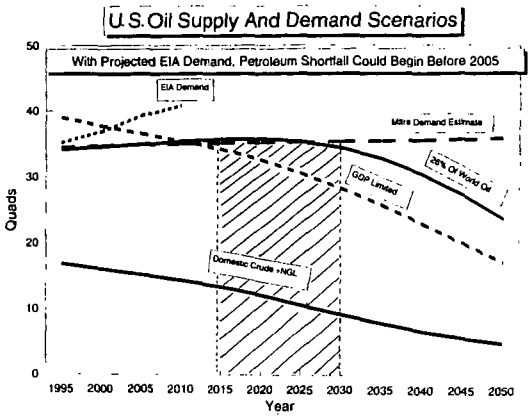

Figure 4

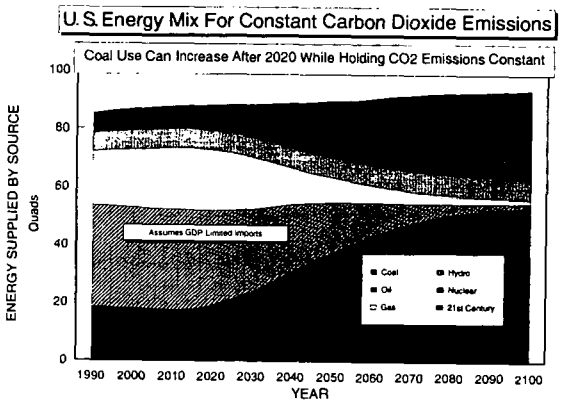

Figure 5

TECHNOECONOMIC ASSESSMENT OF ADVANCED CONCEPTS FOR DIRECT LIQUEFACTION OF SUBBITUMINOUS COALS

Michael Peluso
LDP Associates
32 Albert E. Bonacci Drive
Hamilton Square, N. J. 08690

Keywords: Coal Liquefaction, Advanced Concepts, Economics

INTRODUCTION

For the past three years a group headed by the Center for Applied Energy Research of the University of Kentucky has been investigating, under DOE sponsorship, the use of Advanced Concepts for improving the Integrated Two Stage Liquefaction process practiced at the Wilsonville, Alabama pilot plant(1). Among the concepts tested at the batch scale level were: (1) extraction, dewaxing and hydrotreating of the distillate recycle solvent to improve coal conversion, (2) oil agglomeration of the feed coal to liquefaction to reduce its ash content and improve supported catalyst life, and (3) preparation and use of alternate dispersed and particulate catalysts to improve process performance and/or reduce dispersed catalyst cost.

BASE CASE ASSESSMENT - WILSONVILLE RUN# 263J

Wilsonville pilot plant operation with Black Thunder subbituminous coal was chosen as the basis for defining state-of-the art TSL technology. During Wilsonville Runs #262 & 263, the pilot plant unit was operated in the so-called hybrid mode with dispersed iron and molybdenum catalysts used in the first reaction stage and a supported nickel-moly catalyst used in the second stage ebullated bed reactor. Material balance period #263J was chosen as the basis for developing a baseline conceptual commercial plant case against which the results of this program could be compared(2). An all-distillate product Base Case was formulated in which resid extinction was achieved in the system via a reduction in reactor space velocities as predicted by first order reaction kinetics. All liquefaction distillates are assumed to be upgraded to a common basis (all-gasoline finished product) so that consistent comparisons are assured (3). The Base Case conceptual commercial plant is an all-coal facility located at a mine-mouth Wyoming location. The hydrogen needed for liquefaction is generated by water slurry gasification of ash concentrate from the ROSE unit and coal. Light hydrocarbon gases produced in liquefaction and upgrading are used to close the fuel gas balance. Any excess gas is used to generate hydrogen via the steam reforming process. It is assumed that the electricity needed to help operate the plant is purchased from a nearby utility power plant. A simplified block flow diagram of the conceptual commercial plant is shown in Figure 1. The plant converts 17,929 T/D of Black Thunder coal (MF basis) fed to liquefaction into 68,100 barrels per day(BPSD) of gasoline product. An additional 5,204 T/D of Black Thunder must be gasified in order to meet the plants hydrogen requirements. Overall MAF coal conversion for the Base Case is 92%. A high process solvent to coal ratio of 2.33 is employed since significant quantities of both IOM and ash are recirculated via the ashy recycle technique. Recycled ash is approximately 3.3 times the quantity of ash rejected from the process via the ash concentrate. As a result, the effective concentration of moly on coal to liquefaction is approximately 430 ppm at the Base Case fresh addition level of 100 ppm. Four liquefaction reactor trains in parallel are required to process the 17,929 T/D of coal to liquefaction. Reactor gas rates were determined based on the estimated average reactor partial pressures which existed during Wilsonville Run #263J and the recycle hydrogen gas purity. Actual reactor residence times and space velocities were also based on estimated WR#263J operation with appropriate corrections for the required resid plus IOM conversion level. Organic rejection (i.e. resid, IOM & DAS) from the liquefaction process amounts to 14.5% on an MF coal basis.

ADVANCED CONCEPTS CASE

Three main process variations from the Base Case are incorporated in the ACC. They are:

1. Coal impregnation with moly salt via incipient wetness,
2. Oil agglomeration of the feed coal at low pH, and
3. Distillate solvent quality improvement via solvent extraction, solvent dewaxing and hydrotreating. Used together these three techniques seek to significantly increase product yield per unit of coal feed while reducing solvent recycle rate and liquefaction system additive costs.

• Coal Impregnation:Moly Salt via Incipient Wetness

The cost of dispersed iron and moly catalysts in the Base Case aocounts for almost $3/Bbl.of gasoline product selling price. A significant portion of this cost results from the use of an expensive moly source, the oil soluble Molyvan L. A significant reduction in moly cost is achieved when a much cheaper moly salt such as Ammonium Octomolybdate is used. Even when processing costs for preparing the salt solution , impregnating a small portion of the feed coal to liquefaction and driving off the extra water added to the coal are added, the cost of the impregnated moly is still only about 25% of the cost of using Molyvan L. Experimental results indicate that performance with moly impregnated coals is approximately equivalent to the performance with Molyvan L. The cost of using moly for the ACC drops below the cost of using particulate iron oxide at the 1 wt.% on MF coal dosage level of the Base Case. Therefore, the use of iron is questionable and has not been included in the ACC.

• Oil Agglomeration at Low pH

Results indicate that the use of oil agglomeration at low pH can remove approximately 50% of the ash in Black thunder coal. Ash reduction at the front end of the liquefaction process reduces organic rejection at the back end of the process, thereby increasing product yield. It also reduces the ash recirculation rate within the process while still maintaining the same catalyst recycle enhancement factor as in the Base Case. At low pH, potential supported catalyst poisons, such as calcium, sodium, magnesium and potassium are also removed. For the ACC it has been assumed that the second stage reactor supported catalyst replacement rate can be reduced by 30%. Tests have indioated that impregnated iron and moly are retained on the coal during agglomeration. The oil agglomeration process is well suited for liquefaction. Distillate recycle solvent can be used as the agglomerating agent. Sour water can be used as makeup water to the system and the slurry reject of solids and dissolved salts can be utilized in the gasification slurry mixing systems. In fact, the dissolved salts may even act as a catalyst in the gasification process. A significant amount of sulfuric acid is consumed in the oil agglomeration unit.

• Distillate Solvent Quality Improvement

For the ACC, three process steps are used to treat the waxy distillate recycle solvent used in the Base Case. These processes are Solvent Extraction, Solvent Dewaxing and Hydrotreating. In combination these processes effectively remove and recover the waxy material from the distillate solvent and enhance its donor solvent capabilities (see Figure 3). Both solvent extraction and solvent dewaxing are commercial processes used in the petroleum refining industry.

The benefit of applying these three processes are:
1. Reduction of distillate solvent recycle while improving quality
2. Recovery of a valuable byproduct wax
3. Increased product yield via coal conversion improvement.

It is estimated that the wax yield on MAF coal is 4 wt.%. However, this wax builds up in the distillate recycle solvent until its cracking rate equals production rate. Based on Wilsonville Run#263J data the wax concentration in the distillate recycle solvent is estimated to be approximately 24 wt.%. Removal of a substantial portion of the wax, significantly reduces the distillate solvent recycle rate. The wax that is removed and recovered is a valuable material with an estimated selling price (34¢/lb.) more than double that of gasoline. The solvent extraction process is used upstream of the solvent dewaxing process as a means of significantly reducing the feedrate and the cost of the much more expensive solvent dewaxing process. In the solvent extraction process, a solvent such as N-Methyl-2-Pyrrolidone is used to absorb aromatics from the feed stream. The paraffinic wax is not absorbed and passes thru the unit. For the ACC approximately 70% of the distillate solvent feed to the extraction unit is absorbed, thereby reducing the solvent dewaxing unit feedrate by a factor of 3. In the solvent dewaxing prooess ,

the paraffinic wax is separated from the feed stream by chilling, precipitation and filtration in the presence of a suitable solvent such as methyl ethyl ketone (MEK). When wax production is desired, as in the ACC, a three stage filtration system is used along with a wax finishing step. Conventional fixed bed hydrotreating is used to make the final improvement in distillate solvent quality. For the ACC, a single train system operating at conditions favorable to aromatics hydrogenation (650 to 7500F & 1,800 psig) is used.
The average MAF coal conversion improved 2.4 percentage points when the distillate recycle solvent was fully dewaxed and hydrotreated as compared to using the as-is distillate solvent. Hydrogen uptake in the small scale hydrotreating runs was less than half of what was expected based on Exxon EDS operation. For the ACC it is assumed that the full dewaxing and hydrotreating of the distillate recycle solvent will improve MAF coal conversion by 3 percentage points(95% vs 92% in Base Case). This improvement further increases product yield and reduces the IOM recycle rate.

COMPARATIVE RESULTS

A simplified block flow diagram of the ACC is shown in Figure 2. At the same coal feedrate to liquefaction, gasoline production increases by 4.5% while a significant quantity of the valuable wax byproduct is also recovered. This increase in product yield is directly related to the reduction in Rose unit organic rejection by 6.0% on MF coal. At the same time, recycle solvent rate is reduced by 20% because of wax removal, lower feed ash and higher coal conversion. Moly catalyst recirculation enhancement remains constant. In order to achieve higher product yield, the required per pass resid plus IOM conversion increases in both reaction stages. This increased conversion is achieved by a space velocity reduction (predicted by first order kinetics) of approximately 15% versus the Base Case. Although reactor space velocities are lower, reactor weights are only slightly higher due to the offsetting effect of lower recycle solvent rates. Hydrogen consumption increases in proportion to the increased product rate. With the significant decrease in organic rejection, additional gasification of coal is required to close the hydrogen balance. The total electrical power requirement for the ACC increases by approximately 12% due to increased gasification quantities and the requirements of the added units.
The capital and operating cost estimates for the Base Case were developed using the relevant portions of previous liquefaction plant studies, as well as in-house information (4,5,6). Comparative process units capital costs for the ACC are shown in Table 1. Process units investment increases by $452 million due to the added units and the increased gasification requirements. Interestingly, liquefaction system capital cost decreases despite the higher distillate production rate. As shown in Table 2, the total capital required increases by $ 522 million over the Base Case. However, as shown in Table 3 net operating costs drop by approximately $6.94 per barrel of gasoline product due to the lower liquefaction system additive costs and the significant impact of byproduct wax revenue. At a 15% capital charge factor, the required gasoline product selling price for the ACC is $4.64/Bbl.lower than that for the Base Case.

REFERENCES

1.Center for Applied Energy Research, Phase 1 Final Report (draft), "Advanced Direct Liquefaction Concepts for PETC Generic Units", DOE/PC/91040-55, March 1995.

2. Southern Electric International,Inc., Technical Progress Report, "Run 263 with Black Thunder Mine Subbituminous Coal from Powder River Basin (with Dispersed Slurry/Supported Catalysts)", DOE Contract No.DE-AC22-90PC90033, October 1992.

3. H.A. Frumkin, "Refining and Upgrading of Synfuels from Coal and Oil Shales by Advanced Catalytic Processes - Tenth Interim Report, Revised Stock Balances and Updated Cost Estimates", DOE# FE-2315-115,March 1985.

4. Ashland Synthetic Fuels Inc. and Airco Energy Company Inc., "The Breckinridge Project Initial Effort, Report VIII, Capital Cost Estimate", DOE/OR/20717-8, 1981.

5. Exxon Research and Engineering Company, "EDS Coal Liquefaction Process Development, Phase V, EDS Wyoming Coal Bottoms Recycle Study Design Addendum - Interim Report", DE 84005843, December 1983.

6. Bechtel Corporation, "Draft Final Report on Design, Capital Cost and Economics for the Low Rank Coal Study", DOE Contract No.DE-AC22-90PC89857, October 1994.

TABLE 1
BLACK THUNDER COAL STUDY
ADVANCED CONCEPTS CASE vs BASE CASE
DIFFERENCES IN PROCESS UNIT INVESTMENT

UNIT	Millions of Mid '94 $:Wyoming Location
OIL AGGLOMERATION	+ 60
COAL SLURRY PREPARATION & DRYING	- 6
FIRST STAGE REACTION SYSTEM	- 23
SECOND STAGE REACTION SYSTEM	- 4
LETDOWN SYSTEM	- 3
VACUUM FRACTIONATION	- 14
ROSE UNIT	- 7
DISTILLATE SOLVENT EXTRACTION	+ 74
DISTILLATE SOLVENT DEWAXING	+ 207
DISTILLATE SOLVENT HYDROTREATING	+ 95
GAS PLANT HYDROGEN RECOVERY & RECYCLE	Same
ASH CONCENTRATE & COAL GASIFICATION	+ 49
OXYGEN PLANT	+ 17
STEAM REFORMER	- 8
MAKEUP HYDROGEN COMPRESSION	Same
UPGRADING UNITS	+ 15
Difference in Process Unit Investment	**= + 452**

TABLE 2
BLACK THUNDER COAL STUDY
ADVANCED CONCEPTS CASE vs BASE CASE
DIFFERENCES IN TOTAL CAPITAL REQUIREMENT

	Millions of Mid '94 $: Wyoming Location
PROCESS UNITS	+ 452
OFFSITE UNITS	+ 54
WORKING CAPITAL	Same
START-UP COSTS	+ 8
INITIAL CATALYSTS & CHEMICALS	+ 8
Difference in Total Capital Required	**= + 522**

TABLE 3
BLACK THUNDER COAL STUDY
ADVANCED CONCEPTS CASE vs BASE CASE
DIFFERENCES IN ANNUAL OPERATING COST

	$/Bbl. of Gasoline
TOTAL MF COAL: @ $7.14/T	+ 0.152
PURCHASED ELECTRICAL POWER, @ 4¢/ Kw-hr.	+ 0.364
LIQUEFACTION SYSTEM ADDITIVES :	
- Iron Oxide @ 12¢/lb. & H2S @ 7.5¢/lb.	- 0.802
- Moly Impregnating/ Dispersed Catalyst	- 1.582
- Supported Ni-Moly @ $3/lb.	- 0.782
MAKEUP DEASHING UNIT SOLVENT	- 0.222
OTHER LIQ'N CATALYSTS & CHEMICALS	+ 0.577
UPGRADING UNITS CATALYSTS & CHEM.	Same
RAW WATER @ $ 2.50/1,000 Gallons	+ 0.035
ASH DISPOSAL @ $5/Ton	- 0.007
OPERATING LABOR	+ 0.075
ADMINISTRATION & OPERATIONS SUPPORT	+ 0.013
MAINTENANCE @ 1.5% of TIC + ICC	+ 0.233
INSURANCE & LOCAL TAXES @ 1% of TPC + ICC	+ 0.156
BYPRODUCT CREDITS:	
• Ammonia, Sulfur & Phenols	- 0.019
• Fully Refined Paraffin Wax	- 5.133
Difference in Annual Operating Cost	**= - 6.942**
Diff. in Annualized Capital Cost (15% Cap'l Charge Factor)	**= + 2.302**
ADVANCED CONCEPTS CASE ADVANTAGE	**= - 4.640**

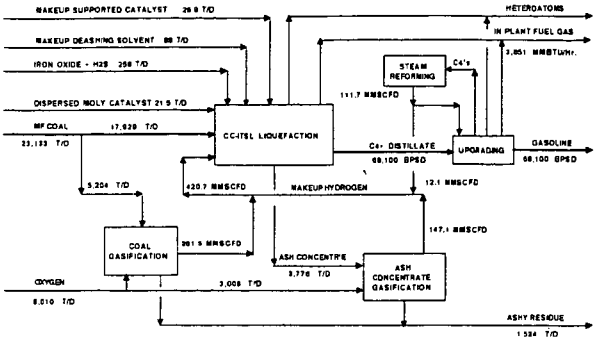

FIGURE 1
BLACK THUNDER LIQUEFACTION STUDY - HYBRID MODE
SIMPLIFIED BLOCK FLOW DIAGRAM - CONCEPTUAL COMMERCIAL PLANT
BASE CASE (SO_2-Free Ash, Wilsonville Run # 263J)

LDP ASSOCIATES

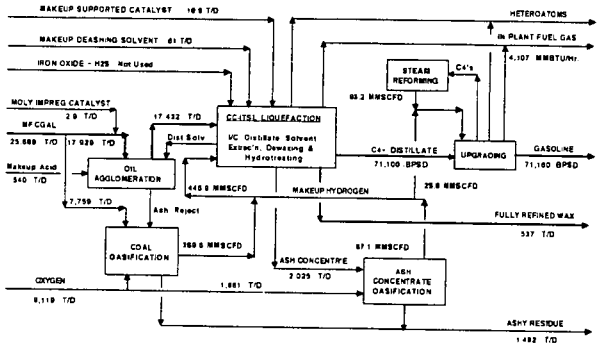

FIGURE 2
BLACK THUNDER LIQUEFACTION STUDY - HYBRID MODE
SIMPLIFIED BLOCK FLOW DIAGRAM - CONCEPTUAL COMMERCIAL PLANT
ADVANCED CONCEPTS CASE (SO_2-Free Ash, W'ville Run # 263J)

LDP ASSOCIATES

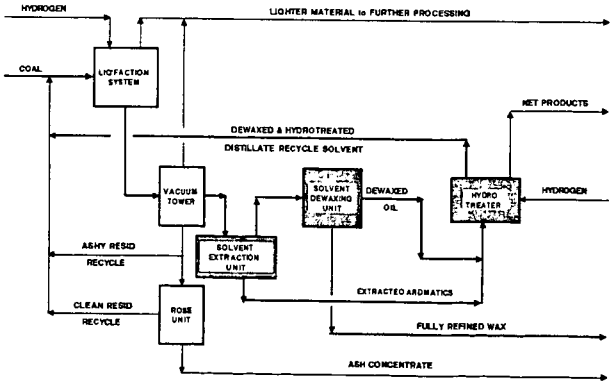

FIGURE 3
ADVANCED CONCEPTS CASE SIMPLIFIED BLOCK FLOW DIAGRAM
SOLVENT EXTRACTION, SOLVENT DEWAXING & HYDROTREATING
OF THE DISTILLATE RECYCLE SOLVENT

LDP ASSOCIATES

Continuous Bench-Scale Slurry Catalyst Testing Direct Coal Liquefaction of Rawhide Sub-bituminous Coal

R. F. Bauman, L. A. Coless, S. M. Davis, M. C. Poole, M. Y. Wen
Exxon Research and Development Laboratories, Baton Rouge, LA 70805

KEYWORDS: Coal liquefaction, Slurry reactor, Dispersed catalysts.

Introduction

In 1992, the Department of Energy (DOE) sponsored research to demonstrate a dispersed catalyst system using a combination of molybdenum and iron precursors for direct coal liquefaction. This dispersed catalyst system was successfully demonstrated using Black Thunder sub-bituminous coal at Wilsonville, Alabama by Southern Electric International, Inc. The DOE sponsored research continues at Exxon Research and Development Laboratories (ERDL).

A six month continuous bench-scale program using ERDL's Recycle Coal Liquefaction Unit (RCLU) is planned, three months in 1994 and three months in 1995. The initial conditions in RCLU reflect experience gained from the Wilsonville facility in their Test Run 263. Rawhide sub-bituminous coal which is similar to the Black Thunder coal tested at Wilsonville was used as the feed coal. A slate of five dispersed catalysts for direct coal liquefaction of Rawhide sub-bituminous coal has been tested. Throughout the experiments, the molybdenum addition rate was held constant at 100 wppm while the iron oxide addition rate was varied from 0.25 to 1.0 weight percent (dry coal basis). This report covers the 1994 operations and accomplishments.

Objective

The objective of this DOE sponsored project is to test advanced and novel slurry phase catalysts for direct coal liquefaction. These novel slurry phase catalysts were developed in other DOE sponsored research programs. The properties of the catalysts are presented in Table 1. A number of such catalysts have shown initial promise in laboratory-scale research, typically by experimentation in small batch autoclaves. The efficacy and application of these catalysts is expected to be strongly dependent upon the process steps and overall configuration envisioned for a particular liquefaction process. The most favorable catalysts and relevant approaches must be evaluated in a continuous flow bench-scale facility in order to define and verify the steady-state product yield structures in response to operating parameters and process changes.

In order to help guide the research effort a set of goals was targeted. A summary of the major project goals as listed in DOE's Statement of Work is presented below:

- Demonstrate mechanical operability of continuous bench unit.
- Verify suitability of system design, including use of plug flow reactors.
- Define suitable catalyst screening conditions.
- Test three iron catalysts.
- Test two molybdenum catalysts.
- Conduct limited optimization studies.
- Obtain mass and elemental balances for chosen data periods.
- Define product yield structures for chosen data periods.

Process Overview and Simplified Process Flow Plan

The Recycle Coal Liquefaction Unit (RCLU) is located at the Exxon Research and Development Labs in Baton Rouge, Louisiana. RCLU is a highly automated, highly instrumented pilot plant designed to process 34 kg (75 lbs.) of coal per day. It has redundant computer control and data acquisition systems allowing for efficient trouble shooting, data analysis and material balance calculations. Over the years, RCLU has been re-configured many times to meet specific data requirements for coal and heavy hydrocarbon conversion. Hence, RCLU is versatile and easy to re-configure. RCLU has been a very reliable tool in the past, with many runs over 1000 continuous hours. An overview of the process is described below and a simplified process flow plan is presented in Figure 1.

Slurry Mixing

In this process, coal, make-up catalysts, recycle solvent and recycle bottoms are prepared in 6 to 8 hour batches in the mix tank to form a homogeneous feed slurry. The equipment in the slurry mix area are the mix tank, spared recirculation pumps, the coal/bottoms bin and the solvent tank. The mix tank is totally enclosed to prevent dust and vapors from entering the process streams. The slurry temperature is typically held around 135-143 °C (275-290 °F) to ensure an easily pumpable slurry. The pressure is held at atmospheric or slightly above during non-charging periods. However, a vacuum can be drawn on the solvent tank to aid during feed charging. The tank is equipped with a mixer to mix the coal, bottoms, solvent and catalyst. The feed slurry is further mixed by the recirculation pump.

Slurry Feed

The slurry feed section is used to provide continuous slurry flow to the liquefaction reactors. The major equipment in the area include the feed tank, spared recirculation pumps, and high pressure feed pumps. Periodically, the feed tank is charged with a fresh batch of slurry from the mix tank. The slurry is continuously mixed and recirculated to ensure a homogeneous slurry in the feed tank. The high pressure pumps are used to pump a slip-stream of slurry from the recirculation loop to the liquefaction reactors. Typical holding tank operating conditions are 135 - 143 °C (275 - 290 °F) and atmospheric pressure.

Liquefaction Reactors

The liquefaction reactor system consists of a pretreater and two reactors in series and their associated sandbaths. The pretreater consists of two or three 25 mm (1") ϕ 316 stainless steel pipes and each reactor consists of four or six 25 mm (1") ϕ 316 stainless steel pipes. The reactor pipes are 1.22 m (4 ft) in length and are connected by 9.5 mm (3/8") ϕ 316 stainless steel tubing. The reactors operate in an upflow mode and are capable of having interstage hydrogen addition. The sandbaths are electrically heated and are used to control the reactor temperatures.

The slurry is pumped from the feed tank to the pretreater at a rate of 3.6 to 5.5 kg/hr (8 to 12 lbs/hr). The purpose of the pretreater is to activate the catalyst by sulfiding the iron oxide. The catalyst is activated by treat gas containing 10 volume percent H_2S in H_2. The activated slurry leaving the pretreater is blended with pure H_2 treat gas before it is fed to the first stage reactor. Most of the coal is converted to liquid hydrocarbons and gas via a combination of thermal and catalytic processes in the two liquefaction reactors.

The residence time within the pretreater and each reactor can be varied by varying slurry feed rate or by varying the number of reactor pipes in each sandbath. The nominal residence time of the pretreater ranges from 20 to 30 minutes while the nominal residence time of each reactor ranges from 40 to 55 minutes. The pretreater and liquefaction reactors operate at 17.2 Mpa (2500 psig). The pretreater operates between 296 - 302 °C (565 - 575 °F) while the liquefaction reactors operate between 427 - 454 °C (800 - 850 °F). A slight exotherm exists in the first two tubes of the first stage reactor. Otherwise, the reactors operate close to isothermal operation and have minimal pressure drop.

High Pressure Separations

RCLU uses high pressure separation vessels to separate the heaviest fraction of the reactor product from the lighter fraction. The high pressure separations consist of both hot and cold separators operating at slightly below reactor pressure. The hot separator is used to split the reactor effluent into two streams; an overhead stream consisting of gases, water and light oil and an underflow stream consisting of heavy oil and mineral matter. The overhead stream from the hot separator passes through two heat exchangers before entering the cold separator. The exchangers cool the stream, thus condensing some of the light oils which are captured in the cold separator. The hot separator underflow stream proceeds to the bottoms stripper where it is stripped with the offgas from the cold separator. The cold separator underflow stream proceeds to fractionation.

Bottoms Stripping

The bottoms stripper separates nominally 1000 °F- hydrocarbons from heavier hydrocarbons and mineral matter (bottoms). Bottoms are periodically withdrawn into a bucket and allowed to cool and solidify. The bottoms is then crushed and a fraction is recycled to the mix tank. The overhead gas and the stripped hydrocarbons are cooled before going to fractionation

Fractionation

The cold separator underflow stream and the bottoms stripper overhead stream are combined in the fractionator feed surge tank. The product gas passes through several

flowmeters before the stream is released to the flare vent. A slipstream of the gas is sent to an online process gas chromatograph (GC) system after the flowmeters. The GC system samples the product gas continuously and analyzes the stream for H_2, H_2O, CO, CO_2, N_2, H_2S, O_2, C_1, C_2, C_3, C_4 and C_5+. The information from the product gas flowmeters and GC system are used to develop daily online material balance closures and later for the complete data workup.

The liquid is pumped from the fractionator feed surge tank to a preheater before it is fed to the fractionator. The fractionator is designed to split the nominally 1000 °F- stream into two components, solvent (also called VGO) and light oil. The heavier component has an initial boiling point (IBP) between 550 °F and 650 °F depending upon tower temperatures. The lighter component has a C_5 IBP. The tower underflow stream is periodically removed and partially recycled to the mix tank. The overhead stream is condensed, refluxed and periodically removed.

Material Balancing and Analyses Procedures

Material balances are based on a 24 hour operating period at constant conditions. Ideally, the conditions are at or near steady state before a yield period (material balance period) is initiated. There is a compromise between the number of conditions and the approach to steady state for a given amount of operating time. For these experiments, some approach to steady state was sacrificed for maximizing the number of operating conditions. The yield periods were initiated when the bottoms conversion started to level off.

From past experience at Exxon, the ash content of recycle bottoms provides a good indication of coal conversion level with known feed coal ash content. In typical bottoms recycle pilot plant operations, the ash content of the recycle bottoms are monitored daily in a screening test. The final ash content in the recycle bottoms is conducted by the analytical labs several weeks later. The procedure for both tests are essentially the same. The main differences are that the analytical tests are automated and use a different purge gas. The ash content of bottoms are measured in duplicate by combustion of small samples of bottoms at 950°C for at least three hours. The average ash content of bottoms and known feed coal ash content are input to a computer model with an equation built in assuming 100% ash balance. The model calculates DAF coal conversions and data are plotted daily to monitor the trend of new conditions vs. the previous conditions. In a typical case, a significant change in the coal conversion is observed in the first few days after starting a new condition. The coal conversion gradually levels off in about 3-5 days after the change to the new condition. The yield periods are initiated when the bottoms ash content begins to level off. The screening tests compare well with the analytical lab tests.

Material balances are conducted after a yield period is complete. RCLU utilizes two levels of material balancing. The first level is on-line material balancing and the second level is material balancing that utilizes data reconciliation techniques. The on-line material balances are often completed within 24 hours after the end of the yield period. They are used to guide unit operations, identify data acquisition problems, and provide preliminary product yields leading to the determination of subsequent run conditions.

The raw data and process variables of each yield period are stored in the RCLU computer system. The on-line material balancing program retrieves these raw data from the RCLU computer system along with input data from unit engineers to calculate the overall material balance, DAF coal conversion, hydrogen consumption, and gaseous and distillate yields for each yield period. The input data from unit engineers include moisture and ash contents of feed coal, and percents of 1000°F+ material in the recycle solvent and 1000°F- material in the recycle bottoms. In order to cross-check the data, balances and yields are calculated using three different slurry feed bases. If balances are poor or yields deviate substantially from the expected then the weights and analyses are re-checked for errors. If no errors are found, an investigation is initiated to determine possible unit material losses and/or errors in data acquisition.

The second level of material balancing utilizes the results of the on-line material balances as well as elemental analyses of each feed and product stream, and simulated distillation by gas chromatography (GCD) analyses of hydrocarbon streams. The reconciled balances are usually not finalized until at least three weeks after the end of a given yield period. Reconciled balances are considered the finalized results and are the results most often reported. Once finalized, reconciled results are used to compare the effects of process variables and/or catalysts on product yields and product distribution.

In order to reconcile the data, a mainframe computer program which utilizes geometric programming techniques is used to adjust the data to comply with a set of constraint equations. The objective of data reconciliation is to legitimately adjust data values to balance elemental weights of feed and product streams. Data is therefore adjusted by taking into account the

reliability of each data measurement. Those variables which have poor reliability are preferentially changed in order to achieve data consistency. Neither the constraint equations nor variable reliabilities are changed from yield period to yield period.

Data reconciliation is an iterative procedure that is designed to be used only when "as-measured" balances are good. Typically, data reconciliation requires that the total material balances are between 98 and 102%. However, material balances between 95 and 102% are tolerable. If the balances do not meet the above criterion, the data is re-analyzed for obvious errors and suspect samples are resubmitted for analyses.

Data from any single reconciled yield period should not be used in data comparisons due to operational variations. Rather, the results from several yield periods (≥ 3) at one condition should be used for comparison purposes.

Results and Discussion

Eight conditions were tested during the 1994 operations, covering the impact of solvent to coal ratio, time-temperature trade off, and type and make-up rate of iron oxide catalyst as shown in Table 2. The molybdenum make-up rate remained constant throughout the experiments. However, the source of molybdenum was varied. A summary of the operating conditions are presented in Table 3. Three 24 hour balances (yield periods) were performed at each condition. A summary of the reconciled yields and overall conversion are presented in Table 4. The values shown in Tables 3 & 4 are the average values at each condition.

General Observations

In general, catalyst changes had very small impact on performance. Of all of the changes tested, one process change, reducing the recycle ratio had the most striking impact. Apparently, recycle ratio has more impact on performance than catalyst over the range of the tests. It may be that the constant addition of 100 wppm molybdenum is masking other changes, such as type and amount of iron catalyst addition rate. Discussions with PETC have indicated to us that the constant molybdenum addition rate was specified based on results at Wilsonville.

Reduced Recycle

The impact of reduced recycle is shown by comparing condition 1 with 2A. The total recycle was reduced from 1.92 to 1.65 on dry ash free (DAF) coal. The result was a significant shift towards a heavier product slate, and higher conversion.

Reduced Sulfur Addition Rate

The impact of reduced sulfur addition rate is shown by comparing condition 2A and 2B. The result was a small reduction in gas yields and hydrogen consumption. No other statistically significant changes were observed. While statistically significant, a small systematic error in the feed gas or product gas sulfur content may have clouded the data. Thus our interpretation of the test result is that the reduction in sulfur had no significant impact on yields or conversion.

Increased Stage 1 Temperature and Mass Velocity

The impact of increasing the first stage reactor temperature and the mass velocity can be seen by comparing condition 3 with 2B. Conversion and liquid yields dropped. Conversion went from 88.60 to 86.88 wt % on DAF coal. C_5-1000°F dropped from 59.1 to 56.5 wt% DAF coal. The temperature and mass velocity were increased to make the impact of a better catalyst easier to detect.

Changed Iron Oxide Catalyst

The impact of iron catalyst type, Bailey vs. Bayferrox is shown by comparing conditions 3 and 4. There was an unintended drop in the first stage reactor temperature of about 2 °C during condition 4, otherwise, conditions were held nominally constant. Conversion, gas yield, and hydrogen consumption all dropped significantly. As with all of these tests, the molybdenum addition rate was held steady at 100 wppm on dry coal. Liquid yields held their own and gas selectivity (100 x C_1 to C_4 yield/total conversion) decreased. Directionally this seems to indicate that an improved iron catalyst could lead to a more selective liquefaction process.

Reduced Iron Oxide Addition Rate

The impact of reducing the iron oxide addition rate from 1.0 to 0.25 wt% DAF coal is shown by comparing condition 4 and 5. The temperature control was improved during condition

5, resulting in an apparent increase of 2 °C in the first reactor stage temperature. The most notable changes were a significant increase in conversion, gas yield, and hydrogen consumption. Conversion increased from 85.62 to 87.01 wt%, C_1 to C_4 increased from 12.48 to 14.08, and hydrogen consumption increased from 5.43 to 5.76 wt % on DAF coal, all statistically significant. Liquid yields remained steady. Notionally, the small increase in temperature may have contributed to the small but significant increase in conversion, while the reduction in catalyst may have lead to the deterioration in gas/liquid selectivity (100 x C_1 to C_4/C_1 to 1000 ^{o}F).

Changed Iron Oxide Catalyst

The impact of iron catalyst type, Bayferrox vs. Mach 1 are shown by comparing conditions 5 vs. 6. The results were small, but significant drops in conversion, C_1 to C_4, and hydrogen consumption. Conversion dropped from 87.0 to 85.2 wt% DAF coal, while C_5 to 537.7°C (1000°F) liquid yields held steady at 57.0 wt % on DAF coal.

Changed Molybdenum Source

The impact of changing the Molybdenum source from Organic, Molybdenum Van L, to inorganic, ammonium heptamolybdate is shown by comparing conditions 5 and 7. The change resulted in a significant drop in conversion, from 87.0 to 85.7, and lower C_1 to C_4 from 14.1 to 12.6. Even though conversion and gas yields dropped in going from the organic to the inorganic molybdenum source, selectivity to liquids improved.

ACKNOWLEDGEMENTS

This work was sponsored by the U. S. Department of Energy under contract No. DE-AC22-94PC94051.

Figure 1
Schematic Flow Plan of RCLU Pilot Plant

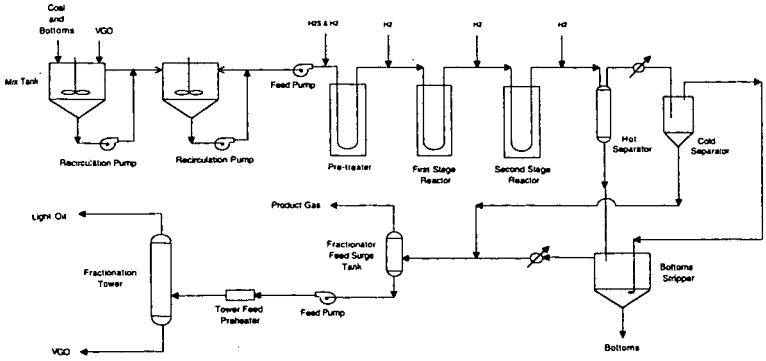

Table 1
Properties of Slurry Catalysts

Catalyst	Particle Size, Microns	Surface Area, m^2/g	Bulk Density, g/cm^3	Physical Form	Composition wt %
NANOCAT® Superfine Iron Oxide (SFIO)	0.003	250	0.05	Reddish-brown powder	100 % Fe_2O_3
Bayferrox PK 5210 Technical Iron Oxide	0.020	123	n/a	Reddish-brown powder	100 % Fe_2O_3
Bailey Iron Oxide	96 wt% <44 µm	n/a	n/a	Reddish-brown powder	100 % Fe_2O_3
MOLYVAN L, Molybdenum containing lubricant	n/a	n/a	1.08	Dark green liquid	8.1 % Mo
MOLYVAN A, Molybdenum containing powder	5 to 10	n/a	1.58	Yellow-orange powder	30.0 % Mo
Ammonium heptamolybdate	n/a	n/a	2.50	White powder	54.3 % Mo

Table 2
Summary of Experimental Design

Condition	Comment	Yield Periods of Interest
1	Initial conditions.	409-411
2A	Reduced solvent to coal ratio compared with initial conditions.	412-414
2B	Reduced H_2S treat rate compared with conditions 1 and 2A	415, 416, 418
3	Increased first stage reactor temperature and increased mass flow rate compared with previous conditions.	419-421
4	Switched from Bailey iron oxide to Bayferrox PK5210 iron oxide catalyst.	422-424
5	Reduced iron oxide addition rate from 1.0 to 0.25 wt% on dry coal.	425-427
6	Switched from Bayferrox PK5210 to Mach 1-Nanocat SFIO catalyst.	428-430
7	Switched from organic to inorganic source for molybdenum catalyst and switched back to Bayferrox PK5210 iron oxide.	431-433

Table 3
Summary of Test Conditions

Condition	Fe_2O_3 Type	Fe_2O_3 wt %	Mo Type	S/C: B/C	H_2S as S wt %	NRT, min.	Reactor Temperature 1st °C (°F)	2nd °C (°F)
1	Bailey	1.03	Org.	1.07:0.85	5.8	49	430.6 (807.0)	450.6 (843.0)
2A	Bailey	0.99	Org.	0.94:0.71	6.0	53	431.1 (808.0)	451.1 (844.0)
2B	Bailey	1.00	Org.	0.90:0.75	2.7	50	431.3 (808.3)	449.3 (840.7)
3	Bailey	1.02	Org.	0.95:0.79	3.4	41	441.3 (826.3)	450.0 (842.0)
4	Bayferrox	1.00	Org.	0.94:0.76	3.3	41	439.3 (822.7)	449.6 (841.3)
5	Bayferrox	0.25	Org.	0.91:0.80	3.0	41	441.5 (826.7)	450.6 (843.0)
6	Mach 1	0.26	Org.	0.91:0.83	3.1	42	440.9 (825.7)	450.4 (842.7)
7	Bayferrox	0.26	Inor.	0.98:0.85	3.1	41	440.9 (825.7)	450.0 (842.0)

Table 4
Summary of Reconciled Yields and Conversion,
(wt% Based on Dry Ash-Free Coal)

Condition	Yield Period	H_2	C_1-C_4	C_5-350	350-650	650-1000	Conversion
1	409-411	-6.12	15.34	14.48	33.93	9.06	88.56
2A	412-414	-6.11	14.51	13.54	32.55	13.57	89.26
2B	415-418	-5.77	13.69	12.86	31.35	14.87	88.60
3	419-421	-5.76	13.31	12.30	29.61	14.59	86.88
4	422-424	-5.43	12.48	12.71	31.33	13.70	85.62
5	425-427	-5.76	14.08	12.24	31.22	13.54	87.01
6	428-430	-5.46	12.82	11.66	30.69	14.67	85.19
7	431-433	-5.65	12.61	12.27	32.14	12.57	85.74

DOE PROOF-OF-CONCEPT DIRECT COAL LIQUEFACTION PROGRAM
Activity of Recovered Catalysts from POC Run No.1

L.K. Lee, A.G. Comolli and E.S. Johanson
Hydrocarbon Technologies, Inc. P.O.Box 6047, Lawrenceville, NJ 08648

Keywords: Coal Liquefaction, Catalyst Activity

INTRODUCTION

In POC Run No. 1 HRI's Catalytic Two-Stage Liquefaction (CTSL) process was evaluated using Illinois No. 6 coal from Crown II Mine in a 3 ton/day process development unit. Solid Separation was accomplished using a vacuum still and subsequently switched to a Kerr McGee residual oil solvent extraction unit (ROSE-SR^{SM}). Akzo AO-60 1/16" extrudate catalyst, a Ni/Mo supported catalyst, was used in both stages. The temperature of the first stage reactor was in the range of 407° to 414°C and about 16° to 27°C lower than that of the second stage. Throughout most of the 57 days operations, catalysts were added and withdrawn from each reactor to maintain consistent process performance. In this paper the activity of the withdrawn catalysts from both reaction stages at selected operation periods is discussed in respect to the degree of carbon lay down and total contaminations.

EXPERIMENTAL

The catalytic activity of fresh and withdrawn catalysts was characterized by its ability to convert a resid containing coal derived liquid to lighter products using a 20 cc shaking microautoclave reactor. As a common test oil the filtered liquid (227-55-23A PFL) that had been obtained during the CTSL Bench Unit operations with Black Thunder Mine coal of Period 23A of Run 227-55, was used. The experiments were all carried out with 13.8 MPa hydrogen pressure, and 30 minutes time after insertion of the autoclave into a fluidized sand bath heater maintained at 440°C. At the end of this time the temperature of autoclave was dropped rapidly by plunging the autoclave into a water bath. The catalyst tested was held in a wire basket in the autoclave and catalyst-oil contact was promoted by the vertical agitation of the autoclave during the experiment. Each experiment used 2 grams of the test oil, and, usually, an amount of oil-free catalyst (toluene extracted) that corresponded to 2 grams of uncontaminated fresh catalyst after correction for the estimated contaminant content, so that the experiments had an approximately common severity of around 30 minutes x grams uncontaminated catalyst/gram test oil.

The product oil was washed from the autoclave and the catalyst using THF as a wash solvent. The THF was removed from the washings by vacuum evaporation using a roto-evaporator in a hot oil bath at 46°C. The residual oil (524°C+) content in the reference oil and product oils were determined by using a TGA procedure.Typcially, the 227-55-23A PFL reference oil containing 29.6 W% 524°C+ residual oil, as determined by ASTM D-1160 procedure, was reported as having 29.6-30.6 W% residual oil content by TGA analysis. Several analyses were performed to determine the amount of contaminants on the oil-free catalysts withdrawn during the POC program. These analyses were bulk and particle densities, elemental (CHNS), ignition loss and major metals (Mo, Ni, Fe, Na, Ca).

CARBONACEOUS AND OTHER CONTAMINANTS

Considering four possible methods of using different analyses (particle density, sum of individual contaminants, nickel and molybdenum content) for estimation of the actual contaminant content in the catalysts, these methods do not agree very closely, as follows comparing the average results for the 13 cases where all of the four methods could be used.

Nickel	47.3%	Molybdenum	46.8%
Particle Density	32.6%	Total Measured Contaminants	25.9%

The Ni and Mo analyses appear to be erratic, with a possibility the Mo and Ni contents of the fresh catalyst are not as high as the cited analyses. The difference in apparent contaminant content based on particle density and contaminants analyses, by an average of 6.7% more contamination indicated by the particle density values, could have been caused by failure to determined all of the metallic contaminants. Titanium content of one of the sample (Period 26), which proved to be higher than the Fe, Na, and Ca contents of the first stage catalyst and also higher than the average of those others elements in the second stage catalyst, have been determined. However, the amounts of Ti (as TiO_2) were only 1.6 and 0.7 W%, which were considerably less than the above difference in indicated total contaminants content. *Figure 1* compares the amounts of catalyst contamination, Period by Period, based on the latter methods. The actual contaminants analyses persistently indicated more

contamination of the second stage catalyst, but the catalyst density values indicate more contamination of the first stage catalyst. Because it was uncertain that all of the contaminating constituents had been determined by chemical analyses, and uncertainty concerning the reliability of such analyses, the estimated fresh catalyst contents that were used were those indicated by the particle density measurements.

CATALYST ACTIVITIES

The activity of the tested catalysts are expressed as percentage of that of a reference catalyst. The reference catalyst was Criterion C-317 catalyst that had been presulfided with a TNPS/gas oil mixture using a fixed bed. The nominal accuracy of the tests was estimated on the basis of the four pairs of replicate tests, as follows:

Test No.	Catalyst	Relatives Activities (%)	Oil Recovery (%)
72 & 73	Fresh AO-60	70, 70	94, 92
90 & 91	Presulfided AO-60	167, 164	89, 90
99 & 104	Period 33 1st Stage	98, 98	92, 100
97 & 103	Period 33 2nd Stage	62, 62	88, 98

The charge catalyst to Run POC-01, Akzo AO-60 catalyst, when not presulfided was of lower activity (70%) than the reference catalyst. Upon presulfidation with dimethyl disulfide or thiononyl polysulfide in tetralin increase the catalyst to 164-167% of the reference catalyst. Similar observation was obtained when Shell S-317 catalyst was presulfided. It's activity increased to 182% of the reference catalyst.

Figure 2 compares the activities of withdrawn catalysts from various periods of Run POC-01. The first samples, Period 1, were less active, 50-62% of the reference activity, than the fresh (unpresulfided) AO-60 catalyst. This pattern was caused by incomplete presulfiding and accumulating of contaminants on the catalysts. These catalysts contained only 35-53% of theoretical sulfur content as compared to values averaging 97% of theoretical sulfur content for catalyst samples later in the run. The activities of the catalysts can be grouped into two regions corresponding to the changes in the operating conditions. In the initial period, Periods 4 to 20, the first and second stage catalysts ranged from 88 to 104 % of the activity of the reference catalyst. There were no on-line catalyst addition/withdrawal in the first 9 operating periods, during which the aging of the catalysts were accelerated to the equilibrium values. Catalyst addition/withdrawals were initiated in Period 10 but on reduced rates on alternate days basis (0.5 lb/ton coal tot he first stage and 1.0 lb/ton coal tot he second stage). The first and second stage temperatures ranged from 399° to 407°C and 427° to 432°C, respectively. Also, the unit was in an ashy recycle mode in the initial periods and was phased out gradually when the ROSE-SR^{SM} solid separation unit was introduced since Period 13. Solid-free recycle mode was implemented from Period 21 onward.

Catalyst samples from the later periods, Periods 26 to 57, were of relatively low activity at 59-72% of the reference catalyst activity. In these later periods, coal feed rate was increased 50% with higher reactor temperatures. The first and second stage temperature were raised by approximately 3° and 5° to 8°C, respectively to cope with the higher coal feedrate. These higher temperatures resulted in higher coke lay down on the catalyst, especially that of the second stage catalyst, as shown in *Figure 3*. Also, starting from Period 20, catalyst addition rates were increased to target equilibrium values of daily additions of 1.5 and 3.0 lb/ton to first and second stages, respectively.

With the exception of Period 1 catalyst, the activities of the other catalyst samples were largely related to the degree of contamination, as shown in *Figure 4*. A correlation considering contents of both carbon and other contaminants gave the following equations:

$$\text{Relative Activity} = A + B * W_{carbon} + C * W_{others}$$

	A	B	C	Confident Limited (%)
All Catalysts	187.4	-5.11	2.72	>99.99
Without Presulfided Catalysts	179.7	-4.82	2.44	99.91

where, W_{carbon} and W_{others} are the weight percent of carbon and other contaminants on the catalysts, respectively. Despite the lower catalyst replacement rate to the first stage (by a factor ½), first stage

catalysts were generally more active than the second stage catalysts by an average of 7%. The relative activity of the first and second stage catalysts appears to be related principally to the lower content of carbon on the first stage catalyst and not to the total amount of contaminants. Excepting the Period 1 catalysts, where the first stage and second carbon contents were virtually the same, in the other six pairs of first and second catalysts (as given in *Figure 3*) the second stage catalyst contained more carbon, by 0.8 to 7.8 W%. The following tabulation gives average values of these factors for the first and second stage catalysts that have been tested:

Stage	Catalyst Activity	Carbon Content (%)	Catalyst Content (%)
First	80	14.56	73.0
Second	72	17.93	75.0

The multiple correlations summarized above indicated that the average activity of the first stage catalysts would be 4% higher than that of the second stage catalysts.

COMPARISON OF EVALUATIONS WITH PROJECTED ACTIVITIES

The residual oil yields in CTSL Bench Unit coal liquefaction operations have been correlated as being dependent on catalyst age by a functionality that assumed catalyst activity declined by a constant proportion for each day of operations at the liquefaction conditions. Projections were calculated for the first and second stage catalyst activities during the course of Run POC-01, using the actual pattern of catalyst addition/withdrawal that occurred during the run. In these calculations, the catalyst deactivation factors for the two stages were based on those given in the Final CTSL topical report. For the interval of Run POC-01, Period 26 through 43, during which equilibrium catalyst addition rates were maintained the average of the microautoclave catalyst evaluation results were lower for the first stage catalyst, and higher for the second stage catalyst, than the projected values. The trends in the evaluated caalyst activities for this interval of the run were directionally in agreement with of those of the projections, showing a possible small decline in the first stage catalyst activity and essentially no change in second stage catalyst activity.

However, the evaluation results differ even more markedly from the projected values for the first interval of the run before Period 20 where there were low rates of catalyst addition to "aged" the initial charge of catalysts, and for the final interval of the run after Period 45 where there was no catalyst addition to the second stage with reduced catalyst input to the first stage.

Figure 5 summarizes the results of calculations for projection activities using the first and second stage deactivation factors adjusted to give a close fit to the evaluations for Periods 26, 32, and 43. This figure also includes the experimental evaluations throughout the run. The adjustments of the deactivation factors were approximately 42% higher for the first stage and 51% lower for the second stage, as compared with he CTSL Bench unit factors.

SUMMARY AND CONCLUSION

The un-presulfided form, "fresh", of Akzo AO-60 catalyst was 2.5 times less active in term of converting to lighter products. Due to the addition of "fresh" catalyst directly into the reactor, the equilibrated catalyst activity was only half of the fully presulfided fresh catalyst, while the second stage equilibrated catalyst was even lower and was similar to that of the un-presulfided fresh catalyst. These microautoclave evaluation results correlated with carbon content of the catalyst, and more strongly with total contamination, including metal contamination. A multiple regression correlation indicated significant effects of both carbon content and other contaminants with the greater impact of the carbon content.

ACKNOWLEDGMENT

The authors would like to acknowledge the support of the Pittsburgh Energy Technology Center for providing funding under the contract DE-AC22-92PC92148.

FIGURE 1

CONTAMINATION OF CATALYST DURING RUN POC-01

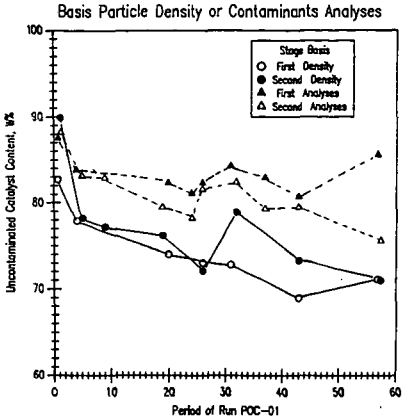

FIGURE 2

RELATIVE ACTIVITY OF RUN POC-01 CATALYSTS

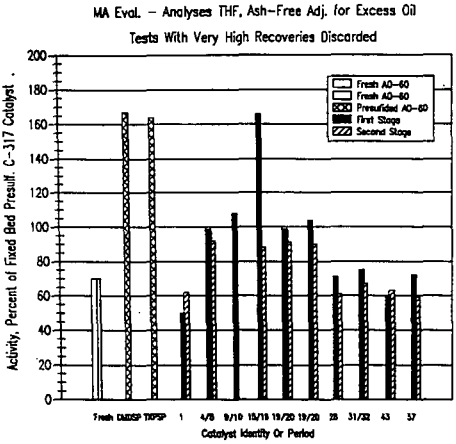

FIGURE 3

CARBON CONTENT OF CATALYSTS DURING RUN POC-01

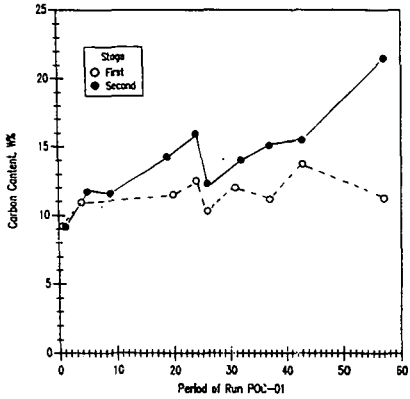

FIGURE 4

ACTIVITY OF POC-01 CATALYSTS IN MICROAUTOCLAVE TESTS

Versus Contamination (Basis Particle Density)

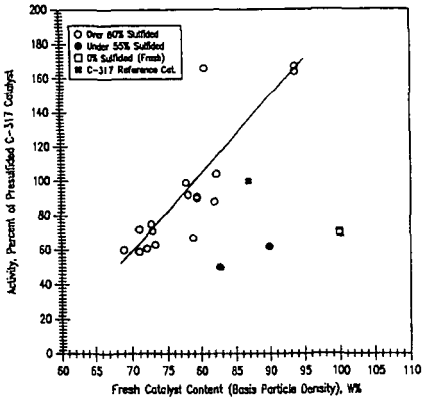

FIGURE 5

POC-01 CATALYST ACTIVITY – EVALUATIONS AND PROJECTIONS

Deactivation Factors to Fit Period 26 to 43 Results

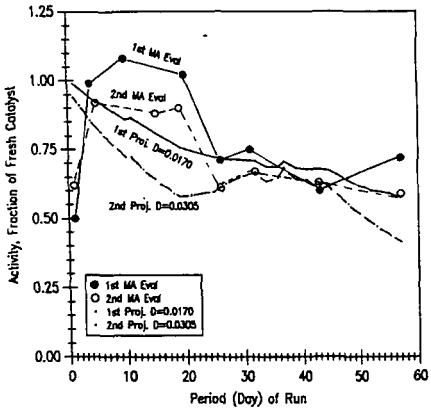

PROMOTING COAL HYDROLIQUEFACTION THROUGH CO-USE OF WATER AND DISPERSED MOLYBDENUM SULFIDE CATALYST

Russell Byrne* and Chunshan Song
Fuel Science Program, 209 Academic Projects Building,
The Pennsylvania State University, University Park, PA 16802, USA

Keywords: Coal liquefaction, water, dispersed catalyst, synergism

INTRODUCTION

Work in our laboratory has demonstrated a remarkable synergism between water and a dispersed molybdenum sulfide catalyst for promoting liquefaction of Wyodak subbituminous coal at relatively low temperature (350-375°C). These results appear to be contrary to conventional wisdom regarding the detrimental effects of water during the catalytic hydroliquefaction of coal [1-4]. Our findings, to date, indicate that both reaction temperature range and water/coal ratio are key factors in determining the net influence of water upon the catalytic liquefaction of this particular coal [5-9]. Significantly, we have observed the same promotional trends arising from the co-use of water and dispersed molybdenum sulfide catalyst both in solvent-free experiments, and in liquefaction experiments performed in the presence of either a non-donor (1-methylnaphthalene), or a H-donor (tetralin) [6,9]. In contrast, however, for catalytic runs at higher temperature (400-450°C), using ATTM without added water always gives the highest conversion, either with or without an organic solvent [6,9]. These interesting results have demonstrated unequivocally that within a specific temperature window, and in the correct proportion, water can have a dramatic promoting effect on the catalytic liquefaction of Wyodak subbituminous coal.

Our findings with Wyodak coal have provided the impetus behind an ongoing fundamental and exploratory study on the promotional effects of water on catalytic coal liquefaction. Although the synergistic enhancement in conversion through co-use of water and dispersed Mo sulfide catalyst has been amply demonstrated for Wyodak subbituminous coal, one of our present primary interests is to determine whether this potentially significant phenomenon is observable with other coals, particularly coals of different rank. In this paper preliminary results from recent work using Pittsburgh #8 high-volatile bituminous coal are presented which indicate a similar marked improvement in coal conversion upon addition of a small amount of water in the presence of dispersed molybdenum sulfide catalyst. The overall improvement in conversion observed for the higher-rank coal, however, is somewhat less dramatic than that for Wyodak coal. Reactions performed at two different temperatures (350 and 400°C) are discussed and compared to those for Wyodak coal. Effects of catalyst loading levels are also described.

EXPERIMENTAL

The coals used were Wyodak subbituminous coal and Pittsburgh #8 high-volatile bituminous coal. These are Department of Energy Coal Samples (DECS-8 and DECS-12, respectively) maintained in the DOE/Penn State Coal Sample Bank, ground to ≤ 60 mesh, and stored under argon atmosphere in heat sealed, argon-filled laminated foil bags consisting of three layers. Wyodak subbituminous coal contains 28.4% moisture, 32.4% volatile matter, 29.3% fixed carbon and 9.9% ash, on as-received basis; 75.8% C, 5.2% H, 1.0% N, 0.5% S, and 17.5% O, on dmmf basis. Pittsburgh #8 high-volatile bituminous coal contains 2.4% moisture, 35.2% volatile matter, 52.4% fixed carbon and 10.0% ash, on as-received basis; 84.8% C, 5.7% H, 1.4% N, 0.8% S, and 7.4% O, on dmmf basis. Both fresh raw coals, and coals pre-dried in a vacuum oven (vd) at 100°C for 2h were used. Reagent grade ammonium tetrathiomolybdate (ATTM, obtained from Aldrich with 99.97% purity) was employed as the dispersed catalyst precursor. The water-soluble inorganic salt ATTM is expected to generate molybdenum sulfide particles on the coal surface upon thermal decomposition at ≥ 325°C. ATTM was dispersed onto either the raw coal or vacuum-dried coal samples by incipient wetness impregnation from its aqueous solution. The metal loading was kept constant at 1 wt% Mo on dmmf coal basis, unless otherwise specified. Following impregnation, the coal samples were dried in a vacuum oven at 100°C for 2h prior to use.

Liquefaction experiments were carried out in 25 ml tubing bomb reactors with around 4g of coal at 350 or 400°C for 30 min (plus an additional 3 min for reactor heat-up time). For both thermal and catalytic experiments with added water, the weight ratio of water to dmmf coal was kept at around 0.46. All reactions described in this paper were performed in the absence of any organic solvent. The reactors were purged several times with H_2 and finally pressurized with 6.9 MPa H_2 (cold). A fluidized sandbath maintained at the desired temperature was used as the heater. After the desired reaction time, the reactors were removed from the sandbath and quenched in a cold water bath to rapidly bring down the temperature < 150°C, then were allowed to cool down to ambient temperature in air. The reactors were vented and the mass of product gases (including residual H_2) determined. Gaseous products were analyzed by GC, with the aid of gas standards for quantitative calibration of GC responses of CO_2, CO, H_2 and C_1-C_4 hydrocarbon gases. H_2 consumption was determined by subtracting the mass of residual H_2 found in the product gases (determined by GC) from the mass of H_2 initially charged. The liquid and solid products were carefully recovered from the reactor and transferred to an extraction thimble. The products were subsequently separated by sequential Soxhlet extraction into oil (hexane solubles), asphaltene (toluene soluble but hexane insoluble), preasphaltene (THF soluble but toluene insoluble), and residue (THF insoluble). Further experimental details may be found elsewhere [6-8].

RESULTS AND DISCUSSION

Experimental results for the catalytic and non-catalytic solvent-free reactions of Pittsburgh #8 coal, performed in both the presence and absence of added water, are illustrated in Figure 1 (350°C) and Figure 2 (400°C). Equivalent data for Wyodak coal is also given in Figure 3 (350°C) and Figure 4 (400°C), respectively. The catalyst loading level employed in these experiments was 1 wt% Mo on dmmf coal basis. The effects of reducing catalyst loading to 0.1 wt% Mo for reactions of Wyodak coal at 350°C are summarized in Figure 5.

Positive Effect of Added Water in Catalytic Liquefaction at 350°C. Our earlier findings concerning the strong promotional effects of added water on the catalytic liquefaction of Wyodak subbituminous coal at 350°C are exemplified in Figure 3. These results have been previously discussed in detail elsewhere [7]. In brief, it can be seen that adding water to the non-catalytic run of vacuum dried Wyodak coal increased coal conversion from 14.5 to 22.5 wt% (dmmf). Using only ATTM improved coal conversion to 29.8 wt%. When both water and ATTM are used in combination, however, there is a remarkable increase in coal conversion to 66.5 wt%.

Referring now to Figure 1 for the runs of Pittsburgh #8 coal at 350°C, it can be seen that compared to the non-catalytic run of vacuum-dried coal, adding water increased coal conversion from 21.9 to 33.6 wt% (dmmf). Surprisingly, using ATTM at 350°C had little apparent benefit on conversion for this coal, giving a conversion of only 25.1 wt%. This is in stark contrast to the results for Wyodak subbituminous coal. Adding water to the catalytic run, however, significantly increased conversion of Pittsburgh #8 coal to 48.0 wt%, representing a 91% increase from the catalytic run without water, and a 119% increase from the non-catalytic run without water. Clearly, as previously seen for Wyodak coal, there is an apparent synergistic enhancement in conversion at 350°C for Pittsburgh #8 coal resulting from co-use of water and dispersed Mo sulfide catalyst. These interesting findings reveal that dispersed Mo sulfide catalyst and added water can act in concert to promote coal liquefaction at relatively low temperature. It is noteworthy, however, that the overall improvement in conversion obseved for the higher-rank coal Pittsburgh #8 is somewhat less dramatic than that for Wyodak subbituminous coal. Considering product quality, it is apparent from Figure 1 that Pittsburgh #8 high-volatile bituminous coal is converted largely to preasphaltenes (ie. THF-soluble but toluene-insoluble) at 350°C. The enhancement in conversion through co-use of water and catalyst is also manifest primarily as an increase in preasphaltene yields. As one might expect, gas yields from Pittsburgh #8 coal (particularly CO_2) are significantly lower than from Wyodak subbituminous coal. Interestingly, however, we observed that CO_2 yields are doubled or even tripled for all reactions with added water. Similar observations have also been made for the hydrous experiments with Wyodak coal [7]. This suggests that water is interacting with certain coal functionalities, ultimately resulting in the evolution of CO_2 through oxidative processes and/or enhanced decarboxylation.

Comparing the conversion data for Pittsburgh #8 (Figure 1) at 350°C to that for Wyodak coal (Figure 3), it is interesting to note that for the non-catalytic reactions, the high-volatile bituminous coal is apparently more reactive than the lower-rank subbituminous coal, both in the absence and presence of water (ie. 21.9 wt% vs 14.5 wt% for anhydrous experiments) and (33.6 wt% vs 22.5 wt% for hydrous experiments), respectively. In contrast, however, for the catalytic reactions, Wyodak coal always gives higher conversion than Pittsburgh #8 (ie. 29.8 wt% vs 25.1 wt% for anhydrous experiments) and (66.5 wt% vs 48.0 wt% for hydrous experiments). These results clearly demonstrate that in the presence of an effective dispersed catalyst, lower-rank subbituminous coals are more reactive than first thought [10], and may in fact be more amenable feedstocks for direct liquefaction than bituminous coals (similar trends are also apparent for the reactions of these coals at 400°C).

Effect of Temperature on Coal Conversion with H_2O and ATTM. For Wyodak coal runs at 400°C (Figure 4), using ATTM without water always gave the highest conversions. The use of ATTM alone at 400°C afforded a very high conversion for this coal (85.4 wt% (dmmf)), and a high oil yield (45.8 wt%), illustrating that, at this temperature, dispersed Mo sulfide catalyst is highly effective at promoting the hydroliquefaction of Wyodak subbituminous coal. However, addition of water to the catalytic run decreased coal conversion (to 62.1 wt%) and oil yield (to 28.2 wt%). An important implication from Figure 4 is that the presence of water at 400°C apparently decreased the effectiveness (or activity) of the dispersed catalyst. This is in distinct contrast to the strong promotional trends observed in the corresponding runs at 350°C.

Considering now the runs at 400°C for Pittsburgh #8 high-volatile bituminous coal (Figure 2), it can be seen that the addition of water to the non-catalytic run of vacuum-dried coal resulted in an increase in conversion from 36.3 wt% to 43.5 wt%. The use of ATTM alone resulted in only a modest increase in conversion (to 54.0 wt%). Adding water to the catalytic run gave a similar conversion to that from the use of catalyst alone (54.9 wt%), though interestingly, did not result in a reduction in conversion as was seen for the catalytic run of Wyodak coal at this temperature. Indeed, addition of water to the catalytic run of Pittsburgh #8 appeared to have some benefit, in terms of product quality, in that there was a notable shift from largely preasphaltenes to an increased yield of asphaltenes isolated in the added water reaction. As was the case for Wyodak coal, however, it is apparent that the strong synergistic enhancement in conversion achieved through co-use of water and dispersed catalyst at 350°C, is lost at higher temperature (400°C). As at 350°C, it is interesting to note that in the absence of catalyst at 400°C, Pittsburgh #8 is apparently more reactive than Wyodak coal. In the catalytic reactions, however, Wyodak coal always gives the

highest conversion. The dispersed Mo sulfide catalyst generated from ATTM does not appear to be a very effective catalyst for promoting the hydroliquefaction of the higher-rank coal.

Effect of Catalyst Loading on Conversion of Wyodak Coal at 350°C. Figure 5 summarizes conversion data for Wyodak coal at 350°C obtained using a reduced catalyst loading of 0.1 wt% Mo on dmmf coal basis. Compared to the original data obtained at a loading of 1 wt% Mo on dmmf coal basis (Figure 3), it can clearly be seen that this reduction in the catalyst concentration significantly reduces the overall effectiveness of the catalyst for promoting conversion of Wyodak coal, both in the catalytic runs and catalytic runs with added water. For the catalytic runs, conversion fell from 29.8 wt% to 20.5 wt%. In the case of catalytic runs with added water, conversion fell from 66.5 wt% to 40.3 wt%. This latter observation indicates that the magnitude of the promotional effect arising through co-use of water and ATTM is not only sensitive to the water/dmmf coal ratio but is also dependent upon the catalyst concentration employed.

SUMMARY

We have found that there are strong synergistic effects between water and a dispersed molybdenum sulfide catalyst (1 wt% Mo on dmmf coal basis) for promoting the low temperature (350°C) liquefaction of both Wyodak subbituminous and Pittsburgh #8 bituminous coals. Relative to the catalytic runs of the dried coal, the co-use of catalyst and water (at water/dmmf coal = 0.46) can more than double the coal conversion at 350°C for 30 min, from 29.8 wt% to 66.5 wt% for Wyodak coal. In the case of Pittsburgh #8 coal, under the same prevailing conditions, the overall improvement in conversion on addition of water to the catalytic run is less dramatic, ie. from 25.1 to 48.0 wt%. One of the contributing factors to this observation may be that the dispersed Mo sulfide catalyst generated from ATTM is, in general, less effective for promoting the hydroliquefaction of the higher-rank coal. At higher temperature (400°C) the promotional effects of adding water are lost and, in the case of Wyodak coal, actually inhibits catalyst activity resulting in a reduction in conversion. For Pittsburgh #8 coal, adding water to the catalytic run at 400°C results in a similar conversion to that from the use of catalyst alone. There is, however, some apparent benefit in terms of a slight improvement in product quality for the added water reaction. We plan to perform a more thorough study of the effects of reaction temperature (ie. 325-425°C) on the water-promoted catalytic liquefaction of Pittsburgh #8 coal in order to construct a temperature vs conversion profile, as we have already done for Wyodak coal [5,9]. In this way, we hope to identify the optimum temperature window in which water-dispersed catalyst synergistic interaction is maximized for conversion of Pittsburgh #8 coal.

In the present study, the water/dmmf coal ratio employed was kept constant at around 0.46. This ratio was selected for this preliminary series of reactions with Pittsburgh #8 as it was previously found to be the optimum ratio for Wyodak coal experiments. Clearly, however, it may not necessarily be the most suitable for Pittsburgh #8, we therefore intend to perform a series of catalytic runs at various H_2O/coal ratios in order to determine the optimum ratio for maximizing conversion of this particular coal.

We observed that dropping the catalyst loading, from 1.0 wt% to 0.1 wt% Mo on dmmf coal basis, had an adverse effect on conversion for Wyodak coal at 350°C both for catalytic runs and catalytic runs with added water. The latter finding demonstrates that the magnitude of the promotional effects arising through co-use of ATTM and water is dependent upon the catalyst concentration. We further plan to investigate the effectiveness of a 0.5 wt% Mo catalyst loading.

ACKNOWLEDGEMENT

We are grateful to Prof. H. H. Schobert for his encouragement and support. Financial support was provided by U.S. DOE and U.S. Air Force. We also thank Mr. W. E. Harrison III of AFWL and Dr. S. Rogers of PETC for their support.

REFERENCES

1. Bockrath, B.C.; Finseth, D.H.; Illig, E.G. *Fuel Process. Technol.* **1986**, 12, 175.
2. Ruether, J.A.; Mima, J.A.; Kornosky, R.M.; Ha, B.C. *Energy & Fuels.* **1987**, 1, 198.
3. Kamiya, Y.; Nobusawa, T.; Futamura, S. *Fuel Process. Technol.* **1988**, 18, 1.
4. Weller, S. *Energy & Fuels*, **1994**, 8, 415.
5. Song, C.; Saini, A.K. *Energy & Fuels*, **1995**, 9, 188.
6. Song, C.; Schobert, H.H.; Saini, A.K. *Am. Chem. Soc. Div. Fuel Chem. Prepr.* **1993**, 38, 1031.
7. Song, C.; Schobert, H.H.; Saini, A.K. *Energy & Fuels.* **1994**, 8, 301.
8. Song, C.; Saini, A.K. *Am. Chem. Soc. Div. Fuel Chem. Prepr.* **1994**, 39, 1103.
9. Song, C.; Saini, A.K.; Mc Connie, J. *Proc. of 8th Int. Conf. Coal Science*, Oviedo, Spain, Sept 10-15, **1995**, in press.
10. DOE COLIRN Panel. *"Coal Liquefaction"*, Final Report, DOE-ER-0400, **1989**, Vol. I and II.

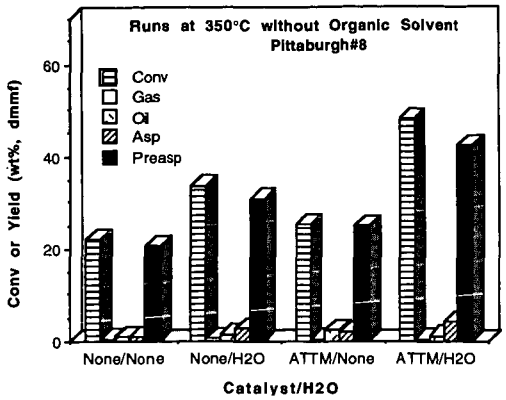

Figure 1 Effect of water on catalytic liquefaction of Pittsburgh #8 coal at 350°C for 30 min.

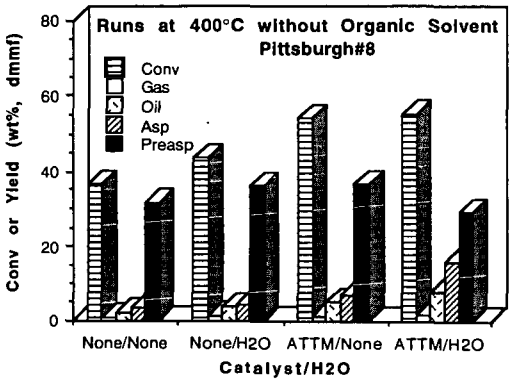

Figure 2. Effect of water on catalytic liquefaction of Pittsburgh #8 coal at 400°C for 30 min.

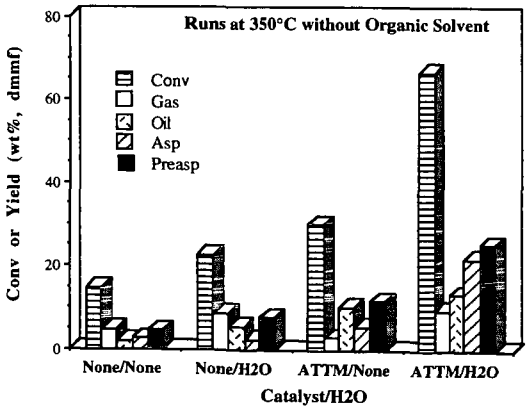

Figure 3. Effect of water on catalytic liquefaction of Wyodak coal at 350°C for 30 min.

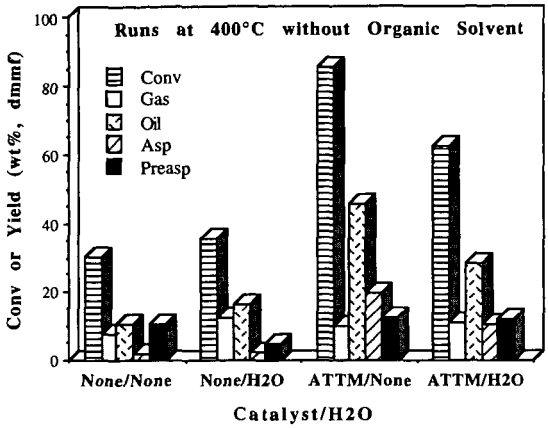

Figure 4 Effect of water on catalytic liquefaction of Wyodak coal at 400°C for 30 min.

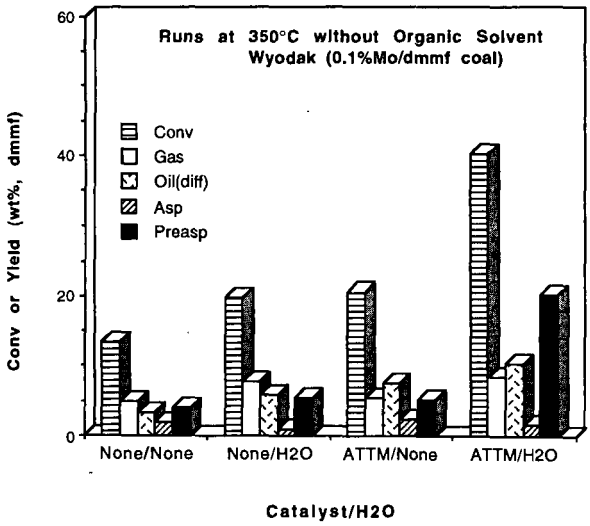

Figure 5 Effect of water on catalytic liquefaction of Wyodak coal using catalyst loading of 0.1 wt% Mo to dmmf coal at 350°C for 30 min.

PROCESS DESIGN OF A NOVEL CONTINUOUS-MODE MINI-PILOT PLANT, FOR DIRECT LIQUEFACTION OF COAL AND UPGRADING OF COAL LIQUIDS

P. Vijay, Chunshan Song*, and Harold H. Schobert

Fuel Science Program
Dept. of Materials Science and Engineering
209 Academic Projects Bldg.
The Pennsylvania State University
University Park, PA 16802-2303

ABSTRACT

On the basis of existing coal liquefaction process units, and our own laboratory research efforts on microautoclave reactor systems, a continuous flow process reactor system for the direct liquefaction of coal and upgrading of coal liquids was designed. In our mini-pilot plant scale process system, two novel technologies have been coupled to improve the economics over existing coal liquefaction processes. The "technologies" incorporated are temperature programmed liquefaction (TPL) of coal and the co-use of water and dispersed metal catalyst in the low-temperature catalytic coal conversion. Details of this continuous-mode process reactor scheme along with its peripheral units will be presented. The progress of this ongoing project will be updated and presented.

Keywords: Direct Liquefaction of Coal, Upgrading of Coal Liquids, and Continuous Flow Process Reactor System.

INTRODUCTION

Extensive research studies on various aspects of the liquefaction of coal including temperature programmed liquefaction (TPL), and effect of water and dispersed molybdenum catalyst for promoting low-severity liquefaction, in the presence of a solvent were conducted earlier [1, 2]. All these batch-mode experiments were successfully conducted in a 25 mL tubing bomb microautoclave reactor. Coal liquefaction experiments in the presence of dispersed catalyst, water, and solvent are currently being performed in a 300 mL batch-mode reactor system.

In order to simulate conditions prevalent in an industrial-type reaction atmosphere, it is necessary to conduct liquefaction of coal and upgrading of coal liquids in a continuous-mode reactor system. Besides, in this system the dispersed catalyst moves with the products rather than staying in the reactor for extended periods, thus enhancing the once-through reactor productivity. The reactor system can be operated in a continuous-mode for a longer time, leading to an increase in the quantity of the products obtained. If the coal liquefaction products stay in the reactor for a prolonged period of time, retrograde reaction occurs that converts desirable small product molecules into less desirable larger macromolecules, by the recombination of small product molecules or by addition of these product molecules back onto the coal [3]. Since the coal liquefaction products that are formed are continuously removed from the flow reactor system, there would be an alleviation in the effect of retrograde reactions thereby increasing the yield and quality of coal liquids, that can be upgraded to produce transportation fuels, particularly jet fuels.

BRIEF OVERVIEW OF EXISTING COAL LIQUEFACTION UNITS

Three of the following well-documented liquefaction processes were studied, before embarking on the process design and assembly of our novel mini-pilot plant reactor system for liquefaction of coal and upgrading of coal liquids.

Advanced Coal Liquefaction Facility at Wilsonville, Alabama. The liquefaction facility at Wilsonville initially operated with two ebullated-bed reactors in series, with supported catalysts in both the reactors [4]. Due to the several well documented advantages of using dispersed catalysts in the 1st reactor [4], a few experiments using dispersed catalysts in the 1st reactor and supported catalysts in the 2nd reactor were conducted. This hybrid catalyst system improved the distillate production by 30-60 %, and increased the coal & resid conversions compared to using dispersed and supported catalysts separately. This Wilsonville Facility was closed down in 1992.

Hydrocarbon Research Institute (HRI) Inc. Unit, New Jersey. The reactor configuration in the HRI unit is similar to that in Wilsonville [5]. Since very few runs were performed in the Wilsonville facility in the hybrid catalyst mode, HRI, Inc. decided to conduct a few more runs with this reactor scheme. An interstage separator was added between the 2 reactors. Experiments were performed using both pure H_2 feed and syngas (H_2 + CO) feed to the 1st reactor, and pure H_2 feed to the 2nd reactor [5]. A higher distillate yield, coal, and residuum conversion were obtained when syngas was used in the 1st stage instead of H_2.

For a few runs an on-line hydrotreater was in service to further remove heteroatoms from the separator and atmospheric still overhead products. The coal conversions were the highest values obtained for this type of coal. The light distillates (IBF-650 °F) contained ten times less nitrogen

* To whom all correspondence should be addressed.

and 17 wt% more hydrogen than that of the 2 ebullated-bed reactors in series configuration. Other studies in the HRI Inc. unit included an addition of a fixed-bed finishing reactor (second or third stage) after the ebullated bed reactors, a three stage CSTR system with an addition of a third ebullated bed reactor in series along with 2 ebullated bed reactors (plug flow simulation), and lowering the solvent/coal ratio to 0.9 in two ebullated bed reactors in series [6].

Pittsburgh Energy Technology Center (PETC) Coal Liquefaction Unit. In PETC, coal liquefaction research studies are being conducted in a computer-controlled bench-scale continuous unit. In this process, coal-catalyst-solvent slurry continuously flows through a 1-liter reactor, where it reacts in the presence of hydrogen to generate coal liquids [7].

PROCESS DESIGN OF A NOVEL CONTINUOUS MODE MINI-PILOT PLANT FOR LIQUEFACTION OF COAL AND UPGRADING OF COAL LIQUIDS

Mini-Pilot Plant for Coal Liquefaction Process

On the basis of existing coal liquefaction units, and our laboratory research efforts in the 25 mL microautoclave reactor system and the 300 mL batch-mode reactor system, a novel continuous flow process scheme for the liquefaction of coal and upgrading of coal liquids was designed. The process flow diagram of this continuous-mode reactor scheme for the liquefaction of coal is presented in Figure 1. The typical operating conditions of the system are shown in Table 1.

The size of the coal particles is small (≤ 60-200 mesh) in order to reduce mass transfer limitations. The solvent used will either be a process solvent (e.g., Wilsonville middle distillates) or petroleum resids. The advantages of employing dispersed catalysts instead of supported catalysts in the coal liquefaction reactors include, a lesser amount of catalyst, good control of retrogressive reactions at preconversion conditions and hence reducing char formation and catalyst deactivation, reduced reaction severity, faster hydrogen transfer rate, improved economics due to enhanced yields of desired products, and higher coal conversion.

In our process, two novel technologies have been coupled in an attempt to improve the economics over existing coal liquefaction processes. The technologies incorporated are temperature programmed liquefaction (TPL) of coal [1] and the co-use of water and dispersed catalysts in the coal liquefaction process [2]. Studies conducted in the 25 mL microautoclave reactor and in the 300 mL batch-mode reactor scheme, will help to provide some basic information in guiding the selection of the various operating conditions for the continuous unit.

Features of the Continuous Flow Reactor Scheme. The significant features of this novel reactor scheme for the coal liquefaction process are:

§ Use of dispersed catalysts in the coal-solvent slurry.
§ Temperature-programmed liquefaction (TPL) in a multistage (2 stages) reactor scheme.
§ Option of adding water to the coal-catalyst-solvent slurry to the 1st stage reactor.
§ Incorporation of an interstage separator between the two stages of the reactor.
§ A feed gas compression system.
§ Continuous sampling and G.C. analysis of gas and liquid from the slurry lines at several vantage points to periodically monitor the progress of the reaction.

Details of the Multistage Continuous Flow Reactor System for Coal Liquefaction Process.

* Slurry Feed Mix Tank - Feed slurry to the reactors consisting of coal, dispersed catalyst, and solvent (or petroleum resids) will be thoroughly mixed in this 3 gallon feed mix tank equipped with an agitator, to maintain this slurry in suspension. The temperature and the pressure of this vessel will be maintained at around 80-100 °C and at 50-80 psi., respectively.

* Slurry Pump - The slurry from the feed mix tank will be fed to the reactors through a preheater by the slurry pump. This pump will be capable of handling high concentration of solids loading in slurry (35 wt %) and pressures as high as 4000 psi.

Prior to entering the preheater, the slurry will be contacted by pure feed gas (H_2 or syngas - $H_2 + CO$). CO will be used in an attempt to improve the economics by incorporating the water-gas shift step. Although it is necessary to recycle gas in an industrial-scale process, we have eliminated all recycle gas streams and the compressors in these lines in our design of the laboratory-scale reactor system, due to budget and space limitations.

* Feed Gas Compression System - The maximum pressure of the feed gas from the manufacturer's gas cylinders is 2500 psi. Since we will require a steady flow of feed gas at pressures around 2500 psi., it was necessary to design a feed gas compression system. The feed gas (H_2 or syngas - H_2 + CO) will flow from the gas cylinders into a pneumatic compressor, where it is compressed to the desired high pressure and stored in the compressed gas storage tanks. The pneumatic compressor will be capable of compressing the inlet feed gas to pressures as high as 5000 psi, depending on the inlet pressure and the desired exit flow rate to the compressed gas storage tanks.

The outlet lines from the compressed gas storage tanks are provided with a vent line, to depressurize the system at the completion of the experimental runs. The outlet from these storage tanks serves as the feed inlet to the reactor system. The feed gas inlet to the slurry line before the preheater, is equipped with a forward pressure regulator and a mass flow controller.

* Preheater - The gas and slurry that enters the 300 mL agitated autoclave vessel that serves as a preheater, will be maintained at a temperature of 200-300 °C. The preheated gas and slurry then flows into the 1st stage reactor.

* 1st Stage Coal Liquefaction Reactor - The 1st stage reactor is a 1-liter vessel equipped with a dispersimax turbine type impeller, that will be maintained at a temperature of 350-400 °C. The gas and slurry entering from the preheater, will undergo primary reactions here.

Provision is made for continuous injection of water from the water feed reservoir (3 gallon), into the 1st stage reactor, with the aid of a water pump. This water reacts with the gas and slurry to form primary products which includes the product vapors and the coal liquids which remains in the slurry. The unreacted gas, product vapors, and slurry (along with the product liquids) then flows into the interstage separator. A sampling loop for G.C. analysis of liquid is provided.

* Interstage Separator - This interstage separator is a 1-liter vessel equipped with a turbine type impeller, whose main function is to ensure the complete removal of water remaining in the system. The product vapors exiting this separator flows through a condenser to remove any condensables remaining in the system like H_2O, H_2S, and NH_3, that are collected in the 300 mL liquid collection bomb. The noncondensables (H_2, C_1-C_4) initially flows through a back pressure controller and a flow meter, and then vented to atmosphere. Provision is made for analysis of gas and liquid from this separator.

* 2nd Stage Coal Liquefaction Reactor - The process stream consisting of gas and slurry from the exit of the interstage separator, and pure gas from the compressed gas storage tank, is the feed to the 2nd stage reactor, which is a 1-liter vessel equipped with a turbine type impeller, and maintained at 400-440 °C. The gas and slurry entering this reactor undergo secondary reactions to form more coal liquids. The reactor effluent flows into a vapor-liquid separator. A sampling line for G.C. analysis of the liquid reacting in the 2nd stage reactor will be installed.

* Vapor-Liquid Separator - The gas and slurry products exiting the 2nd stage coal liquefaction reactor flows into the vapor-liquid separator, which is a 1-liter vessel equipped with a turbine type impeller. The gas exiting this separator is first contacted with water from the reservoir and then cooled by a condenser. The condensables fill the liquid collection bomb, which is a 300 mL cylinder. Provision is made for G.C. analysis of the liquid collected in this bomb. The noncondensables initially flows through a back pressure controller and a flow meter, and then vented to atmosphere. Provision is made for G.C. analysis of this gas exiting the V/L separator.

The gas and slurry exiting the vapor-liquid separator initially flows through a condenser, and is then sent through a Bureau of Mines (BOM) valve which will be capable of handling this slurry, at high temperature and high pressure process conditions. The process stream (gas and slurry) then flows into an atmospheric flash tank.

* Atmospheric Flash Tank - The effluent from the V/L separator enters the atmospheric flash tank which is a 1-liter agitated vessel. The flow rate of the gas exiting this vessel is measured and then vented to atmosphere. Periodic G.C. analysis of this exiting gas will be performed. The slurry exiting this atmospheric flash tank flows into a coal liquids collector tank.

* Coal Liquids Collector Tank / Coal Liquids Upgrading Feed Tank - The slurry exiting the atmospheric flash tank, enters a 3 gallon coal liquids collector tank through a filter bag placed in the process line. This would aid in the separation of solids from the liquid in the slurry stream. The liquids are collected in this tank, which is also the feed tank for the upgrading section of the mini-pilot plant system. The solids containing insolubles, unreacted coal, resids, and catalysts are removed. The coal liquid is then pumped to the upgrading section of the mini-pilot plant.

Mini-Pilot Plant for Coal Liquids Upgrading Process

The schematic of the process flow diagram of the mini-pilot plant for upgrading of coal liquids is presented in Figure 2. The typical operating conditions of the reactor scheme for upgrading coal liquids is shown in Table 1.

Details of Continuous Flow System and Peripheral Units for Coal Liquids Upgrading Process.

* Coal Liquids Upgrading Feed Tank - The feed to the reactor consisting of coal liquids from the liquefaction section of the mini-pilot plant will be stored in this 3 gallon feed tank equipped with an agitator. The temperature and the pressure of this vessel will be maintained at around 80-100 °C and at 50-80 psi., respectively.

The coal liquids from this feed tank is pumped through a feed pump, into the Preheater. Please refer to the earlier section regarding details about the pump and the preheater. Prior to entering the preheater, the liquid feed will be contacted by pure feed gas (H_2) from the compressed gas cylinder. The gas and slurry from the preheater flows into the coal liquids upgrading reactor.

* Coal Liquids Upgrading Reactor - This reactor is a 1-liter autoclave vessel equipped with a Robinson-Mahoney Spinning Catalyst Basket, and will be maintained at a temperature of 375 - 440 °C. The catalysts in the spinning catalyst basket that will assist in the upgrading reactions, will include conventional supported catalysts, and catalysts prepared in the laboratory, such as mesoporous alumino-silicate molecular sieve based catalysts. Provision is made for periodic analysis of the liquid inside the reactor to monitor the progress of the reaction.

The effluent from this upgrading reactor consisting of unreacted gases, product gases, and upgraded coal liquid products, flows into the vapor-liquid separator. Please refer to the earlier section regarding the detailed functions of this separator.

* Atmospheric Flash Tank - The gas and liquid flowing from the V/L separator, flows through a BOM valve and then enters the atmospheric flash tank which is a 1-liter agitated vessel. The flow rate of the gas exiting this vessel is measured and then vented to atmosphere. Periodic G.C. analysis of this product gas and the liquid collected in the vessel will be performed to monitor the progress of the reaction. The upgraded coal liquid stays in the vessel.

STATUS OF THE MINI-PILOT PLANT REACTOR SYSTEM AND FUTURE PLANS

According to the process configuration in the continuous-mode reactor scheme for coal liquefaction and upgrading of coal liquids, a cost estimation for the various individual components and accessories, that includes the reactors, slurry pump, water pump, etc., was performed. According to the cost analysis study and depending on budgetary constraints, the continuous-mode mini-pilot plant scheme will either have only manual controls, or have computer controls for selected equipments, or will be an entirely computerized system.

Several of the major process equipments (reactors, separators, flash tank, feed tanks, water reservoir, slurry pump, water pump, pneumatic compressor, compressed gas cylinders, liquid collection bombs, etc.) were ordered to be delivered from the manufacturers, and a few of them have been received. The other equipments and accessories will be ordered from the manufacturers soon. The assembly of this mini-pilot plant is expected to commence soon.

ACKNOWLEDGMENT

This project was supported by the U.S. Department of Energy, Pittsburgh Energy Technology Center (PETC), and the Air Force Wright Laboratory at the Wright Patterson Air Force Base (WPAFB), Dayton, Ohio. We wish to thank Mr. W.E. Harrison III of WPAFB and Dr. S. Rogers of PETC for their support. We also thank Dr. A. Cugini and Dr. D. Krastman of PETC for the helpful discussions on the liquefaction reactor system.

REFERENCES

1. Song, C., Parfitt, D. S., and Schobert, H. H.; *Energy & Fuels*, Vol. 8, No. 2, 313-319, 1994; Huang, L., Song, C., and Schobert, H.H.; *Am. Chem. Soc. Div. Fuel Chem. Preprints*, 37(2), 223-227, 1992.

2. Song, C. and Saini, A.K.; *Energy & Fuels*, Vol. 9, No. 1, 188-189, 1995; Song, C. and Saini, A. K.; *Am. Chem. Soc. Div. Fuel Chem. Preprints*, 39(4), 1103-1107, 1994; Song, C., Saini, A.K., and Schobert, H.H.; *Am. Chem. Soc. Div. Fuel Chem. Preprints*, 38(3), 1031-1038, 1993.

3. Provine, W. D., Porro, N. D., LaMarca, C., Klein, M. T., Foley, H. C., Bischoff, K. B., Scouten C. G., and Cronauer, D. C.; *Ind. Eng. Chem. Res.*, Vol. 31 (4), 1170-1176, 1992.

4. Lee, J. M., Vimalchand, P., Cantrell, C. E., and Davies, O. L.; *Proceedings of the Liquefaction Contractors' Review Conference*, September 22-24, 1992, Pittsburgh Energy Technology Center, U.S. Department of Energy, pp 35-96.

5. Lee, L. K., Comolli, A. G., Pradhan, V. R., and Stalzer, R. H.; *Proceedings of the Coal Liquefaction and Gas Conversion Contractors Review Conference*, September 27-29, 1993, Pittsburgh Energy Technology Center, U.S. Department of Energy, pp 547-559.

6. Pradhan, V. R., Comolli, A. G., Johanson, E. S., Lee, L. K., Stalzer, R. H., *Proceedings of the Coal Liquefaction and Gas Conversion Contractors Review Conference*, September 27-29, 1993, Pittsburgh Energy Technology Center, U.S. Department of Energy, pp 425-454.

7. Cugini, A. V., Krastman, D., Hickey, R. F., and Lett, R. G.; *Proceedings of the Liquefaction Contractors' Review Conference*, September 22-24, 1992, Pittsburgh Energy Technology Center, U.S. Department of Energy, pp 203-209.

Table 1. Typical Operating Parameters of the Continuous Flow Reactor Scheme

	Coal Liquefaction Reactor	Coal Liquids Upgrading Reactor
Reactor Feed	Subbituminous Coal / Bituminous Coal	Coal Liquids Product from Liquefaction Reactor
Solvent	Wilsonville Middle Distillates	Wilsonville Middle Distillates
Catalyst	MoS_2 Catalyst from Soluble Precursors (Dispersed State)	Mesoporous Supported Catalysts
Reactor Temperature	1st Stage 350 - 400 °C 2nd Stage 400 - 440 °C	375 - 440 °C
Reactor Pressure	2500 psi of H_2	2500 psi of H_2

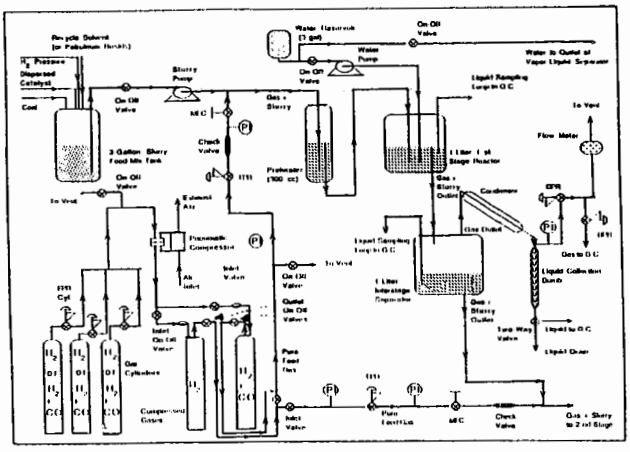

Figure 1. Process Flow Diagram of the Mini-Pilot Plant for Liquefaction of Coal

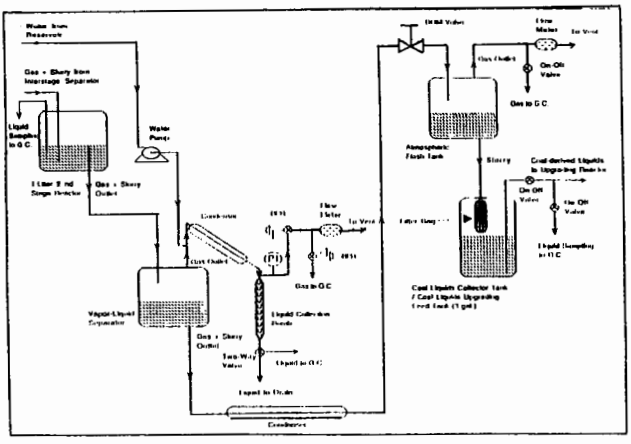

Figure 1 (contd.). Process Flow Diagram of the Mini-Pilot Plant for Liquefaction of Coal

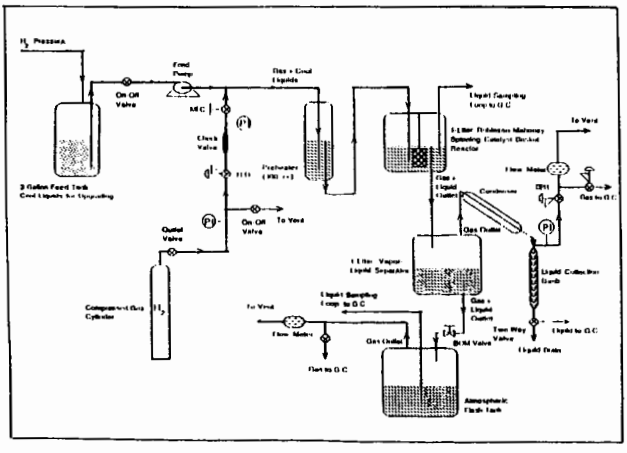

Figure 2. Process Flow Diagram of the Mini-Pilot Plant for Upgrading of Coal Liquids

STRATEGY FOR LARGE SCALE SOLUBILIZATION OF COAL - CHARACTERIZATION OF *NEUROSPORA* PROTEIN AND GENE

Ashish Patel, Y.P. Chen, N.C. Mishra
Department of Biological Sciences
University of South Carolina
Columbia, South Carolina 29208

Key words: coal biosolubilization, involvement of a fungal protein and genetic approach

INTRODUCTION

Coal represents an important source of energy (1,2). Its utilization for generating energy has been offset by environmental problem that it creates by the release of SOx and NOx, which are major causes of acid rain and deforestation. Some of these problems can be tackled by the use of industrial scrubbers. However, a biotechnological approach to these problems may prove more efficient and environment friendly. We have employed certain genetically characterized fungi for the biosolubilization of coal in order to yield chemicals that can be converted into utilizable energy and can be rendered free of SOx and NOx at the source. Here we describe the purification of a protein which is responsible for the biodegradation of low rank coal both *in vivo* and *in vitro*. We also report the characterization of the biochemical nature of the coal derived products obtained after the biosolubilization of coal by this protein *in vivo* and *in vitro*. Identification and characterization of this fungal protein is expected to help the cloning of the gene encoding this protein which is needed to construct a super strain of *Neurospora* capable of large scale solubilization of coal.

MATERIALS AND METHODS

Neurospora crassa is a very well characterized fungus (3). The wildtype strains of *Neurospora crassa* were used for the *in vivo* solubilization of coal and for the extraction and purification of proteins capable of coal solubilization *in vitro*. The low rank coal used was the North Dakota lignite generously supplied by Dr. Charles Scott of the Oak Ridge National Laboratory. The coal was ground to fine mesh 1-3 mm in size and autoclaved before use. The coal granules were not subjected to any other treatment. The *in vivo* solubilization of coal was determined by the liquefaction of coal granule sprinkled over the fungal mat on a Petri dish obtained after a 5-day growth of *Neurospora crassa*. The *in vitro* solubilization of coal was determined by changes in optical density of coal derived products as measured spectroscopically at 254 nm of UV light in a quartz cuvette after incubation of coal granules with *Neurospora* protein preparation in a microfuge tube containing Bis Tris buffer pH 6.5-7.0.

Protein Purification: *Neurospora* protein capable of coal solubilization was purified by ammonium sulfate precipitation, ion exchange chromatography, and HPLC. The amount of protein was determined by methods of Lowry or Bradford, or spectroscopically via absorption at 280 and 260 nm of light.

Determination of the biochemical nature of the coal derived products: Coal derived products obtained after *in vivo* or *in vitro* solubilization were separated by HPLC or by electrophoresis and then examined by mass spectroscopy to reveal their chemical nature. A large volume of liquid culture was grown with continuous aeration. After five days, the culture was treated with tritone X-100 (conc 0.1 ~ 0.5% of total volume). After allowing the reaction to run overnight, the mycelial mass was separated using Whatman 3MM paper. The filterate (crude extract) was centrifuged to remove any debris; 500 ml of the crude extract was loaded directly on a DE-52 (DEAE cellulose) 3.8x11cm (Whatman Labsales, Hillsboro, OR) column which was pre-equilibrated with 0.1M phosphate buffer (pH 7.0). Proteins were eluted with a linear gradient of NaCl from 0.0 to 1M in 600 phosphate buffer. The protein profiles obtained from the ion exchange column showed several peaks. The enzyme peak eluted at 150 ml was equivalent to approximately 0.25M NaCl. The activity of two fractions was twice that obtained with the crude extract. The enzyme peak was pooled and concentrated by ultrafiltration. This solution was applied to a Bio Rad A 0.5M (BioRad, Richmond, VA) 1.8x68cm column which had been pre-equilibrated with phosphate buffer. Proteins were eluted using the same buffer. The enzymes were analyzed by SDS polyacrylamide gel electrophoresis.

RESULTS

It was found that the coal was biosolubilized both *in vivo* and *in vitro*. The possibility of the solubilization by the ingredients of the media was eliminated by performing the same treatment of coal with the ingredients used to make the media.

In vivo Solubilization: Vogel's and WM media were used to grow *N. crassa* on the plates. After five days of growth, coal particles were scattered on the fungal mat. The coal granules appeared as liquid droplets after three to five days (Fig. 1). Two wildtype strains of *N. crassa* viz. Yeehaw Junction and Everglades were used. It was observed that maximum growth was obtained with Yeehaw Junction and in Vogel's media.

In vitro Solubilization: Liquid cultures were grown with Vogel's minimal media with constant aeration. After five days, the mycelium was separated using Whatman 3MM paper. The filterate was used for further experiments. 30mg of coal powder was weighed in an Eppendroff tube and 1ml of filterate was added to it. Absorbance increased with time with maximum increase during the first 4-6 hours. The filterate was kept in cold room and ammonium sulfate was added slowly to it to a concentration of 90%. Centrifuged at 6000 rpm for 20 minutes. Pellet obtained was collected by mixing with 50mM Bis Tris (pH = 7.0). Supernatant left after centrifugation did not show any activity after being treated with coal. Treatment of coal with the sample (pellet + Bis Tris) showed considerable activity. The sample was passed through Sephadex G-25 and dialyzed against 50mM Bis Tris (pH = 7.0) overnight to remove any salts or low molecular weight substrates, if present. By running a pH gradient, it was observed that low and high pH aggravates the biosolubilization reaction and that pH has minimum effect on the reaction between the range of 6.5-7.0. Elevated temperatures also have similar effects on the solubilization and hence the experiments were carried at room temperature.

Protein Purification: The protein was purified using column-chromatography (as described) and at each stage of purification the samples were subjected to solubilization assay, thus discarding the ones without any activity. Finally, the protein was concentrated by collection in a dialysis bag and then covering it with PEG (4000-8000) from all sides. The concentrated protein was dialyzed overnight against the buffer to remove impurities. Bradford test and the Lowry test performed with this sample gave the concentration to be around $1\mu g/\mu l$. The protein was analyzed for temperature stability and it was found that it was stable even after treatment to higher temperatures like 80°C for half an hour or more. The amino acid composition analysis shows that it is an unusual protein in which tyrosine was absent but a sugar moiety was present. The SDS gel containing the protein could not be stained with Coomassie blue. But, it was stained with the silver stain.

Product of Coal Solubilization: Nature of the products obtained from biosolubilization of coal was established using HPLC and mass spectroscopy. The products so obtained are described in Table 2. The products obtained by biosolubilization were extracted by Pentane. In the future, extraction will also be performed with acetone, etc., in order to establish the identity of the productions. The products were compared with ones in NBS library for establishment of chemical structures. The products of coal solubilization are mostly hydrocarbons of low molecular weights (see Table 2).

DISCUSSION

A number of fungi have been described to biosolubilize coal (3-7), however, we are the first one to demonstrate the role of a genetically characterized fungus such as *Neurospora* in this process. Here we describe a method for the large scale purification of a protein from a genetically characterized fungus capable of solubilization of coal. The availability of purified proteins in abundant amount will help in determining the N-terminus sequence of the protein (8) required for the generation of the oligonucleotides for the cloning of the gene encoding this protein capable of coal solubilization. Alternatively the large amount of purified proteins will be used to develop antibody against this protein which will be useful for the screening of the *Neurospora* genomic library harboring a clone containing the gene for this protein. Also, here we describe the identification of the coal solubilization product for the first time. Such information will provide an insight into the mechanism of the action of *Neurospora* protein during coal solubilization. These data can be used to develop a bioreactor capable of conversion of coal product into utilizable chemicals (9).

REFERENCES

1. Specks, R. and A. Kughman. 1982. Energy Process 2:2-6.
2. Starr, C., M.F. Searl, and S. Aupert. Science 256:981-986.
3. Mishra, N.C. Advances in Genetics 29:1-62.
4. Scott, C.D., G.W. Strandberg, and S.N. Lewis. 1986. Biotech. Progress 2:131-139.
5. Shepard M. and L. Aterton. 1987. EPRI Journal 12:28-35.
6. Ward, B. 1985. System. Appl. Microbiol. 6:236-238.
7. Fakoussa, R. 1981. Ph.D. Thesis. Friendrich-Wilhelms. University Bonn Germany.
8. Matsudaira, P. 1987. J. Biol. Chem. 262:10035-10038.
9. Faison, B.D. 1991. Critical Rev. Biotech. 11:347-366.

Table 1. *In vivo* biosolubilization

STRAIN	CULTURE MEDIUM	NO. OF COAL GRANULES		% SOLUBILIZATION
		TOTAL	SOLUBILIZED	
Yeehaw	Vogel's Medium	50	47	94
	WM	50	05	10
Everglades	Vogel's	50	13	26
	WM	50	01	02

Table 2. Characteristics of coal derived products

MOLECULAR WT.	POSSIBLE FORMULAS	INFERENCE
84	C_6H_{12}	may be a contaminant sugar molecules present in growth medium
82	C_6H_{10}	hydrocarbons
326	$C_{25}H_{26}$ or $C_{24}H_{38}$ or $C_{26}H_{14}$	hydrocarbons
278	$C_{16}H_{22}O_4$	probably a contaminant from the plastic tube used during the handling of samples

Figure 1. Coal solubilization by *Neurospora crassa*

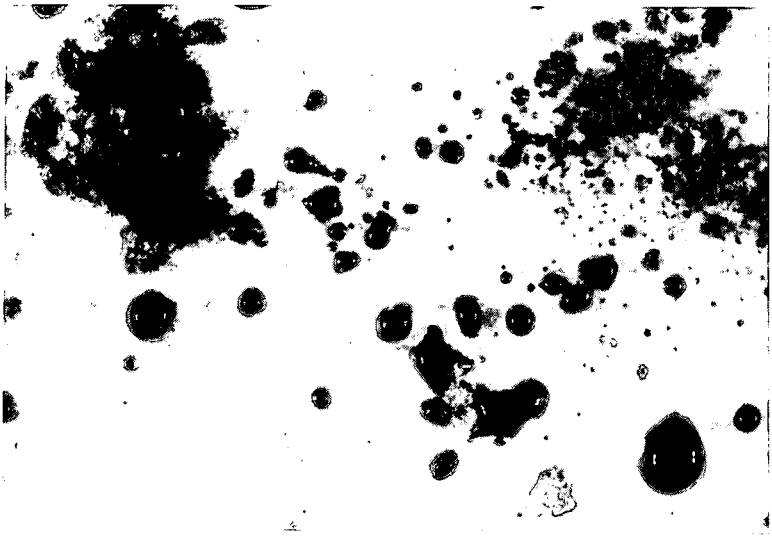

KINETICS OF COAL LIQUEFACTION AT VERY SHORT REACTION TIMES

He Huang, Keyu Wang, Shaojie Wang, M.T. Klein and W. H. Calkins*
Department of Chemical Engineering
University of Delaware, Newark, Delaware 19716

INTRODUCTION

The direct liquefaction of coal is a complex combination of physical and chemical processes. Initially, extractable material is removed from the coal by the process solvent in an amount that depends upon the coal and the solvent characteristics at the temperature of the process. In the subsequent chemical processes, chemical bonds are cleaved thermally or catalytically to form lower molecular weight products. In competition, bond forming (retrograde) reactions of the coal and coal liquefaction intermediates lead to high molecular weight products. These products can foul catalysts, plug the reactor system, and otherwise obscure the underlying chemical fundamentals. This motivated the investigation of the coal liquefaction process at very low conversions, where secondary and retrograde reactions are minimized and the initial liquefaction products can be isolated and studied. This also permits changes in the still solid but partially reacted coal to be investigated.

The study of coal liquefaction under the typical process conditions of high-temperature and high-pressure requires relatively massive equipment. Such equipment has a high heat capacity and is therefore slow to heat up and cool down. This makes a kinetic study at very low conversion quite difficult. To avoid these problems, a special Short Contact Time Batch Reactor (SCTBR) (1-3) was devised which allows the heat up of the process stream to reaction temperature in less than 1 second. The removal and quenching of the reaction products occurs in a similar time period. This paper presents the results of coal liquefaction kinetic experiments with Illinois #6 coal in this novel equipment.

EXPERIMENTAL

Apparatus and Operation. The reactor system, which has been described previously (1-3), is shown in Figure 1. The reactor itself is constructed of 3/4" stainless steel tubing of approximately 12" in length with a wall thickness of approximately 0.433". The preheater and precooler consist of 21 feet of coiled stainless steel tubing with a wall thickness of 0.035".

In operation, both the empty preheater and the reactor are immersed in a sand bath and brought up to the desired reaction temperature prior to the start of the liquefaction reaction. Using high pressure gas, the reaction mixture is driven into the reactor from a small blow case through the preheater. The temperature of the reactants (ca. 30 ml), initially at ambient temperature, approaches the desired reaction temperature to within 5 - 8 °C in approximately 0.3 sec. It reaches the full reaction temperature within 30 seconds. The temperature in the reactor remains quite constant (within ± 2 °C) throughout the liquefaction experiment. The rapid heat up and stable temperature profile are due to both the small quantity of the reaction mixture relative to the massive reactor and the turbulent flow of the reactants through the preheater.

The liquefaction mixture in the reactor is agitated by gas bubbles introduced from the bottom of the reactor. The degree of agitation is controlled by both regulating the exit gas flow rate from the top of the reactor and the configuration of the gas orifices. A small water cooled condenser is situated above the reactor with a disengaging space above it before the let-down valve to prevent the loss of volatile products from the system and to improve operability.

At a preselected time, the contents of the reactor are driven from the reactor through a precooler into the product receiver with high pressure gas. The total contents of the reactor are not recovered in the receiver (usually only 80 - 90 %) due to the wetting of the walls of the system, and the conversion and other kinetic data are determined by analysis of aliquots.

Product Work-up. The liquefaction products were separated into liquid and partially reacted solids by filtration through a sintered glass filter, and the liquids and solids were analyzed separately. The liquids were bottled and nitrogen blanketed for subsequent analysis. The solids were washed with fresh tetralin (to remove residual coal liquids) and then methylene chloride to remove any tetralin remaining. The washed solids were dried in a vacuum oven at 105°C for 48 hours.

Determination of Percent Conversion. During coal liquefaction, the mineral matter (which is insoluble in tetralin) remains with the partially reacted solid coal and does not go into the liquid (4). When the liquefaction is carried out without catalyst, this provides a means of measuring the conversion of the coal to liquid product by the ash content of the solid residue. The ash content is determined by TGA, and provides the conversion as shown in Eq. 1:

$$Conversion = (1 - \frac{X_0}{X}) \times 100 \quad (wt\%) \qquad (1)$$

In Eq. 1, X_o and X are the ash contents of a control sample and the coal liquefaction residue, respectively. The control sample is the original coal, which is processed exactly as a liquefaction residue except at room temperature. Multiple experiments have shown that the ash content can be determined by TGA with a standard deviation of 0.1%.

When the liquefaction is carried out in the presence of an inorganic catalyst, the conversion calculation must include an ash value corrected for the ash derived from the catalyst.

Catalysts Used. Sulfided molybdenum naphthenate has been the principal liquefaction catalyst used to date. This catalyst has been prepared by dissolving molybdenum naphthenate in tetralin and reacting the solution with methyl disulfide. That this catalyst is only active for liquefaction in the presence of hydrogen is shown in Table 1. Without sulfidation, the molybdenum naphthenate itself is inactive, as is the sulfiding agent.

Table 1 Catalysis of coal liquefaction by molybdenum naphthenate (Illinois #6; 8 of T/C; 390 C; 5 min.)

molybdenum naphthenate g	methyl disulfide g	Mo wt%	Conversion wt%
under 1000 psig nitrogen gas			
0.00	0.00	0.00%	28.1%
0.00	1.03	0.00%	27.5%
0.59	0.00	0.85%	28.0%
0.62	1.07	0.86%	28.4%
under 1000 psig hydrogen gas			
0.00	0.00	0.00%	33.8%
0.00	1.03	0.00%	32.3%
0.61	0.00	0.87%	33.5%
0.61	1.15	0.87%	41.8%

TGA Methods. A typical TG curve and its differential (DTG) for unreacted Illinois #6 bituminous coal at 10°C/min heating rate and 100 ml/min nitrogen gas sweep are shown in Figure 2. The TG curve (solid line) shows a small drop below 200 °C due to loss of moisture. In the neighborhood of 350 - 400 °C, a large loss of weight is observed. When the weight loss has leveled off at 950°C, the temperature is held for 7 minutes. This loss in weight is designated as "Volatile Matter". After oxygen is then introduced, another large drop in weight, designated "Fixed Carbon", follows to a steady weight representing the "Ash Content". The Volatile Matter, Fixed Carbon, and ash are important parameters to follow during the liquefaction process.

The DTG curve is also of interest since it clearly shows the volatilization processes occurring during the TG analysis. This DTG curve changes very significantly during the liquefaction process as shown in Figure 3.

RESULTS AND DISCUSSION

Figure 4 shows conversion vs time curves for Illinois # 6 coal in nitrogen and in hydrogen in the absence of a catalyst at 390°C. The initial conversion in the first minute is due to the physical extraction of a soluble fraction of the coal into the tetralin, which occurs in both a nitrogen and a hydrogen environment. This is followed by an induction period and then the slow conversion of the coal structure to liquid product. As the liquefaction temperature is increased (Figure 5), the amount of extraction increases and the induction period becomes shorter. In the absence of a catalyst, however, increases in temperature above about 408°C result in little increase in soluble product. The reason for this can be found in the TG analysis of the residue. The rate of removal of Volatile Matter increases steadily as the temperature increases (Figure 6a), regardless of whether the system is in hydrogen or nitrogen. However the Fixed Carbon increases at a very rapid rate above 408 °C (Figure 6b). This is the retrograde process which results in low liquid yields and the formation of tar and coke.

Figure 7 summarizes the conversion vs time for liquefaction of Illinois #6 in

hydrogen at 390°C in the presence of about 1% sulfided molybdenum naphthenate in tetralin. A rapid extraction is again observed in the first minute, followed by the induction period. The subsequent conversion is faster than is observed for the uncatalyzed liquefaction. Figure 8 shows the content of Fixed Carbon in the residue as a function of time. The retrograde process is very significantly reduced. The precursors to the retrograde reactions are apparently being hydrogenated in the presence of hydrogen and the catalyst.

SUMMARY AND CONCLUSIONS

1). In the first minute of the liquefaction process, in the presence or absence of a catalyst, and in hydrogen or nitrogen, there is a very rapid conversion to liquid product (approximately 25 - 30 % for Illinois #6 coal) due to the extraction of tetralin-soluble material from the coal into the liquid phase.

2). The initial conversion is followed by an induction period and then a slower conversion, presumably of the coal structure itself, which represents the breaking of chemical bonds. This is more rapid in the presence of a sulfided molybdenum naphthenate catalyst.

3). At higher temperatures, the degree of extraction is higher and the induction period shorter. However, in the absence of hydrogen and a catalyst, the breakdown of the coal structure into coal liquid is offset by the build up of retrograde products.

ACKNOWLEDGEMENTS

The support of this work by the Department of Energy under DE22-93PC93205 is gratefully acknowledged. The use of Argonne Premium Coal Samples provided by Dr Karl Vorres is also acknowledged.

REFERENCES

1. Huang, H., Calkins, W.H., Klein, M.T., *Prepr. Pap.-Am. Chem. Soc, Div. Fuel Chem.* 1994, 39 (2) 581.
2. Huang, H., Calkins, W.H., and Klein, M.T. *Energy & Fuels* 1994, **8**, 1304-1309.
3. Huang, H., Fake, D.M., Calkins, W.H., and Klein, M.T. *Energy & Fuels* 1994, **8**, 1310-1315.
4. Calkins, W.H., Huang, H., Klein, M.T. *Proceedings of 1994 Pittsburgh Coal Conference* pp 475-480.
5. Vorres, K.S. 'User's Handbook for the Argonne Premium Coal Sample Program' *ANL/PCSP-93/1.*

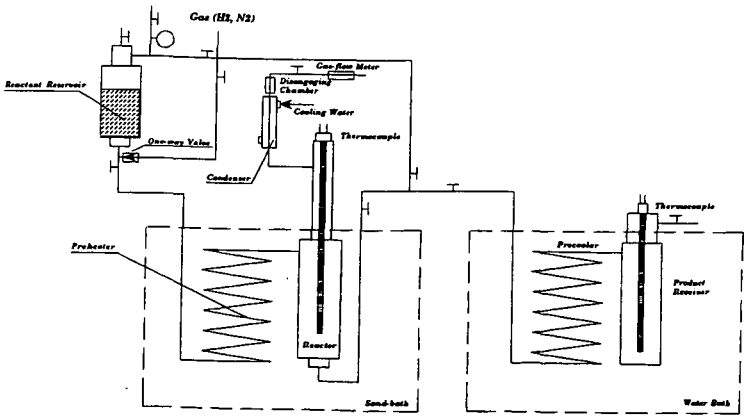

Figure 1 SCTBR system for studying direct coal liquefaction from the initial stages

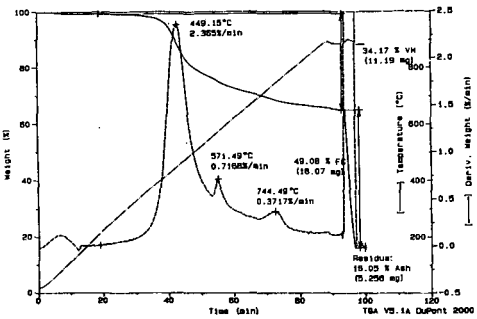

Figure 2 A TG scan on the Illinois #6 coal at 10 °C/min

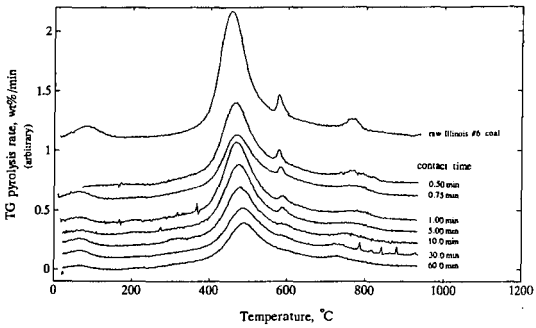

Figure 3 DTG profiles for residues of the Illinois #6 coal after liquefaction in tetralin at the selected contact times (TG scan at 10 °C/min; Liquefaction run at 390 °C under 1000 psig N_2)

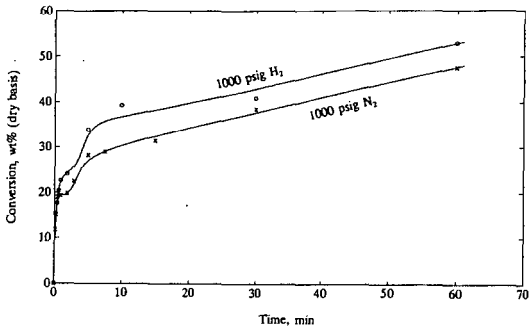

Figure 4 Liquefaction conversion of the Illinois #6 coal at 390 °C

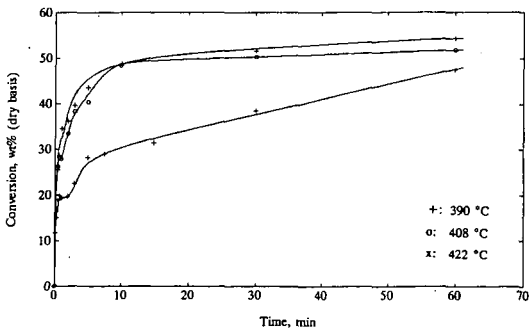

Figure 5 Kinetics of the Illinois #6 coal liquefaction in tetralin under 1000 psig N_2

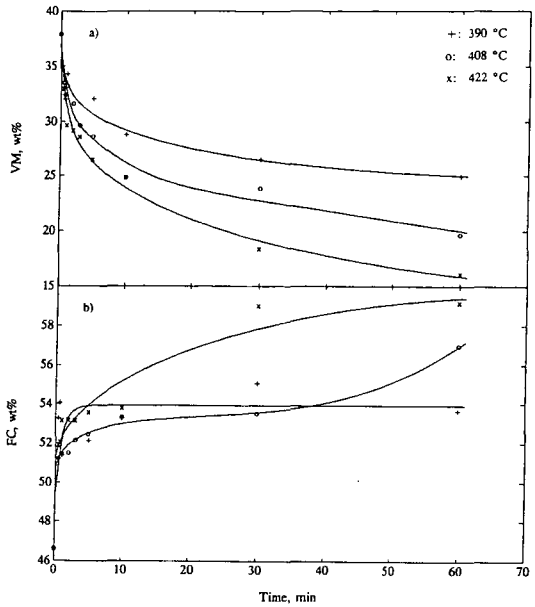

Figure 6 VM (volatile matter) (a) and FC (fixed carbon) (b) in liquefaction residues determined by TGA (Liquefaction: Illinois #6 coal, T:C = 8:1, 1000 psig N_2; TGA: 100 cm^3(STP)/min N_2, 100 °C/min)

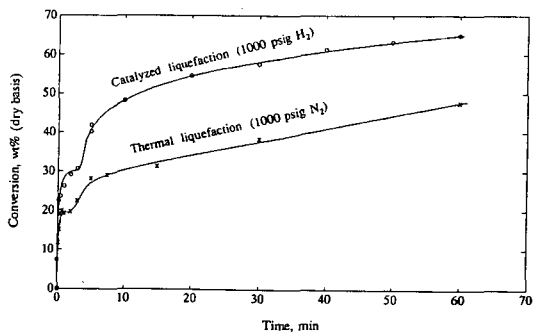

Figure 7 Conversion of the Illinois #6 coal in the thermal and catalyzed liquefaction at 390 °C (Catalyst: ca. 0.9 wt% molybdenum naphthenate; T:C = 8:1)

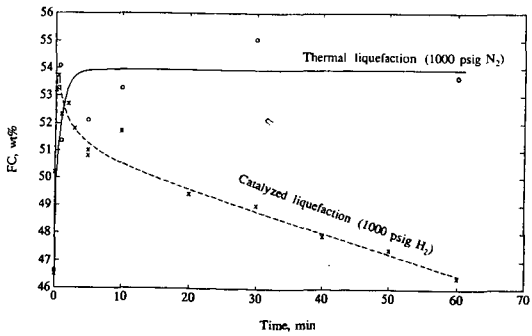

Figure 8 FC (fixed carbon) in liquefaction residues determined by TGA (Liquefaction: Illinois #6 coal, 390 °C, T:C = 8:1; TG scan: 100 cm^3(STP)/min N_2, 100 °C/min)

NEW APPROACH TO IMMOBILIZATION OF COAL-MODEL COMPOUNDS ON SILICA USING A CALCIUM CARBOXYLATE LINKAGE

Sreekumar Ramakrishnan
Robert D. Guthrie
Department of Chemistry
University of Kentucky
Lexington, KY 40506

Phillip F. Britt
A. C. Buchanan, III
Oak Ridge National Laboratory
P. O. Box 2008
Oak Ridge, TN, 37381

Burtron H. Davis
Kentucky Center for Applied Energy Research
3572 Iron Works Pike, Lexington, KY 40511

Keywords: hydroliquefaction, surface-attached, H/D exchange

INTRODUCTION

In an earlier report,[1] we described our efforts to study the hydrothermolysis of surface-immobilized coal model compounds by attaching 1-(4'-hydroxyphenyl)-2-phenylethane to the surface of fumed silica via a Si-OAr linkage using procedures developed by Buchanan, Poutsma and coworkers[2] and heating the resultant material (**SiO-DPE**) under D_2 pressure. These studies were complicated by the fact that phenolic compounds present in equilibrium with ether-linked materials react with thermolytically-produced radicals to form phenoxyl radicals which then react with D_2 to give DOAr compounds. These provide D for ring-deuteration via a silica-catalyzed process which is restricted to hydroxyl-substituted aromatic rings. It is believed that the free phenol present in **SiO-DPE** experiments is due to small amounts of water which is known to be generated continually through the formation of siloxane bonds as silica is heated. In simple thermolysis experiments carried out in vacuum,[2] any water produced is driven out of the reaction zone. In our experiments, however, the reaction proceeds under D_2 pressure (14 MPa) and reaction products are necessarily available for secondary processes.

Coincident with this process, the benzylic radicals produced under these conditions react with D_2 to form D atoms. The D atoms react both with gas-phase reaction products and surface-attached substrates. We found that much of the behavior of the surface-attached material was similar to that of free diphenylethane, **DPE**, under these conditions,[3] particularly that the differences between thermolysis and hydrothermolysis were preserved. Also, the increased tendency to rearrangement and cyclization for surface-attached radicals was still observed under D_2. Because of the phenol-specific exchange process we could follow the D-atom-induced aromatic substitution only in the non-phenolic rings. We could also demonstrate that the D-atom induced part of H-D exchange is greater for gas-phase than for surface-bound materials.

Despite the successes noted, we sought to find a method for constructing links between silica and organic materials which might better survive hydroliquefaction conditions. Attachment of long-chain aliphatic carboxylic acids to silica through Mg^{++} or Ca^{++} ions is a patented method for silica flotation[4] which we thought might be adapted to our purposes. This preprint is a preliminary report on the preparation, thermolysis and hydrothermolysis of materials believed to have the general structure, $SiO^- Ca^{++} {}^-O_2CAr$.

EXPERIMENTAL

Preparation of Ca^{++}-Linked Arene Carboxylates. Aqueous $Ca(OH)_2$ (ca. 0.02 M) which had been prepared with deaerated, deionized water was mixed with sufficient fumed silica (Cab-O-Sil M5 Cabot Corporation) to provide a coverage of 0.35 to 0.50 mmoles/g. The aqueous slurry was filtered under an argon blanket and washed with deaerated deionized water. When the filter cake was partially dry, it was remixed with acetonitrile in the filter funnel and the solvent pulled through the filter. This process was repeated and the cake sucked dry under argon. The base-treated silica was then stirred with an acetonitrile

solution of the appropriate carboxylic acid and filtered. The resultant solid was stirred with additional acetonitrile and filtered. The acetonitrile washing was repeated and the coated silica dried in an oven at 110 °C. Evaporation of the combined acetonitrile washings showed that most of the acid was removed by the base-treated silica. In the case of 4-(2'-(4''-methylphenyl)ethyl)benzoic acid, the acid was not completely soluble in acetonitrile and it was necessary to add some methanol. Scanning electron microscopic studies on the **DPECO$_2^-$**-coated material indicated that with the 200 Å resolution of the equipment used, calcium was evenly distributed on the surface.

Synthesis of 4-(2'-Phenylethyl)benzoic Acid. A modified version of a literature procedure[5] was used. Silver nitrate (2.62 g, 15.4 mmole) in 60 mL water was mixed with sodium hydroxide (1.25 g, 31.2 mmole) in 60 mL water. To this solution was added *trans-p*-stilbene carboxaldehyde, Aldrich Chemical Co. (2.00 g, 9.6 mmole). This was refluxed for 16 h. The reaction mixture was cooled to room temperature and neutralized with concentrated nitric acid. The resultant mixture was extracted with a solvent mixture of equal amounts of CH_2Cl_2 and ethyl acetate. The solvent was removed by rotary evaporation to give 2.11 g of product which was 92 % *trans-p*-stilbene carboxylic acid (86 %). Purification by base extraction and reacidification gave pale yellow crystals, mp 222-223 °C, ^{1}H NMR ($CDCl_3$) δ 8.10 (d, 2 H), 7.5 - 7.7 (m, 4 H), 7.1 - 7.4 (m, 5 H). This material (0.475 g, 2.12 mmole) was dissolved in a mixture of 40 mL CH_2Cl_2 and 20 mL methanol. Palladium (5 %) on carbon (200 mg) was added and the mixture shaken under 35 psi H_2 at 25 °C in a Parr apparatus for 24 h. The catalyst was removed by filtration and the solvent removed by rotary evaporation. The product was recrystallized from aqueous ethanol to give a first crop of 280 mg, 58 %, of the desired product, mp 148-150 °C. ^{1}H NMR ($CDCl_3$) δ 8.03 (d, 2 H), 7.1 - 7.3 (m, 7 H), 2.92 - 3.04 (m, 4 H). MS, 226, 91. Trimethylsilylation of this material and GC analysis showed it to be >99% pure.

Synthesis of 4-(2'-(4''-Methylphenyl)ethyl)benzoic Acid. This material was synthesized by a Wittig reaction following a literature procedure[6] using α-bromo-*p*-xylene and 4-carboxybenzaldehyde producing a mixture of *cis*- and *trans*-4-methyl-4'-carboxystilbene which is hydrogenated using the procedure described above for stilbene carboxylic acid. This gives the desired product as white crystals, mp 201-202 °C. ^{1}H NMR ($CDCl_3$) δ 7.95 (d, 2 H), 7.1 - 7.16 (m, 4 H), 2.90 - 3.03 (m, 4 H), 2.28 (s, 3 H). Trimethylsilylation of this material and GC analysis showed it to be >99% pure.

General Procedure for Reactions. Hydrogenations of coated solids were carried out in glass tubes with capillary openings in a manner essentially identical to that described earlier[1] for **SiO-Ar** type materials. Volatile products were pumped out and collected in a liquid N_2 trap and materials remaining on the surface were recovered by hydrolysis of the silica and trimethylsilylation of the carboxylic acids obtained. Deuterium analysis was carried out by gas chromatography/mass spectrometry (GC/MS).

RESULTS AND DISCUSSION

Product distribution for the volatile products of the thermolysis of Ca^{++}-immobilized 4-(2'-phenylethyl)benzoate, **SiO$^-$ Ca^{++} $^-$O$_2$CDPE**, is given in Table I. The distribution of products in the residual solid is given in Table II.

Table I. Distribution[a] of Volatile Products from Thermolysis of **SiO$^-$ Ca^{++} $^-$O$_2$CDPE** under D_2 and under N_2.

	Time(N_2 or D_2)			
	10 min (D_2)	30 min (D_2)	50 min (D_2)	30 min (N_2)
PhMe	<1%	2.8	5.7	1.1
PhEt	<1%	3.3	4.2	ca. 0.4
DPM	<1%	1.2	1.0	ca. 0.5
1,1-DPE	<1%	1.5	2.2	ca. 1
DPE	78.6	65.7	62.7	94.7
STB	2.6	2.8	2.4	2.3

[a] Distribution is given as approximate weight % of total volatiles. The totals are less than

100 % due to the presence of an unidentified product which appears to be an oxidation product of **DPE**. Some benzene was produced in the reaction but analysis was unreliable in this set of runs. **DPM** = diphenylmethane, **STB** = stilbene.

Table II. Distribution[a] of Materials Remaining on the Surface after Thermolysis of **SiO⁻ Ca⁺⁺ ⁻O₂CDPE** under D_2 and under N_2.

	Time(N_2 or D_2)			
	10 min (D_2)	30 min (D_2)	50 min (D_2)	30 min (N_2)
$PhCO_2^-$	1.1	1.4	1.3	0.7
$MePhCO_2^-$	1.4	3.1	4.2	1.7
$EtPhCO_2^-$	<0.2	0.5	0.7	<0.2
$DPMCO_2^-$	0.6	1.0	1.1	0.6
1,1-$DPECO_2^-$	1.8	3.8	5.7	2.7
$DPECO_2^-$	91.5	86.9	83.9	84.1
$STBCO_2^-$	3.3	2.5	0.4	3.1

[a] Values given are approximate weight %s of materials recovered from hydrolysis of residual solids after trimethylsilylation.

It is clear from these data that the major volatile product of thermolysis, both under N_2 and under D_2 is **DPE**. This result contrasts with the thermolysis of **SiO-DPE** where **DPE** represents a relatively minor fraction of the volatile products (of the order of 10%). This suggests the possibility that the **DPE** might be arising by a decarboxylation process.

To determine whether the **DPE** formed in this reaction is the result of decarboxylation or recombination of benzyl radicals formed from fragmentation, we have also prepared 4-(2'-(4''-methylphenyl)ethyl)benzoic acid, **$HO_2CDPEMe$**, and attached it to silica in the same manner to give **SiO⁻ ⁺⁺Ca ⁻O₂DPEMe**. Thermolysis of **SiO⁻ ⁺⁺Ca ⁻O₂DPEMe** both in the presence and absence of D_2 gives 1-phenyl-2-(4'-methylphenyl)ethane, **DPEMe**, as the major volatile product. A small amount of 1,2-di(4'-methylphenyl)ethane was present, but this was formed in less than 10% of the amount of **DPEMe**. This clearly demonstrates that decarboxylation is a major reaction path, at least in the initial stages of the reaction. The fact that **DPE** remains the major product when **SiO⁻ ⁺⁺Ca ⁻O₂DPE** is subjected to thermolysis under N_2 suggests that protons rather than hydrogen atoms are involved in its production. A reasonable path is that shown in Scheme I wherein the silica surface (directly or indirectly) supplies a proton to the *ipso*-position of the attached substrate, releasing **DPE**. As this reaction proceeds, the surface should increase in basicity and, possibly, the release of **DPE** will decrease. The increase in other products relative to **DPE** supports this hypothesis.

Scheme I

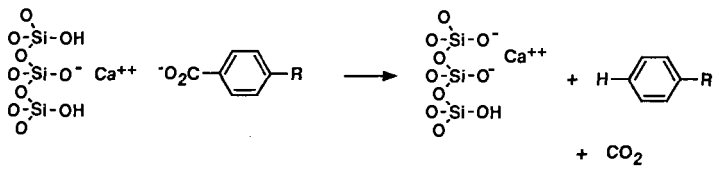

The remainder of the products are analogous to those observed in the thermolysis and hydrothermolysis of **SiO-DPE**. Toluene, **PhMe**, results from thermolysis of the central bond in the DPE moiety to give benzyl radicals which react either with D_2 or with residual $-CH_2CH_2-$ groups to lead to PhCH=CHPh, stilbene (**STB**), or $^-O_2CC_6H_4CH{=}CHPh$, **$STB\text{-}CO_2^-$**. D atoms produced from the reaction $R^\cdot + D_2 \rightarrow RD + D^\cdot$ react to give "hydrocracking" products via $D^\cdot + Ar\text{-}R \rightarrow Ar\text{-}D + R^\cdot$ and also H/D exchange via $D^\cdot + Ar\text{-}H \rightarrow Ar\text{-}D + H^\cdot$. Compared to the **SiO-DPE** case, there is more hydrocracking

Table III. Deuterium Distribution in Products from Thermolysis of **Ca^{++} $^{-}O_2CDPE$** under D_2 at 420 °C.

Product (time - min)	d_0	d_1	d_2	d_3	d_4	d_5	d_6
PhMe (10)	76.0	23.0					
PhMe (30)	24.9	31.5	23.8	11.4	6.1	2.1	
PhMe (50)	18.6	26.6	29.3	8.1[a]	10.5[a]	6.9[a]	
EtPh (10) → $PhCH_2^+$	44 58.1	56 33.8	 8.1				
EtPh (30) → $PhCH_2^+$	12.8 29.9	24.1 32.8	21.8 20.8	15.7 10.2	11.7 4.4	8.8 1.6	5.0 0.3
EtPh (50) → $PhCH_2^+$	8.0 19.5	18.5 30.5	22.5 25.0	19.1 15.0	14.6 7.1	10.7 2.6	6.5 0.3
DPM (30)	18.1	20.5	20.0	15.9	10.6	6.6	3.8
DPM (50)	14.7	18.2	20.7	18.9	13.9	8.9	4.6
1,1-DPE(30)	13.8	14.6	26.5	24.8	16.1	7.9	4.2
1,1-DPE(50)	2.1	7.9	19.3	26.6	22.5	6.3	2.8
DPE (10) → $PhCH_2^+$	13.5 45.7	45.1 36.8	27.8 13.6	9.6 3.1	2.5 0.6	0.8 0.2	
DPE (30) → $PhCH_2^+$	5.8 26.4	16.8 31.9	27.9 24.6	24.6 12.1	14.7 3.7	6.5 0.9	2.6 0.2
DPE (50) → $PhCH_2^+$	3.2 17.9	8.6 25.1	20.1 23.0	26.2 15.4	21.7 6.4	12.4 1.7	5.4 0.3
$PhCO_2^-$ (10)	43.1	30.2	19.5	6.2	0.9		
$PhCO_2^-$ (30)	16.3	34.2	34.0	12.7	2.2	0.5	
$PhCO_2^-$ (50)	9.1	27.1	41.7	18.6	3.6	0.9	
$MePhCO_2^-$ (10)	44.6	34.3	14.0	1.8	1.7		
$MePhCO_2^-$ (30)	12.9	32.1	32.4	15.5	4.9		
$MePhCO_2^-$ (50)	7.2	22.3	34.9	24.1	8.8	2.2	0.5
$EtPhCO_2^-$ (10)	41.5	33.8	15.2	6.1	3.4		
$EtPhCO_2^-$ (30)	13.1	30.8	31.2	17.1	6.8	0.9	
$EtPhCO_2^-$ (50)	4.4	20.4	32.4	26.0	12.5	4.2	
1,1-$DPECO_2^-$ (10)	48.3	33.2	12.7	4.2	1.4		
1,1-$DPECO_2^-$ (30)	15.7	30.8	31.1	16.3	6.1		
1,1-$DPECO_2^-$ (50)	5.2	18.9	32.8	25.2	12.1	4.5	1.4
$DPECO_2^-$ (10) → $PhCH_2^+$	49.5 87.3	35.0 11.3	11.9 1.0	2.7 0.8	0.6		
$DPECO_2^-$ (30) → $PhCH_2^+$	12.8 65.1	30.2 27.9	32.2 5.9	17.0 0.8	5.6 0.2	1.6	0.4
$DPECO_2^-$ (50) → $PhCH_2^+$	3.5 51.2	18.1 35.2	32.0 11.1	27.3 1.9	13.3 0.3	4.4 0.1	1.2

Notes for Table III: [a] Errors accumulate in calculation for toluene at high D content due to large P-1 fragment.

of this substrate and, most strikingly, a marked increase in the amount of rearrangement

of the surface-bound substrate in that 1-phenyl-1(4'carboxyphenyl)ethane, **1,1-DPECO$_2$H**, has become the major reaction product remaining on the surface. The tendency to increased rearrangement of surface-bound radicals has been discussed earlier.[1]

For the runs carried out under D_2, the deuterium distribution of the major products is given in Table III. Many of the features of these data are similar to those noted for hydrothermolysis of **SiO-DPE**. Gas-phase products continue to undergo exchange after separation from the surface so that initially formed **PhMe** (10 min) contains 0.23 atom of D per molecule, more than present in the PhCH$_2$ part of surface-bound substrate, whereas after 30 min, the D content of **PhMe** averages 1.5 atoms of D per molecule while PhCH$_2$ in surface-bound substrate averages only 0.43 atoms. It is interesting that the PhCH$_2$ part of surface-bound **DPECO$_2^-$** appears to be protected from exchange relative to gas-phase molecules, showing 0.13, 0.43 and 0.65 atoms of D per molecule in the three runs. These contrast with values of 0.50, 1.32 and 1.69 in the PhCH$_2$ fragment from **PhEt** and 0.77, 1.38, and 1.53 in this fragment from **DPE**. Thus, PhCH$_2$ moieties on the surface appear to be less susceptible to D-atom attack by at least a factor of 3 compared with PhCH$_2$ parts of free molecules. In surface-bound **DPECO$_2^-$** exchange in the carboxy-substituted benzyl group exceeds that in the unsubstituted benzyl moiety by a factor of three to four. This could be due either to preference for D-atom attack on the carboxy-substituted ring or to some special mechanism for exchange of carboxy-substituted aromatics. We do not have sufficient evidence to distinguish these alternatives at present.

SUMMARY

A new method for surface attachment has been devised to attach arene carboxylic acids to fumed silica via a SiO$^-$ Ca^{++} $^-$O$_2$Ar linkage. This has been used to attach coal-model compounds such as **DPECO$_2$H** to the surface and the resultant **SiO$^-$ Ca^{++} $^-$O$_2$DPE** has been subjected to thermolysis and hydrothermolysis. Part of the material undergoes decarboxylation to give **DPE** and part reacts via the usual homolytic pathways. Radical rearrangement leads to the main surface-retained product and surface-attached molecules are partially protected from D-atom induced exchange. Exchange in carboxy-substituted rings is favored and mechanistic reasons for this are under investigation.

ACKNOWLEDGEMENTS

The authors gratefully acknowledge support from the Department of Energy, Office of Basic Energy Sciences, Division of Chemical Sciences, under Contract No. DE-AC05-840R21400 with Martin Marietta Energy Systems, Inc. (PFB and ACB) and from the United States Department of Energy, Pittsburgh, for a grant, DE-FG22-91-PC91291 (RDG, SR and BHD).

REFERENCES

1. Guthrie, R. D.; Ramakrishnan, S.; Britt, P. F.; Buchanan, III., A. C.; Davis, B. H. Prepr.,Div. Fuel Chem., Am. Chem. Soc. **1994**, 39, 668.

2. Buchanan, A. C., III, Dunstan, T. D. J.; Douglas, E. C.; Poutsma, M. L. J. Am. Chem. Soc. **1986**, 108, 7703-7715.

3. (a) Guthrie, R. D.; Shi, B.; Sharipov, R.; Davis, B. ACS Div. Fuel Chem. Prepr., **1993**, 38, 526-533. (b) Rajagopal, V.; Guthrie, R. D.; Shi, B.; Davis, B. H. ACS Div. Fuel Chem. Prepr., **1993**, 38, 1114. (c) Ramakrishnan, S.; Guthrie, R. D.; Shi, B.; Davis, B. H. ACS Div. Fuel Chem. Prepr., **1993**, 38, 1122. (d) Guthrie, R. D.; Shi, B.; Rajagopal, V.; Ramakrishnan, S.; Davis, B. H., J. Org. Chem. **1994**, 46, 7426-7432.

4. Iler, R. K. "The Chemistry of Silica" Wiley-Interscience, New York, 1979, p. 688.

5. Campaigne, E.; Lesuer, W. M. in *Organic Syntheses*, Coll. Vol IV, N. Rabjohn, Ed., John Wiley and Sons, 1963, p 919.

6. Daniel, H.; LeCorre, M. Tetrahedron Letters **1987**, 28, 1165-1168.

IMPACT OF ORGANIC-MINERAL MATTER INTERACTIONS ON THERMAL REACTION PATHWAYS FOR COAL MODEL COMPOUNDS

A. C. Buchanan, III, Phillip F. Britt, and John A. Struss

Chemical and Analytical Sciences Division
Oak Ridge National Laboratory
P.O. Box 2008
Oak Ridge, Tennessee, 37831-6197

Key Words: Pyrolysis, mineral matter, model compounds

INTRODUCTION

Coal is a complex, heterogeneous solid that includes interdispersed mineral matter. However, knowledge of organic-mineral matter interactions is embryonic, and the impact of these interactions on coal pyrolysis and liquefaction is incomplete.[1] Clay minerals, for example, are known to be effective catalysts for organic reactions.[2] Furthermore, clays such as montmorillonite have been proposed to be key catalysts in the thermal alteration of lignin into vitrinite during the coalification process.[3] Recent studies by Hatcher and coworkers on the evolution of coalified woods using microscopy and NMR have led them to propose selective, acid-catalyzed, solid state reaction chemistry to account for retained structural integrity in the wood.[4] However, the chemical feasibility of such reactions in relevant solids is difficult to demonstrate. We have begun a model compound study to gain a better molecular level understanding of the effects *in the solid state* of organic-mineral matter interactions relevant to both coal formation and processing. To satisfy the need for model compounds that remain nonvolatile solids at temperatures ranging to 450°C, model compounds are employed that are chemically bound to the surface of a fumed silica (Si-O-C_{aryl} linkage).[5-9] The organic structures currently under investigation are phenethyl phenyl ether ($C_6H_5CH_2CH_2OC_6H_5$) derivatives, which serve as models for β-alkyl aryl ether units that are present in lignin and lignitic coals. The solid-state chemistry of these materials at 200-450°C in the presence of interdispersed acid catalysts such as small particle size silica-aluminas and montmorillonite clay will be reported. Our initial focus will be on defining the potential impact of these interactions on coal pyrolysis and liquefaction.

EXPERIMENTAL

The synthesis of the precursor phenol, *p*-$HOPhCH_2CH_2OPh$ (HOPPE), has been reported.[10] The *ortho*-methoxy derivative, *p*-$HOPhCH_2CH_2OPh$-*o*-OCH_3, was synthesized[11] by a similar route except the sodium salt of guaiacol, made from guaiacol and NaH in DMF, was used to alkylate the tosylate, *p*-$PhCH_2OPhCH_2CH_2OTs$,[10] in toluene. The benzyl protecting group was removed by hydrogenolysis with 10% Pd on carbon in CH_3CO_2H with 0.5% H_2SO_4. The phenols were purified to >99.8% (by GC) by elution through a silica column using toluene, followed by multiple recrystallizations from benzene/hexanes.

Detailed procedures for the synthesis of silica-attached diphenylalkanes have been previously described.[5-9] Briefly, the precursor phenols were covalently attached to the surface of a dried (200°C), nonporous silica (Cabosil M-5, Cabot Corp., 200 m^2g^{-1}, ca. 4.5 OH nm^{-2}) by a condensation reaction (225°C, 0.5 h) with the surface hydroxyl groups. For these substrates, unreacted phenol was removed by soxhlet extraction with benzene, rather than high temperature sublimation. The resulting immobilized model compounds are attached to the silica surface by a thermally robust Si-O-C_{aryl} linkage. Surface coverages (*ca.* 0.25 mmol g^{-1}) were determined by GC analysis using internal standards following a standard base hydrolysis assay.[5-9]

The silica-immobilized substrates were blended 1:1 with a dried, fumed silica-1% alumina (Aerosil MOX 170, Degussa, 170 m^2g^{-1}; 15 nm average particle size), silica-15% alumina (Aerosil COK 84, Degussa, 170 m^2g^{-1}), or montmorillonite clay (Montmorillonite K-10, Aldrich, 220-270 m^2g^{-1}, <1μ particle size).[5,11] Similar results were obtained when the solids were either dry mixed or when they were dispersed in benzene followed by solvent evaporation. Thermolyses were performed at 200-450°C (±1.5°C) in sealed tubes under vacuum in a temperature controlled, fluidized sandbath, or in a temperature controlled tube furnace as

previously described.[5-9] Volatile products were trapped in liquid nitrogen, and analyzed by GC and GC-MS with the use of internal calibration standards. Surface-attached products were liberated as phenols following digestion of the silica with aqueous base, silylated to the corresponding trimethylsilyl ethers, and analyzed as above.

RESULTS AND DISCUSSION

The two model compounds examined thus far are silica-immobilized phenethyl phenyl ether (≈$PhCH_2CH_2OPh$, or ≈PPE) and the corresponding methoxy derivative (≈$PhCH_2CH_2OPh$-*o*-OCH_3, or ≈PPE-*o*-OMe) as shown in Figure 1. These compounds are models for the β-aryl ether linkages present in lignin and low rank coals. ≈PPE-*o*-OMe contains the guaiacyl unit that is abundant in gymnospermous lignin.[12]

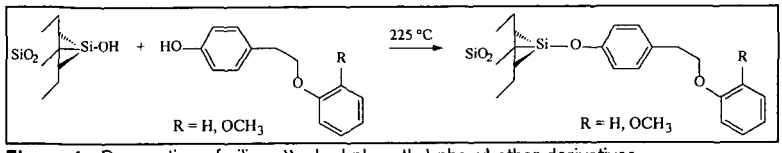

Figure 1. Preparation of silica-attached phenethyl phenyl ether derivatives.

A comparison of the principal products from the thermal and SiO_2-1% Al_2O_3-catalyzed reactions for ≈PPE at 400°C is shown in Figure 2. In the absence of the silica-alumina, the products are readily explained by a free-radical chain decomposition pathway.[11] In the presence of the small particle size silica-alumina, the rate of reaction for ≈PPE is increased by a factor of three (from 69 to 216 % h^{-1}), and the product distribution is substantially altered. At 400°C where the free-radical and acid-catalyzed reactions can compete, the product distribution is dominated by acid-catalyzed cracking products. A similar product distribution is obtained when the silica-alumina catalyzed reaction is performed at the lower temperature of 300°C, where the free-radical reaction is suppressed.

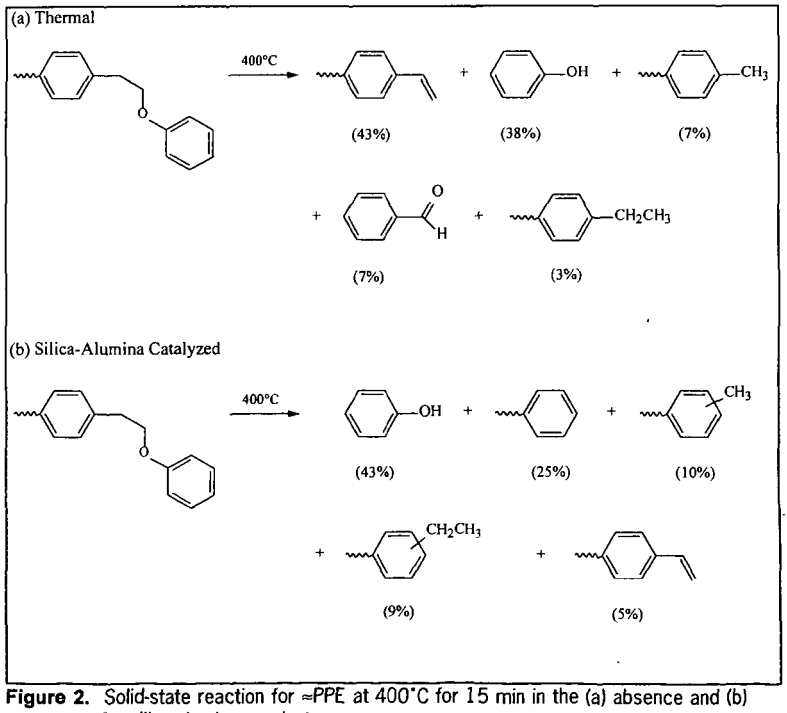

Figure 2. Solid-state reaction for ≈PPE at 400°C for 15 min in the (a) absence and (b) presence of a silica-alumina catalyst.

The acid-catalyzed products arise from two reaction pathways involving (1) initial protonation of the ether oxygen followed by cracking of the ether linkage to form phenol and silica-attached phenethyl cation (≈$PhCH_2CH_2^+$), or (2) protonation of the surface-attached phenyl ring followed by cleavage to produce ≈PhH (*ipso*-protonation) or ≈$PhCH_3$ (*ortho- or para*-protonation).[11] The silica-attached alkyl benzene products are found to be isomerized to *ortho*-, *meta*-, and *para*- isomers. Furthermore, we observe that alkenes are not stable under these conditions and represent minor products in the presence of the silica-alumina. The mass balances, which are excellent in the non-catalyzed runs (*ca.* 99%), are substantially diminished in the presence of silica-alumina. The mass balances are 79% at 400°C and 54% at 450°C principally as a consequence of coking reactions on the silica-alumina.

Similar behavior is observed for ≈PPE-*o*-OMe whose thermally induced, free-radical reaction (Figure 3) parallels that for ≈PPE, but whose rate is *ca.* seven times faster as a consequence of the *ortho*-methoxy substituent.[11] Again in the presence of the silica-alumina, acid-catalyzed reactions dominate and are analogous to those observed for ≈PPE. Protonation of the β-aryl ether, followed by cleavage produces guaiacol (*o*-methoxyphenol) as the major product at 300°C (46%). However, at 400°C (Figure 3) as a result of the higher reactivity of ≈PPE-*o*-OMe, conversions in excess of 85% are obtained in only 10 min. The dominant products at 400°C are the alkylated benzenes, ≈PhH, ≈$PhCH_3$, and ≈$PhCH_2CH_3$ with guaiacol accounting for only 13% of the products.[11] Isomerized (**1**) and alkylated (**2**) starting material are also detected. Coking of the aluminosilicate is again significant and mass balances are low (*ca.* 40%). Small amounts (2-5%) of catechol (*o*-$Ph(OH)_2$) are obtained at 275-400°C indicating that demethylation at the methoxy substituent is a minor reaction pathway under these conditions.

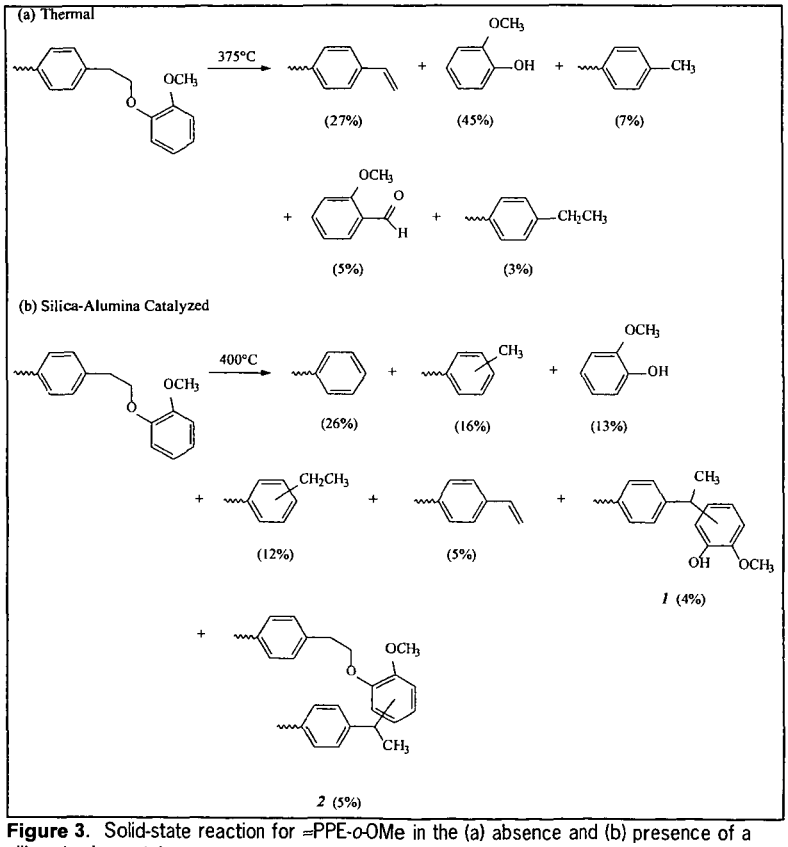

Figure 3. Solid-state reaction for ≈PPE-*o*-OMe in the (a) absence and (b) presence of a silica-alumina catalyst.

SUMMARY

The solid-state chemistry of silica-immobilized phenethyl phenyl ethers is being investigated in the presence of interdispersed silica-aluminas at temperatures (300-450°C) relevant to coal processing to gain a better understanding of the impact of related mineral matter on coal pyrolysis and liquefaction mechanisms. The results demonstrate the dramatic effect that silica-aluminas can have in altering the normal thermal reaction pathways for these models of ether linkages in lignin and low rank coals. At temperatures where free-radical reactions and acid-catalyzed reactions can compete, the products are dominated by acid-catalyzed cracking reaction pathways. The yields of alkenes are dramatically reduced, while new products from aromatic dealkylation, rearrangement, and alkylation are observed. Although the presence of silica-alumina assists in the cracking of the ether models, they also lead to the formation of nonvolatile, higher aromatic residues, i.e. coke. An investigation of the chemistry of these model compounds at low temperatures (*ca.* 150-200°C) in the presence of silica-aluminas, including montmorillonite, is also in progress to delineate the chemical transformations that can occur during lignin maturation.

ACKNOWLEDGEMENTS

This research was sponsored by the Division of Chemical Sciences, Office of Basic Energy Sciences, U.S. Department of Energy, under Contract No. DE-AC05-840R21400 with Martin Marietta Energy Systems, Inc. The authors also thank Ms. Kimberly Thomas for technical assistance.

REFERENCES

1. Buchanan, III, A. C.; Britt, P. F. *Prepr. Pap.-Am. Chem. Soc., Div. Fuel Chem.* **1994**, *39(1)*, 22.
2. Laszlo, P. *Science* **1987**, *235*, 1473.
3. Hayatsu, R.; McBeth, R. L.; Scott, R. G.; Botto, R. E.; Winans, R. E. *Org. Geochem.* **1984**, *6*, 463.
4. Hatcher, P. G.; Faulon, J.-L. *Prepr. Pap.-Am. Chem. Soc., Div. Fuel Chem.* **1994**, *39(1)*, 7.
5. Buchanan, III, A. C.; Dunstan, T. D. J.; Douglas, E. C.; Poutsma, M. L. *J. Am. Chem. Soc.* **1986**, *108*, 7703.
6. Britt, P. F.; Buchanan, III, A. C. *J. Org. Chem.* **1991**, *56*, 6132.
7. Buchanan, III, A. C.; Biggs, C. A. *J. Org. Chem.*, **1989**, *54*, 517.
8. Buchanan, III, A. C.; Britt, P. F.; Biggs, C. A. *Energy Fuels* **1990**, *4*, 415.
9. Buchanan, III, A. C.; Britt, P. F.; Thomas, K. B.; Biggs, C. A. *Energy Fuels* **1993**, *7*, 373.
10. Britt, P. F.; Buchanan, III, A. C.; Hitsman, V. H. *Prepr. Pap.-Am. Chem. Soc., Div. Fuel Chem.* **1991**, *36*, 529.
11. Britt, P. F.; Buchanan, III, A. C.; Thomas, K. B.; Lee, S.-K. *J. Anal. Appl. Pyrolysis* **1995**, in press.
12. Faulon, J.-P.; Hatcher, P. G. *Energy Fuels* **1994**, *8*, 402.

SODIUM METALCARBONYLATES AS POTENTIAL CATALYSTS FOR COAL LIQUEFACTION INVOLVING CO/H_2O OR H_2

C.E. Burgess, C.J.K. Hulston, P.J. Redlich, M. Marshall, and W.R. Jackson
Monash University, Department of Chemistry, Clayton, Victoria, AUSTRALIA

Keywords: sodium metalcarbonylate catalysts, coal liquefaction catalysis

INTRODUCTION

Alkalis such as $NaAlO_2$ and NaOH catalyze CO/H_2O/coal reactions at 350-400 °C [1-5]. Nickel, molybdenum, and cobalt are effective hydrogenation catalysts above 350 °C [6-13]. Previous work has shown that when using 1,2,3,4 -tetrahydroquinoline (THQ) [14-15] and molybdenum sulfide catalyst, individually or together, relatively high conversions can be obtained [16]; by synthesizing a catalyst with THQ and molybdenum sulfide, a synergism was noted with a slight increase in conversion for a subbituminous coal [16]. A combination of transition metals and alkali catalysts, added as separate species to the coal, gives higher conversions than metal or alkali catalysts alone for no-solvent CO/H_2O and $CO/H_2/H_2O$ reactions[17-18], particularly for lower-rank Australian coals. We have synthesized catalyst precursors containing sodium and metal carbonylates to determine in the preliminary stages if the combined precursor would increase coal conversion compared to coal reactions without catalyst and other catalyst systems.

EXPERIMENTAL

Elemental analyses of the two coals used are listed in Table 1. The particle size of both coals are -60 mesh (-250 μm). Loy Yang ROM (run of mine) (LYROM) was obtained from the Loy Yang open cut in Australia, and Surat Basin (SSB) was obtained from the Surat Basin deposit in Australia.

Three methods were used to prepare the sodium metal carbonylates. The first method was used to prepare $NaHFe(CO)_4$ from $Fe(CO)_5$ and NaOH [19]. The reaction is such that all the $Fe(CO)_5$ is consumed and NaOH is in excess. For the preparation, 0.48 g of NaOH dissolved in 50 mL of deoxygenated water was added to an evacuated flask containing 0.75 g of $Fe(CO)_5$. The reactants were stirred for 24 h under argon. The compound of interest ($NaHFe(CO)_5$) was not isolated and the resulting aqueous mixture was loaded directly onto 10g of coal, stirred under vacuum for 1h, and the water evaporated under vacuum [17-18].

A similar method was used to prepare $NaCo(CO)_4$ [20] from $Co_2(CO)_8$ and NaOH (again in excess). For the preparation, 0.53 g of NaOH dissolved in 50 mL of deoxygenated water was added to an evacuated flask containing 0.60 g of $Co_2(CO)_8$. The reactants were stirred for 24 h under argon. The compound of interest ($NaCo(CO)_4$) was not isolated and the resulting aqueous mixture was loaded directly onto 10g of coal, stirred under vacuum for 1h, and the water evaporated under vacuum [17-18]. Since the catalyst of interest was not isolated, we refer to these mixtures as "catalyst mixtures."

A third method was used to prepare $NaCo(CO)_4$ not contaminated with NaOH [21-22]. (Increased coal conversions were noticed with the catalyst mixtures (Table 2), but it was not certain whether the increases were due to the carbonylate or to the excess NaOH in the catalyst mixture.) In this method, dry NaOH (1.8 g, excess) and $Co_2(CO)_8$ (1.6 g) were added to a flask in the absence of air. Dry tetrahydrofuran (THF) was added very slowly as the reactants can ebullate violently if THF is added quickly. The mixture was stirred for 2 h until a notable color change from deep orange to a pinkish-lavender occurred. The solid was filtered out, and the THF removed by vacuum distillation from the filtered solution. The $NaCo(CO)_4$ is not air-stable, so it was prepared under vacuum or argon then solubilized in deoxygenated water in a glove bag before being exposed to the air and loaded onto the coal. The coal/catalyst was stirred under vacuum for 1h, and the water evaporated under vacuum.

Several other catalyst precursors were used as comparisons to the precursors synthesized. The following reagent grade chemicals, all added from aqueous solution [17-18], were used as catalyst precursors: the alkalis sodium aluminate and sodium hydroxide (500 mmol Na/kg dry coal); cobalt (II) acetate and iron (II) acetate (300 mmol metal/kg dry coal); and combined ammonium heptamolybdate (100 mmol Mo/kg dry coal)/nickel (II) or cobalt (II) acetate (40 mmol /kg dry coal). The coal/catalyst was stirred under vacuum for 1h, and the water evaporated under vacuum. When combining the alkalis with the metal catalysts, the alkali was added after the metals unless otherwise noted (it was later found the order of addition caused changes in conversion with mixed catalyst systems).

The reaction took place in a 30 mL horizontal microautoclave as described in other publications [23]. One gram of treated coal was loaded into the reactor. For CO/H_2O reactions, 2.5 g of H_2O was added, and the reactor was pressurized to 3.0 MPa of CO (cold). For hydrogenation reactions, the reactor was pressurized to 6 MPa of hydrogen (cold). The reactors were heated in an ebullating sandbath to the required temperature (2 min to heat the reactor and held at temperature for 30 min).

The work-up procedure was as described previously [17-18, 24-25]. The reactors were vented and scraped out using dichloromethane (DCM). The water was removed from the products by Lundin distillation. The products were ultrasonicated for 10 min and filtered. The residues were dried at 105 °C under nitrogen for 2 h. The DCM was vacuum distilled from the DCM-solubles, and then Shell X4 (40-60 °C b.p. petroleum, mainly hexanes) was added for the extraction of the oil fraction. The product was ultrasonicated for at least 2 min, and the DCM-solubles/X4-insolubles (asphaltenes) were filtered out. Total conversion was calculated by (dry coal with catalyst - dry residue with catalyst)/coal (daf). The oil, gas, and water fraction (OGW) was determined by total conversion minus asphaltene fraction.

RESULTS

Table 2 contains the conversion data for Loy Yang run-of-mine (LYROM) coal for two sets of reaction conditions. The CO/H_2O reactions were all at 365 °C for 30 min. The conversion for this reaction condition of LYROM is 30%, mainly to OGW. Addition of the alkali catalysts gives significantly higher conversions, with sodium aluminate increasing conversion to 51% (45% OGW) and sodium hydroxide increasing conversion to 60% (53% OGW). Metal hydrogenation catalysts give much smaller increases in conversion. Iron increases the conversion to 36% (34% OGW) and cobalt to 42% (41% OGW). For the alkali catalyst and the metal catalyst acting together, the conversion (~50-55%) is similar to the conversion for the reaction when using the alkali alone. The sodium metalcarbonylate catalyst precursors were first tested by reacting sodium hydroxide with iron pentacarbonyl or dicobalt octacarbonyl and loading the mixture of the carbonylate and excess NaOH on to the coal. Increases in conversion were noted (to 55-63%), but the conversion was similar to that for sodium hydroxide alone (60%). Finally, sodium cobalt tetracarbonyl was used as catalyst, but the conversion is similar to that with cobalt alone (40%). The low conversion with sodium cobalt tetracarbonyl may be due to the non-alkaline form of the sodium.

Some of these catalyst combinations were also used in coal hydrogenation reactions with LYROM at 400 °C for 30 min. The conversion for this reaction condition of LYROM is 32%, mainly to OGW. With cobalt and alkali catalysts, the conversion is 71-77%, with 62-67% OGW. The metal carbonylate catalysts only give 41 to 48% conversion. On-going work in this laboratory has focused on the use of Ni/Mo metal catalysts with sodium aluminate [18]. The work has shown that the order of addition of the alkali and the metals, and the metal "promoter" of Mo, significantly affect the conversion. When the Ni/Mo is added first, conversion is about 75 %, 60% OGW. When sodium aluminate is added first, the conversion increases to 87% with 69% OGW. Co/Mo gives significantly lower conversions than Ni/Mo. It appears that sodium can greatly influence the reaction, but its effect depends on the form and amount of sodium added and the metal used as the hydrogenation catalyst.

Table 3 contains the conversion data for Surat Basin coal (SSB) for two sets of reaction conditions. The CO/H_2O reactions were at 365 °C for 30 min. The conversion for this reaction condition of SSB is 27%, mainly to OGW. Addition of sodium aluminate catalyst gave slightly higher conversions (to 36%, OGW). Cobalt alone did not increase conversion. However, the sodium aluminate and cobalt give a conversion only slightly lower than with the alkali alone (~33%), but with a decrease in asphaltene yield to 4%. Sodium cobalt tetracarbonyl (300 mmols/kg dry coal for each metal) gives a similar conversion to that for cobalt and sodium aluminate (33%). Although sodium aluminate does increase the conversion for the CO/H_2O reactions, the increase in conversion is much smaller for LYROM.

Some of these catalyst combinations were also used in coal hydrogenation reactions with SSB at 400 °C for 30 min. The conversion for this reaction condition using SSB (CS_2 was also in this reaction) is 25%, mainly to OGW. The sodium cobaltcarbonylate catalyst gives a conversion of 62%. For sodium aluminate and Ni/Mo (Ni/Mo loaded first), conversion is 51%, 37% OGW. When sodium aluminate was loaded first, the conversion decreases to 46% with 35% OGW.

DISCUSSION

For LYROM coal, the alkali catalysts containing sodium do significantly increase conversion for CO/H_2O reactions at 365 °C; adding metals to the alkalis for this reaction condition does not increase the conversion. Sodium cobalt tetracarbonyl does increase conversion compared to no catalyst, but the increase in conversion is about the same as only by the same amount as cobalt alone. For SSB coal, alkali catalysts are effective in increasing conversion, but not to the same extent as for LYROM coal. Cobalt/sodium aluminate and to a lesser extent the sodium cobalt carbonylate improve the oil yield compared to sodium aluminate.

However, for hydrogenation reactions at 400 °C, sodium has had varying effects on conversion depending on the coal used, hydrogenation catalyst metals used, the order of addition of catalyst, and the form of sodium added. On-going work in this laboratory has shown Ni/Mo combined with sodium aluminate also produces increased conversions, particularly when adding the sodium aluminate before the metals (conversion under similar reaction conditions is 87% on a DCM-soluble basis, with 69% yield of OGW) [18]. With LYROM, the sodium metalcarbonylates under these reaction conditions only increase conversion from the baseline condition about 10-15%,

whereas cobalt/alkali increase conversion by 40%. It is possible the sodium aluminate alters the coal surface of LYROM coal to increase dispersion of the Ni/Mo catalyst [18], and clearly a mixed sodium-metal compound may not affect the metal surface in the same way. However, the catalysts behave differently with SSB coal for hydrogenation at 400 °C for 30 min. Sodium cobalt tetracarbonyl does significantly increase the conversion under hydrogenation reaction conditions, the conversion being 61% with a OGW yield of 39%. Reactions of SSB coal with Ni/Mo and sodium aluminate give conversions around 50%. The order of addition of the alkali and metal catalysts does not alter the conversion significantly with SSB coal as it does with LYROM; yet a higher conversion is obtained when using the sodium cobalt tetracarbonylate than when using Ni/Mo/$NaAlO_2$ with SSB coal.

CONCLUSIONS

The use of sodium cobalt tetracarbonyl with LYROM coal does increase coal conversion from baseline conditions for both CO/H_2O reactions and hydrogenation reactions; but adding cobalt acetate and alkali as separate precursors gives much higher conversions. For SSB coal, sodium cobalt tetracarbonyl does increase conversion for hydrogenation reactions at 400 °C to a higher level than $NaAlO_2$/Ni/Mo. The differing effects of these catalysts when using different coals is not yet understood.

ACKNOWLEDGMENTS

We thank the National Science Foundation for a postdoctoral fellowship (to C.E.B.). This work is part of a collaborative program established by the New Energy and Industrial Technology Development Organization of Japan (NEDO) to promote efficient methods for the production of fluid fuels for power generation from coal, and we thank NEDO for financial support to W.R.J., P.J.R., and M.M.

REFERENCES

1. Del Bianco, A. and Girardi, *Fuel Proc. Tech.*, **23**, 205, (1989).
2. Fischer, F. and Schrader, H., *Brennst. Chem.*, **2**, 257, (1921) (*Chem. Abst.*, **15**, 3900, 1921).
3. Ross, D.S., Blessing, J.T., Nguyen, Q.C. and Hum, G.P., *Fuel*, **63**, 1206, (1984).
4. Lim, S.C., Jackson, W.R., and Marshall, M., submitted for publication in Fuel.
5. Hughes, C.P., Sridhar, T., Lim, S.C., Redlich, P.J., Jackson, W.R., and Larkins, F.P., *Fuel*, **72**, 205, (1993).
6. Derbyshire, F.J., *Catalysis in Coal Liquefaction*, IEA Coal Research, London, IEA CR/08, (1988).
7. Weller, S., *Energy & Fuels*, **8**, 415, (1994).
8. Derbyshire, F.J., Davis, A., Lin, R., Stansberry, P.G., and Terrer, M-T., *Fuel Proc. Tech.*, **12** (7), 127, (1986).
9. Anderson, R.R. and Bockrath, B.C., *Fuel*, **63**, 329, (1984).
10. Utz, B.R., Cugini, A.V., and Frommel, E.A., *Amer. Chem. Soc. Div. of Fuel Chem. Preprints*, **34** (4), 1423, (1989).
11. Cugini, A.V., Martello, D.V., Krastman, D., Baltrus, J.P., Ciocco, M.V., Frommel, E.F., and Holder, G.D., *Amer. Chem. Soc. Div. of Fuel Chem. Preprints*, **40** (2), 1423, (1995).
12. Cusumano, J.A., Dalla Betta, R.A. and Levy, R.B., *Catalysis in Coal Conversion*, Academic Press: New York, p. 155, (1978).
13. Song, C., Hanaoka, K. and Nomura, *Energy & Fuels*, **6**, 619, (1992).
14. Bockrath, B.C., in *Coal Science*, Gorbaty, M.L., Larsen, J.W., and Wender, I., Editors. Academic Press: New York. p. 65, (1983).
15. Derbyshire, F.J., Odoefer, G.A. and Whitehurst, D.D., *Fuel*, **60**, 201, (1981).
16. Burgess, C.E. and Schobert, H.H., *Fuel*, **70**, 392, (1991).
17. Hulston, C.K.J., Redlich, P.J., Jackson, W.R., Larkins, F.P., and Marshall, M., "Reactions of Coals of Different Ranks With CO/H_2 Mixtures of Varying Composition With and Without Sodium Aluminate", accepted for publication in Fuel, 1995.
18. Hulston, C.K.J., Redlich, P.J., Marshall, M., and Jackson, W.R., "Nickel Molybdate Catalysed Hydrogenation of Brown Coal Without Solvent or Added Sulphur," submitted to Fuel, 1995.
19. Sternberg, H.W., Markby, R., and Wender, I., *J. Am. Chem. Soc.*, **79**, 6116 (1957).
20. Wender, I., Sternberg, and Orchin, M. *J. Am. Chem. Soc.*, **74**, 1216 (1952).
21. Edgell, W.F. and Lyford IV, J. *Inorg. Chem.*, **9** (8) 1932 (1970).
22. Schroeder, N.C., Richardson Jr., J.W., Wang, S-L, Jacobson, R.A., and Angelici, R.J. *Organometallics*, **4**, 1226 (1985).
23. Hulston, C.K.J., Redlich, P.J., Jackson, W.R., Larkins, F.P., and Marshall, M., "The Effect of Tubular Reactor Orientation on Conversion of Coal to Liquid Products," submitted to Fuel, 1995.
24. Cassidy, P.J., Jackson, W.R., Larkins, F.P., Sakurovs, R.J. and Sutton, J.F., Fuel, 65, 374, (1986).
25. Jackson, W.R., Larkins, F.P., Thewlis, P. and Watkins, I., Fuel, 62, 606, (1983).

Table 1: Elemental and Ash Analyses for Coals

Coal	Rank	Elemental Analysis (wt % daf)					Atomic H/C Ratio[a]	Ash (wt% dry)
		C	H	N	S	O (by diff)		
LYROM[b]	lignite	70.7	4.91	0.7	0.51	23.2	0.86	0.5
SSB[c]	hvb[d]	81.0	6.08	1.8	0.56	10.5	0.9	9.8

[a] CO_2-free basis
[b] Loy Yang run-of-mine coal
[c] Surat Basin coal
[d] high volatile bituminous

Table 2: Conversion Data for Loy Yang brown coal (LYROM) Using Various Catalysts and Reaction Conditions

Coal	Metal Catalyst[a]	Alkali Catalyst[b]	Temp (°C)	Gas Atm.	Total Conv.[c]	Asph.[d]	OGW[e]
LYROM	none	none	365	CO/H_2O	30	0.6	29
	none	$NaAlO_2$	365	CO/H_2O	51	5.7	45
	none	NaOH	365	CO/H_2O	60	6.9	53
	Fe	none	365	CO/H_2O	36	1.9	34
	Co	none	365	CO/H_2O	42	1.0	41
	Fe	$NaAlO_2$	365	CO/H_2O	55	9.8	45
	Co	$NaAlO_2$	365	CO/H_2O	53	7.8	45
	Co	NaOH	365	CO/H_2O	54	6.5	48
	$NaHFe(CO)_4$[f]	--	365	CO/H_2O	55	6.7	48
	$NaCo(CO)_4$[f]	--	365	CO/H_2O	63	11.6	52
	$NaCo(CO)_4$[g]	--	365	CO/H_2O	40	0.1	40
	none[h]	none	400	H_2	32	2	30
	Co	$NaAlO_2$	400	H_2	71	8.5	62
	Co	NaOH	400	H_2	77	9.8	67
	$NaHFe(CO)_4$[f]	--	400	H_2	48	6.6	41
	$NaCo(CO)_4$[g]	--	400	H_2	41	0.1	41
	Ni/Mo[i]	$NaAlO_2$	400	H_2	87	18	69
	Ni/Mo[j]	$NaAlO_2$	400	H_2	75	15	60
	Co/Mo[i]	$NaAlO_2$	400	H_2	48	5	43

[a] Metal Catalysts - Loaded as aqueous solutions of salts, i.e. cobalt acetate, nickel acetate, ammonium molybdate. Cobalt and nickel salts loaded 300 mmol metal/kg dry coal unless used as mixed catalyst with molybdenum, then cobalt and nickel loaded 40 mmol and molybdenum 100 mmol metal/kg dry coal.
[b] Alkali Catalysts - Loaded as salts, 500 mmol/kg dry coal
[c] Total Conversion - based on DCM-insolubles, [Coal (dry) - Residue (dry)]/Coal (daf)]
[d] Asphaltenes - DCM-solubles/hexane-insolubles
[e] OGW - Oil, Gas, (Total Conversion - Asphaltenes)
[f] Sodium metalcarbonylates - loaded as mixture of NaOH and metal carbonyl
[g] Sodium Cobalt Carbonyl - loaded as actual salt, 300 mmol metal/kg dry coal
[h] Reaction contains CS_2, no baseline data available at this time
[i] Sodium Aluminate loaded before nickel and molybdenum precursors
[j] Sodium Aluminate loaded after nickel and molybdenum precursors

Table 3: Conversion Data for Surat Basin coal (SSB) Using Various Catalysts and Reaction Conditions

Coal	Metal Catalyst[a]	Alkali Catalyst[b]	Temp (°C)	Gas Atm.	Total Conv.[c]	Asph.[d]	OGW[e]
SSB	none	none	365	CO/H_2O	27	4.3	23
	none	$NaAlO_2$	365	CO/H_2O	36	12	24
	Co	none	365	CO/H_2O	27	3.2	23
	Co	$NaAlO_2$	365	CO/H_2O	33	3.7	29
	$NaCo(CO)_4$[f]	--	365	CO/H_2O	33	7.0	26
	none	none	400[g]	H_2	25	2	23
	$NaCo(CO)_4$[f]	--	400	H_2	61	22.3	39
	Ni/Mo[h]	$NaAlO_2$	400	H_2	46	11	35
	Ni/Mo[i]	$NaAlO_2$	400	H_2	51	14	37

[a] Metal Catalysts - Loaded as aqueous solutions of salts, i.e. cobalt acetate, nickel acetate, ammonium molybdate. Cobalt and nickel salts loaded 300 mmol metal/kg dry coal unless used as mixed catalyst with molybdenum, then cobalt and nickel loaded 40 mmol and molybdenum 100 mmol metal/kg dry coal.

[b] Alkali Catalysts - Loaded as salts, 500 mmol/kg dry coal

[c] Total Conversion - based on DCM-insolubles, [Coal (dry) - Residue (dry)]/Coal (daf)

[d] Asphaltenes - DCM-solubles/hexane-insolubles

[e] OGW - Oil, Gas, Water, (Total Conversion - Asphaltenes)

[f] Sodium Cobalt Carbonyl - loaded as actual salt, 300 mmol loading

[g] Reaction time 60 minutes

[h] Sodium Aluminate loaded before nickel and molybdenum precursors

[i] Sodium Aluminate loaded after nickel and molybdenum precursors

MOLYBDENUM HEXACARBONYL AS A CATALYST PRECURSOR FOR DIRECT COAL LIQUEFACTION

Robert P. Warzinski and Bradley C. Bockrath
U.S. Department of Energy
Pittsburgh Energy Technology Center
Pittsburgh, PA 15236

Keywords: coal liquefaction, dispersed catalyst, molybdenum hexacarbonyl

INTRODUCTION

Various transition metal carbonyls of the formula $M_x(CO)_y$ - where M is Cr, Fe, Co, Ni, Mo, Ru, Rh, W, Re - have been used effectively as catalyst precursors in laboratory-scale investigations of direct coal liquefaction (1-6). Most notable are the use of iron pentacarbonyl (4) and molybdenum hexacarbonyl (5). In particular, $Mo(CO)_6$ in the presence of sulfur has been shown to be an excellent catalyst precursor for the liquefaction of coal (5,6) and for promoting reactions with coal model compounds (7).

At PETC, $Mo(CO)_6$ has been used to study the influence of a catalyst on the liquefaction of coal (5,8,9). The inherent volatility of $Mo(CO)_6$ permits it to form an active liquefaction catalyst in the presence of sulfur with no special preparation, impregnation, or dispersion techniques. The liquefaction of coal is effectively accomplished by the simple direct addition of $Mo(CO)_6$ to the liquefaction reactor even in the absence of any added solvents or vehicles. The work reported here describes the activation and reactivity of the catalysts formed from $Mo(CO)_6$.

EXPERIMENTAL

The $Mo(CO)_6$ was used as received from Strem Chemical Company. Purity was given as 98+% with moisture being the only major contaminant. Ammonium tetrathiomolybdate (ATM) was purchased from Alfa Products and used as received. Elemental analysis of the ATM showed that it contained some oxygen; however, the S:Mo ratio was 4:1. In all of the experiments with coal, DECS-17 coal from the Penn State Coal Sample Bank was used. The coal was minus-60 mesh and was riffled prior to use. The elemental analysis (on a dry basis) provided with the coal was as follows: 76.3% carbon, 5.8% hydrogen, 1.3% nitrogen, 0.4% sulfur, 6.6% ash, and 9.7% oxygen (by difference).

Microautoclave experiments were performed according to previously described procedures (5,8,9). When $Mo(CO)_6$ was used with coal, no special impregnation or mixing procedures were used; it was simply added directly to the microautoclave containing the coal sample. Unless otherwise indicated, all of the experiments were conducted for 1 hour using a slow heat-up and rapid cool-down. The products were recovered according to the referenced procedures (5,8,9). Elemental analyses of the products were performed at Huffman Laboratories in Golden, Colorado. ESCA and X-ray diffraction analyses were performed at PETC.

RESULTS AND DISCUSSION

Conversion of $Mo(CO)_6$ to an Active Catalyst. $Mo(CO)_6$ is a sublimable solid that decomposes without melting at 150°C (10). In the absence of a liquid phase, the reactions involved in the transformation of $Mo(CO)_6$ to MoS_2 appear to take place in the gas phase as the carbonyl sublimes and decomposes. We have observed the conversion of $Mo(CO)_6$ in H_2S to MoS_2 in a high-pressure, windowed view cell. A description of the view-cell system has been published (8). In this experiment, 0.37 mmol of $Mo(CO)_6$ and 4.4 mmol of H_2S were added to the cell. At 90°C and 7.0 MPa, a brown coating started to cover the $Mo(CO)_6$ particles and the interior surface of the glass window. At 110°C the coating on the window prevented further visual observation. Inspection of the brown, mirrorlike coating on the window by XPS indicated that it was similar in composition to MoS_2.

To determine the fate of $Mo(CO)_6$ in our microautoclave liquefaction system, experiments were performed at several temperatures with $Mo(CO)_6$ and the results compared to those obtained from similar experiments with ATM, a nonvolatile liquefaction catalyst precursor. In these experiments, 0.9 g of the catalyst precursor and 9.1 MPa of a hydrogen/10% hydrogen sulfide gas mixture were charged to the microautoclave. The products from reactions with $Mo(CO)_6$ and ATM were recovered as methylene chloride-insoluble and tetrahydrofuran (THF)-insoluble residues, respectively. The S:Mo atomic ratios of the products determined from both elemental analysis and ESCA are contained in Table 1 along with the complete elemental composition.

Table 1. Activation of $Mo(CO)_6$

Temperature, °C	Precursor	Atomic S/Mo Ratio		Elemental Composition
		Elemental	ESCA	
175	$Mo(CO)_6$	2.5	---	---
250	$Mo(CO)_6$	2.0	1.3	$MoS_2C_{0.3}H_{1.7}O_{1.1}N_{0.1}$
250	ATM	2.3	1.8	$MoS_{2.3}C_{0.3}H_{2.4}O_{2.3}N_{0.3}$
375	$Mo(CO)_6$	2.3	1.8	$MoS_{2.3}C_{0.3}H_{0.9}O_{0.3}$
375	ATM	2.3	1.9	$MoS_{2.3}C_{0.3}H_{2.7}O_{1.8}N_{0.1}$

At 175°C, the lowest temperature investigated, approximately 45% of the carbonyl reacted to form a product with a S:Mo ratio of 2.5. Unreacted $Mo(CO)_6$ was also observed. An experiment with ATM was not performed under these conditions. At 250°C, no unreacted $Mo(CO)_6$ was observed. At this temperature, 97% of the carbon monoxide in the carbonyl was detected in the product gas. The products formed from $Mo(CO)_6$ and ATM at 250°C have slightly different S:Mo ratios. However, at 375°C, the products were similar in composition and close to the expected value of 2:1 for MoS_2. ESCA analyses of the samples indicated a lower S:Mo ratio on the surface, which was probably due to surface oxidation of the samples. Direct oxygen analyses of these samples confirmed the presence of oxygen.

X-ray diffraction analysis was also performed at PETC to determine the degree of crystallinity of the products from $Mo(CO)_6$ and ATM. At 175°C and 250°C, the products were essentially amorphous compounds; however, at 375°C the development of some crystallinity was observed.

Similar work on the transformation of $Mo(CO)_6$ and ATM under liquefaction conditions was reported by Artok et al. (6). Results with ATM are in agreement with those in Table 1; however, they reported lower S:Mo ratios (1.1 to 1.7) when using $Mo(CO)_6$. One possible reason may be that in our experiments, the H_2S:Mo ratio in the microautoclave system was initially about 6.3:1; whereas, in the work by Artok et al. it was reported as 2.5:1. Under typical coal liquefaction conditions in our system, at 1000 ppm Mo, the H_2S:Mo ratio was initially about 150:1.

The pressure and temperature data collected during microautoclave experiments were used to follow the change in the total number of moles of gas in the system with time. This provided information concerning the transformation of $Mo(CO)_6$ to an active catalyst and the temperature of the onset of catalytic activity. Determining the amount of gas in the system, especially during the heat-up period, from the pressure and temperature data was complicated by the fact that a significant portion of the reaction space is outside the heated sandbath. This cooler region consists of the internal volumes of the pressure transducer, connecting tubing, and associated valves. During heat-up and reaction, the gas in the cooler region would be at a higher density than the gas in the microautoclave. Therefore, calculating the moles of gas in the microautoclave system using the ideal gas law would result in an apparent decrease in the moles of gas as temperature increases.

An empirical correction procedure was developed that compensated for both the nonisothermal nature of the microautoclave system and the nonideality of the gas phase. This procedure involved determining a correction factor from pressure and temperature data from experiments with only H_2 or H_2/3% H_2S in the microautoclave system. This correction factor was obtained by fitting a polynomial equation to the apparent change in the moles of gas calculated using the ideal gas law as a function of the microautoclave temperature in these experiments. This correction factor was then applied to the moles of gas calculated using the ideal gas law from experiments with catalyst. This correction procedure is performed for each microautoclave reactor and is checked on a regular basis. Using this method, changes in gas content greater than $\pm$ 1 mmol can be reliably observed.

Figure 1 presents changes in the amount of gas present in the microautoclave system and the thermal history as functions of time for an experiment in which 3.7 mmol of $Mo(CO)_6$ was heated to 425°C under an initial pressure of 7.8 MPa H_2/10% H_2S. In section A of Figure 1, a rapid rise in amount of gas is first observed that starts at about 160°C as $Mo(CO)_6$ begins to decompose and liberate CO. This is close to the decomposition temperature of 150°C reported for $Mo(CO)_6$ (10). The amount of gas in the microautoclave continues to increase until, at 280°C, the trend reverses and a gradual decrease is observed. In another similar experiment, the reaction temperature was stabilized at 250°C for one hour after the heat-up period. After reaching 250°C, the gas content continued to increase smoothly to a level of 22 mmol and

remained there for the duration of the experiment. This is equal to the maximum amount of CO that could have been liberated from the $Mo(CO)_6$ charged. Analysis of the gas composition by gas chromatography indicated that CO accounted for 95% of the carbon-containing gases produced.

To investigate the cause of the abrupt halt in the increase in gas content at 280°C and the onset of a gradual decrease, an experiment was terminated immediately upon reaching 325°C. Analysis of the recovered gases showed that some methanation and water/gas shift conversion had occurred, although carbon monoxide still accounted for 93% of the carbon-containing gases produced. The former reaction accounts for a reduction in the net moles of gas, while the latter gives evidence that water produced in the methanation undergoes catalytic reaction with CO.

In section B of Figure 1, a rapid decrease in the amount of gas occurs at temperatures above 350°C. This may be associated with an increased rate of methanation of the CO released from $Mo(CO)_6$. A fairly uniform rate of gas consumption (0.39 mmol/mmol Mo/min) occurred in the range of 370°C to 410°C.

At the end of one hour at 425°C the reaction was quenched (section C). Gas analysis indicated that all of the CO was utilized with 90% selectivity towards methane formation. The number of moles of gas present after quenching is lower than at the end of the reaction prior to quenching owing to the condensation of water vapor formed as a result of the methanation reaction. The amount of water indicated in Figure 1 (23 mmol) is in reasonable agreement with that expected based upon the amount of $Mo(CO)_6$ charged and the methane formed (20 mmol).

In Figure 2, the activation of $Mo(CO)_6$ in the H_2/10% H_2S environment is compared to similar experiments conducted in N_2 and H_2. The use of CS_2 as a source of sulfur in place of H_2S is also shown. In all four cases, the liberation of CO is observed. The largest and most uniform release of CO to the gas phase occurred when both H_2 and H_2S were present. In another experiment (not shown in Figure 2), the rate of release of CO was similar with N_2/10% H_2S to that observed with H_2/10% H_2S. The data in Figure 2 also show that the most active methanation catalyst was formed in the presence of just H_2. This is evidenced by the sharp decrease in gas content that occurred at 363°C. The rate of decrease in the temperature range of 380°C to 410°C was 0.55 mmol/mmol Mo/min. When N_2 was used, no significant drop in gas content occurred, either with (Figure 2) or without H_2S (not shown).

X-ray diffraction analyses of samples collected from the above experiments indicated that, in the presence of H_2/10% H_2S, the strongest peak was from MoS_2. The average crystallite size was 75 Å with a stacking height of 30 Å. The MoS_2-containing catalyst formed in the presence of N_2/10% H_2S had similar dimensions. When either N_2 or H_2 alone was used, the strongest peak was from Mo_2C. In these cases, the crystallites were more uniform in size with an average diameter of between 14 Å and 20 Å. Referring to the data in Figure 2, the carbide formed in the presence of H_2 appears to be a more reactive catalyst for methanation than the sulfided species. This agrees with published results obtained at 350°C and 101.3 KPa (11).

Effect of catalyst precursors on coal liquefaction. We have previously shown that $Mo(CO)_6$ is an effective catalyst precursor for coal liquefaction even in the absence of added liquids and special impregnation procedures (5,9). Compared with uncatalyzed reaction, the conversion of DECS-17 coal to primary (THF-soluble) products was facilitated over a wide temperature range by the catalyst formed from $Mo(CO)_6$. A different behavior was observed for the conversion of the primary to secondary (cyclohexane-soluble) products. In this case, the onset of catalytic conversion occurred between 375°C and 400°C.

Additional experiments were performed using the DECS-17 coal with various combinations of $Mo(CO)_6$, hydrogen, hydrogen sulfide, carbon disulfide, and nitrogen. When $Mo(CO)_6$ was used it was added at a level of 1000 ppm Mo based on daf coal. All of the experiments were performed at 425°C. The conversion results are shown in Figure 3. The error bars represent the range of values obtained about the average. The first set of data illustrates the high conversions obtained using $Mo(CO)_6$ with H_2/3% H_2S without added solvents or vehicles. The second and third sets of data show that a drop in both THF and cyclohexane conversions occurs if H_2S is eliminated; however, the conversions are still relatively high. Compared to no added sulfur (third set of data), using CS_2 appears to have no benefit. The fourth and fifth sets of data represent thermal conversions in the absence of catalyst. A small improvement is observed when H_2S is present, even in the absence of catalyst. Finally, the last two sets of data represent experiments performed in N_2. The presence of $Mo(CO)_6$ had no effect in the absence of H_2.

In the work with DECS-17 coal and $Mo(CO)_6$, it is assumed that $Mo(CO)_6$ sublimes and disperses onto the coal from the gas phase either prior to being sulfided or as it is converted to the sulfide phase. The previously described experiments in the view cell support this assumption. At the levels of Mo used in the experiments represented in Figure 3 (1000 ppm), the fate of the $Mo(CO)_6$ could not be determined using X-ray crystallography on the THF-insoluble residues owing to the small amount present and to interferences from the coal mineral matter in the residue. However, the residue from a similar experiment at 425°C in which $Mo(CO)_6$ was used at a higher level (10,000 ppm) could be examined if the mineral matter was first removed with hydrofluoric acid. In this case, X-ray diffraction analysis identified molybdenum disulfide in the THF insoluble product with a crystallite size of approximately 80 Å and a relatively low degree of stacking.

CONCLUSION

The results presented above confirm that $Mo(CO)_6$ forms a finely divided active catalyst for coal liquefaction even in the absence of added liquids or special impregnation procedures. Experiments with $Mo(CO)_6$ in an H_2/H_2S mixture show that the onset of hydrogenation activity related to methanation in the microautoclave system begins near 280°C and increases dramatically at about 350°C. Primary dissolution of coal assisted by the catalyst follows the same pattern; a small catalytic effect is observed at 325°C that increases in magnitude with temperature (5).

The decomposition of $Mo(CO)_6$ and the liquefaction of coal in the presence of this compound are both facilitated by the presence of H_2S. Substituting CS_2 for H_2S adversely affected $Mo(CO)_6$ decomposition and liquefaction conversion. In the absence of added sulfur, $Mo(CO)_6$ forms a carbide phase that is even a more active catalysts for methanation than the sulfide phase; however, this increased activity is not noted in liquefaction experiments with a low-sulfur coal. A different catalyst phase may be formed when coal is present.

The above work also demonstrates that with appropriate correction, the microautoclave pressure and temperature data can be used to follow changes in the amount of gas in the system during an experiment. Using this procedure, information on catalyst activation and reactivity were obtained. The same procedure has also been used to observe the influence of a catalyst on gas uptake during coal liquefaction (5).

ACKNOWLEDGMENTS

The author would like to thank Richard Hlasnik and Jerry Foster for performing the microautoclave work, Sidney Pollack and Elizabeth Frommell for X-ray diffraction analysis and interpretation, and Rodney Diehl for performing the XPS and ESCA analyses.

DISCLAIMER

Reference in this report to any specific product, process, or service is to facilitate understanding and does not imply its endorsement or favoring by the United States Department of Energy.

REFERENCES

1. Sharma, R.K.; Moffett, G. Prepr. Pap. - Amer. Chem. Soc., Div. Fuel Chem. **1982**, 27(2), 11-17.
2. Yamada, O.; Suzuki, T.; Then, J.H.; Ando, T.; Watanabe, Y. Fuel Process. Technol. **1985**, 11, 297-311.
3. Suzuki, T.; Yamada, H.; Yunoki, K.; Yamaguchi, H. Energy Fuels **1992**, 6, 352-356.
4. Suzuki, T. Energy Fuels **1994**, 8, 341-347.
5. Warzinski, R.P. Prepr. Pap. - Amer. Chem. Soc., Div. Fuel Chem. **1993**, 38(2), 503-511.
6. Artok, L.; Davis, A.; Mitchell, G. D.; Schobert, H. H. Energy Fuels **1993**, 7, 67-77.
7. Suzuki, T; Yamada, H; Sears, P. L.; Watanabe, Y. Energy Fuels **1989**, 3, 707-713.
8. Warzinski, R. P.; Lee, C.-H.; Holder, G. D. J. Supercrit. Fluids **1992**, 5, 60-71.
9. Warzinski, R.P. Proc. Int. Conf. Coal Sci. **1993**, 2, 337-340.
10. CRC Handbook of Chemistry and Physics; Weast, R. C., Ed.; CRC: Boca Raton, **1988**, B-108.
11. Saito, M.; Anderson, R.B. J. Catal. **1980**, 63, 438-446.

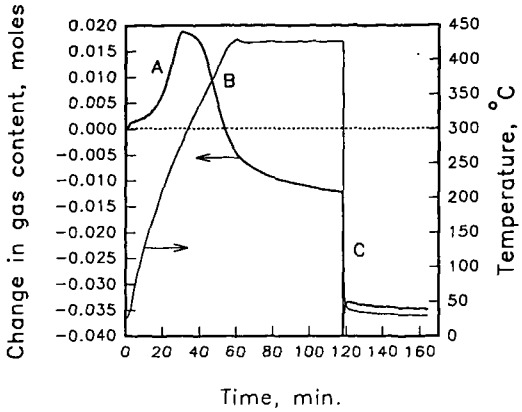

Figure 1. Reactivity of $Mo(CO)_6$ in H_2/10% H_2S

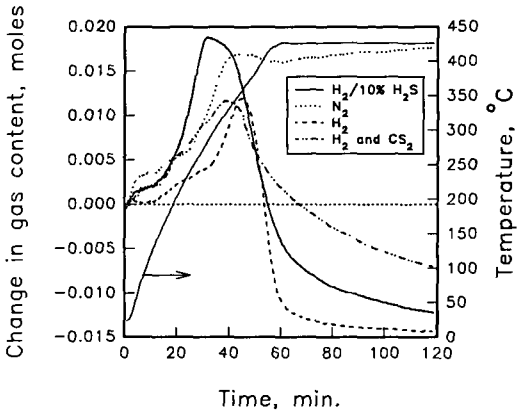

Figure 2. Reaction of $Mo(CO)_6$ in different systems.

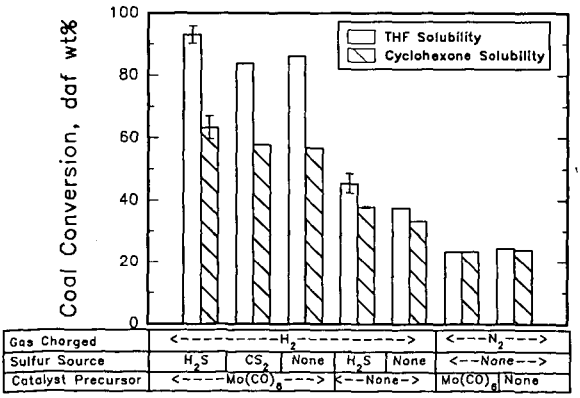

Figure 3. Effect of a catalyst, initial gas composition, and form of sulfur addition on the conversion of DECS−17 coal.

COMPARISON OF THE MEANS OF INTRODUCTION OF MoS_2 LIQUEFACTION CATALYSTS ON PERFORMANCE

Robert P. Warzinski, Anthony V. Cugini, and Bradley C. Bockrath
U.S. Department of Energy
Pittsburgh Energy Technology Center
Pittsburgh, PA 15236

Keywords: coal liquefaction, molybdenum sulfide catalysts, molybdenum hexacarbonyl

INTRODUCTION

The performance of dispersed coal liquefaction catalysts depends on many factors. One long recognized issue is the key importance of intimate contact between the catalyst and the reacting coal. The development of evidence for this critical relationship has been recently reviewed (1). The method of catalyst addition bears directly on this problem. For example, impregnation of coal with a catalyst precursor provides improved liquefaction conversion when compared to adding the precursor as a powder or as a particulate in a liquefaction solvent (2). Exploitation of the advantages obtained by impregnation of a catalyst or its precursors is still pursued.

Unlike most liquefaction catalyst precursors, $Mo(CO)_6$ has been found to be an effective catalyst precursor even in the absence of such impregnation procedures (3). The purpose of this paper is to compare the activity of the catalyst formed from $Mo(CO)_6$ with that of preformed MoS_2-containing catalysts known to be active for coal liquefaction. All of the liquefaction experiments were performed without the addition of liquefaction solvents or vehicles to avoid the leveling effect they may exert, especially if they are good hydrogen donors. The elimination of added solvents or vehicles also amplifies the importance of coal/catalyst contacting because mass transport becomes more restricted in reacting phases of higher viscosity.

EXPERIMENTAL

Coal and Chemicals: All experiments were performed with DECS-17 (Blind Canyon) coal (minus 60 mesh) from the Penn State Coal Sample Bank. The elemental analysis (on a dry basis) provided with the coal was as follows: 76.3% carbon, 5.8% hydrogen, 1.3% nitrogen, 0.4% sulfur (0.02% pyritic sulfur), 6.6% ash, and 9.7% oxygen (by difference). The moisture content of the as-received coal was 3.7%. The coal was riffled prior to use. $Mo(CO)_6$ was obtained from Strem Chemical Company, ammonium heptamolybdate (AHM) was obtained from Fisher Chemical Company, and Panasol (a mixture of alkylated naphthalenes) was obtained from Crowley Chemical Company. All of the chemicals were used as received.

Catalyst Preparation: Three methods of introducing catalyst were used; addition of a catalyst precursor, recycle of the catalyst-containing residue from coal liquefaction experiments with the precursor, and addition of preformed catalyst particles. The catalyst precursor, $Mo(CO)_6$, was simply added directly to the microautoclave containing the coal sample without a special impregnation or mixing procedure. A MoS_2-containing liquefaction residue was prepared in a microautoclave using 6.6 g DECS-17 coal and $Mo(CO)_6$ (10,000 ppm Mo based on daf coal) under 7.2 MPa H_2/3% H_2S at 425°C for 1 h. Finely divided MoS_2-containing particles were prepared in a 1-L semi-batch stirred autoclave using 400 g Panasol and 10,000 ppm Mo (based on Panasol) as aqueous AHM (12% by weight) under 17.3 MPa, 30 mL/s H_2/3% H_2S at 400°C for 0.5 h (4). The MoS_2-containing particles and liquefaction residue were both recovered from tetrahydrofuran (THF) by pressure filtration following extraction of the respective reaction products. The dried liquefaction residue and MoS_2-containing particles contained 4.4% and 30% Mo, respectively.

Microautoclave Liquefaction Experiments: Microautoclave experiments were performed according to procedures described previously (3,5). The $Mo(CO)_6$, the liquefaction residue, or the MoS_2-containing particles were added directly to the microautoclave along with the coal (3.3 g) to give a Mo loading of 1,000 ppm (based on daf coal). No solvents or vehicles were used for catalyst addition or in the liquefaction experiments. All of the experiments were conducted for 1 hour at reaction temperatures from 350°C to 425°C under 7.2 MPa H_2/3% H_2S (cold pressure) using a slow heat-up and rapid cool-down. The products were recovered using sequential extractions with THF and cyclohexane according to the referenced procedures (3,5).

Catalyst Characterization: X-ray diffraction and BET surface area analyses were performed at PETC. A JOEL 200CX TEM located at the University of Pittsburgh was also used to obtain images of the MoS_2-containing particles. Additional details have been published (4).

The catalysts were also characterized by their activity for CH_4 production from CO in the absence of coal in the microautoclave under conditions similar to those used in the liquefaction experiments. In these experiments, either the liquefaction residue or the MoS_2-containing particles were added to the microautoclave at a level of approximately 0.4 mmol Mo. In the case of $Mo(CO)_6$, the MoS_2-containing catalyst phase was first formed in a separate experiment using 1.0 g of $Mo(CO)_6$ under 7.7 MPa H_2/10% H_2S and 1 h at 425°C (slow heat-up). A portion of the product sufficient to provide 0.4 mmol Mo was then added to the microautoclave. CO and a H_2/3% H_2S mixture were then combined in the microautoclave to give a gas mixture of approximately 75% H_2, 23% CO, and 2% H_2S at 7.7 MPa. Both slow and rapid heat-up experiments were performed at 375°C with a 1-h residence time at reaction temperature. The rates of gas uptake associated with the methanation reaction were obtained from records of the change in pressure with time. These data were used to calculate the change in moles of gas present in the system at reaction temperature.

RESULTS AND DISCUSSION

Microautoclave experiments were performed with Blind Canyon (DECS-17) coal to investigate the effect of the means of introducing catalysts on liquefaction. The catalyst was introduced either in the form of the chemical precursors $Mo(CO)_6$ and H_2S, or as MoS_2-containing compounds. Two MoS_2-containing compounds were used: (1) a liquefaction residue prepared from the precursors and the DECS-17 coal, and (2) high-surface-area MoS_2-containing particles prepared prior to the liquefaction experiments from AHM and Panasol.

We have previously shown that $Mo(CO)_6$ is an effective catalyst precursor for coal liquefaction even in the absence of added solvents or vehicles and special impregnation procedures (3). Table 1 contains the liquefaction conversion results from experiments using only the DECS-17 coal with and without 1000 ppm Mo added as $Mo(CO)_6$ in one-hour reactions at temperatures from 325°C to 425°C. All results are the average of at least two experiments. The influence of native catalyst precursors is negligible, owing to the low levels of pyrite in this coal.

Table 1. Liquefaction of DECS-17 coal using $Mo(CO)_6$ without added solvents or vehicles

Reaction Temperature, °C	THF Conversion, %		Cyclohexane Conversion, %	
	Thermal	Catalytic	Thermal	Catalytic
325	14	19	7	9
350	29	46	12	15
375	46	83	23	25
400	48	94	31	52
425	45	93	38	65

Compared to the uncatalyzed reaction, the conversion of coal to primary (THF-soluble) products was facilitated by the catalyst formed from $Mo(CO)_6$ even at the lowest temperature used, 325°C. The difference between catalytic and non-catalytic coal conversion continuously increased with temperature. In the case of secondary (cyclohexane-soluble) products, the onset of a significant catalytic effect occurred between 375°C and 400°C.

The observation of a catalytic effect at the lowest temperature used in the liquefaction experiments implies an active catalyst is formed at even lower temperatures. A detailed investigation of the activation of $Mo(CO)_6$ in the absence of coal under conditions similar to those used in the microautoclave liquefaction experiments has been reported (6). $Mo(CO)_6$ is a sublimable solid that decomposes without melting at 150°C (7). In microautoclave experiments, the evolution of CO associated with the decomposition was observed to begin at about this temperature. If H_2S was present, MoS_2 formed readily. When heated in an H_2/H_2S mixture, the development of catalytic activity was indicated by the conversion of the evolved CO to CH_4. The onset of catalytic methanation was detected near 280°C and increased dramatically at about 350°C. This result and the THF-conversion data shown in Table 1 confirm that an active catalyst is formed before significant thermal conversion of the coal begins.

A series of catalysts were formed in the microautoclave by heating $Mo(CO)_6$ in H_2/10% H_2S to various temperatures (6). The products were submitted to analysis by X-ray diffraction to determine the degree of crystallinity. At 175°C or 250°C, the products were essentially amorphous compounds. The development of some crystallinity was observed on raising the reaction temperature to 375°C. At 425°C, a higher degree of crystallinity was observed. The average crystallite size formed at this temperature was 75 Å with an average stacking height of 30 Å (~5 layers).

When the catalyst is formed in conjunction with coal, the $Mo(CO)_6$ apparently sublimes and disperses onto the coal from the gas phase either prior to being sulfided or as it is converted to the sulfide phase (6). At the levels of Mo used in the liquefaction experiments with $Mo(CO)_6$ (1000 ppm), it was not possible to determine the fate of the $Mo(CO)_6$ using X-ray crystallography on the THF-insoluble residues owing to the small amount of catalyst present and to interferences from the coal mineral matter which was concentrated in the residue. It was possible, however, to examine the MoS_2-containing liquefaction residue prepared from the DECS-17 coal and $Mo(CO)_6$ (see Experimental) by X-ray diffraction if the mineral matter was first removed by digestion with hydrofluoric acid. In this case, X-ray diffraction analysis identified MoS_2 in the THF insoluble residue with a crystallite size of approximately 80 Å and a relatively low degree of stacking as indicated by a very broad 002 line.

An alternative method for forming MoS_2-containing particles from AHM in Panasol has been reported (4). Elemental analysis of the MoS_2-containing particles was consistent with a composition of 50 wt% carbon and 50 wt% MoS_2 (4). X-ray diffraction showed that the MoS_2 was poorly crystalline. The average size in the basal plane was 25 Å. Absence of the 002 line implied the MoS_2 was essentially single layer. The dimensions obtained by X-ray diffraction were confirmed by TEM. The surface area of the particles determined by the BET method with nitrogen was 262 m^2/g.

To compare the three different means of introducing MoS_2, liquefaction experiments were carried out in the microautoclave using the DECS-17 coal at temperatures from 350°C to 425°C. All of the experiments were performed at least in duplicate. A comparison of the results for the two preformed catalysts with those obtained using $Mo(CO)_6$ (Table 1) was made by taking the difference between the conversion values for the catalysts. These differences are shown in Figure 1. The large error bars indicated on the zero line represent the range of conversion values obtained using $Mo(CO)_6$. The small error bars associated with the symbols for the two preformed catalysts represent the range of values obtained for these experiments. Error bars are not shown if they are smaller than the size of the symbol.

With respect to conversion to primary (THF-soluble) products, the data in Figure 1 show that the form of introduction of the catalyst has a significant effect on the primary dissolution and liquefaction of the coal. The catalyst formed in-situ from $Mo(CO)_6$ consistently yielded the highest conversions, especially at the lower temperatures. The MoS_2-containing particles were better than the MoS_2-containing liquefaction residue except at the lowest temperature where the conversions were similar. At 425°C, the MoS_2-containing particles did yield high levels of conversion similar to when $Mo(CO)_6$ was used.

A different picture emerges from Figure 1 regarding secondary conversion of the primary products to cyclohexane-soluble material. The form of introduction of the catalyst did not appear to have any significant effect at any temperature in this case.

The changes in the total number of moles of gas in the microautoclave system during experiments with and without the catalysts were determined from the pressure and temperature data collected during the experiments. A correction procedure was used to compensate for the nonisothermal nature of the microautoclave system and for nonideality in the gas phase (6). After subtracting the thermal results from the respective results obtained with the catalysts, plots of moles of gas versus reaction time show decreasing amounts of gas at all temperatures investigated. The onset of rapid hydrogen consumption differed for the different forms of catalyst. For $Mo(CO)_6$, the liquefaction residue, and the preformed particles, the onset of rapid hydrogen consumption occurred at approximately 370°C, 400°C, and 390°C, respectively. At 350°C, the rate of consumption for all catalysts was nearly constant for the entire reaction time at this temperature. At the higher temperatures, the rates of consumption were initially constant but decreased with time as the reaction proceeded.

The increment in coal conversion due to catalyst is plotted against values for the initial rates of gas uptake caused by catalyst in Figure 2. The increase in THF conversion attributed to catalyst correlates well with the initial rates of gas uptake when the uptake is plotted on a logarithmic scale. No such correlation is evident for conversion to cyclohexane soluble material.

MoS_2 is known to catalyze the hydrogenation of CO to form CH_4 (8). As an independent measure of catalyst activity, the rates of gas uptake associated with the conversion of a CO/H_2 mixture were obtained in the presence of the three forms of the catalyst. The preformed catalysts were simply added to the microautoclave as in the liquefaction experiments. For $Mo(CO)_6$, the catalyst species was first formed in a separate experiment without coal and a portion of this product was then used in the methanation test. Details are contained in the

Experimental section. Table 2 contains the rates of gas uptake observed using both slow and rapid heat-up to 375°C along with the respective conversions to THF-soluble products observed in the previously described liquefaction experiments at this same temperature (no rapid heat-up liquefaction experiments were performed).

Table 2. Comparison of methanation activity and liquefaction conversion at 375°C for different forms of MoS_2-containing catalysts.

Catalyst	Heat-up	Gas Uptake Rate (mmol gas/mmol Mo/min)	Liquefaction Conversion, daf wt%[1]
Mo-containing THF insols	slow	0.029	63
	rapid	0.041	--
MoS_2 Particles	slow	0.079	76
	rapid	0.085	--
Derived from $Mo(CO)_6$[2]	slow	0.032	83
	rapid	0.044	--

[1]THF conversions. The cyclohexane conversions were the same (25% to 26%) in all cases. [2]The methanation tests were performed with catalyst prepared in the absence of coal. The catalyst was formed in situ in the liquefaction tests.

The highest rate of gas uptake is that of the preformed MoS_2 particles derived from AHM and Panasol. The rates for the two materials derived from $Mo(CO)_6$ are lower and nearly the same whether the catalyst was formed with or without coal present. There is no direct correlation between the gas uptake rates observed for methanation and the values for coal conversion. A rationale for the different order of catalytic performance found for the gas-phase methanation and the coal liquefaction reactions may be more easily constructed when more data is in hand. For the present, it is worth noting that the experimental reactions are quite different with regard to rate restrictions that may be imposed by mass transport. Thus, coal/catalyst contacting may be a significant determining factor in the liquefaction experiments. The solvent-free character of these experiments accentuates the importance of mixing and contact with the reacting coal. For example, the most intimately mixed catalyst, that formed in situ from $Mo(CO)_6$, provides the highest coal conversion. When recovered in the liquefaction residue and recycled, conversion drops significantly. However, the activity determined by the gas-phase reaction for the liquefaction residue is not much less than observed for the catalyst made in the absence of coal. On the other hand, the particulate catalyst formed from AHM and Panasol shows higher activity for the gas-phase reaction, but does not perform as well as the more intimately mixed catalyst in the liquefaction experiment. The solvent-free liquefaction experiment reflects a combination of catalyst activity and coal contacting, while the gas-phase methanation test more nearly reflects a catalytic activity. It should also be borne in mind that the catalytic sites responsible for the two different reactions may not be the same. In view of the importance of establishing what factors limit the performance of dispersed catalysts, for example catalyst activity versus transport limitations, experiments now in progress are aimed at further exploring the relationship between methanation activity and liquefaction results.

CONCLUSION

The results show that the means of introduction of MoS_2-containing catalysts has a significant effect on the initial dissolution and conversion of coal to THF-soluble products, especially at temperatures below 425°C. The self-dispersing $Mo(CO)_6$ precursor provided the best conversions under the conditions of these experiments. More intimate contact between the catalyst and the reacting coal is thought possible in this case than with the preformed catalysts. Better contact could promote more hydrogen transfer from the gas phase to the reacting coal, preventing retrogressive reactions. The initial softening point of the DECS-17 coal is 385°C, and maximum fluidity is achieved at 420°C (Gieseler plastometer data provided with the coal). This increase in fluidity may be the reason performance of the different catalysts becomes more similar at the higher temperatures. Experiments with coals with different softening characteristics might be used to test this hypothesis.

On the other hand, the conversion of the coal to cyclohexane-soluble products was not affected by the form of introduction of the catalyst. This would imply that the reactions involved in forming these lighter materials occur at a point in the liquefaction process when all of the catalysts would be more uniformly distributed throughout the reaction mass.

Finally, the presence of coal appears to have an influence on the character of the catalyst formed from $Mo(CO)_6$. The X-ray data presented indicates that a reduced degree of stacking is observed for catalyst samples prepared in the presence of coal.

ACKNOWLEDGMENTS AND DISCLAIMER

The author would like to thank Richard Hlasnik and Jerry Foster for performing the microautoclave work, Sidney Pollack and Elizabeth Frommell for X-ray diffraction analysis and interpretation, and Donald Martello for performing the TEM analysis. Reference in this report to any specific product, process, or service is to facilitate understanding and does not imply its endorsement or favoring by the United States Department of Energy.

REFERENCES

1. Weller, S. W. Energy & Fuels **1994**, 8, 415-420.
2. Derbyshire, F. J. Catalysis in Coal Liquefaction: New Directions for Research; IEA Coal Research: London, 1988.
3. Warzinski, R.P. Prepr. Pap. - Amer. Chem. Soc., Div. Fuel Chem. **1993**, 38(2), 503-511.
4. Cugini, A.V.; Martello, D.V.; Krastman, D.; Baltrus, J.P.; Ciocco, M.V.; Frommell, E.F.; Holder, G.D. Prepr. Pap. - Amer. Chem. Soc., Div. Fuel Chem. **1995**, 40(2), 370-376.
5. Warzinski, R. P.; Lee, C.-H.; Holder, G. D. J. Supercrit. Fluids **1992**, 5, 60-71.
6. Warzinski, R.P. and Bockrath, B.C. Prepr. Pap. - Amer. Chem. Soc., Div. Fuel Chem. **1995**, this volume.
7. CRC Handbook of Chemistry and Physics; Weast, R. C., Ed.; CRC: Boca Raton, **1979**, B-99.
8. Saito, M. and Anderson, R. B. J. Catal. **1980**, 63, 438-446.

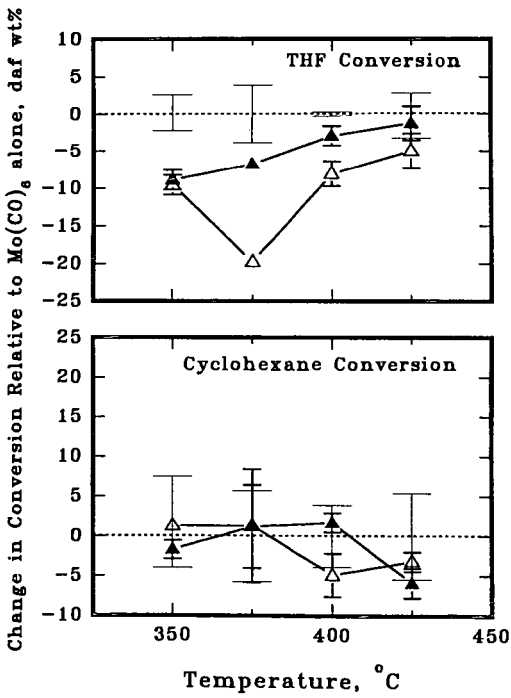

Figure 1. Effect of the means of introduction of catalyst on conversion of DECS-17 coal relative to direct addition of $Mo(CO)_6$. (△ MoS_2-containing liquefaction residue: ▲ preformed MoS_2-containing particles.)

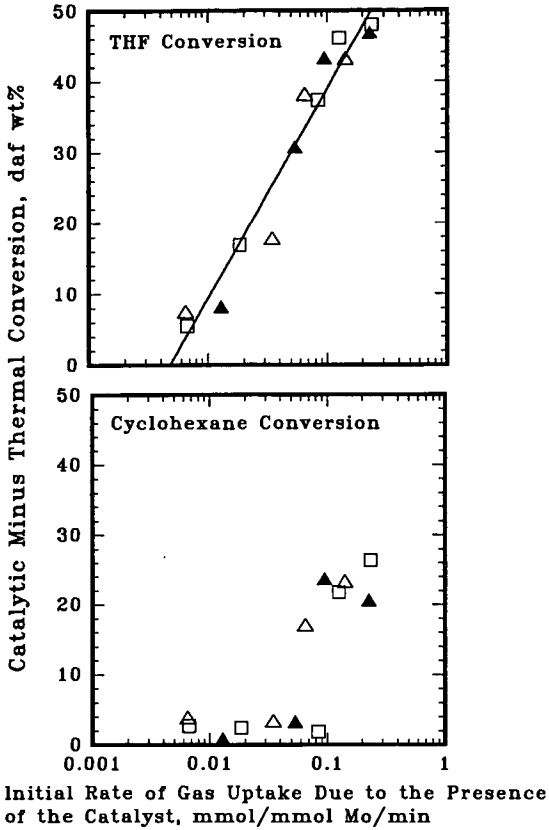

Figure 2. The dependence of catalyst-assisted conversion on the initial rate of gas uptake caused by the catalyst. (□ $Mo(CO)_2$; △ MoS_2-containing liquefaction residue; ▲ preformed MoS_2-containing particles.)

INFLUENCE OF SULFUR ADDITION AND S-INDUCED WALL CATALYTIC EFFECTS ON C-C BOND CLEAVAGE AND AROMATICS HYDROGENATION

Eckhardt Schmidt*, Chunshan Song and Harold H. Schobert

Fuel Science Program, Department of Materials Science and Engineering, 209 Academic Projects Building, The Pennsylvania State University, University Park, PA 16802

Catalytic hydrocracking of 4-(1-naphthylmethyl)bibenzyl, designated as NMBB, predominately yielded naphthalene and 4-methylbibenzyl. Sulfur addition to most catalyst precursors lead to substantially higher catalyst activity and subsequently higher conversion. NMBB was also treated with sulfur alone in the absence of catalysts in concentrations of 1.2 to 3.4 wt, corresponding to conditions present in catalytic runs with added sulfur to precursors. It was found that increasing sulfur concentrations lead to higher NMBB conversion. Furthermore, sulfur had a permanent influence on the reactor walls. It reacted with the transition metals in the stainless steel to form a microscopic black iron sulfide layer on the surface, which could not be removed mechanically. The "non-catalytic" runs which were done after experiments with added sulfur yielded higher conversions than normal runs done in new reactors. This "wall catalytic effect" can be reduced by treating sulfided reactors with hydrochloric acid for a short period of time and subsequent immersing into a base bath overnight. These results demonstrate the significant influence of sulfur addition and S-induced residual wall-effect on C-C bond cleavage and hydrogenation of aromatics in batch reactors.

Keywords: Model reactions, hydrocracking, dispersed catalysts, wall-effect.

INTRODUCTION

Since the early 90's, modern coal liquefaction has reached a point where only minor improvements to the process have been made (1). Sophisticated catalysts have been developed to increase efficiency. Much work still needs to be done in order to fully understand the mechanism on a molecular level, which in turn might lead to an optimized liquefaction process. Model compounds, like NMBB serve as excellent examples of a simplified coal model. Recent work (2,3) examined the effect of various catalysts on hydrocracking of this model compound. It turned out that certain precursors, such as Mo-based and bimetallic systems, show very high activity which can generally be increased by sulfur addition. This finding stimulated our interest to study the influence of S in model compound hydrocracking reactions.

We selected for comparison organometallic compounds and inorganic complexes. Good solubility of catalyst precursors in the liquefaction media generally leads to better catalyst dispersion and greater effectiveness for liquefaction reactions (4). One way to achieve better dispersion is by using soluble organometallic precursors. Ligand loss at elevated temperatures results in an in situ preparation of finely dispersed active catalyst particles. Hirschon and Wilson (5) demonstrated that highly dispersed catalysts from organometallic precursors can be effective for hydrogenating the coal with molecular hydrogen without relying upon a donor solvent. Thus the following work describes our efforts to investigate the influence of dispersed catalyst precursors and sulfur on hydrocracking of NMBB.

EXPERIMENTAL SECTION

Catalyst Precursors

A sample of superfine iron oxide was graciously provided by Mach I Inc. in Pennsylvania. NMBB and sulfur was purchased from TCI America. GC-MS confirmed sufficient purity of NMBB (> 99 %) and it was used without further purification.

Model compound reactions

Runs with NMBB were carried out in 33 mL stainless steel reactors (tubing bomb) at 400 °C for 30 min. In a typical run, a reactor was loaded with ca. 0.25 g NMBB, 2.11 wt % catalyst precursor and 0.14 g solvent (tridecane). The reactor was purged three times with H_2 and then pressurized with 6.9 MPa H_2 at room temperature for all experiments. A preheated fluidized sand bath was used as the heating source and the horizontal tubing bomb reactor was vertically agitated to provide mixing (about 240 strokes/min.) After the reaction the hot tubing bomb was quenched in cold water and the gaseous products collected in a gas bag for further analysis. The liquid contents were washed with 15 ml CH_2Cl_2 through a low speed filter paper for qualitative and quantitative GC analysis of the filtrate. All runs were carried out at least twice to confirm reproducibility.

The products were identified by GC-MS using a Hewlett-Packard 5890 II GC coupled with a HP 5971A mass-selective detector operating at electron impact mode (EI, 70 eV). The column used for GC-MS was a J&W DB-17 column; 30-m X 0.25-mm, coated with 50 % phenyl 50 %. -methylpolysiloxane with a coating film thickness of 0.25 μm. For quantification, a HP 5890 II GC with flame ionization detector and the same type of column (DB-17) was used. Both GC and GC-MS were temperature programmed from 40 to 280 °C at a heating rate of 4 °C/min and a final holding time of 15 min. The response factors for 10 of the products were determined using pure compounds. More experimental details may be found elsewhere (2).

RESULTS AND DISCUSSION

Hydrocracking of NMBB

Initial tests using superfine iron oxide (SFIO), a commercially available sample with a high surface area (250 m^2/g), yielded only moderate conversion (27.1 %), even at elevated temperatures (400 °C). The beneficial effect of sulfur addition could once more be demonstrated. Sulfur added to SFIO led to a considerable increase in conversion (78.2 %). A series of experiments was carried out to determine the impact of sulfur concentration on NMBB conversion. It was found that increasing sulfur concentration (starting at 1.2 wt %) led to increasing model compound conversion. As shown in Tables 1 and 2, several catalysts in combination with S were tested to study the impact of sulfur addition for catalytic hydrocracking of NMBB at 400 °C.

Among the tested catalyst precursors (Figure 1), ferrocene is more effective in hydrocracking reactions of NMBB than the inorganic iron complex $FeSO_4$ x 7 H_2O, which is the least active. However, in the presence of sulfur, $FeSO_4$ x 7 H_2O shows remarkable activity. The active form from iron sulfate is considered to be pyrrhotite. High temperature activation of ferrous sulfate transforms the inorganic complex in an H_2S atmosphere into an active pyrrhotite phase (6). Adding sulfur to ferrocene had a negative effect on its. This is possibly due to the formation of iron carbide during the initial stage of the catalyst activation. It is known (7) that sulfur addition to iron oxide, or iron pentacarbonyl initiates the transformation into pyrrhotite ($Fe_{1-x}S$, where $0 \leq x \leq 0.125$, because of Fe^{3+} impurities). This activation reaction is difficult to perform and iron carbonyls tend to form less reactive iron carbides and oxides during the activation process. Precursor molecules without CO ligands, but cyclopentadienyl groups, are expected to form much more iron carbide. In most reactions, S-presence attains higher conversion than a reaction for the same precursor in a hydrogen atmosphere. Even though molybdenum-based precursors are generally superior to iron-containing complexes, S-addition transforms the latter compound class into a more active phase, probably by providing a better dispersion of iron (8).

It was also found that sulfur had a permanent effect on the stainless steel reactor walls. Even new reactors turn black inside after reactions with S, depending on the sulfur concentration. We assume that added S reacts with iron on the surface of the reactor walls to form FeS. This black FeS layer can not be removed mechanically, and is not removed by base (KOH/i-Propanol/H_2O) for an extended period of time (1 - 3 days). Further experiments of sulfided reactors with NMBB alone gave dramatically higher conversion than identical thermal runs in new reactors. This so called "wall effect" can be reduced by immersing sulfided tubing bomb reactors in a 6 N HCl bath for 5 min. Subsequent treatment of the same reactor in base bath brings "background activity" down by more than 50 %. However, repeated acid washing leaches out steel components and weakens the steel. Furthermore, the surface characteristics of so treated reactors are changed permanently.

The influence of remaining sulfur in the tubing bomb reactors was also investigated. The question arises whether sulfur itself, of sulfided reactor walls are responsible for NMBB cleavage. To clarify this problem, we washed sulfided reactors subsequently with chloroform and ethanol to remove material trapped in the upper part of the tubing bomb reactors. Experiments after this treatment revealed no difference compared to runs without washing the reactor. Therefore, the "residual" catalytic effect seems to be due mainly to the formation of a sulfided layer on the reactor wall. Treatment of tubing bomb reactors with hydrochloric acid partially removes unwanted FeS particles but does not restore the original low activity of a new reactor. More work still needs to be done to understand the influence of sulfur on coal liquefaction experiments. Coal is going to be studied too, because of varied sulfur concentrations which can activate S-free precursors and change their activity substantially.

PRODUCT DISTRIBUTION

The following compounds can be found as main products: tetralin, naphthalene, bibenzyl and 4-MBB. The identified products can be classified into hydrocracking, hydrogenation and isomerization products. Those coming from hydrocracking reactions form the major pool of reaction products, followed by hydrogenation and isomerization products. Hydrocracking of NMBB yields three product categories from cleavage of the bonds between the aromatic moieties. Figure 1 and 2 show the product distribution from catalytic hydrocracking experiments of NMBB. All iron-containing catalyst precursors give a ratio of main products similar to each other. It is apparent that ferrous catalysts cleave NMBB preferably in position at the C-C bond α to the naphthyl ring. Increasing conversion leads in most experiments to a proportional increase in the yields of major products. When added in larger amounts (3.4 vs. 1.2 wt %), S not only increased NMBB conversion, but also altered product distribution (Table 2).

Several studies, including the present work, have shown that NMBB tends to undergo cleavage of the C-C bond connecting the naphthyl group to the remainder of the molecule when subjected to a variety of catalytic reactions under a variety of conditions. Farcasiu et al. (3) suggested a reaction mechanism in which the first stage consists of the formation of a radical cation. The loss of electron density leads to a weakened α-bond which can then be broken relatively easily. This is in contrast to model studies in which phenyl-containing compounds prefer β-cleavage (9). In the work of Penn and Wang (9) radical cations were generated in the mass spectrometer under a variety of conditions but had little impact on the bond cleavage pathway. Preference for β-cleavage was observed. Which was explained by resonance stabilization of the intermediates. Both intermediates are resonance stabilized. Thermochemical calculations (10) show that reaction pathway β is 30 kcal/mol lower for both neutral and radical cationic species than pathway α. In contrast, neither of the intermediates resulting from bond α cleavage are stabilized. However, in the presence of a catalyst, the major reaction pathway mainly involves the cleavage of bond α.

These studies indicate that a new decomposition pathway mechanism must be developed to explain the results of bond cleavage involving model reactions on NMBB.

ACKNOWLEDGMENTS

This project was supported by the U.S. Department of Energy, Pittsburgh Energy Technology Center under contract DE-AC22-92PC92122. We are grateful to Dr. U. Rao of PETC for his support. We also thank Mr. R. Copenhaver for the fabrication of reactors, and Mach I Inc. for providing the SFIO sample.

REFERENCES

1. Mochida, I. and Sakanishi, K. *Advances in Catalysis*, **40**, **1994**, 39-85.
2. a) Schmidt, E. and Song, C. *Prepr. Pap. - Am. Chem. Soc., Div. Fuel Chem.*, **35**, **1994** 733-737.
   b) Song, C.; Schmidt, E. and Schobert, H. H. *DOE Coal Liquefaction and Gas Conversion, Contractors' Review Meeting, Pittsburgh*, (September 7-8, **1994**), 593-604.
3. a) Farcasiu, M.; Smith, C. *Prepr. Pap. - Am. Chem. Soc., Div. Fuel Chem.* , **1990**, **35**, 404-13.
   b) Farcasiu, M.; Smith, C. *Fuel Processing Technology* , **1991**, **29**, 199-208.
   c) Farciasiu, M.; Smith, C. and Ladner, E. P. *Prepr. Pap. - Am. Chem. Soc., Div. Fuel Chem.*, **1991**, **36**, 1869-77.
4. Artok, L.; Davis, A.; Mitchell, G. D.; Schobert, H. H. and Schobert, H. H. *Energy Fuels* , **1993**, **7**, 67-77.
5. a) Hirschon, A. S.; Wilson Jr, R. B. *Coal Science II* , *ACS Sym. Ser.*, **1991**, 273-83.
   b) Hirschon, A. S.; Wilson Jr, R. B. *Fuel*, **1992**, **71**, 1025-31.
6. Artok, L.; Schobert, H. H.; Davis, A. *Fuel Process Technol.*, in press.
7. a) Herrick, D.; Tierney, J.; Wender, I.; Huffmann, G.P. and Huggins, F.E. *Energy and Fuels*, **4**, **1990**, 231.
   b) Weller, S. *Energy Fuels*, **1994**, **8**, 415-420.
8. Song C.; Schmidt, E. and Schobert, H. H. *8th ICCS, Oviedo Spain*, September 10-15, **1995**, submitted.
9. Penn, J. H.; Wang, J.-H. *Energy Fuels*, **1994**, **8**, 421-425.
10. Ades, H. F.; Companion, A. L.; Subbaswamy, K. R. *Prepr. Pap. - Am. Chem. Soc., Div. Fuel Chem.*,**1991**, **36**, 420-4.

Table 1: Effect of Catalyst Precursors on Hydrocracking Reactions of NMBB at 400 °C.

Catalyst Precursors[a]	Cp_2Fe	Cp_2Fe + S	$FeSO_4$ x 7 H_2O	$FeSO_4$ x 7 H_2O+ S	Superfine Fe_2O_3	Superfine Fe_2O_3 + S
Products [mol %]						
Toluene	1.6	1.1		1.3	1.3	1.9
Tetralin	0.4	0.3		0.6	3.0	4.0
Naphthalene	13.8	10.3	4.5	24.0	16.4	64.1
2-Methylnaphthalene						1.4
1-Methylnaphthalene	5.6	.0.5		1.5		5.8
Bibenzyl	2.6	0.6	0.6	2.5	1.0	8.9
4-Methylbibenzyl	9.4	7.4	2.6	19.1	17.4	59.6
Conversion [wt %]	**15.8**	**9.6**	**3.7**	**23.9**	**27.1**	**78.2**

[a]When sulfur was added, the atomic ratio of S:Fe was 1:1.

Table 2: Effect of Sulfur Addition on Hydrocracking Reactions of NMBB at 400 °C.

Catalyst Precursors	None Catalytic	Sulfur [1.2 wt %][a]	Sulfur [3.4 wt %][a]	None [sulfided reactor]	None [reactor HCl treated]
Products [mol %]					
Toluene	0.3	1.4	4.9	1.0	1.0
p-Xylene					
Tetralin	0.2	0.8	2.9	0.8	0.4
Naphthalene	0.6	24.8	74.4	19.1	10.8
2-MTHN[b]			0.4		
2-Methylnaphthalene			7.8		
1-Methylnaphthalene		1.7	9.5	0.8	0.7
Benzylnaphthalene	0.9				
Bibenzyl		2.4	42.5	1.0	1.2
4-Methylbibenzyl	1.3	22.1	32.3	18.3	9.7
Conversion [wt %]	**3.9**	**26.1**	**82.5**	**23.0**	**11.6**

[a]Based on NMBB, [b]methyltetrahydronaphthalene.

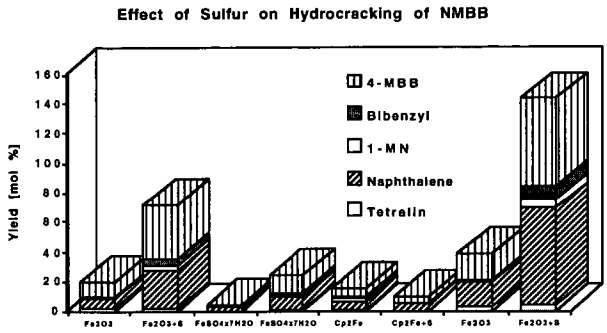

Figure 1: Effect of catalytic hydrocracking of NMBB at 400 ° for 30 min.

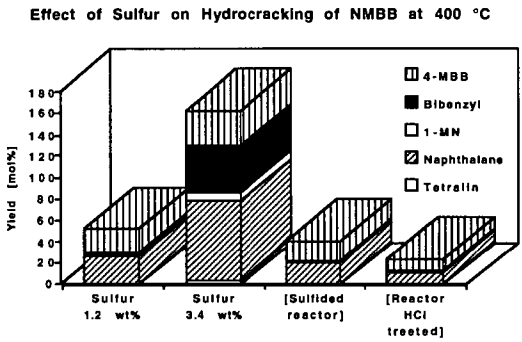

Figure 2: Effect of sulfur on NMBB hydrocracking product distribution at 400 °C for 30 min.

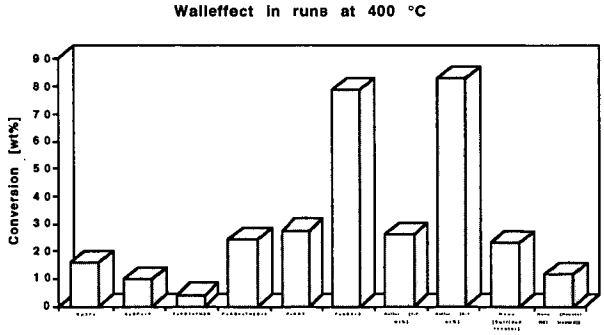

Figure 3: Effect of sulfur on NMBB conversion at 400 °C for 30 min.

A STUDY OF CHEMICAL DEHYDRATION OF COALS AND ITS EFFECT ON COAL LIQUEFACTION YIELDS

D.A. Netzel, F.P. Miknis, J.C. Wallace, Jr., C.H. Butcher, J.M. Mitzel, T.F. Turner
Western Research Institute, 365 N. 9th Street, Laramie, WY 82070-3380,
and R.J. Hurtubise, Dept. of Chemistry, University of Wyoming, Laramie, WY 82071

Keywords: Coal Drying, Chemical Dehydration, Coal Liquefaction

INTRODUCTION

Although great strides have been made in developing the technology of coal liquefaction processes in recent years, many unsolved problems still remain before a viable and economical process can be achieved. The technological problems that still exist can be solved through a more fundamental understanding of the chemistry associated with each stage of the coal liquefaction process, starting with any pretreatment steps that may be carried out on the coal itself. One pretreatment process which can improve the economics of coal liquefaction is coal drying, particularly for the lower rank coals. However, there is also considerable evidence to show that drying has a detrimental effect on the liquefaction behavior of coals.[1-3] The problem that needs to be solved is that of economically drying coal without adversely affecting its liquefaction reactivity. Only recently have there been any systematic studies of the methods of coal drying on coal structure and the role water plays in enhancing or lessening coal reactivity toward liquefaction.[4-5] Thermal methods of drying can alter the physical structure of coal as well as promote undesirable chemical reactions. Low-temperature drying of coal, on the other hand, should preserve the structural integrity, reduce retrograde reactions, reduce thermal degradation, and provide information on nonbonded, chemisorbed, and physisorbed water. Chemical drying of coals is a relatively unexplored technique for removing water at low temperature.

A common chemical dehydrating agent is 2,2-dimethoxypropane. This agent has been used in inorganic chemistry to remove water of hydration in inorganic compounds[6] and in biological sciences for drying tissues for microscopic examination.[7,8] The reaction of 2,2-dimethoxypropane (DMP) with water is shown in scheme I.[9]

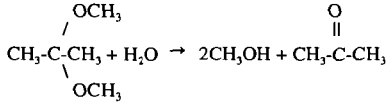

Scheme I

This reaction is rapid and endothermic. The reaction products, methanol and acetone, are removed by vacuum at ambient temperature. Removing water by chemical means rather than by physically forcing exchange by mass action preserves the ultrastructural integrity of the coal cellular components. The use of the dehydration agent, 2,2-dimethoxypropane, in this study to dry coals is a novel and innovative approach to the understanding of the role of water in coal chemistry.[10]

EXPERIMENTAL

Of the six coals used in this study four were obtained from the Pennsylvania State University, Coal Research Section, and two were obtained from the Powder River Basin in Wyoming. The coals selected for study consisted of a lignite, three subbituminous, and two bituminous coals. Bulk samples of these coals were premoisturized in a constant humidity chamber at 30°C for 24 hours. The moisture content determined thermally was used as the reference moisture content for the coals.

Coal samples were dried with DMP before coal liquefaction. Depending upon the amount of moisture in the coal, between 22 and 72 grams of DMP, and between 6 and 25 mL of 0.2 N methanesulfonic acid in methanol were added to a 20 g sample of coal. The acid-methanol solution was added to the sample, followed by DMP. The contents of the flask were shaken to ensure good mixing and contact. The mixture was allowed to stand for 24 hrs. The liquid was then decanted and a vacuum was applied to remove the remaining liquid (excess DMP and methanol).

A modified "Borgialli" microreactor[1] was used for the liquefaction of the coals. The key features of this reactor system are: rapid heating through submergence in a fluidized sandbath,

pneumatic control of the extent of autoclave submergence, and continuous stirring using a magnetically-coupled stirrer. The gases produced during the coal liquefaction process were collected in a gas bomb and analyzed using an HP 5890 Series II GC fitted with both FID and TCD detectors. A 6 ft, Porapak N, packed column was used to separate the gases. Upon completion of the coal liquefaction experiment, the reactor was opened, and the soluble coal products and residue were rinsed using CH_2Cl_2 into a Soxhlet thimble. Soxhlet extraction was carried out for 30 hr at the refluxing temperature of CH_2Cl_2. The solid residue in the Soxhlet thimble and the thimble were placed into a furnace set at ~ 100°C for 20 hrs to remove solvent. The coal residues were characterized using solid-state carbon-13 NMR. Solvent swelling of the coal samples was conducted using the procedure described by Green et al.[12]

Solid-state ^{13}C NMR measurements were made using a Chemagnetics 100/200 solids NMR spectrometer. Carbon aromaticity measurements were made at 25 MHz using the technique of cross polarization (CP) with magic-angle spinning (MAS) and high-power decoupling. These measurements were made using either a large-volume sample spinner (2.1 mL) at a spinning rate of ~ 3.8 kHz or a 7.5 mm (OD) sample spinner at a spinning rate of 4.5 kHz. Between 3,600 and 7,200 transients were recorded. Other instrument parameters were a pulse delay of 1 s, a contact time of 1 ms, a 6.2 μs (large volume spinner) and 5 μs (7.5 mm spinner) pulse widths, a sweep width of 16 kHz, and 1 K data acquisition points. A 25 or 50 Hz exponential multiplier was applied to the free induction decay of each ^{13}C spectrum before integration.

A TA instruments 2910 Differential Scanning Calorimeter (DSC) with a liquid nitrogen cooling accessory (LNCA) was used in this study to determine the amount of solvents retained by the coals after chemical dehydration.

RESULTS AND DISCUSSION

A. Effects of Chemical Drying Process on the Structure of Coals

1. Chemical Drying Kinetics. A typical plot of the weight percent of moisture removed from the coal samples as a function of time in which the coals are in contact with DMP is shown in Figure 1. In all cases a significant amount of moisture is removed in the first minute of the reaction. The initial reaction is DMP with physisorbed surface water and free water in the pores near the surface of the coal. Removal of the remaining moisture requires longer times and is due to diffusion control of DMP into the smaller pores within the coals.

The chemical drying data after the fast initial reaction were fit to 1st- and n^{th}-order kinetic equations. The kinetic parameters are listed in Table I. The initial concentration, C_i, shown in the table is defined as the percent of physisorbed and free surface moisture removed from the coal during the initial reaction of water and DMP. This reaction occurs almost instantaneously. The value of C_i for both the first order and n^{th} order reactions increases with decreasing coal rank. That is, the higher rank coals are generally less porous and have less adsorbed water than the lower rank coals. For Wyoming Black Thunder coal, the C_i value is higher than expected and may be due to the smaller mesh size of the coal sample compared to the other coals.

The percent of moisture in coal at $t = \infty$, but not including the water removed during the initial reaction, is M_∞. The sum of C_i and M_∞ gives the total amount of water in each coal sample. These values exceed their respective thermal moisture values especially for the low rank coals.

Table I also lists the percent of readily accessible water (sorbed surface water) for each coal. As shown in the table, the percent of loosely bound surface water increases with decreasing rank of the coal. Based on a first-order kinetics analysis of the data, the Utah Blind Canyon coals have the lowest amount of surface water (12.2%) whereas the Texas Bottom coal and North Dakota Beulah lignite have almost two-thirds of the total water near or on the surface and readily accessible to react with DMP (62.0 and 64.4%, respectively). Figure 2 is a plot of the percent of surface water as a function of the rank of coal based upon the fixed carbon content. Wroblewski and Verkade[12] also measured the different types of moisture in coals using several extraction solvents and measuring the moisture content in the extracts over an eight hour period. These authors found that of the total moisture content, the higher rank coals have less surface water than the lower rank coals in qualitative agreement with the results shown in Figure 2.

2. ^{13}C NMR. The ^{13}C CP/MAS NMR spectra of the premoisturized and chemically dried Wyoming Eagle Butte coal is shown in Figures 3a and 3b. There appears to be enhanced resolution in the aromatic (100-210 ppm) and aliphatic (0-80 ppm) carbon regions of the spectra. Decarboxylation in the aromatic region is not apparent. The enhanced resolution in the aliphatic carbon region may be due to (1) the tightly bound residual solvents and/or reaction products such as methanol that had replaced the water and (2) increased mobility of some coal

components because of less secondary interactions resulting from the loss of the strongly hydrogen bonded water. Only slight changes (within experimental error) are noted for the carbon aromaticity values for chemical dried coals relative to the premoisturized coals. Thus, chemical drying had little or no effect on the organic composition of the coals. However, the extent of physical association of the coal molecule had been altered due to the loss of water which may have affected the overall coal structure.[13]

3. Differential Scanning Calorimetry of Coals. The solid-state ^{13}C NMR spectra of chemically dried coals showed additional carbon resonances and/or increased resolution in the aliphatic carbon region. The changes in the spectra were assumed to be due to sorbed solvents and/or reaction products occupying surface and pore sites previously held by water. DSC was used to identify and quantify the sorbed species for the chemically dehydrated coals. For the chemically dried coal samples, losses could conceivably be from vaporization of methanol, acetone, water, or a combination of the three. Fortunately, the heats of vaporization of the three materials are significantly different, and a tentative identification of the material is possible if it is assumed that only one material is lost. For all chemically-dried coals, except Utah Blind Canyon, the material lost appears to be methanol with an average heat of vaporization of 1136 J/g and a standard deviation of 100 J/g. The literature value is 1224.5 J/g. The measured heat of vaporization for the Utah coal is close to the literature value for acetone, however, the weight loss for this material and the transition energy are small decreasing the accuracy of both measurements and placing the identification of the material in some doubt.

4. Swelling Index. The swelling index profile parameter[14] of the chemically dehydrated coals is given in Table II. This parameter for Illinois # 6 and Texas Bottom coals shows a small decrease relative to the swelling index parameter of the premoisturized coals, whereas, Utah Blind Canyon, Wyoming Eagle Butte, Wyoming Black Thunder, and North Dakota Beulah coals show a significant increase. The data show that only a small increase or no change in the cross-linking internal structure for the Illinois # 6 and Texas Bottom coals had occurred as a result of chemical dehydration. However, a significant decrease in the cross-linking structure ($1 - X > 1$) is observed for the other four coals. The incorporation of CH_3OH at the sites previously occupied by water molecules would decrease the extent of relatively strong secondary interactions involving ionized groups, charge-transfer complexes and π-π interactions as well as hydrogen bonding and weak van der Waal's forces.[15] A decrease in these interactions, in effect, would reduce the cross-linking due to physical association relative to the premoisturized coal.

B. Effects of Chemical Drying Process on the Reactivity of Coals

Table III gives the results of the coal liquefaction of the six coals that were chemically dried. The table contains data on the percentage of gas, liquid, and residue produced, and the percent conversion. Relative to the premoisturized coals (0% water removed), drying the coals by chemical dehydration, in general, increased the conversion yield. Utah Blind Canyon and North Dakota Beulah coals showed little or no change in the conversion yield.

Except for the chemically dried coals, the conversions are generally less for coals dried by thermal methods.[1-4,16] The reason for the differences in liquefaction behavior of the chemically dried and the thermally dried coals appears to be due to the retention of the reaction products and solvents by the chemically dried coals. DSC has shown that some of the methanol was incorporated into the coal pore structure in place of the water, thus possibly preventing collapse of the pore structure during the dehydration reaction. This would allow for greater diffusion of tetralin during liquefaction and hence greater conversion. Relative to the premoisturized coal, all chemically dried coals show an increase in the coal liquid yield. This increase may also be the result of replacement of water by CH_3OH in the internal structure of coal thereby reducing the strong hydrogen bonding effect caused by water. In general, there is increase in total percent of gas produced with decreasing rank of the premoisturized coals (Utah to North Dakota). Both the Utah and North Dakota coals show a significant decrease in gas produced when completely dried. The total amount of gases produced from the other four dried coals is essentially the same as their corresponding premoisturized coals. The amount of coal residue produced during liquefaction of the premoisturized coals (Table III) decreases with the increase in the moisture content of the coal (decrease in coal rank).

The ^{13}C CP/MAS NMR spectra of the coal liquefaction CH_2Cl_2 extracted residues from the premoisturized and chemically dried Texas Bottom coals are shown in Figures 4a and 4b. When compared to the starting coal spectrum, the NMR spectra of the residues show a significant reduction in the aliphatic component relative to the aromatic component. There is also a shift in the resonance position from ~ 30 ppm to ~ 20 ppm for the aliphatic carbons. The residual

aliphatic component at ~ 20 ppm could be due to methyl groups attached to aromatic rings that would not be cleaved during liquefaction at 425°C.

The significant difference in the residue NMR spectra of the Texas Bottom coal as well as for the other five coals is the enhanced resolution of the aliphatic carbons for the coals dried via chemical dehydration. This enhanced resolution of the aliphatic carbons in the ^{13}C NMR spectra was also noted in the NMR spectra of the chemically dried coals before liquefaction. However, it is unlikely that the carbon resonances observed are due to solvent and reaction products of the chemical drying technique unless the methanol is strongly adsorbed even at the liquefaction temperature of 425°C. It may be that the methanol solvent removed some of the soluble aliphatic carbon substituents (decreasing the chemical shift dispersion) and, thus, in effect giving higher resolution of the remaining carbons types.

REFERENCES

1. Silver, H.F., and W.S. Frazee, EPRI Report AP-4193, 1985.
2. Silver, H.F., P.J. Hallinan, and W.S. Frazee, ACS Div. of Petrol. Chem. Preprints, 1986, 31(3): 755-760.
3. Serio, M.A., P.R. Solomon, E. Kroo, R. Bassilakis, R. Malhotra, and D. McMillen, ACS Div. of Fuel Chem. Preprints, 1990, 35(1): 61-69.
4. Song, C., A.K. Saini, and H.H. Schobert, Energy and Fuels, 1994, 8: 301.
5. Okuma, O., M. Masuda, K. Murakoshi, S. Yanai, and T. Matsumura, Nenryo Kyokaishi, 1990, 69: 259.
6. Donoghue, J.T., and R.S. Drago, Inorg. Chem., 1962, 1: 866-872.
7. Adams, R.F., J. of Chrom., 1974, 95: 189-212.
8. Muller, L.L., and T.J. Jacks, J. of Histochemistry and Cytochemistry, 1975, 23: 107-110.
9. Critchfield, F.E., and E.T. Bishop, Anal. Chem., 1961, 33: 1034-1033.
10. Netzel, D.A., F.P. Miknis, J.C. Wallace, Jr., C.H. Butcher, J.M. Mitzel, T.F. Turner, and R.J Hurtubise, DOE Final Report, Western Research Institute, WRI Report No. WRI-95-R023.
11. Green, T.K., J. Kovac, and J.W. Larsen, Fuel, 1984, 63: 935-938.
12. Wroblewski, A.E., and J.G. Verkade, Energy and Fuels, 1992, 6: 331.
13. Nishioka, M., Fuel, 1994, 73: 57.
14. Solomon, P.R., M.A. Serio, G.V. Deshpande, and E. Kroo, Energy and Fuels, 1990, 4: 42.
15. Nishioka, M., 1992, Fuel, 1992, 71: 941.
16. Saini, A.K., C. Song, and H. Shobert, ACS Div. Fuel Chem. Preprints, 1993, 38 (2): 593.

Table I. Kinetic Parameters for the Chemical Dehydration of Coals

Coal		Kinetic Parameters					
		Order n	Rate Constant k, hr^{-1}	Initial Concentration of water, C_i (%)	Final Concentration of water, M_∞ (%)	Total Concentration of Water (%) $C_i + M_\infty$	Percent of Surface Water $C_i/(C_i+M_\infty)$
Utah Blind Canyon	1st order	1	3.59×10^{-3}	0.89	6.41	7.3	12.2
	nth order	0.893	4.15×10^{-3}	0.94	6.31	7.3	13.0
Illinois # 6	1st order	1	1.93×10^{-2}	4.6	6.5	11.1	41.4
	nth order	1.07	2.49×10^{-2}	4.5	6.6	11.1	40.5
Wyoming Eagle Butte	1st order	1	2.17×10^{-3}	12.5	11.5	24.0	52.1
	nth order	3.62	0.157	11.2	18.8	30.0	37.3
Wyoming Black Thunder	1st order	1	1.85×10^{-3}	19.9	2.2	22.1	90.1
	nth order	0.943	1.62×10^{-2}	15.3	7.1	22.4	68.3
Texas Bottom	1st order	1	8.39×10^{-3}	18.4	11.3	29.7	62.0
	nth order	5.61	12.8	13.0	23.6	36.6	35.5
North Dakota Beulah	1st order	1	1.11×10^{-3}	24.6	13.6	38.2	64.4
	nth order	1.32	4.29×10^{-4}	24.6	15.4	40.0	63.1

Table II. Solvent Swelling Profile Parameter[a] of Premoisturized Coals and Chemically Dried Coals

Coal	Swelling Parameter (1-X) using 1,4-Dioxane	
	Premoisturized Coal	Chemically Dried
Utah Blind Canyon	1.0	1.61
Illinois # 6	1.0	0.95
Wyoming Eagle Butte	1.0	1.50
Wyoming Black Thunder	1.0	1.51
Texas Bottom	1.0	0.84
North Dakota Beulah	1.0	1.10

[a] $X = (Q_{coal} - Q_{v,dry}) / (Q_{coal} - 1)$ where X = swelling index; Q_{coal} = swelling ratio of the premoisturized coal; and $Q_{v,dry}$ = swelling ratio of the dried coal.

Table III. Percentages of Gas, Liquid, Residue, and Conversion from the Liquefaction of Coals Dried using the Chemical Dehydration Method

Coal	Percent Water Removed	Percent Gas	Percent Liquid	Percent Residue	Percent Conversion
Utah Blind Canyon	0 100	9.1 4.0	61.0 63.7	30.0 32.3	70 67.7
Illinois # 6	0 100	3.4 5.3	64.3 74.4	32.4 20.2	67.6 79.8
Wyoming Eagle Butte	0 100	10.9 10.0	62.3 75.1	26.8 14.9	73.2 85.1
Wyoming Black Thunder	0 100	11.4 9.7	67.6 72.4	21.0 17.9	79.0 82.1
Texas Bottom	0 100	12.4 10.2	70.0 77.2	17.6 12.6	82.4 87.4
North Dakota Beulah	0 100	35.6 12.1	38.8 62.1	25.6 25.8	74.4 74.2

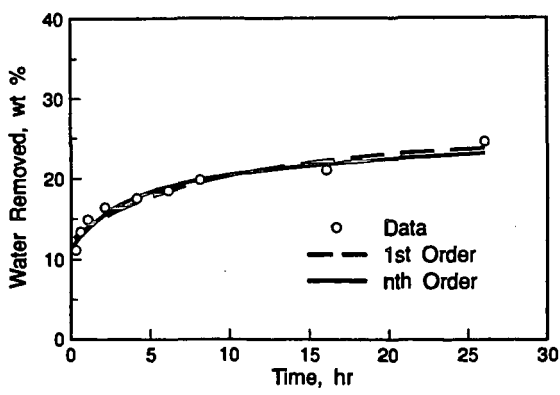

Figure 1. Weight Percent of Water Removed by DMP in Wyoming Eagle Butte Coal as a Function of Time

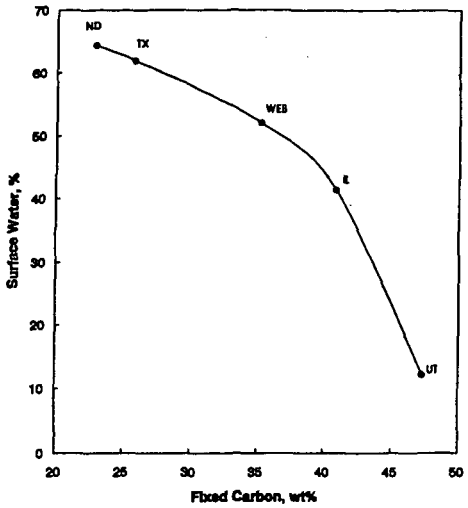

Figure 2. A Plot of the Percent Surface Water for Coals as a Function of the Coal Rank (wt % of fix carbon)

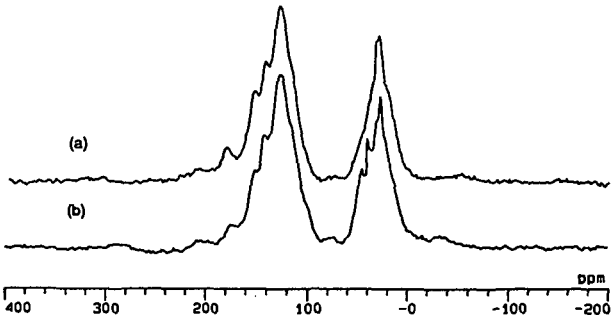

Figure 3. Carbon-13 NMR Spectra of Wyoming Eagle Butte Coal: (a) Premoisturized Coal and (b) Chemically Dried Coal

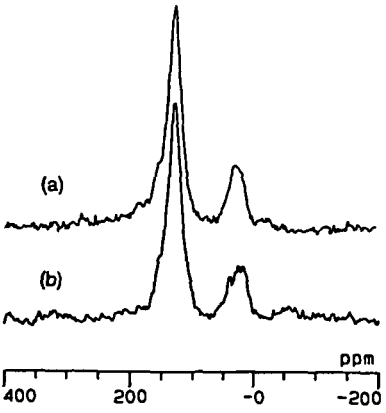

Figure 4. Carbon-13 NMR Spectra of Texas Bottom Coal Residues from Coal Liquefaction of (a) Premoisturized Coal and (b) Chemically Dried Coal

INFLUENCE OF BINARY SWELLING SOLVENTS: MECHANISM OF ACTION

R. Ding, D. Tucker and Lowell D. Kispert
Department of Chemistry, Box 870336
The University of Alabama
Tuscaloosa, AL 35487-0336

KEYWORDS: Binary, Swelling Solvents, Hydrogen Bonding, Spin Probes

ABSTRACT

This study addresses the dramatic up-take of a poor swelling solvent in Argonne Premium Coal Samples (APCS), Illinois #6, Beulah-Zap and Lewiston-Stockton when such a solvent is spiked with various amounts of the strong swelling solvent, pyridine. The unexpected up-take can be explained in terms of four different processes: (1) disruption of weak hydrogen bonds which isolate the interconnected micropore system; (2) disruption of weak hydrogen bonds which protect individual micropores; (3) competition of pyridine for the active sites involved in the hydrogen bonds or the "poisoning" of active sites; and (4) disruption of stronger hydrogen bonds within the macromolecules which causes an opening of the structure. When more than 5% pyridine is used, no additional disruption of the hydrogen-bonded network occurs. The structural changes were monitored by spin probe incorporation which was measured by EPR spectroscopy.

INTRODUCTION

In swelling coals with chlorobenzene, it has been observed by Green and Larsen that when small amounts (0.35 mmol/g coal) of pyridine are added to chlorobenzene, the up-take of chlorobenzene by the coal is dramatically increased.[1] Since the EPR spin probe method has been shown to be very sensitive to changes in the physical and chemical structure of coal during this swelling process,[2] it was thought that some insight into the effect of pyridine on the coal structure could be gained by applying this method to a binary swelling solvent. Toluene was used as the swelling solvent because it does not significantly swell the coal or disturb any cross-linking, so that the interactions between the coal structure and pyridine can be studied.

Previously, Painter has asserted that hydrogen bonds in coal are short lived and do not make major contributions to the cross-linked structure.[3] A recent model assumes that coal is made up of interconnected chains which are solubilized during this swelling process.[4] These connected chains have segments referred to as dangling ends, whose mobility is limited by the surrounding solubilized chain segments suggesting a dynamic structure for coal during the swelling process. The same conclusion can be reached from the results of short term oxidation studies,[5] where removal of water during exposure to dry gas causes changes in as little as 30 seconds. It is possible that hydrogen bonding can establish cross-linking within a macromolecule causing a blockage of the micropore areas, making them inaccessible to guest molecules until they are disrupted by a swelling solvent as supported by observations of Larsen and Wernett.[6] It was observed that the surface area measured for Beulah Zap lignite by N_2 or hydrocarbon surface analysis was 30 times less than by CO_2 surface analysis. This was attributed to the greater solubility of CO_2 in coal and it was concluded that an interconnected micropore network does not exist.

Two assumptions are necessary to explain the observations made in the current study: one, that coal has a dynamic structure and two, that hydrogen bond interactions form cross-links which inhibit accessibility of guest molecules to the coal micropores. The two spin probes used in this study were TEMPAMINE (VII) and TEMPO (VIII) (Figure 1). These compounds have similar molecular volumes, but VII contains an amino group which can interact with hydrogen bonding sites in the coal structure.

EXPERIMENTAL

Swelling solvent/spin probe solutions were prepared in 1 millimolar concentrations of VII or VIII in toluene. Each spin probe solution was split into 16 aliquots of 10 mL and spiked with 0% to 9% pyridine.

APCS coal samples (Beulah-Zap, Illinois #6 and Lewiston-Stockton) were opened under argon and 30 mg portions were immediately placed into vials and covered with 2 mL of a toluene spin probe solution spiked with pyridine. Each sample was then swelled for 18 hours and worked up as previously described.[7] The concentration of the incorporated spin probes was determined by EPR spectroscopy.

RESULTS AND DISCUSSION

Illinois #6 Subbituminous Coal

The retention of spin probe VII (amine substitutent) in Illinois #6 is shown in Figure 2. It can be seen that oscillations occur in the concentration of spin probe retained as the amount of pyridine that is added to the swelling solvent is increased. These oscillations decrease in intensity as the concentration of pyridine in the solvent solution is increased up to 2% pyridine in toluene. From a 2% up to 5% pyridine concentration (not shown) there is no significant change in the retention of spin probe VII. The largest changes in spin probe retention are observed for concentrations of pyridine less than 0.5%. A three fold increase in spin probe retention is observed upon the addition of 500 ppm pyridine (0.05%) to the toluene swelling solvent.

Figure 3 illustrates the effect of pyridine concentration in toluene on the retention of spin probe VIII in Illinois #6, where the size of the probe is the controlling factor. The effects are similar to those observed for the retention of spin probe VII, although the extent of retention is decreased by 90%. Significant oscillations in spin probe retention are observed for concentrations of pyridine less than 2%. As above, increases in pyridine concentration beyond 2% have very little effect on the retention of spin probe VIII.

Since retention of spin probe VII was much greater than that observed for spin probe VIII, it seems that structural changes, brought about by small amounts of pyridine, provide for significantly increased accessibility of the spin probe to active sites in Illinois #6 APCS coal. The enhanced retention of VII indicates that the active sites are capable of strong interactions with the amino group.

The fact that the addition of 0.1% pyridine causes a large decrease in retention for both spin probes shows that a structural change is primarily responsible since spin probe VIII has no functional interactions. The decrease in retention of spin probe VIII indicates either that the structure of the coal collapsed, blocking access to the coal micropores, or that the structure opened up to such a large extent that the spin probes could not be trapped. It seems likely at this point that the structure is opened to an extent such that the spin probes are removed during the cyclohexane wash since the concentration of spin probe VII is still greater than the retention observed in the absence of pyridine. Evidently very small amounts of pyridine open the structure of the coal enough so that "pockets" of active sites are made accessible to the spin probes.

It is possible that opening the structure only slightly allows for diffusion of the spin probes into the structure, while somewhat greater opening of the structure allows for pockets to be formed which trap the spin probes more effectively. In this way, the coal pockets could trap polar spin probes of the requisite size with hydrogen bond interactions exactly like an inclusion compound (as opposed to a simple intercalation process). As the structure is opened further, the larger pockets can no longer trap the guest molecules, and so the retention of the spin probes in the structure decreases.

At 0.2% pyridine, the concentration of the retained spin probe VIII drops even further; however, the retention of spin probe VII increases again. This shows that the structure has opened even further (decrease in spin probe VIII), allowing greater accessibility to hydrogen-bonding sites (increase in spin probe VII), but not creating any additional pockets which might trap the non-hydrogen bonding probes (spin probe VIII).

As the amount of pyridine is increased to 0.4%, a decrease in retention is observed for spin probe VII while an increase in retention is observed for spin probe VIII. This indicates that pyridine causes a poisoning of the active sites available for interaction with the polar spin probe, while at the same time opening the structure to create more areas that are able to trap small spin probes. It should be noted that the amount of amino substituted spin probes retained at this pyridine concentration is still much greater than that of the non-substituted spin probes, indicating that there is still a significant number of active sites available for trapping polar spin probes.

At 0.6% pyridine, an increase in retention is observed for spin probe VII while a decrease is observed for spin probe VIII. At this point and beyond, further oscillations in the retention of each spin probe appear to be due to competing processes of opening micropores, opening larger structural areas, and poisoning of active sites with pyridine.

With higher concentrations of pyridine both the period and the amplitude of the oscillations decreased. After the concentration of pyridine reached 10%, the spin retention observed is similar to that observed for pure pyridine. The data suggest that complete structural opening occurs so that if this is desired, it may be possible to achieve this goal without wasting large amounts of an expensive, toxic, strong swelling solvent.

Beulap-Zap Lignite

Spin probe VII retention in Beulah-Zap lignite swelled in toluene spiked with up to 1.2% of pyridine is expressed as a function of pyridine concentration in Figure 4. Again an oscillatory behavior is observed for spin probe retention as the concentration of pyridine in the swelling solvent solution is increased. Similar to the behavior of Illinois #6, the oscillations observed for the retention of spin probe VII in Beulah-Zap have decreasing periods as the concentration of pyridine is increased. Increasing the pyridine concentration above 4% has little effect on the amount of spin probe retention. It is likely that the structure of the lignite has then been completely opened by disrupting all hydrogen bonded networks, as was observed when pure pyridine was used as the swelling solvent.

The retention of spin probe VIII (size dependence) in Beulah-Zap lignite as a function of pyridine concentration in the toluene swelling solvent is shown in Figure 5. Oscillatory behavior similar to that of Illinois #6 is observed. However, after 0.6%, additional pyridine has a negligible effect on the incorporation of the spin probe. Addition of 100 ppm pyridine (0.01%) to the swelling solvent for Beulah-Zap has almost no effect on the retention of spin probe VIII. When the concentration of pyridine is increased to 200 ppm (0.02%), a large increase in the retention of spin probe VIII is observed, while a small, yet significant decrease in the retention of spin probe VII is observed. The large increase in spin probe VIII retention indicates that hydrogen bonds which block access to the interconnected micropore network have been disrupted without significantly affecting the macromolecular structure. Although a greater number of micropores was made available, a decrease in the retention of spin probe VII was observed. This would seem to indicate that in Beulah-Zap the pyridine necessary to provide initial access to the micropore structure competes significantly for the active hydrogen bonding sites available to the amino spin probes.

As the concentration of the pyridine in the swelling solvent is increased from 200 ppm to 500 ppm (0.05%), a large decrease in the retention of spin probe VIII occurs, but a corresponding increase in the retention of spin probe VII is observed. The large decrease in retention of spin probe VIII indicates that the macromolecular structure was opened to a significant extent. This disruption of hydrogen bonds in the macromolecular structure caused a dramatic increase in the available active sites for hydrogen-bonded interactions, as evidenced by the large increase in retention of spin probe VII.

A further increase in the concentration of pyridine to 700 ppm (0.07%) results in an increase in retention of spin probe VIII and a huge decrease in retention of spin

probe VII. Again, additional micropore structure is made available to guest molecules (indicated by an increase in spin probe VIII retention), but as the concentration of pyridine approaches the concentration of the spin probes, a large percentage of the active sites in the micropore system is poisoned (indicated by the large decrease in spin probe VII retention).

When the concentration of pyridine is 0.1%, a decrease in retention of both spin probes is observed. At this point, the macromolecular structure is opened to such an extent that the spin probes can no longer be trapped in the available micropores.

Further increases in pyridine concentration do not significantly affect the retention of spin probe VIII. The retention of spin probe VII continues to oscillate as the concentration of pyridine increases. At this point the structure of the coal is opened extensively. Variations in the retention of spin probe VII are primarily due to increases in available micropore structure and decreases in active sites due to pyridine site competition.

The observed data can be explained in terms of the following four processes: one, disruption of weak hydrogen bonds which protect or isolate the interconnected micropore system; two, disruption of weak hydrogen bonds which protect individual micropores; three, competition of pyridine for the active sites capable of establishing hydrogen bonds or the "poisoning" of active sites; four, disruption of stronger hydrogen bonds within the macromolecular structure which causes more extensive opening of the structure. The contributions of each of these factors to the spin probe retention with increasing concentrations of pyridine vary to a significant extent up to 1% pyridine. At concentrations above 1% pyridine, the first factor becomes less significant, and variations in the others require greater change in pyridine concentration.

The spin probe retention does not vary to such a degree with percent added pyridine in a higher rank coal such as Lewiston-Stockton where a larger amount of covalent cross-linking and a smaller degree of hydrogen bonding occur. Furthermore, it was found that the spin probe VIII retention as a function of % added pyridine decreased nearly exponentially. The reduced hydrogen bonding in the higher rank coals is reflected by the reduced number of available micropore structures and decreases in active sites due to pyridine site competition.

CONCLUSION

Inclusion of guest molecules into the macromolecular structure of coal can be achieved by spiking a "poor" swelling solvent with as little as 100 ppm of a strong swelling solvent. The optimum amount varies with rank. Dramatic oscillations in spin probe retention are most severe below 0.5% for IL and below 0.1% pyridine for BZ and LS. Above this amount any additional break-up of the hydrogen-bonded structure is not detectable by use of spin probes.

ACKNOWLEDGMENT

This work was supported by the U. S. Department of Energy, University of Coal Grant Program, Grant No. DE-FG22-93PC93202.

REFERENCES

1. Green, T. K.; Larsen, J. W. *Fuel* **1984**, *63*, 1538.
2. Sady, W.; Tucker, D.; Kispert, L. D.; Spears, D. R. *Prepr. Pap. Am. Chem. Soc., Div. Fuel Chem.* **1993**, *38*, 1323.
3. Painter, P. *Am. Chem. Soc. Div. Fuel Chem. Symp. Macrom. Str. Coal.* August 22-26, **1993**, Chicago, IL.
4. Painter, P. *Prepr. Pap. Am. Chem. Soc., Div. Fuel Chem.* **1993**, *38*, 1304.
5. Tucker, D.; Kispert, L. D. *Prepr. Pap. Am. Chem. Soc., Div. Fuel Chem.* **1993**, *38*, 1335.
6. Larsen, J. W.; Wernett, P. C. *Prepr. Pap. Am. Chem. Soc., Div. Fuel Chem.* **1992**, 37(2), 849.
7. Kispert, L. D.; Tucker, D.; Sady, W. *Prepr. Pap. Am. Chem. Soc., Div. Fuel Chem.* **1994**, *39*, 54.

Figure 1
Spin probes VII and VIII.

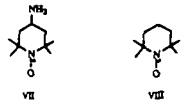

Figure 2
The retention of spin probe VII in Illinois #6 APCS coal after swelling with toluene spiked with pyridine.

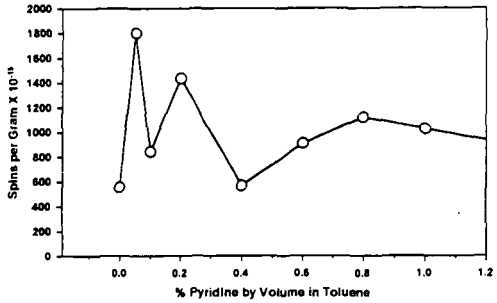

Figure 3
The retention of spin probe VIII in similarly swelled Illinois #6 APCS coal.

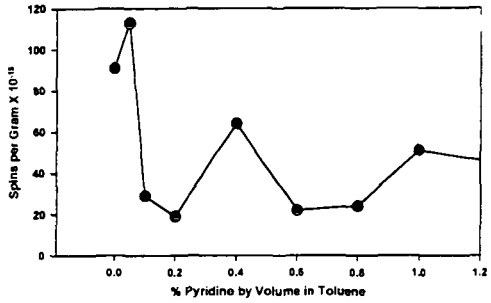

Figure 4
The retention of spin probe VII in similarly swelled Beulah-Zap APCS coal.

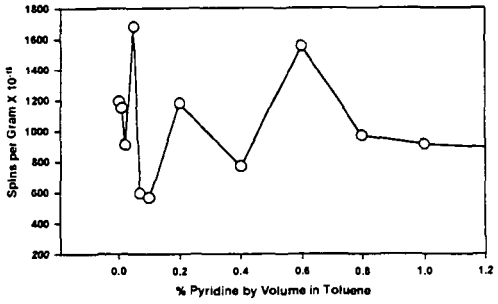

Figure 5
The retention of spin probe VIII in similarly swelled Beulah-Zap APCS coal.

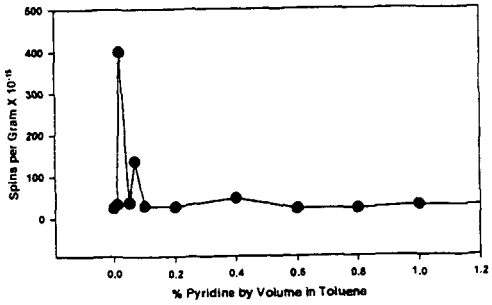

NAPHTHENE UPGRADING WITH PILLARED SYNTHETIC CLAY CATALYSTS

Ramesh K. Sharma and Edwin S. Olson
University of North Dakota
Energy & Environmental Research Center
PO Box 9018
Grand Forks, ND 58202

Keywords: Naphthene, Hydrocracking, Hydroisomerization

ABSTRACT

Catalytic hydrotreatment of methylcyclohexane was investigated to model upgrading of coal-derived naphthenes. Nickel-substituted synthetic mica montmorillonite (NiSMM), alumina-pillared NiSMM, and zirconia-pillared NiSMM were prepared and tested for hydrocracking and hydroisomerization of methylcyclohexane. Infrared and thermal desorption studies of the pyridine-adsorbed catalysts indicated the presence of Lewis as well as Brønsted acid sites. Total acidity and surface area increased with pillaring of NiSMM with polyoxy aluminum and polyoxy zirconium cations. Most of the products were branched alkanes (isoparaffins). These compositions are highly desirable for environmentally acceptable transportation fuels. Furthermore, dehydrogenation was not a major pathway, as indicated by the minimal formation of aromatic hydrocarbons, coke, or other oligomeric materials. This paper describes the effect of various operating conditions, which included reaction temperature, contact time, hydrogen pressure, and catalyst on the product distribution.

INTRODUCTION

A growing need exists for new and improved catalysts to improve the overall economics of coal liquefaction. Coal-derived liquids are heavy, viscous, aromatic, hetero-compound-rich, and are very difficult and expensive to refine into transportation fuels. Natural clays were used as catalysts in petroleum cracking until replaced by more active and selective zeolites (1). Synthetic clays (SMM) containing a hydrogenation component were more active for hydrocracking and hydroisomerization (2-4). Synthetic clays such as nickel-substituted synthetic mica montmorillonite (NiSMM) were effective for cleaving carbon-carbon bonds and isomerizing the alkyl chains to give branched alkanes without extensive formation of aromatic hydrocarbons (5-8). These catalysts have also been found to be effective in hydrocracking and reforming of biomass materials to the isoparaffinic composition desired for transportation fuels (9-10). In the pillared clays, intercalation of hydroxylated or complexed metal cations maintains the clay layer structure after loss of water and generates large pore sizes. These structures are stable to 450° and 500°C. Pillared clays containing a hydrogenation component could be used for hydrogenation and hydrocracking processes.

The goal of this study was to develop an understanding of the hydrocracking and hydroisomerization of coal-derived cycloalkanes (naphthenes). Catalytic hydrotreating reactions of methylcyclohexane (MeCH) were conducted to evaluate the potential of synthetic and pillared synthetic clay catalysts for the upgrading of coal-derived liquids to an isoparaffinic product. The reactions of MeCH were carried out under several conditions to determine the effects of temperature, reaction time, and hydrogen pressure on the hydrocracking and hydroisomerization activity of NiSMM, alumina-pillared NiSMM, and zirconia-pillared NiSMM.

EXPERIMENTAL

Catalyst Preparation and Characterization

NiSMM was prepared by the procedure of Heinerman (11). Pillaring of NiSMM was carried out according to the procedure described earlier (12). The acidity of the solid acid catalysts was determined by pyridine adsorption and desorption studies. A small amount of sample (100 mg) was placed in a glass chamber attached to a vacuum pump, a gas inlet, and a gas outlet. The chamber was evacuated, and argon saturated with pyridine was introduced into the chamber until the weight increase ceased. At this stage, the chamber was evacuated until the physisorbed pyridine was removed, as indicated by the constant weight of the base absorbed sample. The amount of pyridine chemisorbed was used to determine total acidity of the catalyst. Surface area measurements were performed with Micromeritics AccuSorb 2100E static unit for nitrogen physisorption at 77K (BET method).

Catalytic Reactions

In a typical experiment, 0.5 g of MeCH and 0.25 g of the catalyst were placed in a tubing bomb (15-mL microreactor). The microreactor was evacuated, pressurized with desired amount of hydrogen, and placed in a rocking autoclave preheated to the desired temperature. At the end of the reaction period, the microreactor was cooled in a dry ice-acetone slurry, degassed, and opened. The

desired amount of the internal standard was added to the product slurry; the product slurry was transferred into a centrifugation tube by washing with methylene chloride; and the solid catalyst removed by centrifugation. Quantitative gas chromatography-flame ionization detection (GC-FID) analyses of the liquid samples were performed with a Hewlett-Packard 5890a gas chromatograph equipped with a Petrocol capillary column. The solid was dried in vacuum at 110°C for 3 hours. Since it was not found in the reaction products, octadecane was added as the internal standard. Alkane components were determined from the area percent ratio with respect to octadecane, assuming the same response factor.

RESULTS AND DISCUSSION

Total acidity of the NiSMM as measured by the amount of chemisorbed pyridine was found to be 0.84 mmol/g of catalyst, indicating the presence of acidic sites in the catalyst. These sites may be Lewis as well Brønsted acids. Pillaring the clay with polyoxyaluminum cations increased the total acidity to 1.02 mmol/g of catalyst. The increase in acidity is due to the additional acidic sites created by the dehydroxylation of the hydroxylated aluminum cations.

The surface area of the NiSMM was found to be 240 m^2/g. Pillaring the clay with polyoxy zirconium cations resulted in an increase in the surface area (274 m^2/g). The increase in surface area may be due to the micropores created by the dehydroxylation of the intercalated hydroxylated metal cations (pillars).

The results from the catalytic hydrocracking/hydroisomerization reactions of MeCH are given in Tables 1 and 2. In all these tests, conversion to liquid and gas products was 100%, and no coke or insoluble materials were detected on the recovered catalyst.

Temperature effects

A reaction of MeCH was carried out with alumina-pillared NiSMM at 350°C for 30 min in the presence of 1000 psi of initial hydrogen pressure. This reaction gave only 29% conversion of MeCH to products. The yields of liquid and gas products were 23% and 6% respectively. A reaction at 400°C gave considerably higher conversion (93%) of MeCH to liquid (72%) and gas (21%) products. There is therefore a large temperature effect and this experiment established that 400°C is a more appropriate temperature. Subsequent reactions were performed at 400°C.

The reaction products were a complex mixture of hundreds of components formed as result of the extensive rearrangements or isomerization of the primary cracked products. The major products from higher-temperature reactions were the desired isoparaffins (mono-, di-, and trimethylalkanes) with lower amounts of *n*-alkanes. The amount of aromatic hydrocarbons was insignificant.

Pressure effects

Reactions of MeCH were conducted under different initial hydrogen pressures to determine the effect on product yields and distribution. The reaction of MeCH with NiSMM at 400°C for 90 min in the presence of 1000 psi of initial hydrogen pressure gave almost complete conversion of the substrate to liquid (41%) and gas (58%) products. The reaction at 500 psi resulted in significant improvement in the yield of liquid products (72%), and gas yield was significantly lower (25%), owing to lower hydrocracking of MeCH and rearrangement products at the lower pressure. Pillared clay catalysts exhibited the same effect. The reaction of MeCH with alumina-pillared NiSMM (AlPNiSMM) at 400°C for 90 min in the presence of 200 psi of hydrogen (initial) gas only 36% conversion of the substrate to liquid (25%) and gas (11%) products. Increasing the hydrogen pressure to 500 psi resulted in substantial increase in the conversion of MeCH (90%) to give 68% yield of liquid products and 22% of gas products. The reaction with 1000 psi initial hydrogen pressure gave significantly high conversion of MeCH (99%), but the yield of liquid products was significantly lower (42%) with the remaining gas. The reaction of zirconia-pillared NiSMM (ZrPNiSMM) with MeCH at 400°C for 90 min in 500 psi (initial) hydrogen pressure gave 98% conversion to liquid product (68%) and gas product (30%). However, similar reaction with 1000 psi hydrogen pressure gave significantly lower amounts of liquid products and high gas yield (Table 1). Thus there is a large pressure effect on conversion of MeCH and also a large pressure effect on gas yield.

Reaction Time

The effect of reaction time on the product yields and product distribution was investigated with AlPNiSMM. The 30-min reaction gave 93% conversion of MeCH to products; the yields of liquid and gas products were 72% and 21% respectively. The reaction for 90 min resulted in almost complete conversion of MeCH to give a liquid product yield of 42%. The remaining substrate was converted into gaseous products. After 180 min, MeCH was completely converted into liquid (21%) and gaseous (79%) products. The effect of time was also studied by comparing the reactions of MeCH with AlPNiSMM for 30 and 90 minutes at 400°C in the presence of 200 psi of initial

hydrogen pressure. These reactions gave similar conversions of MeCH to volatile products (Table 1). The liquid product yield was somewhat higher for the 30-min reaction than for the 90-min reaction. Thus, over a longer period of time, primary cracked products are further cracked to form undesirable gaseous components, and a shorter reaction time favors liquid isoparaffinic products.

Selectivity

A comparison of the conversions obtained with the three catalysts at 500 and 1000 psi at 400°C indicate that there is no difference in activity. There is also no difference in the selectivity for total liquid product at 500 psi. At 1000 psi, the ZrPNiSMM appeared to give a somewhat better liquid yield (54%) than the NiSMM and AlPNiSMM.

Further information on the selectivity for hydrocracking and hydroisomerization reaction of the MeCH can be gained from comparison of the cyclic and isoparaffinic components in the products (Table 2). The reaction of MeCH with AlPNiSMM in 200 psi hydrogen gave larger amounts of dimethylcyclopentane (DMCP), indicating that hydrocracking is incomplete at lower hydrogen concentrations. The formation of four DMCP isomers (1,1-DMCP, *trans*-1,2-DMCP, *cis*-1,3-DMCP, and *trans*-1,3-DMCP) indicates that carbonium ions form initially on all carbons of the MeCH ring and rapidly rearrange via protonated cyclopropane (actually bicyclohexane) intermediates to the isomeric DMCPs.

The products at 500 psi with the three catalysts are mainly the isoparaffins. Thus, at higher pressures, cracking of the DMCP rearrangement products as well as the MeCH via carbonium ion intermediates increases, giving branched C_7 isomers and subsequently other isoparaffins. The ZrPNiSMM appears to be the most efficient catalyst for the ring hydrocracking reaction. This result is consistent with the higher acidity of this pillared catalyst. Previous work demonstrated that there is no difference in the three catalysts with respect to shape selectivity (9); hence, the effects seen here are likely the result of the acidity effects. The amounts of aromatic hydrocarbons were found to be minimal with all the catalysts, so dehydrogenation is not a major reaction of the MeCH.

The AlPNiSMM gives a quite different distribution of products from those of the other two catalysts. Since the *n*-heptane yield is high, the initial carbonium ion reaction may favor the rearrangement of 2-methylcyclohexylcarbonium ion to 2-ethylcyclopentylcarbonium ion, which cracks to *n*-heptane rather than branched heptanes. Ethylcyclopentane is one of the larger components in the products from this reaction. The lowered content of branched alkanes increased the DMCP:BA ratio. Thus the acidic AlPNiSMM is also efficient at hydrocracking but different initial rearrangements lead to different products.

ACKNOWLEDGMENT

This work was performed under the auspices of the U.S. Department of Energy, Contract No. DOE-FC21-86MC10637.

REFERENCES

1. Gates, B.C.; Katzer, J.R.; Schuit, G.C.A. *Chemistry of Catalytic Processes*; McGraw-Hill: New York, 1979; p 1.
2. Jaffe, J.; Kittrell, J.R. U.S. Patent 3 535 229, 1970.
3. Mulaskey, B.F. U.S. Patent 3 682 811, 1972.
4. Csicsery, S.M.; Mulaskey, B.F. U.S. Patent 3 655 798, 1972.
5. Swift, H.E.; Black, E.R. *Ind. Eng. Chem. Prod. Res. Dev.* **1974** *13*, 106.
6. Black, E.R.; Montagna, A.A.; Swift, H.E. U.S. Patent 4 022 684, 1977.
7. Black, E.R.; Montagna, A.A.; Swift, H.E. U.S. Patent 3 966 642, 1976.
8. Olson, E.S.; Sharma, R.K., *Prepr. Pap.—Am. Chem. Soc., Div. Fuel Chem.* **1994**, *39*, 706.
9. Olson, E.S.; Sharma, R.K. *Energy from Biomass and Wastes XVI*; Klass, D.L. Ed.; Institute of Gas Technology: Chicago, IL, 1993; p 739.
10. Sharma, R.K.; Olson, E.S. *Prepr. Pap.—Am. Chem. Soc., Div. Fuel Chem.* **1994,** *39*, 1040.
11. Heinerman, J.J.L.; Freriks, I.L.C.; Gaaf, J.; Pott, G.T.; Coqlegem, J.G.F. *J. Catal.* **1983,** *80*, 145.
12. Gaaf, J.; van Santen, R.; Knoester, A.; van Wingerden, B. *J. Chem. Soc. Chem. Commun.* **1983,** 655.

Table 1. Catalytic Reactions of Methylcyclohexane[a]

Catalyst	Time, min	Temp, °C	Hydrogen, psig	Conversion, %	Products, %	
					Liquid	Gas
NiSMM[b]	90	400	500	97	72	25
NiSMM	90	400	1000	99	41	58
AlPNiSMM[c]	30	350	1000	29	23	6
AlPNiSMM	30	400	1000	93	72	21
AlPNiSMM	30	400	200	37	28	9
AlPNiSMM	90	400	500	90	68	22
AlPNiSMM	90	400	200	36	25	11
AlPNiSMM	90	400	1000	99	42	57
AlPNiSMM	180	400	1000	100	21	79
ZrPNiSMM[d]	90	400	500	98	68	30
ZrPNiSMM	90	400	1000	99	54	45

[a] Substrate = methylcyclohexane; catalyst:substrate ratio = 0.5.
[b] Nickel-substituted synthetic mica montmorillonite.
[c] Alumina-pillared NiSMM.
[d] Zirconia-pillared NiSMM.

Table 2. Products from Reactions of Methylcyclohexane[a]

Catalyst	Hydrogen, psig	BA[b] / nA[d]	DMCP / BA	OCA[c] / BA	i-C_4 / n-C_4	i-C_5 / n-C_5	i-C_6 / n-C_6	i-C_7 / n-C_7
NiSMM	500	3.2	0.2	0.2	2.2	5.1	5.7	3.1
ZrPNiSMM	500	2.7	0.1	0.1	2.1	4.3	5.2	4.2
AlPNiSMM	500	1.9	0.6	0.2	2.6	6.6	7.5	0.7
AlPNiSMM	200	4.9	6.7	2.3	2.3	7.9	10.6	12.4
AlPNiSMM	1000	3.3	0.6	0.3	2.5	6.6	8.4	2.6

[a] Reaction temperature = 400°C; reaction time = 90 min; catalyst:substrate ratio = 0.5.
[b] Branched alkanes.
[c] Cycloalkanes other than DMCP.
[d] Normal alkanes.

HYDRODESULFURIZATION OF DIBENZOTHIOPHENE OVER Mo-BASED DISPERSED CATALYSTS

William S. Cooke, Eckhardt Schmidt*, Chunshan Song and Harold H. Schobert

Fuel Science Program, Department of Materials Science and Engineering, 209 Academic Projects Building, The Pennsylvania State University, University Park, PA 16802

The hydrodesulfurization (HDS), hydrocracking (HC) activity and selectivity of several Mo, Co and Fe-based catalyst precursors have been examined in model compound reactions of dibenzothiophene (DBT). Reactions were carried out at 400 °C with 6.9 MPa of H_2 for 30 min. A metal loading of 0.5 mol % (based on DBT) in tridecane as solvent resulted in a low conversion rate and only hydrogenation products. Even the addition of sulfur to the catalyst in a 4:1 molar ratio only led to a minor increase in conversion and HDS. However, a change in the molar ratio of solvent to model compound from 1:1 to 19:1 and a metal loading of 36.16 mol % lead to a dramatic increase in conversion, HDS, and HC. Furthermore, the use of higher boiling point solvents such as hexadecane and octadecane had a beneficial effect on both HDS and HC. The addition of sulfur in a 6:1 ratio of S:metal to the higher-metal-loaded runs had varying effects that were dependent upon the catalyst used.

Keywords: Model reactions, hydrocracking, dispersed catalysts.

INTRODUCTION

The objective of this work is to examine the hydrodesulfurization activity of dispersed catalysts under coal liquefaction conditions. Most coal hydroliquefaction reactions (1) are performed at temperatures in excess of 400 °C and 6.9 MPa H_2 for at least 30 min. These severe conditions are required to break the heteroatom and alkyl bridges that connect the aromatic species. Different metal catalysts, in particular molybdenum (2), have been known to be effective in coal liquefaction reactions. The complex nature of coal renders the study of reactions of a specific coal molecule impossible and thus obscures the effectiveness of a particular catalyst. Some catalysts are particularly effective for HC, others better for desulfurization and denitrogenation. Coals with a high heteroatom (sulfur) content, are of concern in combustion processes and pose an environmental risk. Multistage liquefaction is expected to improve selectivity for specific reactions, such as desulfurization, to meet current refining regulations. The model compound chosen for the examination of the hydrodesulfurization was dibenzothiophene (DBT). The catalysts chosen for this study were, ammonium tetrathiomolybdate (ATTM), molybdenum hexacarbonyl, $MoCl_3$, $Co_2(CO)_8$, $Fe(CO)_5$ with and without added sulfur, and the thiocubane type bimetallic catalyst precursor $Cp_2Co_2Mo_2(CO)_2S_4$ [MoCo-TC2].

EXPERIMENTAL

Materials

The model compound dibenzothiophene (98% purity) and the solvents tridecane, heptadecane, and octadecane (all 99% purity) were obtained from Aldrich; $Mo(CO)_6$ obtained from Johnson Matthey, ATTM and $MoCl_3$ from Aldrich, $Fe(CO)_5$ and $Co_2(CO)_8$ from Strem. The thiocubane type complex $Cp_2Co_2Mo_2(CO)_2S_4$ [MoCo-TC2] was prepared according to the method of Brunner and Wachter (3). Elemental sulfur was obtained from J. T. Baker Chemical Co. All chemicals and precursors were used as received.

Conditions and Procedures

Experimental runs with the model compound DBT were carried out in 33 mL reactors using ca. 1 g of DBT and various solvent to model compound ratios at 400 °C for 30 min, in the presence of catalyst precursors (0.5-36.16 mol % metal based on DBT). When sulfur was added to a S-free precursor, the S:metal atomic ratio was 4:1, unless otherwise mentioned. For those experiments involving water, the above procedure was used with the addition of water in a H_2O:DBT molar ratio of 10:1. The remainder of experiments involved a metal loading of 36.16 mol % (with respect to DBT). In another set of experiments, catalysts were added to a reaction solution consisting of 1% DBT and 99% solvent. Sulfur was added to S-free precursors in a S:metal ratio of 6:1. The reaction temperature primarily employed was 400 °C, except for those experiments involving water in which case 350 °C was used. The reactor was purged three times with H_2 and then pressurized with 6.9 MPa H_2 at room temperature for all experiments. A preheated fluidized sand bath was used as the heating source and the horizontal tubing bomb reactor was vertically agitated to provide mixing (about 240 strokes/min). After the reaction the hot tubing bomb was quenched in cold water. The liquid contents were washed with 15 ml CH_2Cl_2 through a low speed filter paper for qualitative and quantitative GC analysis of the filtrate. Most runs were carried out twice to confirm reproducibility.

Analysis

The products were identified by GC-MS using a Hewlett-Packard 5890 II GC coupled with a HP 5971A mass-selective detector operating at electron impact mode (EI, 70 eV). The column used for GC-MS was a J&W DB-17 column; 30-m X 0.25-mm, coated with 50 % phenyl-50 % methylpolysiloxane with a coating film thickness of 0.25 μm. For quantification, a HP 5890 II GC with flame ionization detector and the same type of column (DB-17) was used. Both GC and GC-MS were temperature programmed from 40 to 260 °C at a heating rate of 4 °C/min. The response

factors for 5 of the products were determined using pure compounds. Conversion was determined by the amount of unreacted DBT recovered after the reaction. Yields of products were calculated as molar percentage based on DBT reactant. More experimental details may be found elsewhere (4).

RESULTS AND DISCUSSION

Initially, DBT hydrodesulfurization tests were performed at 400 °C over ATTM and $Mo(CO)_6$ using a metal loading of 0.5 mol % with and without added sulfur in a S:metal ratio of 4:1. Table 1 and Figure 1 show the results of these runs. At such a low loading level, both precursors displayed only moderate catalytic activity. However, when S was added to the S-free precursor, conversion increased significantly. The HDS activity of $Mo(CO)_6$ was improved when a higher metal loading of 5 mol % Mo (with respect to DBT) was used. This suggests that a much higher metal concentration would be needed to completely convert and hydrodesulfurize DBT under the conditions used.

To study the impact of different metal concentrations on DBT conversion, a much higher metal loading, 36 mol % with respect to DBT, was also used in examining the performance of various catalyst precursors. Table 2 and Figure 2 give the results with $Mo(CO)_6$ and ATTM. The reactions with $Mo(CO)_6$ and ATTM were performed using tridecane and octadecane as solvents. The liquid products identified from these reactions were biphenyl (BP), tetrahydro-dibenzothiophene (TH-DBT), cyclohexylbenzene (CHB), bicyclohexyl (BCH), and benzene (BNZ). It should be noted that there are un-identified products, which are not included in Table 2. One of them has MW of 166. It could be cyclopentylmethylcyclohexane, but this needs to be confirmed. For the runs with $Mo(CO)_6$, increase in Mo loading from 0.5, to 5 and to 36 mol % with respect to DBT increased the DBT conversion with tridecane solvent from 5.5 to 26.2 to 53.4 mol %. Adding sulfur further increased the catalytic activity for DBT conversion. A comparison of the results for ATTM with different metal loadings (Tables 1 and 2) showed a substantial increase of DBT conversion and HDS degree (as expressed by the sum of HDS products). Reactions with ATTM at 0.5 mol % metal loading gave DBT conversions up to 21.2 %, with only HDS and partial hydrogenation products (Table 1). A great impact on conversion, HDS, and product distribution could be found in model reactions with ATTM at 36 mol % metal loading (Table 2). The products include not only HDS products such as BP and CHB, but also hydrocracking products such as benzene. Highest conversions were achieved using octadecane as a (high boiling) solvent in combination with added S.

As shown in Table 3 and Figure 3, the precursors used in the high metal-loading runs also included were $MoCl_3$, $Co_2(CO)_8$, $Fe(CO)_5$ with and without sulfur, and the bimetallic catalyst MoCo-TC2, in addition to ATTM and $Mo(CO)_6$. Again, most of these catalysts were run with tridecane and octadecane as solvents, and in some cases heptadecane was also used. The ratio of S:metal ratio employed was 6:1. As seen in Tables 2 and 3 the use of high metal concentrations dramatically increased conversion and HDS.

From the DBT conversion data in Tables 2 and 3, $Mo(CO)_6$ appears to be the most active precursor and showed highest selectivity. The reactions of $Mo(CO)_6$ lead to 50.8 % HDS and a conversion of 53.4 % using tridecane as a solvent. These percentages increase when tridecane was replaced with octadecane. The use of octadecane increased HDS (50.8 % to 80.0 %) and increased conversion (53.4 % to 75.8 %). When sulfur was added in a 6:1 S:metal ratio the results for tridecane were 41.2 % HDS and 100 % conversion, and for octadecane 43.2 % for HDS. The influence of S was studied in a set of experiments using a 2:1 and a 6:1 S:metal ratio. Both runs were conducted with heptadecane as a solvent. Sulfur addition resulted in high HDS yield and complete conversion but different product distribution. In the latter reaction cyclohexylbenzene (CHB), bicyclo-hexyl (BCH), and benzene (BNZ) accounted for most of the products. This effect is also present when using a higher boiling point solvent. CHB, BCH, and BNZ accounted for 100 % of the products of the run with $Mo(CO)_6$, added sulfur and octadecane, as compared to runs, using heptadecane and tridecane under the same conditions. These results indicate that oil-soluble $Mo(CO)_6$ may be used for HDS reactions. Curtis (5) demonstrated that catalytic desulfurization can be achieved in high yields by using molybdenum naphthenate, which is another oil-soluble precursor.

The 36 mol % metal loaded samples of ATTM easily outperformed the 0.5 mol % samples. The total yields of HDS products with ATTM, however, are lower than those with $Mo(CO)_6$ without sulfur and much lower than those with $Mo(CO)_6$ with sulfur. This is surprising, considering that ATTM has a S:metal ratio of 4:1 compared to no precursor sulfur for $Mo(CO)_6$, and ATTM was shown to be more effective than $Mo(CO)_6$ in our coal liquefaction experiments. The performance of ATTM, like $Mo(CO)_6$, was also affected by the solvent used. The use of octadecane increased HDS from 24.8 % to 36.0 % and conversion from 40.4 % to 74.6 %. The product distribution also changed. An increase in HDS and hydrogenation products, such as BP, TH-DBT, and CHB could also be observed.

$MoCl_3$ gave about the same results as ATTM, in terms of HDS and conversion in both solvents (Table 3). However, the addition of sulfur to $MoCl_3$ resulted in a considerable decrease in both HDS and conversion. The use of $Co_2(CO)_8$ in octadecane gave relatively low conversion, which indicates that the material from $Co_2(CO)_8$ itself is less active for DBT conversion under the conditions employed. Although sulfur was not used, it could possibly increase the activity of $Co_2(CO)_8$ as it did for $Mo(CO)_6$. The use of the bimetallic catalyst MoCo-TC2 did not give an improvement over the individual Co or Mo catalysts. In fact, the results were almost identical to runs using $Co_2(CO)_8$. It should be mentioned that the above results apply only to the HDS using in situ generated catalyst from MoCo-TC2. The last precursor used was $Fe(CO)_5$, with and without

added sulfur. They were the least active precursors, among all those tested with octadecane solvent. This is probably due to the low hydrogenation activity and HDS activity of the Fe catalysts. An additional reason for the lack of activity of $Fe(CO)_5$ is the preferred formation of less reactive iron carbides (6) and iron oxides over iron sulfides.

$Mo(CO)_6$ and ATTM were also used at 0.5 mol % metal loading in reactions at 350 °C involving water. Previous work by Song (7) demonstrated the promoting effect of water addition in coal liquefaction experiments under low severity reaction conditions. Water was added in a H_2O:DBT molar ratio of 10:1. The results obtained so far were not conclusive. The product recovery was poor with CH_2Cl_2 as the solvent for recovering products from the reactions with H_2O. It is considered that replacing CH_2Cl_2 with acetone as the wash solvent may improve the product recovery.

CONCLUSIONS

Dibenzothiophene appeared to be relatively stable under thermal conditions and reacts only with very active catalysts and high metal loadings to form hydrodesulfurized products. $Mo(CO)_6$ (36 mol % metal loading) with added sulfur in a S:metal ratio of 6:1 and octadecane as solvent was found to be the most active catalyst yielding 100% HDS and conversion at 400 °C. ATTM and $MoCl_3$ appear to be less active for DBT HDS under similar conditions. The other catalyst precursors, $Co_2(CO)_8$, MoCo-TC2, and $Fe(CO)_5$, showed only moderate activity. The use of high boiling solvent seems to be beneficial to HDS, conversion, and the formation of hydrogenation products.

In model reactions using ATTM and $Mo(CO)_6$ (0.5 mol % metal loading) with and without added sulfur only low catalytic activity could be observed. The product distribution in runs using a metal loading of 0.5 mol % revealed only hydrogenation products.

REFERENCES

1. Kamiya, Y.; Nobusawa, T. and Futamura, S. *Fuel Process. Technol.*, **18, 1988**, 1.
2. a) Artok, L.; Davis, A.; Mitchell, G. D. and Schobert, H. H. *Energy & Fuels*, **1993, 7**, 67-77.
   b) Garg, D. and Givens, E. N. *Fuel Process. Technol.*, **8, 1984**, 123-34.
3. Brunner, H. and Wachter, J. J. *J. Organomet. Chem.*, **C41-44, 1982**, 240.
4. a) Schmidt, E. and Song, C. *Prepr. Pap. - Am. Chem. Soc., Div. Fuel Chem.*, **35, 1994** 733-737.
   b) Song, C.; Schmidt, E. and Schobert, H. H. *DOE Coal Liquefaction and Gas Conversion, Contractors' Review Meeting in Pittsburgh*, (September 7-8, **1994**), 593-604.
5. Kim, H. and Curtis, C. W. *Energy & Fuels*, **Vol. 4, No. 2, 1990**, 206.
6. Herrick, D.; Tierney, J.; Wender, I.; Huffman, G. P. and Huggins, F. E. *Energy & Fuels*, **Vol. 4, 1990**, 231.
7. Song, C. and Saini, A. K. *Energy & Fuels*, **9, 1995**, 188-9.

Table 1. Catalytic Hydrodesulfurization of Dibenzothiophene with Mo-Based Precursors [0.5 - 5 mol % metal loading].

Experiment #	BLDA3/4	BLDA5	BLDM5/6	BLDM12	BLDM10/11	BLDMS1/2	BLDMS5
Catalyst Precursor	ATTM[a]	ATTM[b,#]	$Mo(CO)_6$[a]	$Mo(CO)_6$[b]	$Mo(CO)_6$ [5 mol %[a]]	$Mo(CO)_6$+ S[a]	$Mo(CO)_6$+ S[b]
Products [mol %][c]							
TH-DBT	5.4	4.6	0.4	0.8	2.5	7.7	8.0
BP	2.5	2.0	1.9	3.0	5.6	3.9	4.3
CHB	1.2	0.9	0	0.1	0.4	1.8	2.1
BCH	0		0	0	0	0	0
BNZ	0		0	0	0	0	0
HDS products	3.7	2.9	1.9	3.1	6.0	5.7	6.3
Conversion [wt%]	**21.2**	**7.4**	**5.5**	**17.1**	**26.2**	**38.2**	**17.8**

Solvent: [a]tridecane, [b]octadecane. [c] biphenyl (BP), tetrahydro-dibenzothiophene (TH-DBT), cyclohexylbenzene (CHB), bicyclohexyl (BCH), and benzene (BNZ).
Needs to be re-run to check the reproducibility.

Table 2. Catalytic Hydrodesulfurization of Dibenzothiophene with Mo-Based Precursors [36 mol % metal loading].

Experiment #	BCDA5	BCDA4	BCDM1/2	BCDM6/5	BCDMS1/2	BCDMS5/6	BCDMS7	BCDMS8
Catalyst Precursor	ATTM[a]	ATTM[b]	$Mo(CO)_6$[a]	$Mo(CO)_6$[b]	$Mo(CO)_6$ +S[a]	$Mo(CO)_6$ + S [2:1][c]	$Mo(CO)_6$ + S [6:1][c]	$Mo(CO)_6$ + S [6:1][b]
Products [mol %]								
TH-DBT	3.3	4.7	2.1	2.1	5.5	0	0	0
BP	6.4	11.4	39.1	48.3	26.6	9.9	2.6	0
CHB	11.7	17.7	8.5	14.1	41.7	20.7	23.0	19.1
BCH	3.2	3.2	0	14.6	0	2.5	4.7	11.0
BNZ	3.5	3.7	3.2	3.0	25.7	15.8	10.9	13.8
HDS	24.8	36	50.8	80.0	94.0	48.9	41.2	43.9
Conversion [wt%]	**40.4**	**74.6**	**53.4**	**75.8**	**70.5**	**99.1**	**100.0**	**100.0**

Solvent: [a]tridecane, [b]octadecane, [c]heptadecane.

Table 3. Catalytic Hydrodesulfurization of Dibenzothiophene with Mo-Based Precursors [36 mol % metal loading].

Experiment #	BCDT3	BCDT2	BCDTS3	BCDTS2	BCDC1	BCDC2	BCDMC1	BCDF1	BCDFS1
Catalyst Precursor	$MoCl_3$[a]	$MoCl_3$[b]	$MoCl_3$ +S[a]	$MoCl_3$ +S[b]	$Co_2(CO)_8$ a,#	$Co_2(CO)_8$ b	MoCo-TC2[b]	$Fe(CO)_5$[b]	$Fe(CO)_5$ +S[b]
Products [mol %]									
TH-DBT	0	6.9	4.1	4.5	0	0	2.5	0	0
BP	33.3	42.5	11.3	12.0	0	5.6	7.0	4.4	4.5
CHB	0	2.3	2.8	11.5	0	13.1	11.5	10.0	15.1
BCH	0	0	0	3.8	0	13.1	0	0	0
BNZ	7.0	13.2	7.4	5.0	0	0	0	0	0
HDS	40.3	58.0	21.5	32.3	0	31.8	18.5	14.4	19.6
Conversion [wt%]	**52.6**	**67.3**	**45.2**	**48.4**	**0**	**19.6**	**16.3**	**5.0**	**8.5**

Solvent: [a]tridecane, [b]octadecane. # Needs to be re-run to check the reproducibility.

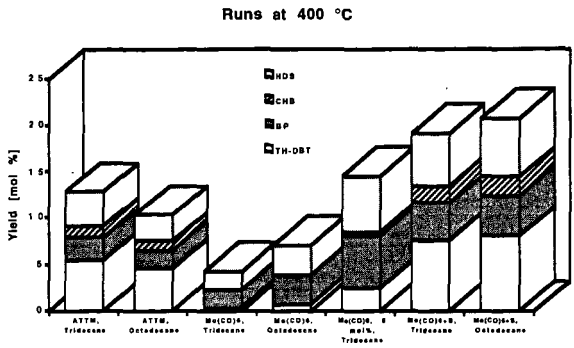

Figure 1. Catalytic Hydrodesulfurization of Dibenzothiophene with Mo-Based Precursors [0.5 - 5 mol % metal loading].

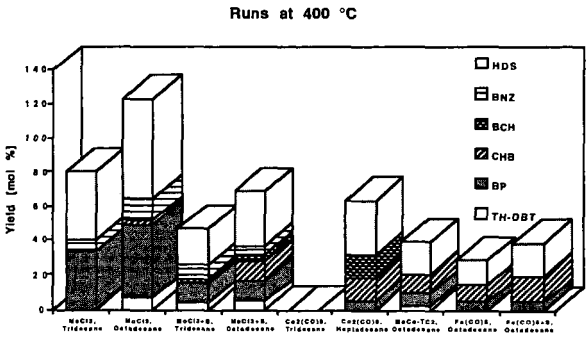

Figure 2. Catalytic Hydrodesulfurization of Dibenzothiophene with Mo-Based Precursors [36.16 mol % metal loading].

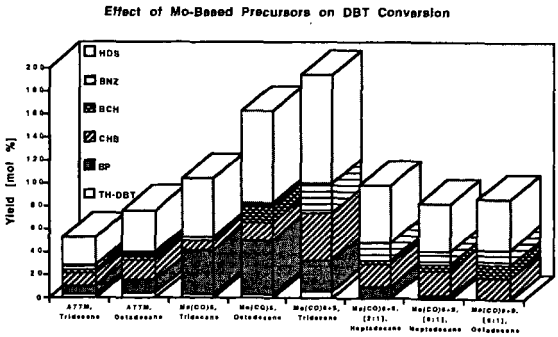

Figure 3. Catalytic Hydrodesulfurization of Dibenzothiophene with Mo-Based Precursors [36 mol % metal loading].

CATALYTIC HYDRODESULFURIZATION OF BITUMEN

Ramesh K. Sharma and Edwin S. Olson
University of North Dakota
Energy & Environmental Research Center
PO Box 9018
Grand Forks, ND 58202
(701) 777-5000

Keywords: Catalytic hydrodesulfurization, Bitumen

ABSTRACT

Investigations of the catalytic hydrodesulfurization of Venezuela bitumen and its water emulsion (Orimulsion) were carried out. This material contained a large amount of sulfur and organometallics, such as vanadium and nickel compounds. A variety of nickel and molybdenum catalysts were prepared. These, as well as two commercial catalysts, were tested with Orimulsion and vacuum-dried, pentane-insoluble and -soluble bitumen. Catalytic hydrotreatment removed up to 75% of sulfur from the bitumen. Hydrodesulfurization was found to be affected by reaction temperature, reaction time, catalyst, and feed material. Moisture-free bitumen and a pentane-soluble bitumen fraction were desulfurized more effectively than Orimulsion. Zeolite-based catalysts gave higher desulfurization than synthetic clay catalysts.

INTRODUCTION

The sulfur content of many coals, crude oils, and bitumens results in serious problems in the utilization and processing of these resources, both as fuel and nonfuel materials. Emission regulations demand that cleaner fuels be utilized. The production of low-sulfur, low-metal petroleum coke (petcoke) is also being sought for the manufacture of needle cokes, carbon electrodes, metallurgical reductions, and fuels. Unfortunately, the feedstocks available for production of fuels and carbon products tend to have higher sulfur contents, e.g., the very large reserves of crude oil and bitumens that are available in South America with sulfur contents of greater than 3 wt%. Lower-value sour crudes are also an increasing problem for oil production in parts of the United States.

Previous work at the Energy & Environmental Research Center (EERC) was concerned with the development of catalysts for production and upgrading of coal liquids, including hydrodesulfurization. The types of catalysts investigated included zinc chloride-silica complexes (1), metal-impregnated natural and synthetic clays (2–5), and zeolites (5). Molybdenum sulfide impregnated in a nickel-substituted synthetic mica montmorillonite (NiSMM) and in a hydrotalcite clay were demonstrated to be highly effective catalysts for hydrodesulfurization of coal-derived products.

Further demonstrations of the activities and stability of these catalysts for desulfurization of petroleum resids and bitumens are needed. Currently used resid desulfurization catalysts experience severe deactivation as a result of plugging of the catalyst pores or sintering of the metal sulfides. Several catalysts that previously exhibited activity for hydrodesulfurization of coal-derived materials were tested for desulfurization of a Venezuela bitumen. This material is marketed as a water emulsion product called Orimulsion.

EXPERIMENTAL

The hydrodesulfurization tests were conducted in a small batch reactor with hydrogen pressures of about 1000 psi at a temperature of 390°C. The emulsion form (a 70% bitumen-30% water emulsion) is convenient for weighing and transferring the bitumen, and therefore the emulsion as well as the moisture-free bitumen (71 wt%) obtained by drying the water emulsion were used in tests. The moisture-free bitumen was further fractionated into pentane-soluble (83 %) and pentane-insoluble (17 %) fractions.

Catalysts

Catalysts used in this study included the following: 1) chromia-pillared clay +molybdenum (6), NiSMM + molybdenum (7, 8), 2) Y-Zeolite + nickel-molybdenum (9), 3) Y-Zeolite + nickel-tungsten (9), 4) Y-Zeolite-aluminosilicate (10) + nickel-molybdenum, 5) Hydrotalcite + molybdenum (4), 6) uranium oxide-nickel oxide (11), 7) uranium oxide-nickel oxide + molybdenum prepared by impregnation of above catalyst, 8) AMOCAT and HDN-30.

Catalytic Reactions

The catalysts were presulfided by heating with elemental sulfur plus hydrogen (200 psig) at 400°C for 2 hr. In a typical experiment, 1.50 g of Orimulsion or 1.0 g of dry bitumen or 1.0 g of pentane-soluble fraction and 0.5 g of the catalyst were placed in a tubing bomb (15-mL microreactor). The microreactor was evacuated, pressurized with 1000 psig of hydrogen, and placed in a rocking autoclave heated to the desired temperature. Heating was continued for 1 or 3 hours. At the end of the reaction period, the microreactor was cooled to room temperature, degassed, and opened. The product slurry was extracted

with tetrahydrofuran, and the solid catalyst removed by centrifugation. The supernatant liquid was evaporated to remove solvent, and the dried product was analyzed for sulfur. Total sulfur determinations were done with a LECO Model 532 sulfur analyzer using the American Society for Testing and Materials (ASTM) D1551 method.

RESULTS AND DISCUSSION

Synthetic and Pillared Clay-Supported Molybdenum

In a 1-hr test with the as-received emulsion (Orimulsion), the synthetic clay-supported molybdenum catalyst (NiSMM + 5% molybdenum, presulfided) gave a product with 3.0% sulfur (dry basis), which is a 23% reduction in the sulfur content of the bitumen (Table 1). Minimal hydrocracking and gas formation occurred under these conditions, although it is likely that some asphaltene hydrogenation occurred. The viscosity was not significantly changed.

A chromia-pillared clay containing impregnated molybdenum (molybdenum-high-chromium-pillared clay [Mo-HCPC]) was presulfided, and the catalyst was tested for hydrodesulfurization activity with the Orimulsion (Table 1). This catalyst exhibited a similar poor desulfurization activity (10% sulfur reduction).

The reaction of Orimulsion with the molybdenum sulfide-impregnated hydrotalcite (MoHT) catalyst gave a product with 3.6% sulfur (8% reduction) (Table 1). This catalyst gave respectable desulfurization with coal-derived liquids as well as model compounds (4), but apparently it is hindered by the aliphatic content of the bitumen, which may inhibit diffusion into the small pores of the catalyst.

Commercial Catalysts

The presulfided commercial molybdenum catalysts, AMOCAT and HDN-30, both removed 39% of the sulfur of the Orimulsion (dry weight basis) in the 1-hr batch hydrodesulfurization test (Table 1). On this basis, we concluded that the EERC catalysts that previously showed desulfurization activities with coal liquids were far inferior to the commercial catalysts for desulfurization of the highly aliphatic bitumen. The form of sulfur present in the bitumen is likely to be partly heterocyclic as it is in the coal, but the matrix is entirely different in the bitumen.

Y-Zeolite-Supported Catalysts

Further catalyst screening was carried out with zeolite catalysts modified by metal impregnation and also by coating the zeolite with aluminosilicate (cogel) as is done with fluid catalytic cracking (FCC) refining catalysts. The zeolite-supported nickel-molybdenum catalyst gave a 32% reduction of sulfur, and a similar zeolite-supported nickel-tungsten catalyst gave only a 22% sulfur reduction in 1-hr tests (Table 1).

More encouraging results were obtained with the catalyst prepared by impregnating nickel and molybdenum into a zeolite-aluminosilicate cogel (Table 2). The cogel-supported nickel-molybdenum catalyst gave 43% removal of sulfur in a 1-hr test. This catalyst is similar to that recently reported by a Canadian group (12). Further testing with Orimulsion for 3 hours gave 58% removal. When a dry fraction of the bitumen was hydrotreated with this catalyst for 3 hours, 37% of the sulfur was removed. Similar reaction with a pentane-soluble fraction of the bitumen resulted in 74% sulfur removal to give a product with 1.0% (dry weight basis) sulfur content. However, when the same reaction was carried out using 10 wt% of the catalyst, only 25% sulfur was removed.

Mixed Oxide Catalysts

Good results were also obtained with a nickel catalyst supported on uranium oxide, which gave 38% removal of sulfur from the as-received Orimulsion in the 1-hr period (Table 3). The function of the uranium oxide is to prevent sintering of the nickel during regeneration of the catalyst. A hydrodesulfurization reaction of the moisture-free bitumen with this catalyst for 3 hours gave the same reduction in sulfur as that obtained with the Orimulsion. Thus with this catalyst, the water present in the emulsion does not appear to interfere with the reaction. Impregnation of molybdenum (5%) into this nickel catalyst resulted in a slight increase in catalytic activity (41% sulfur reduction). Better desulfurization was expected for this catalyst, but since far superior results were obtained with the zeolite catalyst, further work with the molybdenum-nickel-uranium oxide catalyst was suspended.

CONCLUSIONS

Two catalysts that had previously exhibited activity for hydrocracking coal tar constituents were active for hydrodesulfurization of the high-sulfur Venezuelan bitumen. The most active catalyst for hydrodesulfurization was a nickel- and molybdenum-impregnated Y-zeolite-aluminosilicate cogel. This catalyst removed 75% of the sulfur from the moisture-free bitumen and 58% of the sulfur from the Orimulsion. A nickel-molybdenum catalyst supported on uranium oxide gave slightly better results than

desulfurization with the commercial catalysts. Other catalysts that had exhibited activity for desulfurization of coal-derived liquids were less active for desulfurization of the bitumen than the commercial hydrotreating catalysts.

ACKNOWLEDGMENTS

The support of the U. S. Department of Energy is gratefully acknowledged.

REFERENCES

1. Sharma, R.K.; Diehl, J.W.; Olson, E.S. "Hydrodesulfurization with a New Solid Acid Catalyst," In *Processing and Utilization of High-Sulfur Coals III*; Markuszewski, R.; Wheelock, T.D., Eds.; Elsevier: Amsterdam, 1990; pp 735–743.
2. Olson, E.S.; Buchwitz, C.M.; Yagelowich, M.; Sharma, R.K. *Prepr. Pap.—Am. Chem. Soc., Div. of Fuel Chem.* **1993**, *38*, 156–162.
3. Olson, E.S.; Yagelowich, M.C.; Sharma, R.K. *Prepr. Pap.—Am. Chem. Soc., Div. Fuel Chem.* **1992**, *37*, 262–267.
4. Sharma, R.K.; Olson, E.S. "Catalytic Hydrodesulfurization with Hydrotalcites," In *Processing and Utilization of High-Sulfur Coals IV*; Dugan, P.R.; Quigley, D.R.; Attia, Y.A., Eds.; Elsevier: Amsterdam, 1991; pp 377–384.
5. Olson, E.S.; Sharma, R.K. "New Catalysts for Production of Synthetic Fuels," *In* Proceedings of the Australian/U.S.A. Workshop on Low-Rank Coals, Billings, MT, May 23–24, 1991; EERC publication.
6. Sharma, R.K.; Olson, E.S. *Prepr. Pap.—Am. Chem. Soc., Div. Fuel Chem.* **1994**, *39 (3)*, 702.
7. Heinerman, J.J.L.; Freriks, I.L.C.; Graaf, J.; Pott, G.T.; Coglegem, J.G.F. *J. of Catal.* **1983**, *80*, 145.
8. Olson, E.S.; Sharma, R.K. *Prepr. Pap.—Am. Chem. Soc., Div. Fuel Chem.* **1994**, *39 (3)*, 706.
9. Haynes, H. W., Jr. *Ind. Eng. Chem. Process. Des. Dev.* **1983**, *22*, 401.
10. Pecorara, T.A. U.S. Patent 5 001 097, 1991.
11. Berry, F.J.; Murray, A.; Parkyns, N.D. *Appl. Catal. A* **1993**, *100*, 131.
12. Diaz-Real, R.A.; Mann, R.S.; Sambi, I.S. *Ind. Eng. Chem. Res.* **1993**, *32*, 1354.

Table 1. Hydrodesulfurization Reactions of Bitumen

Catalyst	Substrate	Subst.: Cat. Ratio[a]	Time, hr	Sulfur in Substrate,[b] %	Sulfur in Product, %	Sulfur Removed, %
Mo-NiSMM	Orimulsion	2	1	3.9	3.0	23
Mo-HCPC	Orimulsion	2	1	3.9	3.5	10
NiMo-Y-Zeolite	Orimulsion	2	1	3.9	2.7	32
NiW-Y-Zeolite	Orimulsion	2	1	3.9	3.0	22
MoHT	Orimulsion	2	1	3.9	3.6	8
AMOCAT	Orimulsion	2	1	3.9	2.3	39
HDN-30	Orimulsion	2	1	3.9	2.4	39

[a] Ratio is based on the dry weight of bitumen contained in the Orimulsion.

[b] Percent sulfur is based on the dry weight of bitumen contained in the Orimulsion.

Table 2. Hydrodesulfurization Reactions of Bitumen with NiMo-Y-Zeolite-Aluminosilicate Cogel

Substrate	Substrate: Cat. Ratio	Time, hr	Sulfur in Substrate,[a] %	Sulfur in Product, %	Sulfur Removed, %
Orimulsion	2[b]		3.9	2.3	43
Orimulsion	2[b]	3	3.9	1.8	58
Dry Bitumen	2	3	3.7	2.5	37
Pentane-Soluable	2	3	3.6	1.0	74
Pentane-Soluable	10	3	3.6	2.8	25

[a] Ratio is based on the dry weight of bitumen contained in the Orimulsion.

[b] Percent sulfur based on the dry weight of the bitumen contained in the Orimulsion.

Table 3. Hydrodesulfurization Reactions of Bitumen with Ni-U Oxide Catalysts.

Catalyst	Substrate	Subst. : Cat. Ratio	Time, hr	Sulfur in Substrate,[a] %	Sulfur in Product, %	Sulfur Removed, %
Ni-U Oxide	Orimulsion	2[b]	1	3.9	2.5	38
Ni-U Oxide	Dry bitumen	2	3	3.7	2.4	39
Ni-U Oxide + 5% Mo	Dry bitumen	2	3	3.7	2.4	41

[a] Ratio is based on the dry weight of bitumen contained in the Orimulsion.

[b] Percent sulfur is based on the dry weight of the bitumen contained in the Orimulsion.

CAUSTIC WASHING FOR REFINING OF DIRECT COAL LIQUEFACTION PRODUCTS

Richard A. Winschel, Peizheng Zhou*, Francis P. Burke,
Gary A. Robbins, Susan D. Brandes
CONSOL Inc., Research & Development, 4000 Brownsville Road, Library, PA 15129
*Burns and Roe Services Corp., P.O. Box 18288, Pittsburgh, PA 15236

KEYWORDS: Liquefaction, Refining, Phenols

INTRODUCTION

Extensive research and development sponsored by the U.S. DOE/PETC over the past two decades has resulted in dramatic improvements in the quality of direct coal liquefaction products. High-quality coal-derived distillates are obtainable from catalytic two-stage liquefaction (TSL) processes, such as those developed at the Wilsonville, AL pilot plant and the Hydrocarbon Technologies Inc. (HTI) pilot plant and bench units. The products of the Wilsonville and HTI TSL operations are suitable as high quality feedstocks for producing transportation fuels in a refinery. These products have important quality advantages over crude petroleum: they are distillates boiling below about 700°F and are thus virtually free of resid and metals, and they have very low sulfur contents and low nitrogen contents.[1-3] The coal liquids have carbon and hydrogen contents and Watson characterization factors within the range of crude petroleums.[1-3] However, relative to crude petroleum, the crude coal products have elevated oxygen contents[(1-3)]. Although these oxygenated species are found at elevated concentrations throughout the boiling range of the coal liquids, they are most frequently concentrated in the heavy naphtha and light kerosene fractions. For example, when the oxygen content of coal liquids is plotted as a function of boiling point, there is often a maximum in the curve between 355 °F and 465 °F (Figure 1 and References 1, 2, and 4).

Phenolic compounds are the predominant oxygen-containing components in the coal liquids;[4] the curve maximum represents phenols with zero to three alkyl carbon substituents. Phenolic compounds must be reduced to low concentrations to produce finished transportation fuels. In a typical modern petroleum refining scheme, this would be accomplished by hydrotreating. However, because coal liquids have high concentrations of phenolics, it may be advantageous to reduce their concentration prior to hydrotreating by some other route, for example, by caustic extraction. Although caustic washing could not replace hydrotreating to produce finished fuels from the oils described here, this route for pre-removal of phenols could have several advantages over hydrotreating the phenolic containing oils: it would reduce the overall hydrogen demand, it could produce a valuable by-product (cresylic acid), and it would simultaneously strip from the oil mercaptans and hydrogen sulfide in addition to the phenolics. Indeed, caustic washing was once a common unit operation in petroleum refineries because of its ability to sweeten light distillates.[5] The cresylic acid could be sold as a by-product or perhaps methylated to produce methyl aryl ethers,[6] which could be used as a high octane oxygenate gasoline extender. Presented here are results of experiments conducted to recover a cresylic acid by-product from crude coal liquids, while simultaneously improving the quality of the liquid. The quality improvement in the coal liquid and the characterization of the by-product cresylics are discussed.

EXPERIMENTAL

The net products of three liquefaction runs that represent variations of state-of-the-art technology were characterized in detail. The three samples were generated at the Wilsonville 6 ton/day pilot plant (Run 260D) and the HTI 2 lb/hr bench unit (Runs CC-15 and CMSL-2), as described in Table 1. The characterization scheme included fractional distillation and analysis and inspection of the fractions. Some of the distillation fractions were caustic washed to remove phenolics and the recovered raffinate and caustic extract fractions were also characterized. The exact caustic washing procedure used varied among the samples; however, the general scheme was to contact the oil in a separatory funnel multiple times with NaOH (either 20 wt % or 6 wt % solutions) then with water, to acidify the extract with concentrated aqueous HCl, then to extract the phenols with methylene chloride and to remove the methylene chloride by rotary evaporation. Raffinate and caustic extract yields are determined gravimetrically. Some losses resulted from evaporation and handling during the extraction scheme. The complete backgrounds of the samples, details of all experimental methods and characterization data appear in the original reports of this work.[7-9] Phenolic -OH concentrations were determined by Fourier-transform infrared spectroscopy.[10] The caustic extracts also were characterized by gas chromatography/mass spectrometry (GC/MS) with a HP 5970 system equipped with a 30 m x 0.25 mm DB-5 column (0.25 μm film thickness) as follows: 20 psig He carrier gas; splitless injection as 1% solutions in THF; injection port at 300 °C; column temperature program - 5 min at 35 °C, to 100 °C at 35 °C/min, to 320 °C at 4 °C/min; scan from 45 to 300 amu; spectra searched against the Wiley/NBS mass spectral library; identifications based on search results and supplemented by

retention times; normalized quantitation is based on peak area divided by total peak area of all phenolics found.

DISCUSSION

The oxygen contents, determined by difference, of the distillation fractions of the three crude coal liquids are plotted in Figure 1 as a function of the mid boiling point of the fraction. Two of the three curves show maxima between 355 and 465 °F. Material in this boiling range tends to have relatively high concentrations of phenolic compounds. For example, Table 2 shows that the 380-510 °F fraction has the highest phenolic -OH concentration of the four distillation fractions of the Wilsonville Run 260D sample.

The fractions of the Wilsonville Run 260D sample that were caustic washed include the naphtha (IBP-380 °F), jet or kerosene (380-510 °F), diesel fuel (510-650 °F), and residuum (650 °F+) fractions. Table 2 shows the yields of raffinate and extract from each extraction and the phenolic -OH concentration in each fraction. The phenolic -OH concentrations (Table 2) of the raffinates show that caustic washing was quite effective at removing phenolics from the fractions boiling below 510 °F. In fact, for these raffinates, phenolic -OH was near or below detection limits. Caustic washing was not very effective for the higher boiling fractions. Not only was caustic washing less effective for the higher boiling fractions, it was also less selective; GC/MS analyses showed that the caustic extracts of the higher boiling fractions were contaminated with hydrocarbons. For this reason, and because the highest concentration of phenolics tend to exist in fractions that boil between 355 and 465 °F (Figure 1 and References 1, 2, and 4), only the naphtha (IBP-380 °F) and kerosene (380-510 °F) fractions of the HTI Run CC-15 sample and the "swing cut" (350-400 °F) fraction of the HTI Run CMSL-2 sample were caustic washed. The raffinates of the fractions from HTI Runs CC-15 and CMSL-2 were characterized by the same set of inspection tests as the original, unextracted fractions. The caustic extracts of the fractions from all three runs were characterized by GC/MS analysis and phenolic -OH determination.

The caustic extract yields range from 1.1 to 4.6% and losses (100% - yield of raffinate - yield of extract) range from 0.1 to 4.7%. The variations result from the different properties of the fractions, and perhaps from the use of different caustic washing procedures.

Table 3 compares the inspection data of the raffinates with the corresponding data of original, unextracted fractions. For the IBP-380 °F fraction of Run CC-15, the lower Reid vapor pressure of the raffinate appears to result from the loss of light material during the caustic wash. Properties of that fraction that showed improvement from caustic washing include acidity, copper strip corrosion, existent gum, bromine number, basic nitrogen, oxidation stability, heat of combustion, and mercaptan sulfur. The quality of the fraction in terms of its suitability as gasoline are somewhat improved relative to the unextracted fraction. The major improvements in the 380-510 °F fraction of Run CC-15 from caustic washing include acidity and mercaptan sulfur. Other improvements include oxygen (by diff.), viscosity and bromine number.

For the 350-400 °F fraction of HTI Run CMSL-2, the property which showed the greatest improvement from caustic washing is the mercaptan sulfur content. Many other properties (e.g., bromine number, acidity, oxygen by diff.) show some changes that indicate the raffinate is a better stock for production of transportation fuels. The oxidation stability decreased; this may result from the removal of hindered phenols, which are known to act as antioxidants. However, the opposite effect was seen with the IBP-380 °F fraction of HTI Run CC-15, as discussed above.

The major components of the caustic extracts, as determined by GC/MS analysis, are provided in Table 4. Although the extracts of the higher boiling fractions contained some hydrocarbons, each caustic extract consisted primarily of phenolics. The high measured phenolic -OH concentrations of the caustic extracts (Table 2) confirm this. Depending on the boiling point of the fraction extracted, the caustic extracts consist of phenols with zero to four alkyl substituents.

SUMMARY

Caustic washing was found to be highly efficient and highly selective for the extraction of phenolics from the light distillate fractions (b.pt. <510 °F) of the products of modern two-stage direct coal liquefaction products. The extracts were composed almost entirely of phenolics and the lower boiling raffinates were almost devoid of phenolics. The properties of the raffinates as feedstocks or blendstocks for transportation fuels were moderately improved relative to the unextracted materials. Notable improvements included reduced acidity, mercaptan sulfur, oxygen (by diff.) and copper corrosion; other minor improvements also were seen. The composition of the caustic extracts (cresylic acids) depends on the boiling point of the material extracted, but primarily consists of phenols with zero to four alkyl substituents.

ACKNOWLEDGEMENT
This work was supported by the U.S. Department of Energy under contracts DE-AC22-89PC89883, DE-AC22-89PC88400, and DE-AC22-94PC93054. The inspection data and caustic washing of the HTI samples were performed by G. Sturm, J. Kim and J. Shay of the National Institute for Petroleum and Energy Research.

REFERENCES

1. Zhou, P.-Z.; Winschel, R. A.; Klunder, E. B., *Am. Chem. Soc. Div. Fuel Chem. Prepr.* 1994, *39*(4), 1205-1209.
2. Zhou, P.-Z.; Rao, S. N. "Assessment of Coal Liquids as Refinery Feedstocks", DOE Contract No. DE-AC22-89PC88400, February 1992.
3. Zhou, P.-Z. "Characterization of Direct Liquefaction Distillate Products", DOE Contract No. DE-AC22-89PC88400, 1994.
4. Zhou, P.-Z. "Recovery of Phenols From Coal Liquids", DOE Contract No. DE-AC22-89PC88400, March 1993.
5. Nelson, W. L., *Petroleum Refinery Engineering*, Fourth Ed.; McGraw-Hill: New York, 1958; Chapter 10.
6. Singerman, G. M. "Methyl Aryl Ethers from Coal Liquids as Gasoline Extenders and Octane Improvers", Report DOE/CE/50022-1, November 1980.
7. Kramer, R. L. in Report DOE/PC89883-34, November 1991.
8. Sturm, Jr., G. P.; Kim, J.; and Shay, J. in Report DOE/PC89883-92, January 1994.
9. Robbins, G. A.; Brandes, S. D.; Winschel, R. A.; Burke, F. P., Reports DOE/PC89883-43, March 1992, DOE/PC89883-86, March 1994, and DOE/PC 93054-4, October 1994.
10. Burke, F. P.; Winschel, R. A.; Robbins, G. A., Report DOE/PC30027-61, March 1985.

TABLE 1. SOURCE DATA OF COAL LIQUID SAMPLES

Plant/Run	Feed Coal Seam	Process Description		
		Operating Mode	Catalyst	Reactor Temps., °F
Wilsonville 260D	Wyodak and Anderson	Catalytic/Thermal	Shell 324/Fe_2O_3	790/774
HTI CC-15	Wyodak and Anderson	Thermal/Catalytic	Fe_2O_3/Shell 317	800/775
HTI CMSL-2	Illinois No. 6	Catalytic/Catalytic	Shell 317/Shell 317	752-777/795-811

TABLE 2. YIELDS AND PHENOLIC -OH CONCENTRATIONS OF FRACTIONS

Fraction	Yields, wt % of Feed Fraction		Phenolic -OH Concentration, meq/g Sample		
	Raffinate	Caustic Extract	Feed Oil	Raffinate	Caustic Extract
Wilsonville Run 260D					
IBP-380 °F	92.7	3.7	0.40	0.02(a)	-
380-510 °F	94.7	3.6	0.92	0.07(a)	-
510-650 °F	94.4	4.6	0.52	0.27	-
650 °F$^+$ - Trial 1	95.4	1.9	0.41	0.28	-
650 °F$^+$ - Trial 2	97.9	2.0	0.41	0.31	-
HTI Run CC-15					
IBP-380 °F	92.9	2.4	0.13(b)	(c)	8.90
380-510 °F	92.1	4.0	0.24(b)	(c)	7.49
HTI Run CMSL-2					
350-400 °F	95.4	1.1	(c)	(c)	5.02

(a) Quantitation is uncertain at these extremely low concentrations
(b) Amine signal probably contributing to reported phenolic -OH concentrations
(c) Amine observed, no phenolic -OH detected

TABLE 3. INSPECTIONS OF ORIGINAL AND RAFFIANTE FRACTIONS

Property	HTI Run CC-15				HTI Run CMSL-2	
	<380 °F		380-510 °F		350-400 °F	
	Original	Raffinate	Original	Raffinate	Original	Raffinate
Spec. Gravity @ 60 °F (D4502)	0.7798	0.7775	0.8899	0.8882	0.8492	0.8484
API Gravity (calculated)	50.0	50.5	27.5	27.8	35.1	35.3
Elemental Analysis, wt %						
Carbon (D5291)	85.93	86.12	87.12	87.75	86.78	86.86
Hydrogen (D5291)	13.96	13.77	11.77	11.68	12.72	13.08
Sulfur (D3120)	0.03	0.03	0.03	<0.01	0.01	0.01
Nitrogen (D4629)	0.09	0.07	0.33	0.33	0.03	0.02
Oxygen (by diff)	0.00	0.01	0.75	0.23	0.46	0.03
Basic Nitrogen (UOP269)	0.082	0.058	0.274	0.264	0.023	0.023
Mercaptan Sulfur (D3227), ppm	51.5	9.7	45.2	<0.1	19.0	6.0
Viscosity (D445), cSt						
@ 210 °F	-	-	-	-	0.6653	0.8741
@ -20 °C	-	-	10.80	9.665	4.683	4.359
Refractive Index (D1218), @ 20 °C	1.42882	1.42836	1.49196	1.49072	-	-
Freezing Point (D2386), °F	-	-	-12	-13	-99	-95
Cloud Point (D2500), °F	-	-	-	-	<-60	<-60
Pour Point (D97), °F	-	-	-	-	<-60	<-60
Reid Vapor Pressure (D5191), psi	2.54	2.09	<0.01	<0.01	0.02	<0.01
Flash Point (D56, D93), °C	-	-	83	82	50	57
Group Analy. (ASTM D5134 & HC22)						
Paraffins, vol %	38.0	34.7	9.6	9.1	7.5	8.0
Naphthenes, vol %	45.7	48.8	43.1	46.0	61.3	61.5
Aromatics, vol %	8.7	9.2	41.4	41.9	28.4	27.6
Olefins, vol %	4.6	4.2	5.8	3.0	2.6	2.5
Benzene (PIANO, mod D5134)	0.089	0.078	-	-	-	-
Naphthalenes (D1840), vol %	-	-	4.23	3.74	0.48	0.32
Bromine Number (D1159)	3.62	2.37	5.08	2.69	3.00	2.71
Aniline Point (D611), °F	103.8	108.0	71.5	75.2	-	-
Smoke Point (D1322), mm			10.9	11.6	15.8	15.4
Acidity (D3242), mg KOH/g	0.05	<0.01	0.04	0.01	0.01	<0.01
Copper Corrosion (D130)	3b(dark)	2d(mod)	1a(slight)	1a(slight)	1a(slight)	1a(slight)
Existant Gum (D381), mg/100 mL	11.2	9.0	-	-	6.4	6.2
Oxidation Stability (D525), min	105	1440	-	-	1440	720
Thermal Stability (JFTOT) (D3341)	-	-	Fail	Fail	-	-
Octane No., Motor Method (D2700)	60.7	58.1	-	-	-	-
Octane No., Rarch Method (D2699)	61.6	60.2	-		-	-
Heat of Combustion (D2382, D240), Net Btu/lb	16,509	18,651	17,918	18,043	16,401	18,411
Luminometer Number (D1740)	-	-	-	-	27.3	27.0

TABLE 4. COMPOSITIONS OF CAUSTIC EXTRACTS

Component	GC/MS Intensity, as % of Total Phenolic Intensity (No. of Resolved Peaks in Parentheses)				
	Wilsonville Run 260D		HTI Run CC-15		HTI Run CMSL-2
	IBP-380 °F	380-510 °F	IBP-380 °F	380-510 °F	350-400 °F
phenol	24(1)	0.4(1)	13(1)	-	-
o-cresol	15(1)	1(1)	21(1)	-	1.5(1)
m/p-cresol	31(2)	4(1)	24(1)	0.4(1)	1.5(1)
dimethyl phenol	13(6)	14(6)	21(5)	13(6)	32(5)
ethyl phenols	16(2)	13(3)	17(2)	8(2)	10(2)
C_3-phenols	1(5)	31(12)	4(6)	51(12)	37(11)
C_4-phenols	-	16(10)	-	24(12)	17(9)
indanol	-	18(1)	-	4(1)	0.3(1)
dihydroxytoluene	-	1(1)	-	-	-
tetralinol	-	2(1)	-	-	-

Only traces of hydrocarbon contaminants found in IBP-380 °F extracts.
Some hydrocarbon contaminants found in others.

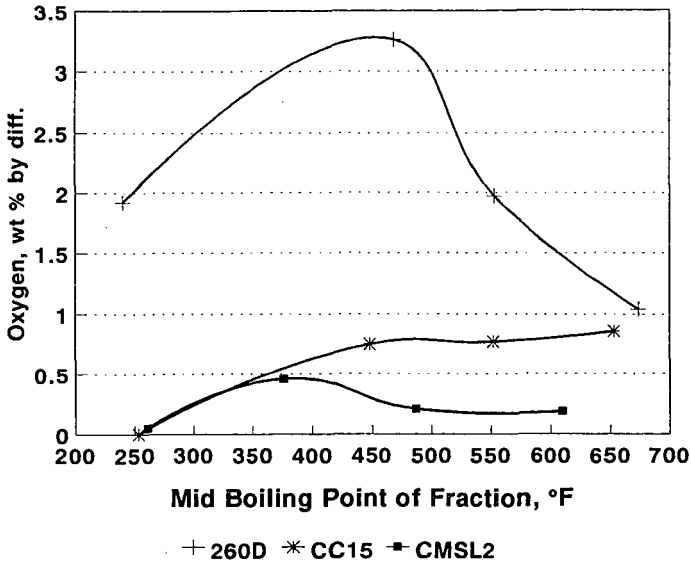

Figure 1. Oxygen Content (by diff.) versus Mid Boiling Point of Coal Liquid Fractions.

HYDRODENITROGENATION WITH NiMo SUPPORTED ON Al_2O_3-$AlPO_4$

R. Menon, H.S. Joo, J.A. Guin, Department of Chemical Engineering
Auburn University, Auburn, Alabama, 36849
P. J. Reucroft and J.Y. Kim, Department of Chemical and Materials Engineering
University of Kentucky, Lexington, Kentucky, 40506

Aluminum phosphate - metal oxides can be used as nonconventional supports for NiMo hydrotreating catalysts. Several Al_2O_3-$AlPO_4$ (AAP) supports were prepared by coprecipitation. Effect of variations in Al/P atomic ratios, precipitation method, final pH, and washing agent on various support properties were examined. Catalysts containing 3 wt% Ni and 13 wt% Mo were prepared by incipient wetness and characterized by several methods. Hydrodenitrogenation (HDN) activities of the catalysts were examined in model compound and coal liquid reactions.

Keywords : catalyst support, aluminum phosphate, solid acid catalyst, HDN

INTRODUCTION

New and more stringent environmental regulations are expected to have a major impact on the refining industry. To achieve future government specifications for fuels, significant changes will likely be required in refinery operations to produce products with good combustion characteristics and reduced emissions. Emphasis in this research is on the development of new and improved catalysts for upgrading coal-liquids and coal/waste liquefaction liquids (CWL) to clean transportation fuels. Because coal liquids contain significant quantities of heteroatoms, (S, O, and N) and have higher aromaticity than their petroleum based counterparts, hydroprocessing operations will form the nucleus of technology for their upgrading.

One of the latest studies in catalysis (Catalytica, 1994) suggests solid acids (metal oxides, heteropoly acids, metal sulphates, *metal phosphates* etc) as important industrial catalysts. The incentive for developing new solid acid and base catalysts to replace hazardous or corrosive liquid ones is again environmental considerations (Tanabe., 1994; Catalytica,1994). The use of phosphorous as a promoter element for Co-Mo and Ni-Mo/ Al_2O_3 catalysts has received significant attention in coal-liquids upgrading (Tischer et al ., 1987), with varying degrees of success; however, actual metal phosphate supports have received little attention as upgrading catalyst supports. There is considerable evidence of their utility as a possible catalyst support material in light of their high stable surface area, pore geometry, surface acidity properties and surface chemistry (Marcelin et al.., 1983; Moffat, J.B., 1978; Rebenstorf et al., 1991). Chen et al (1990) studied hydrodesulfurization reactions of residual oils over CoMo/Alumina-Aluminum phosphate catalysts. They reported that larger surface area, smaller acid amount and weaker interaction of AAP supports made the metal more highly dispersed, produced more active sites and resulted in high initial HDS activity. In this study we explored the performance of metal phosphates of aluminum, zirconium and titanium as potential new supports for HDN upgrading catalysts. Preparation of cogels of $AlPO_4$ and Al_2O_3 by coprecipitation of an aluminum salt and H_3PO_4 has been discussed in the literature (Kearby, K., 1961; Mitchell et al., 1987; Vogel et al ., 1982; Campelo et al., 1986).

EXPERIMENTAL SECTION

PREPARATION OF ALUMINA-ALUMINUM PHOSPHATES (AAP)

The experimental procedures used here in were based on earlier works (Chen et al ., 1990; Cheung et al .,1986; Marcelin et al., 1983). Various factors taken into consideration were an appropriate aluminum compound, precipitating agent, gelation conditions, washing agent, drying and calcination temperatures. Three methods were examined.

METHOD A: Supports were prepared by a coprecipitation method. Phosphoric acid solution (H_3PO_4, 85 wt%) was added to an aqueous solution of aluminum nitrate nona hydrate $Al(NO_3)_3 \cdot 9H_2O$, slowly in an amount to give the desired Al/P ratio. After the addition, the acidic solution was well stirred for at least 10 minutes. A basic solution was prepared by mixing ammonium hydroxide(NH_4OH, 28-30%) and distilled water with a volume ratio 1:1. Both the acidic and basic solutions were added slowly to a third well stirred vessel containing 1L of distilled water. The pH value in the third vessel was maintained at 8.0 throughout the precipitation process by adding small amounts of the acidic and basic solutions. This process was continued until the acidic solution was consumed. The resulting precipitates were centrifuged, washed three times with distilled water, dried overnight at 393K in a vacuum oven, and calcined in a muffle furnace for 12h at 773K. Varying the Al/P ratio allowed various AAP composites to be obtained. Each support is designated based on the Al/P mole ratio.

METHOD B: Certain modifications were made in Method A. [1] Coprecipitation was done at 273K; not at room temperature, [2] A ripening period of 12h was allowed at room temperature, [3] The washing agent was chosen as isopropanol and [4] pH =5.0 instead of 8.0 during precipitation.

H_3PO_4 (85wt%) was added to a solution of $Al(NO_3)_3 \cdot 9H_2O$. The acidic solution was well-stirred and cooled to 0°C. A basic solution was prepared by mixing ammonium hydroxide and distilled water with a volume ratio 1:1. Both the acidic and basic solutions were added slowly to a third vessel of distilled water at 0°C. After standing overnight, the gel was thoroughly extracted with isopropanol three times, allowed to stand at room temperature overnight to evaporate residual isopropanol, dried at 106-110°C for 12h in a vacuum oven, and calcined at 500°C for 12h in a muffle furnace. Two sets of experiments were done to study the effects of pH on the textural properties of AAPs. The first set of experiments was done with varying Al/P ratio and keeping the pH constant at 5.0 during precipitation. In a second set of experiments, Al/P ratio was kept constant at 1.0 and constant values of pH 5.0, 6.0, 7.0, 8.8 and 9.2 were used during precipitation. Heat treatment was same as above.

METHOD C: The precipitation methods were modified. Solutions of $Al(NO_3)_3 \cdot 9H_2O$ and H_3PO_4 were stirred together to form an acidic solution to which ammonium hydroxide solution (13%) was added rapidly. Precipitation occurred rapidly at 0°C. During precipitation pH was not held constant. As ammonia was added to the acidic solution, the pH rose from less than 1.0 to neutrality, and precipitation occurred during a 1-2 min interval. A ripening period of 12h was allowed. The gel was centrifuged and washed with isopropanol three times, followed by drying in the vacuum oven for 12h at 108°C and calcination in the muffle furnace at 649°C for 3h. The samples prepared were AAP1, AAP2, AAP3.5, AAP4, AAP5, AAP6 and AAP8. An Al_2O_3 support also was prepared for comparison purposes.

PREPARATION OF NiMo/AAP CATALYSTS

Supports AAP1, AAP2, AAP4, AAP5, AAP8, and Al_2O_3 prepared in the lab using Method C were chosen for final catalyst preparation. All were made by Method C. Three commercial materials were also used: Shell 424 NiMo/Al_2O_3 as catalyst and $AlPO_4$-G (Grace Davison), and Al_2O_3-H (Harshaw) as supports. The metal compounds chosen were ammonium molybdate tetrahydrate $(NH_4)_6Mo_7O_{24} \cdot 4H_2O$ and nickel nitrate hexahydrate, $Ni(NO_3)_2 \cdot 6H_2O$. The compounds were dissolved in an exact amount of water to fill the pore volume of the support. The supports were impregnated with ammonium molybdate first, dried for 16h at 120°C in a vacuum oven, and calcined at 500°C for 5h in a muffle furnace. Then, they were impregnated with nickel nitrate solution, dried for 16h at 120°C and calcined again for 5h at 500°C.

CHARACTERIZATION OF CATALYSTS

Surface area and pore volume measurements: Surface area was determined by nitrogen adsorption (BET Method) using a Quantasorb adsorption unit manufactured by Quantachrome Corp. The samples were degassed for 4.5h at 350°C prior to the measurements. The pore volumes were measured by using water as a pore filling medium.

XPS Studies: X-Ray photoelectron spectroscopy was used for the surface (in the top 2-5 nm of the solid) elemental analysis of the catalysts.

X-ray Diffraction studies: Catalysts were characterized by X-ray diffraction to investigate their crystallographic properties. A powder diffractometer was used, at 40 kV and 40 mA with Cu Kα radiation.

ICAP: Bulk metal analysis was done by a Jarrell Ash ICAP (Inductively Coupled Argon Plasma) 9000. The values are given in Table 1.

MEASUREMENT OF HDN ACTIVITY: All reactions were performed in 20cc 316 ss tubing bomb microreactors (TBMR) which were agitated in a fluidized sand bath and replicated at least twice. A reactant solution (6g) containing 2 wt% pyridine in hexadecane was used for model compound studies and coal liquid (3g) for upgrading. Experiments were charged with 1000 psig cold hydrogen pressure and performed at 350°C for 20 min using 0.1 g catalyst for model compound reactions and at 375°C for 1 hr using 0.4 g catalyst for upgrading coal liquid. Catalyst was sulfided *in situ* with dimethyl disulfide.

RESULTS AND DISCUSSION

Elemental Analysis : Bulk metal concentrations calculated, based on the amount of reagents used and the amount of the support formed (experimental) and actual analysis by ICAP is shown in Table 1. A comparison between the experimental and theoretical (based on weight of support expected) weights of the supports (Method C) are given in Table 3.

XPS Studies: The Al/P ratios were similar for both bulk and surface with a slight depletion of Al or enrichment of P on the surface compared to the bulk (Table 1). AAP4, AAP8 and Al_2O_3 -H

showed lower Mo/Ni values on the surface compared to the bulk.

Surface areas and pore volumes: In METHOD A, the surface area of AAPs increased as the Al/P ratio varied from 1.0 to 8.0 (Fig.1a). The area of AAP1 was only 41 m^2/g. The modifications done to Method A, in Method B, provided an AAP1 with much higher surface area (141 m^2/g). However, the AAPs showed a different trend and the highest area did not exceed 200m^2/g. In Method C, the AAPs exhibited higher surface areas, the maximum being at 267 m^2/g (AAP5). With increasing pH surface areas of AAPs declined (METHOD B), but above pH= 8 it showed a tendency to increase (Fig 1b). The pore volume and pore diameter (Method C) increased with increasing P/Al ratio (Fig 1c & Fig 1d). After impregnation with Mo and Ni, the catalyst surface areas (Fig 2) were reduced considerably (Table 2), possibly due to the plugging of small pores. By studying the effect of gelation condition, precipitating agent, washing agent etc, on the textural properties of AAPs, a systematic method of preparation for these catalysts can be recommended. Rapid precipitation at 273K, a ripening period before centrifuging the gel, choice of isopropanol as washing agent and an optimum calcination temperature can provide catalysts with desired pore size for hydrotreating reactions.

X-Ray Diffraction Patterns: For NiMo/AAP1 the position of the main peaks (at 2θ= 27.3 and 26.6) suggested the presence of MoO_3 and $Al(PO_3)_3$ phases. This also agrees partially with those of aluminophosphates with P/Al = 1.0 (Cheung et al., 1986) and with CoMo/AAP1 (Chen et al., 1990). For NiMo/AAP2, the peaks at 2θ= 23 and 26.4 were in partial agreement as those of MoO_3 and $AlPO_4$. No characteristic peaks of Al_2O_3 was observed. This may be due to the formation of a mixture of crystalline bulk oxide and surface compounds and can be attributed to the metal oxide-support interaction. Reducing the phosphorous content (NiMo/AAP4 and NiMo/AAP8) demonstrated an amorphous (X-Ray indifferent) pattern, giving no hint of alumina, NiO or MoO_3. The broad XRD pattern of NiMo/Al_2O_3 (Method C) indicated a low order of crystallinity. Al_2O_3-H showed a more crystalline pattern than the above, but after impregnation with Ni and Mo, the catalyst gave an amorphous pattern. The $AlPO_4$ -G sample gave a broad peak around 2θ = 28 which is characteristic of the tetrahedral structure in amorphous $AlPO_4$. The main peaks (2θ = 23, 27.0) for NiMo impregnated $AlPO_4$ -G indicated the presence of an MoO_3 phase.

HDN Activity: Pyridine HDN occurs through a sequential pathway as shown in Fig. 3 in which pyridine is saturated to form piperidine followed by the formation of pentylamine through piperidine hydrogenolysis. Subsequent nitrogen removal from pentylamine results in pentane and ammonia as final products. Pentylpiperidine is formed in a side reaction from the alkyl-transfer reaction of piperidine and pentylamine. Di-n-pentylamine was also found to a minor extent in our experiments. In this experiment, a loss of N can be caused by the adsorption of N-containing compounds (pyridine, piperidine, pentylamine, and pentylpiperidine) on catalyst and the wall of reactor and evaporation (Joo et al., 1995). Because of these losses, in this paper, all values of pyridine HDN are considered as semi quantitative. Pyridine and coal liquid HDN activities of a series of catalysts which have different Al/P atomic ratio and the same Ni/Mo content are in Fig. 4a. HDN activity generally increased with the increase of Al/P ratio (or surface area of catalyst). As shown in Fig. 4b, generally HDN activity is linearly correlated with surface area of catalyst. The surface area is directly related to pore size. When the size of reactants are small enough in comparison with pore size, *hindered* internal diffusion is not the rate determining step. In this type of reactions, higher surface area of catalyst can give higher catalytic activity due to higher metal dispersion (Ni and Mo). However, *hindered* diffusion may take place with very heavy feeds. It has been reported that an optimum pore diameter for hydrodemetallization (HDM) of heavy oil exists around 20 nm (Smith et al., 1994). AAP catalyst having an optimum pore size obtained by manipulating Al/P ratio and other preparation conditions can be effective in this type of reaction.

REFERENCES

1. *Appl.Catal:*.A: General, Volume 113, No.1-9, June 1994.
2. Tanabe, K., *Appl.Catal. A: General* 113, p147-152 (1994).
3. Tischer, R.E., *Ind. Eng. Chem. Res.* 1987, 26, 422-426.
4. Marcelin, G., *J. Catal.* 83, 42-49 (1983)
5. Moffat, J.B., *Catal. Rev.-Sci. Eng.*, 18(2), 199-258 (1978).
6. Rebenstorf, B., *J. Catal.* 128, 293-302 (1991).
7. Kearby, K., Proc. of the Second International Congress on Catalysis (1961), p2567, Paris.
8. Chen et al., *Ind. Eng. Chem. Res.* 29, 1830 (1990).
9. Cheung et al., *J. Catal.* 102, 10-20 (1986).
10. Mitchell, S.F., *J. Catal.* 105, 521-524 (1987).
11. Vogel, R.F., *J. Catal.* 80, 492-493 (1983).
12. Campelo et al., *J.Catal.* 101, 484-495 (1986).
13. H.S. Joo, X. Zhan, J.A. Guin, No.41d., AICHE Spring Meeting Houston, 1995.
14. K.J. Smith and L. Lewkowiccz, *Canadian J. of Chem. Eng.*, 72, August, 637-643, 1994.

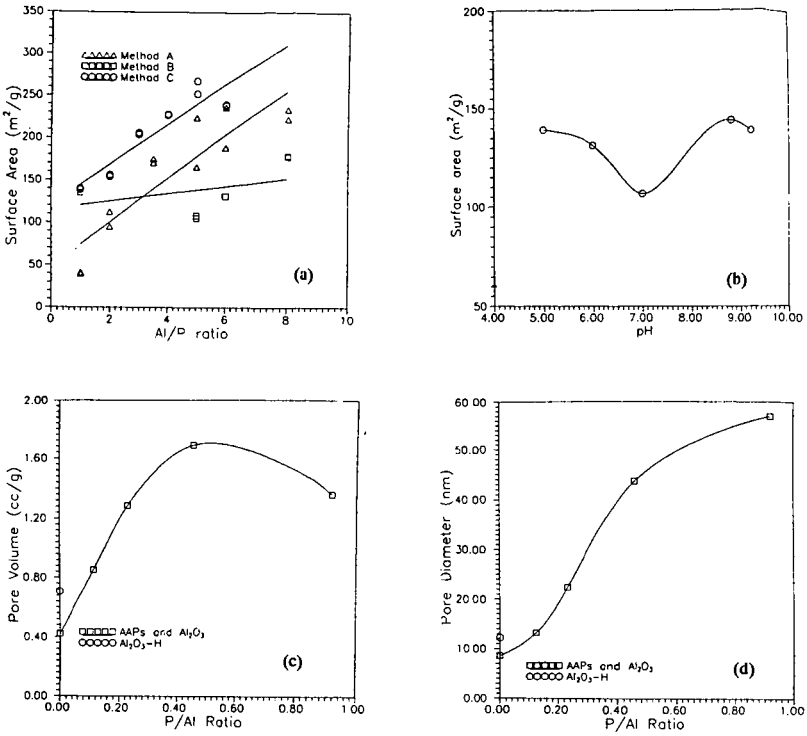

Fig 1. Effect of variables on support properties
(a) Surface area (m^2/g) Vs Al/P ratio (b) Surface area (m^2/g) Vs pH
(c) Pore volume (cc/g) Vs P/Al ratio (d) Pore diameter (nm) Vs P/Al ratio

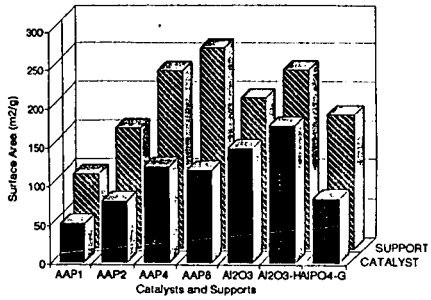

Fig 2. Surface Area of Catalysts

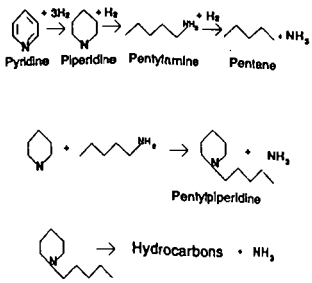

Fig 3. Reaction Pathways for Pyridine HDN

Support	Al		Mo		Ni		P		Al/P mole ratio-calc	Al/P mole ratio XPS	Mo/Ni mole ratio XPS
	ICP	calc	ICP	calc	ICP	calc	ICP	calc			
AAP1	19.0	18.2	na	13.3	3.06	3.23	19.1	19.1	1.09	1.2	21
AAP2	20.7	22.8	12.7	13.5	2.79	3.25	14.9	12.0	2.18	1.55	high
AAP4	na	41.8	12.8	13.3	2.84	3.21	na	11.1	4.3	4.25	2.07
AAP8	24.1	36.2	12.6	13.2	2.87	3.1	5.67	4.8	8.6	6.5	2.23
Al_2O_3	na	43.9	15.5	13.3	na	3.22	0.006	0			na
Al_2O_3 -H	na	41.5	12.7	13.3	na	3.22	0.002	0			1.77
$AlPO_4$ -G	14.9	17.1	11.8	13.3	na	3.21	22.1	20.2	0.97	0.93	9.33

na: not available

Table 1. Calculated and Measured Catalyst Composition (wt%)

Support	Support Pore Volume (cc/g)	Surface Area(m^2/g)	
		Support	Catalyst
AAP1	1.37	96	50
AAP2	1.69	154	79
AAP4	1.29	229	123
AAP8	0.85	259	118
Al_2O_3	0.42	194	146
Al_2O_3 -H	0.71	230	176
$AlPO_4$ -G	1.02	172	82

Table 2. Physical Characteristics of Supports (Method C) and Catalysts

Support	Support Weight (g)	
	Expt	Calc
AAP1	29.18	28.99
AAP2	46.78	41.82
AAP4	25.2	33.71
AAP5	62.0	79.9
AAP8	57.0	59.19
Al_2O_3	12.03	12.73

Table 3. Comparison of Support Weights (g)

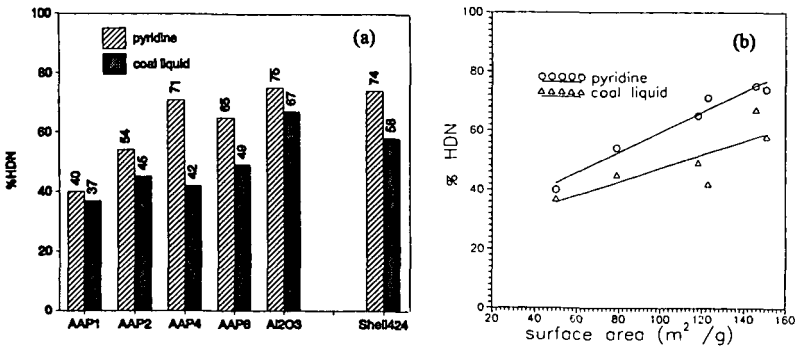

Fig 4. HDN with AAP Catalysts
(a) HDN Activity
(b) %HDN vs. Surface Area

HYDROTREATING OF COAL-DERIVED LIQUIDS*

Frances V. Stohl, Stephen E. Lott, Kathleen V. Diegert,
David C. Goodnow, John B. Oelfke

Sandia National Laboratories
Process Research Department 6212
Sandia National Laboratories
P.O. Box 5800
Albuquerque, NM 87185-0709

KEYWORDS: Refining, Coal Liquids, Hydrotreating

ABSTRACT

The objective of Sandia's refining of coal-derived liquids project is to determine the relationship between hydrotreating conditions and product characteristics. The coal-derived liquids used in this work were produced in HTI's first proof-of-concept run using Illinois #6 coal. Samples of the whole coal liquid product, distillate fractions of this liquid, and Criterion HDN-60 catalyst were obtained from Southwest Research Inc. Hydrotreating experiments were performed using a continuous operation, unattended, microflow reactor system. A factorial experimental design with three variables (temperature, (310°C to 388°C), liquid hourly space velocity (1 to 3 g/h/cm^3(cat)), pressure (500 to 1000 psig H_2)) is being used in this project. Sulfur and nitrogen contents of the hydrotreated products were monitored during the hydrotreating experiments to ensure that activity was lined out at each set of reaction conditions. Results of hydrotreating the whole coal liquid showed that nitrogen values in the products ranged from 549 ppm at 320°C, 3 g/h/cm^3(cat), 500 psig H_2 to <15 ppm at 400°C, 1 g/h/ cm^3(cat), 1000 psig H_2.

INTRODUCTION

DOE/PETC's refining of coal liquids program is aimed at determining the most cost effective combination of existing refinery processes and blending options necessary to upgrade direct and indirect coal liquids into transportation fuels that meet year 2000 specifications. A main reason for this program is that coal liquefaction processing has improved significantly since the last refining evaluation was done by Sullivan and Frumkin (1) at Chevron in the early 1980s. In addition, a recent publication by Zhou, Marano and Winschel (2) indicates that blending coal liquids with petroleum may allow refiners to produce specification products with less refining than if each fraction was processed separately. Sandia's role in this program is to develop a database relating hydrotreating parameters to feed and product quality by experimentally evaluating options for hydrotreating whole coal liquids, distillate cuts of coal liquids, petroleum, and blends of coal liquids with petroleum. Sandia's project is unique because our small-scale, continuous operation flow reactor system enables us to evaluate many hydrotreating options in a cost effective manner while keeping waste production to a minimum. Sandia's project is integrated with other program participants including participants in the Refining and End-Use of Coal Liquids Study project (Bechtel, Southwest Research Inc. (SwRI), Amoco, M. W. Kellogg), Hydrocarbon Technology Inc. (HTI, formerly HRI) the MITRE Corporation, and PETC. Sandia's data will be used by other program participants in refinery linear programming models to identify the most cost effective options for introducing and processing coal liquids in a refinery. This paper will cover results obtained from hydrotreating whole coal liquid product from HTI's first proof of concept run with Illinois #6 coal.

EXPERIMENTAL PROCEDURES

Sandia's experimental procedures included using a factorial experimental design, hydrotreating the whole coal-derived liquid, characterizing the feeds and hydrotreated products, and reporting results to other program participants.

Continuous Operation Reactor System: Sandia's hydrotreating studies are being performed using a continuous operation, trickle-bed, microflow reactor system. The system has all required safety features to enable it to be operated unattended. The capabilities of this reactor system include catalyst loadings up to 25 cm^3, liquid flow rates from 0.05 to 4 cm^3/min, gas flows for hydrogen and nitrogen up to 2 l/min, gas flows for H_2S/H_2 up to 0.5 l/min, maximum temperature of 620°C, and a maximum pressure of 1800 psig. The reactor volume is 59 cm^3. Four samples can be collected automatically during unattended operation. For liquid hourly space velocities (LHSV) of 1 and 3 g/h/cm^3(cat), samples would weigh about 7 and 22 g respectively.

Factorial Experimental Design: Based on experience, three parameters were chosen for the factorial experimental design (Figure 1): temperature, pressure, and LHSV. The ranges of hydrotreating conditions used with the design were temperatures of 310 to 388°C, pressures of 500 to 1000 psig H_2, and LHSVs from 1 to 3 g/h/cm^3(cat). Evaluation of the first set of hydrotreating conditions (388°C, 500 psig H_2, 1 g/h/cm^3(cat)) was repeated once during the run and once at the end of the run so that effects of catalyst deactivation could be determined. Prior to the use of the testing using the factorial experimental design, two additional sets of reaction conditions were evaluated to see the effects of high pressure and temperature: 388°C, 1500 psig H_2, 1 g/h/cm^3(cat) and 362°C, 1500 psig H_2, 1 g/h/cm^3(cat).

Reactor Feeds and Catalyst: Sandia received (from SwRI) a sample of fresh Criterion HDN-60 catalyst and about 3.5 gallons of whole coal liquid product that was produced in HTI's first proof-of-concept run using Illinois #6 coal. The whole coal liquid product was collected when HTI's third stage reactor was not on line and while catalyst replacement was being used. Sandia's reactor was loaded with 10g of fresh catalyst that was sulfided in situ using temperature staging. The presulfiding procedure consisted of heating the catalyst to 177°C under He, starting the flow of a 10 mol% H_2S/H_2 mixture and maintaining

177°C for 1 hour. The catalyst was then heated to 288°C under flowing H_2S/H_2 and maintained at 288°C for 1 hour. Next the catalyst was heated to 404°C under flowing H_2S, the temperature was maintained at 404°C for 1 hour. H_2S flow was stopped and H_2 flow started.

Figure 1: Factorial experimental design (temperature = °C, LHSV = g/h/cm³(cat), pressure = psig)

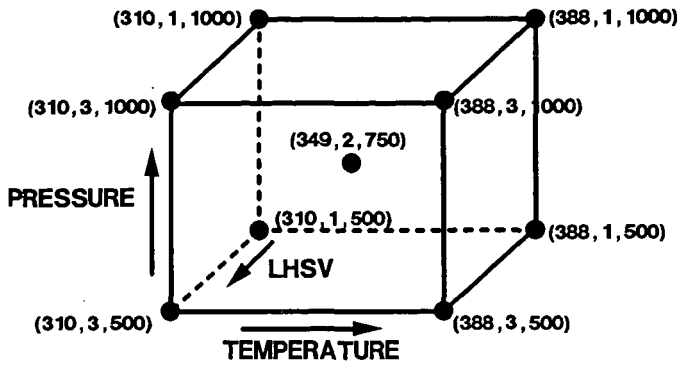

Analytical Procedures: Small samples were collected either manually or automatically throughout the run. Nitrogen and sulfur analyses were used to determine when line out was achieved at each reaction condition. These analyses were performed using an Antek 7000 Sulfur & Nitrogen Analyzer with an automatic sampler. Standards were prepared using phenanthridine for nitrogen, thianthrene for sulfur, toluene for the solvent, and four to five dilutions. Standards were measured at least twice and a polynomial fit of the intensity versus concentration data was used for analysis of unknowns.

RESULTS AND DISCUSSION

Analyses of the whole coal liquid by HTI, SwRI, and Sandia are shown in Table 1. SwRI used their measured specific gravity. Sandia used 0.9 g/ml for the first and second samples. Data for the second sample was also calculated using SwRI's specific gravity to show the effect of different values. Results show some variability but indicate the whole coal liquid has about 600 ppm nitrogen and 400 ppm sulfur.

Table 1. Sulfur and nitrogen analyses of whole coal liquid. Specific gravities used: HTI unknown; SwRI = 0.8628 g/ml; Sandia = 0.9 g/ml (except as noted).

HTI		SwRI		Sandia	
N	S	N	S	N	S
581	345	529	405	616	428
				621	399
				649*	417*

* *Same data as second analysis but calculated with specific gravity = 0.8628.*

The first condition used in the run was 388°C, 1500 psig H_2, and LHSV = 1 g/h/cm³(cat). This condition was chosen to line out the freshly sulfided catalyst and to evaluate high severity conditions as a check on parameters for the factorial experimental design. Product analyses showed no detectable nitrogen or sulfur. Therefore, temperature was decreased to 362°C with pressure and LHSV remaining the same. At this condition, nitrogen and sulfur contents of the hydrotreated products were still very low (less than 5 ppm). Since hydrogen pressure is the most restrictive variable in a refinery and because low pressure gives more versatility for processing, the maximum pressure used in the factorial experimental design was decreased to 1000 psig H_2. In addition, the lower limit for temperature was also decreased. The goal was to have as broad a range of parameters as possible without decreasing sensitivity to the parameters. The order in which the various conditions were evaluated is shown in Figure 2.

Figure 2 shows the nitrogen contents that were obtained at the various processing conditions. Results were considered lined out when the temperature, pressure and LHSV were relatively constant and the nitrogen and sulfur results were relatively constant. The brackets above each grouping of nitrogen values show which results met these criteria. These results were used to determine the average nitrogen content at that condition. The average nitrogen contents and standard deviations are shown along the X-axis. In addition, the order in which conditions were evaluated is also shown. No data is shown for conditions 6 or 15 because the reactor went down before there were enough data points for analysis. Sample 17 was a large batch (about 890 ml) of hydrotreated product collected at the same condition used for sample 16 (368°C, 1000 psig H_2, 3 g/h/cm³(cat)). Sample 19 was a large batch (865 ml) collected at the same condition as sample 16 (368°C, 1000 psig H_2, and 1 g/h/cm³(cat)). These large batches were collected so that there would be enough hydrotreated product for additional analyses. Samples 17 had 151 ppm nitrogen, which is a little lower than sample 16, which had 178 ppm nitrogen. Samples 19 and 18 had similar nitrogen contents, 42 and 44 ppm respectively. Both samples 17 and 19 had <7 ppm sulfur.

Figure 2. Nitrogen (ppm) vs reaction conditions. Temperature (°C), Pressure (psig), LHSV g/h/cm³(catalyst). Dashed line = Reactor Shutdown.

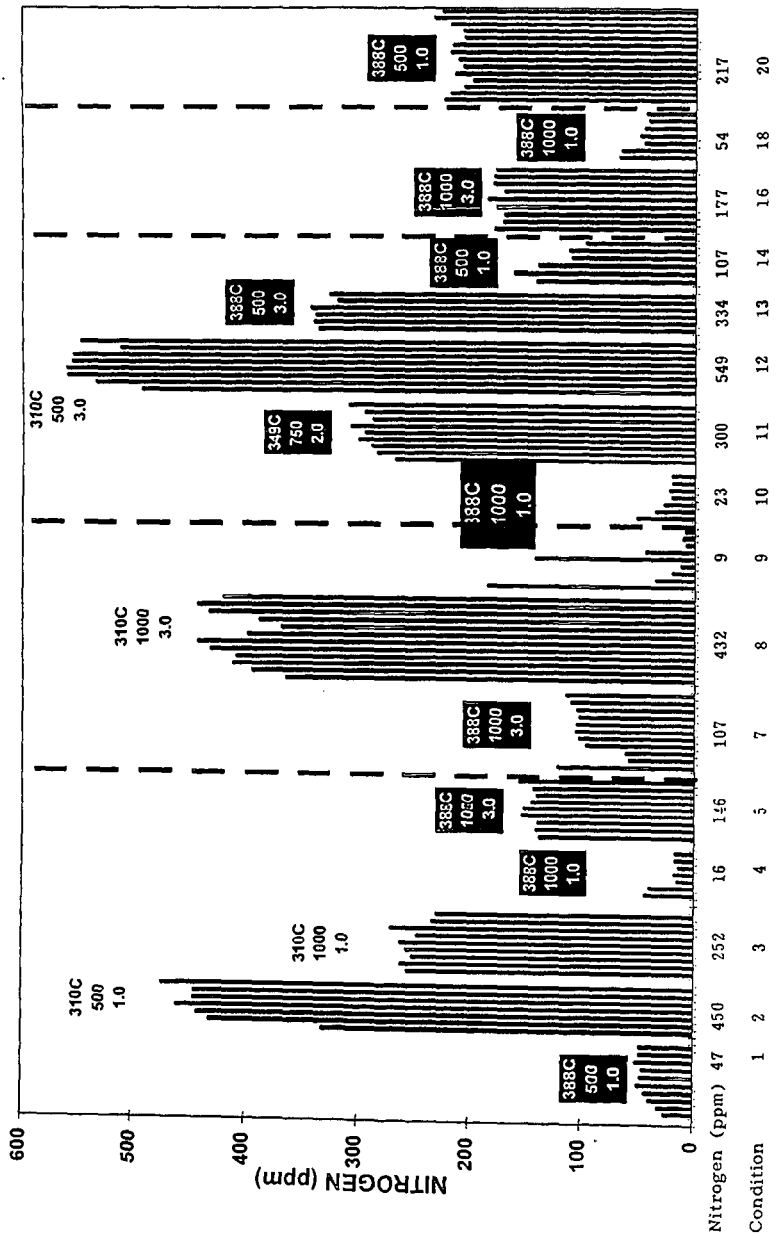

Figure 3 shows nitrogen contents as related to the conditions for the experimental design. Multiple values at a given condition show effects of catalyst deactivation. The total amount of reaction time (excluding down time) for this run was just over 32 days. Comparison of results for conditions 1 and 20 shows the effects of catalyst deactivation. Figure 4 shows the sulfur contents for the conditions of the factorial experimental design.

Figure 3: Average nitrogen values (ppm) with standard deviations.

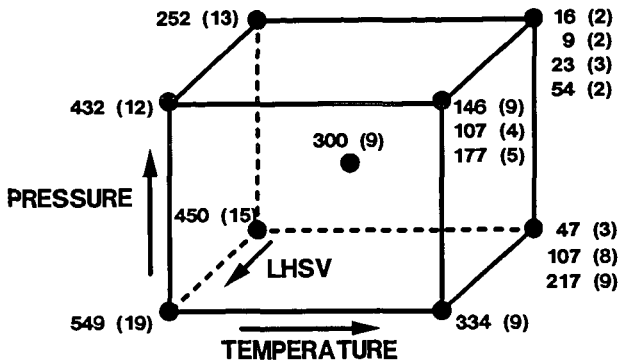

Figure 4: Average sulfur values (ppm) with standard deviations.

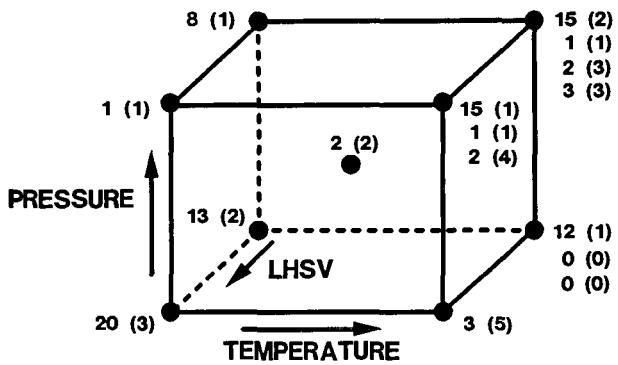

CONCLUSIONS AND FUTURE WORK

Results of this work show that good denitrogenation and good desulfurization can be obtained under relatively mild conditions with coal liquids from current processes. At the lowest severity condition, there is only about 10% nitrogen removal, whereas at the highest severity condition, there is about 97% nitrogen removal. Sulfur removal is good over the whole range of conditions and is greater than 95%. Ongoing and future work will involve additional characterization of reaction products by techniques such as distillation, PONA or PIONA analyses, density determinations, and proton NMR for hydrogen distributions. Results will be corrected for catalyst deactivation and analyzed statistically to determine the effects of process conditions on product quality. Future hydrotreating experiments will be performed with distillate fractions of this coal liquid and with coal-derived liquids from subbituminous coal.

• **Acknowledgment:** This work was supported by the U. S. Department of Energy at Sandia National Laboratories under contract DE-AC04-94-AL85000.

References:

1) Sullivan, R. F., Frumkin, H. A., ACS Div. of Fuel Chem. Preprints 31(2), 325, 1986.
2) Zhou, P.-Z., Marano, J. J., Winschel, R. A., ACS Div. of Fuel Chem. Preprints 37(4), 1847, 1992.

INVESTIGATION OF HYDROGEN TRANSFER IN COPROCESSING USING MODEL SYSTEMS

Jing Shen and Christine W. Curtis
Chemical Engineering Department
Auburn University, AL 36849

Introduction

The objective of this research was to evaluate the role of the resid in the coprocessing of coal and petroleum resid. The question being asked was whether the resid is an active solvent in coprocessing reactions and whether resid donates any hydrogen to coal during coprocessing. An effective means of determining whether resid participates in the reactions at coprocessing conditions is to use model systems and trace their reaction pathways. The research performed in this study evaluated the hydrogen donability of a naphthenic compound perhydropyrene, a compound type prevalent in resids that are hydrogen-rich. Model species were also used as acceptors that represented the aromatic aspect of coal. The model acceptors that were used were anthracene and phenanthrene.

Perhydropyrene has been used previously as a model donor representing resids by Owens and Curtis (1994) and Wang and Curtis (1994). In a N_2 atmosphere, perhydropyrene donated hydrogen to anthracene, increased the conversion of coal to THF soluble material, and reduced retrogressive reactions of petroleum resid (Owens and Curtis, 1994). Reactions of a number of hydrogen donor compounds such as cyclic olefins, hydroaromatic compounds, and naphthenes like perhydropyrene under equivalent reaction conditions showed that perhydropyrene had the least propensity for hydrogen donation among those compounds in both N_2 and H_2 atmospheres (Wang and Curtis, 1994). In the current study, the model perhydropyrene was used to represent petroleum and was reacted individually and with model acceptors primarily in a H_2 atmosphere to simulate coprocessing although some reactions were performed in N_2 to provide a reference point.

The model acceptors that were used included anthracene and phenanthrene, both of which are aromatic and represent molecules typically found in coal. Anthracene and phenanthrene have been used as coal model compounds and evaluated according to their ability to accept hydrogen from either a model donor or molecular hydrogen. Hydrogenation reactions of anthracene and phenanthrene were performed at temperatures of 325 °C (Salim and Bell, 1984) and 400 °C (Nakatsuji et al., 1978; Song et al., 1989 and 1991; Fixari and Perchec, 1989; Miyak et al.,1982) for 60 min with a hydrogen pressure of 5 to 9.8 MPa at ambient temperature. Different catalysts were used by the researchers including $NiMo/Al_2O_3$, $NiCl_2$, and sulfided $NiMo/Al_2O_3$ at loadings of 10 to 15 % on a reactant charge basis. The catalyst used in this study was a slurry phase catalyst molybdenum naphthenate which was added directly to the reactor contents along with excess sulfur. Mo naphthenate has been used extensively in coal and resid coprocessing reactions (Cassell and Curtis,1988; Pellegrino and Curtis, 1989; Kim and Curtis 1990, 1990a, 1990b, 1991; Ting et al.1992; Brannan et al.1995).

Experimental

Materials. The chemicals used in these experiments included anthracene (ANT, 99%), phenanthrene (PHEN, 98+ %), biphenyl, dihydroanthracene (DHA), pyrene (PYR), hexahydropyrene (HHP), and perhydropyrene (PHP). These chemicals were obtained from Aldrich Chemical Company and were used as received. The slurry phase catalyst, Mo naphthenate (MoNaph, Mo 6 wt %), was obtained from Shephard Chemical Company and was used as received. Sulfur added to the MoNaph reactions was introduced as elemental sulfur and was obtained from Aldrich. The solvent used to recover the reaction products was HPLC grade THF from Fisher Scientific Company.

Reaction Procedures. The reactions were conducted for 30 min in stainless steel tubular microreactors with a volume of ~20 mL. Each reaction was duplicated. The reactors were charged with the model reactants and with H_2 at 3.4 or 8.7 MPa at ambient temperature. When reacted individually, the model donor or model acceptors were added at ~ 0.1 g each of the donor or acceptor. When the donor and acceptor were charged simultaneously at a 1:1 ratio, each reactant was charged at 0.05 g, but when the ratio charged was 5:1, then 0.1 g of donor and ~ 0.02 g of acceptor were added. The reactions were performed at two different temperatures: 400 and 440 °C. The reactors were situated horizontally in a heated sand bath and were agitated at 400 cpm during the reaction. After 30 min of reaction the reactors were quickly quenched in

room temperature water. The liquid and solid products were removed from the reactor after being washed with 5 mL of THF and recovery obtained is given in the data tables.

Catalytic reactions were performed with MoNaph being charged to the reactors at a loading level of 1000 ppm of Mo on a total reactant charge basis. Elemental sulfur was added to MoNaph reaction in a 3:1 S to Mo ratio since MoS_2 was shown to be produced under these reaction conditions (Kim et al. 1989). The catalyst generated in situ at reaction temperature formed finely divided catalyst particles.

Analysis. The products that were recovered with THF from the reaction were analyzed on a Varian Model 3300 gas chromatograph equipped with an SGE HT-5 column and flame ionization detector. The HT-5 column had a 0.1 μm coating thickness, 0.33 mm in diameter and 25 m in length. The temperature program started at 60 °C with a final temperature of 320 °C and with a program rate of 2.5 °C/min. The temperatures of the injector and detector were 320 and 325 °C, respectively. Biphenyl was used as the internal standard.

Results and Discussion

The reactions were conducted at liquefaction conditions and in the absence of a solvent. The reaction systems were composed of the model donor and model acceptors reacted individually and combinatorially under thermal and catalytic conditions. The model donor used in all of this work was perhydropyrene and two model acceptors were anthracene and phenanthrene.

Reactions of the Model Acceptors. The two model acceptors used in this study had different propensities for accepting H_2 from the naphthenic donor and from molecular H_2. Reactions of anthracene and phenanthrene were performed individually in N_2 and H_2 at 400 and 440 °C and are described in Tables 1 and 2. Reactions of anthracene in N_2 resulted in less than 2% conversion of anthracene to DHA. The source of the hydrogen most likely came from anthracene itself when anthracene dimerized and the released H_2 which hydrogenated anthracene to form DHA.

Coprocessing of coal and petroleum resid is typically performed at temperatures ranging from 400 to 440 °C and under a H_2 pressure of 18 to 20 MPa at reaction temperature. H_2 pressure was used in these model reactions to simulate actual reaction conditions. Therefore, reactions of the two model acceptors were performed in H_2 at temperatures of 400 and 440 °C and at H_2 pressures of 18 to 20 MPa at reaction temperature. (The corresponding pressure at ambient temperature is 8.7 MPa.) The reaction products obtained from anthracene were DHA and THA; the products from phenanthrene were dihydrophenanthrene (DHPN) and tetrahydrophenanthrene (THPN). The amount of H_2 that was accepted in each reaction is given in the tables by the column headed by the "H_2 accepted" which is the moles of H_2 accepted per 100 moles of acceptor. Comparison of these quantities gives a measure of the amount of H_2 that had been accepted by the given acceptor under specific reaction conditions.

Anthracene was reactive in a thermal reaction with molecular H_2 present, yielding nearly 86% conversion to partially saturated products at both 400 and 440 °C (Table 1). The primary product formed was DHA at 440 °C which accounted for nearly 81% of the product; the minor product was THA which only accounted for about 5% of the product. At 400 °C, the same products were formed although the quantities were somewhat different; a lesser amount of DHA, 67.5%, and greater amount of THA, 18.4%, were formed.

Phenanthrene, in contrast to anthracene, had a lesser propensity for accepting molecular H_2 at 400 and 440 °C as evidenced by the conversion of phenanthrene being 4.7% and 9.1%, respectively (Table 2). The products from phenanthrene were DHPN and THPN which were produced in equivalent amounts in the 400 °C reaction and in an almost 2:1 ratio of DHPN to THPN in the 440 °C reaction. This lower proclivity for accepting molecular H_2 made phenanthrene the reactant of choice in the reactions with the naphthene perhydropyrene. The donation of H_2 and acceptance of H_2 from perhydrophyrene would be more apparent when hydrogenation from molecular H_2 was minimized.

These model acceptors were also reacted with the slurry phase catalyst, MoNaph+S, at the same temperatures and pressures as the thermal reactions; the result of these reactions are shown in Table 1 for anthracene and Table 2 for phenanthrene. Fairly small increases in the conversion were obtained in the reactions with anthracene and phenanthrene. For example, the conversion for phenanthrene increased from 4.7 to 9.0% at 400 °C and from 9.1 to 18.7% at 440 °C with the addition of MoNaph+S. Similarly, the conversion of ANT increased at both reaction

temperatures; the increase at 400 °C was from 85.9 to 88.6% conversion, while at 440 °C the increase was from 85.8 to 96.9% conversion.

Reaction of the Model Donor. The model donor used in this study was the naphthene, perhydropyrene. Perhydropyrene was used in the current study as a test naphthene molecule to examine if hydrogen transfer occurred between the model naphthene and aromatic species in H_2 and N_2 atmospheres. Perhydropyrene was reacted alone in H_2 and N_2 atmospheres thermally and catalytically at 400 and 440 °C. Perhydropyrene was stable showing almost no reactivity at these conditions. At 400 °C in N_2, no conversion of perhydropyrene occurred thermally while with MoNaph+S 1% conversion to pyrene occurred. At 440 °C in N_2, slightly higher conversion of perhydropyrene occurred. In H_2 at both 400 and 440 °C, perhydrophyrene was stable yielding at most 3% conversion. The MoNaph+S catalyst promoted conversion.

Reactions of Model Donor and Acceptors. Reactions were performed that combined the model donor perhydropyrene with the model acceptors anthracene and phenanthrene. The reactions of perhydropyrene with anthracene at 1:1 and 5:1 ratio under thermal and catalytic conditions are given in Table 1. The moles of H_2 accepted per 100 moles of anthracene or phenanthrene as well as the conversion of anthracene or phenanthrene served as a measure of the activity of the system.

The thermal reaction of perhydropyrene with anthracene at 400 °C and a 1:1 ratio gave a H_2 accepted of 103.9 while the addition of MoNaph+S increased the amount of H_2 accepted to 120.9. Increasing the ratio of perhydropyrene to ANT to 5:1 did not change the amount of H_2 accepted; the H_2 accepted in the thermal reaction was 104.0 while the addition of MoNaph+S increased H_2 accepted to 121.2. The primary product in all of these reactions was DHA but the addition of MoNaph+S increased the amount of THA produced. These conversion and H_2 accepted values were nearly equivalent to those obtained without perhydropyrene at 400 °C.

Phenanthrene accepted much less donor and molecular H_2 than anthracene at equivalent reaction conditions. For example, when perhydropyrene and phenanthrene were reacted together thermally at a 1:1 and 5:1 ratio at 400 °C, the amount of conversion was 2.9 and 4.6% and the H_2 accepted was 1.2 and 1.8 moles, respectively, as shown in Table 2. The respective values for anthracene ranged from 80 to 95% conversion and 104 to 120 moles of H_2 accepted. The primary product from phenanthrene was usually DHPN with THPN being the secondary product.

Although the reactivity of phenanthrene was much lower than that of anthracene, reactions of phenanthrene with perhydropyrene responded to the presence of perhydropyrene, to change in reaction temperature, and to the type of catalyst used. The reactivity of the perhydropyrene and phenanthrene systems is given on Table 2. Comparison of the conversion and H_2 acceptance values at two different temperatures but at otherwise equivalent conditions showed that reactions at 440 °C promoted a higher level of conversion and H_2 accepted than those at 400 °C.

Despite this lower reactivity at 400 °C, notable differences in the reactivity were observed in the thermal reactions of phenanthrene and perhydropyrene compared to catalytic reactions containing MoNaph+S. Reactions at 5:1 ratio of donor to acceptor in N_2 at 400 °C showed that a small amount of perhydropyrene donated to phenanthrene yielding THPN as product. By comparison, the reaction of phenanthrene in N_2 at 400 °C did not convert any phenanthrene and, hence, did not yield any hydrogenated product. Thermal reactions at 400 °C in H_2 with a 1:1 ratio of perhydropyrene to phenanthrene converted 2.9% phenanthrene while the 5:1 ratio converted 4.6%. The amount of H_2 accepted gave a corresponding amount of 4.4 and 7.4 moles of H_2 accepted per 100 moles of phenanthrene. The increased amount of naphthene present in the reaction at 400 °C increased the amount H_2 accepted by phenanthrene.

In the catalytic reactions using MoNaph+S, an excess amount of perhydropyrene at 400 °C also increased the amount of phenanthrene conversion and the amount of H_2 accepted by phenanthrene. MoNaph+S promoted hydrogenation of phenanthrene to DHPH and THPN. Comparing the combined donor and acceptor reactions to the acceptor reaction alone showed that perhydropyrene being present in the thermal reaction did not increase either phenanthrene conversion or the amount H_2 accepted. However, the addition of MoNaph+S with perhydropyrene present increased both conversion and H_2 accepted at 400 °C when compared to the catalytic reaction with phenanthrene alone.

Reactions of perhydropyrene and phenanthrene at 440 °C (Table 2) showed an overall higher reactivity than at 400 °C at corresponding reaction conditions. In N_2 with MoNaph+S, the amount of phenanthrene conversion to DHPN and THPN was 2.2%. The source of H_2 in the reaction was H_2 donated from perhydropyrene. In the reaction perhydropyrene produced pyrene

and several partially saturated pyrene compounds, thereby donating 8.9 moles of H_2 per 100 moles of perhydropyrene. In H_2 at 440 °C, the ratio of perhydropyrene to phenanthrene affected the amount of phenanthrene conversion as well as the amount of H_2 accepted. Both the thermal and catalytic reactions at the higher ratio gave larger amounts of these quantities than at the lower 1:1 ratio. The thermal reaction at 400 °C resulted in 9.3 moles of H_2 accepted per 100 moles of phenanthrene while at 440 °C 16.8 moles of H_2 were accepted. The MoNaph+S catalyst promoted hydrogenation of phenanthrene at both ratios yielding at the 1:1 ratio 15.8 moles of H_2 accepted by phenanthrene while at the 5:1 ratio 26.2 moles of H_2 were accepted.

Perhydropyrene reacted in these reactions with phenanthrene to form decahydropyrene (DCP), hexahydropyene (HHA), tetrahydropyrene (THP), dihydropyrene (DHP), and pyrene (PYR). More different products were made from perhydropyrene when phenanthrene was present than when perhydropyrene was reacted alone, where only pyrene was produced. A calculation of the amount of H_2 donated from these products is given in the tables and is designated as the moles of H_2 donated per 100 moles of donor or H_2 donated. In the H_2 atmosphere at 400 °C, the amount of H_2 donated from perhydropyrene remained nearly the same except for reactions containing MoNaph+S which increased H_2 donated to 6.3 from 1 to 2 in the thermal reactions. At 440 °C, higher amounts of H_2 were donated from perhydropyrene to the acceptors.

Summary

Determining whether hydrogen donation occurred from perhydropyrene as a representative of a resid naphthene at typical coprocessing conditions was a goal of this investigation. The reactions of the model naphthene perhydropyrene and the model acceptors, anthracene and phenanthrene, clearly showed that different chemical species present in the coal have different propensities for accepting H_2 regardless of its source, molecular or donor. The model naphthene under some circumstances, like in the anthracene reaction, was a positive influence on the reaction, causing the overall amount of H_2 accepted to increase. Catalytic reactions with MoNaph+S also promoted the apparent transfer of H_2 from perhydropyrene to anthracene. Phenanthrene was not as active an acceptor as anthracene. Thermal hydrogenation of anthracene and phenanthrene with molecular hydrogen at 400 °C yielded 85% and 4.7% conversion, respectively. Excess donor model was required to observe a positive effect of the naphthene on the H_2 accepted by the model acceptor.

References

Cassel, F.N.; Curtis, C.W. *Energy Fuels, 2,* 1, 1988.

Faxari, B. and Perchec, P.L., *Fuel,* 1989, Vo. 68, February, 218-221.

Kamiya, Y., Futamura, S., Mizuki, T., Kajioka, M. and Koshi, K. *Fuel Processing Technology, 14,* 79-90, 1986.

Kim, H.; Curtis, C.W. *Energy Fuels, 4,* 214, 1990a.

Kim, H.; Curtis, C.W. *Energy Fuels, 4,* 206, 1990b.

Kim, H.; Curtis, C.W. *Fuel Sci. Tech Intl. 9,* 229, 1991.

Kim, H.; Curtis, C.W.; Cronauer, D.C.; Sajkowski, D.J. ACS Fuel Dive Prep. 34, 4, 1446, 1989.

Miyak, M., Sakashita, H., Norura, M. and Kikkawa, S. *Fuel,* 1982, Vol 61, February, 124-128.

Nakatsuji, Y., Kubo, T., Nomura, M., and Kikkawa, S., *Bulletin of the Chemical Society of Japan,* Vol. 51 (2), 618-624, 1978.

Owens, R.; Curtis, C.W. *Energy Fuels, 8,* 823, 1994.

Pellegrino, J.L.; Curtis, C.W. *Energy Fuels, 3,* 160, 1989.

Salim, S.S. and Bell, A.T. *Fuel,* 1984, Vol 63, April, 469-476.

Song, C.; Nomura, M. and Ono, T. *Preprint - Am. Chem. Soc. Div. Fuel Chem., 36, 2,* 586-596, 1991.

Song, C.; Ono, T.; and Nomura, M. *Bulletin Chemical Society Japan 62,* 630-632, 1989.

Ting, P.S.; Curtis, C.W.; Cronauer, D.C. *Energy Fuels, 6,* 511, 1992.

Wang S.L.; Curtis, C.W. *Energy Fuels, 8,* 446, 1994.

Acknowledgements

The support of the United States Department of Energy under contract No. DE-AC22-91PC91055 for this work is greatly appreciated.

Table 1. Anthracene at Reactions 400 °C and 440 °C: Reacted Alone and With Perhydropyrene

Reaction Condition	Reactants	Atmosphere	T (°C)	Product Distribution (mol%)			Recovery (%)	ANT Conversion, %	H_2 Accepted / H_2 Donated
				ANT[c]	DHA	THA			
Thermal	ANT	N_2	400	98.3±0.17	1.70±0.17	0±0	92.5	1.7	1.7
Thermal	ANT	H_2	400	14.1±0.8	67.5±0.4	18.4±1.2	90.1	85.9	104.3
MoNaph + S	ANT	H_2	400	11.4±0.6	70.0±9.3	26.6±8.6	94.4	88.6	123.2
Thermal	ANT	H_2	440	14.2±0.40	80.9±0.42	4.9±0.82	84.4	85.8	90.75
MoNaph + S[b]	ANT	H_2	440	3.8±0.06	55.8±0.62	40.4±2.1	80.1	96.9	136.58
Thermal	PHP: ANT 1:1	N_2	400	94.0±1.8	6.0±1.8	0.0±0.0	82.5	6.0	6.5±0.7
MoNaph + S	PHP: ANT 1:1	N_2	400	95.4±1.1	3.2±1.2	1.4±0.1	85.2	4.6	6.0±0.9
Thermal	PHP: ANT 1:1	N_2	440	94.4±0.4	4.6±0.1	1.0±0.3	83.8	5.6	6.5±0.7
MoNaph + S	PHP: ANT 1:1	N_2	440	96.3±0.1	3.7±0.1	0.0±0.0	87.1	3.7	4.3±0.3
Thermal	PHP: ANT 1:1	H_2	400	5.9±0.5	84.3±4.5	9.8±4.0	98.2	94.1	103.9
MoNaph + S	PHP: ANT 1:1	H_2	400	3.4±0.8	72.5±5.2	24.1±6.0	96.8	96.6	120.9
Thermal	PHP: ANT 5:1	H_2	400	6.3±2.1	83.4±0.6	10.3±2.7	92.2	93.7	104.0
MoNaph + S	PHP: ANT 5:1	H_2	400	5.3±2.0	68.2±6.5	26.6±4.5	82.9	94.7	121.2

[a] Reaction time = 30 min; 8.7 MPa H_2 or N_2 at room temperature.
[b] MoNaph + S = Mo naphthenate with added elemental S.
[c] ANT = anthracene; DHA = dihydroanthracene; THA = tetrahydroanthracene; H_R = (1 x DHA mol% + 2 x THA mol%) x 100.
[d] Reactant loading: Aproximately 0.05 g of each ANT and PHP in PHP:ANT = 1:1 thermal and catalytic reactions; Approximately 0.02 g of ANT and 0.1 g of PHP in PHP:ANT = 5:1 thermal and catalytic reactions. Mo naphthenate loading is approximately 0.0017 g = total reactant charge (0.1 g)/ 60, computed according to 1000 ppm MoS_2 and 6 wt% Mo in Mo naphthenate.

Table 2. Phenanthrene Reactions at 400 and 440 °C: Reacted Alone and With Perhydropyrene

Reaction Condition	Reactant	Atmosphere	T(°C)	Product Distribution (mol %)			Recovery (%)	PHEN Conversion (%)	H_2 Accepted[b]	H_2 Donated[c]
				PHEN	DHPN	THPN				
Thermal	PHEN	N_2	400	100±0.0	0.0	0.0	86.6	0.0	0.0	NA[d]
MoNaph	PHEN	N_2	400	100±0.0	0.0	0.0	85.5	0.0	0.0	NA
Thermal	PHEN	H_2	400	95.3±0.7	2.6±0.5	2.1±0.2	83.5	4.7	6.8±0.9	NA
MoNaph+S[b]	PHEN	H_2	400	91.0±0.0	6.0±0.0	3.0±0.1	87.3	9.0	12.0±0.1	NA
Thermal	PHEN	N_2	440	100 ±0.0	0.0	0.0	87.6	0.0	0.0	NA
MoNaph+S	PHEN	N_2	440	100 ±0.0	0.0	0.0	85.3	0.0	0.0	NA
Thermal	PHEN	H_2	440	90.9±1.2	5.9±0.7	3.2±0.5	91.8	9.1	12.3±1.7	NA
MoNaph+S	PHEN	H_2	440	81.3±3.8	12.8±2.4	5.9±1.4	82.0	18.7	24.6±5.2	NA
Thermal	PHP: PHEN1:1	H_2	400	97.1±0.2	1.5±0.0	1.4±0.2	88.5	2.9	4.4±0.3	1.2±0.1
MoNaph+S	PHP: PHEN1:1	H_2	400	86.9±2.0	9.0±1.5	4.1±0.5	90.0	13.1	17.2±2.5	6.2±0.0
Thermal	PHP: PHEN5:1	N_2	400	98.4±0.2	0.0±0.0	1.6±0.2	92.3	1.6	3.2±0.4	3.8±0.0
MoNaph+S	PHP: PHEN5:1	N_2	400	99.0±0.0	0.0±0.0	1.0±0.0	86.6	1.0	2.0±0.0	3.9±0.0
Thermal	PHP: PHEN5:1	H_2	400	95.4±0.2	1.8±0.4	2.8±0.8	86.9	4.6	7.4±2.1	1.8±0.0
MoNaph+S[b]	PHP: PHEN5:1	H_2	400	82.8±0.1	10.7±0.6	6.5±0.1	92.9	17.2	23.7±0.1	6.3±0.0
Thermal	PHP: PHEN 1:1	H_2	440	93.2±1.4	4.4±0.8	2.4±0.6	92.5	6.8	9.3±2.1	0.9±0.1
MoNaph+S	PHP: PHEN 1:1	H_2	440	87.2±1.3	9.9±0.7	2.9±0.6	94.8	12.8	15.8±1.9	7.5±0.1
Thermal	PHP: PHEN 5:1	H_2	440	87.1±1.1	9.0±0.0	3.9±1.2	86.0	12.9	16.8±2.3	8.6±0.1
MoNaph+S[b]	PHP: PHEN 5:1	H_2	440	79.5±3.6	14.9±2.1	5.6±1.5	80.0	20.5	26.2±5.1	10.7±0.6
MoNaph+S	PHP: PHEN 5:1	N_2	440	97.8±0.2	0.5±0.1	1.7±0.7	86.4	2.2	3.9±1.0	8.9±0.1

[a] Reaction Conditions: 30 min; 8.7 MPa H_2 or N_2 at ambient temperature; catalyst loading = 1000 ppm on total reactant charge basis; the total amount of reactant charged is approximately 0.1 g.
[b] Moles of H_2 Accepted per 100 moles of PHEN; H_2 accepted = (2 x THPN mol% + 1 x DHPN mol%) x 100.
[c] Moles of H_2 Donated per 100 moles of PHP; H_2 Donated = (3 x DCP mol% + 5 x HHP mol% + 6 x THP mol% + 7 x DHP mol% + 8 x PYR mol%) x 100.

EFFECT OF TETRALIN ON THE DEGRADATION OF POLYMER IN SOLUTION

Giridhar Madras, J.M. Smith, and Benjamin J. McCoy
Department of Chemical Engineering and Materials Science
University of California at Davis
Davis, CA 95616

Keywords : polymer, hydrogen donor, thermal degradation, continuous kinetics, solvent effect

ABSTRACT

The effect of a hydrogen-donor solvent tetralin on thermal degradation of poly(styrene-allyl alcohol) in liquid solution was investigated in a steady-state tubular flow reactor at 1000 psig at various tetralin concentrations, polymer concentrations, and temperatures. The experimental data were interpreted with continuous-mixture kinetics, and rate coefficients determined for the specific and random degradation processes.

Introduction

Thermolytic degradation of polymers is similar in some respects to other important thermal decomposition processes like petroleum cracking and coal thermolysis. All these processes involve complex mixtures, both as reactants and as products. Polymer degradation usually occurs in a polydisperse mixture, and observing the temporal change of the molecular weight distribution (MWD) caused by degradation affords a means to test kinetic models. Due to the advance of technology in analytical instrumentation, dynamic MWD data can be obtained by gel permeation chromatography (GPC). A continuous-mixture approach is applicable for these cases, since it is based on mass balance equations that govern the temporal change of a distribution function (Aris and Gavalas, 1966; Cheng and Redner, 1990). This approach has been used for a theoretical discussion of polymer degradation (Ziff and McGrady, 1985,1986), for the kinetics of reactions in reversible oligomerization (McCoy, 1993), as a model for coal liquefaction (Prasad et al., 1986), and for coal thermolysis (Wang et al., 1994). Recently, Wang et al. (1995) measured the rates of specific and random scission for the degradation of poly(styrene-allyl alcohol) in t-butanol using the continuous-mixture approach.

There is little information of the effect of hydrogen-donor solvents on the degradation of polymer in solution. Sato et al. (1990) investigated the solvent effect on the thermal degradation of polystyrene at 300-450 C and 2 MPa. They observed that solvents with higher hydrogen donating capability produced less conversion of polystyrene. These experiments indicated that the degradation behavior, and the conversion of the polymer are affected by the solvents. Murakata et al. (1993) investigated the effect of hydrogen-donor solvents on the degradation of poly-α-methylstyrene and observed that there was no effect of the solvent on the degradation mechanism and the conversion of the polymer. The effect of hydrogen-donor solvents has been extensively investigated for coal liquefaction. The literature on this subject, including generally accepted pathways for hydrogen transfer from a donor solvent, was summarized by Chawla et al. (1989).

The objective of this study was to investigate the effect of the hydrogen-donor solvent, temperature, and residence time on the degradation of the poly(styrene-allyl alcohol). The experimental data was obtained by passing the polymer solution through a steady-state flow reactor, and analyzing the products using HPLC-GPC. Continuous kinetics ideas were employed to interpret the experimental data and fundamental data.

Experiments

The polymer used in this study was poly(styrene-allyl alcohol) (Polysciences, Inc.) of number-average molecular weight 1100. The polymer was pretreated to remove components in the lower molecular weight range, which would interfere with the analysis of the product peaks. A detailed explanation of the pre-treatment is given by Wang et al. (1995). The polymer was pre-treated by dissolving 50 grams of the polymer in 500 ml of t-butanol. The polymer solution was continously stirred using a magnetic stirrer and heated to 40 C on a heating plate. A volume of 1350 ml of distilled water was added drop by drop to this polymer solution. The high molecular-weight polymer precipitated and settled at the bottom. The dried precipitate was blanketed under nitrogen in a closed bottle to avoid oxidation. The MW of the treated polymer was 1640.

The experiments were carried out at high pressure, 1000 psig (6.8 MPa), to prevent the vaporization of the solvent, 1-butanol, at high temperatures and to ensure that the reaction of the polymer occurs in the liquid phase. The polymer solution was prepared by dissolving the polymer in 1-butanol at a known concentration in the range of 1-4 g/L. The polymer solution flows through the reactor, a water cooled heat exchanger, two pressure reduction valves placed in series, and finally exits through a rotameter. The flow rate (and hence the residence time of the

fluid in the reactor) is controlled by the rotameter. Degradation experiments were carried out at three different polymer concentrations, four different temperatures, and four different tetralin concentrations to study the effects of these parameters on the rate of polymer degradation. At each condition, the experiment was conducted at four different residence times (i.e., four different flow rates). Since the flow rates were measured at ambient conditions, the residence times for each temperature were corrected with the density calculated from Lee-Kesler equation (Lee and Kesler, 1975). After reaching steady state, two 20 ml samples were collected at each residence time for the HPLC-GPC analysis. Experiments of 1-butanol and 10 to 50% tetralin, in the absence of polymer, were conducted at 150 to 200 C to investigate interactions between the solvents. The GPC analysis of samples from these experiments indicated no products.

The significant difference of these experiments compared to pyrolysis experiments in gas or vacuum is that all the reactions take place in the liquid phase, and thus the residence time for both the reactants and products is the same. Further, the mild temperatures limit the amount of random chain scission and eliminate repolymerization.

Before analyzing the effluent sample by GPC, one needs to concentrate the sample and dissolve the reactant and products in tetrahydrofuran. Hence, 20 ml of the effluent sample is concentrated to 4 ml by evaporating the 1-butanol under vacuum at 353 C. The molecular weight distribution of the effluent samples was determined by gel permeation chromatography using PLgel columns (Polymer Labs) in a high performance liquid chromatograph (Hewlett Packard 1050). For this purpose, two columns packed with crosslinked poly(stryene-divinyl benzene) of 100 and 500 A pore size, respectively, were used in series after a guard column. Tetrahydrofuran (THF, HPLC grade, Fisher Chemicals) was continuously pumped through the columns at a constant flow rate of 1 ml/min. A sample of 100 microliters was injected at the start of each run and the ultraviolet detector was used to measure the absorbance of the compounds in the effluent samples. The wavelength of 254 nm was chosen since this wavelength provided the maximum absorbance of the reactant and products. The molecular weight corresponding to the retention time in the columns was calibrated with polystyrene samples obtained from Polymer Lab. The calibration procedure is described in detail by Wang et al. (1995).

Mechanism

The mechanism of degradation of polymer is similar to that of Wang et al. (1995). The thermal degradation of the polymer is of two kinds: random scission at any position along the polymer chain, and specific scission leading to specific products. Both types of scissions occur in the degradation of poly(styrene-allyl alcohol), as seen from Figure 1, which is the MWD plotted as concentration distribution (g/L MW) versus Log_{10} MW. The figure shows three distinct peaks in the molecular weight range 100-500 indicating specific scission products. The higher MW range peak shifts to a lower MW range relative to the feed polymer indicating random scission.

Though only three distinct peaks are observed in the figure, we expect the formation of styrene, since it was observed by Wang et al. (1995). The styrene peak should appear at a MW of 104. However, since tetralin and styrene have comparable MW of 132 and 104, respectively, the peaks of these two compounds are superimposed. Lacking a method to distinguish styrene from tetralin, we therefore removed this peak from the chromatogram and its subsequent analysis. The remaining peaks in the effluent chromatograms were approximately of MW 162, 222, and 486, respectively, and are proposed to be the oligomer of an allyl alcohol and a styrene molecule (SA), and an oligomer of two allyl alcohols and one styrene molecule (ASA), and a trimer of SA ($(SA)_3$). Any allyl alcohol (A) produced during the degradation would evaporate during the sample preparation.

Theoretical Model

The theoretical model is similar to the one proposed by Wang et al. (1995). The MWD of the feed polymer is described by a gamma distribution. The parameters of the gamma distribution are obtained by calculating the zeroth, first, and the second moments of the experimental peak. This gamma distribution is used as the initial MWD in the kinetics model.

A continuous mixture can be defined as a mixture of a very large number of different-size polymer molecules, whose distribution can be expressed by a continuous index such as the molecular weight. We consider that all the degradation products are dissolved in solution, that no repolymerization reactions occur, and that the flow reactor can be treated as a steady-state plug-flow reactor. Model equations based on continuous kinetics for polymer degradation were developed by Wang et al. (1995).

Results and Discussion

For the degradation of poly(styrene-allyl alcohol) in a solvent of pure t-butanol, both random and specific scission of the polymer occurred at 130-200 C and 1000 psig (Wang et al., 1995). However, in the present case of 1-butanol solvent, no degradation of the polymer was observed at these conditions in the absence of tetralin. This suggests that t-butanol was involved in the reaction, possibly as a hydrogen donor. Sato et al. (1990), on the other hand, reported decreased degradation of several polymers in presence of hydrogen donors. These results indicate the significance of the solvent effect in thermolytic degradation reactions, and the importance of continued investigation along these lines.

An experimental MWD and model simulation are presented in Figure 2. As explained earlier, a peak of styrene has been removed since the peak of tetralin is superimposed on it. The three distinguishable peaks, SA, ASA, $(SA)_3$, are the products of specific chain scission. The same products (S, SA, ASA, $(SA)_3$) are produced with either t-butanol or 1-butanol plus tetralin.

The parameters in the model are the parameters of the gamma MWD describing the feed polymer and the rate coefficients for specific and random degradation. The rate coefficients for specific degradation are determined from the equation (Wang et al., 1995):

$$q = k_i \, p \, t \qquad (1)$$

where p is the feed concentration (mol/L), t is the residence time, and q is the concentration of the specific product (mol/L). These concentrations are the zeroth moments of their MWDs divided by MW. Since the zeroth moment is the area under the curve, the area of each specific product peak was determined by numerical integration using the trapezoidal rule. The slope of the line gives the rate coefficient for specific degradation, k_i. The rate coefficients for random degradation are obtained by fitting the experimental MWD data of random degradation with gamma distribution parameters, using the relationship derived by Wang et al. (1995).

The dependence of the specific and random degradation rate coefficients on the temperature, concentration of the polymer, and concentration of the hydrogen-donor solvent (tetralin) are shown in the Tables 1-3. The rate constants are independent of polymer concentration, confirming that the reactions for both specific and random degradation are first-order. This is consistent with the assumption of Wang et al. (1995).

The activation energies for random and specific degradation are extracted from the temperature dependence of the rate coefficients (Figure 3) and are given in Table 4. The dependence of the rate constants on the concentration of tetralin were modeled by the following equation:

$$k = k_t C_t / (1 + \kappa \, C_t) \qquad (2)$$

where k is the rate constant and C_t is the vol% of tetralin. Parameters k_t and κ are obtained by plotting the inverse of the rate versus the inverse of tetralin concentration and are given in Table 5. Tetralin is essential for the degradation of the polymer at this temperature and pressure. A tetralin concentration of 25% produces rate coefficients nearly an order of magnitude higher than the rate coefficients obtained by Wang et al. (1995), who degraded the same polymer using t-butanol without tetralin. However, the activation energies for the specific and random degradation of the polymer by 1-butanol and 25% tetralin are comparable to the activation energies for the specific and random degradation of the polymer by t-butanol.

Acknowledgement

The financial support of Pittsburgh Energy Technology Center Grant No. DOE DE-FG22-94PC94204, and of the University of California UERG is gratefully acknowledged.

References

Aris, R.; Gavalas, G.R. *Phil. Trans. R. Soc., London* **1966**, A260, 351.
Cheng, Z.; Redner, S. *J. Phys. A : Math. Gen.* **1990**, 23, 1233.
Chawla, B.; Keogh, R.; Davis, B.H. *Energy and Fuels* **1989**, 3, 236-242.
Lee, B.F.; Kesler, M.G. *AIChE. J.* **1975**, 21, 510-527.
McCoy, B. J. *AIChE J.* **1993**, 39, 1827.
Sato, S.; Murakata, T.; Baba, S.; Saito, Y.; Watanabe, S. *J. Appl. Poly. Sci.* **1990**, 40, 2065.
Murakata, T.; Saito, Y.; Yosikawa, T.; Suzuki, T.; Sato, S. *Polymer* **1993**, 34, 1436.
Wang, M.; Zhang, C.J.; Smith, J.M.; McCoy, B.J. *AIChE J.* **1994**, 40, 131.
Wang, M.; Smith, J.M.; McCoy, B.J. *AIChE J.* **1995**, 41 (6), In press.
Ziff, R. M.; McGrady, E.D. *J. Phys. A: Math. Gen.* **1985**, 18, 3027.
Ziff, R. M.; McGrady, E.D. *Macromolecules* **1986**, 19, 2513.

Table 1. Rate coefficients (1/sec) for specific and random degradation of the polymer at various temperatures and at a constant polymer concentration of 2 g/L and a tetralin concentration of 25%.

Temperature	k for SA ($x10^3$)	k for ASA ($x10^3$)	k for $(SA)_3$ ($x10^3$)	k_r ($x10^4$)
130	1.68	2.52	3.36	0.22
150	1.89	3.09	4.05	2.1
170	3.9	4.68	5.85	18
200	5.95	6.43	7.14	130

Table 2. Rate coefficients (1/sec) for specific and random degradation of the polymer at various polymer concentrations and at a constant temperature of 150 C and a tetralin concentration of 25%.

Polymer Conc. (g/L)	k for SA ($x10^3$)	k for ASA ($x10^3$)	k for $(SA)_3$ ($x10^3$)	k_r ($x10^4$)
1	1.73	3	4.2	2.3
2	1.89	3.09	4.05	2.1
4	1.75	2.89	3.9	2.3

Table 3. Rate coefficients (1/sec) for specific and random degradation of the polymer at various tetralin concentrations and at a constant temperature of 150 C and a constant polymer concentration of 2 g/L.

Tetralin Conc.	k for SA ($x10^3$)	k for ASA ($x10^3$)	k for $(SA)_3$ ($x10^3$)	k_r ($x10^4$)
5 %	0.58	1.6	1.78	0.4
10 %	0.8	2.3	2.5	1.0
25 %	1.89	3.09	4.05	2.1
50 %	2.09	3.57	4.9	2.5

Table 4. Activation energies for specific and random degradation

Specific Product	Activation energies (kcal/mol)
SA	7.5
ASA	5.2
$(SA)_3$	4.4
Random degradation	33.1

Table 5. Parameters for the dependence of rate coefficients of polymer degradation on tetralin concentration.

Specific Product	k_t ($x10^4$) (1/sec/vol%)	κ (1/vol%)
SA	1.33	0.043
ASA	5.59	0.138
$(SA)_3$	4.96	0.085
Random degradation	1.07	0.012

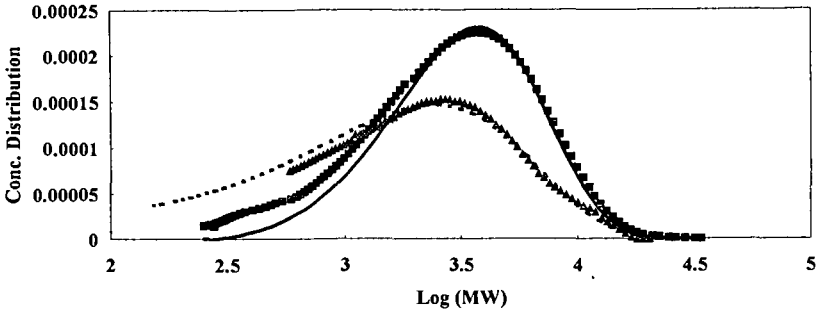

Figure 1. The MWD before and after thermal degradation (■: chromatograph before degradation, ▬ : Gamma Distribution fit ; ▲ : chromatograph after degradation at 150 C, 25% tetralin, and residence time of 42.51 min. ; ..... : Gamma Distribution fit).

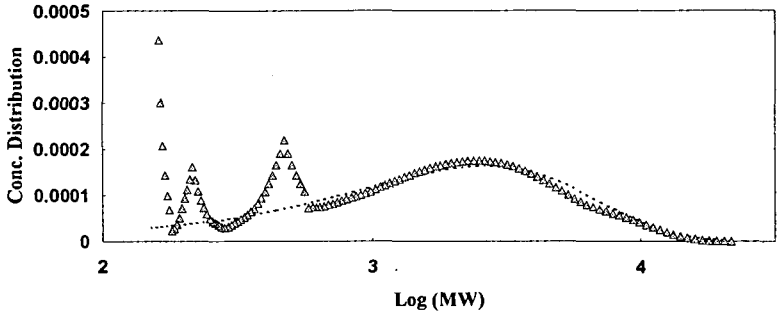

Figure 2. Comparison of experimental results of MWD with model simulation at 150 C, 25% tetralin and at a residence time of 42.51 minutes (Δ : experimental data; ..... : Gamma Distribution fit). .

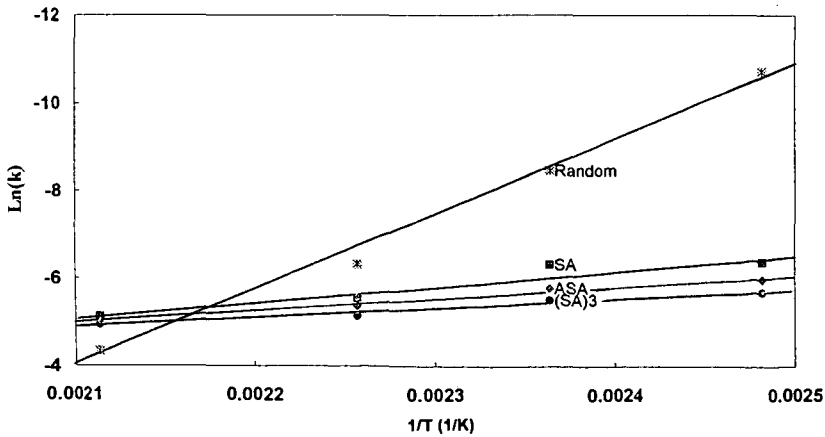

Figure 3. Arrhenius plot of the degradation coefficients versus temperature to determine the activation energies of the specific scission and random degradation.

WASTE OILS UTILIZED AS COAL LIQUEFACTION SOLVENTS ON DIFFERENT RANKS OF COAL

Edward C. Orr, Yanlong Shi, Jing Liang, Weibing Ding,
Larry L. Anderson, and Edward M. Eyring
Department of Chemistry and Department of Chemical and Fuels Engineering, University of Utah, Salt Lake City, UT 84112

Keywords: tires, plastic, coal, liquefaction

Introduction

Solvent plays an important role in direct coal liquefaction. The solvent acts as a medium to transport hydrogen, as a heat transfer medium, as an additional reactant along with the coal, as a coal dissolution medium, and as the medium to transport coal liquefaction products away from the coal matrix. Recent investigations of coprocessing coal with solid waste materials (plastics, rubbers, cellulose) to raise the hydrogen content of the coal products with a concomitant decreased need for the addition of hydrogen gas have involved reacting solid waste plastics and solid waste rubbers directly with coal with little preparation other than grinding or shredding the waste material.[1-4] (An indirect benefit to coprocessing waste with coal is that less waste must be disposed of in landfills or by incineration.) Dry mixing of coal and waste materials may be the most cost effective method for coprocessing waste with coal because there is less preparation of the waste material. However, the metals, anti oxidants, carbon black, and plasticers present in the waste materials make some preparation of the reactants necessary. A possible pretreatment of the waste materials would be a vacuum pyrolysis of the waste materials that would produce cleaner oils. To examine this issue, we have recently carried out coal liquefaction experiments in which coals of different ranks were reacted with oils obtained by the vacuum pyrolysis of waste materials, specifically plastics and rubber tires. We have also used waste automotive oils to determine whether the automotive oil is effective, and whether trace heavy metals found in the waste automotive oil can be scavenged by the coal.

Experimental

Coal samples were obtained from the Penn State Coal Sample Bank. Six different coals were used as received: Pocahontas DECS-19 (low volatile bituminous coal), Blind Canyon DECS-2 (high volatile A bituminous coal), Illinois-6 DECS-2 (high volatile B bituminous coal), Wyodak-Anderson DECS-26 (subbituminous B coal), Smith-Roland DECS-8 (subbituminous C coal), and Buelah DECS-11 (lignite A). Waste automotive crankcase oil was obtained from Book Cliff Energy, Green River, Utah. Oils from the vacuum pyrolysis of waste rubber tires and from waste plastics were obtained from Conrad Industries, Chehalis, Washington. All oils were stored under ambient conditions. All coals were ground to a -60 mesh. Samples were mixed in a 1 part coal to 1 part solvent ratio determined by weight. Each sample was placed in a 27 cm^3 stainless steel tubing reactor with no catalyst. Solvents were stirred prior to being placed in the tubing reactor. Tubing reactors were purged with N_2 and pressurized with H_2 to 1000 psig (cold). Tubing reactors were placed in a sandbath heated to 430 °C and shaken vertically for one hour. The tubing reactor was then removed from the sandbath and allowed to cool for 5 minutes. The tubing reactor was then quenched using cold water. The tubing reactors were left sealed over night. Products were then removed and placed in soxhlet extractor thimbles and extracted with THF. Soxhlet extraction was continued until the extraction solvent appeared clear. The THF was then removed with a rotary evaporator leaving behind the soluble product. The THF soluble product was then dried under vacuum for two hours and weighed. The sum of the THF soluble mass and THF insoluble mass was subtracted from the original coal (daf) weight to account for gas mass. The dried THF soluble portion was then extracted with cyclohexane. The remaining insoluble portion is referred to as asphaltenes and the soluble portion as oil. An effort was made to keep samples under a nitrogen atmosphere in order to minimize air oxidation. GC-MS analyses were completed on a Hewlett Packard 5890 series II Gas Chromatograph coupled to a Hewlett Packard 5971 Mass Spectrometer. A J & W 100 meter long DB-1 column was used for the GC-MS analyses. Trace metals were analyzed by ICP (Data Chem. Laboratories, Salt Lake City, UT).

Results

The waste automotive crankcase oil from Book Cliff Energy is a mixture of many automotive oils received onsite at their refinery. The vacuum pyrolyzed plastic oil and the vacuum pyrolyzed tire oil from Conrad Industries were prepared from large samples of various plastics and tires. Thus the oils used in this study are representative of those that would be supplied to a coal liquefaction refinery instead of working with oils vacuum pyrolyzed from only one plastic sample or rubber sample.

ICP analysis of the waste automotive oil in Table 1 indicates the presence of many heavy metals. Of specific interest are the high zinc and phosphorous concentrations. This suggests the presence of a lubricant additive identified by Tarrer and coworkers.[5]

ICP analysis of the pyrolyzed plastic oil (Table 1) shows the presence of calcium, iron, and zinc. The calcium arises from the addition of calcium oxide during the pyrolysis of plastic to react with any hydrochloric acid formed from the breakdown of polyvinyl chloride polymers. GC-MS analysis indicates the presence of alkanes as large as C_{36}, as well as the presence of cyclic rings, and aromatic species such as benzene and naphthalene.

The ICP results for pyrolyzed tire oil (Table 1) show that zinc is the only heavy metal present. The vacuum pyrolyzed tire oil is low in zinc relative to a standard rubber tire. Past analysis indicates that a rubber tire contains on average 1.5 % by weight zinc oxide. Vacuum pyrolysis of the waste rubber tire circumvents the problems associated with removal of carbon black from the products.[6] Vacuum pyrolysis of waste rubber tires also permits formation of polyaromatics.[7] These polyaromatics are known to be useful in coal reactions because of their hydrogen shuttling and hydrogen donating characteristics.[8,9] Analysis by GC-MS indicated the presence of benzene, methylated forms of benzene, naphthalene, methylated forms of naphthalene, anthracene, methylated forms of anthracene, phenanthrene, methylated forms of phenanthrene, pyrene, methylated forms of pyrene, and naphthacene.

Table 2 contains the product distributions for conversion results obtained from reacting coals of differing ranks with waste oils at 430 °C for 1 hour. It is important to note that the total conversions reported are for the combination of both the coal and the solvent. This appears to be a better way of comparing all three solvent systems because the solvents react differently.

The coals are listed according to rank with Pocahontas being the highest ranking coal used and Buelah being the coal of lowest rank. The Pocahontas coal was not effectively converted using any of the three solvents. This is not surprising since higher rank coals are harder to depolymerize than are lower rank coals. The waste automotive oil solvent and the plastic solvent show similar overall coal rank trends with respect to total conversion. The asphaltene yield was slightly higher for runs using automotive oil solvent than runs using plastic solvent. This is surprising because the plastic oil with its abundance of large alkanes would be expected to increase asphaltene percentages even if larger alkanes did not react with other coal fragments. This indicates some cracking of the plastic solvent during coprocessing. Examination of the reactors indicated some char formation for the plastic solvent whereas no charring was observed for the automotive oil solvent. The lack of charring for the waste automotive oil solvent is what one might predict for an automotive lubricant but increased asphaltenes were not foreseen. It is interesting that trace metals identified in the automotive solvent have no detectable effect in promoting conversion of the coal.

The total conversion yields for the tire solvent indicated no rank correlation in contrast to the automotive oil solvent and the plastic oil solvent. The tire solvent did produce more measurable asphaltenes than did the other two solvents. Visual examination of the tubing reactors revealed enhanced charring with the tire oil present. This is not surprising with char precursors pyrene and anthracene in the initial reaction mixture. These molecules are also known to be beneficial to coal reactions because of their capacity to act as hydrogen donors and shuttlers.[9] The tire oil did not seem to be beneficial for the lower rank coals. The lower rank coals may be too reactive and combine with the solvent to form asphaltenes. The greatest total conversion for all three solvents came from tire oil solvent coprocessed with Illinois #6 coal. The Illinois #6 has a greater proportion of sulfur and iron oxide. These are known to form a sulfided iron which then can act as a catalyst in coal liquefaction. Previous experiments have shown that the pyrolyzed tire oil is beneficial

only in the presence of hydrogenation catalysts. It may be that the hydrogenation catalyst partially hydrogenated the pyrolyzed tire oil which could then act as a hydrogen donor.[10]

The ICP analyses for metals in the product oils for the three solvents coprocessed with the six different coals are shown in Table 3. The ICP analysis shown in Table 1 for the automotive oil solvent before it was coprocessed with any coal is also presented at the far right hand column of the Table in order to compare the amount of metal present in products derived from three coal/solvent distributions. Table 3 shows a decrease in almost every metal detected in the original solvent. A substantial decrease is observed for zinc, phosporous, magnesium, iron, copper, barium, and aluminum. Tarrer and coworkers have indicated that the high content of zinc and phosporous is due to the presence of zinc dialkyldithiophosphate.[3] It appears that the oils produced from the Illinois #6 coal and the Wyodak-Smith coal are the cleanest overall with respect to trace heavy metals.

The results from oils and asphaltenes indicate that no one coal is significantly more efficient than the others at capturing heavy metals. Therefore, it is difficult to say if there is any rank effect correlation for capturing heavy metals. The data appear to indicate that all coals have to some degree an ability to capture heavy metals. It is possible that the heavy metals in the automotive oil solvent were not plentiful enough to saturate the scavenging abilities of the coals in order to determine which coal would be the best scavenger. This scavenging or capture may involve the chemistry of the coal or a physical effect of incorporating the heavy metals into the carbon matrix of the coal. In past studies[11] using Electron Probe Microanalysis (EPMA), heavy metals were observed to reside in coal particles after coprocessing coal with waste rubber tires. In the EPMA micrographs the area of high heavy metal localization also coincided with areas of high sulfur concentration indicating that metals were present as sulfides. Therefore, sulfur in the coal may be beneficial for scavenging. This was also reported by Tarrer and associates for work completed on scavenging of zinc dialkyldithiophosphate. They found the scavenged zinc from the automotive oil residing in coal in the form of zinc sulfide. The ultimate analysis shows that the Illinois #6 has an abundant amount of sulfur. Illinois #6, along with the Wyodak-Anderson appeared to localize trace metals only slightly better than the other metals according to Table 3.

Conclusion

The Pocahontas coal is not a good coal to be coprocessed with any waste oil solvent to produce liquid transportation fuels. The other coals showed similar conversions with waste oil solvents except the Illinois #6. Results for different coal ranks liquefied in different solvents indicate that the Illinois #6 gives the best total conversion when reacted with oil derived from the vacuum pyrolysis of waste rubber tires. As for the heavy metals in waste automotive oils, coprocessing the automotive oils with the coal diminishes the amount of metal found in the products. Scavenging of metal did not appear to be coal rank dependent under the experimental conditions used in this study.

Acknowledgments

We gratefully acknowledge Lester J. Thompson and Eugene Dalton with Book Cliff Energy, Green River, UT for their generous donation of waste automotive crankcase oil. We gratefully acknowledge Phillip Bridges of Conrad Industries, Chehalis, WA for his generous donations of pyrolyzed plastic oil, pyrolyzed tire oil, and for insights regarding our results. Financial support by the U.S. Department of Energy, Fossil Energy Division, through the Consortium for Fossil Fuel Liquefaction Sciences, Contract No. UKRF-4-21033-86-24, is gratefully acknowledged.

References

1. Farcasiu, M.; Smith, C, **1992**, Prepr. Pap. Am. Chem. Soc., Div. Fuel Chem., 37 (1), 472.

2. Anderson, L. L.; Tuntawiroon, W., **1993**, Prepr. Pap. Am. Chem. Soc., Div. Fuel Chem., 38 (4), 810.

3. Huffman, G. P.; Feng, Z.; Mahajan, V.; Sivakumar, P.; Jung, H.; Tierney, J. W.; Irving, W., **1995**, Prepr. Pap. Am. Chem. Soc., Div. Fuel Chem., 40 (1), 34.

4. Parker, R. J.; Carson, D. W., **1995**, Prepr. Pap. Am. Chem. Soc., Div. Fuel Chem., 40 (1), 51.

5. Tarrer, A., Technical Report on DOE Contract No. DE-FC22-93PC93053, Period: May1, **1994**-October 31, **1994**.

6. Orr, E. C.; Ding, W. B.; Bolat, E.; Rumpel, S.; Eyring, E. M.; Anderson, L. L., **1995**, Prepr. Pap. Am. Chem. Soc., Div. Fuel Chem., 40 (1), 44.

7. Williams, P. T.; Taylor, D. T., **1993**, Fuel, 72, 1475.

8. Grint, A.; Jackson, W. R.; Larkins, F. P.; Louey, M. B.; Marshall, M.; Trewhella, M. J.; Watkins, I. K., **1994**, Fuel, 73 (3), 381.

9. McMillen, D. F.; Malhotra, R.; Tse, D. S.; Nigenda, S. E., **1988**, Prepr. Pap. Am. Chem. Soc., Div. Fuel Chem., 33 (1), 58.

10. Badger, M. W.; Harrison, G.; Ross, A. B., **1994**, Prepr. Pap. Am. Chem. Soc., Div. of Petroleum Chem., 39 (3), 438.

11. Orr, E. C.; Tuntawiroon, W.; Anderson, L. L.; Eyring, E. M., **1994**, Prepr. Pap. Am. Chem. Soc., Div. Fuel Chem., 39 (4), 106

Table 1 ICP Analysis of Automotive Solvent, Pyrolyzed Plastic Solvent, and Pyrolyzed Tire Solvent

Metal	**Automobile Oil Solvent µg/g**	**Pyrolyzed Plastic Oil Solvent µg/g**	**Pyrolyzed Tire Oil Solvent µg/g**
Aluminum	81		
Antimony			
Arsenic			
Barium	9.3		
Beryllium			
Cadmium	1.4		
Calcium	920	520	
Chromium	1.7		
Cobalt			
Copper	54		
Iron	310	50	
Lead	27		
Lithium			
Magnesium	240		
Manganese	7		
Molybdenum			
Nickel	13		
Phosphorous	870		
Potassium	510		
Selenium	1.3		
Sodium	34		
Silver			
Strontium	2.7		
Thallium			
Vanadium			
Zinc	850	20	40

Blank areas indicate that none of the element was detected

Table 2 Comparison of Total Conversions (Percent by Weight) for Coals of Different Coal Rank Coprocessed With Waste Oils at 430 °C for 1 Hour

	Automotive Oil Solvent	Pyrolyzed Plastic Oil Solvent	Pyrolyzed Tire Oil Solvent
Pocahontas			
Gas + Oil	54.5	54.3	47.0
Asphaltenes	2.4	0.5	9.0
Total Conversion	56.9	54.8	56.0
Blind Canyon			
Gas + Oil	65.4	66.5	60.4
Asphaltenes	3.7	3.6	10.3
Total Conversion	69.1	70.1	70.7
Illinois #6			
Gas + Oil	66.1	64.4	65.8
Asphaltenes	10.4	7.2	17.8
Total Conversion	76.5	71.6	83.6
Wyodak			
Gas + Oil	70.2	71.5	63.1
Asphaltenes	3.7	1.4	5.1
Total Conversion	74.0	72.9	68.3
Smith - Roland			
Gas + Oil	74.8	73.4	67.9
Asphaltenes	3.2	1.4	4.8
Total Conversion	77.9	74.7	72.7
Beulah			
Gas + Oil	74.2	77.2	66.1
Asphaltenes	2.0	0.4	3.8
Total Conversion	76.2	77.6	69.9

Table 3 Comparison of ICP Analyses of Oils Produced From Coal and Waste Automotive Oil Solvent Coprocessed at 430 °C for 1 Hour

Oil	Pocah.	Blind Canyon	Illinois #6	Wyod.-And.	Smith-Roland	Beulah	Auto Oil
Aluminum							81
Antimony							
Arsenic					31		
Barium							9.3
Berryllium							
Cadmium		1.2		0.9			1.4
Calcium	260	56	42	51	64	200	920
Chromium	1.1	1.4			3.4	2.5	1.7
Cobalt						10	
Copper		2.2			7.4		54
Iron	23	62	19	77	42	45	310
Lead							27
Lithium					3.4		
magnesium							240
Manganese							7
Molybdenum							
Nickel	11	10		6.2	16		13
Phosporous							870
Potassium	690	400	470		770	340	510
Selenium	31						1.3
Silver					1.3	1.3	34
Sodium		400					
Strontium							2.7
Thallium							
Vanadium							
Zinc	15	14	8	11	15	11	850

PLASTICS PYROLYSIS AND COAL COPROCESSING WITH WASTE PLASTICS

M. S. Mulgaonkar, C. H. Kuo, A. R. Tarrer
Chemical Engg Dept
Auburn University
Auburn, Al-36849

Keywords: pyrolysis, plastics, coal liquefaction

ABSTRACT

Pyrolysis of waste plastics is one of the routes to waste minimization that has been gaining in interest in recent times. A compact unit is designed that can pyrolyze a mixture os waste plastics and used oil. The product of the process is a liquid oil that has considerably reduced viscosity and which can be either used a s fuel directly or as a feedstock for refineries. Pyrolysis was carried out for the waste oil alone and for its mixture with plastics of one type(HDPE). Different temperatures of reaction and the product viscosities related to the temperatures of operation. Residence times were as low as 2-8s. The reactor was divided into two parts, the first part at the inlet was deliberately kept at a lower temperature to first bring up the Reynolds numbers (>15,000) to high values before introduction to the high temperature second section.

The liquid product of pyrolysis can be used for the co-liquefaction of coal. Several coal liquefaction studies were carried out to determine the effect of the use of the waste plastic-used oil product of pyrolysis as solvent. The result indicate considerable enhancements of the conversions and selectivities of coal for such prepyrolyzed liquid.

Introduction

Plastics form a major portion of all municipal wastes. It was reported (1) that some 30 billion pounds of plastic waste are generated in the US per year. Also the demand for plastics would reach 76 billion pounds by the turn of the century. Currently, only about 1% of the plastics waste is recycled. The recycling of the plastic can be costly and difficult because of the constraints on water contamination and inadequate separation prior to recycled.

Therefore several new processes are currently under development for the treatment of waste plastics. Two processes have shown promise, pyrolysis and hydrolysis, in recovering the basis chemicals and fuels from the waste plastics. In pyrolysis, the plastics are heated in the absence of oxygen in a closed environment, with the resulting products of pyrolysis available for use as a chemical feedstock, or fuel. Hydrolysis decomposes plastic wastes through a series of chemical reactions. These new processes will reduce the cost of monomers and the consumption of petroleum. In one instance, scientists have demonstrated a new process for sequential pyrolysis for waste carpet recycling. In this case caprolactum, the starting material for nylon production, was separated with yields of around 85% without separating the nylon from the backing material of the carpet. It is reported that a commercial plant could produce high grade caprolactum at a cost of $0.15-0.50/lb compared to the commercial cost of $1.00/lb. Thus costs could be reduced by as much as 50%. Thus pyrolysis appears to be an attractive alternative to plastics landfilling or incineration.

Many companies are already showing considerable interest in pyrolysis of waste plastics. The Japanese company, Fuji has started a commercial scale plastics to gasoline plant at Aioi, that is capable of processing 11 million lb/yr of waste plastic. In this process the plastic is first preheated to 250°C. The preheated plastic is then fed by an extruder to a furnace, and then to a cracking unit that uses aluminosilicate catalyst. The process yields 40% gasoline, 20% kerosene, 20%gas-oil mixture, 15% gas and 5%residuals. Retrieved energy is used to power the plant. Annually the plant would produce one million gallons of gasoline (2)

Chuo Kagaku Co.,the largest PS food tray manufacturer in Japan has a 2-million-lb/yr plant for reclaiming PS waste that is based on the Fuji design. The plant is anticipated to yield on startup, a fuel mixture of 90% aromatics, 6% paraffins and 4% olefins. When blended with gasoline, it produces a high octane fuel.

Amoco Chemical, Chicago, is also concentrating on the development of a pyrolysis unit. Scientists at Amoco have concluded that use of a small scale pyrolysis unit to crack mixed plastics into liquid chemical prior to feeding them to a refinery unit appears to be the optimal route. Liquids being easily transportable, this would avoid the costly step of shipping bulk plastic scrap to far-flung U.S. oil refineries (2). Also in the U.S., the American Plastics Council, Washington, DC, is sponsoring two pyrolysis projects by recycler Conrad Industries, Chehalis,

WA. One of the plants is already on stream. A drum of the pyrolyzed plastic oil (PPO) of this company was obtained and was used in the coal coprocessing experiments as indicated in Table 2. Typical composition of household wastes is shown in Table 1.

System Design

The new compact pyrolysis unit has been designed to pyrolyze a mixture of waste molten plastic and waste oil. This unit operates at very low residence times (2-8 seconds) and can operate continuously. The reactor consists of a 125 ft long 2.5 mm diameter S.S. tube that is divided between two different heating or reaction sections. The temperatures of operation can be finely controlled so as to give liquid products of various viscosities. The temperatures of operation range from 350-600°C, the pressures are low (ambient) to medium (100-300 psi). The reaction is carried out in two stages. In the first reactor tube section the temperatures are kept low (300-400°C) to allow the viscosity to reduce sufficiently to give high Reynolds numbers in the subsequent high temperature (450-600°C) section. As a result, Reynolds numbers higher than 15,000 are obtained in this section. A detailed schematic of the process is included. Two sand baths are used for the liquefaction process and the temperatures of the two are set independently to give the required temperature steps in the operation.

The feed liquid which consists of waste oil and waste plastics (which is kept molten) at 250-300°C are subjected to nitrogen pressure to push the liquid through the cracking sections. The tube outlet pressure can be controlled by means of a back pressure regulator that can be adjusted to any required set point. Thus complete variation in operational pressure is possible. The reaction can be carried out at different pressures and the effect of operation pressure can be investigated almost independently of the residence times.

Several runs of pyrolysis with waste oil were carried out in the laboratory. Two typical temperature profiles are included and the corresponding viscosities of the product are also included in the figures.

Decomposition temperature ranges of the plastics are usually obtained from thermogravimetric methods (4). These methods have been used by other investigators for obtaining the reaction rate parameters, i.e., the pre-exponential factors and the activation energies. These constants are used in the present experiments to decide on the residence time variations that would be necessary to treat plastics of different compositions and also to predict the properties of the products where possible, using model based simulation.

Several pyrolysis runs were carried out with plastics dispersed in the oil and the pyrolysis products obtained. The temperature profile for one run with 2.5% HDPE pellets are included.

Results and Discussion

Once the pyrolysis products of the plastics are obtained, they can be used to carry out the liquefaction of the coal in a batch or continuous manner. Here, the results of tubing bomb experiments based on batch coal coprocessing show that the reaction of liquefaction occurs to increased levels of conversion with the addition of (waste) plastics, such as polystyrene or HDPE. Increases in conversions of around 20% are obtained with the unpyrolyzed waste plastics, and selectivities are enhanced by 15-25% on an average. The conversions further increase if the plastics and the waste oil solvents are in addition prepyrolyzed (two stage liquefaction). This is the basis for the design of the pyrolysis section followed by the coal coprocessing.

The main design parameters are the residence time, feed temperature, the two stage temperatures, and the flow inducing pressure difference. These parameters have to be very carefully chosen in order to get the right conversions and yields of liquids. The effects of temperature and residence times are relatively well understood for the pyrolysis reactions. Too high a residence time results in excessive gas formation and when the temperatures are high to high coke formation. The temperatures that are attainable in any pyrolysis unit thus determines the yields of gas, liquids and coke. Usually the threshold temperatures for pyrolysis depends on the type of material to be processed. In general the lower limit of temperature for most pyrolysis is 350-400°C. The actual temperatures chosen are usually much above this. Since thermal cracking reactions proceed with significant activation energies, temperatures has an important effect on rate. Activation energies are in the range of 55-65 kcal/mol (6).

Temperature is also known to have a very important effect on the selectivities of paraffin pyrolysis. In the present case the aim is to maximize the formation of liquids and therefore the temperatures are lower, of the order of about 500-700°C. The exact temperature chosen would then depend on the nature of the material to be processed. If the feed material is simply waste lubricating oil, then the temperatures of 450-500°C are found to be sufficient for the maximization of liquids. If in addition we are adding waste plastics then the temperature of cracking must usually be raised in order to bring about sufficient chain scission and obtain products in the liquid form suitable for use as liquid fuels or as feed to a refinery unit.

Conclusions

Exploratory batch reaction studies have shown two-stage coal coprocessing with waste plastics and oils to yield high conversions of coal (>80%) with a high selectivity for oil(>60%). the waste oils and plastics were first thermally cracked in a first stage to yield a liquid solvent for the second-stage coal coprocessing. A pilot scale unit was constructed for performing the first stage cracking studies. Waste oil mixed with HDPE were successfully cracked using this unit, there being no significant amounts of coke or solids produced.

The use of low residence time cracking would offer a number of advantages. Two of these are(1)transportation costs could be significantly reduced by removing contaminants close to the generation site and by reducing the bulk density of the plastics; and (2) handling of waste plastics/oils during coal coprocessing would be simplified due to the low viscosities and fluidic properties of the cracked products.

References

1) J. E. Lynx, American Dyestuff Reporter, Dec. 1993, pp. 9
2) R. D. Leaversuch, Modern Plastics, June 1992, pp. 49-50
3)C.-H. Wu et al.,Waste Management, Vol. 13, pp 221-235
4) P. Mapleston, Modern Plastics, Nov. 1993, pp 58-61
5) Textbook Of Polymer Science, F. W. Billmeyer, Third Edition, Wiley-Interscience
6) Pyrolysis: Theory and Industrial Practice, L. F. Albright et al., Academic Press, 1983

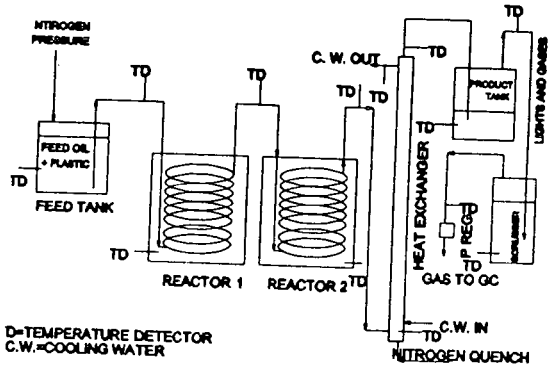

Figure 1: Pyrolysis Unit

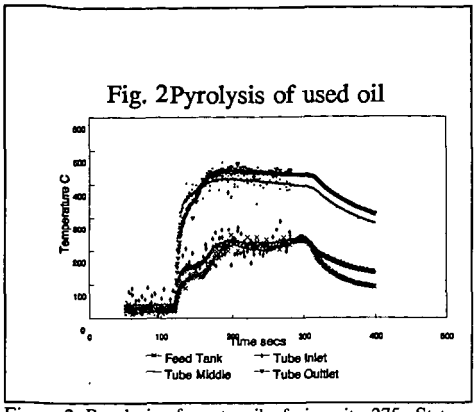

Figure 2. Pyrolysis of waste oil of viscosity 275 cSt to give product of viscosity 50 cSt

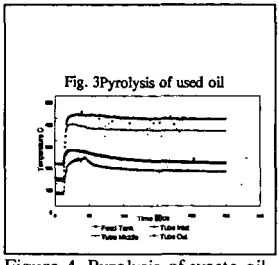

Figure 4. Pyrolysis of waste oil of viscosity 275 cSt to give product of viscosity 130 cSt

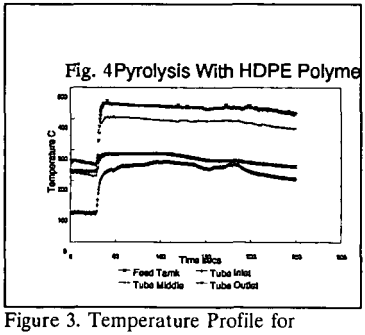

Figure 3. Temperature Profile for Pyrolysis of HDPE (2.5%) Dispersed in Used Oil, Product Viscosity was 80cSt @30°C

Table 1. Composition Of Mixed Plastics Wastes:

Composition (% wt)	
Polyethylene	60
Polypropylene	05
Polyvinylchloride	10
Polystyrene	15
Polyethyleneterephthalate	05
Polyamide	05

Table 2. Response of coal conversion /selectivity to addition of pyrolyzed plastic , PS & waste oil

Solvent	Hexane Convrsn(%)	Total Conversn(%)	Selectivity(%)
Waste Oil	43	73	59
Waste Oil/polystyrene(PS) 1:1	39	60	65
Prehydrocracked waste oil	60	86	70
Waste oil/PS prehydrocracked1:1	63	97	65
Pyrolyzed plastic oil(PPO)	64	91	70
Prehydrocracked PS/waste oil 1:1	73	100	73
PPO/waste oil 1:1	56	81	69

Reaction conditions: 2.5g DECS-6 coal, 10g solvent, 0.25g Fe_2O_3, 425°C, 1250 psig H_2, 1 hour

COPROCESSING OF WASTE PLASTICS WITH COAL AND PETROLEUM RESID

Hyun Ku Joo and Christine W. Curtis
Chemical Engineering Department
Auburn University, AL 36849

Introduction

Waste plastics have become an increasing problem in the United States since land filling is no longer considered a feasible disposal method. Since plastics are petroleum-derived materials, coprocessing them with coal to produce transportation fuels is a feasible alternative. In this study, catalytic coprocessing reactions were performed using Blind Canyon bituminous coal, Manji and Maya petroleum resids, and plastics. Model polymers including polystyrene, low density polyethylene and poly (ethylene terephthalate) were selected because they represent a substantial portion of the waste plastics generated in the United States. The objective of this research is to determine the effect of using resid as a solvent in the coprocessing of coal and waste polymers on the conversion and product distribution obtained. This study was conducted by first evaluating the reactivity and conversion of the individual systems at coprocessing reaction conditions. Then systems containing binary combinations of either coal, resid, or waste plastic were performed. The last set of reactions performed were ternary systems of coal, resid and waste plastic. All reactions that contained combinations of reactants were reacted catalytically using presulfided $NiMo/Al_2O_3$. The effect of each component on the coprocessing reaction was evaluated.

Experimental

Materials. The model plastic compounds, low density polyethylene (LDPE), polystyrene (PS), and poly(ethylene terephthalate) (PET), used in this study were obtained from Aldrich Chemical Co. and were used as received. The coal used was Blind Canyon bituminous coal (DECS-17) obtained from the Penn State Coal Sample Bank. The proximate analysis of the coal is 45% fixed carbon, 45% volatile matter, 6.3% ash and 3.7% moisture. The ultimate analysis of the coal is 82.1% C, 6.2% H, 0.4% S, 1.4% N, and 0.12%Cl. The resids used were Manji and Maya obtained from Amoco. The analyses of the resids were 85.1% C, 10.8% H, 0.7% N, 2.6% S, 231 ppm V, 220 ppm Ni and 23 ppm Fe for Manji and 84.1% C, 9.9% H, 0.7% N, 5.1% S, 550 ppm V, 100 ppm Ni and 17 ppm Fe for Maya. The solvents used for extraction analyses were HPLC grade hexane, toluene, and tetrahydrofuran (THF) from Fisher Scientific.

Reactions and Procedures. Reactions were performed using a single component, two components, and three components to evaluate the reactivity and mutual effects among the reactants. All reactions were performed in 20 cm^3 stainless steel tubular microreactors at 430 °C for 60 min with 8.3 MPa of H_2 introduced at ambient temperature. The microreactors were agitated horizontally at 450 rpm in a fluidized sand bath and were immediately quenched in water after reaction. The reactants were charged at 1.0 g for coal and polymer and 1.5 g for resid, giving resid to polymer and resid to coal ratios of 3:2 in binary system and coal to resid to polymer ratios of 2:3:2 in ternary systems. The coal was stored in a vacuum desiccator before being used. Reactions were performed thermally and catalytically using 1 wt % of powdered, presulfided $NiMo/Al_2O_3$ on a total charge basis. Reactions with LDPE and coal or resid were performed at higher catalysts loadings of 3 and 10 wt %. The $NiMo/Al_2O_3$ catalyst was composed of 2.72 wt % Ni and 13.16 wt % Mo. The procedure for presulfiding $NiMo/Al_2O_3$ began with predrying $NiMo/Al_2O_3$ with N_2 for one hr at 300 °C. Then, 10 vol % H_2S/H_2 gas mixture was flowed over the catalyst at 225 °C for one hr, at 315 °C for one hr, and 370 °C for two hr. The final step was flowing N_2 at 370 °C over $NiMo/Al_2O_3$ for one hr.

The reaction products were determined by using solvent fractionation and by weighing the gaseous products. The liquid products were fractionated using a series of solvents into hexane soluble materials (HX); toluene soluble, hexane insoluble material (TOL); and THF soluble, toluene insoluble material (THF), and THF insoluble material or IOM which is defined as insoluble organic matter that is ash-free. Solvent fractionation was also performed on the unreacted materials to determine their solubility. Low recoveries for PS and PET resulted from volatile material being produced during reaction and being lost during the rotary evaporation of hexane. When rotary evaporation was performed at 25 °C with minimal vacuum, the PS reactions products were so volatile that 75% loss occurred while PET lost 67%. The definition for conversion used in this study is the conversion of the reactant to THF soluble material. For coal, the definition for conversion is

$$\% \text{ conversion} = \left[1 - \frac{g\ IOM}{g\ maf\ coal} \right] \times 100 .$$

Plastics and resids have the same definition; however, the plastics are solids at room temperature and have varying but limited solubility in THF, while resids are a semi-solid at room temperature and are totally soluble in THF .

Results and Discussion

The product distributions for the unreacted plastics were determined at ambient temperature to establish a baseline for comparison with their reactivity at coprocessing conditions (Table 1). Previous research performed by Luo and Curtis (1995) has shown that under typical thermal coprocessing conditions only limited conversion of the waste plastics occur. Therefore, the plastics used in this study were reacted under catalytic conditions only using presulfided $NiMo/Al_2O_3$. This catalyst was chosen because it has been used almost as a standard in coal liquefaction reactions and because it was used as the catalyst in the waste plastics and waste tire coprocessing pilot scale run performed by HRI and sponsored by the Department of Energy (Pradhan et al., 1994).

Table 1. Product Distributions from Unreacted and Thermally Reacted Material

Reactants[a]	Product Distribution (%)					Conversion (%)	Recovery (%)
	Gas[b]	HX	TOL	THF	IOM		
Unreacted							
PS	0.0	0.0	21.0	14.1	64.9	35.1	112
LDPE	0.0	0.0	1.4	3.1	95.5	4.5	104
PET	0.0	0.0	0.7	0.7	98.6	1.4	104
Manji	0.0	87.1±0.4	12.9±0.4	0.0	0.0	100	103
Maya	0.0	63.0±0.8	37.0±0.8	0.0	0.0	100	101
Thermal Reactions							
Coal	19.1±0.6	15.9±1.1	3.5±0.5	6.2±4.2	55.5±5.4	44.6±5.4	98
Manji	11.6±1.1	71.0±2.1	9.9±0.6	4.9±1.5	2.7±0.1	97.4±0.2	85
Coal/Manji	9.8±0.2	56.9±0.8	8.6±0.4	11.8±1.8	13.1±3.3	87.0±3.3	84

[a] Coal = Blind Canyon DECS-17, Manji and Maya resid. PS = Polystyrene; LDPE = low density polyethylene; PET = poly(ethylene terephthalate). [b] Gas = gaseous product; HX = hexane solubles; TOL = toluene solubles; THF = THF solubles; IOM = insoluble organic matter.

Single Component Reactions. The conversions and product distributions for all of the coprocessing reactions are given in Table 2. The conversions for the single component reactions showed that coal and LDPE yielded lower conversions than the others; their respective conversions were 64.7 and 69.8%. The other plastics, PET and PS, and both resids yielded high conversions, ranging from a low of 94.7% for PET to 100% for PS. A positive influence of the catalyst was observed in the system since coal conversion increased from 44.6% in the thermal reaction to 64.7% in the catalytic reaction. Likewise, when the catalytic conversion of the three plastics are compared to the conversions of the unreacted materials and to the thermal conversions at 440 °C given by Luo and Curtis (1995) the effects of temperature, compared to the unreacted materials, and of catalyst, compared to the thermally reacted and unreacted materials, were positive.

The product distributions of the three plastics reacted at 430 °C with presulfided $NiMo/Al_2O_3$ were quite different. Although PS and PET both yielded high conversions, the gas produced from PET was substantially higher yielding 36.8% compared to 8.0% for PS. The yield of hexane solubles from PS was the highest obtained at 91%; however, these hexane soluble materials were very volatile as shown by the low recovery that was discussed in the experimental section. The products produced from the conversion of the plastics were primarily the lighter fractions of gas or hexane solubles. Very small amounts of THF and toluene soluble materials were produced.

The catalytic reaction of the resids produced a small amount of heavier material, IOM and THF soluble material, that was not present in the original resid. The majority of the products were hexane soluble, although the amounts produced were slightly less than in the original resids. At 430 °C and with $NiMo/Al_2O_3$, 10 to 15% gas was produced from the resids so that the total amount of hexane solubles and gas produced was equal to the unreacted Manji hexane solubles and higher than the Maya unreacted hexane solubles indicating that Maya was upgraded at these reaction conditions.

Binary Systems. Reactions containing different combinations of the coal, resid, and plastics used in this study were performed, and the conversion and product distributions were obtained. High conversions of 90 to 100% were obtained for the binary combinations of coal plus resid and resid plus polymer, although conversion of resids with LDPE at 77.4 to 80.9% were lower than resid with the

other two plastics. The binary combination of coal and plastics yielded much lower conversions of 47.7 to 66.9% than the other systems, indicating that plastics and coal did not provide a mutually beneficial solvating medium.

Table 2. Reacton Results from Coprocessing Polymers with Coal and Resid[a]

Reactants	Product Distribution (%)					Conversion (%)	Recovery (%)
	Gas	HX	TOL	THF	IOM		
Single Component							
PS	8.0±2.5	91.0±2.7	0.5±0.6	0.5±0.7	0.0	100	42
LDPE	20.0±1.3	41.8±2.8	4.4±1.8	3.6±0.3	30.3±0.6	69.8±0.6	91
PET	36.8±1.6	54.7±1.6	2.0±1.2	1.3±0.1	5.4±1.2	94.7±1.2	56
Coal	18.3±0.1	22.6±1.8	4.2±0.1	19.6±2.5	35.4±3.9	64.7±3.9	94
Manji	10.4±0.4	78.3±0.3	8.5±0.2	1.9±0.8	0.7±0.8	99.3±0.8	85
Maya	14.5±0.4	65.8±0.9	15.1±1.4	1.5±0.4	3.3±0.4	96.8±0.4	93
Two Components							
Coal/Manji	10.8±0.3	64.1±1.6	12.2±0.0	9.7±0.8	3.2±0.6	96.8±0.6	88
Coal/Maya	10.6±0.4	59.4±0.1	20.4±0.1	1.9±0.2	8.0±0.8	92.1±0.8	85
Maya/PS	8.3±0.3	80.4±1.8	8.3±0.6	1.5±0.2	1.7±0.6	98.4±0.6	57
Maya/LDPE	9.5±0.2	58.0±2.0	7.5±0.8	2.5±0.8	22.7±2.2	77.4±2.2	90
Maya/PET	19.0±0.8	65.8±0.1	7.6±0.4	2.4±0.1	5.4±0.4	94.7±0.4	67
Manji/PS	4.7±0.1	86.5±0.9	5.9±0.4	1.4±0.1	1.6±0.6	98.4±0.6	58
Manji/LDPE	9.0±0.3	63.5±0.9	5.7±0.8	2.8±0.1	19.1±0.0	80.9±0.0	89
Manji/PET	18.2±0.4	70.7±0.1	5.5±0.1	1.9±0.1	3.7±0.6	96.3±0.6	63
Coal/PS	7.6±0.1	54.0±2.9	0.8±0.4	2.0±0.5	35.7±2.2	64.4±2.2	56
Coal/LDPE	11.6±1.0	30.1±2.8	4.6±0.1	1.6±0.1	52.3±1.8	47.7±1.8	95
Coal/PET	21.6±0.6	41.6±3.2	1.4±0.6	2.5±1.2	33.1±5.5	66.9±5.5	67
Three Components							
Coal/Maya/PS	7.7±0.4	69.2±0.8	9.4±0.5	5.9±0.1	8.0±0.9	92.1±0.9	66
Coal/Maya/LDPE	9.0±1.8	52.9±2.1	9.1±0.0	5.7±0.1	23.4±0.4	76.7±0.4	90
Coal/Maya/PET	16.9±1.5	55.9±2.5	7.5±0.0	6.8±0.1	13.0±0.9	87.1±0.9	74
Coal/Manji/PS	5.4±0.4	75.5±1.7	7.5±0.4	6.6±0.2	5.2±1.6	94.8±1.6	62
Coal/Manji/LDPE	9.4±1.9	57.2±1.1	9.1±0.6	5.0±0.0	19.4±0.3	80.6±0.3	88
Coal/Manji/PET	14.9±0.1	61.6±0.6	7.1±0.4	7.0±0.0	10.1±1.1	89.9±1.1	71
Two Components at Higher Catalyst Loading							
Coal/LDPE	10.7±0.4	36.1±1.8	3.5±0.2	3.8±1.3	46.0±2.6	54.1±2.6	90
Maya/LDPE	9.2±0.1	57.4±0.5	6.9±0.9	3.2±0.6	23.5±0.4	76.6±0.4	90
Manji/LDPE	8.3±0.1	61.0±1.5	4.1±0.1	2.2±1.3	24.5±0.1	75.5±0.1	93
Three Components at Higher Catalyst Loading							
Coal/Manji/LDPE	6.9±0.1	60.7±1.1	8.4±0.3	4.7±0.6	19.4±0.6	80.7±0.6	88

[a] Reaction Conditions 430 °C, 8.3 MPa H_2, and one hour; 1 wt% $NiMo/Al_2O_3$ of total feedstock for catalytic reactions.

A parameter, termed coprocessing effect factor (f_i), was defined that evaluated the effect of combining two materials rather than reacting them individually. The three coprocessing effect factors that were evaluated were the conversion, hexane soluble, and gas coprocessing effect. The equation that defines this parameter is

$$f_i = \frac{(\% CP_i - \% HM_i)}{\% CP_i} \times 100$$

where i is either gas, hexane solubles, or conversion, HM is the hypothetical mean, and CP is the coprocessing result.

The reactions of coal and resid showed positive coprocessing effect factors for hexane solubles and conversion which means that more hexane soluble material was produced and more conversion of material occurred when coal and resid were reacted together than when they were reacted individually. The coprocessing effect factor for gas products was negative for both coal and resid combinations, meaning that less gas was produced during coprocessing than in the individual reactions. Similarly, the reaction of Maya resid with each of the plastics resulted in each binary

combination having a positive hexane soluble coprocessing effect factor and negative gas coprocessing effect factor. The conversion coprocessing effect factor for Maya and the three plastics varied according to the type of plastic: Maya and PS gave a slightly positive factor while the other two combinations gave negative values. Manji resid reacted with each of the three plastics resulted in a less positive hexane coprocessing effect factor than Maya/polymer and large negative values for the gas coprocessing effect factor. The combination of coal and PS or LDPE was detrimental to the production of hexane soluble material from the coprocessed materials, while the combination of coal with PET was favorable for the production of hexane soluble material. The amount of gas produced during coprocessing was less with the coal and polymers as it was with combined reaction of all the other systems. The coprocessing effect factor for conversion of the coal and polymer systems yielded negative values that were quite large ranging from −19.1 for coal and PET to −41.0 for coal and LDPE. The combination of coal and polymer was detrimental to the conversion compared to that obtained in individual reactions.

Ternary Systems. The coprocessing effect factors for the ternary systems were calculated two ways. The first method of calculation shown on Table 3 used the hypothetical mean of the individual reactions where the ratio of the components in the ternary system was used to weight the various terms. The second method of calculating the hypothetical mean was to use the results of reactions of a single component and a binary system to calculate hypothetical mean in which of the reactants involved were weighted according to the relative amount of each material in the ternary systems.

The results with the calculational method using the individual reactions are given in Table 3. All of the ternary reaction systems showed a positive coprocessing effect factor for the hexane soluble material when compared to the hypothetical mean calculated from the individual reaction systems. The gas coprocessing effect factor for each ternary reaction system resulted in large negative values. Particularly, the ternary systems containing PS and LDPE gave large negative values; PET also gave negative values but the decrease compared to the individual systems was not nearly as large. Reacting the three components yielded a much reduced gas make compared to the individual reactions. Coprocessing the three materials together resulted in positive effects on the conversion of ternary systems containing PS and PET for both coal and resid combinations; however, the systems containing LDPE gave negative values. Reaction with Manji resid was more beneficial to each of the polymers than was Maya.

The coprocessing effect factor calculation with the hypothetical mean from the single component plus binary systems gave negative gas coprocessing effect factors. The hexane soluble coprocessing effect was positive for the coal plus resid/polymer systems and for the resid plus coal/polymer systems; however, only half the polymer plus coal/resid systems gave positive values. LDPE gave negative values for both resids indicating that the binary system did not increase the hexane solubles compared to the hypothetical mean. The conversion coprocessing effect factor was positive for the hypothetical means using coal plus resid/polymer and resid plus coal/polymer. However, all of the conversion coprocessing effect factors for polymer plus coal/resid were negative, indicating that addition of the polymer to the coal/resid system was detrimental to overall conversion.

Effect for Catalyst Loading. The binary and ternary systems containing LDPE gave lower conversions and hexane solubles than the other polymers. The effect of increasing catalyst loading to 3 and 10 wt % based on the total charge on coal conversion and hexane soluble yield in binary and ternary systems containing LDPE was determined. The 3 wt % addition increased the conversion in the coal/LDPE from 47 to 54 % (Table 2); the effect on conversion from the other binary and ternary systems were minimal and with the resids even decreased the conversion slightly. Increasing the catalyst loading to 10 wt % had a similar effect as the 3% loading.

Summary and Conclusions

The coprocessing of coal, plastics and resid yielded favorable results. The amount of gas produced decreased as the number of components in the reaction increased. For binary and ternary systems containing resid, increases in the amount of hexane solubles and in conversion were apparent. The binary reaction of coal and plastics did not show this effect; the combination appeared to be detrimental to both materials. However, when resid was added to the system in the ternary systems, the positive hexane soluble and conversion coprocessing effect factors were obtained. Increasing catalyst loading improved the conversion of and the hexane soluble yield in the coal/LDPE system. Increased catalyst loading had little effect on the binary and ternary systems containing resids.

Table 3. Coprocessing Effect Factors for Binary and Ternary Systems

Reaction Combinations	Coprocessing Effect Factor (f_i)		
	Gas	HX	Conversion
Two Components			
Coal/Manji	-25.6	12.6	11.7
Coal/Maya	-51.1	18.3	8.8
Maya/PS	-43.4	5.6	0.3
Maya/LDPE	-75.8	3.1	-11.1
Maya/PET	-15.2	6.8	-1.3
Manji/PS	-100.9	3.6	-1.2
Manji/LDPE	-58.2	-0.3	-8.2
Manji/PET	-15.2	2.6	-1.2
Coal/PS	-73.0	-5.2	-27.9
Coal/LDPE	-65.1	-7.0	-41.0
Coal/PET	-27.5	7.1	-19.1
Ternary Systems with Hypothetical Mean of Individual Components[b]			
Coal/Maya/PS	-78.3	12.4	3.9
Coal/Maya/LDPE	-90.6	11.9	-4.2
Coal/Maya/PET	-29.9	10.1	0.1
Coal/Manji/PS	-121.7	12.6	5.5
Coal/Manji/LDPE	-63.8	9.2	-0.5
Coal/Manji/PET	-35.6	9.7	2.0
Ternary Systems with Hypothetical Mean of Single and Binary Systems[b]			
Coal + Maya/PS	-44.9	7.7	3.6
Coal + Maya/LDPE	-33.5	9.5	3.8
Coal + Maya/PET	-11.2	4.4	1.1
Coal + Manji/PS	-59.0	9.6	6.4
Coal + Manji/LDPE	-24.0	9.4	5.4
Coal + Manji/PET	-22.3	7.5	2.9
Maya + Coal/PS	-37.1	14.7	15.0
Maya + Coal/LDPE	-42.7	14.2	10.4
Maya + Coal/PET	-9.8	7.0	8.5
Manji + Coal/PS	-63.0	14.7	16.3
Manji + Coal/LDPE	-18.0	11.3	13.4
Manji + Coal/PET	-12.8	6.9	10.1
PS + Coal/Maya	-28.0	1.1	-2.5
PS + Coal/Manji	-85.2	4.9	-3.1
LDPE + Coal/Maya	-47.6	-2.8	-11.8
LDPE + Coal/Manji	-42.9	-0.9	-10.5
PET + Coal/Maya	-7.0	-3.9	-6.6
PET + Coal/Manji	-22.3	0.3	-7.0

[a] HM = Hypothetical Mean of reactants which is defined as

$$HM_i = \frac{(\%\ coal_i + 1.5\ x\ \%\ resid_i + \%\ polymer_i)}{total\ charged\ (g)}$$

[b] Calculations using different hypothetical mean which is defined as

$$HM_i = \frac{(x) \times \%\ one\ component + (y) \times \%\ two\ components}{3.5}$$

where x is 1.0 for coal and polymer and is 1.5 for resid; y is 2.0 for coal and polymer and 2.5 for resid.

Acknowledgements

The support of the United States Department of Energy through Contract No. DE-FC22-93PC93053 for the work is sincerely appreciated.

References

Luo, M.; Curtis, C.W. Consortium for Fossil Fuel Liquefaction Science, Final Report, June, 1995.

Pradhan, V.R.; Comoli, A.G.; Lee L.K.; Stalzer, R. H. *ACS Fuel Chem Div. Preprints,40*(1) 82-86, 1995.

VACUUM PYROLYZED TIRE OIL AS A COAL SOLVENT

Edward C. Orr, Yanlong Shi, Qin Ji, Larry L. Anderson, and Edward M. Eyring
Department of Chemistry and Department of Chemical and Fuels Engineering,
University of Utah, Salt Lake City, UT 84112

Keywords: tires, coal, coprocessing, EPMA

Introduction

Recent interest in coprocessing coal with hydrogen rich waste materials in order to produce liquid transportation fuels has given rise to interesting twists on standard coal liquefaction.[1-5] In general, coprocessing coal with a waste material has been approached with the idea that the waste material would be mixed with the coal under liquefaction conditions with little or no preliminary processing of the waste material other than shredding into smaller size particles. Mixing the waste material with the coal would occur in the primary stage of liquefaction. The primary stage would accomplish the dissolution of the coal and breakdown of the waste material. The products would then be introduced into the secondary stage where uprgading of product would occur.

Recent work with waste rubber tires directly coprocessed with coal has shown that this is a feasible scheme, but that additonal pretreatment of the tires is beneficial to the coprocessing. This additional step is the vacuum pyrolysis of the waste rubber tire to yield an oil that is highly aromatic. The vacuum pyrolysis of the waste rubber tires is also beneficial in separating out the carbon black and ash from the volatile constituents. It has been shown that the breakdown of waste rubber tires during vacuum pyrolysis produces polyaromatic hydrocarbons.[6] Polyaromatics are known to be beneficial in coal liquefaction.[7-9] The present paper explores the usefulness of oil derived from pyrolysis of waste rubber tires as a reactant in a coal coprocessing scheme or as a coal liquefaction solvent.

Experimental

Blind Canyon (Utah) coal (DECS-6, -60 mesh) (**BC6**) was obtained from the Penn State Coal Sample Bank and stored under nitrogen at 0 °C. Oil obtained from vacuum pyrolysis of waste rubber tires (**PTO**=pyrolyzed tire oil) was produced by Conrad Industries, Chehalis, WA. The **PTO** was stored under ambient conditions. GC-MS analysis of the **PTO** was completed on a Hewlett Packard 5890 series II gas chromatograph coupled to a Hewlett Packard 5971 Mass spectrometer. A J & W 100 meter long DB-1 column was used for the GC-MS analyses. Elemental analyses were completed by Atlantic Microlabs, Norcross, Georgia. The precursor catalyst (ammonium tetrathiomolybdate, Aldrich) was used as received to impregnate the **BC6** from aqueous solution by the incipient wetness technique to obtain a 1 % by weight loading of the catalyst. The catalyst was added to the **PTO** in solid, dry form to achieve a 1 % by weight presence of the catalyst. The **BC6**/catalyst mixture was vacuum dried for two hours at 100 °C to remove all moisture. The **PTO/BC6** samples were placed directly in 27 cm^3 tubing reactors, purged with N_2, and pressurized to the pressure of interest. Pressures reported are for H_2 or N_2 and are initial pressures at room temperature before immersion in the sandbath. Reactors were heated by a fluidized sandbath held at various reaction temperatures. The tubing reactors were shaken vertically at 160 rpm for the duration of the experiment, removed and allowed to cool at room temperature for 5 minutes, and then quenched in cold water. Reaction products and solids were removed and extracted with tetrahydrofuran (THF). The THF was removed with a rotary evaporator, and the THF soluble portion was dried under vacuum for two hours and weighed. The THF insoluble residue remaining in the soxhlet extractor thimble was also dried for two hours under vacuum. The sum of the THF solubles and the THF insoluble residue, corrected for ash, was subtracted from the initial coal mass (daf) and solvent mass to calculate the total gas produced. Total conversion was defined as the sum of the gas and THF solubles. The dried THF solubles were then extracted with cyclohexane. The cyclohexane was removed from the oil sample using a rotary evaporator. The cyclohexane insoluble residue is referred to as asphaltenes. The cyclohexane soluble portion is referred to as oil. EPMA samples were prepared by grinding the THF insoluble portions and mixing with Petropoxy 154 (Pullman, Washington). The plug was polished with

a syntron diamond paste polisher for eight hours. Micrographs were obtained using a CAMECA Model SX-50 electron microprobe (Courbevoie, France). Two different micrographs are presented: secondary electron micrographs (SEM) and the characteristic X-ray micrograph for specific elements of interest. (All micrographs shown are for a 50 μm x 50 μm field of view).

Results

In Table 1 the analysis of the **BC6** is reported. Table 2 contains elemental analysis results for the **PTO**. The NMR results indicate the **PTO** is highly aromatic. The GC-MS analysis of the **PTO** indicated the presence of benzene, methylated forms of benzene, naphthalene, methylated forms of naphthalene, anthracene, methylated forms of anthracene, phenanthrene, methylated forms of phenanthrene, pyrene, methylated forms of pyrene, and naphthacene. These results are similar to what Williams and Taylor found for oil derived from the vacuum pyrolysis of waste rubber tires.[6]

Figure 1 contains the product yields based on the original coal (daf) and **PTO** masses. The data show good overall total conversion for the **PTO/BC6** mixtures. The results indicate that a 30 to 40 minute heating period is optimum for maximizing the conversion of **BC6/ PTO** with molybdenum catalyst present under a hydrogen atmosphere at 430 °C. Initial conversion is suprisingly high at 10 and 20 minutes. This may indicate that the **PTO** is very effective in solublizing the coal. In all samples, charring was observed, but charring was more significant in the 50 and 60 minute samples. The significant charring is probably due to the **PTO**. The polyaromatic molecules are char precursors, thus it is not surprising that charring increased with reaction time.

Figure 2 shows the yields based only on coal. These values were calculated on the assumption that **PTO** is only present in the products as gas and oil. Therefore we can subtract out 50 % of the gas and oil and double the remaining conversion value to obtain the coal total conversion. From the new total conversion we subtract twice the amount of asphaltenes in order to obtain the new gas and oil values. This assumes no **PTO** forms char, which is very unlikely, but this permits an approximate calculation of the amount of coal that was actually converted. Thus, it could be predicted that at 30 minutes 92 % of the coal would be converted into gas, oil, and asphaltenes.

Table 3 contains the carbon and hydrogen percentages for the oils, asphaltenes, and char/ash produced from the above reactions. The carbon and hydrogen values were converted to molar values to obtain carbon/hydrogen ratios. The oil quality remained constant throughout the six time periods.

In past work, it was found that Electron Probe Microanalysis (EPMA) was useful in spotting the location of catalysts and metals in coal.[10-12] EPMA is a qualitative tool for determining the degree of dispersion of metal catalysts in coal particles.

The EPMA data in Fig. 3 show a coal particle taken from a sample which containsed **BC6** coprocessed with **PTO** at 430 °C for only 20 min. For the coal particle, a secondary electron micrograph (SEM), a sulfur X-ray image, and a molybdenum X-ray image are shown. The SEM image and sulfur X-ray image are presented to show the location of the coal particle. The **BC6** contains approximately 0.4 % by weight sulfur which the EPMA detects. Fresh coal contains no molybdenum, therefore detection of molybdenum by the EPMA indicates the presence of catalyst. The detection limit of the EPMA for molybdenum is approximately 200 ppm. Thus catalyst may be present in samples even though it may not be detected by EPMA.

The molybdenum micrograph in Figure 3 indicates the presence of the molybdenum catalyst in the coal particle. It is somewhat surprising to find catalyst inside the coal particle at such an early time in the liquefaction period. In previous unpublished work we found that when **BC6** was reacted at 350 °C without any solvent and the molybdenum was not incorporated into the coal matrix until 50 to 60 minutes of coprocessing had occurred. The high total conversion

observed after 20 minutes for the **PTO/BC6** system indicates that dissolution and thermal cracking of the coal occurred rapidly. **PTO** probably induces swelling thus allowing for greater dispersion of the catalyst throughout the coal particles. This suggests that increased dispersion of the molybdenum catalyst observed in the coal particles by EPMA may be partially responsible for the high conversion values.

Conclusion

Tire oil obtained by vaccum pyrolysis of waste rubber tires is better than shredded tires for coprocessing with coal. The **PTO** appears to be a good dissolution solvent for the coal and an effective hydrogen donor. EPMA data indicate that the solvent readily enters the coal matrix thus aiding catalyst dispersion.

Acknowledgements

We gratefully acknowledge Lester J. Thompson and Eugene Dalton with Book Cliff Energy, Green River, UT for providing us with pyrolyzed tire oil. We also acknowledge Phillip Bridges with Conrad Industries, Chehalis, WA for his generous donation of pyrolyzed tire oil and discussions of this work. Financial support by the U.S. Department of Energy, Fossil Energy Division, through the Consortium for Fossil Fuel Liquefaction Sciences, Contract No. UKRF-4-21033-86-24, is gratefully acknowledged.

References

1. Farcasiu, M.; Smith, C., **1992**, Prepr. Pap. Am. Chem. Soc., Div. Fuel Chem., 37 (1), 472.

2. Orr, E. C.; Tuntawiroon, W.; Ding, W. B.; Rumpel, S.; Eyring, E. M.; Anderson, L. L., **1995**, Prepr. Pap. Am. Chem. Soc., Div. Fuel Chem., 40 (1), 44.

3. Stiller, A. H.; Dadyburjor, D. B.; Wann, J.; Tian, D.; Zondlo, J. W., **1995**, Prepr. Pap. Am. Chem. Soc., Div. Fuel Chem., 40 (1), 77.

4. Robbins, G. A.; Winschel, R. A.; Burke, F. P., **1995**, Prepr. Pap. Am. Chem. Soc., Div. Fuel Chem., 40 (1), 92.

5. Huffman, G. P.; Feng, Z.; Mahajan, V.; Sivakumar, P.; Jung, H.; Tierney, J. W.; Wender, I., **1995**, Prepr. Pap. Am. Chem. Soc., Div. Fuel Chem., 40 (1), 34.

6. Williams, P. T.; Taylor, D. T., **1993**, Fuel, 72, 1475.

7. Orr, E. C.; Tuntawiroon, W.; Anderson, L. L.; Eyring, E. M, Fuel Processing Technology, in press.

8. Grint, A.; Jackson, W. R.; Larkins, F. P.; Louey, M. B.; Marshall, M.; Trewhella, M. J.; Watkins, I. K., **1994**, Fuel, 73 (3), 381.

9. McMillen, D. F.; Malhotra, R.; Tse, D. S.; Nigenda, S. E., **1988**, Prepr. Pap. Am. Chem. Soc., Div. Fuel Chem., 33 (1), 58.

10. Sommerfeld, D. A.; Jaturapitpornsakul, J.; Anderson, L. L.; Eyring, E. M., **1992**, Prepr. Pap. Am. Chem. Soc., Div. Fuel Chem., 37 (2), 749.

11. Sommerfeld, D. A.; Tuntwiroon, W.; Anderson, L. L.; Eyring, E. M., **1993**, Prepr. Pap. Am. Chem. Soc., Div. Fuel Chem., 38 (1), 211.

12. Orr, E. C.; Tuntawiroon, W.; Anderson, L. L.; Eyring, E. M., **1994**, Prepr. Pap. Am. Chem. Soc., Div. Fuel Chem., 39 (4), 1065.

Table 1 Analysis of Blind Canyon DECS-6 Coal*

Proximate	Percentage
% Ash	5.84
% Volatile	44.50
% Fixed Carbon	49.66
Ultimate	Percentage
% Carbon	81.28
% Hydrogen	6.24
% Nitrogen	1.55
% Sulfur	0.42
% Oxygen	10.5

* Penn State Coal Sample Bank

Table 2 Elemental Analysis of Oil Derived From The Vacuum Pyrolysis of Waste Rubber Tires

Element	Percentage
Carbon	87.7
Hydrogen	11.0
Nitrogen	0.3
Sulfur	0.6

Figure 1 Conversion results for Blind Canyon DECS-6 and oil obtained from the pyrolysis of waste rubber tires. Coprocessing was carried out in tubing reactors at 430 °C under hydrogen gas with a molybdenum catalyst present. The ratio of coal to oil was 1:1 by weight.

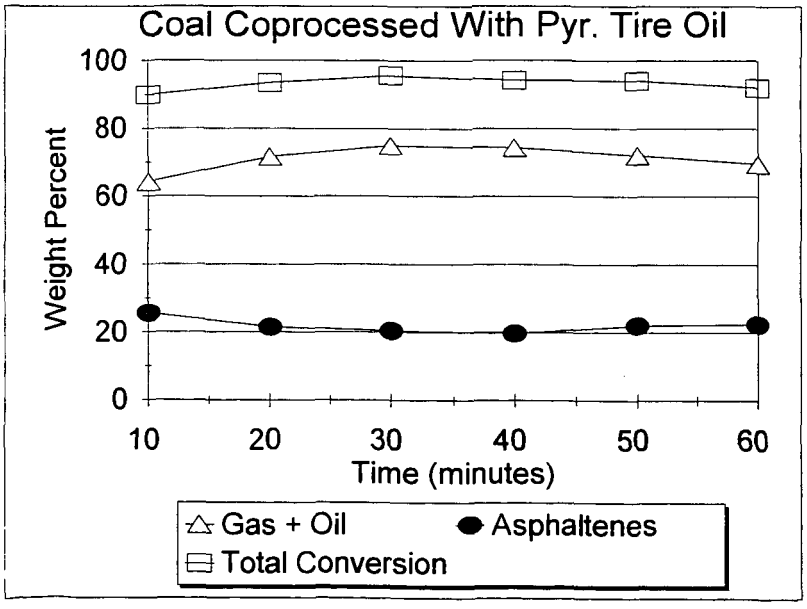

Figure 2 Conversion results for Blind Canyon DECS-6. Coprocessing was carried out in tubing reactors at 430 °C under hydrogen gas with a molybdenum catalyst present. The ratio of coal to oil was 1:1 by weight.

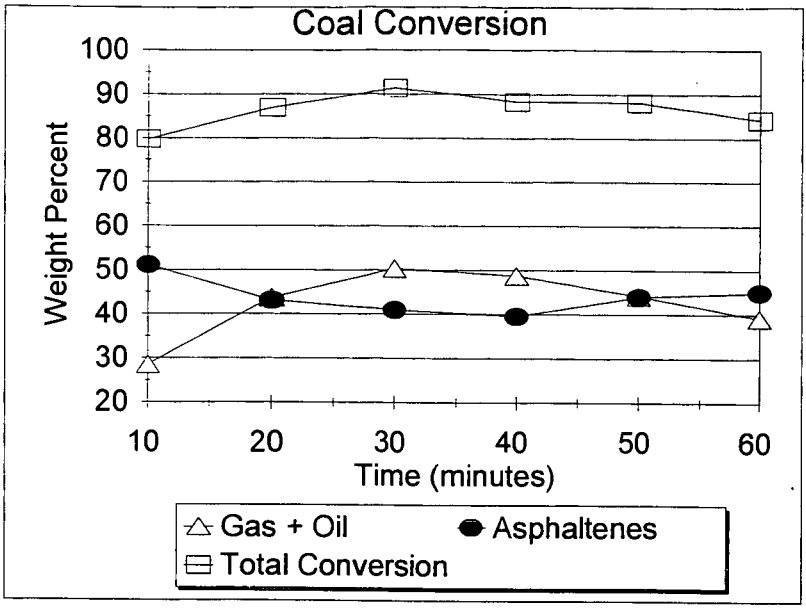

Table 3 Carbon and Hydrogen Analysis of Oil, Asphaltenes, and Char/Ash

	Oil	Asphaltenes	Char/Ash
10 Minutes			
Carbon	86.8	84.3	57.6
Hydrogen	8.6	5.8	3.2
Molar Ratio	.8	1.2	1.5
20 Minutes			
Carbon	86.0	85.6	53.4
Hydrogen	8.4	5.5	2.8
Molar Ratio	.9	1.3	1.6
30 Minutes			
Carbon	84.3	87.1	43.0
Hydrogen	8.3	5.6	2.2
Molar Ratio	.9	1.3	1.6
40 Minutes			
Carbon	86.4	86.9	38.9
Hydrogen	8.5	5.5	2.0
Molar Ratio	.9	1.3	1.6
50 Minutes			
Carbon	84.9	87.6	56.0
Hydrogen	8.3	5.4	2.9
Molar Ratio	.9	1.4	1.6
60 Minutes			
Carbon	85.1	87.7	59.9
Hydrogen	8.1	6.0	2.8
Molar Ratio	.9	1.2	1.8

Figure 3
Blind Canyon DECS-6 coal in pyrolyzed tire oil
1 % ammonium tetrathiomolybdate
Hydrotreated for 20 minutes, 430° C, 1000 psig (cold) H_2
EPMA micrograph dimensions (50 μm x 50 μm)

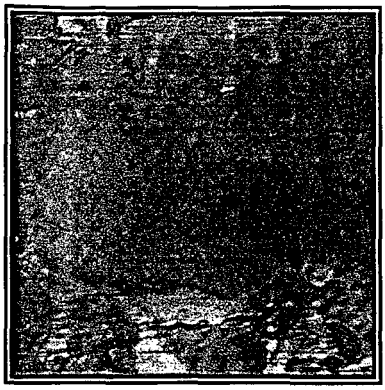

Secondary Electron Image

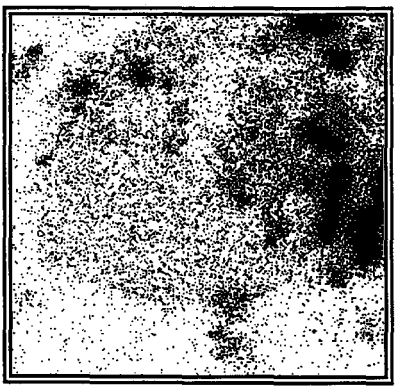

Sulfur K_α

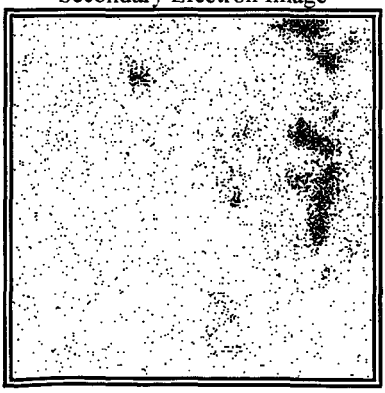

Molybdenum L_α

Technical Support of the U.S. DOE Biomass Power Program in the Development of Biomass to Electricity Technologies.

Richard L. Bain and Ralph P. Overend
National Renewable Energy Laboratory
Industrial Technologies Division
1617 Cole Boulevard
Golden, CO 80401-3393

Keywords: Biomass, Electric Power, R&D

INTRODUCTION

In the USA the period since 1973 to the present, has resulted in a dramatic upswing in bioenergy use and applications uses especially in thermal and electrical applications of mainly wood residues. The wood processing and pulp and paper sectors became about 70% self sufficient in energy in that period and the amount of grid connected electrical capacity increased from less than 200 MW in 1978 to over 7,500 MW_e today. This dramatic growth stimulated in part by federal tax policy and state utility regulatory actions, occurred after the Public Utilities Regulatory Policies Act (PURPA) of 1978 guaranteed small electricity producers that utilities would purchase electricity at a price equal to the utilities' avoided cost.

More than 70 percent of biomass power is cogenerated with process heat. Wood-fired systems account for 88 percent, agricultural waste (3%), landfill gas (8%), and anaerobic digesters (1%). There are nearly 1000 wood-fired plants in the U.S., typically ranging from 10 to 25 MW_e. Only a third of these plants offer electricity for sale. The rest are owned and operated by the paper and wood products industries for their own use. Most of today's biomass grid connected power installations are the smaller scale independent power and cogeneration systems. To date, utilities have been involved in only a handful of dedicated wood-fired plants in the 40 to 50 MW_e size range, and in some co-firing of wood and municipal solid waste in conventional coal-fired plants.

Net plant heat rates for 25 MW_e plants in the California PG&E service territory average approximately 18 percent efficiency (17,000 Btu/kWh). By comparison the 43 MW_e utility-operated plant at Kettle Falls, Washington has a reported heat rate of 26% efficiency (14,382 Btu/kWh). However, the advantageous power purchase agreements that were negotiated under PURPA in the 1980s are no longer available at high rates of avoided costs. As a result a number of plants are closing as their power contracts come up for renewal. They could be competitive in today's environment using low cost waste and residue fuels if their efficiency was much higher as has been demonstrated in the sugar industry of Hawaii where the power plants operate for a major part of the year as CHP installations. Investments in efficient steam cycles has resulted in a competitive rate of power generation under PURPA. Low pressure boilers were systematically replaced by higher pressure boiler systems of larger capacity in the period 1960 through 1980 with the average steam pressure and temperature increasing from 1.3 MPa and 210 °C to 4.4 MPa and 380 °C. Meanwhile the net steam consumption in the mills decreased significantly from 600 kg /tc to about 300-400 kg/tc; resulting in a power output of about 60 kWh/tc on average with the best mills reaching over 100 kWh/tc.

Biomass Power Efficiency Advances are Needed in order to be competitive with low cost fossil fuels, especially in stand alone power generation, will require a considerable Increase in the power to heat ratio and will require advanced technologies - such as the use of IGCC (Integrated Gasification Combined Cycles) as illustrated in Table 1.

As can be seen, the increase in efficiency has two effects: it reduces the capital cost on a kW basis, and it reduces the sensitivity of the final cost of electricity to the fuel cost component.

The USDOE Biomass Power Program is working to address the issues of making biomass competitive by working with today's industry to increase its reliability and to develop advanced systems for increased efficiency and environmental performance.

The pathways under discussion are included in Figure 1.

Support for today's Industry: In general the biomass power industry has displayed good reliability, however, in the case of the IPP Biomass fueled stations in California, operational difficulties

rapidly emerged when using non-wood biomass fuels[1]. The operational difficulties were caused by the deposition of mineral matter on the heat exchange surfaces (boiler tubes, superheaters, and water walls) and by the agglomeration of ash and inert fluid bed materials. This problem is one that is costly as it results in down-time for tube cleaning and repair, and because there is considerable interest in the development of dedicated crops such as short rotation woody crops and herbaceous energy crops for bioenergy applications it could be a problem that would affect the long term large scale deployment of biomass fuels in both electricity generation and the production of liquid fuels. For this reason the USDOE through NREL initiated a collaborative study with industry on the ash deposition problem[2] with the goal of establishing the root cause of the difficulties in using non-traditional biomass fuels.

While the nature of the direct combustion boiler problem is of current concern, NREL also recognized that these same issues may have to be addressed in the non-combustion processes such as fast pyrolysis, and gasification that convert biomass into intermediate fuels that would be used in very high efficiency generation systems based on gas turbines. Gas turbines are extremely sensitive to both mineral matter and to alkali metals. For the state-of-the-art turbines with turbine inlet temperatures of 1260°C (2300 °F) the manufacturer's specifications call for less than 300 ppb of alkali metal in the hot section. Since high efficiency biomass to electric conversion is a goal of the USDOE Biomass Power Program[3] a program of testing non-woody and short rotation biomass feedstocks in gasifiers and fast pyrolysis processes was instituted.

The Ash Deposition Problem was addressed by conducting extensive fuels and deposits analysis and through an extensive collaboration the cause was identified. The project received over 700 different fuels analyses from the participants, however, the majority of these did not have the critical ash analysis data. However, this may not have been such a bad omission since the project has established that there are major problems with the standard ash determination methods that are accepted as standards for coal materials. The ASTM methods for coal prepare an ash at 800 °C which is then used for the pyrometric cone analysis to determine if there will be a slagging or sticky problem. Unfortunately the critical element causing the ash deposition and fouling problem is potassium and it is known that this and other mineral matter from biomass will evaporate from the ash at 800 °C, decreasing its mass and altering its fusion properties[4]. Potassium is a key component of cellular function and in plants it can be present at 1000 times the concentration of sodium. As much as 35% of the ash in annual plants can be alkali which drastically reduces the ash fusion temperature from greater than 1300 °C in the case of wood ash to about 700 °C where the potassium can form a eutectic with the plant's silica or the sand medium of the fluidized bed[5]. Work with the MBMS system at NREL has shown that the form in which potassium is transported can be very diverse including oxides, hydroxide, sulphite/ate, and chlorides as volatiles[6].

Gasification Developments: Commercial biomass gasifiers are already in use to generate process heat and steam. Current development activities are focused on producing electricity and, to some extent, liquid fuels, and involve integrating gasification with various cleanup systems to ensure a high-quality and reliable gas product. At this time, there is no clear preference for a single gasifier system. The Global Environment Facility[7], is evaluating two systems offered by Scandinavian commercial developers for the CHESF project in NE Brasil. The evaluation will compare the advantages and disadvantages of using air gasification at high pressure (Bioflo) or at low pressure (the TPS system). High-pressure gasification would have to meet the pressure requirements of the chosen turbine on all system components, including the gas clean-up system; the low-pressure system would carry out the gas cleaning before compressing the fuel gas to the turbine operating pressure. Air blown systems only produce a low-heating value gas (less than 150 Btu/ft^3, 5-6 MJ/Nm^3), and a significant loss in efficiency is imposed if the gas must be cooled to ambient temperatures prior to being compressed. For this reason, the American and Scandinavian gasification programs are emphasizing using hot gas clean-up systems for the air-blown, low heating value gasifiers that will be operated at pressure.

The U.S. program has a dual-pathway strategy involving both low and medium heating value gas production. One high pressure system is capable of generating either low or medium heating value gases according to whether it is an air- or oxygen-blown variant, and is the Renugas® system developed by IGT. The low-pressure strategy in the U.S. is based around two developers of medium heating value gas systems who do not use oxygen, rather use indirect gasification to produce gases having heating values of 350-450 Btu/ft^3(15 - 20 MJ/Nm^3). Cooling and quenching the gas does not incur a significant efficiency penalty and, compared with low-heating value gas, there are essentially no modifications required in the turbine combustors to handle the

medium-heating value gas fuels.

The Pacific International Center for High Technology Research (PICHTR) Project (>6 MW_e): The U.S. Department of Energy (DOE) and the state of Hawaii have joined with PICHTR in a cost-shared cooperative project to scale up the Institute of Gas Technology (IGT) Renugas® pressurized air/oxygen gasifier to a 45-90 ton/day engineering development unit (EDU) operating at 1-2 MPa using bagasse and wood as feed. The site is the HC&S sugar mill at Paia, Maui, Hawaii, and NREL is providing project oversight in addition to systems analysis. The first phase, which is now being commissioned consists of the design, construction, and preliminary operation of the gasifier to generate hot, unprocessed gas. The gasifier is designed to operate with either air or oxygen at pressures up to 2.2 MPa, at typical operating temperatures of 850°-900°C. In Phase 1, the gasifier will be operated for about four months at a feed rate of 45 ton/day at a maximum pressure of 1 MPa. Following the end of Phase 1 in late 1995, a hot-gas cleanup unit and gas turbine will be added to the system to generate 3–5 MW of electricity.

The Vermont Gasifier Project with FERCO and the McNiel Generating Station (>15MW_e) Future Energy Resources Company (FERCO) of Atlanta, GA, is the licensee of the Battelle indirect gasification system, and the scaleup is at the site of the Burlington Electric Department's McNeil station in Burlington, VT. The project, which is in two phases, will first take feedstock from the 50 MWe station and after gasification will return the gas to the boiler. The scale of operation is about 200 tpd. The second phase will incorporate approximately 15 MW_e of turbine electricity generation. The project is jointly funded by USDOE and FERCO and presently construction forecast to start in Fall 1995.

National Renewable Energy Laboratory (NREL) Activities: The research strategy is guided by systems analysis and technoeconomic assessments of gasifier-based power cycles. In the laboratory, research is ongoing to develop catalysts for hot gas conditioning, and use of advanced instrumentation and chemometrics for feedstock characterization and evaluation. One element of this research is using advanced mass spectrometry to characterize alkali metal speciation under gasification and combustion of biomass conditions. This work has been extended to develop and using a transportable molecular beam mass spectrometer (TMBMS) for real time measurement of hot stream composition to 500 atomic mass units (amu). The TMBMS is being used by both Battelle and IGT to measure gasifier and catalyst performance in the field.

ACKNOWLEDGMENTS

This work was performed under contract № DE-AC36-83CH10093 to the US Department of Energy. Special thanks go to our colleagues at NREL: Foster Abglevor, Thomas A. Milne, David Dayton, Jim Diebold, David Gratson, Esteban Chornet, Robert Evans, John Scahill, Steven Czernik, and Kevin Craig for their helpful discussions on this theme.

REFERENCES

1. Jane Hughes Turnbull. 1993 *Use of Biomass in Electric Power Generation the California Experience*, Biomass and Bioenergy Vol. 4. pp 75-84.

2. Alkali Deposits found in biomass power plants: a preliminary investigation of their extent and nature. NREL Subcontract TZ-2-1-11226-1. Principal Investigator Thomas R. Miles of Thomas R. Miles Consulting Design Engineers. Participants: Delano Energy Company Inc.; Electric Power Research Institute; Elkraft Power Company (Denmark); Foster Wheeler Energy Corporation; Hydra Co Operations Inc.; Mendota Biomass Power; Inc.; National Wood Energy Association; Sithe Energies, Inc.; Thermo Electron Energy Systems; Wheelabrator Environmental Systems Inc.; Woodland Biomass Power Ltd.; Western Area Power Authority; Sandia National Laboratories; Hazen Research Inc.; Al Duzy and Associates; University of California Davis; U.S. Dept. of the Interior, Bureau of Mines; Appel Consultants, Inc.

3. Electricity from Biomass National Biomass Power Program Five-Year Plan (FY1994-FY1998) Solar Thermal and Biomass Power Division, Office of Solar Energy Conversion, U.S. Department of Energy, Washington, D.C. Draft April 1994.

4. M.K. Misra, K.W. Ragland, and A.J. Baker. 1993 *Wood Ash Composition as a Function of the Furnace Temperature*, Biomass and Bioenergy Vol. 4. pp 103-116.

5. A. Ergundler, and A.E. Ghaly. 1993 *Agglomeration of Silica Sand in a Fluidized Bed Gasifier Operating on Wheat Straw*, Biomass and Bioenergy Vol. 4. pp 135-147. See also the phase diagram for SiO_2 - $K_2O.SiO_2$ in E.M. Levin, H.F. McMurdie, and F.P. Hall, 1956. *Phase Diagrams for Ceramists*. The Am. Ceramic Soc. Inc.:Columbus OH.

6. D. Dayton, and T.A. Milne. "Alkali, Chlorine, SOx, and NO_x Release During Combustion of Pyrolysis Oils and Chars." in Ed. T.A. Milne. Proceedings Biomass Pyrolysis Oil Properties and Combustion Meeting. September 26-28, 1994 Estes park Colorado. NREL-CP-430-7215. pp 296-308.

7. P. Elliott, and R. Booth. 1993. *Brazilian Biomass Power Demonstration Project*. Special Project Brief. Shell International:London, U.K.

Table 1. Comparison of present day steam generation with IGCC

Cost factors (¢/kWh)	Steam Generation	IGCC
Operations and Maintenance	0.5	0.5
Fuel only Cost	3.6	1.6
Capital Recovery	4.2	3.0 -3.5
Cost of Electricity	8.3	5.1-5.6

Notes to Table 1. Assuming a marginal cost of fuel of $2/million Btu (or approximately $40/tonne of dry biomass), a load factor of 85% (base loaded), and a return on capital invested of 8%/year, it is possible to see the effect of the new technology. Both plants are approximately 50 MW_e capacity. The efficiency of the steam plant is about 20%, while the IGCC is estimated to have an efficiency of 45%. The capital cost of the steam plant is $1.8/W, while that of the IGCC is expected to be in the range of $1.3 to $1.5/W.

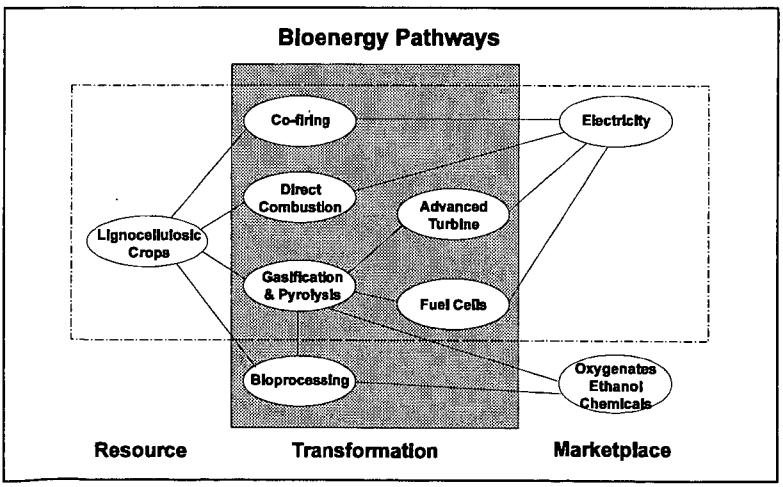

FIGURE 1: Bioenergy pathways.

HOT GAS CLEANUP IN BIOMASS GASIFICATION - REVIEW OF ACTIVITIES WITHIN EC SPONSORED R&D PROGRAMS

Anders L. Hallgren, Dept. of Chem. Eng. II
P.O.B. 124, Chemical Center, University of Lund
S-221 00 Lund, Sweden

Keywords: biomass gasification, hot gas cleanup, filtering, alkali measurements

INTRODUCTION

The use of biomass as an alternative fuel source attracts presently considerable interest in the European Community. A variety of R&D projects are currently active in investigating the prospects for biomass conversion processes in power and heat production.

Renewable energies in general are seen as one of the major options for energy supply, offering substantial advantages regarding environmental protection and CO_2 emissions. Because of their decentralize character they may also offer considerable potential in rural areas.

Within the European Commission (EC) research and technical development programs, several R&D and demonstration projects are being carried out reflecting issues in utilizing biomass or alternative solid fuels for power and heat production. Apart from being a potential environmental-friendly conversion route, the motives for introducing biomass in heat and power production is of course being able to replace the use of fossil fuels and to find alternative applications for existing agricultural areas.

One of the main technical issues is the gas cleanup process for clean gas utilizations and IGCC (Integrated Gasification Combined Cycle) concepts. Potential advantages are expected if the gas cleaning process can be accomplished at enhanced temperatures. Available options for integrated hot gas cleanup are being tested ranging from particulate removal to emission control. An overview of the ongoing projects in the area is presented in the following.

A new generation of gasifiers suitable for gasification of biomass and so called alternative solid fuels are under development. A PFB biomass gasifier test rig (Figure 2) has been installed at the Dept. of Chem. Eng. II (University of Lund). The system includes an integrated hot gas cleanup system that forms the basis for the activities at the department within two EC Joule II programs [1]. Progress from these efforts are presented and discussed.

PROSPECTS FOR BIOMASS UTILIZATION

At present about 80 % of the energy consumption within the European Union is from the use of fossil fuels. Within the power and heat production, some 40 % of the production is produced from coal utilization. These production systems have often modest efficiency and contribute to a large extent to the global emissions of nitrogen oxides, sulfur oxide, carbon oxide, and particulate matter [2]. Until today natural gas and fossil fuels have been regarded as the most economic and appropriate fuel for heat and power production where biofuels (biomass, agro- and forestry residues) may be believed to be the more environmental friendly alternative in the long run.

In many regions of Europe there is a steady and continuous production of biomass residues. The growing of biomass for energy production, combined with the utilization of agricultural and forestry residues, is an alternative energy resource in many areas that today is likely to be not too far from a commercial status. One driving force for this development is the tax structure including the exclusion of biomass from recently imposed CO_2 tax on fossil fuels. In some regions farmers may even be

encouraged to grow energy crops on land that during the last years has been taken out of production to balance the farming industry.

To meet the environmental challenges, improved technologies are needed. The current technologies involve combined cycle concepts where improved performances are needed. Novel solutions and continuous developments of integrated systems offer encouraging prospects for enhanced efficiency and more economical power generation. The improvements also have to involve fuel flexible systems accepting a broad variety of different solid fuels. Since the awareness of potential environmental-friendly alternatives has increased and the restrictions with respect to emissions has been reinforced, the interest for utilizing renewable fuels in heat and power production has correspondingly grown. With IGCC technology and renewable energy sources it is possible to get a both ecological acceptable and a highly efficient concept for heat and power production.

INTEGRATED HOT GAS CLEANING FOR IGCC PROCESSES

For a successful implementation of biomass gasification in commercial fuel gas production, the effluent gas must conform to allowable limits regarding particulate and other impurities. For IGCC applications there are potential advantages with gas cleanup at high temperatures and elevated pressures.

The fuel gas from gasification processes contains various amounts of impurities and particulate originating from the solid fuel and attrition products from the bed material. Advanced filtration technology today partially offers solutions to some of these problems. Especially the integration of these systems in larger scales has to be surveyed more carefully.

Hot gas cleaning also imply chemical manipulations of the product gas to meet environmental as well as technical standards. High molecular weight products, tars, and other components like alkali trace elements may cause in the condensed phase severe operational problems. These have to be removed before the gas product can qualify as fuel for gas engine or gas turbine purposes.

Within the so called JOULE II NON-NUCLEAR ENERGIES research framework several multi-partner projects have been drawn together embracing technical programs from a variety of R&D organizations, including industrial partners, from the current member states of the European Community. An unique opportunity is hereby given to establish expert networks designed to address key technical issues. Some of the networks are dealing with issues connected with particulate removal and emission control. A presentation of three projects working with biomass related hot gas cleanup is given below.

Current research projects in the EC Joule II Non-Nuclear Energy Program

- INTEGRATED HOT FUEL GAS CLEANING FOR ADVANCED COMBINED CYCLE PURPOSES (JOU2/CT93/0431) is a sub-project incorporated in a vast EC program project called CLEAN COAL TECHNOLOGY R&D. As the name implies, the project essentially deals with topics reflecting coal gasification and combustion. Likewise the sub-project is aimed to cover integrated gas cleanup issues in coal related advanced gasification systems. However, the need for fuel flexibility for such systems has been recognized and alternative solid fuels are considered and included in the studies.

The project organization and work, as for most EC project programs, is based on a close scientific and technical co-operation between the project partners organized in groups based on scientific areas. A typical project structure is shown in Figure 1. This project is one of the bigger projects within the Joule II program and the activities comprise a broad range of research tasks within hot gas cleaning. From techno-economic modeling studies via cycle control studies to fundamental and applied emission control investigations, the project has a total budget of close to 8 million ECU, an equivalent of 6 million USD. The grant from the European Commission is here about 3.5 million USD. The project is co-ordinated by CRE (Coal Research Establishment) in England.

- COMPARISONS OF ENTRAINED PHASE AND FLUIDIZED BED GASIFICATION OF BIOMASS WITH RESPECT

TO PROBLEMS RELATED TO FEEDING AND HOT GAS CLEANING (JOU2/CT93/0347) is another Joule II project focusing on integrated gas cleanup for advanced gasification systems. The project work is a co-operation between Coal Research Establishment (CRE) in the UK, Deutsche Montan Technologie (DMT) in Germany, and LIT in Sweden. The objective with the project is to collect end-user-oriented information for process development in advanced thermochemical conversion of biomass. Integrated pressurized hot gas cleansing units at DMT and LIT have been provided with different filters (filter types; materials) to find the most suitable filtering system for biomass gasification purposes. The project is co-ordinated by DMT and has a total budget of 1 million ECU (750.000 USD).

- ADVANCED AND INTEGRATED BIOMASS GASIFICATION WITH HOT AND CATALYTIC FLUE GAS CLEANING FOR ELECTRICITY PRODUCTION AND OTHER END PRODUCTS (JOU2/CT93/0399) is a project coordinated by the University of Madrid (Spain) dealing with catalytic reforming and optimization of the gas product. Specific focus is put upon catalytic methane steam reforming, hydrocracking, and the use of water-gas shift catalysis. Together with Danish Technical Institute (DTI) in Denmark cereal straw is converted in a fluidized bed gasifier with a down stream catalytic reformer. The total budget for a 36 months work period is 300.000 ECU (225.000 USD).

The above mentioned project are being carried out during 1994-96. Periodically, technical meetings as well as progress meetings are held through out the course of the projects to monitor and to assess the project progress. Apart from the Joule II program other EC sponsored research programs as well as various national research programs are undertaken within the individual countries in the European Community.

Project work at Lund Institute of Technology (LIT)

LIT takes part in two of the above mentioned projects with studies investigating the influence of different bed materials, the effect from biomass ash on the bed behavior in PCFB gasification of biomass, and hot gas particulate removal. The distribution of alkali species in the gasification products is additionally studied including an assessment for their reduction or removal [3].

Vapor-phase alkali metals (Na, K) may form condensed compounds in the temperature interval 400-550 °C. These alkali compounds are capable of drastically enhance hot corrosion on metallic surfaces in the process system, cementing deposited particulate, and support agglomeration tendencies of the bed material in a fluidized bed gasifier. Enhanced tendency for agglomerations in the bed, due to sticky layers of alkali condensations on the particle surfaces, has been found in systems utilizing biomass.

Specifically of interest is to what extent the alkali compounds in the fuel are converted into the gas phase and how to reduce the alkali concentration. At equibrillium the alkali content in the gas phase is strongly influenced by the temperature as well as by the pressure. At increasing pressures in the system the alkali content in the gas phase is reduced largely due to condensation mechanisms. The temperature in certain parts of the conversion system must be kept high enough to suppress such condensation mechanisms. Consequently, to reach efficient reduction this suggests that gas phase alkali capture must take place at temperatures above 600 °C that put distinct requirements on adequate on-line monitoring.

At LIT sorbents for hot gas alkali removal are studied and the efficiency of these sorbents are being evaluated. Routine on-line methods for monitoring alkali components directly in the hot gas phase are very scarcely reported in the literature. Current alkali measurements techniques are mainly based on batch sampling and laser spectroscopy, methods that both are being tested and evaluated within the Joule II program.

An instrument for plasma assisted alkali monitoring in the gas phase, developed by the University of Tampere (Finland), will be tested with the test rig at LIT. The method is based on optical spectroscopy of alkali metals heated by a thermal plasma at process temperature.

In addition, another novel device for on-line measuring of alkali metals in the gas phase will be used at LIT. The device and method, developed by Chalmers Technical University in Gothenburg

(Sweden), is suitable for determinations of trace alkali components in hot fuel gas. The technique is based on surface ionization of the alkali components and has been tested with pure alkali sources as well as with different biofuel with very encouraging results. Alkali concentrations in the range of 0.1 ppb to well above 1 ppm have been detected and measured. A setup was designed and constructed for the LIT test rig and preparation for measurement campaigns is presently in progress.

As a second main part of the EC project work at LIT, hot gas particulate removal is being studied in the LIT gasification test rig. The primary solid phase separation step is achieved by an internal axial cyclone that has shown a separation efficiency between 96-98% on a solid/gas phase ratio basis. A secondary step is performed by means of a single SiC-based candle filter with effluent gas dust concentration lower than 10 mg/Nm^3. However, the operational time on the candle filter has so far been short to make adequate predictions regarding the suitability in biomass gasification.

Comparable filter test are additionally being carried out together with DMT in Germany where metallic filter are tested and evaluated for biomass gasification purposes. Advanced ceramic candle filters offer promising solutions and have good filtration efficiency but integrated in biomass gasification specific issues have to be covered before the technology can be fully accepted for biofuel based IGCC applications.

CONCLUSIONS

A growing interest in utilizing biomass and other so called alternative solid fuels is today seen among various countries in the European Community. Alternative solid fuels as a domestic resource for energy production is important not only for the energy supply but also for the potential benefits regarding the environment and rural and regional development[4].

Key issues in implementing the technology associated with sustainable biomass utilization for both power and heat production have been identified and are emphasized in different R&D programs sponsored by the European Commission. An important area is the integration of gas cleaning systems for IGCC and similar applications.

Dept. of Chem. Eng. II at LIT is involved in two so called Joule II research projects studying hot gas particulate removal and alkali reduction. In these studies particular interest is in hot gas solid phase separation including filtering systems suitable for biomass gasification processes. Additionally, research efforts have been made in investigating the effects from fuel alkali in the fluidized bed gasification process and studies including an assessment for the reduction or removal of alkali components in the gas phase. So far the preliminary results indicate that most of the alkali in the LIT test rig is adsorbed on the surface of the ash collected in the filter unit. Two individually developed systems for monitoring alkali species in hot fuel gas will be tested and evaluated.

REFERENCES.

1. A. Hallgren, I. Bjerle & L. Chambert, "PCFB Gasification of Biomass", paper presented and published in the proceedings to the 206th ACS National Meeting, Chicago, IL., Aug. 22-27, 1993
2. Minchner, A., "Integrated Hot Fuel Gas Cleaning for Advanced Gasification Combined Cycle Processes", project description Contract No. JOU2/CT93/0431, 1994.
3. A. Hallgren, "Hot Gas Particulate and Alkali Removal in PCFB Gasification of Biomass", paper presented and published in the proceedings to the AIAA 29th Intersociety Energy Conversion Engineering Conference, Monterey, August 7-11, 1994.
4. "Research and Technological Development Programme in the field of Non-Nuclear Energy (1990-1994) JOULE II; Project Synopses", European Commission, EUR 15893 EN, 1994.

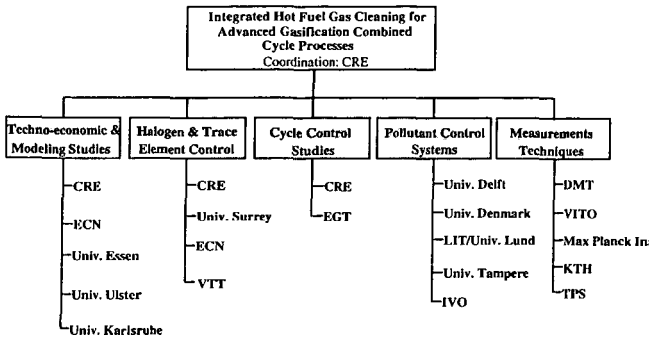

Figure 1. Project organization and activities

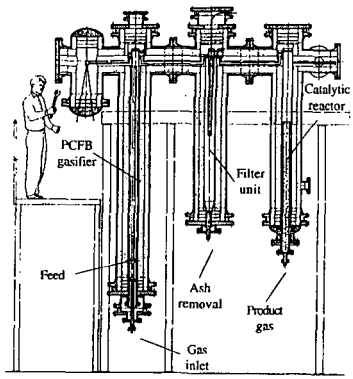

Figure 2. The PCFB biomass gasification test rig at LIT

HIGH EFFICIENCY ELECTRICITY PRODUCTION IN THE SUGAR INDUSTRY OF THE FUTURE: THE PACIFIC INTERNATIONAL CENTER FOR HIGH TECHNOLOGY RESEARCH PROJECT (>6 MW_e)

Andrew R. Trenka
Pacific International Center for High Technology Research
2800 Woodlawn Drive • Honolulu, Hawaii 96822

Keywords: Sugarcane Bagasse, Electric Power, Gasification Demonstration

INTRODUCTION

The Pacific International Center for High Technology Research (PICHTR) is presently starting up a 100 tpd bagasse Renugas® gasifier which was developed under license from the Institute of Gas Technology (IGT).

For thousands of years, mankind has used biomass for energy, burning it first in campfires. In more modern times, combustion boiler systems were developed such as those fueled by coal. Through inefficient, these systems answered an increasing need for energy brought on by the industrial revolution. Yesterday's systems are being replaced with more efficient methods of energy conversion and extraction. Recognizing the untapped potential for biomass power to provide clean and efficient energy, the U.S. Department of Energy established the National Biomass Power Program in 1991. The State of Hawaii Department of Business, Economic Development & Tourism is collaborating in this national program to complement the development of its own sustainable resource program. As a key player in this program, PICHTR will design, construct, and operate a biomass gasification facility that will be the centerpiece of the nation's biomass gasification technology.

Current Power Generation by the Sugar Industry in Hawaii

Worldwide, the sugarcane industry has the potential to be a major generator of electric power for the electricity grid through the use of the by-product of sugarcane processing called bagasse as a fuel source. Initially, bagasse was used as a fuel solely for the evaporation of water in order to concentrate the sugar, since animal or hydropower was originally used to crush the cane. In time, the benefits of using steam power for in-plant power needs resulted in increased use of these by-products in energy production. The history of the industry in Hawaii was that although[1] some export of electricity to communities took place in the industry prior to 1970, the really major growth in generating capacity took place in the 1970s as the sugar industry consolidated its low pressure boilers into higher pressure units to produce more electricity. The passage of the 1978 Federal Public Utilities Regulatory Policies Act (PURPA) further stimulated the use of bagasse to the point where, in 1991, the industry burning bagasse in conjunction with fossil fuels supplied about 5.5% of the grid electricity. The generation in that year[2] was 495 TWh, down from a high of 681 TWh in 1988. Further, Biomass energy in Hawaii was provided in the form of energy recovered from the H-power plant in Honolulu, an ultra-modern Waste-to-Energy plant recovering steam and electricity from municipal waste generated on Oahu.

Global Sugarcane Power Potentials

The sugar industry worldwide offers the potential to produce about 500 TWh of electricity for export if significant energy-efficient gains could be made internally to the process of sugar production and advanced power generation technology was to be adopted along with increased residue collection from sugarcane growing[3]. To reach this output would require a power generation rate of 450–600 kWh/tc where tc is a tonne of cane processed. Table 1 shows the world cane production statistics from two viewpoints, the geographic area, and the development status. It can be seen that the majority of the sugarcane production is in developing countries.

---

1 C.M. Kinoshita. *Cogeneration in the Hawaiian Sugar Industry*, Bioresource Technology. 35(3). pp 231–237. 1991

2 DBEDT. *The State of Hawaii Data Book 1992*. A Statistical Abstract. Table 476, 477

3 R.H. Williams, and E.D. Larson. Advanced Gasification based Biomass Power Generation in Eds. T.B. Johansson, H. Kelly, A.K.N. Reddy, and R.H. Williams. Renewable Energy: Sources for Fuels and Electricity. Chapter 17, pp 729–785, Island Press: Washington, D.C. 1993

The current average rate of power generation from sugarcane in most developing countries is much less than 500 kWh/ton cane processed (tc)—typically less than 10 kWh/tc. Average values range from 15 to 25 kWh/tc in plants that do not require any fossil fuel input. This is barely sufficient to meet the internal needs of these sugarmills. Traditionally, the industry need has been for only sufficient electric power to meet the in-plant or factory demand, with the steam exhaust in balance with the thermal energy requirements. Essentially, the boilers are operated as a bagasse disposal unit since there is a need to maintain an equilibrium between bagasse production and utilization.

Additionally, the sugarcane industry does not normally operate on a year round basis—the cane harvesting and processing season in Hawaii can be quite long at 200 days, but in many places the season is less than 150 days. It is only when there is an incentive to sell power to the grid that the sugar industry can undertake the necessary investments in higher pressure steam boilers and turbogenerators along with energy efficiency improvements. In the Hawaiian industry (footnote 1) low pressure boilers were systematically replaced by higher pressure boiler systems of larger capacity in the period 1960 through 1980, with the average steam pressure and temperature increasing from 1.3 MPa and 210°C to 4.4 MPa and 380°C. Meanwhile, the net steam consumption in the mills decreased significantly from 600 kg/tc to about 300–400 kg/tc; resulting in a power output of about 60 kWh/tc on average, with the best mills reaching over 100 kWh/tc. The thermal efficiency to generate electricity is approximately 15%–20% in such combined heat and power arrangements. Increasing the power to heat ratio will require advanced technologies—such as the use of integrated gasification combined cycles (IGCC). The estimated steam that would be available from an IGCC is only 275 kg/tc and necessitate severe energy efficiency improvements in the sugar production process but would increase the electricity output in the sugarcane season to about 600 kWh/tc. For this to be produced on a year round basis would require additional fuels such as the tops and leaves from the sugarcane harvest (called *Barbojo* in Spanish-speaking countries) other Biomass fuels including wood and wastes or additional fossil fuel input.

PICHTR's development of the Renugas® gasifier is targeted towards this global market, as well as the needs of Hawaii. Recent studies of the profitability of using sugarcane and energy cane crops to increase the power output to the grid have shown that increasing both the power output and the power to heat ratio of the Pioneer Mill on the island of Maui will lead to a rate of return of 30% under a set of selling price assumptions that include sale of electricity at 5 c/kWh. A typical steam plant under the same conditions would not be profitable[4]. The typical performance and economic improvement according to NREL is given in Table 2.

The PICHTR Gasifier

The U.S. Department of Energy (DOE) and the State of Hawaii joined with PICHTR in this cost-shared cooperative project, with the objective of scaling up the process development unit (PDU) of IGT Renugas® pressurized air/oxygen gasifier to a 45–90 ton/day engineering development unit (EDU) operating at 1–2 MPa using bagasse and wood as feed. Other participants in the project are IGT, the Hawaii Natural Energy Institute (HNEI), the Hawaii Commercial and Sugar Company (HC&S), and the Ralph M. Parsons Company, the architectural and engineering firm for the project. The site is the HC&S sugar mill at Paia, Maui, Hawaii. The National Renewable Energy Laboratory is providing project oversight in addition to systems analysis.

The scaleup will be completed in several stages, as shown in Figure 1.

The first phase, which is now being commissioned, consists of the design, construction, and preliminary operation of the gasifier to generate hot, unprocessed gas. The gasifier is designed to operate with either air or oxygen at pressures up to 2.2 MPa, at typical operating temperature of 850°–900°C. In Phase 1, the gasifier will be operated for about four months at a feed rate of 45 ton/day at a maximum pressure of 1 MPa. Following the end of Phase 1 in late 1995, a hot-gas cleanup unit will be added and operated for a planned period of about 500 hours to generate design data and experience with third generation ceramic candle filters. In late 1997, a gas turbine will be added to the system

to generate 3 to 5MW of electricity. In this phase, the gasifier feed rate will be 90 ton/day, and the system will operate at pressures up to 2.2 MPa. In a projected but not yet funded Phase 3, the system will be operated in an oxygen-blown mode to produce a clean syngas for methanol synthesis in addition to producing electricity. Discussions are underway with interested commercial partners which could focus on a 1–2 MW power producing system.

A key element of the development in Hawaii will be to prove the suitability of ceramic barrier filters in gas turbine applications. PICHTR is working with Westinghouse, IGT, Gilbert Commonwealth, and the National Renewable Energy Laboratory to demonstrate this technology and have just completed short duration testing of a hot gas cleanup train on the Renugas® pressurized air-blown fluidized bed gasifier at IGT in Chicago. The tests in Chicago demonstrated that ceramic barrier filtration technology is effective in this application; however, the first generation ceramic filters used will not have a sufficiently long service life at the severity projected in this application. More advanced and more stable filters are now available for the following on testing at the BGF.

The project in Hawaii will establish the operational experience and broad data base needed to demonstrate full scale viability of the technology.

---

4 PICHTR Sustainable Biomass Energy Program, NREL LOI—Maui Project. Draft Report dated May 1995

Table 1. Sugarcane Production Statistics

WORLD CANE PRODUCTION
Source FAO—Agristat database 1990
Data in 1,000 tonnes (kt)

BY DEVELOPMENT CLASS			GEOGRAPHICAL DISTRIBUTION		
World	1,035,096				
Developed	72,193				
North America		24,575	N&C America	173,278	
Europe		256	USA		24,576
Oceana		26,226	South America	332,016	
Other		21,135	Africa	72,982	
Developing	962,903		Asia	426,006	
Africa		38,839	Europe	256	
Latin America		480,718	Oceana	30,559	
Near East		17,316			
Far East		421,698			
Other		433			
Least Developed		25,021			

Table 2. Comparison of Present Day Steam Generation With IGCC[5]

COST FACTORS (¢/kWh)	STEAM GENERATION	IGCC
Operations and Maintenance	0.5	0.5
Fuel Only Cost	3.6	1.6
Capital Recovery	4.2	3.0–3.5
Cost of Electricity	8.3	5.1–5.6

Notes to Table 2. Assuming a marginal cost of fuel of $2/million Btu (or approxmately $40/tonne of dry Biomass), a load factor of 85% (base loaded), and a return on capital invested of 8%/year, it is possible to see the effect of the new technology. Both plants are approximately 50 MW_e capacity. The efficiency of the steam plant is about 20%, while the IGCC is estimated to have an efficiency of 45%. The capital cost of the steam plant is $1.8/W, while that of the IGCC is expected to be in the range of $1.3 to $1.5/W.

Fig. 1

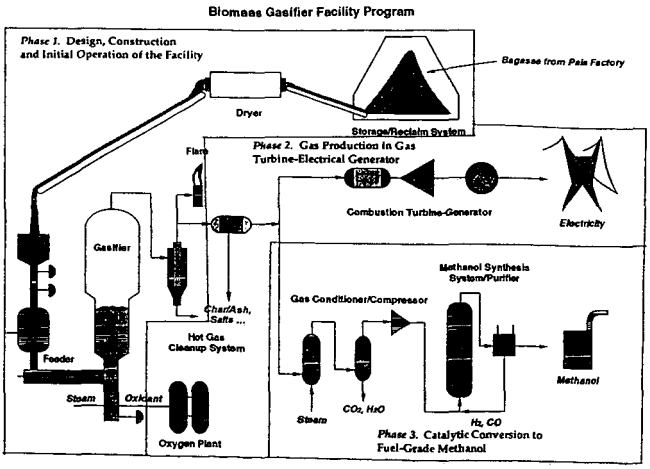

[5] Table generated from systems studies by Kevin Craig and R.P. Overend, NREL

NUMERICAL MODELING OF A DEEP, FIXED BED COMBUSTOR

Kenneth M. Bryden, M.S., Graduate Student; and Kenneth W. Ragland, Ph.D., Professor
Department of Mechanical Engineering
University of Wisconsin - Madison
Madison, WI 53706 USA

Keywords: Computational Modeling, Biomass Combustion, Whole-Tree-Energy

INTRODUCTION

A steam power plant utilizing whole trees as the renewable fuel (Whole-Tree-Energy™) is being developed by Energy Performances Systems, Inc. of Minneapolis, MN [1]. Hardwood trees are grown and harvested on energy plantations, or harvested from inferior, over-aged standing trees, transported in trucks as whole trees, and stored in a large covered stack at the power plant site where the stack is dried with waste heat from the power plant. When dried to the desired moisture content, the whole trees are burned in a fixed bed boiler. This innovative system completed stacking, drying and combustion tests at a site near Aurora, MN in August, 1992 [2].

The advantages of the proposed system are 1) time, energy and processing costs are saved by not chipping the wood, 2) a 30 day supply of wood may be stored on site without degradation of the fuel, and 3) the combustion heat release per unit plan area is greater than with wood chips. The concept is envisioned for 25 MW to 400 MW Rankine cycle power plants.

In the WTE combustor a ram feeder located 6 m above a fixed grate injects batches of trees trimmed to 8 m in length (for a 100 MW plant) with trunks up to 20 cm in diameter. The fuel feed rate is set to maintain a fuel bed 3 to 5 m deep on a grate. Preheated air is blown upwards through the fuel bed such that the lower section of the bed has an oxidizing environment and the upper part of the fuel bed has a reducing environment. Combustion is completed by means of overbed air jets.

Tree sections are fed onto the top of a deep, fixed bed of reacting wood. These sections are dried further and pyrolized forming a char layer on the outside of the log. Pyrolysis products and moisture flow outward through the char layer. Typically the oxygen flux will be zero in the upper part of the bed, and the char will react with the carbon dioxide and water vapor. The surface of the char will be heated by the gaseous products and cooled by the reducing reactions of carbon dioxide and water vapor with the char. As the fuel moves downward in the bed, the char layer will grow in thickness as the inner core of the undisturbed wood is pyrolized more rapidly than the outer char surface is consumed. In the lower portion of the bed oxygen becomes available to react with the pyrolysis products. When the log is completely dried and pyrolized in the lowest portion of the bed the oxygen reacts directly with the char and the char is consumed rapidly, causing the entire bed to move downward. The overall bed heat release rate depends on the heat and mass transfer to the logs, the formation of the char layer, the reaction rate of the char with oxygen, carbon dioxide, and water vapor, and the nature and rate of reaction of the pyrolysis products.

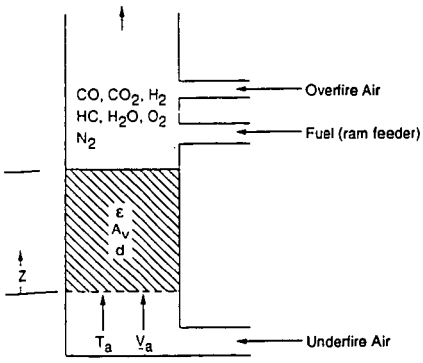

Fig. 1. Schematic of deep bed combustor.

DESCRIPTION OF THE MODEL

The model is a one-dimensional, steady state model for a top feed, updraft, packed bed combustor (Fig 1). It is assumed that the walls are adiabatic. The char reaction is assumed to be the rate limiting step and sets the pyrolysis rate [4]. An initial log diameter and a constant void fraction are used to characterize the pile, and the logs are assumed to be oriented across the gas flow. The surface area to volume ratio of the fuel is determined at each distance step in the bed as a function of diameter. As the log shrinks due to reaction with oxygen, carbon dioxide, and water vapor; moisture and wood volatiles are released

Table 1. Chemical Reactions Used in the Model.

Reaction #	Chemical Reaction	Heat of Reaction (kJ/kg)
1	$2\,C + O_2 \rightarrow 2\,CO$	9,211
2	$2\,CO + O_2 \rightarrow 2\,CO_2$	10,107
3	$C + CO_2 \rightarrow 2\,CO$	-14,372
4	$C + H_2O \rightarrow H_2 + CO$	-14,609
5	$CH_{0.152}O_{0.028} + 0.867\,O_2 \rightarrow 0.761\,H_2O + CO$	17,473
6	$2\,H_2 + O_2 \rightarrow 2\,H_2O$	142,919

from the wood. For dry wood the ratio of wood consumed to char consumed is initially high at the top of the bed as the wood is rapidly pyrolized in the furnace environment and decreases as the diameter shrinks. When a 3 cm diameter is reached, the fuel remaining is assumed to be all char. The ratio is set based on data from the single log combustion tests performed in a specially designed furnace under conditions related to the WTE system [3]. The model solves the equations of conservation of mass and energy for the solid, conservation of mass and energy for the gas, and conservation of gas phase species. Seven gas phase species are considered; oxygen, nitrogen, hydrogen, water vapor, carbon dioxide, carbon monoxide, and nitrogen.

The gaseous species conservation equations in differential form are,

$$\frac{d(G_i)}{dz} = r_i \qquad [1]$$

where G_i and r_i are the mass flux per unit area and chemical reaction rate per unit volume of species i, respectively, and z is the height of the combustor. The chemical reaction rate for each gaseous species is formed from the reactions shown in Table 1 as follows:

$$r_i = \sum_{j=1}^{N_r} b_{i,j}\dot{w}_j + y_i r_{wood} \qquad [2]$$

where $b_{i,j}$ is the stoichiometric yield of species i in reaction j on a mass basis, $\dot{w}_j$ is the rate of reaction j, y_i is the mass fraction yield of species i due to the pyrolysis of wood (Table 2), and N_r is the number of reactions (N_r = 6). The reaction rates include both chemical kinetics and diffusion. The consumption rate of char is

$$r_{char} = b_{char,1}\dot{w}_1 + b_{char,3}\dot{w}_3 + b_{char,4}\dot{w}_4 \qquad [3]$$

The reaction rate of wood is

$$r_{wood} = r_{char}K_{wood} \qquad [4]$$

where K_{wood} is the ratio of wood consumed to char consumed.

The mass flux of the gas is

$$G_g = \sum_{i=1}^{N_s} G_i \qquad [5]$$

where N_s is the number species. Conservation of mass for the solid is

$$(1-\varepsilon)\rho_s \frac{dV_s}{dz} = r_s \qquad [6]$$

where ε is the void fraction of the bed, ρ_s is the density of the solid, r_s is the net reaction rate per unit volume of the solid, and V_s is the downward solid velocity.

Conservation of energy for the gas is,

$$\frac{d(G_g h_g)}{dz} = \sum_{j=1}^{N_r} \Delta H_j \dot{w}_j - y_{H_2O} r_{wood} \qquad (7)$$

where h_g is the enthalpy of the mixture and ΔH_j is the heat of reaction for reaction j. Conservation of energy for the solid is based on a surface energy balance,

$$A_v h_{conv}(T_s - T_g) = \Delta H_1\dot{w}_1 + \Delta H_3\dot{w}_3 + \Delta H_4\dot{w}_4 + \dot{m}_r h_r - \dot{m}_p h_p \qquad [8]$$

where h_{conv} is the convective heat transfer coefficient, A_v is the char surface area per unit bed volume, h_r is the enthalpy of the reactants, and h_p is the enthalpy of the products including pyrolysis products. The convective heat transfer coefficient is obtained from a correlation for non-reacting beds [5] with a screening factor to account for mass transfer [6].

Table 2. Mass Fraction Yield of pyrolysis products of dry, ash free wood [7].

char	0.200
water	0.250
hydrocarbons	0.247
carbon monoxide	0.183
carbon dioxide	0.115
hydrogen	0.050

The boundary conditions for the inlet air velocity, temperature, and the gas composition are specified at the grate ($z = 0$). The solid velocity of the fuel at the grate is zero. Log size and as-received moisture content are specified at the top of the bed. Eqs. 1 through 8 are solved by using a differential-algebraic implicit solver.

VALIDATION OF THE WTE COMBUSTOR/GASIFIER MODEL

Combustion tests were run at Aurora, MN in August 1992 using a 1.4 m by 2.6 m by 3.7 m deep bed of hardwood logs with an average top size of 20 cm and an average as-received moisture content of 31.6%. The fuel was supported by cooled steel tubes 6.4 cm diameter on 22 cm centers. The underfire air was preheated to approximately 275°C and the average air flow rate was 565 kg/min, which gave an inlet velocity under the bed of 3.8 m/s to 4.1 m/s. The average wood burning rate during the 2 hr test was 162 kg/min, and the average burning rate per plan area was 2670 kg/hr-m². The heat release rate per unit plan area was 10.1 MW/m², and the peak was 12.9 MW/m². These heat release rates are high compared to a coal-fired spreader-stoker because of the deep fuel bed and the high inlet air velocity.

The simulation model was run for the above conditions assuming a representative fuel size of 17.8 cm, a bed void fraction of 0.60, inlet air temperature of 260° C, and an inlet air velocity of 3.95 m/s. The lowest portion of the fuel bed consists of small diameter char where the oxygen is rapidly consumed and the temperature rises rapidly. Above the oxidizing region is an extended reducing region where the logs slowly are dried and pyrolyzed and the char layer reacts with carbon dioxide and water vapor. The predicted burning rate per unit area for these conditions and assumptions is 2960 kg/hr-m², which compares well with the measured burning rate of 2670 kg/hr-m². Assuming a higher heating value of 19.1 MJ/kg for dried wood, the corresponding heat release rate is 10.7 MW/m², which is within 6% of the Aurora test.

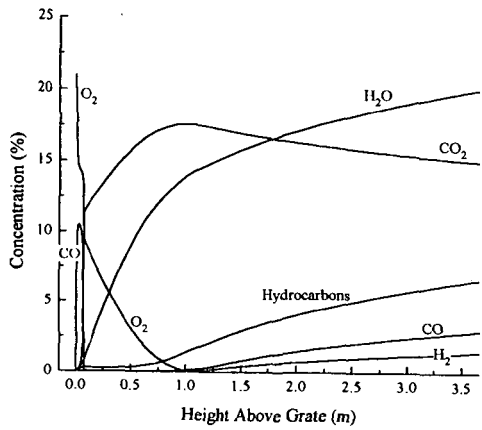

Fig. 2. Gas species concentration vs. height above grate. Inlet air preheat of 400°C, fuel moisture content of 23%, underfire inlet air velocity of 3.7 m/s, and bed height of 3.7 m.

SIMULATED PERFORMANCE OF THE WTE COMBUSTOR/GASIFIER

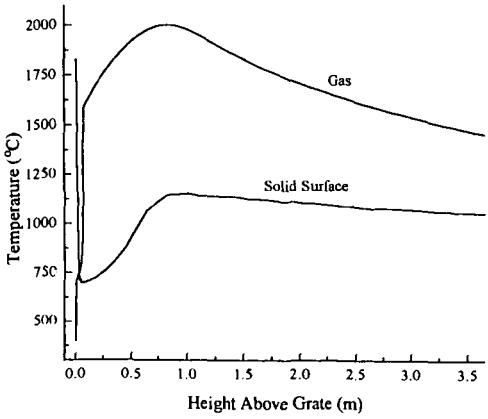

Fig. 3. Solid surface and gas temperature vs. height above grate. Inlet air preheat of 400°C, fuel moisture content of 23%, underfire inlet air velocity of 3.7 m/s, and bed height of 3.7 m/s.

The proposed design conditions for the combustor/gasifier for a 100 MWe WTE power plant specify a 4.3 m by 8.5 m by 3.7 m deep fuel bed of hardwood logs with a average top size of 20 cm diameter with 23% as-received moisture, and 400°C inlet air temperature. Keeping all the other model parameters the same as the validation run above, the predicted heat release rate is 9.5 MW/m² with an inlet air velocity of 3.2 m/s. Overfire air is needed to complete combustion, and the predicted overfire air to underfire air ratio is 0.85. The predicted gaseous species profiles in the fuel bed for the design case with an inlet air velocity of 3.7 m/s are shown in Fig. 2. The first 25% of

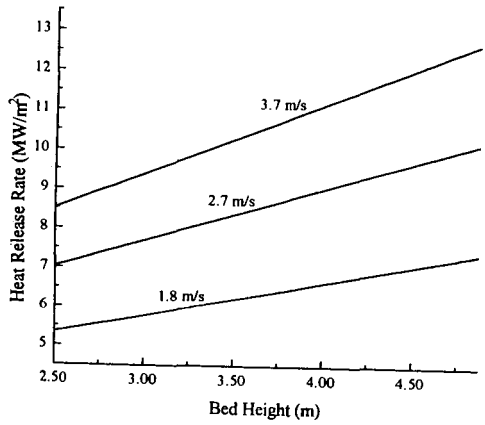

Fig. 4. Heat release rate vs. bed height and underfire air velocity. Inlet air preheat of 400°C and fuel moisture content of 23%.

the bed (~1 m) is an oxidizing region in which the oxygen is completely consumed. The upper 75% of the bed is a reducing region in which the char-carbon dioxide and char-water vapor reactions dominate. The hydrocarbons, carbon monoxide, and hydrogen that are formed in reducing region, are burnt out in the overfire air region. The fuel is pyrolyzing in the upper 98% of the bed and pure char exists only in the lowest 2% of the bed. The predicted gas and solid surface temperatures are shown in Fig. 3. The solid surface temperature just above the grate is high because the high oxygen concentration is reacting with pure char. As the char surface reaction decreases and as the volatiles and moisture escape through the surface of the fuel, the surface temperature is reduced rapidly, but then rises further above the grate due to heat transfer from the gaseous combustion products. At about 1 m above the grate the oxygen is consumed and the char reducing reactions gradually decrease the temperatures. The gas velocity at the top of the bed, prior to the overfire air, is 12.5 m/s when the inlet air is 3.2 m/s.

Several different options are available to the designer and operator to meet the goal of producing a given heat release rate to meet a given load. The underfire inlet air velocity may be changed by changing the air flow rate. The underfire air temperature may be changed by adjusting the air preheat. The fuel bed height may be increased or decreased by adjusting the fuel feed rate, and the fuel moisture content may be changed by adjusting the drying time. The impact of these is as follows:

1. Increasing the underfire air velocity causes a higher burning rate as the oxygen penetrates further into the bed. This consumes more char increasing the overall temperature, increasing the heat transfer to the fuel. This in turn increases the drying and pyrolysis of the fuel. However, excessive air velocity will cause higher pressure drop across the bed, more carry-over of partially burned fuel particles, and possible tube erosion. The predicted combined effect of increasing the inlet air flow and the bed height on the heat release rate is shown in Fig. 4.
2. Increasing the bed height lengthens the gasification zone and also increases the heat release rate, provided more overfire air is used.
3. Increasing the underfire air preheat decreases the fuel burning rate for a fixed underfire air velocity, because less air mass flow is delivered to the fuel bed (Fig. 5). Although the chemical reaction rates tend to be increased by increased temperature, the reactions in the bed are more limited by mass transfer than kinetics.
4. Increasing the fuel moisture content decreases the pyrolysis rate because the temperatures are lowered, thus lowering the heat release rate, all else remaining constant (Fig. 6).

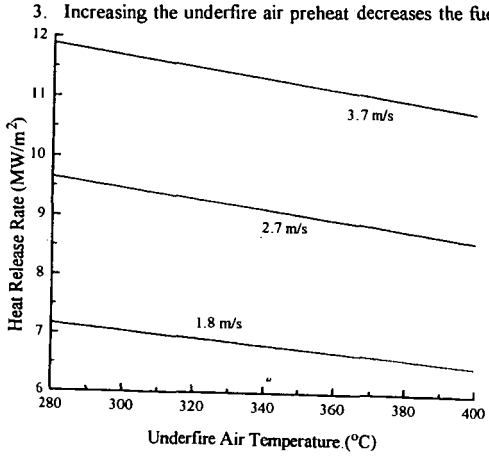

Fig. 5. Heat release rate vs. underfire air temperature and underfire air velocity. Bed height of 3.7 m and fuel moisture of 23%.

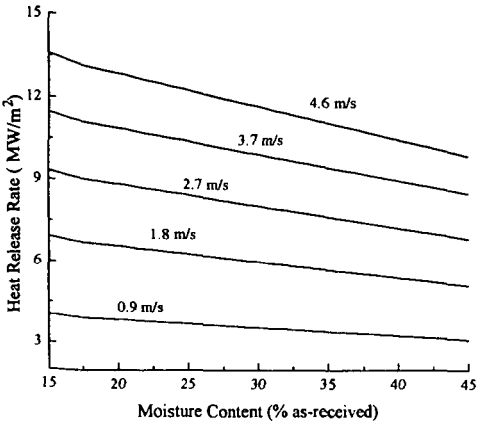

Fig. 6. Heat release rate vs. fuel moisture content and underfire air velocity. Inlet air preheat of 400°C and bed height of 3.7 m.

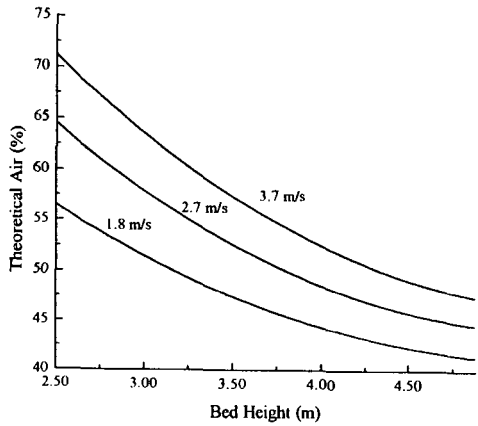

Fig. 7. % theoretical air vs. bed height and underfire air velocity. Inlet air preheat of 400°C and fuel moisture content of 23%.

The theoretical air required for complete combustion varies primarily with bed height and underfire inlet air velocity (Fig. 7). As the bed height is increased, more fuel is gasified, but a limit is reached because the gas temperature drops too low to support the reduction reactions and the carbon dioxide is consumed.

CONCLUSIONS

A computational model for the WTE combustor has been developed and adjusted to within 6% of heat output of 10.1 MW/m2 of the Aurora, MN test run. The deep, fixed bed combustor obtains high energy release rates due to the high air velocity and extended reaction zone. The lowest portion of the bed is an oxidizing region and the remainder of the bed acts as a gasification and drying zone. For the 100 MW design case with 23% fuel moisture, inlet air preheat of 400°C, and underfire air inlet velocity of 3.2 m/s; the predicted heat output per unit bed area is 9.5 MW/m². The heat output of the combustor/gasifier can be changed by altering the underfire air flow rate, the bed height, the air preheat, and the fuel moisture.

ACKNOWLEDGMENTS

This work is funded by the Electric Power Research Institute under contract RP3407-07 and directed by Evan Hughes, EPRI project manager.

REFERENCES

1. Lamarre, L., "Electricity from Whole Trees," *EPRI Journal,* 19(1):16-24 (1994).

2. Schaller, B. J., L. D. Ostlie, and R. E. Sundberg, "Program to Test Key Elements of the WTE™," EPRI Report TR-101564 (1993).

3. Bryden, K. M. and K. W. Ragland, "Burning Rate of Single Logs in a Controlled Convective Environment," Unpublished Paper (1995).

4. Ragland, K. W., J. C. Boerger, and A. J. Baker, "A Model of Chunkwood Combustion," *Forest Products Journal,* 38(2):27-32 (1988).

5. Wakao, N. and S. Kaguei, *Heat and Mass Transfer in Packed Beds,* Gordon and Breach, p. 292 (1982).

6. Kays, W. M. and M. E. Crawford, *Convective Heat and Mass Transfer,* McGraw-Hill, Third Ed., p. 507 (1993).

7. Ragland, K. W., D. Aertz, and A. J. Baker, "Properties of Wood for Combustion Analysis." *Biosource Technology,* 37:161-168 (1991).

MATEMATICAL MODELLING OF STRAW BALE COMBUSTION IN CIGAR-BURNERS

Niels Bech
Department of Combustion Research
Risø National Laboratory
DK-4000 Roskilde
Denmark

Lars Germann
Danish Technological Institute
Teknologiparken
DK-8000 Århus C
Denmark

Lars Wolff
I/S VESTKRAFT
Vestkraftkaj 2
DK-6701 Esbjerg
Denmark

Keywords: Combustion, Mathematical Modelling, Straw

ABSTRACT

This paper describes a computer model for the calculation of the steady and non-steady behaviour of straw bales subject to surface combustion in cigar burners. The mathematical formulation is one-dimensional and the flow of gas through the straw bales is described by means of Darcy's law for flow through a porous medium. The computer model is able to predict flow rate, temperature and composition of gas and straw as function of axial length and time. Calculated results are compared to measurements of temperature- and gas composition profiles within the burning straw bales. It is observed that the straw bale temperatures as well as the outlet gas composition are predicted reasonably well. Calculations have been carried out in order to assess the implication of a straw bale feed stop in a 3 MW district heating plant fueled with Heston straw bales. The results indicate serious disturbancies in the performance of the burner.

INTRODUCTION

A computer model, STRAW, has been developed for the calculation of the steady and non-steady behaviour of surface combusting straw bales[1]. Parallelling the theoretical efforts experiments have been carried out with the purpose of measuring temperature and concentration profiles within the burning straw bales as well as in the furnace room[2-3]. The measurement have been used in the validation of STRAW.

The principle of surface combustion of straw bales is illustrated in figure 1 after Gundtoft[4].The straw bales are fed from the left at a rate corresponding to the combustion rate in such a way that the burning bale front remains at a fixed position. The figure shows the different process areas. Due to diffusion and subsequent condensation of water vapour a zone of straw with a water content higher than that of raw straw may appear. As the temperature rises the straw is dried and after that it undergoes pyrolysis. The required heat is transported from the burning surface through thermal conduction and radiation. When the devolatilization of the straw is finished straw char remains. The burning of the char finally results in a layer of ash or slag. Primary air is injected for the combustion at the straw surface, while oxygen for the combustion in the furnace room of the remaining gases is provided by a secondary air stream.

THE COMPUTER MODEL STRAW

For a more detailed description of the mathematical model conf. reference 1.

Assumptions. The following assumptions are made:

1. The system is one-dimensional in space.
2. The cross sectional area of the straw bales is constant.
3. The gas is described as an ideal gas.
4. The flow of gas through the straw grid is described by means of Darcy's law for flow through a porous medium.

5. The velocity of the straw grid is constant in the axial direction(but not in time).
6. The porosity and the permeability of the straw grid depends upon time and the location in the bale.
7. Only water vapour diffusion is considered at the moment.
8. Straw-gas and gas-gas thermal radiation is neglected in the straw bales.

Basic Equations.
Mass conservation for component no. i in the gas phase:

$$\frac{\partial m_g^i}{\partial t} + \frac{\partial \left(m_g^i u_g^i\right)}{\partial x} = \Gamma^i + S_g^i \tag{1}$$

Mass conservation for component no. i in the straw:

$$\frac{\partial m_h^i}{\partial t} + u_h \times \frac{\partial m_h^i}{\partial x} = -\Gamma^i - S_h^i \tag{2}$$

Energy equation for the gas phase:

$$\frac{\partial e_g}{\partial t} + \frac{\partial \left(e_g u_g\right)}{\partial x} = Q_g + \sum_i \left(\Gamma^i h_p^i + S_{inj}^i h_{inj}^i\right) \tag{3}$$

Energy equation for the straw:

$$\frac{\partial e_h}{\partial t} + u_h \times \frac{\partial e_h}{\partial x} = Q_h - \sum_i \Gamma^i h_p^i + \frac{\partial}{\partial x}\left(\lambda_h^* \frac{\partial T_h}{\partial x}\right) \tag{4}$$

Momentum for the gas phase (Darcy's law):

$$u_g = u_h - \frac{K}{\mu_g}\left(\frac{dp}{dx} + g\, cos\Theta \rho_g\right) \tag{5}$$

Symbols:

g	Acceleration of gravity [m/s^2]
K	Permeability of straw grid [m^2
p	Gas pressure [Pa]
Q	Heat production per unit volume [W/m^3]
S	Mass source/sink [kg/m^3/s]
T	Temperature [C]
u	Velocity [m/s]
Γ	Transfer of mass from straw grid to the gas phase per unit volume and time [kg/s/m^3]
h	Enthalpy [J/kg]
λ^*	Effective thermal "conductivity" of straw grid which takes into account heat conduction as well as thermal radiation [W/m/C]
μ	Dynamic viscosity of gas [kg/m/s]
ρ	Density of gas [kg/m^3]
Θ	Angle between x-axes and vertical [degrees]

EXPERIMENTAL DESIGN

A test facility for burning straw bales has been constructed (see fig. 2). It is capable of burning straw packed in small bales of 10-12 kg each by means of surface combustion, i.e. the bale is not torn up, but is burnt from one end to the other. Primary air is being injected directly to the straw surface by means of air nozzles. The remaining part of the air is being added in the main duct, giving an excess air ratio of about 1.7. Directly in front of the straw surface is an electrically heated zone giving a heat flux to the straw, and thereby illuding a combustion chamber with hot walls. By means of probes inside the straw bale, measurements of temperatures and gas concentrations during the whole combustion process have been performed. For a more detailed description see references 2 and 3.

COMPARISON TO MEASUREMENTS

Straw bales constitute a very inhomogeneous fuel. Fig. 3 shows measured temperatures for four "near identical" experiments. The calculated temperatures are shown as well. The burning straw bale surface is located where the temperature reaches its first maximum around 1000 centigrade (around $x = 230$ mm in the figure). It is seen that the rise in straw bale temperature close to the burning surface as well as the temperature at the surface are predicted reasonably well.

The measured concentrations at the burning surface shown in table 1 are averages for the four experiments. It is seen that the gas concentrations of CO_2, CO and C_xH_y are also predicted reasonably well although the amount of C_xH_y is slightly underestimated. The gas composition inside the straw bale close to the burning surface (which is not shown here) is not predicted well enough. This is believed to be due to the fact that the model does not account for turbulent diffusion of the gas phase components. In the calculation it has been assumed that 80 % of the primary air is available for combustion at the straw bale surface.

CALCULATED FEED STOP IN CIGAR BURNER

One event which is known to cause problems in a cigar burner in terms of a deterioration of the combustion and increased pollution is the stop in the straw bale feeding which occurs in some plants in connection with the delivery of a new straw bale. Calculations have been carried out in order to assess the implication of a straw bale feed stop in a 3 MW district heating plant fueled with Heston straw bales.

The straw bale feed and air injection are interrupted for 60 seconds and then continued from $t = 75$ sec. at the previous rates. In fig. 4 are shown the inlet and exit mass flow rate of straw carbon W^C_{hin} and W^C_{hex}, respectively. The amount fed at the inlet drops to nil after 15 sec. and increases to the initial rate at 75 sec. The exit value is zero initially at the normal operating conditions. This means that all the straw carbon is burned at the straw surface. It is seen however, that when the feeding starts again at $t = 75$ sec then W^C_{hex} becomes positive for a short period of time ($\simeq 5$ sec). In other words, unburned straw carbon falls into the combustion chamber when the straw feeding is restarted. The reason is that the temperature at the straw surface drops about 200 degrees during the feed stop, conf. fig. 5.

SUMMARY AND CONCLUSIONS

A computer model, STRAW, has been developed for the calculation of the steady and non-steady behaviour of surface combusting straw bales. Model predictions have been compared to measurements of temperature- and gas composition profiles within the burning straw bales and calculations have been carried out in order to assess the implication of a straw bale feed stop in a 3 MW district heating plant fueled with Heston straw bales.

Comparisons between calculated and measured results show that:

- The rise in straw bale temperature close to the burning surface as well as the temperature at the surface are predicted reasonably well.
- The concentrations of CO_2, CO and C_xH_y in the exit gas are also predicted reasonably well although the amount of C_xH_y is slightly underestimated.
- The gas composition inside the straw bales close to the burning surface is not predicted well enough probably because the model does not account for turbulent diffusion of the gas phase components.

It has been shown that an interruption of the feed for 60 sec causes violent disturbancies in the computed performance of the burner. Unburned straw carbon is pushed into the combustion chamber when the straw feeding is restarted. In order to maintain good burner performance it is essential to avoid this behavior. This can be done by introducing a continuous feeding system which maintains the straw bale feeding rate at the operating value.

ACKNOWLEDGEMENTS

The work which has been supported by the Danish Ministry of Energy's energy research programme EFP-92 has been carried out in cooperation with the Department of Energy Technology at the Danish Technological Institute in Aarhus and Vølund R & D Center in Kolding.

REFERENCES

1. Bech, N. "Modelling of the Vølund Cigar Burner by means of the Computer Model STRAW", Risø-R-817, Risø National Laboratory, Roskilde, Denmark, 1995.
2. Wolff, L. "Forsøgsopstilling til forbrænding af halmballer ('Pyrolyseforsøg)", Risø-R-721 (DA) Forskningscenter Risø, december 1993.
3. Wolff, L. and Bech, N. "Surface combustion of straw bales, a test facility for pyrolysis investigations", 8'th European Conference on Biomass for Energy, Environment, Agriculture and Industry, Vienna, 3-5 October, 1994.
4. Gundtoft, S. "Forbrænding af halm i mindre anlæg", Jysk Teknologisk, august 1989.

	O_2	CO_2	CO	C_xH_y
Measured	0.04	0.14	0.14	0.015
Calculated	0.04	0.15	0.14	0.011

Table 1: Comparison of measured and calculated concentrations in the gas at the burning straw bale surface

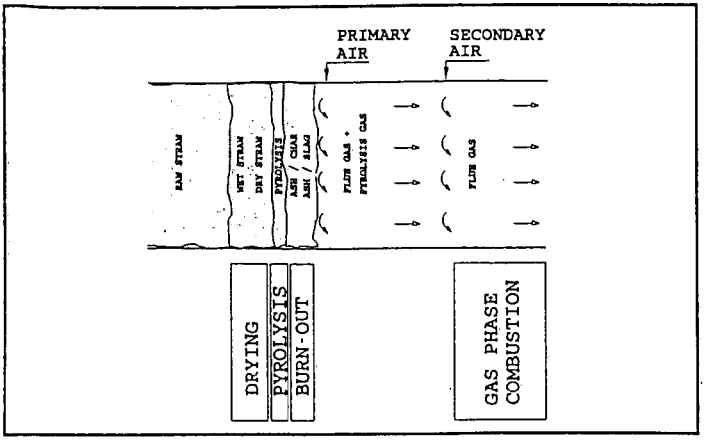

Figure 1: Surface combustion of straw. Definition of processes and zones.

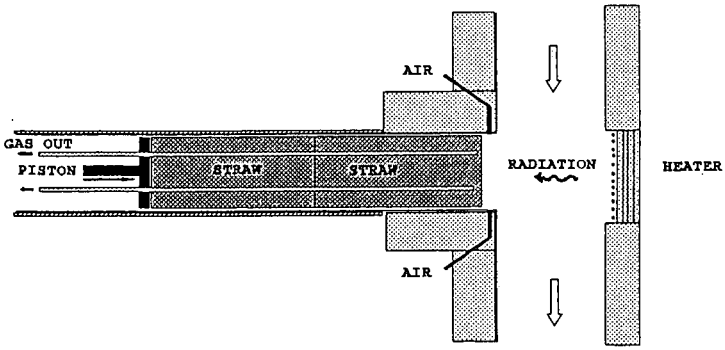

Figure 2: Experimental setup.

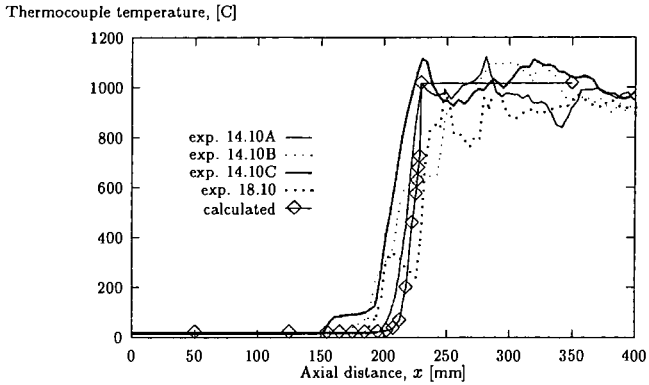

Figure 3: Comparison of measured and calculated thermocouple temperatures

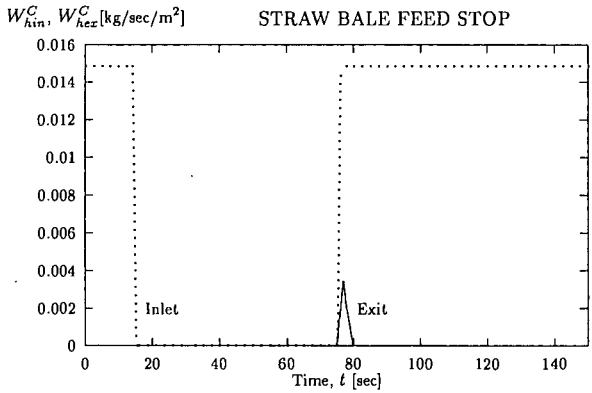

Figure 4: Inlet and exit mass flow rate of straw carbon for straw bale feed stop

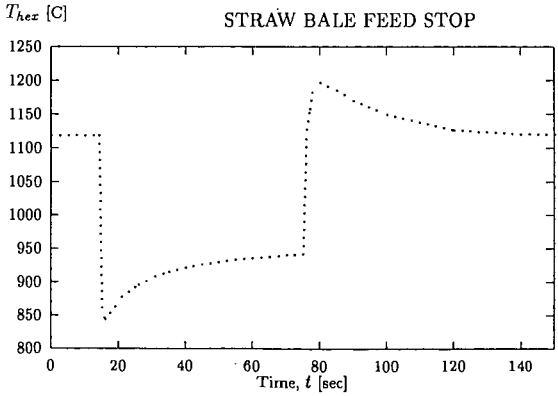

Figure 5: Calculated exit straw temperatures for straw bale feed stop

ORGANIC EMISSIONS FROM COMBUSTION OF PLYWOOD AND PARTICLEBOARD

Jeffrey M. Hoerning, Michelle A. Evans, Danny J. Aerts, and
Kenneth W. Ragland
Department of Mechanical Engineering
University of Wisconsin-Madison, Madison, WI 53706

Keywords: wood combustion; volatile organic emissions

INTRODUCTION

Large amounts of wood, wood waste and manufactured wood products are burned on grates to produce process heat and electricity in industrial boilers. Industrial combustion chambers generate high temperatures for relatively long residence times, however emissions of volatile organic substances are of concern if the residence time, temperature and turbulence are inadequate. The typical industrial plant does not measure volatile organic emissions, but does measure oxygen and carbon monoxide concentrations. With sufficient excess O_2 and low enough CO, the organic emissions are thought to be acceptably low. For example, the Wisconsin Department of Natural Resources specifies good combustion practice as CO less than 600 ppm corrected to 7 % oxygen plus temperatures greater than 675°C for 1.0 s. The purpose of this project was to determine the adequacy of this criteria with respect to volatile organic emissions for selected wood and manufactured wood products in a laboratory combustor.

Manufactured wood products contain wood, wood fiber, and non-wood additives such as adhesives, wood preservatives and fire retarding chemicals. Secondary manufacturing processes can add plastic overlays, paints, varnishes, lacquers, fillers, strength additives, and dyes. Primary wood products include lumber, plywood, composition board, and pulp and paper. Primary residue is in the form of edge trimmings, sawdust, sander dust, shavings, and fiber sludge, which could be used to replace fossil fuels for steam generation at the industrial site. Eventually the manufactured products are discarded, and rather than going to a landfill, the wood products may be burned in a boiler.

Particleboard is made from sawdust and contains 6% phenol-formaldehyde resin solids. Because of the phenol formaldehyde resin, there is concern that the formaldehyde emissions may be higher than in pure wood. Formaldehyde is considered a hazardous air pollutant by the 1990 Clean Air Act. Under proper operating conditions a wood-fired, spreader-stoker boiler has low formaldehyde emissions, however when the temperature and/or excess oxygen are too low, the formaldehyde emissions can be high [1].

TEST SETUP

The combustor is a 13 cm i.d. by 5 m long chamber made from low density Ceraform ceramic risers which are 13 cm i.d., 30 cm o.d. by 30 cm long. The insulation tubes were force fit into a long steel tube assembly which was hung vertically from a fixed platform as shown in Fig. 1. A propane burner was fitted into the bottom of the combustor for startup, and a mullite honeycomb grate was mounted 60 cm above the burner. Two underfire air opposed jets were located 20 cm below the grate and two overfire air opposed jets were located 40 cm above the grate. The fuel feeder was mounted in a stainless steel tee at the top of the combustor. The combustor exhaust flowed to a wet scrubber and induced draft fan.

Single 11 mm pine plywood cubes were fed at constant rate into the top of the combustor and fell quickly by gravity onto the grate. The cube feed rate must be very constant to maintain constant combustion conditions. The cube feeder consisted of a vibrating hopper feeding the cubes onto a stainless steel, Teflon coated chute. Cubes were held at the bottom of the chute until a rod driven by a pneumatic cylinder, pushed the cube into the combustor. A solenoid turned the air to the cylinder on and off. A pulse generator controlled the timing of solenoid and a counter, which gave the time between pulses, indicated the feed rate of the cubes.

The untreated southern pine cubes had a density of 0.55 g/cm^3 and contained about 8% moisture. The particleboard, which was

southern pine with 6% phenol-formaldehyde based resin, had a density of 0.80 g/cm^3. The plywood was made of southern pine and had a density of 0.65 g/cm^3.

MEASUREMENT METHODS

For detection of aromatic compounds during combustion, a known volume of sample gas was drawn through a collection tube which was connected to the side of the combustor through a 200 mm long, 3 mm id. stainless steel transfer line. To obtain an accurate sample volume of gas, a graduated sealed 3 liter acrylic tube was filled to a known level with water. During the sampling process the water was pumped out of the tube at a known rate. Displacing the water in the tube was the sample gas that was drawn through the adsorbent tube. The difference in volume from the initial and final level of water in the acrylic tube indicated the exact volume of gas that passed through the adsorbent tube. Two types of collection tubes were used. The first was a glass lined thermal desorption tube packed with 250 mg of Tenax-GR adsorbent. The second was a solvent desorption tube, ORBO-32 standard charcoal tube (Sulpelco).

The thermal desorption system was attached to the injection port of a Hewlett Packard 5890 Series II GC using both a 5971 Mass Selective Detector and a Flame Ionization Detector. The desorption heater was maintained at 300°C for the 10 min. desorption process. The sample was then cryo focused at the injector end of the GC column. The peaks were identified with the Wiley NBS library using Hewlett Packard Chemstation software. The GC capillary column is a 30 meter 0.53 mm i.d., 0.88 µm film thickness HP-5 Column (Hewlett Packard). A short 0.5 m by 0.53 mm i.d. deactivated fused silica guard column was used on the injection port end of the capillary column to provide an area for cryo focusing and to protect the capillary column. For solvent desorption, NIOSH method 1501 was used. After a known amount of sample gas was drawn through the desorption tube, the contents of the tube were added to 1 ml of carbon disulfide. A 1 µL sample was taken from this solution and injected into the same GC and column described above.

Single point calibration was performed every day for aromatic compounds being analyzed using certified calibration test mixes. For the thermal desorption, a known amount of calibration mix was added to the desorption tube through a special fitting (from Scientific Instruments) while passing He gas through the tube for 30 min. The tube was then analyzed in the typical manner. For solvent desorption a known amount of test mix was injected into the desorption tube, then the tube was capped and let stand overnight. The tube was then analyzed in the usual solvent desorption way.

CO, CO_2 and O_2 were continuously monitored during each run at the same sample point in the combustor that the GC sample was taken. These meters were calibrated daily with certified gas mixes.

TEST RESULTS AND DISCUSSION

Some tests were run using both underfire and overfire air, and some were run using extra nitrogen to lower combustor temperatures. However, the best operation was obtained using only underfire air, which is the condition reported here. Air flow was varied from 0.3 m^3/min. (std) to 0.9 m^3/min. (std) (1 m/s to 4 m/s). Residence time was varied from 0.5 s to 3 s by adjusting the air flow and by changing the sampling location. Sample ports were located at 1.9 m and 3.8 m above the grate. Fuel flow rate was varied to control combustor temperature and ranged from 15 g/min. to 70 g/min. The combustor required about 10 min. to warm up with the propane burner and about 10 min. to reach steady state with the wood cubes feeding. Combustor gas temperatures were measured at the centerline of tube at 0.9 m, 1.9 m, 2.5 m and 3.8 m above the grate. The vertical temperature drop above the first thermocouple was 50°C/m to 100°C/m depending on the conditions. The emissions data was correlated based on the gas temperature at the point of sampling.

The emissions of volatile organic compounds from the wood cubes depended on the excess oxygen, the gas temperature, and the residence time. Under fuel rich conditions high concentrations

of benzene, PAH's and formaldehyde were observed, with major abundances of benzene, naphthalene, acenaphthylene and anthracene. (Fig. 2). With high excess oxygen in the combustion products, polynuclear aromatic compounds were not observed, but benzene, and toluene were observed unless the temperatures were above 650°C. When excess oxygen was greater than 6 %, benzene concentrations ranged from undetected to 2 ppm, and toluene concentrations ranged from undetected to 0.4 ppm as the temperature was decreased.

The wood feed rate and the ppm concentration data were converted to an emission factor basis of μg/g wood. The results are plotted versus temperature at the sampling point, for two groups of residence times and for excess oxygen above 4% in Figs. 3 and 4 for benzene and toluene. For a residence time of 0.5 s to 1.5 s benzene emission factor averaged 7 ±5 μg/g wood for temperatures above 600°C, whereas below 600°C the emissions increased rapidly. When the residence time was increased to 2 s to 3 s, the emissions did not increase until the temperature dropped below 400°C. Toluene exhibited a similar behavior but the emissions were lower by a factor of 2. Carbon monoxide concentrations were below 1000 ppm when the temperature was above 650°C for residence times of 0.5 s to 1.5 s, and above 450°C for residence times of 2.0 s to 3.0 s. The CO increased rapidly for temperatures below these values. A cross plot of the benzene emissions versus CO concentration (Fig. 5) shows that the benzene is below 20 μg/g wood when the CO is below 4000 ppm. As the CO rises above 4000 ppm, the benzene emissions increase rapidly. Toluene shows a similar behavior.

Formaldehyde concentrations are plotted versus temperature at fuel rich conditions and 3% O_2 for particleboard (Fig. 6). Under rich combustion conditions, as the average temperature is reduced below 700°C the formaldehyde increased rapidly. At 3% oxygen the formaldehyde was less than 25 ppm. For pine plywood, concentrations of formaldehyde plus acetaldehyde were tested with O_2 at 15% and residence times of 0.9 sec. Tests were made using Kitagawa gas detector tubes. At 460°C 11 ppm (500 μg/g) of formaldehyde plus acetaldehyde was detected and at 530°C 3 ppm (130 μg/g) was detected at CO levels of 5000 - 6000 ppm.

Hubbard [1] measured benzene and formaldehyde emissions from a 20 million Btu/hr wood fired stoker boiler at a lumber and veneer plant. Benzene emissions ranged from 1 to 11 μg/g and formaldehyde ranged from 1 to 6 μg/g, and CO levels were between 200 and 700 ppm during the tests. Fritz and Hubbard [2] measured CO emissions from six wood fired boilers with a heat capacity of 7 to 20 million Btu/hr and found many exceedances above 600 ppm with some levels above 10,000 ppm. They suggest an upper CO limit of 1080 ppm in addition to an 8 hr ave. limit of 600 ppm for CO to give low VOC emissions. Fig. 5 indicates that benzene emission increase rapidly when the CO exceeds 4000 ppm. Low formaldehyde emissions require CO levels below several hundred ppm.

REFERENCES

1. Hubbard, J., Encouraging Good Combustion Technology at Wood-Fired Facilities in Wisconsin, National Biofuels Conference, Newton, MA, 1992.
2. Fritz, R.A. and Hubbard, A.J., Control of Hazardous Air Emissions from Wood-Fired Boilers, Bioenergy 94, pp. 335-341, 1994.

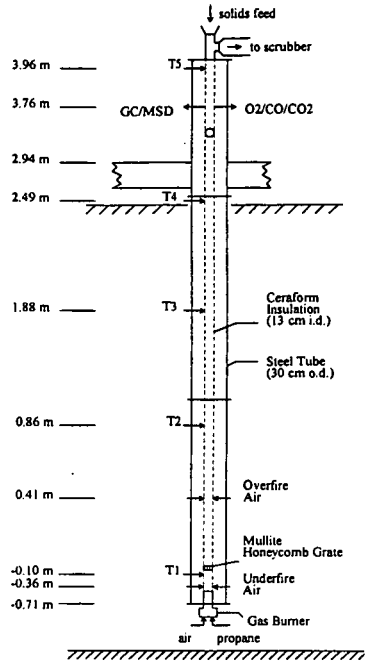

Fig 1. Fixed Bed, Up-Draft Combustor

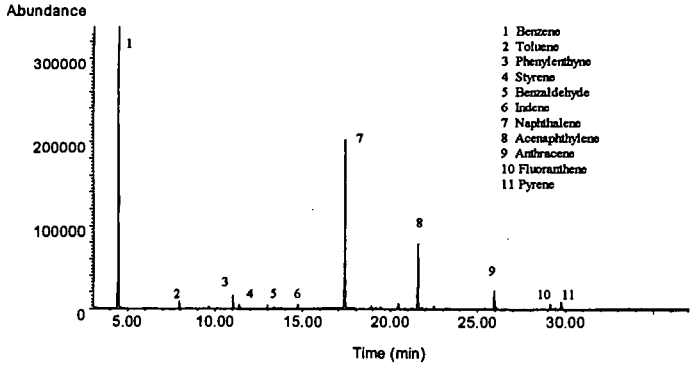

Fig. 2 Chromatogram of rich fuel conditions

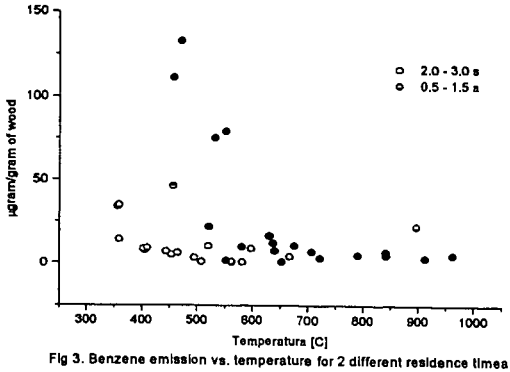

Fig 3. Benzene emission vs. temperature for 2 different residence times

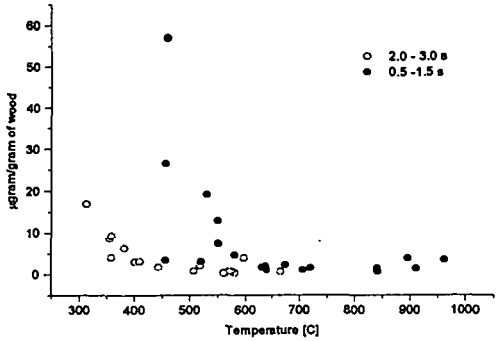

Fig 4. Toluene emission vs. Temperature for 2 different residence times

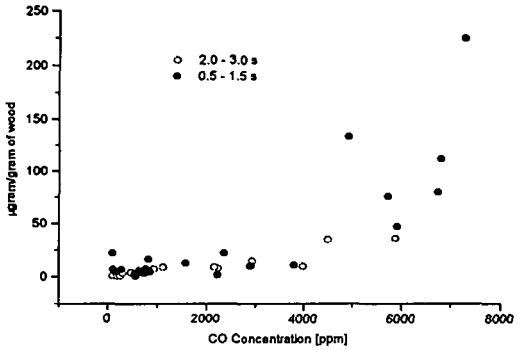

Fig 5. Benzene emission vs. CO concentration for 2 different residence times

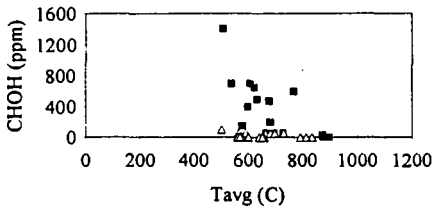

Fig 6. Formaldehyde Concentration vs. Average Temperature for Particleboard
Solid squares indicate rich combustion and open triangle indicates 3% O_2

PRODUCT ANALYSIS FROM THE OPERATION OF A 10 TON/DAY, DIRECT, FLUIDIZED BED, BIOMASS GASIFIER AND HGCU SYSTEM

Matthew A. Ratcliff[a], Michael Onischak[b], David A. Gratson[a], Joseph A. Patrick[a], Richard J. French[a] and Benjamin C. Wiant[c]

a) NREL, Golden, CO, 80401 b) IGT, Chicago, IL, 60632 c) Westinghouse, Orlando, FL, 32826

Keywords: Gasifier Products, Hot Gas Cleanup, Molecular Beam Mass Spectrometry

Introduction

A principal goal of the DOE Biomass Power Program is the development of advanced high efficiency electric power generating cycles, such as integrated gasifier-gas turbine-generator systems. A key technical development required to economically produce electric power with an integrated gasifier-turbine system is the ability to remove chars and alkali metals from the gasifier product gas stream, to protect the turbines, and do so at high temperature and pressure. Westinghouse hot gas cleanup (HGCU) technology, based on ceramic membrane candle filters, has been selected for validation in this application [1]. The HGCU system was tested at the 10 ton/day scale, using a direct, pressurized, fluidized bed gasifier [2]. Two tests were conducted at the Institute of Gas Technology (IGT) RENUGAS process development unit (PDU) in Chicago, IL, during the weeks of October 31-November 5, 1994 and February 5-11, 1995.

The overall objective of the Westinghouse/IGT HGCU performance test program was to evaluate the performance of the hot gas filters with a dust-laden product gas generated from the gasification of bagasse in the RENUGAS PDU. This filter performance information will be used to determine the HGCU operating conditions for subsequent extended testing of the hot gas filters installed in a slipstream from the 100 ton/day bagasse demonstration gasifier in Hawaii [3]. Initially there was concern that tars produced in the gasifier would undergo coking reactions within the ceramic candles, leading to irreversible plugging of the filters. Consequently, a tar-cracking reactor was designed and installed ahead of the HGCU to remove the tars.

In order to characterize the tars and the performance of the process, the National Renewable Energy Laboratory's (NREL) Transportable Molecular Beam Mass Spectrometer (TMBMS) was interfaced with the PDU to monitor the performance of the RENUGAS gasifier, tar-cracker and candle filter unit operations. The development of a comprehensive, on-line, process monitoring capability has been a long term goal of NREL's Industrial Technologies Division. We have realized that goal with the successful demonstration of the TMBMS during the Westinghouse/IGT tests.

Experimental

The design and construction details of the TMBMS have been covered elsewhere [4]. In this application the instrument was interfaced with the PDU by a heat traced sampling system that permitted manual selection of three sampling ports with high temperature ball valves, as shown schematically in Figure 1. The sample ports A, B and C were installed at the tar-cracker inlet, tar-cracker outlet, and HGCU outlet, respectively. The sampling system incorporated the following functions. Particulate was removed from the gas samples with stainless steel filters at process pressure (nominally 300 psig) and at a temperature $\geq 300°C$. The designed sample flow rate was 18.4 lb/h or 1% of the nominal process stream mass flow rate. The sample pressure was let-down in two stages with critical flow orifices (CFO1 and CFO2). The first stage caused the largest pressure drop from process conditions. A regulating valve between the CFO's was manually adjusted to maintain the pressure upstream of CFO2 at 20 psig by diverting most of the sample flow to vent. CFO2 dropped the pressure to 2-3 psig. The two stage CFO/diverted flow design of the sampling system enabled rapid detection of process fluctuations due to the dynamic nature of the sample flow.

The sample gas was then diluted 1:4 with preheated N_2 from a mass flow controller and a small amount of argon was blended (via mass flow controller) with the diluted sample as an internal standard. The sample then flowed through heat traced 0.5 inch stainless steel transfer lines to the TMBMS, while a constant temperature of 300° C was maintained. The diluted gas volumetric flow rate was measured by an orifice plate flow meter, just ahead of the TMBMS. This flow rate signal was recorded with the mass spectral data. The total diluted flow was directed past the TMBMS sampling orifice before being exhausted outside the building.

A port was provided in the sampling system for standards injection into the low pressure N_2 stream ahead of a static in-line mixer (see Figure 1). Multi-level calibration solutions of benzene, naphthalene, anthracene and pyrene were prepared. The standards were injected into the sampling system with a syringe pump several times each day, alone and as standard additions to sampled process gas.

IGT's sampling procedures for the PDU included product gas sampling at two points: downstream of the

gasifier and downstream of the tar-cracker. Gases, condensible liquids and entrained solids were collected from these points with iso-kinetic sampling systems, then separated for off-line analysis. The gases were analyzed with a Carle GC equipped with TCD and FID detectors. Immediately after the HGCU a Westinghouse alkali probe was installed. The product gas stream from this port was condensed and depressurized. The aqueous phase of the condensible liquids was analyzed for sodium and potassium. A breakthrough dust detector probe was installed at this same location. Solids collected on this probe were weighed but not analyzed because the quantity was too small. No gas or organic liquid analyses were performed from this third sample stream.

Results

The product gas composition measured by IGT, exiting the PDU gasifier is shown in Table 1. This raw gas composition reflects the non-optimized input of steam to the PDU and also nitrogen purges that are greater than would be used commercially. The condensed tar components collected after the gasifier measured 1.7 wt% of the bagasse feed on a moisture and ash free basis.

In the case of the TMBMS on-line measurements, tars are defined here as hydrocarbons with molecular weights starting with benzene on up. The TMBMS was programmed to scan to 350 amu (skipping masses 18 and 28 for H_2O, N_2 and CO to avoid saturating the detector) every 10 or 20 seconds. Figure 2 shows the total ion current vs. time trace for a 1 hour sampling period where we cycled through all of the sampling ports. Each point in the trace represents the acquisition of a complete mass spectrum. Thus the TMBMS is essentially a multi-channel on-line chemical analyzer. Figure 3 is the mass spectrum of the tars exiting the gasifier (sample port A), averaged over a six minute period starting at 2:00am (refer to Figure 2). The mass spectrum is representative of the tars produced in the gasification of bagasse in the IGT gasifier. They are of a tertiary nature, dominated by benzene (m/z = 78) and naphthalene (m/z = 128), along with smaller amounts of polycyclic aromatic hydrocarbons (PAH's) such as anthracene (m/z = 178) and pyrene (m/z = 202). Multi-level calibration of the TMBMS with standards allowed quantitative measurement of these species as shown in Figure 4. These data are from the first HGCU performance test and demonstrate that the tar-cracker was destroying about 75% of the tars and the HGCU was not removing much tar from the gas stream (< 10% of the raw tar). During the second test the tar-cracker was operated at a lower temperature and with different fluidizing media. In that test the TMBMS measured no significant change in tar concentration across either the tar-cracker or the HGCU.

The feeder system for the RENUGAS process was originally designed for wood chips. The change to bagasse in these tests forced numerous modifications to be made to the feeder system, many of which were anticipated and implemented before the first test. Further modifications to the feed injection screw, including water cooling and serrated threads, were made before the second test. In the field, analysis of the TMBMS data revealed some unexpected chemical behavior occurring in the process, which eventually lead to a new understanding of the importance of accurate feed level control in maintaining stable gasification.

The TMBMS monitored the concentrations of the various gases and vapors, which varied in a regular periodic fashion, during stabilized PDU operation. Figure 5 shows this behavior for just three of the numerous species monitored simultaneously: carbon dioxide (m/z ≈ 44), benzene (m/z = 78) and methane (m/z = 16), sampled at port A. We observed that this cyclical behavior was correlated with the operation of the bottom feed lock-hopper valve and had a period of approximately 5 minutes. The feed lock-hopper was slightly over-pressurized with nitrogen, relative to the gasifier, to prevent back-flow of gasification product gas containing combustibles and steam. For this reason part of the concentration variation was probably due to nitrogen dilution of the products when the bottom gate valve opened. However, because the relative magnitude of the concentration drops were not the same for all products, we deduced that there were more complex effects of the lock-hopper operation on the gasification process than product dilution.

The concentration variation was not due to process pressure fluctuations because our sample gas flow meter, an orifice plate/differential pressure meter, was stable through this monitoring period. Sampling system artifacts such as distillation or chromatography in the sample transfer lines are largely ruled out by the fact that the variation magnitude was approximately the same for hydrocarbons from benzene through pyrene and only slightly less for methane. The swing effect was attenuated for tar compounds above mass 202, and this may be due to sampling artifacts because of the 300° C temperature of the transfer lines and the relatively low vapor pressures of the higher molecular weight species.

Our explanation for the product concentration swing is a momentary upset of the residence time of the bagasse in the gasifier when the bottom lock-hopper valve opens. At that moment, we believe that bagasse distributed along the feed injection screw was blown into the gasifier at an uncontrolled rate by the over-pressurized nitrogen from the lock-hopper. This was followed by a brief period during which no fresh bagasse was injected into the gasifier, as the feed injection screw grooves refilled. Thus, the bagasse residence time in the gasifier was disrupted causing the product concentrations to drop then return to normal.

Tars and methane are formed early in the gasification process, by pyrolytic mechanisms from the volatile components in the fresh bagasse [5,6]. Their residence time in the gasifier is short, being controlled by the steam and gas flow rate. In contrast, char has a longer residence time in the gasifier and distributes throughout the fluidized bed. Char continues to react with steam producing CO_2, CO and H_2 long after the volatile tars have left the reactor, explaining the less pronounced concentration drop for CO_2 than for tars and methane.

During the second test the TMBMS detected the effects of a feed interruption and change in feeder system operation, while monitoring port C. An overheating tar-cracker forced an interruption in bagasse feeding to permit the tar-cracker to cool down. Mechanical problems with the feed lock-hopper began as feeding was restarted. These problems took about 30 minutes to resolve, and when feeding recommenced the TMBMS made it apparent that the gasifier product concentrations were no longer varying during lock-hopper operation. Figure 6 shows the HGCU outlet concentrations of CO_2, benzene and methane before, during and after the feeder problems, starting at 9:14pm. These observations with the TMBMS were carefully correlated with events in the PDU control room. During the sample time frame of 10-24 minutes we see the concentration swing behavior characteristic of the PDU operation with bagasse to that point. At 24 minutes the PDU operator interrupted feeding to cool down the tar-cracker. The TMBMS detected this interruption as, for example, the drop in benzene concentration to baseline. It remained there until 33 minutes, and the methane behaved similarly, yet the CO_2 concentration remained high. A partial batch of fresh feed was delivered into the gasifier at 33 minutes, when the concentrations of all three products rise. Then the upper lock-hopper valve jammed at about 34 minutes. The TMBMS again detected this as the precipitous drop in methane and benzene concentrations and the more gradual drop in CO_2.

We presently do not have an explanation for the sudden unilateral rise in CO_2 at 46 minutes, but by 54 minutes the feeding problems were resolved and all the product concentrations were near normal by 10:09pm. The TMBMS monitoring of port C was interrupted between 10:09pm and 10:10pm and then sample dilution nitrogen was measured for background for 3 minutes. By 10:14pm the TMBMS was back on-line with port C, and we observed that the average product concentrations were roughly equivalent to those prior to the feed interruption, however, the periodic concentration swings were gone. The TMBMS detected the back-pulse of the HGCU at 104 minutes. The cause of the concentration spike for benzene and methane at 88 minutes has not been determined.

The reason for the improved chemical stability was that the PDU operator had made an operational change that increased the inventory of bagasse in the feeder section between the bottom lock-hopper valve and the injection screw. This change was made possible because the feed level sensor had spontaneously begun to operate in a satisfactory manner, during the correction of the feeder system mechanical problems in the previous half hour. (The capacitance-type feed level sensor had been reliable with wood chips but not with the bagasse up to this point). The higher feed level effectively sealed the gasifier from the pressure bursts associated with the lock-hopper operation. Thus, the actual bagasse feed rate into the gasifier was stabilized, the residence time of the feed in the gasifier was no longer disturbed and the product concentrations stabilized.

Conclusions

A Molecular Beam Mass Spectrometer was successfully interfaced with a high temperature/pressure, PDU scale biomass gasifier, hot gas conditioning and cleanup unit operations. We demonstrated the instrument's ability to continuously sample from the process and measure multiple products simultaneously. Statistical analysis of the calibration standards data demonstrated that the TMBMS response to the analytes was linear and very precise over the range of 10-1000 ppm. Excellent instrument calibration stability was achieved over a period of five days and the standard addition tests revealed no sample matrix effects on the calibration of the TMBMS for these analytes.

The identification and explanation of the process fluctuations and the feeder system operational change described above, as well as other transient phenomena, was facilitated by the on-line multi-species detection capabilities of the TMBMS. The TMBMS process gas measurements showed that the HGCU was not affecting the tar species concentrations, implying that coking would not be a problem. Analysis of the candle filters at Westinghouse showed no evidence of carbon deposition within the filters, confirming our conclusion.

The sampling experience with the TMBMS during transient feeding upsets demonstrated that chemical channels leading to the formation of benzene (and the other PAH's) and methane shut down rapidly in the absence of fresh feed. Thus, these compounds appear to be very sensitive indicators of feeding and gasification stability. Continuous measurement of one or more of these species would be very beneficial to process control.

References

1) NREL sub-contract No. XAZ-3-12092-01-106794, "Hot Gas Cleanup for Operation of a Gas Turbine with a Fluidized Bed Air Blown Biomass Gasifier" awarded to Westinghouse Electric Corporation, in progress.

2) Final report for PNL sub-contract No. B-C5821-A-Q, "Development of Biomass Gasification to Produce Substitute Fuels" details the IGT gasifier, **1987**.

3) In progress, joint project with DOE, Hawaii and the Pacific International Center for High Technology Research (PICHTR) to scale up the IGT RENUGAS gasifier.

4) Ratcliff, M. A. "Design and Construction of a Transportable Molecular Beam Mass Spectrometer, and its Application to the Analysis of Diesel Exhaust", Masters Thesis T4606, Colorado School of Mines **1994**.

5) Evans, R. J.; Milne, T. A. *Energy and Fuels* **1987**, *1*, pp. 123-137.

6) Evans, R. J.; Milne, T. A. *Energy and Fuels* **1987**, *1*, pp. 311-319.

Acknowledgments

The authors are grateful to the numerous people who participated in these tests. Special thanks go to David Dayton, Steve Deutch, Robert Meglen, Steve Phillips, Ralph Overend and Tom Milne from NREL, and Rick Knight, Bob Schlusser, Ken Kozlar, Dave Parham and Jim Wangerow from IGT. This project was funded by the DOE's Solar Thermal and Biomass Power Program directed by Gary Burch. The NREL program manager was Rich Bain.

Table 1. Gasifier Product Gas Composition[a] (vol. %, wet)

H_2	4.23	CH_4	3.81
H_2O	56.14	C_2H_4	0.14
N_2	17.58	C_2H_6	0.06
CO	6.83	C_3H_6	0.00
O_2	0.07	C_3H_8	0.00
CO_2	10.91	C_6H_6	0.23[b]

[a] Reflects non-optimized steam input and nitrogen purges. [b] Includes benzene from condensate.

Figure 1

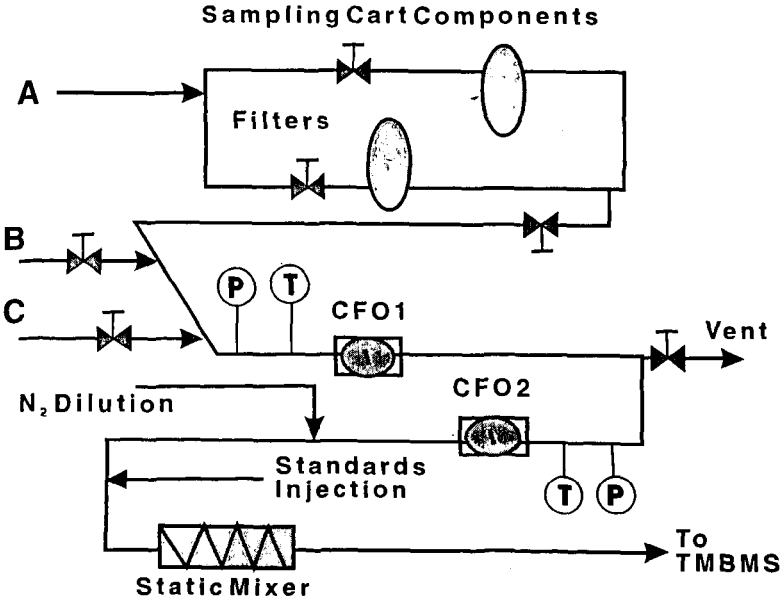

Figure 2

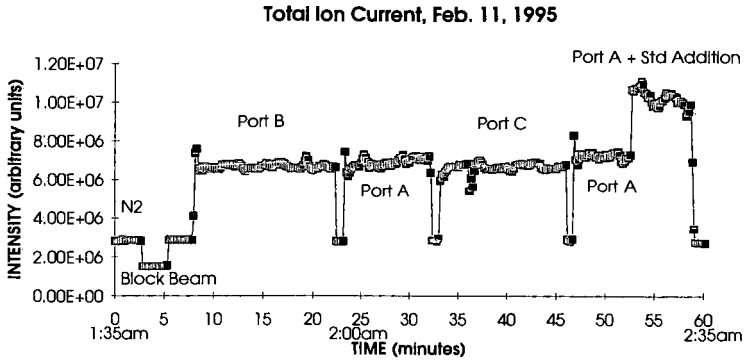

Figure 3

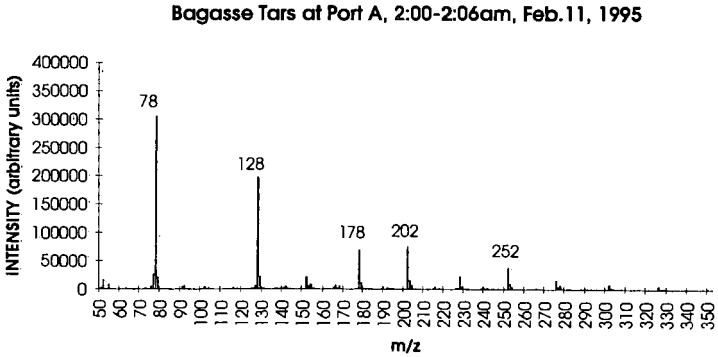

Figure 4

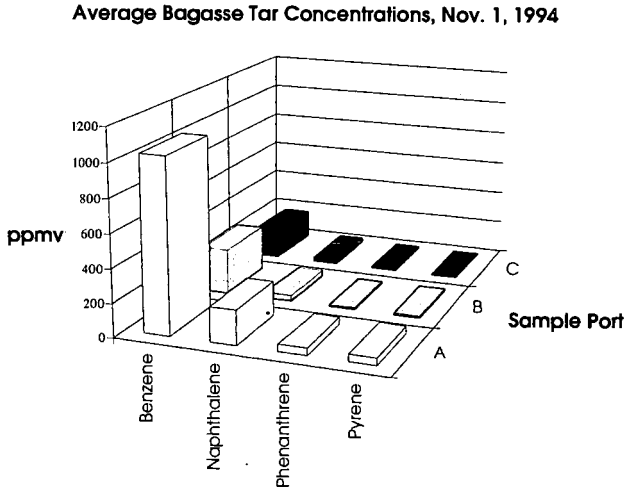

Figure 5

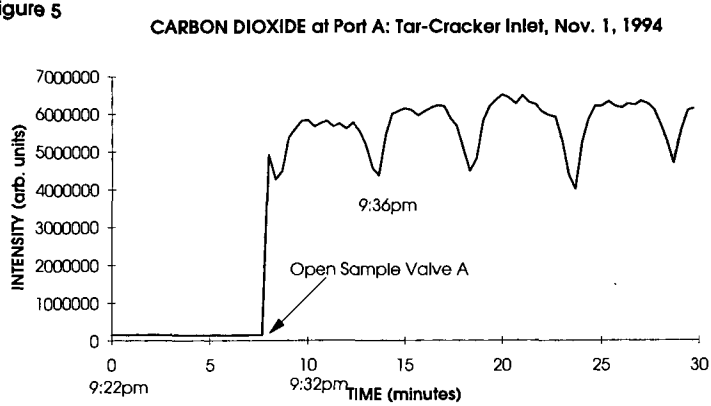
CARBON DIOXIDE at Port A: Tar-Cracker Inlet, Nov. 1, 1994
INTENSITY (arb. units)
7000000
6000000
5000000
4000000
3000000
2000000
1000000
0
9:36pm
Open Sample Valve A
0
5
10
15
20
25
30
9:22pm
9:32pm
TIME (minutes)

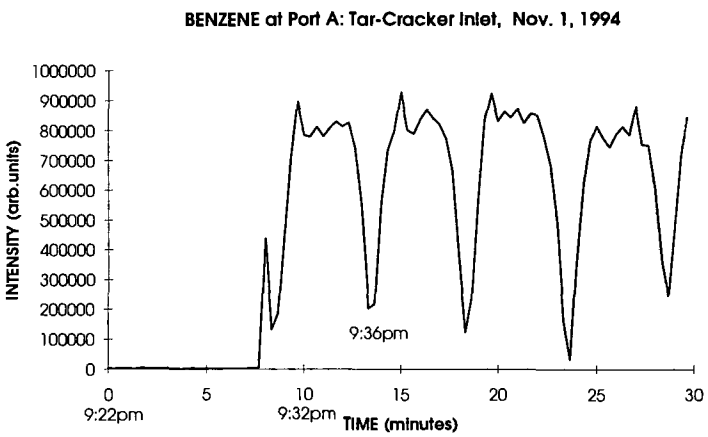
BENZENE at Port A: Tar-Cracker Inlet, Nov. 1, 1994
INTENSITY (arb.units)
1000000
900000
800000
700000
600000
500000
400000
300000
200000
100000
0
9:36pm
0
5
10
15
20
25
30
9:22pm
9:32pm
TIME (minutes)

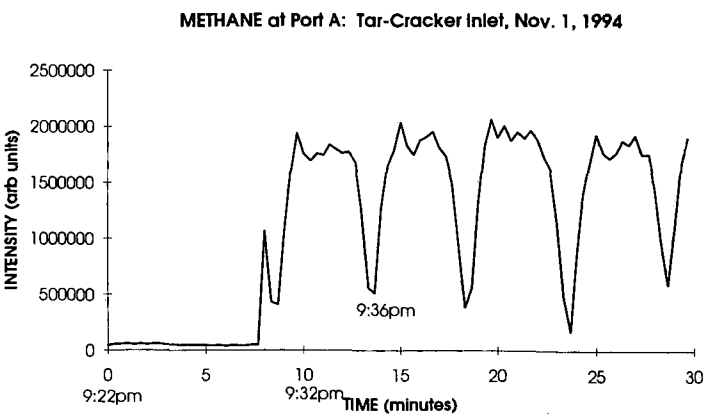
METHANE at Port A: Tar-Cracker Inlet, Nov. 1, 1994
INTENSITY (arb units)
2500000
2000000
1500000
1000000
500000
0
9:36pm
0
5
10
15
20
25
30
9:22pm
9:32pm
TIME (minutes)

Figure 6

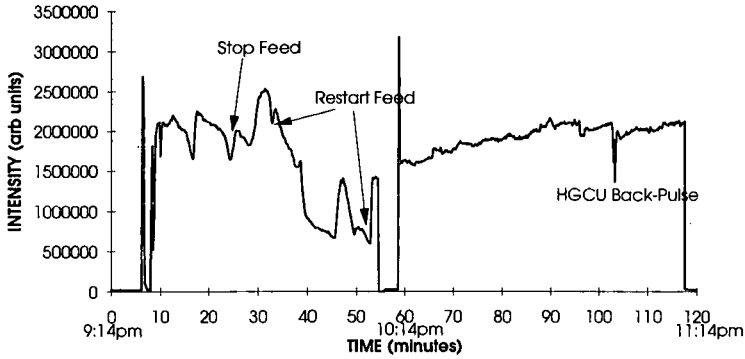
Carbon Dioxide at HGCU Outlet, Feb. 10, 1995
INTENSITY (arb units)
3500000
3000000
2500000
2000000
1500000
1000000
500000
0
Stop Feed
Restart Feed
HGCU Back-Pulse
0 10 20 30 40 50 60 70 80 90 100 110 120
9:14pm
10:14pm
11:14pm
TIME (minutes)

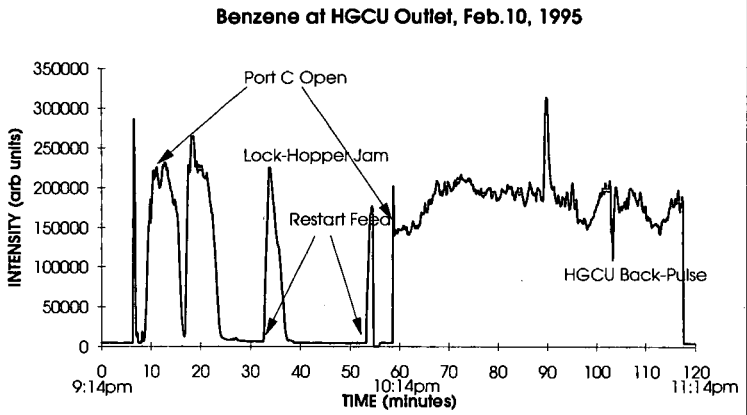
Benzene at HGCU Outlet, Feb.10, 1995
INTENSITY (arb units)
350000
300000
250000
200000
150000
100000
50000
0
Port C Open
Lock-Hopper Jam
Restart Feed
HGCU Back-Pulse
0 10 20 30 40 50 60 70 80 90 100 110 120
9:14pm
10:14pm
11:14pm
TIME (minutes)

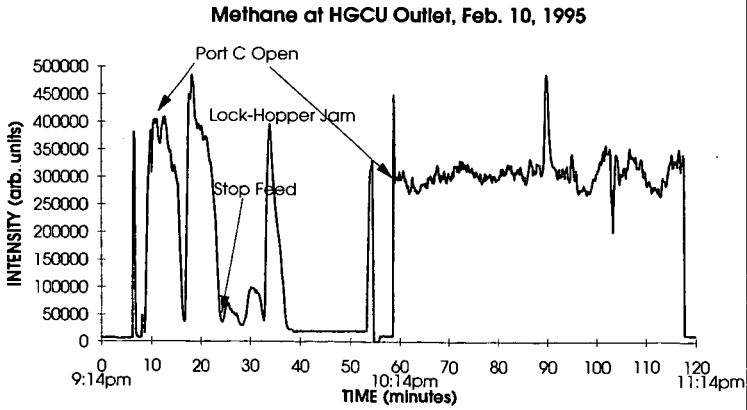
Methane at HGCU Outlet, Feb. 10, 1995
INTENSITY (arb. units)
500000
450000
400000
350000
300000
250000
200000
150000
100000
50000
0
Port C Open
Lock-Hopper Jam
Stop Feed
0 10 20 30 40 50 60 70 80 90 100 110 120
9:14pm
10:14pm
11:14pm
TIME (minutes)

GASIFICATION REACTIVITIES OF SOLID BIOMASS FUELS

Antero Moilanen, Esa Kurkela
VTT Energy, P.O.Box 1601, FIN-02044 FINLAND

Keywords: Biomass, gasification, reactivity

INTRODUCTION

The design and operation of the biomass based gasification processes require knowledge about the biomass feedstocks characteristics and their typical gasification behaviour in the process. In this study, the gasification reactivities of various biomasses were investigated in laboratory scale Pressurised Thermogravimetric apparatus (PTG) and in the PDU-scale (Process Development Unit) Pressurised Fluidised-Bed (PFB) gasification test facility of VTT (Figure 1).

EXPERIMENTAL

In PTG, the effects of individual process parameters (relevant to pressurized fluidised bed gasification) on gasification rate were studied using following parameter ranges: gasification agent (CO_2, H_2O), temperature (700 - 1 000°C), pressure (1-30 bar). With some samples, also the effect of product gas on gasification rate was tested.

The characteristics of the samples are presented in Table 1. The selected samples are part of a biomass sample collection analysed in the EU-project (European Union) belonging JOULE II Program /1/.

The gasification rate measurements were carried out in the pressurised thermobalance (PTG), which is presented schematically in Figure 1. A more detailed description of its operation has been presented in /2/. The tests were carried out isothermally by lowering down the sample of about 50 mg in size to the reactor with the winch system equipped in the PTG. During this time, the sample was pyrolysed when it heated up to the reaction temperature at an estimated rate of above 10K/s. The weight change, which was recorded during this approximately 60 seconds period, was due to, mainly, the pyrolysis of the sample and the buoyancy phenomena. After this period, the weight change due to the gasification (and eventual postpyrolysis) was monitored.

In the fluidized-bed gasification tests, air and a small amount of steam were used as gasification agents. The feedstock and dolomite were fed into the lower part of the bed and part of the fines elutriated from the fluidized-bed were separated in the primary cyclone and recycled back to the bed. The fines separated by the secondary cyclone and the ceramic filter unit were collected, weighed and sampled. The main variable in the tests was the gasification temperature, which was controlled by changing the air-to-fuel ratio.

The carbon conversion data for three biomass fuels are presented together with data for two bituminous coals and Rhenish brown coal. The feedstock analyses are shown in Table 2. Examples of the operation conditions and process data for the different fuels are presented in Table 4.

RESULTS

The gasification rates obtained from the PTG measurements are shown in Table 3 as a function of CO_2 and H_2O pressure measured at 850°C. The gasification rate denoted as r" is indicated as an instantaneous gasification rate, i.e. mass change rate divided by residual ash-free mass (%/min). The conversion used indicates the burn-off of the whole fuel including the mass loss due moisture and pyrolysis release. In Figure 2, the conversion behaviour, i.e. r" vs. conversion, is given for the fuels which were gasified also in the PFB.

The PTG tests show that there are great differences in gasification rates between various fuels. The preliminary correlations between gasification rates and ash composition indicated that, especially,

the rates at higher fuel conversions seemed to decrease with increasing silica content in the fuel. This indicates that catalytically active ash components can loose their activity due to reactions with silica, or due to sintering behaviour. Also, adding a product gas component to the gasification gas decreased radically the gasification rate. For example, the gasification rate (r") of wheat straw decreased from 27 %/min to 10%/min when CO was added 10% to CO_2 at 30 bar pressure.

The carbon conversions of the PFB tests shown in Table 4 are calculated from the material balances. The great differences between the gasification behavior of the five feedstocks used in PFB measurements can be clearly seen by comparing the data shown in Figure 3. Only the two bituminous coals seemed to behave more or less similarly and a strong and clear correlation was found between carbon conversion and equivalence ratio (or temperature). With these fuels it took several hours to reach steady state char inventory in the bed and also in the freeboard and in the recycling loop.

The three different biomass fuels had also clearly different gasification behavior. In gasification of pine sawdust, very high carbon conversions could be achieved already at relatively low temperatures, while bark and straw were more difficult to be completely gasified. In the case of straw gasification high conversion efficiencies could be achieved at above 850°C, but unfortunately sintering of the straw ash caused severe operational problems. Pine bark did not have problematic ash sintering behavior, but has a clearly lower reactivity than wood or straw. Consequently high gasification temperatures and efficient recycling of elutriated fines are required with pine bark to reach high conversion efficiencies.

Rhenish brown coal is an excellent feedstock for fluidized-bed gasification and over 95 % carbon conversion could be reached already at about 900 °C temperature. This fuel has also a high reactivity measured in PTG /3/.

The results of this study shows that gasification reactivities of the biomasses can differ greatly from each other. The comparison of the results between PTG and PFB shows that the gasification rates measured in PTG have the same order as the reactivities in PFB based on achieved carbon conversion calculations.

REFERENCES

1. Wilén, C. et al. The feasibility of electricity production from biomass by gasification systems - Fuel analyses. EU-Joule II Program Contract No. JOU2-CT92-0226, ENEL, VTT, IVO, DMT, Final report. To be published 1995.

2. Saviharju, K, Moilanen, A., van Heiningen, A.R.P., New High Pressure Gasification Rate Data on Fast Pyrolysis of Black Liquor Char. Preprints 1995 International Chemical Recovery Conference TAPPI, April 24-27, 1995, Toronto, Canada, pp. A237-243.

3. Mühlen, H.-J., Sowa, F., van Heek, K.H., Comparison of the gasification behaviour of a West and East German brown coal. Fuel Proc. Tech., 36(1993), pp. 185-191.

Table 1a. The characteristics of the feedstock samples, wt%, dry basis

Sample	V.M. %*)	F.C. %*)	Ash, %	C, %	H, %	N, %	O_{diff}, %	S, %
Pine saw dust	83.1	16.8	0.1	51.0	6.0	0.1	42.8	nil
Pine bark	73.1	25.3	1.7	52.5	5.7	0.4	39.7	0.03
Forest residue (pine)	79.3	19.4	1.3	51.3	5.8	0.4	40.9	0.02
Salix	79.9	18.9	1.2	49.7	6.1	0.4	42.6	0.03
Wheat straw	77.7	17.6	4.7	47.5	5.9	0.6	41.5	0.07
Barley straw	76.1	18.0	5.9	46.2	5.7	0.6	41.5	0.08
Reed canary grass	73.5	17.6	8.9	45.0	5.7	1.4	38.9	0.14
Miscanthus	78.5	18.2	3.3	47.9	6.0	0.6	41.6	0.6
Sweet sorghum	77.2	18.1	4.7	47.3	5.8	0.4	41.7	0.1
Kenaf	79.4	17.0	3.6	46.6	5.8	1.0	42.8	0.1

V.M.: Volatile Matter Content, F.C.: Fixed Carbon

Table 1b. The ash compositions of the samples.

Sample	Ash composition, %									
	SiO_2	Al_2O_3	Fe_2O_3	CaO	MgO	K_2O	Na_2O	TiO_2	SO_3	P_2O_5
Pine saw dust	8.3	4.0	3.7	41.8	11.8	24.6	0.5	0.12	1.9	10.5
Pine bark	1.3	10.6	0.6	40.6	4.5	15.2	1.0	0.12	2.0	9.6
Forest residue (pine)	38.5	9.4	7.4	15.4	4.0	16.6	0.7	0.5	1.6	6.4
Salix	0.4	0.6	0.4	30.8	5.1	53.0	0.5	0.02	3.0	22.9
Wheat straw	59.9	1.6	1.1	7.3	1.8	33.7	0.9	0.04	1.1	4.5
Barley straw	62.0	0.4	0.3	4.5	2.2	38.5	1.0	0.02	1.4	5.0
Reed canary grass	89.8	2.8	2.3	3.5	1.5	6.3	0.3	0.05	1.1	8.2
Miscanthus	42.8	1.0	0.8	7.6	4.8	50.6	1.3	0.03	2.1	10.5
Sweet sorghum	57.8	1.3	1.1	9.0	2.7	16.4	3.0	0.05	3.0	6.0
Kenaf	6.6	3.6	2.4	30.8	6.0	26.5	2.5	0.08	5.7	5.5

Table 2. The analyses of the feedstock materials used in the fluidised bed tests.

	Polish coal	Colombian coal	Rhenish brown coal	Wheat straw	Pine sawdust	Pine bark
Moisture content, wt-%	3.6-6.7	7.6	11.5-12.2	6.1	6.1-16	5.6-6.7
Proximate analysis, wt-% d.b.						
Volatile matter	31.8	34.7	53.0	75.8	83.1	71.8
Fixed carbon	59.9	53.2	42.7	18.2	16.8	26.7
Ash	8.34	12.1	4.3	6.1	0.08	1.6
Ultimate analysis, wt-% d.b.						
C	75.5	71.9	63.8	46.1	51.0	53.9
H	4.7	4.9	4.6	5.6	6.0	5.8
N	1.3	1.5	0.8	0.52	0.08	0.35
S	0.7	1.0	0.3	0.08	< 0.01	0.03
O (diff.)	9.5	8.6	26.2	41.6	42.8	38.4
Ash	8.3	12.1	4.3	6.1	0.08	1.6

Table 3. The instantaneous gasification rates of the samples at the minimum and at the conversion value of 95% measured at 850°C.

Sample	1 bar CO_2		30 bar CO_2		1 bar H_2O		30 bar H_2O	
	r" min.	r" at X=95%	r" min.	r" at X=95%	r" min.	r" at X=95%	r" min.	r" at X=95%
Pine saw dust	27	39	22	43	25	25	50	71
Pine bark	9	16	7	13	7	13	44	71
Forest residue (pine)	18	20	na	na	na	na	na	na
Salix	29	42	23	50	30	130	60	225
Wheat straw	16	19	25	42	13	17	46	58
Barley straw	19	22	na	na	na	na	na	na
Reed canary g.	3	3	10	15	15	19	na	na
Miscanthus	18	25	26	59	24	45	na	na
Sweet sorgh.	20	23	26	51	29	62	na	na
Kenaf	50	83	55	103	67	83	na	na

Table 4. Operational data on typical set points with different fuels.

	Polish Coal	Colombian coal	Rhenish brown coal	Wheat straw	Pine sawdust	Pine bark
Equivalence ratio	0.47	0.49	0.44	0.3	0.39	0.34
Fuel feed rate, g/s	5.33	5.49	11.50	13.30	10.67	11.45
g/s-daf	4.70	4.50	9.70	11.70	9.00	10.40
Air feed rate, g/s	23.67	23.66	35.03	21.2	21.15	23.56
kg/kg-fuel(daf)	5.04	5.26	3.61	1.81	2.35	2.27
Steam feed rate, g/s	4.06	4.50	1.90	3.6	1.77	1.23
kg/kg-fuel(daf)	0.86	1.00	0.20	0.31	0.20	0.12
Purge N_2 feed rate, g/s	3.3	3.4	1.2	4.6	2.1	2.6
Dolomite feed, g/s	0.45	0.45	0	0	0.7	0.39
Pressure, MPa	0.5	0.5	0.5	0.5	0.5	0.5
Bed temperature, °C	1 001	980	824	772	831	871
Freeboard temperature, °C	1023	1014	910	848	968	978
Carbon conversion, wt%						
to gas (C1)	85.0	86.2	95.9	83.4	94.6	87.7
to gas+tars (C2)	85.3	86.7	96.2	93.9	100.3	90.0
incl.dolomite input (C3)	84.2	85.5	96.2	93.9	98.6	89.3
Carbon losses, wt-% of input, Bottom ash	0.5	0.2	0.1	0	0.1	0
Cyclone dust	2.3	3.4	2.4	2.1	0	2.5
Filter dust	13.0	11.1	1.1	2.5	0.8	8.3
Carbon balance closure output, wt % of input	100.0	100.2	99.8	98.5	99.5	100.1
Gas composition, vol%						
CO	8.7	6.9	16.4	9.0	8.8	12.0
CO_2	10.6	10.8	10.0	11.5	13.8	12.8
H_2	8.4	8.1	12.0	4.0	7.8	9.0
CH_4	0.7	0.9	1.1	3.6	3.8	3.1
C_2 hydrocarbons	0.00	0.00	0.02	0.78	0.15	0.20
H_2O	15.6	18.3	7.3	23.9	17.2	12.6
NH_3	0.12	0.14	0.19	0.15	0.026	0.13
H_2S	0.039	0.058	0.017	0.014	0.005	0.009
N_2 (+Ar)	55.8	54.8	53.0	47.1	48.4	50.2

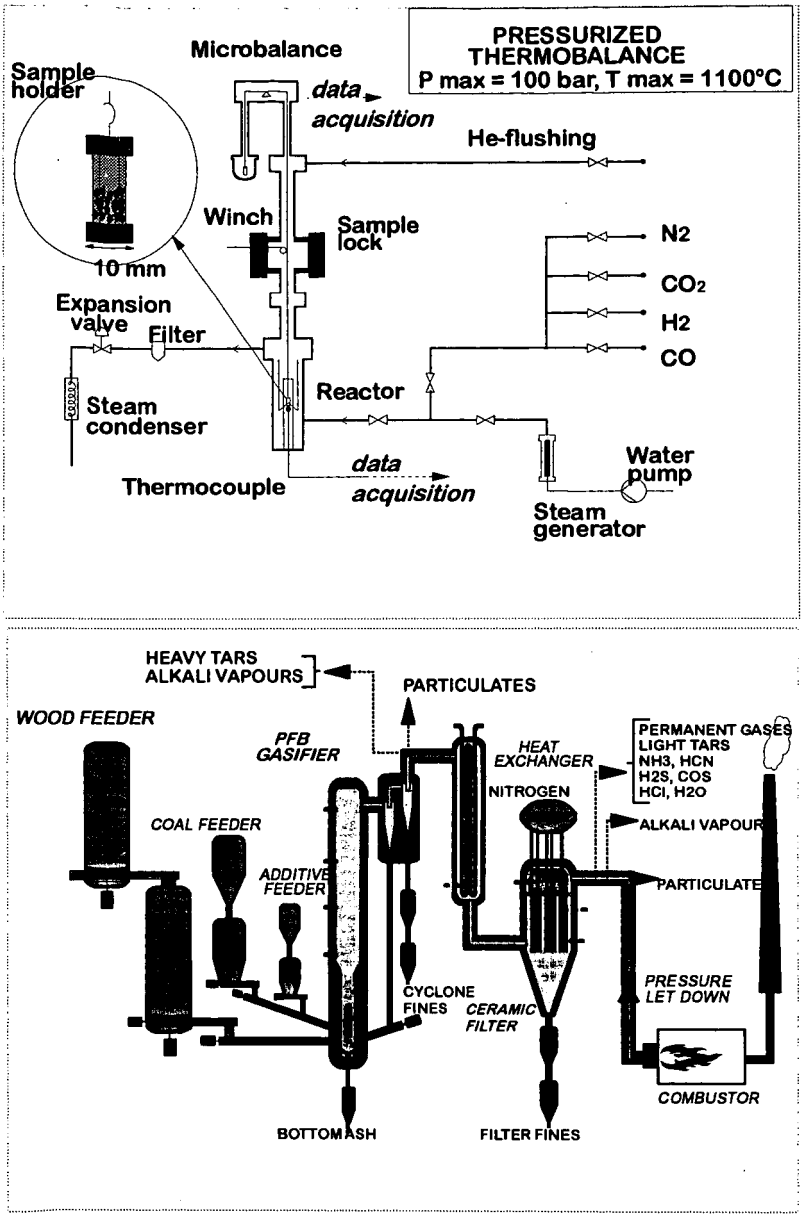

Figure 1. The pressurised thermogravimetric apparatus and pressurized fluidized-bed gasification test facility used in the study.

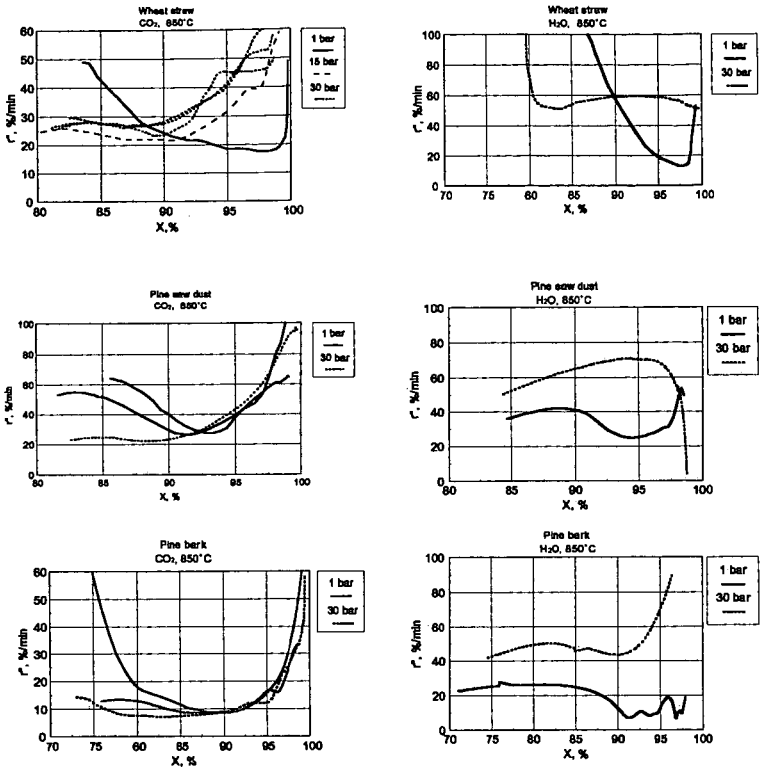

Figure 2. The gasification rate r" vs. fuel conversion X of CO_2 and H_2O gasification in 1 and 30 bar pressures and at 850°C.

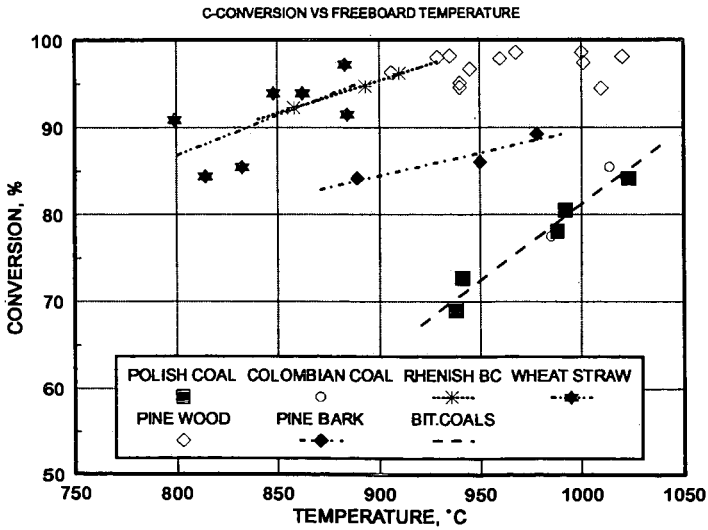

Figure 3. The achieved carbon conversions as a function of freeboard temperature in the PFB.

COMPARISON OF BIOMASS AND COAL CHAR REACTIVITIES

Sidney P. Huey, Kevin A. Davis[1], Robert H. Hurt[2], and Mary J. Wornat[3]

Sandia National Laboratories
Combustion Research Facility
Livermore, CA 94551-0969

[1]Current Address: Reaction Engineering International
77 West 200 South, Suite 210
Salt Lake City, UT 84121

[2]Current Address: Brown University
Division of Engineering, Box D
Providence, RI 02912

[3]Current Address: Princeton University
Department of Mechanical & Aerospace Engineering
Princeton, NJ 08544

Keywords: biomass, char reactivity, extinction behavior

ABSTRACT

Char combustion is typically the rate limiting step during the combustion of solid fuels. The magnitude and variation of char reactivity during combustion are, therefore, of primary concern when comparing solid fuels such as coal and biomass. In an effort to evaluate biomass' potential as a sustainable and renewable energy source, the change in reactivities with the extent of burnout of both biomass and coal chars were compared using Sandia's Captive Particle Imaging (CPI) apparatus. This paper summarizes the experimental approach used to examine biomass and coal char reactivities and extinction behaviors and presents results from CPI experiments.

The reactivity as a function of extent of burnout for six types of char particles, two high-rank coal chars, two low-rank coal chars, and two biomass chars, was investigated using the CPI apparatus. Results indicate that both of the high-rank coal chars have relatively low reactivities when compared with the higher reactivities measured for the low-rank coal and the biomass chars. In addition, extinction behavior of the chars support related investigations that suggest carbonaceous structural ordering is an important consideration in understanding particle reactivity as a function of extent of burnout. High-rank coal chars were found to have highly ordered carbon structures, where as, both low-rank coal and biomass chars were found to have highly disordered carbon structures.

INTRODUCTION

Char combustion is typically the rate limiting step during the combustion of solid fuels. Incomplete combustion of solid fuels in utility boilers has long been an important concern for power generation facilities [Hottel and Stewart, 1940]. The result of incomplete combustion is a high level of unburned carbon in a boiler's flyash. This, in turn, causes a number of deleterious effects, including, a significant decrease in combustion efficiency, an adverse effect on heat transfer and electrostatic precipitator operation, and a greater difficulty marketing the flyash for recycling (i.e., for carbon contents greater than 3 to 6 percent). Determining the relative level of unburned carbon from burning coal and biomass fuels in boilers motivates this investigation.

This paper concentrates on biomass chars produced from the pyrolysis of two biomass feedstocks—a soft wood, Southern Pine; and an herbaceous material, switchgrass. The biomass chars were formed by pyrolyzing pine and switchgrass particles in a vortex reactor at 625 °C, described elsewhere [Diebold and Scahill, 1988]. Previous work on biomass chars has focused on (1) structural and compositional changes [Wornat *et al.*, 1995] and (2) quantitative measurements of global reactivity at early and intermediate levels of combustion under pulverized-fuel conditions [Wornat *et al.*, 1994]. This paper focuses on the reactivity of chars during the late stages of combustion, which is critical to unburned carbon in flyash.

In practice, the level of unburned carbon in the flyash is related to the fuel's rank. Coal rank is a measure of volatile matter contained in the coal and is generally considered an indicator of its geologic

age. Our earlier work [Hurt, 1993; Hurt and Davis, 1994; Davis *et al.*, 1995] indicates that the carbonaceous structure of young materials (biomass and low-rank coal chars) is less susceptible to the structural ordering process that bituminous and high-rank coals can undergo. The more amorphous nature of the younger materials during the latter stages of combustion should maintain their initially high level of reactivity throughout the entire combustion process, insuring lower levels of unburned carbon in the flyash.

Bituminous and high-rank coals produce high levels of unburned carbon, whereas, low-rank coals produce lower levels of unburned carbon. Biomass, with a very high volatile matter content, high oxygen content, and a correspondingly low heating value, is thermochemically similar in many respects to a low-rank coal. Given the thermochemical similarity of low-rank coals and biomass chars, we expect both fuels to exhibit comparable reactivities and to produce similarly low levels of unburned carbon. This paper presents an investigation of char reactivity as a function of burnout for biomass chars and compares them to our observations for coal chars of various ranks.

A relationship exists between a char's reactivity and extinction behavior and its temperature-time profile [Hurt, 1993]. Temperature-time profiles of chars provide the relative magnitude of reactivities for different chars, where as, normalized temperature-time profiles of chars are best suited to illustrate and compare the extinction behavior of different chars. Because maximum temperatures and extinction times vary greatly for different types of chars, temperatures and times were normalized to allow for a comparison of extinction behaviors for various types of chars.

EXPERIMENTAL METHODS

The high-temperature reactor in Sandia's Coal Combustion Laboratory (CCL) was used to measure the temperature-time profiles during combustion of two high-rank coal chars (Illinois #6 and Pocahontas #3), two low-rank coal chars (Beulah and Dietz), and two biomass chars (pine and switchgrass). Data were obtained with the Captive Particle Imaging (CPI) diagnostic system that has been discussed in previous reports [Hurt and Davis, 1994]. Figure 1 presents a schematic of the CPI. The system provides optical access for high-resolution video imaging of complete particle combustion for individual 100 μm to 200 μm char particles in a well-controlled combustion environment. Particles are placed on an alumina fiber bed supported by fine platinum wires. The particles are oxidized in a laminar flow of vitiated air with 6 mole-% excess oxygen at a temperature of approximately 1600 K. The particle is positioned along the reactor centerline at the focal point of a long-focal-length microscope. During the positioning process a water-cooled coil surrounding the particle holder provides local cooling and therefore prevents premature reaction of the particle. This microscope is connected to a video system capable of simultaneously imaging both reflected light and near infrared (IR) emission from the reacting particles. The IR images can be used for determination of radiance temperatures. Radiance temperature is defined as the temperature of a hypothetical black body emitting the same radiative power as the real object (particle) in the wavelength range of interest (here 700 to 1000 nm). For particles that have undergone low to intermediate extents of burnout, emissivities are approximately 0.8 [Baxter *et al.*, 1988] and true particle temperatures will be approximately 20 K greater than the reported radiance temperatures.

For the temperature-time profiles, the radiance temperatures are normalized to their corresponding maximum temperatures (i.e., normalized temperature equals the actual temperature divided by the maximum temperature). The temporal data are normalized by the time at which near-extinction (in the case of the higher rank coals) or extinction (in the case of lower rank coals and biomass chars) of the combustion process occurs. These extinction (and near-extinction) times correspond to the inflection point in the temperature-time profile that occurs after the peak temperature.

Using the CPI, normalized temperature-time profiles of several coal chars and solid biomass-derived fuels were determined for at least 20 particles of each type. Figures 2, 3, and 4 present the normalized temperature-time profiles for bituminous and high-rank coal chars (Illinois #6 and Pocahontas #3), low-rank coal chars (Beulah and Dietz), and biomass chars (pine and switchgrass), respectively. The figures show that for all the chars the particle temperature increases to a maximum and decreases to the reactor temperature, nominally 1400 to 1500 K. Table 1 summarizes the overall reactivity for various char particles [Wornat *et al.*, 1994].

RESULTS AND DISCUSSION

The general shape of a temperature-time profile is an indicator of a char's reactivity as a function of extent of burnout. A gradual decrease in temperature occurring after a char's peak temperature indicates that the reactivity of that char is decreasing with the extent of burnout, as shown for bituminous and high-rank coals in Figure 2. Chars that remain at or near their peak temperature for a

significant period during combustion then display a sudden decrease in temperature at the end of oxidation are believed to have relatively high reactivities that do not decrease with extent of burnout. Figures 3 and 4 show examples of chars with high reactivities that do not decrease with extent of burnout. These results show that the time or conversion dependence of reactivity for low-rank coal chars and biomass chars are very similar, the reactivities for both types of chars are relatively high, and the reactivities do not decrease with extent of burnout.

In addition to the information regarding extinction behavior, the CPI technique allows one to qualitatively compare the magnitude of the global reactivities of the various chars. Peak temperatures and burnout times obtained from these experiments suggest global reactivities qualitatively similar to the earlier quantitative work of past work [Wornat *et al.*, 1994]. The relative overall reactivities of chars are in the following order.

lignite chars > biomass chars > high-volatile bituminous coal chars

Table 1 lists the quantitative results obtained in the CCL over the past several years. The slightly higher reactivities of the biomass chars under CPI conditions may be a result of the somewhat lower temperatures used for the CPI compared to the CCL.

CONCLUSIONS

Based on our previous work on carbon reactivity and ordering of the carbon structure during coal and char combustion [Davis *et al.*, 1995], the current results for the biomass chars are not surprising. High-rank coals are observed to undergo a significant decline in reactivity with increasing burnout. This is a consequence of carbon structural ordering in the char during exposure to the high-temperature combustion environment. Highly ordered carbon structures offer fewer active sites for heterogeneous surface oxidation, which, therefore, decreases the reactivity of the carbon particle. In our related work on biomass chars [Wornat *et al.*, 1995], short-range ordering of the biomass char carbon is observed in carbon-rich portions of the chars. However, the high levels of oxygen content in biomass fuels favors cross-linking of the carbon chains that inhibits further carbon ordering during combustion This persistence of disorder in the carbon structure during biomass char oxidation is also observed for the high-oxygen-content chars of low-rank coals. We believe that the disorder in the carbon structure is responsible for the high reactivities found in both the low-rank-coal and biomass chars throughout their combustion lifetime. A consequence of this high char reactivity is that the particle temperature remains high for these chars through the entire burnout. In summary, the combustion behavior of biomass chars was found to be similar to that of low-rank coals—high reactivity with no evidence of a decrease with extent of burnout.

REFERENCES

Baxter, L.L., Fletcher, T.H. and Ottesen, D.K. (1988). Energy and Fuels **2**:423.

Davis, K.A., Hurt, R.H., Yang, N.Y.C. and Headley, T.H. (1995). *The Evolution of Char Chemistry, Crystallinity, and Ultra-fine Structure during Pulverized-coal Combustion*, Combustion and Flame **100**:31

Diebold, J. and Scahill, J. (1988). *Pyrolysis Oils from Biomass: Producing, Analyzing, and Upgrading*, ACS Symposium Series 376 (E.J. Soltes and T.A. Milne, Eds.), The American Chemical Society, Washington, D.C., pp. 31-40

Hottel, H.C. and Stewart, I.M. (1940). *Space requirement for the combustion of pulverized coal*, Ind. Eng. Chem. **32**:719.

Hurt, R.H. and Mitchell, R.E. (1992). *Unified High-Temperature Char Combustion Kinetics for a Suite of Coals or Various Rank* 24th International Symposium on Combustion, The Combustion Institute

Hurt, R.H. (1993). *Reactivity distributions and extinction phenomena in coal char combustion*, Energy and Fuels **7**:721.

Hurt, R.H. and Davis, K.A. (1994). *Near-Extinction and Final Burnout in Coal Combustion*; 25th International Symposium on Combustion, The Combustion Institute

Wornat, M.J. (1993). *Combustion Studies of Pyrolysis Oils and Chars — November to February*; Sandia National Labs Quarterly Progress Report, Case No. 4317.000

Wornat, M.J., Hurt, R.H., and Yang, N.Y.C. (1994). *The Combustion Reactivity of Biomass Chars,* Proceedings from the Eastern States Section Meeting of the Combustion Institute. The Combustion Institute

Wornat, M.J., Hurt, R.H., Yang, N.Y.C. and Headley, T.H. (1995). *Structural and compositional transformations of biomass chars during combustion*, Combustion and Flame **100**:131

Table 1. Overall Reactivities of Various Chars

Fuel Name	*Fuel Type*	*Rate*† *(g of C/cm²·sec)*
Southern Pine Char[1]	woody	0.0037
Switchgrass Char[1]	herbaceous	0.0041
Beulah[2]	lignite	0.0065
Lower Wilcox[2]	lignite	0.0056
Smith-Roland[2]	subbituminous	0.0065
Dietz[2]	subbituminous	0.0061
Hiawatha[2]	high-volatile bituminous	0.0059
Blue #1[2]	high-volatile bituminous	0.0045
Illinois #6[2]	high-volatile bituminous	0.0033
Pittsburgh #8[2]	high-volatile bituminous	0.0024
Lower Kittaning[2]	low-volatile bituminous	0.0021
Pocahontas[2]	low-volatile bituminous	0.0012

† rates are calculated from global kinetic parameters at gas conditions of 1500K & 6 mole-% O_2, the value 0.0065 is the diffusion-limited maximum for these conditions

1 Wornat, Hurt, and Yang (1994)

2 Hurt and Mitchell (1992)

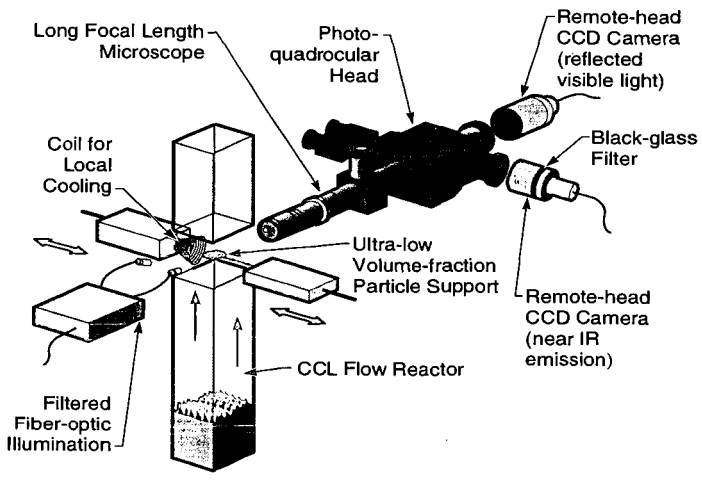

Figure 1. Schematic of the Captive Particle Imaging System

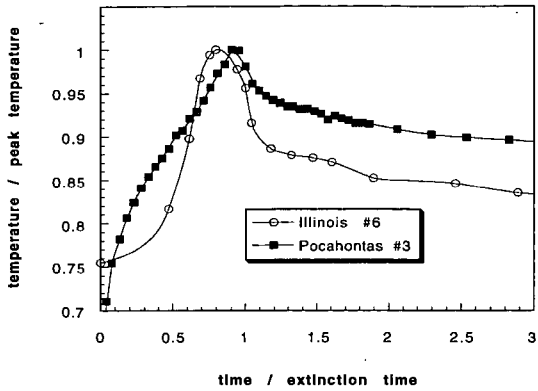

Figure 2. Normalized Temperature versus Normalized Time for Bituminous and High-Rank Coals

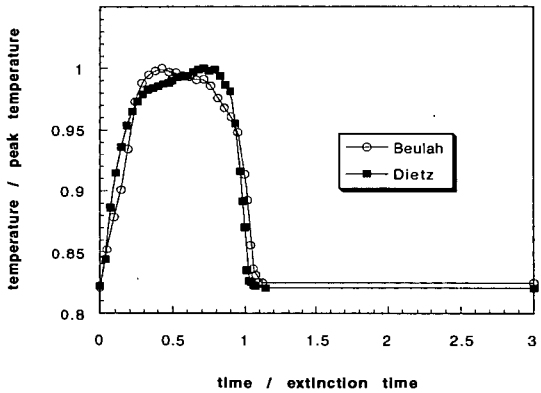

Figure 3. Normalized Temperature versus Normalized Time for Low-Rank Coals

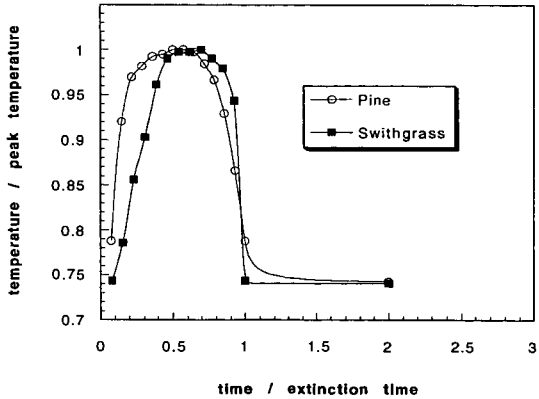

Figure 4. Normalized Temperature versus Normalized Time for Biomass Chars

ALFALFA STEM FEEDSTOCK FOR IGCC POWER SYSTEM FUEL

by
Dr. Max M. DeLong, Northern States Power Company
Dr. Michael Onischak, The Institute of Gas Technology
Michael Schmid, Tampella Power Corporation
Benjamin Wiant, Westinghouse Electric Corporation
Professor Ervin Oelke, University of Minnesota

Keywords: IGCC, alfalfa, gasification

ABSTRACT: A feasibility study was completed for an integrated gasification combined cycle (IGCC) electric power generation plant to operate in conjunction with an alfalfa processing plant that provides the gasification feedstock and a mid-level protein animal feed co-product. Alfalfa stem material was evaluated as a gasification feedstock. The leaf material was evaluated as a mid-level protein animal feed supplement. The alfalfa leaf-stem separation and power generation operations have dual and/or synergistic functions which contribute to a technically and economically compatible combination.

The pressurized biomass gasification process selected is the IGT RENUGAS™ system licensed to Tampella Power Corp. Adaptation of the air-blown gasification process to alfalfa stems results in low-Btu fuel gas suitable for combustion turbines. The gasification process is expected to obtain very high carbon conversion with low tar production, overcome ash agglomeration, and provide for control of volatile alkali species. A hot gas clean-up system removes particulate matter with a ceramic filter system. The collected ash residues are expected to be returned to the land that grew the alfalfa.

The physical and chemical properties of the alfalfa feedstock were evaluated for the gasification process. The alfalfa char carbon-steam reaction, which is the slowest step in the complete conversion of biomass to gases, was measured and the char proved to have a high reactivity. Ash components were measured and evaluated in terms of agglomeration within the gasifier. Using this information, the alfalfa gasification conditions were predicted. A subsequent preliminary gasification test confirmed the alfalfa gasification conditions. To complete the engineering design of the IGCC system, additional testing is required, but the results to date are positive for a successfull process.

INTRODUCTION: In response to a solicitation by USDOE, through the National Renewable Energy Laboratory (NREL), with co-sponsorship by the Electric Power Research Institute (EPRI), Northern States Power Company (NSP) formed a team with the University of Minnesota, The Institute of Gas Technology, Tampella Power Corp.and Westinghouse Electric Corp. to perform a feasibility study of alfalfa crop production coupled to a gasifier/hot gas clean-up/gas turbine/steam turbine power generation system. Figure 1 presents a block diagram of the combined electrical power and alfalfa co-product concept. In accordance with the solicitation by NREL, the study investigated economic development through biomass systems integration, and emphasized: 1) sustainable biomass energy crop production, 2) efficient power generation, and 3) co-product value from alfalfa-leaf meal.

This system concept uses alfalfa from a dedicated feedstock supply system (DFSS); namely, biomass material planted specifically for an energy production facility. The proposed cropping plan involves planting alfalfa in a seven year cycle with 4 years of alfalfa followed by 2 years of corn and one year of soybeans. This seven year rotation is in contrast to the often used current rotation system of corn and soybeans being continously alternated. Alfalfa is a crop that can be grown on a long term basis by a group of farmers with coordination through a closed-end cooperative arrangement (i.e., membership is offered only to producers). The co-op carries on a value added processing and marketing function for the farmer.

Alfalfa provides real benefits for other agricultural crops in the rotation and the land. These benefits result from the inclusion of a perennial (nitrogen-fixing) legume in the crop rotation. The need for external inputs of fertilizers, fossil fuels, herbicides and insecticides are reduced while distinct environmental benefits including reduced soil erosion, improved soil tilth, increased soil organic matter levels, and reduced potential for nitrate leaching are realized. Alfalfa was chosen as a feedstock because it has been sucessfully grown in NSP's service territory including the region surrounding the plant site of the feasibility study, NSP's Minnesota Valley Generating Plant at Granite Falls, MN. Additional acreage of the crop would enhance the regions ability to continue progress towards achieving a sustainable agricultural (i.e., preservation of long term productivity and no adverse environmental impact). The knowledge base, expertise and production capability for producing the crop is well established in the region.

ALFALFA FRACTIONATING PROCESS: The alfalfa fractionating (separating) plant diagram shown in Figure 2 receives sun-cured alfalfa in a conventional round bale package; reduces the particle size of the alfalfa material; dries it to a suitable moisture content for fractionation, storage or further processing. A dual air path (radially and axially) hammermill separates the leaf from the stem material. The separation of leaf from stem enhances the quality of the stem material as fuel, because the leaf fraction has the higher proportion of ash, fuel bound nitrogen and sulfur. Also, the stem material after fractionation has lower particle-to-particle friction and a higher bulk density than a mixture of the two fractions. The leaf fraction benefits from separation because the resulting crude protein concentration is raised, and the subsequent power for pelletizing is reduced as a result of the removal of the fibrous stems. Gas turbine exhaust heat can be used to assist in drying the incoming alfalfa. Low grade steam from the power cycle can be used to roast the leaf fraction to improve the digestibility and value of the crude protein.

ALFALFA FEEDSTOCK PROPERTIES: The alfalfa stem feedstock was analyzed chemically and physically. The analyses were compared with similar biomass feedstocks, namely bagasse and wood chips that have been successfully gasified in the RENUGAS™ fluidized-bed gasifier. The initial results were positive. The alfalfa stem feedstock is expected to be as good as the bagasse feedstock, in terms of gasification operating conditions and feed handling operations.

Important physical properties of alfalfa include its particle shape, particle size distribution, and bulk density. Handling characteristics relate to biomass particle-to-particle friction and biomass particle-to-wall friction factors that are important in solids handling considerations. Tests showed that sized and dried alfalfa should handle and feed well.

Also included with the physical properties is an assessment of the tendency of the ash constituents to combine and form agglomerates within the gasifier or in downstream equipment. Alkali elements such as potassium and sodium can combine with silica to form agglomerates in the gasifier. Unlike woody biomass feedstocks, which tend not to form agglomerates, alfalfa contains amounts of potassium, sodium, and silica that may form a eutectic mixture with a melting point near the expected gasification temperature. Furthermore, alkali compounds may exit the gasifier with the product gases as aerosols. These could potentially pass through the barrier filter and eventually deposit on the blades of the combustion turbine.

The important chemical properties of alfalfa include its moisture level, ultimate analysis, calorific value, and the elemental composition of the ash. Another chemical property important for gasification is char reactivity with steam. Reactivity of the biomass char carbon with steam is a measure of the slowest reaction step in the complete conversion of biomass into gases. After the very rapid devolatilization step, about 5% to 15% of the initial biomass weight remains as char carbon. The char carbon reacts with steam in the gasifier to complete the gasification process forming additional carbon monoxide and hydrogen. The rate of this reaction determines the char residence time in the fluidized bed, hence, is related to the size of the gasifier. Figure 3 shows the measured char reactivity or the steam-char gasification rate for the char of alfalfa stems compared to chars measured previously from a similar agricultural residue, namely, corn stover, and a silvicultural residue, maple wood chips. Also shown in comparison to the three biomass species are the slower char gasification rates measured for peat and bituminous coal. The base carbon entity plotted in the figure is the weight of char carbon that remains after completion of the rapid devolatilization step minus the weight of the ash in the material.

The char reactivity measurements were made in a pressurized thermobalance operating at expected gasification conditions of 1600°F and 300 psig. The composition of the gas in the thermobalance was representative of the gasifier product gas with respect to steam and hydrogen: namely, 45% steam, 5% hydrogen, and 50% nitrogen. Hydrogen is a product of the steam-char reaction, thus the design char gasification rate is measured under similar hydrogen concentration.

As seen in the Figure 3, the alfalfa char reacted at essentially the same rate as the corn stover and the maple chars under similar conditions. Therefore, it is expected that the alfalfa char should gasify at least at the same rate as char from wood chips that have been successfully gasified. In terms of the process design, the alfalfa throughput rate over the same cross-sectional area of the gasifier should be at least equal to that of the maple wood chips, which have been extensively tested in the PDU.

ALFALFA EVALUATION RESULTS: The moisture, ultimate analysis, and heating value results for the alfalfa feedstock are presented in Table 1 for samples of alfalfa obtained from three counties with different soil classifications surrounding the Granite Falls plant site. The alfalfa samples received were separated into stem and leaf fractions and were analyzed individually. The alfalfa stems are intended to be the gasification feedstock. The leaves are to be separated and processed into value-added leaf meal products, although the gasifier system does not preclude the leaves being sent to the gasifier along with the stem material.

The alfalfa compositions shown in Table 1 are within the expected range of most biomass feedstocks considered for gasification. The major distinctions seen in Table 1 are that the leaf fraction has more ash and also a higher nitrogen content than the stems. The higher nitrogen content of the leaves is related to the animal protein feed value. If the leaf fraction is to be gasified along with the stems, then the higher ash and fuel-bound nitrogen levels have to be considered in the design of the plant.

Table 2 presents the ash analyses of the stem and leaf fractions of alfalfa from the three county samples. The leaf fraction is up to 47 wt % of the dried alfalfa plant. The amounts of potassium, sodium, and silicon are important. These elements can combine to form a eutectic that have a melting temperature below the normal gasification temperature. Possible combinations of the oxides of these elements are well known in coal combustion systems and in iron-making. The presence of these species is a concern in combustion boilers with an oxidizing atmosphere which favors the formation of agglomerates that foul the boiler internals. There is a concern that even at lower temperatures and in the reducing atmosphere of a fluidized-bed gasifier these agglomerates may form.

A coal agglomeration test used at IGT was modified for biomass agglomeration to assess the degree of agglomeration under non-oxidizing conditions (the IGT boat test). The general test procedure involves reducing the size of the biomass to 200 mesh and then pyrolyzing the mass in a 3/8-inch by 3-inch ceramic boat under nitrogen at 1800°F followed by cooling under nitrogen to room temperature. The residue is then evaluated in terms of agglomeration strength. The mass of biomass char carbon and ash that remains in the boat after cooling is described in terms of varying degrees of agglomeration ranging from a very strong adhesive mass to completely free-flowing particles.

The boat test conducted with the alfalfa stems alone showed a very weakly agglomerated mass of char and ash. Just the weight of a pencil point could break up the mass and it also could not be extracted intact from the boat. It was weakly held together by the adhesion due to some tar pyrolysis products and ash components. The bagasse feedstock that was successfully gasified in the RENUGAS process development unit (PDU) at IGT showed a more strongly agglomerated mass in the boat test compared to the alfalfa. However, the subsequent PDU bagasse gasification test at 1600°F (871°C) did not show any evidence of agglomeration with the agitation and mixing with the inert material in the fluidized-bed gasifier. Bagasse, however, is washed of most of the potassium and sodium elements in the sugaring process, so a precaution is recommended for initial alfalfa gasification tests.

One possibility for preventing agglomeration in the gasifier is to add small amounts of certain additives that contain magnesium, which is known to combine with alkali and prevent the formation of the lower melting temperature agglomerates. Two such additives were tested in the boat tests. These additives were magnesium oxide and a high magnesium carbonate content dolomite. The amount of these materials that were added to the alfalfa was kept to a minimum and was calculated as a one-to-one weight ratio of the amount of potassium that was measured in the ash of the samples, i.e., 4 wt % magnesium oxide and 8 wt % dolomite.

All of the boat tests conducted with these two additives showed that the char-ash residue became completely free flowing, just like dry sand. Hence, if the alfalfa fluidized-bed gasifier is designed to operate with dolomite as the fluidized-bed media, then alfalfa ash agglomeration will be controlled and not a concern. Furthermore, conditions for alkali capture or removal from the product gas stream should be enhanced with the collection of the dolomite fines by the hot gas filter.

BASIC GASIFICATION PROCESS CONDITIONS: The specification of the basic conditions for the air-blown, fluidized-bed gasification process include the gasification temperature and pressure, and to a lesser degree, the acceptable limits for feed moisture and the amount of steam addition to the fluidized bed. The gasification temperature is the most important operating variable in terms of achieving the highest carbon conversion efficiency, namely, conversion of the feed carbon to gases along with the lowest amount of oil and tar species in the product gas. The incoming feed moisture will affect the amount of air needed to maintain a selected gasification temperature. Hence, the heating value of the product gas is affected due to feed moisture and the additional air that is required to maintain the gasification temperature.

Based on data in Figure 3 from the thermobalance test of the alfalfa char gasification rate at pressure and 1600°F, and from the previous gasification test experience in the IGT RENUGAS™ 10 ton per day process development unit (PDU) with the Hawaiian bagasse feedstock at 1580°F, which yielded 96% bagasse feed carbon conversion, it is expected that an alfalfa gasification temperature near 1600°F should yield similar or greater feed carbon conversions.

PDU TESTS WITH ALFALFA: In a concurrent DOE program, the IGT RENUGAS process development unit (PDU) gasifier system was modified to evaluate the hot gas cleanup for the 100

ton per day bagasse demonstration gasifier being built in Hawaii. One alfalfa gasification test was conducted in that program. The alfalfa was successfully reduced in size with a forage harvester with an increase in the bulk density to about 10 lbs per cubic foot and fed smoothly to the PDU gasifier at the rate of 7.7 tons per day for an 8-hour test duration. The entire alfalfa plant was gasified, including the leaves and stems.

The PDU gasifier results showed that the alfalfa carbon conversion to gases and condensible liquids at the 1470°F gasifier temperature was about 98%, and the product gas composition was similar to bagasse gasification. The alfalfa test in the PDU was conducted with about 8 wt % dolomite added with the alfalfa to the fluidized bed of the inert alumina bead material used for alfalfa gasification. However, in this limited test, the test conditions were not optimized for the alfalfa according to the conditions identified in this feasibility study, but overall, the test indicates alfalfa can be successfully gasified. Additional alfalfa gasification performance testing at the PDU or larger scale is needed to obtain detailed engineering design information. Alfalfa exhibits some variation in the amount and type of ash components between the stem and leaf fractions and also between the different growing regions around the proposed plant site. It is expected that these differences will not impact the proposed alfalfa gasification scheme, but this also needs to be evaluated with gasification tests. The gasification of alfalfa stems in a fluidized bed of dolomite is expected to control ash agglomeration tendencies.

Table 1. ALFALFA ANALYSIS: FROM THREE COUNTIES NEAR THE PLANT SITE

County	*Olivia*		*Montevideo*		*Clarkfield*		*Average*	
Moisture and Ash Analysis, wt %	Stems	Leaves	Stems	Leaves	Stems	Leaves	Stems	Leaves
Moisture	9.99	6.65	8.40	6.91	9.73	6.42	9.37	6.66
Ash	5.18	11.01	4.62	7.37	4.69	9.03	4.83	9.14
Ultimate Analysis, wt %								
Ash	5.65	11.43	4.98	7.68	5.14	9.48	5.26	9.53
Carbon	47.15	47.11	47.47	48.22	46.96	47.02	47.19	47.45
Hydrogen	5.84	5.89	5.94	6.10	5.93	5.92	5.90	5.97
Nitrogen	2.14	4.76	2.07	4.80	1.98	4.53	2.06	4.70
Sulfur	0.08	0.29	0.08	0.28	0.08	0.21	0.08	0.26
Oxygen (by diff.)	39.14	30.52	39.46	32.92	39.91	32.84	39.5	32.09
Total	100.00	100.00	100.00	100.00	100.00	100.00	100.00	100.00
Higher Heating Value, Btu/lb (dry)	8030	8230	8140	8660	8080	8360	8083	8417

Table 2. ELEMENTAL ASH ANALYSIS OF ALFALFA: THREE COUNTIES NEAR THE PLANT SITE

County	Olivia		Montevideo		Clarkfield		Average	
Ash Element, wt % of Ash	Stems	Leaves	Stems	Leaves	Stems	Leaves	Stems	Leaves
Silicon	0.23	0.56	0.26	0.25	0.80	1.21	0.43	0.67
Aluminum	0.00	0.00	0.00	0.00	0.00	0.00	0.00	0.00
Iron	0.00	0.00	0.00	0.00	0.00	0.00	0.00	0.00
Manganese	0.00	0.00	0.00	0.00	0.00	0.00	0.00	0.00
Titanium	0.00	0.00	0.00	0.00	0.00	0.00	0.00	0.00
Phosphorus	0.95	0.76	1.84	1.13	1.57	1.93	1.45	1.27
Calcium	5.67	5.77	6.33	11.40	13.80	11.20	8.60	9.46
Magnesium	1.46	1.18	2.09	1.69	1.65	2.29	1.73	1.72
Sodium	0.56	0.49	0.70	0.37	0.32	0.42	0.53	0.43
Potassium	10.50	7.40	12.60	9.59	6.23	10.50	9.78	9.16
Sulfur	0.52	0.50	0.62	1.24	2.04	1.54	1.06	1.09

Figure 1 Power And Co-Product Plant Concept

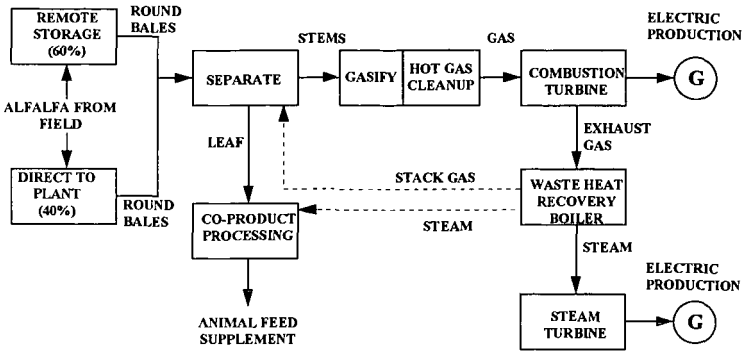

Figure 2 Processing Plant

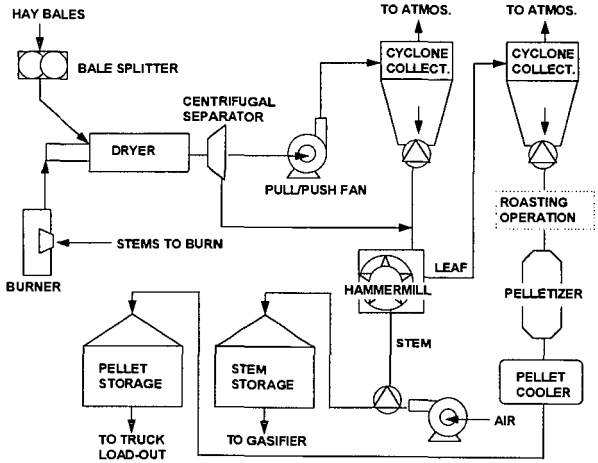

Figure 3. Comparison of Char Gasification Rates

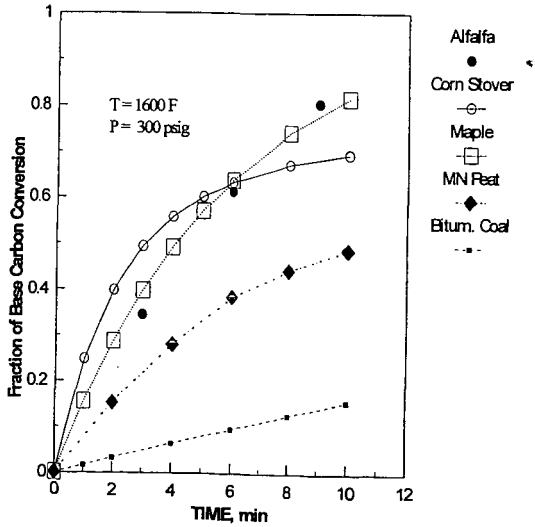

PRESSURIZED THERMOGRAVIMETRIC REACTIVITY STUDY OF WHEAT STRAW COMBUSTION AND CO_2-GASIFICATION.

Ole Rathmann and Jytte B. Illerup
Department of Combustion Research
Risø National Laboratory
DK-4000 Roskilde, DENMARK.

Keywords: Wheat-straw biomass, Pressurized, Gasification reactivity.

Abstract.
Biomass fuel reactivity is interesting since biomass, as e.g. wheat straw, is a relevant fuel for advanced pressurized power plants due to the CO_2 neutrality. In this study combustion- and CO_2-gasification reactivities of pulverized wheat straw char up to 40 bar were investigated by isothermal thermogravimetric analysis, and the results were compared to a typical subbituminous coal. A recently built pressurized thermogravimetric analyzer of the horizontal type, with operating conditions at least up to 1200°C, 45 bar, was used. In the study the effects of temperature and partial pressure of the reactants O_2 and CO_2, respectively, were seen, for gasification also the inhibition effect of CO, whereas a distinct total pressure effect could not be observed. Also the effect of using non-pulverized straw pieces was investigated.

INTRODUCTION

The use of biomass fuels for power generation and heat production has a number of advantages with the CO_2 neutrality and saving of depletable fossil fuels among the most obvious. In addition, national legislation in Denmark urge to use locally available biomass as e.g. wood waste and straw. Considering the future, characterization of biomass fuel will thus be relevant in relation to combustion and gasification for high efficiency pressurized power plant types (as IGCC). As a result, research groups in Scandinavia and elsewhere have been active in characterizing the biomass fuels relevant in their respective countries, and main issues have been influence of pressure, temperature and gas composition on the reaction rate.

Especially wood, straw and black liquor char gasification reactivities at moderate reaction rates have been studied using large-sample vertical Pressurized ThermoGravimetric Analyzer (PTGA) instruments. Blackadder & Rensfelt (1985) studied pyrolysis of wood, cellulose and lignine up to 800 °C at 1 to 40 bar. Moilanen et al. (1993) investigated atmospheric steam gasification of chars of wood, peat and black-liquor in comparison with coal and brown-coal, while Whitty et al.(1993b) investigated pyrolysis and char CO_2-gasification of coarsely pulverized wood and peat at 850°C at 1-20 bar. Stoltze et al.(1993) studied atmospheric steam gasification of large samples of barley straw char at 750°C-950°C. Black liquor char was investigated by Backman et al. (1993) and by Whitty (1993) regarding pressurized CO_2- and steam gasification in presence of CO at 650-800°C and 1-30 bar. The following overall picture is seen: In pyrolysis, wood char yield increases clearly with increasing pyrolysis pressure, while the reactivity displays a weak decrease. Wood char reactivity is similar to that of peat and brown coal and about 1 order of magnitude faster than for coal, black liquor displays a reactivity 2 orders of magnitude faster than wood, and gasification with steam has a reactivity about 4 times faster than with CO_2. The reactvity increases strongly with increasing temperature and as seen for coal. Increase in total pressure at constant gas percentage composition has a weak, enhancing effect for wood while for black liquor the effect is directly reducing, attributed to inhibition by CO or H_2 inside the char pores.

In this work we have investigated combustion and CO_2-gasification reaction rates of straw as this fuel is expected to be one of the important biomass fuels in future advanced Danish power/heating stations. The work was performed under contract with and the Danish utility associations Elsam and Elkraft within the European Union APAS programme, and was supported by the Danish Ministry of Energy.

EXPERIMENTAL

The fuel samples were prepared from wheat straw normally used in Danish electrical-power/district-heating stations. Entire straws were ground to pulverized, average straw samples with a particle diameter smaller than 200μm. Char of pulverized straw, straw inter-node pieces, straw nodes and grains were produced in a furnace by a 7 minutes 900 °C pyrolysis heat treatment at atmospheric pressure without oxygen access. The raw fuel compositions given in table 1 indicate rather similar proximate compositions while ash compositions differ, especially with respect to K_2O and P_2O_5.

The PTGA-instrument used for the study (fig.1) is a modified DuPont thermogravimetric analyzer of the horizontal type, recently built at RISØ. The fuel sample is placed on a small 1cm diameter Platinum tray hanging on a horizontal balance arm, situated in a reaction tube together with thermocouples. The reaction tube is heated from outside by a heater element, and the entire thermobalance arrangement is placed inside a 35 l pressure vessel. Pressure and flow control are performed by a number of valves and gas mass flow controllers. The test gas, selectable from either an inert gas (N_2) source or a premixed reactive gas source, is supplied to the rear end of the reaction tube with a filler element to heat the test gas to operating temperature. A test gas rate corresponding to a linear velocity in the reaction tube of about 1 cm/s at 1000 °C is used giving a switching time for the gas composition at the sample position of about 100 s. The balance sytem is the original DuPont component, while reaction tube, oven and all external systems are new. The PTGA can operate up to 45 bar and 1200°C simultaneously. Samples up to about 150 mg can be investigated, but for low density fuels the practical limit is set by the fuel volume and may be 5 to 10 mg. Data logging is performed once per 2 seconds.

Pyrolysis experimcnts were performed in an inert test gas with a ramped temperature. The combustion and gasification reactivity experiments were performed isothermally with the operating temperature established in inert test gas after which the reactive test gas (N_2/O_2 or $N_2/CO_2/CO$ mixture) was selected. The maximum conversion rate that could be measured was set by the test gas switching time and the maximum diffusion rate of reactant to the sample and within the sample.

The experimental weight signals were compensated for bouyancy and balance arm length expansion, based on calibration tests. For the reactivity experiments a transformation then followed of the compensated weight to a conversion degree X and a reactivity R(= reaction rate per remaining char)

$$X = (m_{c0}-m_c)/m_c \qquad (1)$$
$$R = -dm_c/dt /m_c = dX/dt /(1-X) \qquad (2)$$

where m_c and m_{c0} are the instantaneous and initial char mass on dry and ash free basis, respectively. Each reactivity experiment was characterized by the reactivity at 50% conversion, $R_{0.5}$, and the variation of R with conversion X was, as an approximation, described by a single normalized reactivity profile f(X) (normalized to 1.0 at X=0.5) for each of the reaction types, i.e. $R(X) \approx R_{0.5} f(X)$. An estimate of the reaction time to a certain conversion degree could then be calculated as

$$t_X = 1/R_{0.5} \int_0^X f(X')/(1-X')dX' \qquad (3)$$

RESULTS

A minor number of pyrolysis experiments were performed on raw, pulverized straw samples to see the influence of heating rate and pressure in the temperature range 150-1000°C. At 20 bar, heating rates of 10, 30 or 50°C/min had no effect on char yield. With a heating rate of 30°C/min the char yield seemed to increase weakly with pressure: 15%, 20% and 22% char yield (2.5% uncertainty) for 1.5, 20 bar and 40 bar, and the maximum pyrolysis rate occurred in a narrow range from 342°C to 355°C. More accurate experimental results are necessary to quantify the pressure effect on the char yield. As these results showed little effect of pyrolysis pressure it was assumed that the atmospheric pyrolysis pressure was of no importance for the resulting char.

Combustion reactivity was measured at temperatures from 300°C to 410°C, pressures from 1.5 bar to 40 bar and O_2 pressures from 0.08 bar to 0.8 bar. The results for $R_{0.5}$ are shown in fig.2. The reactivity increased with increasing conversion degree, with values at X=0.2 and X=0.8 about 0.6 and 1.7 times the value at X=0.5, respectively. While results at such low temperatures are not directly applicable to practical conditions they permit comparison to corresponding reference coal data. At 400°C and 0.26 bar O_2, the reactivity was found to be about $0.002 s^{-1}$, about 30 times higher than the reactivity for the reference coal. The dependence on temperature and O_2 partial pressure corresponds to an activation energy of 110 kJ/mole and a reaction order of 0.61. The activation energy is similar to that of the reference coal but the reaction order is a little lower. No significant effect of the total pressure was observed.

CO_2 gasification reactivity was measured in the fluidized-bed relevant temperature range 850°C-1050°C at 20 bar and with 3 different gas compositions, including one with the inhibitor-component CO, as shown in fig.3. A few of these experiments were repeated at 4 and 40 bar total pressure with unchanged CO_2/CO partial pressures. At 1000°C the reactivity $R_{0.5}$ was found to be about $0.006s^{-1}$ in 0.7 bar CO_2 and no CO. The reactivity increased with conversion degree, with values at X=0.2 and X=0.8 about 0.6 and 2 times the value at X=0.5, respectively. The present straw reactivity is about 16 times faster than for the reference coal and 1.5-2 times faster than for the wood reactivity as measured by Whitty et al.(1993a). The results for $R_{0.5}$ could be interpreted in terms of Langmuir-Hinshelwood kinetics (see e.g. Laurendeau (1978)):

$$R_{0.5} = k_1 P_{CO2}/(1+aP_{CO} + bP_{CO2}),$$

where k_1, a, and b have Arrhenius temperature dependence, for a and b, however, with negative activation energies. In spite of some unsystematic variation in the experimental data, saturation (described by the 'b' parameter) was clearly observed as the reactivity increased less than proportionally to the increase in CO_2 pressure from 0.7 to 2.2 bar in absence of CO. Also, the clear decrease in reactivity from 1.5 to 5 times, when changing from a 2/0 bar to a 2/2 bar CO_2/CO test gas, indicates clearly inhibition (described by the 'a' parameter) at the test temperatures. Both the saturation and inhibition effects showed an expected reduction with increasing temperature. The present results are too scarce to permit an unambiguous determination of kinetic parameters, but as shown in fig.3, a Langmuir-Hinshelwood representation could be obtained using a- and b-parameters from the reference coal in combination with a fitted k_1-parameter. However, the value of this k_1-parameter in dependence of temperature is strongly dependent on the applied values of the a- and b- parameters. The measurements suggest a moderate reactivity reduction with increasing total pressure, may be up to 2 times when the pressure is increased from 4 to 40 bar at constant CO_2 and CO partial pressures. In contrast to black liquor reactivity, the present data suggest an increasing reactivity when increasing the pressure at constant gas percentage composition.

The reactivity of char of non-pulverized 'straw particles' was measured at 900-1000°C with 20 bar pressure and 2/2 bar CO_2/CO partial pressure. Relative to the char of average, pulverized straw the inter-node particles showed a reactivity more than 2.5 times faster, node-particles showed a reactivity 2 times slower at 900°C while at 950°C and 1000°C it was more than 3 times faster than for pulverized straw. Grains showed a reactivity about 2.5 times slower than pulverized straw. The surprising faster reactions of inter-node and node particles may be due to the non-packed structure of the sample, but for the nodes this behavior may also be due to the higher concentration of the catalyst K_2O in the ash (see table 1).

DISCUSSION AND CONCLUSION

The present PTGA instrument has proved to be a valuable instrument for biomass fuel reactivity analysis at moderate reaction rates, in the present study of wheat straw.

Pyrolysis of pulverized straw suggested a small increase in char yield with increasing pressure. Pressurized combustion and gasification reactivity of straw char samples, pyrolyzed at low heating rate, was investigated up to 40 bar but with the main part of the investigations at 20 bar.

The combustion reactivity at low temperature (around 350°C) with 0.08 to 0.8 bar O_2 was somewhat more than one order of magnitude higher than for a reference coal and with the same relative temperature dependence. The dependence on O_2 partial pressure was weaker, and no significant dependence on total pressure (at constant partial pressure) could be observed.

CO_2-Gasification reactivity was investigated around 950°C at CO_2 and CO pressures around 1 bar. The results, displaying both CO_2-saturation and Co-inhibition, could be understood in terms of Langmuir-Hinshelwood kinetics, but more accurate measurements are necessary to actually determine the kinetic parameters. In absolute magnitude the straw char reactivity was found to be an order of magnitude higher than for the reference coal and also a little higher than for wood biomass. Char of non-pulverized `straw-particles', including grains, displayed reaction rates moderately scattering above (3 times) and below (2 times) that of the pulverized samples, presumably as a combined result of size effect, compactness and composition of the non-pulverized particles. The pulverized fuel reactivity results displayed a moderate decrease with total pressure, but more accurate measurements are needed to tell whether this is a significant effect. Also, experiments with chars pyrolyzed at high heating rates at various pressures would be relevant to distinguish between the effects of total pressure through pyrolysis and through char gasification.

REFERENCES

Backman,R., Frederick,W.J. and Hupa,M., *Basic Studies on Black-Liquor Pyrolysis and Char Gasification.* Bioresource Technology **46** (1993) pp 153-158.

Blackadder, W., Rensfelt,E. (1985). *A pressurized thermobalance for pyrolysis and gasification studies of biomass, wood and peat*, in: Fundamentals of Thermochemical Biomass Conversion, edited by R.P. Overend et.al., Elsevier (1985).

Laurendeau,N.M.(1978). *Heterogeneous Kinetics of Coal Char Gasification and Combustion.* Prog.Energy Combust. Sci. **4** (1978), pp 221-270.

Moilanen,A., Saviharju,K. and Harju,T. (1993). *Steam gasification reactivities of various fuel chars,* in: Advances in Thermochemical Biomass Conversion, pp.131-141, edited by Bridgwater, A.V., Blackie Academic & Professional (1993).

Stoltze,S., Henriksen,U., Lyngbech,T. and Christensen,O. (1993). *Gasification of straw in a large-sample TGA.* Nordic seminar on solid fuel reactivity, Gothenburg, Nov. 24th 1993.

Whitty,K.J. (1993a). *Gasification of black liquor with H_2O under pressurized conditions.* M.Sci. thesis. Report 93-4, Dept. Chem.Engin. Åbo Akademi, Finland.

Whitty,K.J., Sorvari,V., Backman,R.,and Hupa,M.(1993b). *Pressurized pyrolysis and gasification studies of biomasses.* Åbo Akademi, Department of Chemical Engineering, Report 93-7, IFRF Swedish-Finnish Flame Days 1993.

TABLES AND FIGURES

Table 1. Fuel proximate-ultimate analysis.
Most relevant species and compounds are included.

w% in dry non-pyrolyzed fuel	Pulv. straw (average)	Straw-nodes	Grain
Ash	6.4	9.0	1.6
Volatiles	77.3	75.1	83.2
Hydrogen	5.8		6.8
Carbon	47.2		44.6
w% in ash			
SiO_2	62	2.7	1.4
CaO	8.1	11	3.7
MgO	1.8	3.4	11
Na_2O	0.4	0.2	0.2
K_2O	14	55	34
P_2O5	2.4	2.0	45

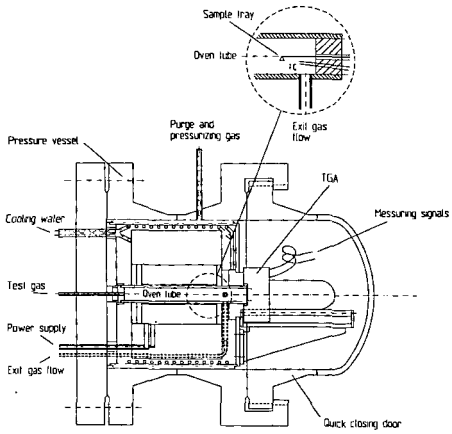

Fig 1. Recently built Pressurized Thermogravimetric Analyzer instrument used in this study. All electrical connection fit-throughs are placed in the rear flange (left side) of the pressure vessel.

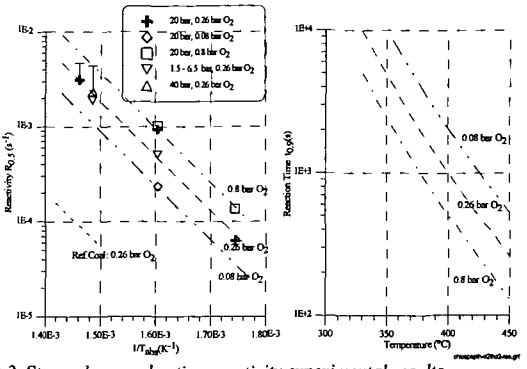

Fig.2. Straw char combustion reactivity experimental results.

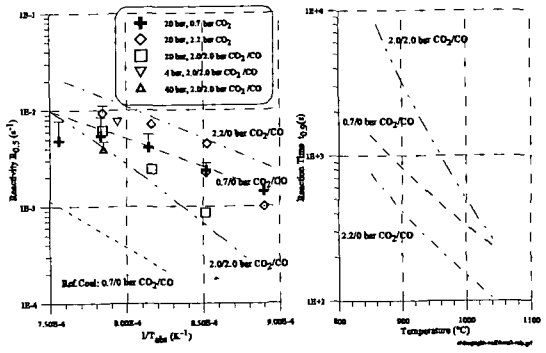

Fig.3. Straw char CO_2-gasification reactivity experimental results.

In both fig.2 and fig.3 representative Langmuir-Hinshelwood kinetic model values are shown by dashed and dash-dotted lines. Error bars indicate uncertainty due to large instrument diffusion limitation. The over-all accuracy is 10-15%. Preliminary results from a reference pulverized coal char (Colombian Cerrejón) are included. Predictions of conversion times to a conversion degree of 0.9 are shown in the right part of the figures.

PYROLYSIS AND COMBUSTION OF PULVERIZED WHEAT IN A PRESSURIZED ENTRAINED FLOW REACTOR

Jan Fjellerup, Erik Gjernes and Lars K. Hansen
Department of Combustion Research
Risø National Laboratory
DK-4000 Roskilde, Denmark

Keywords: Straw, pressurized, reactivity

INTRODUCTION

During recent years there has been an increasing interest for pressurized combustion and gasification of solid fuels in power plants due to the potential for high efficiency. The utilization of new types of solid fuels for pressurized combustion and gasification depends on the reactivity at relevant conditions. Risø's pressurized laboratory was established in 1992 with the aim of studying pressurized pyrolysis, combustion and gasification of solid fuels. At present the laboratory comprises a Pressurized Entrained Flow Reactor (PEFR) and a Pressurized Thermogravimetric Analyzer (PTGA) for the study of reactivity of solid fuels at high pressure. In the present paper the PEFR facility is presented and pyrolysis and combustion of pulverized straw at elevated pressure are shown.

EXPERIMENTAL

The PEFR facility

Pyrolysis and combustion of pulverized wheat were performed in a PEFR [1]. The reactor is operated differentially, which means that the reactant gas flow is large compared to the particle flow. This implies that during combustion or gasification of solid fuels, the bulk concentration and temperature are well controlled. The system layout of the facility is seen on Figure 1. The main components are the gas mixing system, pressure vessels, furnace, moveable probe, gas outlet and conditioning system. The systems consists of a vertical cylindric furnace fed with a reaction gas of a specified composition. The furnace consists of three parts; a gas preheater section and two half cylinder reactor sections each with Super Kanthal heating elements which can give a maximum reactor temperature of 1500°C.

The fuel is fed pneumatically by the primary gas through a narrow ceramic tube and enters near the top of the reaction tube. The fuel tube is mounted through the centre of the gas preheater and cooled by water to avoid reaction of the fuel in the preheating section. The reactor tube is approximately 7 cm ID and 2 m long. The probe can be positioned to collect particles at various distances and thereby various residence times. The probe is water cooled and nitrogen quench gas is added to the top of the probe to stop the chemical reaction instantaneously as soon as the particles enter the probe. The collected particles are trapped on a filter, and they are analyzed for moisture, volatiles and ash content in the TGA. The conversion of the particles is determined using the ash tracer technique.

The furnace is built into a 100 bar pressure vessel. The reaction gas is a mixture of various gases N_2, O_2, H_2, CO_2, CO, CH_4 and H_2O (as steam). The reaction gas is added to the top of the furnace after being preheated to the furnace temperature. The flow is estimated to give the wanted gas velocity in the furnace at the actual furnace temperature and pressure. An average gas velocity of 0.3 m/s is used in all experiments. Assuming a laminar parabolic velocity distribution, the 0.3 m/s average gas velocity corresponds to a gas velocity of 0.6 m/s centrally in the reactor.

The performance of the facility is listed in table 1.

Fuel selection and preparation

The biomass selected for this study was Danish wheat, which were pulverized [2] and sieved with an Alpine sieve. The size distribution based on mass can be seen in Table 2, while the proximate and ultimate analysis are shown in Table 2 and 3, respectively [3].

RESULTS AND DISCUSSION

In the PEFR experiments samples were taken out at five different locations representing a residence time of 0.5 to 2.5 s. The residence time is based on a velocity of 0.6 m/s. All samples have been double analyzed for ash percentage in the TGA, and the conversion is calculated using the ash tracer technique. The results are presented as m/m0, which is the collected DAF (Dried and Ash Free) mass divided by the initial DAF mass.

Pyrolysis

The pyrolysis experiments were performed at 10 bars total pressure in an atmosphere of pure nitrogen, and at temperatures of 700, 800, 900 and 1000°C. Figure 2 shows the m/m0 value plotted versus time for the 1000°C case. The experiments resolved a mass loss profile showing that the m/m0 value is decreasing towards the end point at 2.5 s. The final values for the 700 to 1000°C experiments were 0.14, 0.12, 0.10 and 0.11. For the 900 and 1000°C cases approximate constant m/m0 values were found at the last three probe positions which corresponds to a residence time of 1.2, 1.6 and 2.5 s. By averaging the results from these three probe positions the m/m0 value became 0.10 for both cases. The proximative analysis gave a pyrolysis yield of 81.5%, while in the present experiments the yield is increased to 90%.

Combustion

Combustion experiments were performed in an atmosphere of nitrogen and oxygen at 800°C and 10 bar and at 1000°C using both 10 and 20 bars total pressure. The mass loss profile for the experiments at 800°C is shown in Figure 3 and the pyrolysis level found above is indicated by a solid line. Figure 3 shows that for a residence time of 0.5 s the m/m0 is below the pyrolysis level, which means that the straw has started to burn. For a residence time of 1.2 s the particle has burned more than 98% (pyrolysis+combustion), and the conversion remains constant with residence time. Figure 4 shows that at 10 bar and 1000°C the pulverized straw has burned 95% at 0.5 s residence time. The final conversion at 2.5 s residence time is 99.5%, which is higher than the 800°C case. At 20 bars pressure the conversion at 0.5 s residence time is only 80% compared to 95% at 10 bars pressure, even though, the oxygen partial pressure is higher for the 20 bars experiments. The final conversion at 2.5 s residence time is 97%. Thus the general trend is that the combustion reactivity is decreased with increasing total pressure.

CONCLUSION

The pyrolysis experiments show that the pulverized straw pyrolysis 90 % of DAF in the PEFR at 1000°C and 10 bars pressure, which is above the volatile yield from the proximative analysis (81.5% of DAF). The pyrolysis in the reactor at 900-1000°C reaches its final values in about 1 s.

The combustion experiments show a high reactivity with oxygen, at 10 bar and 1000°C the pulverized straw has burned 95% at a residence time of 0.5 s. Increasing the absolute pressure from 10 to 20 bar for similar temperature and oxygen partial pressure reduces the conversion of the pulverized straw.

ACKNOWLEDGMENTS

This work has been performed within the European Union APAS Clean Coal Technology Programme for the Danish utility associations Elsam and Elkraft and for the Danish Ministry of Energy under the EFP91 programme.

REFERENCES

1. Hansen, L.K., Fjellerup, J., Stoholm, P. and Kirkegaard, M. (1995). *The Pressurized Entrained Flow Reactor at Risø. Design Report.* Risø-R-822(EN).

2. Wenzel, W. et al. (1994). *Versuche zur Grosskornvergasung von Stroh in der Versuchsanlage Freiberg.*(in German). NOELL Energie- und Entsorgungstechnik GmbH, Freiberg.

3. Illerup, J.B. and Ethelfeld, J. (1995). *Combustion and Gasification of Coal and Straw under Pressurized Conditions. Task 1: Preparation and characterization of fuels.* Risø-R-809(EN), Risø National Laboratory, Denmark.

Table 1. The performance of the PEFR facility

Pressure	0.1 - 80 bar
Primary gas flow	0.3 - 6.0 Nm^3/hr
Reaction gas flow	1.5 - 30 Nm^3/hr
Reaction gas preheating	600 - 1500°C
Reactor temperature	600 - 1500°C
Fuel (coal or biomass) up to 10mm	10 - 300 g/h
Optical ports (Used at moderate pressures)	10 (2 in two levels) (3 in two levels)

Table 2. Size distribution based on mass (sieve method) and proximate analysis of pulverized wheat (wt%)

Size (μm)	wt %
> 1000	0
500 - 1000	0.2
250 - 500	6.2
125 - 250	25.0
63 - 125	14.7
32 - 63	9.5
< 32	44.4

	Dry	DAF
Fixed Carbon	17.5	18.5
Volatiles	77.3	81.5
Ash	5.2	---

Table 3. Ultimate Analysis, wt

C	H	N	S	Cl	Na	K	O
47.2	5.8	0.7	0.17	0.17	0.034	0.70	45.2

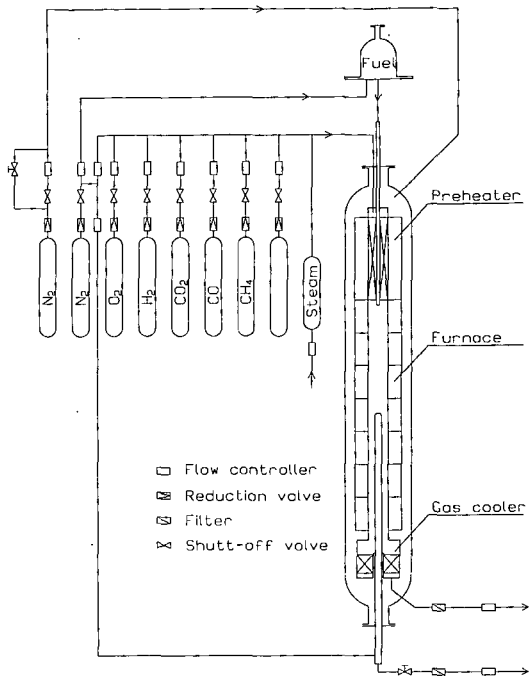

Figure 1. PEFR system layout

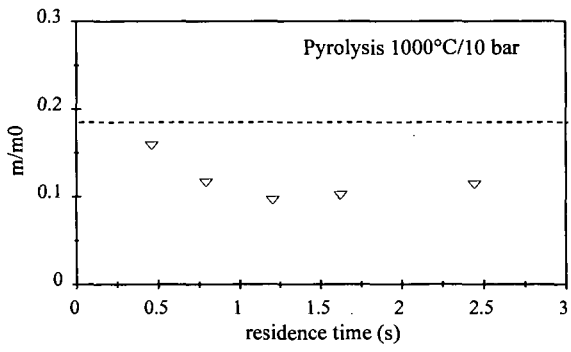

Figure 2. Pyrolysis of pulverized straw at 10 bar and 1000°C. Collected DAF mass divided by the initial DAF mass (m/m0) is plotted versus residence time. The line indicates proximate pyrolysis level.

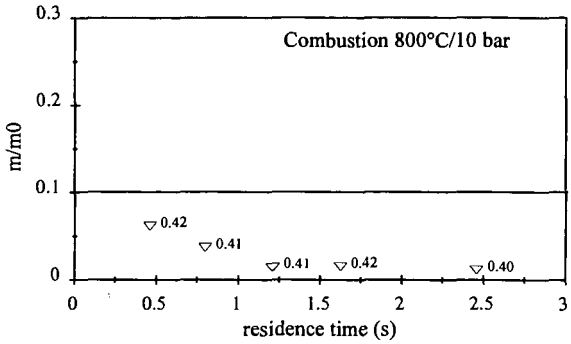

Figure 3. Combustion of pulverized straw at 10 bar and 800°C. Solid line indicates pyrolysis level, and partial pressure of oxygen in bar is written at each point.

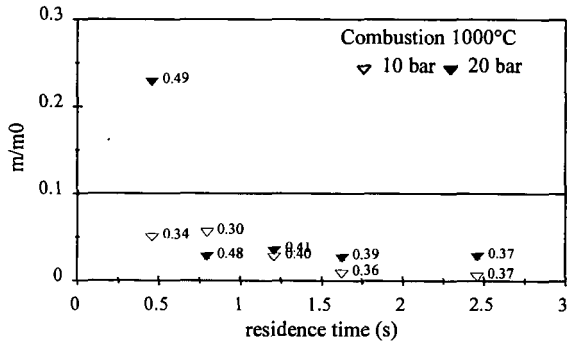

Figure 4. Combustion of pulverized straw at 10 and 20 bar and 1000°C. Solid line indicates pyrolysis level for the 10 bar case, and partial pressure of oxygen in bar is written at each point.

LIFETIME TESTING OF CATALYSTS FOR CONDITIONING THE PRODUCTS OF A BIOMASS GASIFIER

W. A. Jacoby, S. C. Gebhard and R. L. Vojdani
National Renewable Energy Laboratory
1617 Cole Boulevard
Golden, CO 80401

Keywords: synthesis gas, hot-gas conditioning, biomass gasification

INTRODUCTION

The National Renewable Energy Laboratory, in collaboration with its industrial and academic partners, is engaged in a project with the goal of developing and facilitating the commercialization of safe, cost-effective, and environmentally benign technologies for the production of transportation fuels from biomass via thermal gasification. The block diagram below illustrates the steps involved.

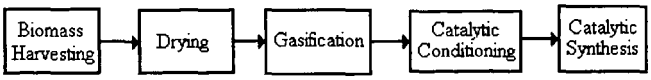

The research presented in this paper focuses on the catalytic conditioning step, also referred to as hot-gas conditioning. The product of biomass gasification is crude synthesis gas, a mixture of hydrogen (H_2), carbon monoxide (CO), carbon dioxide (CO_2), methane (CH_4), steam, and higher molecular weight hydrocarbons and oxygenates (referred to as tar). The goals of synthesis gas conditioning are threefold: 1) reduce the concentration of tar by catalyzing steam reforming reactions; 2) reduce the concentration of methane by catalyzing steam reforming reactions; 3) increase the hydrogen/carbon monoxide ratio from the value of 0.7 (representative of crude syngas from a biomass gasifier) to about 2 (desirable for production of synfuels or H_2) by catalyzing the water-gas shift reaction.

Previous investigations have focused on developing catalysts or disposable solids to achieve hot-gas conditioning. The most promising materials identified in recent work have been commercial supported nickel (Ni)-steam reforming catalysts and dolomite.[1-7] Dolomite is only moderately effective for tar destruction. The primary issue with Ni-based steam reforming catalysts is lifetime. When exposed to the high molecular weight aromatic hydrocarbon and oxygenated compounds found in biomass gasifier tar, supported Ni catalysts deactivate on a time scale that is unacceptable for commercial use.

EXPERIMENTAL METHODS

The experimental apparatus is illustrated in Figure 1. It includes a vaporizer enclosed in a single zone furnace. A high pressure, positive displacement liquid pump feeds water to the vaporizer for steam generation. A second identical pump supplies a mixture of aromatics (benzene, toluene, and naphthalene) to simulate the tar found in syngas from a biomass gasifier. The liquids are vaporized in a stainless steel tube packed with stainless steel balls. Hydrogen and a 3:1:1 mixture of CO, CO_2 and CH_4, are also metered into the vaporizer through mass flow controllers. This model crude syngas solution is fed into a catalytic reactor operating in down-flow mode and heated by a three zone furnace equipped with microprocessor temperature control. Reactors are fabricated from stainless steel with aspect ratios appropriate for catalyst loads between 0.5 grams and 30 grams. Catalyst particles are ground and sieved to 16-20 mesh size (0.841 mm to 1.19 mm). Two basic reactor/catalyst configurations are tested, a commercial Ni-based steam reforming catalyst alone and Ni catalyst in conjunction with an upstream high-temperature water-gas shift co-catalyst in a dual bed reactor. The Ni catalysts are reduced overnight (15 hrs) prior to use in a stream of 14% H_2 in steam and He at 600°C. The composition of the feed and product mixtures is monitored by two computer controlled, on-line gas chromatographs; one for the permanent gases (Carle Refinery gas analyzer) and one for tar (Hewlett Packard 5890II with a DB-5 capillary column). The apparatus is automated and equipped with safety features that allow it to operate unattended during extended lifetime tests.

RESULTS AND DISCUSSION

Supported Ni catalysts will catalyze steam reforming of methane and tar compounds. Figure 2 illustrates the performance of United Catalysts Inc. (UCI) G90B Ni catalyst in treating the model crude syngas mixture with a steam mole fraction of 0.5. The simulated tar solution introduced into the vaporizer was comprised of 5 mole percent naphthalene in benzene. The composition of the effluent gas was monitored hourly. The observations reported were made under steady state conditions more than 60 hours into the run. We observed near complete conversion of tar and a high conversion of methane by steam reforming; however, the effluent mixture did not achieve equilibrium with respect to water-gas shift and CO hydrogenation.

The issue of catalyst lifetime was addressed during a subsequent experiment run under similar conditions. The UCI G90B remained active for 585 hours (the experiment was stopped at this time when a feed line plugged). A significant build up of coke was observed in and around the catalyst bed and many of the catalyst particles had been reduced to a fine powder. The steam content of the syngas produced during biomass gasification can be as low as 0.3-mole fraction[1], therefore the performance of the catalyst at lower steam to carbon ratios is of interest. Figure 3 shows that reducing the steam mole fraction in the feed

shortens catalyst lifetime. Thus, the use of supported nickel catalyst alone may not be practical for the synthesis gas conditioning application.[2-4] In all cases in Figure 2, steam is in excess over that required by stoichiometry for both steam reforming of tar and the water-gas shift reaction. The large effect of steam concentration in this case supports previous assertions that the water adsorption rate is important for these reactions.[8]

Alumina will catalyze the water-gas shift reaction at high temperatures[9]. Figure 4 illustrates this activity for χ-alumina at 815°C. Near equilibrium concentrations of CO, H_2, and CO_2 were observed with and without steam pretreatment (50% steam in He for 10 hours at 850°C) and in the presence and absence of a model tar compound (1 mole percent toluene). In separate experiments, an η-alumina also catalyzed the water-gas shift reaction. Coke was not formed to a significant extent on either of the aluminas.

The combined effect of the alumina and nickel catalyst would fulfill the syngas conditioning objectives if their performance characteristics were additive. Figure 5 shows the results of an experiment addressing this possibility. The primary bed containing Imperial Chemical Industries (ICI) 46-1, K-promoted supported Ni catalyst was combined with an upstream co-catalyst bed of χ-alumina. The ICI catalyst was used in this initial proof of concept run because it has been shown to be active for conditioning of the effluent of a biomass gasifier and is resistant to deactivation.[10] Later experiments involved UCI G90B because it was expected that this catalyst would be more susceptible to deactivation in this application, increasing the sensitivity of investigation of the efficacy of the alumina bed.[11] This dual bed reactor was fed with a model crude syngas mixture containing a 0.5-mole fraction steam and a 0.01-mole fraction toluene. Figure 5 shows that both toluene and methane steam reforming and water-gas shift are achieved simultaneously. Thus, the dual bed concept provides the catalyst activity needed to effectively condition biomass gasifier synthesis gas, but questions of catalyst lifetime remain.

The function of the upstream, co-catalyst bed is to catalyze the water-gas shift reaction. This is postulated to improve the lifetime of the downstream Ni steam reforming catalyst by increasing the concentration of hydrogen adsorbed on the surface of the Ni crystallites. An increased surface hydrogen atom coverage could inhibit coke formation if the rate of hydrogenating adsorbed coke precursors is greater than the rate of precursor polymerization. Table 1 outlines a 2^4 factorial designed to test this hypothesis. The primary response is the elapsed time until the "end of useful life". This transition corresponds to a loss of tar and methane reforming activity, i.e., when gas chromatographic peak areas for methane and tar compounds rose to within experimental error of the areas of the same peaks during control runs.

Table 1 also summarizes the results of the 2^2 factorial subset of this experimental work that has been completed to date. In this work, the model crude syngas mixture contained 0.3-mole fraction steam and a 0.03-mole fraction of tar solution comprised of 5 mole percent naphthalene in benzene. Based on the results of previous work, the total gas flow rates and the amounts of UCI G90B and alumina were chosen to give a gas hourly space velocity (GHSV) of 170,000 h^{-1} for the Ni catalyst, and a GHSV = 2,000 h^{-1} for the alumina catalyst. The response reported for the 2^2 factorial experiment is the loss of tar reforming activity. In some cases, the loss methane of reforming activity occurred more quickly than the loss of tar reforming activity, but our conclusions regarding the use of the alumina co-catalyst bed are not altered.

This 2^2 experimental design investigated the main effects of the presence or absence of an upstream alumina co-catalyst bed and the temperature of the reactor. It shows that the co-catalyst bed significantly increases the lifetime of the Ni catalyst (B = +55 hours). Figure 6 illustrates this effect; increased lifetime was observed with respect to methane, benzene, and naphthalene steam reforming. Data analysis also revealed that the temperature and temperature-co-catalyst interaction are less important (T = +13 hours and B x T = +23 hours). When the entire 2^4 design matrix has been completed, it will be possible to estimate the standard error in the response based on the magnitude of third and fourth order interactions and tests of significance will be performed.

CONCLUSIONS AND FUTURE WORK

Our results show that a dual bed configuration using alumina as a co-catalyst upstream of a conventional Ni-based steam reforming catalyst provides appropriate activity and can increase the catalyst lifetime for catalytic conditioning of a model biomass gasifier product gas. The full experimental design also addresses main effects and interactions involving steam mole fraction and reactor temperature, as well as a comparison of the UCI G90B catalyst and an experimental catalyst (Ni/Al_2O_3 promoted with oxides of chromium, magnesium, and lanthanum). The results of a comprehensive catalyst characterization effort will be reported and the use of mixed metal oxides with perovskite structures as the co-catalyst are also planned. Finally, the optimal configuration identified in the laboratory experiments will be tested with syngas generated in a pilot scale biomass gasifier currently under construction at NREL.

ACKNOWLEDGEMENTS

This work was funded by the Department of Energy's Biofuels Systems Division through the NREL Biofuels Program. The authors would also like to thank Esteban Chornet, Ralph Overend, Robert Evans, and Helena Chum for useful discussions.

REFERENCES

1. Furman, A. H., Kimura, S. G., Ayala, R. E., and Joyce, J. F. Biomass gasification pilot plant study. AEERL-748, 3R, 6/8/93. Prepared for the U. S. Environmental Protection Agency, Office of Research and Development, Washington, DC.

2. Aznar, M. P., Corella, J., Delgado, J., and Lahoz, J. Improved steam gasification of lignocellulosic residues in a fluidized bed with commercial steam reforming catalysts. *Ind. Eng. Chem. Res.* 32, 1-10 (1993).
3. Baker, E. G., Mudge, L. K., and Brown, M. D. Steam gasification of biomass with secondary catalysts. *Ind. Eng. Chem. Res.* 26, 1335 - 1339 (1987).
4. Donnot, A., Magne, P., and Deglise, X. Method of determining catalyst lifetime in the cracking reaction of tar from wood pyrolysis. *J. Anal. and Appl. Pyrolysis*, 22 39 - 46 (1991).
5. Simell, P. A. and Bredenberg, J. B. Catalytic purification of tarry fuel gas. *Fuel* 69, 1219 - 1225 (1990).
6. Simell, P. A., Leppälahti, J. K., and Bredenberg, J. B. Catalytic purification of tarry fuel gas with carbonate rocks and ferrous materials. *Fuel* 71, 211-218 (1992).
7. Vassilatos, V., Taralas, G., Sjöström, K., and Björnbom, E. Catalytic cracking of tar in biomass pyrolysis gas in the presence of calcined dolomite. *J. Canadian Chem. Eng.* 70, 1008 - 1013 (1992).
8. Rostrup-Nielsen, J. R. Activity of nickel catalysts for steam reforming of hydrocarbons. *J. Catal.* 31, 173-199 (1973).
9. Amenomiya, Y. Active sites on solid acid catalysts, II. Water-gas conversion on alumina and some other catalysts. *J. Catal.* 55, 205 - 212 (1978).
10. Zhou, J. Catalytie tar reforming for gasified biomass. Masters Thesis, University of Hawaii, 1994.
11. Mudge, L. K., Baker, E. G., Brown, M. D., and Wilcox, W. A. Bench scale studies on gasification of biomass in the presence of catalyst. Report PNL-5669, Pacific Northwest Laboratories, Richland, WA, 1987.

Table 1: 2^4 Experimental Design and Initial Results

Factors				Variable	Levels	
B	T	S	K		-	+
-	-	-	-	B = Co-catalyst Bed	no	yes
+	-	-	-	T = Temperature	750°C	800°C
-	+	-	-	S = Steam Mole Fraction	30%	40%
+	+	-	-	K = Ni Catalyst	UCI G90B	Exp.
-	-	+	-			
+	-	+	-			
-	+	+	-			
+	+	+	-			
-	-	-	+			
+	-	-	+			
-	+	-	+			
+	+	-	+			
-	-	+	+			
+	-	+	+			
-	+	+	+			
+	+	+	+			

Initial Results: 2^2 Design

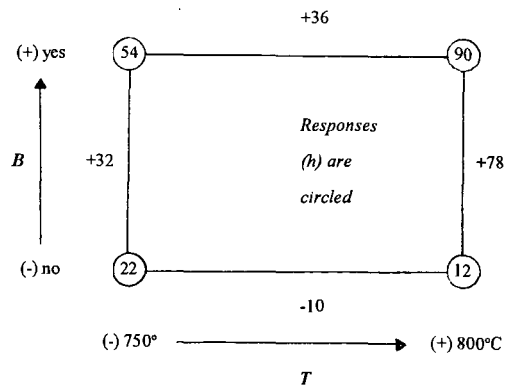

Figure 1: Schematic of Experimental Apparatus

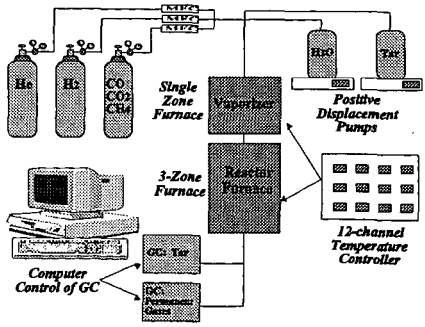

Figure 2: Activity of UCI G90B Catalyst

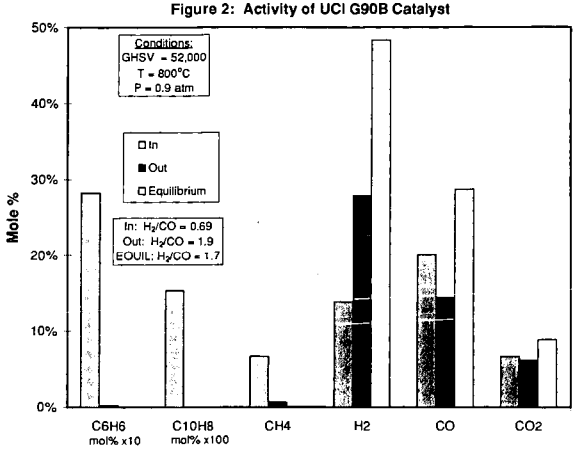

Figure 3: Effect of Steam on Time to Complete Deactivation for UCI G90B

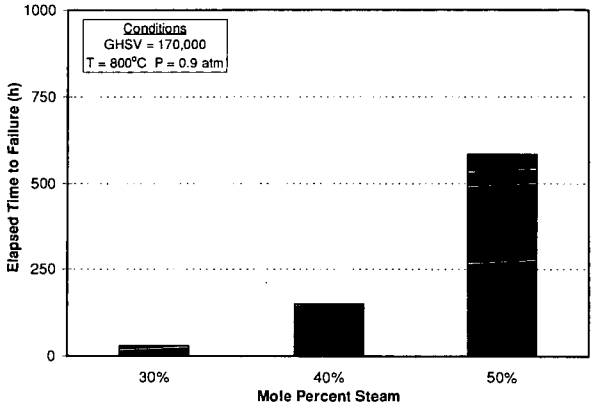

Figure 4: Water Gas Shift Activity of χ-Alumina Catalyst

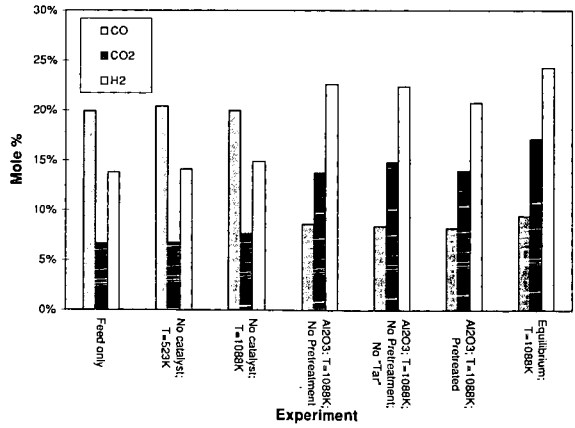

Figure 5: Activity of Dual Bed System with ICI 46-1 and χ-Al_2O_3

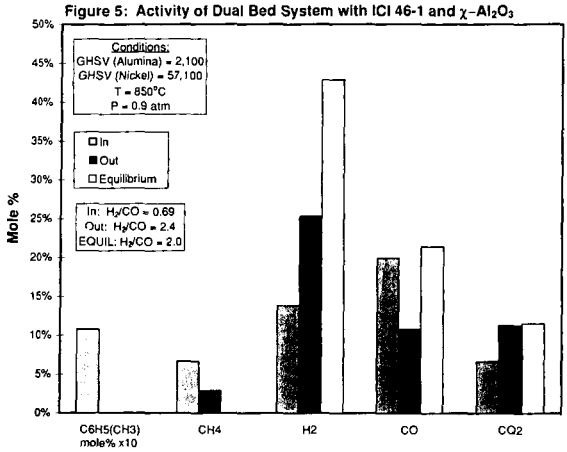

Figure 6: Steam Reforming Activity vs. Elapsed Time

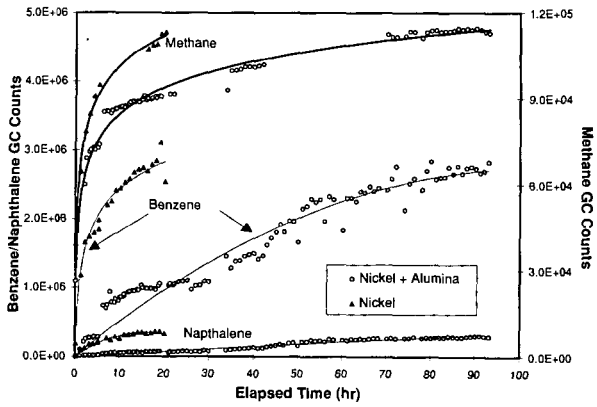

INDIRECT LIQUEFACTION OF BIOMASS: A FRESH APPROACH

J.L. Cox, A.Y. Tonkovich, D.C. Elliott, E.G. Baker
Pacific Northwest Laboratory
Richland, Washington 99352

E.J. Hoffman
P.O. Box 1852
Laramie, Wyoming 82070

Keywords: gasification, liquefaction, biomass

INTRODUCTION

A variety of gaseous products for use as synthetic fuels and chemicals are produced by gasifying biomass. The actual product composition depends on the biomass composition and the reaction conditions. Several different gasification approaches have been investigated, at rather small scale, and reported in the literature (1,2). Many of these methods have their roots in coal gasification, including the work on catalytic gasification presented by Baker and Mudge (3) and Cox et al. (4). Catalytic gasification takes advantage of catalysts to serve two primary functions: 1) to increase the yield of gases, at the expense of tar and char, at lower temperatures than are possible without catalysts, and 2) to catalyze secondary reactions to produce the specific product desired. Sufficiently high rates can be achieved to allow operation at lower temperatures so that oxygen is not needed as a co-reactant, thus eliminating the need for an oxygen plant.

One catalytic approach to producing synthetic fuels and chemicals is indirect liquefaction of biomass, which entails gasifying the biomass to create a synthesis gas consisting of hydrogen and oxides of carbon. These materials, in turn, are converted to the desired liquid fuels and/or chemicals by suitable choice of catalyst, synthesis gas composition, and reaction conditions. This type of approach has been extensively investigated where coal is the carbonaceous feed material, but it has not been extended seriously to biomass and other feedstocks. It is generally recognized that developing gasification methods to produce the synthesis gas poses one of the major technical and economic challenges to improving this technology. This paper reports a different slant on indirect liquefaction that could stimulate advancements in the efficiency and economics of the process for biomass.

BIOMASS GASIFICATION - A NEW APPROACH

The new approach to biomass gasification outlined here is predicated on the concept that it is better to gasify biomass to a CO_2-synthesis gas composed primarily of H_2 and CO_2, rather than a CO-synthesis gas composed primarily of H_2 and CO. The conversion to CO_2-syn gas, and its subsequent utilization, may be superior, both technically and economically, to the route through a CO-syn gas.

A comparison of the stoichiometry of the respective routes is shown in Reactions (1) and (3), respectively.

$$C + H_2O = CO + H_2 \quad (1)$$

$$\underline{CO + H_2O = CO_2 + H_2} \quad (2)$$

$$C + 2H_2O = 2H_2 + CO_2 \quad (3)$$

Both carbon-steam ($C\text{-}H_2O$) gasification reactions are endothermic. The enthalpy of the $C\text{-}H_2O$ reaction to produce CO-syn gas is 31.4 kcal/g-mole, while only 21.6 kcal/g-mole are required for the CO_2-syn gas reaction. The difference between the two reactions is the exothermic (-9.8 kcal/g-mole) CO-shift reaction given in Reaction (2). Clearly, biomass is not carbon; nevertheless, the conclusions are the same except the steam gasification of biomass is even more facile than carbon (i.e., graphite), and the thermodynamics are more favorable.

Minimizing the energy requirements for the gasification portion of the overall sequence in the indirect conversion to fuels and chemicals eases the burden of the most costly and inefficient step in the overall process. Pinto and Rogerson (5) report the cost of the reformer/gasmaking portion of a steam-reforming methanol plant constitutes 45% of the total capital cost. Henery and Louks (6) have shown that the economics of producing synthetic natural gas (SNG), i.e., methane, from coal and lignite depend strongly on the

cost of adding heat to the steam-carbon reaction. The amount of heat supplied and the method by which it is supplied to the gasification reactions are highly critical to the economics. In the case of SNG, Henery and Louks (6) estimate the cost of the gasification heat is 1/3 the cost of product (SNG). Any process that takes advantage of exothermic gasification reactions (e.g., $CO + H_2O = CO_2 + H_2$ and $C + H_2 = CH_4$) in the gasifier can reduce external heat requirements and substantially improve process economics and efficiency. Calculations based on Reactions (1) and (3) indicate that CO_2-syn gas requires 31% less energy to produce than CO-syn gas.

Another advantage of biomass in general is its reactivity allows sufficiently low temperatures (<750°C) to be employed so that reaction enthalpy can be supplied indirectly by a tube still reactant heat exchanger. Consequently, there is no need for pure oxygen or a plant to produce it, and a major expense and energy penalty to the gasification section of the operating plant is eliminated.

Because the reactivity of biomass varies among the different types (7,8), reaction conditions can be selected to favor the production of CO_2-syn gas over CO-syn gas, including temperature, residence time, steam:biomass ratio, and the use of catalysts. The predicted gasification product composition is particularly sensitive to temperature and steam:biomass feed ratios. This sensitivity is shown in the equilibrium data in Table I, which indicate that the optimum conditions for producing CO_2-syn gas are high steam:biomass ratio, low temperatures, and low pressures. At 1 atm, 600°C, and a steam:biomass (i.e., H_2O:C) mole ratio of 10:1, the product gas composition is 65.4% H_2, 31.2% CO_2, 3.0% CO, and 0.4% CH_4. Since biomass has about 30 wt% oxygen, the amount of water required is predicted to be substantially less than 10:1.

While practically all gasification studies, irrespective of carbonaceous feedstock, have been conducted with the goal of producing CO-syn gas, there is sufficient experimental and theoretical evidence to suggest that, through reaction engineering principles, high conversions of feedstocks can be achieved, producing high yields of CO_2-syn gas. Some of the predictions in Table I can be compared with experimental results under similar conditions shown in Table II.

CO- AND CO_2- SYNTHESIS GAS CHEMISTRY

Work on the use of synthesis gas to produce a broad range of products began about 70 years ago in Germany with the production of fuels using cobalt catalysts (11-13). While this chemistry is loosely referred to as Fischer-Tropsch in recognition of the pioneering and extensive contribution of these individuals, there has been literally hundreds of significant contributors. The use of CO-syn gas has been the focus of this work, while CO_2-syn gas has scarcely been considered.

Table III illustrates the range of products that can be produced from CO-syn gas. Interestingly, optimum methanol synthesis over Cu/ZnO catalysts requires about 5% CO_2 in the inlet gas. If the CO_2 content is lower or higher, the methanol formation rate drops. Furthermore, the methanol formation apparently does not occur if the synthesis gas is free of CO_2 and H_2O. Russian investigators (18,19) have accounted for these observations by a mechanism where methanol formation is dominated by hydrogenation of CO_2 formed during reaction by the water gas shift reaction from CO:

$$CO + H_2O + 2H_2 \rightarrow [3H_2 + CO_2] \rightarrow CH_3OH + H_2O \qquad (4)$$

Kuechen et al. (20) reported that a deactivated Cu/ZnO catalyst at 3-5 Mpa (30-50 atm) and 483-543K gave maximum rates of methanol synthesis with H_2-CO-CO_2 syn gas ratio 70:0:30. The activation energy of methanol synthesis from CO_2 and H_2 was considerably lower than that from CO and H_2. Cox et al. (4) reported the methanation of CO-free CO_2-syn gas ($4H_2/CO_2$) in a packed bed reactor over supported nickel catalyst at 375°C, 100 psig, and space velocities of up to 7000 hr^{-1}.

REACTION COMPARISONS

Many of the synthesis schemes that have used CO-syn gas in the past appear to be possible using CO_2-syn gas, as indicated here. The respective stoichiometries of aliphatic, olefin, and alcohol hydrocarbon formation from CO- and CO_2-syn gases are shown in Reactions (5) through (10). The thermochemistry of some of the simpler homologs of these series of compounds is shown in Tables IVA and IVB. The data show that each are exothermic with favorable free energy changes at low temperatures and high pressures.

$$(2n+1)H_2 + nCO = C_nH_{2n+2} + nH_2O \quad (5)$$

$$2nH_2 + nCO = C_nH_{2n} + nH_2O \quad (6)$$

$$2nH_2 + nCO = C_nH_{2n+1}OH + (n-1)H_2O \quad (7)$$

$$(3n+1)H_2 + nCO_2 = C_nH_{2n+2} + 2nH_2O \quad (8)$$

$$3nH_2 + nCO_2 = C_nH_{2n} + 2nH_2O \quad (9)$$

$$3nH_2 + nCO_2 = C_nH_{2n+1}OH + (2n-1)H_2O \quad (10)$$

The advantage of using CO_2-syn gas in place of CO-syn gas may have significant overall process implications and, in some instances, reaction-specific benefits, as discussed below. For example, a comparison of the enthalpies of the CO- and CO_2-syn gases at 300°C shows the methanation to be about 18% less for the CO_2-syn gas (Reaction 8, n=1) than for CO-syn gas (Reaction 5, n=1), 35% less for the olefin formation (Reaction 9, n=2), 39% less for methanol formation (Reaction 10, n=1), and 29% less for ethanol formation (Reaction 10, n=2). Both CO- and CO_2-syn gas reactions are favored by pressure, but the CO-syn gas reactions are more favored than CO_2-syn gas. Comparative volume contractions for CO-syn gas versus CO_2-syn gas reactions are 50% versus 40% for methanation, 50% versus 37.5% for olefin formation, 66.5% versus 40% for methanol formation, and 66.7% versus 50% for ethanol formation. Hence, pressure can be used to considerable advantage to increase equilibrium conversions.

As expected from the enthalpies of reaction, the free energies are less for the respective CO_2-syn gas reactions. At 200°C, the respective free energy change (kcal/mole) for the CO- and CO_2-syn gas reactions are, respectively, -24.6 versus -19.5 for methanation, -13.46 versus -3.25 for olefin formation, 3.8 versus 8.9 for methanol formation, and -9.9 versus 0.3 for ethanol formation. For those reaction conditions with positive free energy changes, elevated pressures can be used to increase equilibrium yields, as is currently practiced in the commercial production of methanol from CO-syn gas. In the alcohol synthesis reactions, where free energy changes are not as favorable as for the other hydrocarbon synthesis reactions, higher pressures would be required to achieve equivalent equilibrium yields with the CO_2-syn gas.

Although some adjustments may be needed, these comparisons show the two synthetic gases to have comparable reactions for producing the desired products. Another salient feature of the new approach is that carbon deposition should not be the problem it is for CO-syn gas since the CO_2 counters the Boudouard reaction.

$$2CO = C + CO_2 \quad (11)$$

In addition, as can be seen from the thermodynamic data in Table IVB, synthesis reactions with CO_2-syn gas are less exothermic, reducing the difficulty of temperature control and expense of extra duty heat transfer equipment encountered when using CO-syn gas. Furthermore, lowering the concentration of CO alleviates a safety concern.

CONCLUSIONS

A new approach to indirect liquefaction of biomass is advocated based on the premise that it is easier to gasify the biomass to a CO_2-syn gas than to a CO-syn gas. Thermodynamic arguments are presented that show an energy savings of about 30%. Experimental data are presented that are consistent with the thermodynamic prediction that a CO_2-syn gas can be achieved through control of gasification conditions. Optimum gasification conditions are about 600°C, atmospheric pressure, and steam:biomass ratio equal to 10:1 in the presence of a gasification catalyst. The CO_2-syn gas under these conditions consists of 65.4% H_2, 31.2% CO_2, 3.0% CO, and 0.4% CH_4. Thermodynamic predictions have also been presented along with experimental results that indicate the range of products produced by catalytic conversion of CO_2-syn gas is comparable to products produced with CO-syn gas. Furthermore, carbon deposition and heat removal and temperature control are predicted to be more easily controlled with CO_2-syn gas chemistry. Even if catalytic conversion diversity with CO_2-syn gas is not as versatile as with CO-syn gas, the gasification to CO_2-syn gas represents an improvement in gasification efficiency, and the process can be used to produce fuel gas and hydrogen. While the discussion has focused on biomass, the concepts presented herein are appropriate for other carbonaceous materials such as coal and natural gas.

ACKNOWLEDGMENT
Pacific Northwest Laboratory is operated for the U.S. Department of Energy by Battelle Memorial Institute under Contract DE-AC06-76RLO 1830.

REFERENCES

(1) Bridgwater, A.V. ed. *Advances in Thermochemical Biomass Conversion.* Blackie Academic & Professional/ Chapman Hall, Glasgow: 1994.
(2) Overend, R.P.; Rivard, C.J. In *Proceedings First Biomass Conference of the Americas*, Vol. 1, pp. 471-497, 1993. NREL/CP-200-5768, National Renewable Energy Laboratory, Golden, Colorado.
(3) Baker, E.G.; Mudge, L.K. *Catalysis in Biomass Gasification.* PNL-5030, Pacific Northwest Laboratory, Richland, Washington: 1984.
(4) Cox, J.L. et al. *The Direct Production of Hydrocarbons from Coal-Steam Systems.* Research and Development Report No. 80, Office of Coal Research, U.S. Department of Interior: 1974.
(5) Pinto, A.; Rogerson, P.L. *Chemical Engineering*, **1977**, 102-108.
(6) Henery, J.P. Jr.; Louks, B.M. *Chem Tech.*, **1971**, 238-247.
(7) Roberts, A.F. *Combustion and Flame*, **1970**, *14*, 261-272.
(8) Schiefelbein, G.F. "Biomass Gasification Research: Recent Results and Future Trends." PNL-SA-12841, Pacific Northwest Laboratory, Richland, Washington: 1985.
(9) Lucchesi, A. et al. "Hydrogen by Pyrolysis-Gasification of Biomass." In *Proceedings of the Second International Symposium on Hydrogen Produced from Renewable Energy*, Cocoa Beach, Florida, October 22-24, 1985.
(10) Mudge, L.K.; Baker, E.G.; Mitchell, D.H.; Robertus, R.J.; Brown, M.D. *Catalytic Gasification Studies in a Pressurized Fluid Bed Unit.* PNL-4594, Pacific Northwest Laboratory, Richland, Washington: 1983.
(11) Storch, H.H.; Golumbic, N.; Anderson, R.B. In *The Fischer-Tropsch and Related Synthesis.* John Wiley & Sons: New York, 1951.
(12) Pichler, H. In *Advances in Catalysis.* Frankenburg, W.G.; Komarewsky, V.I.; Rideal, E.K. eds., Academic Press: New York, 1952, Vol. 4.
(13) Anderson, R.B. In *Catalysis.* Emmett, P.H. ed., Reinhold: New York, 1956, Vol. 4.
(14) Mills, G.A.; Steffgen, F.W. *Catalysis Reviews*, **1973**, *8*(2), 159-210.
(15) Marschner, F.; Moeller, F.W. In *Applied Industrial Catalysis.* Leach, B.E. ed., Academic Press: New York, 1983, Vol. 2.
(16) Hindermann, J. P.; Hutchings, G.J.; Kiennemann, A. *Catal. Rev.-Sci. Eng.*, **1993**, *35(1)*, 1-127.
(17) Iglesia, E.; Reyes, S.C.; Madon, R.I.J.; Soled, S.L. *Adv. in Catalysis*, **1993**, *39*, 221-302.
(18) Rosovskii, A.Y. *Khim. Prom*, **1980**, *11*, 652.
(19) Kagan, Y.B. et al. *Kinet. Catal.*, **1976**, *17*, 440.
(20) Kuechen, C.; Hoffmann, U. *Chem. Eng. Sci.*, **1993**, *48(22)*, 3767-3776.

TABLE I. Predicted Equilibrium Gasification Product Compositions (1 atm)

Product, mol. %	500°C	600°C	700°C	800°C
$H_2O:C = 0.5$				
H_2	38.1	49.3	50.9	49.8
CO_2	36.8	25.1	11.1	2.9
CO	4.9	16.8	34.9	46.2
CH_4	20.2	8.8	3.1	1.1
$H_2O:C = 1.0$				
H_2	38.1	49.3	50.9	49.8
CO_2	36.8	25.1	11.1	2.9
CO	4.9	16.8	34.9	46.2
CH_4	20.2	8.8	3.1	1.1
$H_2O:C = 2.0$				
H_2	38.1	50.7	57.1	57.1
CO_2	36.8	25.3	17.2	14.4
CO	4.9	16.0	24.7	28.4
CH_4	20.2	8.0	1.0	0.1
$H_2O:C = 3.0$				
H_2	46.2	58.8	60.9	60.0
CO_2	35.5	27.1	22.4	20.0
CO	3.9	10.9	16.4	20.0
CH_4	14.4	3.2	0.3	0.0
$H_2O:C = 5.0$				
H_2	56.9	63.8	63.2	62.6
CO_2	33.8	29.3	26.9	25.0
CO	2.7	4.5	6.3	8.0
CH_4	6.6	0.6	0.4	0.0
$H_2O:C = 10.0$				
H_2	64.6	65.4	65.1	64.7
CO_2	32.7	31.2	30.3	29.0
CO	1.5	3.0	4.6	6.3
CH_4	1.2	0.4	0.0	0.0

TABLE II. Experimental Gasification Results

Feed Material	coal char	olive-husks	biomass
Catalysts	$K_2CO_3/Ni\text{-}Al_2O_3$	none	$Ni\text{-}Al_2O_3$
Steam/feed, lb/lb	3.8	-	5.7
Pressure, psia	30	15	15
Temperature, °C	560	747	735
SCF H_2/ton feed	90,000	35,000	not reported
Product(mol%, H_2O free)			
CO	1.9	6	5.8
CO_2	36.6	25	29.9
H_2	61.4	67	64.1
CO	1.9	6	5.8
CH_4	0.0	2	0.2
Reference	4	9	10

TABLE III. Some Products Accessible Through CO-Synthesis Gas

Product	Reaction Conditions	Ref.
CH_4	$3H_2/CO$, 350-400 °C, 50-100atm, 5,000-10,000 h^{-1} GSV, Ni/Al_2O_3 Catalyst	14
CH_3OH	$2H_2/CO$, 230-300 °C, 50-100atm, Cu-ZnO Catalyst	15
$C_nH_{2n+1}OH$ (n>1)	$1.1H_2/CO$, 260 °C, 130atm, 5,000-10,000 h^{-1} GSV, K-promoted MoS_2 Catalyst	16
C_nH_{2n} (n=2-4)	$1.4H_2/CO$, 280 °C, 10atm, 340 h-1 GSV, Fe-Mn Catalyst	16
C_{5+}	$2.1H_2/CO$, 200 °C, 20atm, Co/SiO_2, 360 h^{-1}	17

TABLE IVA. Comparative Thermochemistry of CO- and CO_2- Synthesis Gases (reactants and products in their normal states)

	Free Energy,kcal				
Reaction	25°C	200°C	250°C	300°C	350°C
5(n=1)	-36.04	-24.59	-21.78	-18.94	-16.06
6(n=2)	-31.48	-13.46	- 9.34	- 5.16	- 0.95
7(n=1)	- 6.97	3.76	6.64	9.56	12.50
7(n=2)	-32.89	- 9.90	- 4.17	1.60	7.40
8(n=1)	-31.26	-19.49	-17.15	-14.77	-12.34
9(n=2)	-21.92	- 3.25	- 0.07	3.18	6.49
10(n=1)	- 2.19	8.86	11.27	13.73	16.22
10(n=2)	-23.34	0.31	5.09	9.94	14.85

TABLE IVB. Comparative Thermochemistry of CO- and CO_2- Synthesis Gases (reactants and products in their normal states)

	Enthalpy,kcal				
Reaction	25°C	200°C	250°C	300°C	350°C
5(n=1)	-59.78	-50.96	-51.38	-51.77	-52.13
6(n=2)	-71.26	-52.24	-52.76	-53.25	-53.70
7(n=1)	-30.63	-23.38	-23.72	-24.03	-24.31
7(n=2)	-81.83	-63.85	-64.34	-64.76	-65.13
8(n=1)	-60.47	-41.35	-41.88	-42.38	-42.85
9(n=2)	-72.64	-33.03	-33.76	-34.46	-35.13
10(n=1)	-31.32	-13.77	-14.22	-14.64	-15.02
10(n=2)	-83.21	-44.64	-45.33	-45.97	-46.56

METHANOL FROM BIOMASS VIA STEAM GASIFICATION

John A. Coffman
Wright-Malta Corp.
Plains Road
Ballston Spa, NY 12020

Keywords: steam gasification, biomass, methanol

ABSTRACT

R & D at Wright-Malta on gasification of biomass, and use of this gas in methanol synthesis, has now reached the stage where a demonstration plant is feasible. The gasifier has evolved into a long, slender, slightly declined, graded temperature series of stationary kiln sections, with box beam rotors and twin piston feed. The methanol reactor is envisioned as a smaller, more declined, graded temperature, water-filled stationary kiln, with a multi-pipe rotor. Input to the demo plant will be 100 tons/day of green (45% water) wood chips; output is projected at 11,000 gal/day of methanol and 7500 lbs/hr of steam. The over-all biomass to methanol system is tightly integrated in its mechanical design to take full advantage of the reactivity of biomass under a slow, steady, steamy pressurized cook, and the biomass pyrolysis and methanol synthesis exotherms. This is expected to yield good energy efficiency, environmental attractiveness, and economical operation.

INTRODUCTION

The oral presentation at the biomass symposium will consist primarily of pictures, drawings, graphs, and flow charts, illustrating the novelty in the mechanical equipment aspects of the W-M technology, as it has evolved over the past quarter-century. There is some novelty, too, in the steam gasification chemistry, the raw gas reformation into syngas, and the projected methanol synthesis. These aspects of the development will be emphasized in this written preprint.

STEAM GASIFICATION RESEARCH

Process parameters were determined in two bench-scale equipments: a "minikiln" and a "biogasser". One provided batch experimentation, giving a differential look at the process and an end point; the other permitted continuous operation and gave integrated data.

The minikiln was a rotating autoclave, about 1 ft in diameter and 3½ ft in length, electrically heated, with provision for steam injection under the bed and for product gas sampling and analysis. Test material, such as wood chips, corn stalks, or solid waste and sewage sludge, was placed in the barrel, the door bolted on, heating and rotation started, and the material tumbled in place, gradually heating, going on a simulated trip down a long kiln. At the end of the run, the minikiln was cooled, and the residue removed and weighed.

The biogasser was a long (10 ft), slender (2 in. ID), auger reactor, heated electrically, with provision for continuous feed of moist sawdust through lock valves into the cool end, and controlled release of product gas at the hot end. The solid residue dropped into a pressurized receptacle and was subsequently weighed. Water and condensable organics, if any, were stripped from the gas by passage through a condenser. The gas was analyzed by chromotography; its composition was representative of that expected from a commercial kiln.

The bench-scale research showed that a slow, steady, pressurized cook, with alkaline catalyst and steam, under temperature gradually increasing to a top figure of 1100-1150°F is sufficient to gasify any type of biomass to 95-98% completion. No air or oxygen is required. It also showed that there is a broad optimum pressure at 200-400 psi. Lower pressure tends to slow the gasification process; higher pressure tends to throw the product mix toward higher molecular weight tar and coke, a la LeChatelier. It was determined that steam reformation of the intermediate pyrolysis liquids and steam gasification of the char go to completion under about the same conditions. Perhaps the vapors drift down the kiln, are absorbed into

char, and crack there. When conditions are right and char consumption is essentially complete, the gas also is clean, and burns with a pale blue, non-luminous flame.

The slow, steady temperature rise of the biomass charge, imposed by the inherently sluggish heat transfer of an indirectly heated kiln, is beneficial to the chemistry of steam gasification. Water itself is not sufficiently dissociated, even at 1100°F, to attack the decomposing biomass, although there will be some ionic hydrolysis in the region up to about 500°F. Rather, activation comes from the free radicals formed by breakage of chemical bonds in biomass polymers, starting at about 350°F, the weakest breaking first, then the next stronger, etc. Water participates in the radical chain reactions. With the slow temperature rise, radicals are generated in a slow, steady stream, on up through the brown and black charry stages. Char at, say, 900°F, is still not carbon; it is an amorphous high polymer with about one atom of hydrogen to two atoms of carbon, and still forms radicals (mostly atomic hydrogen) when heated to higher temperatures. And so the decomposing biomass reacts with water/steam all through its slow heat-up, and most of its substance, except inorganic matter, is gone by 1100°F.

(In contrast, a chip dropped into a fluid bed at 1100°F forms its radicals in a rush, wasting most of them. Steam reaction with the decomposing chip is thwarted, too, by the outpouring of gaseous products, and a substantial charry residue remains.)

The over-all gasification process is depicted in the balanced equation below. The proportions of the product gas are experimental data, being the nearest whole number composite of many runs in the biogasser at optimum conditions. (It is of interest to note that they are close to equilibrium even though equilibrium would not be expected at 1100°F in the absence of a metallic catalyst.) Wood is fresh white pine at 45% moisture. The numbers under the formulas represent the heat content in Btu's of each constituent, derived from one pound of dry wood.

$$\underset{\substack{\text{(1 lb. dry wood)}\\ 4C_6H_9O_4\\ 9000\ \text{Btu}}}{} + \underset{\substack{\text{(0.8 lb water)}\\ 29H_2O}}{} \xrightarrow[\text{200-300 psi}]{\text{1100°F}}$$

$$\underset{248}{C} + \underset{6593}{10CH_4} + \underset{1264}{6H_2} + \underset{419}{2CO} + 11CO_2 + 21H_2O + \underset{476}{\text{exotherm}}$$

Experimentation in the minikiln, using it in a differential thermal analysis mode, determined the magnitude and temperature occurrence range of the wood decomposition exotherm. Data obtained were in agreement with the calculated figure and with the literature. There was some degree of overlap between the water evaporation endotherm at higher pressures and the decomposition exotherm, but not enough to blunt it unduly. Calculation indicated that production equipment should be operable in regenerative mode without external heat supply, after initial warm-up and without a 2nd law pinch, provided that the moisture content of the feed material is not more than 50%. That is, the temperature differential between the backcoming gas in the heating pipes on the rotor vanes, and the on-going gasification process in the kiln, will be everywhere sufficiently large to sustain the process. This is particularly true in the methanol system, where the backcoming reformed gas will have unusually high enthalpy.

EQUIPMENT CHANGE AND SCALE-UP

The steam gasification process has been studied in five equipments in this order:

1. Bench-scale, batch type rotary kiln-15 lb charge.
2. Bench-scale continuous auger kiln-20 lbs/hr.
3. Process development unit, steam-heated auger kiln-500 lbs/hr.
4. Bench-scale, batch type rotor kiln-12 lb charge.
5. Mini-process development, rotor kiln-60 lbs/hr.

In all of the equipments, with comparable feed stocks, temperatures, pressures, heat cycles, and alkaline catalyst concentrations, the degree of gasification completeness and the composition of the product gas were, within experimental error, identical. There is no reason to expect this slow, steady process to change appreciably with further scale-up to

projected "standard" production units at, say, 12.5 green tons/hr.

REFORMING TO SYNGAS

If the gas is taken from the hot end of the kiln and raised in temperature from 1100 to 1500°F in the presence of an equilibrating catalyst, its composition will shift as shown in the equation below. This equation was derived from a W-M computer program which calculates the gas composition having the minimum Gibbs free energy as a function of temperature and pressure. Similar programs have been verified experimentally by other investigators in steam-reforming of natural gas.

$$\underset{6593}{20CH_4} + \underset{1264}{12H_2} + \underset{419}{4CO} + 22CO_2 + 42H_2O \xrightarrow[200\ psi]{1500°F}$$

$$\underset{1648}{5CH_4} + \underset{5368}{51H_2} + \underset{2522}{25CO} + 16CO_2 + 33H_2O + \underset{-1363}{\text{endotherm}}$$

Note that most of the methane has been steam-reformed to H_2 and CO, that some of the CO_2 has been reduced to CO, that most of the energy is now in the H_2 and CO, and that the ratio between these gases is now 2.04/1.00, just right for methanol synthesis. This gas composition shift is strongly endothermic, and the heat of reaction must be supplied by external heating.

(It is instructive to combine the gasification and shift equations, giving a situation which would prevail if the gasification were performed at a top temperature of 1500°F and 200 psi. The process is now 476-1363 = -887 endothermic. This does not mean that the wood decomposition exotherm has changed; it remains reasonably constant at about 700 Btu. It does mean that the the over-all gasification process will range among varying degrees of endo- and exothermicity depending upon the final gas composition, which is in turn dependent upon temperature and pressure. Higher temperature and lower pressure throw it toward endothermicity and vice versa.

Wright-Malta favors a lightly exothermic, self-sustaining gasification and a separate gas composition shift for reasons of equipment cost and process efficiency.)

METHANOL SYNTHESIS

As the syngas leaves the reformer, it gives a little of its sensible heat to the incoming gas, and then flows into the backcoming pipes on the gasifier vanes at about 1300°F. It exits the kiln at the feed end, is stripped of its water and all but a couple per cent of its CO_2, and is then compressed adiabatically from 200 to 1500 psi and 600°F.

Rather than use a scaled-down version of a commercial methanol process for the demonstration plant, W-M intends to use a new reactor design. It is, naturally, a stationary kiln (3 ft by 20 ft) declining about 15° from the horizontal, with about a 200 pipe rotor. In each pipe (1 in.) is a loosely fitting chain, and in each link is a copper catalyst pellet, kept bright and active by the mild chafing which occurs as the rotor slowly turns. Syngas drifts downward through the rotor pipes, condensing chemically into methanol vapor and physically into liquid, with the equilibrium shifting toward the right as the temperature falls. Water flows slowly, countercurrently up through the kiln, warmed by the methanol exotherm, its sensible heat, and heat of condensation, and boiling at the top end. Conversion of syngas to methanol is expected to be sufficiently accomplished (perhaps 60%) in a single, slow pass through the reactor so that recycling will be minimal.

The over-all biomass to methanol system is a tightly integrated package, taking full advantage of exotherms and sensible heat. The reformer will be heated by burning part of the purge gas (mostly methane); the remainder will be recycled through the twin piston feed into the gasifier. Steam raised in the methanol reactor, and in a heat recovery boiler atop the reformer, may be used, as in the demonstration plant, for space heating, or to generate electricity for powering the compressor and other auxiliaries. In the latter instance, net energy efficiency, raw biomass to fuel grade methanol, is calculated to be at least 70%.

Momentum is building to take seriously the need to move toward sustainable development through renewable energy. Biomass is, by far, the most versatile and widely distributed form of renewable energy, and environmentally attractive as well. In the present business climate, particularly here in the States, biomass to methanol would seem to be the best renewable energy venture.

A MILD, CHEMICAL CONVERSION OF CELLULOSE TO HEXENE AND OTHER LIQUID HYDROCARBON FUELS AND ADDITIVES.

J. Michael Robinson
Chemistry Department, The University of Texas of the Permian Basin
Odessa, TX 79762

Keywords: Biomass, Liquid fuels, Chemical reduction

INTRODUCTION

Biomass fermentations and high temperature and pressure pyrolysis processes that produce gas or liquid fuels are legion. They all have drawbacks. For example, the theoretical limit of ethanol production is 67% due to the loss of 1/3 of the available carbon as carbon dioxidc gas during the fermentation. Pyrolytic reactions usually lose carbon as char and gases and may achieve about 80% carbon conversion [1] Furthermore, pyrochemical processes usually require nearly dry feedstocks. Obviously, there remains a need for a variety of fuels from many sources, especially conventional liquid fuels. To resolve this fuel problem and to use a renewable resource, a strategy was selected to prepare valuable hydrocarbons from biomass by a chemical process.

Our initial goal was to develop an efficient multistep chemical process for the conversion of the principle components of biomass, cellulose and hemicellulose, into hydrocarbon fuels. Separation of these components and/or the use of selective reactions might allow for 100% carbon conversion by keeping the carbon chain intact. Furthermore, if initial reactions could be conducted in an aqueous medium, then the use of wet feedstocks would be possible. Overall, a six carbon sugar polymer, cellulose, would afford a single pure hydrocarbon product such as hexene. This is precisely what we have developed, a novel *chemical* process.

RESULTS AND DISCUSSION

Our use of the term *chemical* implies the typical mild conditions usually employed in glass vessels. This process consists of three to four separate reactions, the first two of which occur in water. **Scheme I** comprises a brief summary of the main reaction steps that achieve the strategic objectives of the organic portion of the process. For simplicity in this abstract, Scheme I is shown with cellulose rather than raw biomass, although the latter works as well.

Step 1 is a reductive depolymerization of carbohydrate biopolymers. Cellulose is simultaneously hydrolysed in dilute acid and catalytically hydrogenated to glucitol (commonly named sorbitol) in near quantitative yields.[2] Hemicellulose is similarly converted into xylitol and sorbitol. Lignin, if present, is simply removed by filtration after the reaction. While the acid is mild, the highly selective rutheniun catalyst is only active at the temperature shown. Thus, Step 1 uniquely provides the required polyols required for the next reaction and simultaneously provides a facile separation of lignin.

Step 2 of the process is also a key reaction: the chemical conversion of polyhydric alcohols to liquid hydrocarbons. The major part of all the reduction requirements occurs in this conversion. Reduction of five hydroxyl groups of sorbitol occurs while one hydroxyl group gives substitution.

According to an early reference,[3] sorbitol reacts with aqueous HI and red phosphorous to afford 2-iodohexane in 95% yield. By-product I_2 is consumed by phosphorous.

Our strategy to overcome the physical problems of I_2 phase separation as a solid or of using solid red phosphorous was to use homogeneous chemical agents that concomitantly reduce I_2 to regenerate HI.[4] If the I_2 reacts quickly, it does not interfere with the polyol reduction reaction. Such use met with the unexpected results of simultaneous alkene formation and oligomerization. Considerable effort has been extended toward identifying the various products and the variables that control their formation.

Thus in Step 2, polyhydric alcohols such as sorbitol are reduced essentially quantitatively to a mixture of halocarbon and hydrocarbon compounds by reaction with hydriodic acid (HI) and a phosphorous type reducing agent, either phosphorous acid (H_3PO_3) or hypophosphorous acid (H_3PO_2). The reaction occurs in boiling aqueous solution at atmospheric pressure for about 1-2 hours. Reaction conditions were varied to give on one extreme about 99% 2-iodohexane and on the other extreme about 86% hydrocarbons with the remainder being halocarbons. The immiscible products are simply removed as a separate phase from the water solution. So Step 2 not only provides a highly reduced C_6 compound but also C_{12}, C_{18}, and C_{24} hydrocarbons. These groups represent fuels in the range of gasoline, kerosene, diesel, and fuel oil, respectively. Material balances (yields) are 100%(±4%) and were determined by GC/MS analyses of isolated product.

Each hydrocarbon group is a mixture of alkene isomers. The higher homologues typically contain a ring. An example structure for the $C_{12}H_{22}$ isomers (1,2,4-trimethyl-3-propylcyclohexene, MW = 166) is shown in Scheme I. Halocarbons detected were 2-iodohexane, isomers of $C_6H_{12}I_2$, and traces of $C_{12}H_{22}I_2$. Mannitol and xylitol gave similar results.

In contrast, we found that Step 2 products such as these do not form from glucose; it must first be reduced to sorbitol. Such products do not form on treatment of wood with HI.[5] In fact, these authors found that H_3PO_2 greatly "suppresses the yield of oil products." Products obtained in this manner are complex mixtures of high molecular weight oils and tars containing oxygen and high percents of iodine, not specific molecular weight range small hydrocarbons as in our process.

Step 3 might be considered a cleanup reaction in that all of the remaining halocarbons in mixtures from Step 2 are subsequently converted to alkenes by an elimination reaction with potassium hydroxide (KOH) in boiling alcohol. Vast differences in boiling points of hexene (68 °C) from the other higher mass hydrocarbons, 200 °C and 300 °C, allow facile separation by distillation of the final mixture. The mixture of isomers in each group depresses the melting point and helps the fuel remain liquid.

The elimination of HI (Step 3) by KOH produces KI as insoluble by-product. KI can be recycled to KOH and HI by electrochemical means using Aqua-Tech's bipolar cells.[6] Such regenerations are commercially economical. Hexene distilled after Step 3 is very low in iodine impurity, typically ranging from low teens to near 100 ppm. Further lowering of the iodine content is desired for two reasons: (1) potential corrosion due to the HI produced upon combustion, and (2) potentially expensive iodine replacement costs. However, 35 ppm iodine content only increases the cost of hexene by about $0.002/gal.

There are several optional steps, one of which is shown as **Step 4** in Scheme I. Catalytic hydrogenation of hexene furnishes hexane, an important industrial solvent. Hydrolysis of 2-iodohexane to 2-hexanol is another optional reaction to a value added product.

Physical values, H/C ratio, and octane numbers are shown for these fuels and compared to conventional liquid fuels in Table 1. Hexene, for example, has a RON of 93, density of 0.68, and a H/C ratio of 2, all ideal for gasoline. The C_{12} hydrocarbons have several desirable properties (less volatile, highly branched, cyclic, partially unsaturated, and a H/C ratio of 1.8) that should contribute to a high RON. This group might be suitable as a narrow boiling point range gasoline. However, this C_{12} mixture should have a density of 0.8 and a bp of about 200 °C, similar to the values of kerosene. The C_{18} and C_{24} isomer mixtures likely fit into the diesel and fuel oil ranges. Oxygenates marketed today are also compared with 2-hexanol.

SUMMARY AND ECONOMIC PROJECTION

This multistep *chemical* process for reduction of biomass to liquid hydrocarbon fuels is the first of its kind. It stands in sharp contrast to other research areas that follow classical lines of bio-(fermentation) or thermal (pyrolysis) conversion. In fact, uncoupling the reduction process to a series of mild selective chemical reactions was the key to the problem. As a result, economic advantages abound. One particular advantage of this *chemical* process is that both Step 1 and Step 2 reactions take place in water as solvent, which allows the use of wet biomass. The water immiscible organic products of Step 2 simply coalesce as an upper layer facilitating their separation by mere decantation. Another benefit of the process is that the cyclic alkene dimers and trimers produced directly in Step 2 actually require less reduction, 10% and 13%, respectively, than hexene. These oligomeric hydrocarbons also do not require base treatment and subsequent reagent regeneration costs as do the haloalkanes. Step 2 is highly tunable, which allows a choice of products. Each simple reaction step can be driven to essentially quantitative yield resulting in the same high yield for the entire process.

While we may only use hydrogen in Step 1, and the optional Step 4, it is convenient at this time to estimate the total costs of reduction based on a typical price for hydrogen. Using a hydrogen cost of $0.54/lb and a cost range of $10 to $40/ton for biomass (dry weight basis) containing 75% holocellulose, then total feedstock and reduction costs might be estimated as $0.49 to $0.64 per gallon for hexene. Similarly, the C_{12} and C_{18} isomers range from $0.44 to $0.60/gal. However, there are other chemical and mechanical costs associated with this multiple step process that will definitely contribute to overall process economics. Even if the real costs are twice as much, it might still be economical. Establishment of accurate economics will take some time. Total costs depend upon the exact steps, reagents, products, and precisely how the reagents are recycled. It is possible that the high quality, high value products available *via* this process may indeed be economically attractive in the near future, perhaps as fuel additives, even without a change in the margin of fossil fuels. Thanks to strong financial support from several sources, we are continuing to develop this process.

REFERENCES

1. Soltes, E.J. "Of Biomass, Pyrolysis, and Liquids Therefrom", Ch. 1 in ACS Symposium Series #376 "Pyrolysis Oils From Biomass; Producing, Analyzing, and Upgrading" Soltes, E.J. and Milne, T.A., Editors, American Chemical Society, Washington, D.C., **1988**.
2. Sharkov,V.I. "Production of Polyhydric Alcohols from Wood Polysaccharides," *Angew. Chem. I.E.E.* **1963**, *2*, 405.
3. Vincent,C.; Delachanal "Work with Sorbitol" *Compt. Rend*, **1890**, *109*, 677; *Beil.* **1918**, First Work, Band I, System 59, 533.
4. Foster,L.S.; Nahas,H.G.,Jr. "Hydriodic Acid: Regeneration of Oxidized Solutions," *Inorg. Synth.*, Vol. 2, 210, W.C. Fernelius, Ed., **1946**.
5. Cooper,D.; Douglas,M.; Ali,O.; Afrashtehfar,S.; Ng,D.; Cooke,N. "A Low Pressure-Low Temperature Process for the Conversion of Wood to Liquid Fuels and Chemicals Using Hydrogen Iodide" *Canadian Bioenergy R&D Semin. [Proc.] 5th*, **1984**, 455.
6. Mani,K.N. "Electrodialysis Water Splitting Technology," Aquatech Systems Report, Allied Signal, Inc., Warren, NJ, **1990**.

ACKNOWLEDGMENT

This research has been supported by UTPB; the Robert A. Welch Foundation (Texas); the National Renewable Energy Laboratory (NREL); and the U.S. Department of Energy, Basic Energy Sciences, Advanced Research Projects. Special thanks are extended to Dr. Norman Hackerman, President Emeritus of Rice University and Chairman of the Welch Foundation, as well as to Dan Tyndall and Dr. Tom Milne at NREL who have been particular helpful. Many students have participated in the research and development of this process over the span of several years. Their assistance is greatly appreciated.

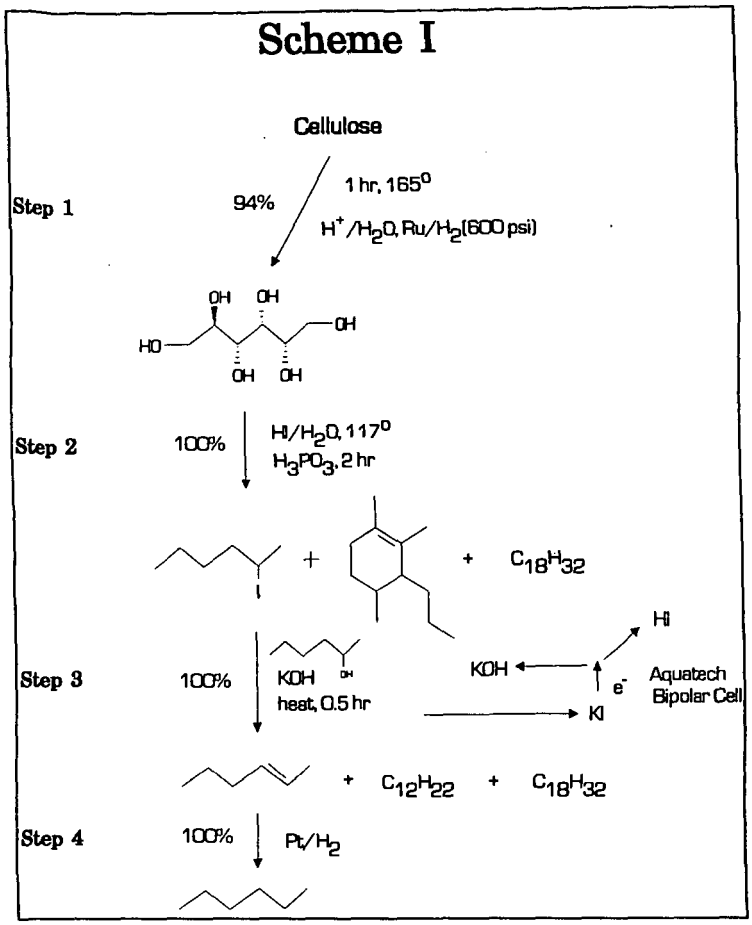

Table 1: Fuel Values

HYDROCARBONS

Compound	Formula	bp °C	RVP	d	H/C	Therm Val	Oct N
Hexane	C6H14	68	35	0.66	2.33	45 MJ/kg	25
Hexene	C6H12	69		0.67	2.0	(44.5)	93
gasoline	C4-C12	27-225	7-8	0.75	2.0	47.3	88
Dimers	C12H22	180-200		(0.76)	1.8		(high)
diesel	C14-C19	240-360	nil	0.84	2.1	43	
Trimers	C18H32	280-300		(0.8)	1.8		

OXYGENATES

Compound	Formula	bp °C	RVP	d	% O	Therm Val	Oct N
Methanol	CH4O	65		0.79	50	22.4 MJ/Kg	106
Ethanol	C2H6O	78	18	0.79	35	29.4	115
MTBE	C5H12O	56	8	0.74	18.2	38	110
ETBE	C6H14O	73	4	0.74	15.7		112
2-Hexanol	C6H14O	136		0.81	15.7	39	(high)

CATALYTIC THERMOCONVERSION OF CELLULOSE TO FUELS IN AQUEOUS MEDIUM

BABUL K. DATTA
Department of Chemical Engineering
Columbia University in the City of New York
NY 10027, USA

Keywords: Catalysts, Thermochemical, Aqueous.

ABSTRACT

Catalytic thermochemical liquefaction in aqueous medium was studied for conversion of cellulose to liquid fuels. There are 8 reactions were done by two different co-catalysts, (alkaline & acidic) with 5% Pt/Al_2O_3 in presence of 35 bar CO and H_2 as a reducing gas, at 300 ^{0} c. The duration of reaction time was 2 hours. During the reactions, catalysts and reaction time affected the process most dramatically. While the initial liquefaction (depolymerisation) of the cellulose is thermally controlled (pyrolysis), the subsequent conversion of the "Proto-oil" to liquid oils (deoxygenation) is mainly catalytically influenced. Some of the catalysts exhibited effective deoxygenation which resulted in the conversion of "Proto-oil" to a low oxygen content product. In run 7, conversion, oil production, H/C atomic ratio, calorific value is higher than others.

INTRODUCTION:

The conversion of cellulose to liquid fuels has been the subject of intensive studies during the last years [1-3].

The key problem in the liquefaction of biomass is the poor control of desired reactions. In pyrolytic liquefaction processes, the reactions are non selective, involving homolytic cleavage and free-radical reactions. In direct liquefaction, which uses CO, H_2, and water as reagent and catalysts, there is a complex sequence of reactions which probably starts out with the thermal breakdown of lignocellulosic materials and continues through the rearrangement, the reduction, the dehydration, the decarboxylation and other reactions to give a host of reactive compounds. These compounds can go further during the severe conditions of liquefaction process to lead to the polymerized, polymerisable and acidic compounds responsible of the poor yield and quality of the cellulose derived oil.

The crystalline regions in the cellulosic material make heterogeneous reactions occur slowly, as the close packing of the cellulose chains does not permit ease penetration by reagent molecules4. The use of homogeneous catalysts in these cases eliminates additional problems arising from the lack of effective contact between two solid phases, namely a heterogeneous catalyst and the biomass feedstock. Lindemuth 5 believed that $HCOO^-$ ion is the active species in a complex sequence of reactions that leads to oil formation.

The objective is to develop a consistant, quantified description of the liquefaction of cellulose, to examine the effect of co-catalysts with 5% Pt/Al_2O_3 in CO and H_2 atmosphere, quality of produced oils, and different types of water soluble components.

EXPERIMENTAL:

One liter capacity stainless steel autoclave (with rocker system) was used for each reaction with 1g different catalysts, 400g distilled water, 35 bar hydrogen gas and 300 ^{0}c temperature. All reactions were done for 2 hours. After cooling the autoclave, gasses were vented to the gas measurement system and collected samples for analysis in IR, GC. Then opened the autoclave for decant the aqueous layer and the rest of solid part was dissolved in acetone and refluxed for 3 hours, then filtered with vacuum pressure.After filtration, the solid part was char and catalyst; and the filtrate was rotaevaporated to separate acetone and oil. The remaining oil was separated by different solvents, such as Heptane and Toluene. The separated parts are called lights, waxes, asphaltenes and resins.

The aqueous phase contains a significant amount of reactive compounds, resulting from the breakdown of the cellulose. To understand of the nature of this complex, water soluble fraction, group separation was necessory before any identification was attempted. This was possible by solvent extraction. Prior to group separation , resinous substances from the water soluble were first precipitated with di-ethyl ether. The resulting ethereal soluble fraction was subsequently fractionated into four basic groups, namely; a) Carboxalic acids, (separated by 10% aqueous Na_2CO_3). b) Carbonyl compounds, (separated by 5% $NaHSO_4$). c) Phenolic compounds, (separated by 10% NaOH) and d) Solubilized/ Neutral hydrocarbons.

The four groups were identified by IR Spectroscopy.

IR - Perkin - Elmer IR Spectrophotometer (model 157) with range of 600 -4000 cm^{-1} was used.

Gas Chromatography - Pye Unicam G. C. (Series 204) fitted with dual detector system and coupled to a data processing computer (Hewlett - Packard - Data Dynamics 390) was used.

Catalysts - Johnson - Matthey Co. **Cellulose** - Powered pure cellulose (Solkaflock Brown Co., N. Y.). **Suspension medium water** - Distilled water. **Reducing gases** - Electrolytic hydrogen and Carbon-monoxide, BOC commercial grade-99.5%.

RESULTS AND DISCUSSIONS:

Table 1, lists the different reaction inputs, operating parameters and product distribution for runs 1-8. K_2CO_3 and $SnCl_2$ were used as a Co-catalysts with 5%Pt/Al_2O_3 for conversion of cellulose (Solka- floc) at 300°C and 35 bar of CO and H_2 as a reducing gas with 400 g water. In case of $SnCl_2$ in H_2 atmosphere, the amount of H_2O formation is larger than with K_2CO_3 and CO atmospheres due to the dehydration and catalytic deoxygenation of cellulose. Here Sn^{+2} plays an important role which enters into the complex scheme of reaction to reduce cellulose fragments and liberate O_2, which reacts with H_2 from atmosphere or (from solvent H_2O) to form H_2O. This homogeneous hydrogenation of acidic catalyst contributes to dehydration of cellulose and leads to produce unsaturated substances that polymerise easily to form char. This effect, is directly proportional to the acidity of the medium. On the other hand, K_2CO_3 with CO atmosphere, CO reacts with H_2O (from solvent) to form CO_2 and H_2 (water gas shift reaction) instead of produce H_2O. Hence, $SnCl_2$ with H_2 produces large amounts of H_2O .

Moreover, $SnCl_2$ with H_2 atmosphere, maximum amount of water-soluble compounds were formed due to the strong hydrolytic action of the acidic catalyst. But in case of K_2CO_3 in presence of CO atmosphere, is reverse due to the neutralization of the organic acid compounds, higher conversion to gasification and decarboxylation (loss of CO_2) of water soluble fractions and cellulose fractions. CO probably has an additional role which inhibits the polymerisation of unsaturated compounds to form char.

The product gas recovery, shown that the gas formation is greater in presence of K_2CO_3 with CO reactions, which is probably due to CO took part in the water-gas shift reaction as well as K_2CO_3 + CO + H_2O can form intermediate compound, possibly a potassium formate, which produces hydrogen, probably as hydried (H^-) ion. This ion reacts with the substrate (cellulose fragments), to remove oxygen as CO_2 and leads to the formation of oil also.

$$K_2CO_3 + H_2O + 2CO \longrightarrow 2H\text{-}C\text{-}OOK + CO_2$$

$$2H\text{-}C\text{-}OOK \longrightarrow H_2 + CO + K_2CO_3$$

Net reaction: $H_2O + CO \longleftrightarrow H_2 + CO_2$

Table 2 shows the elemental analysis of the feeds, char and oil of run (from 1-8).

The H/C atomic ratio is higher (1.26) with 5% Pt/Al_2O_3 + K_2CO_3 + CO atmosphere in run 7, which may be due to elemination of higher amount of oxygen as a CO_2 by water-gas shift reaction. That means one carbon atom can eliminates two oxygen atoms as CO_2 from the reaction mixture. But in case of $SnCl_2$ with H_2, reduction occurs by the elimination of only one oxygen atom (as H_2O) with two hydrogen atoms. The total elemination of oxygen (reduction) is double in case of K_2CO_3 + CO than $SnCl_2$ + H_2. Moreover, the produced hydried (H^-) ion, from potassium formate is more active reducing agent than normal hydrogen atmosphere. So, it can easily more reduced the cellulose fragments for production of high amount and high quality of oils. Hence, the H/C atomic ratio and calorific value of the run 7 is greater than run 6 and others. is also high.

After solvent analysis, high amount of lights was formed than asphaltenes (in run 7) which was probably due to higher conversion of asphaltenes, resins and water-soluble fractions in presence of CO atmosphere into lights as well as gases (as CO_2, CO and hydrocarbon gases) Which is shown in table 3.

From table 4, it is seen that when conversion increases, the production of water soluble fraction decreases and production of gases and oils increases. Moreover, ether soluble fractions from water soluble parts were also decreases on the same way which may due to the conversion of water soluble fractions into gases and oils. The ether soluble fractions were further separated by different solutions into different functional groups as carboxalic acid, carbonyl, phenolic and neutral hydrocarbons and identified by IR spectrum (shown in figure 1A to 2A).

From table 5, the G.C. analysis shown that K_2CO_3 in presence of CO atmosphere, CO_2, CO gases are formed greater than the run with $SnCl_2$ in presence of H_2 which may probably due to water-gas shift reaction. The low concentration of hydrogen gases produced indicated that the hydrogen from the water-gas shift reaction is very reactive and reacts instantly with the cellulose fragments. The gases were identified by IR spectrum and GC chromatograms of run 5 to 8 and shown in figure 3A to 6A.

CONCLUSION:

1) In terms of conversion of cellulose, oil yield, quality of oil, calorific value of oil are higher in run 7, (K_2CO_3 + 5% Pt/Al_2O_3 with CO atmosphere) in comparison with others.

2) The aqueous phase contains a significant amount of reactive compounds, resulting from the breakdown of the cellulose. The acidity of the aqueous phase is high (P^H 3) due to the presence of carboxalic acids. After reaction, when it was decanted from the autoclave, it looks as white after some while it becames brown in color due to oxidation. After analysis of the water soluble fractions, it is seen that it contains carboxalic acids, carbonyl compounds, phenolic compounds and neutral hydrocarbon compounds, Table 5.

3) Using K_2CO_3 as a co-catalyst with 5% Pt/Al_2O_3 in presence of CO atmosphere, increased the yield of gaseous products at the expense of char and water soluble fraction. The improvement in the conversion has an reflection on the quantity and quality of the desired product.

4) The use of K_2CO_3 with 5% Pt/Al_2O_3 in presence of CO atmospheres had an enhanced effect on the catalytic conversion of cellulose.

5) Economically, 5% Pt/Al_2O_3 + $SnCl_2$ in presence of H_2 atmosphere is a viable catalyst for liquefaction of cellulose, because CO is more expensive than H_2.

REFERENCES:

1) Adjaye, J; R. K. Sharma and N.N. Bakhshi, "*Characterization and Stability Analysis of Wood-derived Bio-oil*", Fuel Process, Technol. 31, 241-256 (1992).

2) " *Third liquefaction experts meeting* ", NRCC, Sherbrooke, Que., August 1983.

3) " *Proceeding of the 14th Biomass Thermochemical*" conversion contractor's Meeting, U.S. Department of Energy, Arlington, Virginia, June 1982.

4) J.P. Franzidis and A. Porteous," *Review of Recent Research of the Development of a Contonuous Reactor for thr Acid Hydrolysis of Cellulose*" in " *Fuels from Biomass and Wastes*", D.L.Klass and G. H. Emert, ed.; *Ann. Arbor Science publishers Inc. Ann Arbor, MI*, (1981).

5) T. E. Lindemuth," *Carboxylolysis of Biomass*" in " *Biomass Conversion Processes for Energy and Fuel*" S. S. Sofer, O. R. Zaborsky, ed., 187-200, Plenum Press, NY, 1981.

6) A. R. Bowes, H. G. Shatwell, and A. W. Nash, " *The Thermal Decomposition of Cellulose under Hydrogenation Conditions*", J.Soc.Chem.Ind., **44**, 507-511 T, 526T, 1925

Table 1. Reaction inputs, parameters and product distribution

Run	1	2	3	4	5	6	7	8
Feed type	Cellulose	Cellulose	Cellulose	Cellulose	Cellulose	Cellulose	Cellulose	Cellulose
Feed (g)	50.0	50.0	50.0	50.0	50.0	50.0	50.0	50.0
Catalyst	K_2CO_3	$SnCl_2$	K_2CO_3	$SnCl_2$	5% Pt/Al_2O_3 + K_2CO_3	5% Pt/Al_2O_3 + $SnCl_2$	5% Pt/Al_2O_3 + K_2CO_3	5% Pt/Al_2O_3 + $SnCl_2$
Catalyst (g)	1.0	1.0	1.0	1.0	.5+.5=1.0	0.5+0.5=1.0	0.5+0.5=1.0	0.5+0.5=1.0
Water, g	400.0	400.0	400.0	400.0	400.0	400.0	400.0	400.0
Reducing gas	H_2	H_2	CO	CO	H_2	H_2	CO	CO
Reducing gas (g)	1.6	1.6	22.12	22.12	1.6	1.6	22.12	22.12
TOTAL INPUT (g)	452.6	452.6	473.12	473.12	452.6	452.6	473.12	473.12
Temperature (°C)	300	300	300	300	300	300	300	300
Initial pressure (atm)	35	35	35	35	35	35	35	35
Heating up time (hr)	1.40	1.50	2.30	2.35	2.0	2.10	2.30	2.20
Reaction time (hr)	2.0	2.0	2.0	2.0	2.0	2.0	2.0	2.0
Max. Reaction press(atm) Final	280	280	290	285	295	292	310	300
Reaction press (atm)	37	36	40	38	40	44	38	36
TOTAL OUTPUT (g)	451.0	450.7	471.4	471.8	450.9	450.9	472.0	471.82
% Recovery from Autoclave	99.6	99.6	99.64	99.72	99.6	99.6	99.8	99.72
Product Distribution								
% Gas produced	16.0	11.56	18.76	28.8	12.8	15.96	31.76	26.40
% Water-soluble fraction	12.6	8.6	6.8	8.6	12.4	5.60	3.00	10.40
% Oil	17.6	40.0	38.6	21.2	24.4	40.0	50.00	20.60
% Char	19.0	8.0	6.4	14.6	12.0	7.0	3.00	11.00
% Water-produced	31.6	28.0	26.0	24.2	35.0	28.0	10.00	29.00
% TOTAL RECEIVED	96.8	96.76	96.56	97.4	96.6	96.56	97.76	97.4
% CONVERSION	75.64	89.59	92.28	78.9	78.68	93.73	96.94	81.44

Table 2. Elemental analysis

Run	1	2	3	4	5	6	7	8
Feedstock analysis								
% C	41.5	41.5	41.5	41.5	41.5	41.5	41.5	41.5
% H	6.1	6.1	6.1	6.1	6.1	6.1	6.1	6.1
% O*	52.4	52.4	52.4	52.4	52.4	52.4	52.4	52.4
% Ash	-	-	-	-	-	-	-	-
Char analysis								
% C	53.2	54.0	50.0	60.0	73.7	52.0	42.2	70.0
% H	4.9	4.5	3.9	5.5	4.6	4.2	4.0	4.2
% O*	28.0	15.0	12.0	23.7	21.7	8.9	6.8	10.8
% Ash	13.9	26.5	34.1	10.8		34.9	47.0	15.0
Oil analysis								
% C	75.6	77.8	78.0	68.9	78.0	74.5	75.3	73.9
% H	6.5	7.2	7.5	6.1	7.0	7.6	8.0	6.8
% O*	17.9	12.2	11.0	13.3	15.0	9.8	9.5	12.0
% Ash	-	1.0	3.5	11.7		8.1	7.2	7.3
H/C	1.02	1.10	1.14	1.05	1.07	1.21	1.26	1.09
O/C	0.177	0.117	0.10	0.146	0.144	0.098	0.094	0.146
Calorific value (Kcal/g)	7.5320	8.6512	8.6923	8.2513	8.3520	8.7215	8.7580	8.5571

Table 3. Product oil composition

Run	1	2	3	4	5	6	7	8
Product oil composition								
%Heptane soluble Lights.	35.8	50.2	55.0	38.3	41.6	61.2	63.5	46.7
%Heptane soluble (boil), Waxes.	8.90	13.4	14.8	12.3	12.0	13.8	15.0	12.3
%Toluene soluble Asphaltenes.	33.0	22.7	20.2	31.2	28.9	17.0	15.0	25.8
%Toluene insoluble,Resins.	22.3	13.7	10.0	18.2	17.5	8.0	6.5	15.2

Table 4. Extraction of different functional group(compounds) from ether soluble fraction of water soluble fraction.

Run	1	2	3	4	5	6	7	8
%Ether soluble fraction (from WSF*)	40.0	27.0	25.0	32.0	36.0	22.0	20.0	28.0
% A	14.2	9.0	8.5	9.6	10.2	7.0	6.4	9.0
% B	9.2	6.5	6.2	8.0	8.8	5.0	4.0	6.8
% C	4.5	2.2	2.5	2.0	4.0	2.0	3.0	1.6
% D	8.4	8.2	7.0	8.5	8.6	6.4	5.2	7.5
% E	2.2	0.6	0.5	1.5	2.8	1.0	0.6	1.1
% Total	38.5	26.5	24.7	29.6	34.4	21.4	19.2	26.0
% Recovery	96.25	98.0	98.8	92.5	96.0	97.0	96.0	93.0

A - Carboxalic acids (extracted by aqueous 10% Na_2CO_3 solution).
B - Heavy carboxalic acid
C - Carbonyl compounds (extracted by aqueous 5% $NaHSO_4$ solution).
D - Phenolic compounds (extracted by aqueous 10% NaOH solution).
E - Neutral hydrocarbons (ethereal soluble compounds).
* WSF - Water soluble fraction
** All percentages are wt/wt of ether soluble fraction
*** % of ether soluble fractions were obtained from Water soluble fraction by treating with di-ethyl ether.

Table 5. Product of gas distribution

Run	1	2	3	4	5	6	7	8
% CO	42.64	37.95	31.09	29.86	46.84	36.84	25.97	38.55
% CO_2	24.21	24.68	52.25	50.09	25.06	40.26	61.04	50.90
% CH_4	3.81	2.76	2.91	3.16	2.91	3.01	2.82	2.84
% C_2H_6	0.59	0.57	0.59	1.02	0.60	0.59	0.63	0.65
% C_2H_4	0.83	0.55	0.58	1.04	0.72	0.68	0.71	0.61
% C_3H_8	1.14	0.71	0.66	1.09	0.85	0.55	0.81	0.67
% C_3H_6	0.23	0.24	0.18	0.27	0.26	0.21	0.24	0.16
% n-Butane	-	-	-	-	-	-	-	-
% 1-Butene	-	-	-	-	-	-	-	-
% *iso-butene*	-	-	-	-	-	-	-	-
% Trans-2-butane	1.31	1.50	1.37	1.35	1.53	1.46	1.26	0.93
% Cis-2-butene	0.87	0.42	0.89	0.85	0.88	1.05	0.83	0.61
% Butadiene	1.72	2.09	1.75	1.70	1.72	1.86	1.72	0.85
% Total	77.35	71/47	92.27	90.43	81.37	86.51	87.04	96.77
% H_2 + UP_**	22.655	28.53	7.73	9.57	18.63	13.49	12.96	3.23

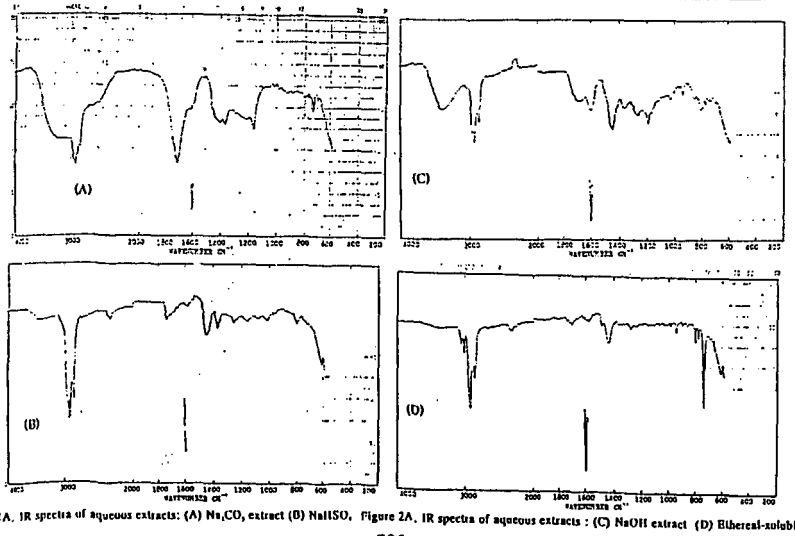

Figure 1A. IR spectra of aqueous extracts: (A) Na_2CO_3 extract (B) $NaHSO_4$ Figure 2A. IR spectra of aqueous extracts : (C) NaOH extract (D) Ethereal-xuluble .

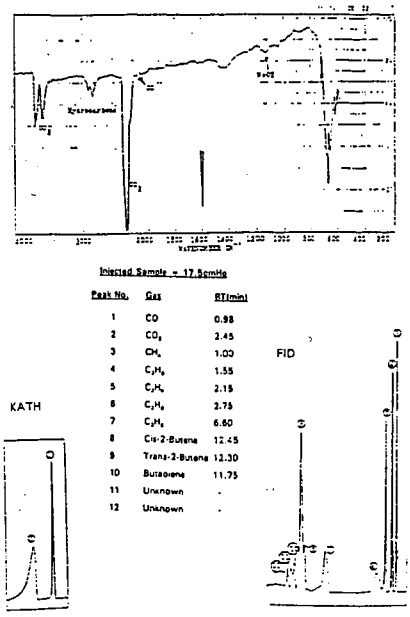

Injected Sample = 17.5cmHg

Peak No.	Gas	RT(min)
1	CO	0.98
2	CO_2	2.45
3	CH_4	1.00
4	C_2H_6	1.55
5	C_2H_4	2.15
6	C_2H_6	2.75
7	C_2H_4	6.60
8	Cis-2-Butene	12.45
9	Trans-2-Butene	12.30
10	Butadiene	11.75
11	Unknown	-
12	Unknown	-

Figure 3A. The IR spectrum and GC chromatograms of the gaseous product from run 5

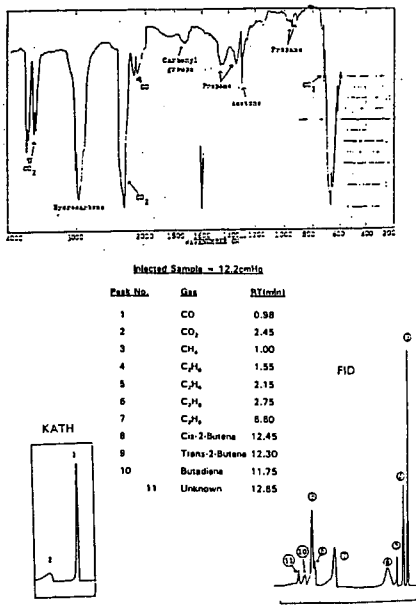

Injected Sample = 12.2cmHg

Peak No.	Gas	RT(min)
1	CO	0.98
2	CO_2	2.45
3	CH_4	1.00
4	C_2H_6	1.55
5	C_2H_4	2.15
6	C_2H_6	2.75
7	C_2H_4	6.60
8	Cis-2-Butene	12.45
9	Trans-2-Butene	12.30
10	Butadiene	11.75
11	Unknown	12.85

Figure 4A.

The IR spectrum and GC chromatograms of the gaseous product from run 6.

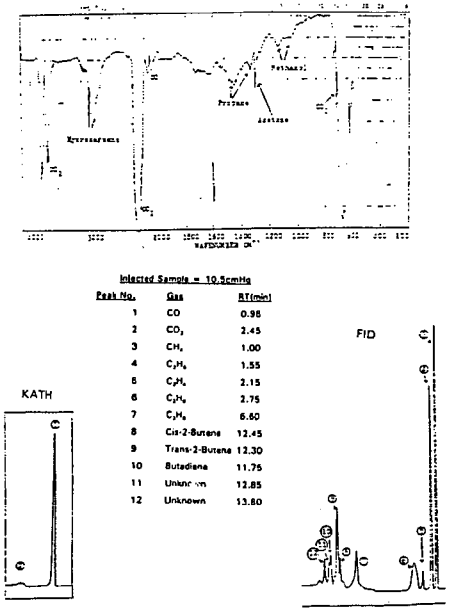

Injected Sample = 10.5cmHg

Peak No.	Gas	RT(min)
1	CO	0.98
2	CO_2	2.45
3	CH_4	1.00
4	C_2H_6	1.55
5	C_2H_4	2.15
6	C_2H_6	2.75
7	C_2H_4	6.60
8	Cis-2-Butene	12.45
9	Trans-2-Butene	12.30
10	Butadiene	11.75
11	Unknown	12.85
12	Unknown	13.80

Figure 5A. The IR spectrum and GC chromatograms of the gaseous product from run 7.

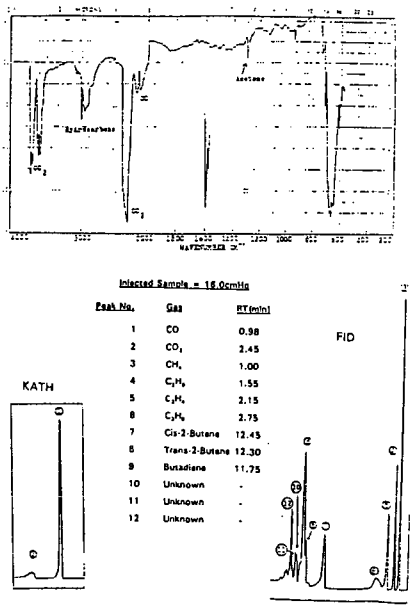

Injected Sample = 18.0cmHg

Peak No.	Gas	RT(min)
1	CO	0.98
2	CO_2	2.45
3	CH_4	1.00
4	C_2H_6	1.55
5	C_2H_4	2.15
6	C_2H_6	2.75
7	Cis-2-Butene	12.45
8	Trans-2-Butene	12.30
9	Butadiene	11.75
10	Unknown	-
11	Unknown	-
12	Unknown	-

Figure 6A.

The IR spectrum and GC chromatograms of the gaseous product from run 8

Deposition investigation in straw fired boilers

P.A.Jensen[1], M.Stenholm[2], P.Hald[1], K.A.Christensen[3].

[1] Risø National Laboratory, Dept. of Combustion Research, P.O.Box 49, DK-4000 Roskilde, Denmark.
[2] dk-TEKNIK, Gladsakse Møllevej, DK-2860 Søborg, Denmark.
[3] Technical University of Denmark, Dept. of Chemical Engineering, DK-2800 Lyngby, Denmark.

Key words: Deposition, straw, combustion.

Introduction

In Denmark straw has been applied as fuel at small combined power and district heating plants since the late 1980's. New equipment have been developed to handle and burn the straw. However, straw is by no means a trivial fuel, problems like fluctuations, deposition in the furnace, corrosion and a poor burn out have been observed at boiler plants. One of the problems has been, the large differences in the amount of deposition in the furnace chamber and on superheater tubes when applying different fuel parcels. Knowledge of how to characterize the straw for predicting the deposition properties in the boiler is needed. We will here present deposition experiments performed at two straw fired power plants with a fuel input of respectively 18 and 30 MW.

Some limited experiments have earlier been performed on smaller scale boilers[1,2], no clear correlation between laboratory analyses of the straw and deposition in the boilers was found. Combustion experiments on a combined wood and straw fired 18 MW stoker fired boiler have been performed[3]. Strong indications, of condensation of the mineral matter at different places in the boiler chamber, were seen.

Serial straw has typically a high content of potassium (0.5-1.3%), chloride (0.2-0.7%) and silicium (0.3-1.0%)[4]. KCl sublimates at typical combustion conditions and equilibrium calculations indicate that most of the potassium is in the gas phase at 900 °C[6]. The equilibrium calculations also indicate that a high Cl to K ratio gives a higher amount of K in the gas phase. The low melting point for some potassium species gives a high risk of the formation of hard deposits on furnace walls and convection tubes. A component as KCl melt at 771 °C, and KCl can contribute to melt formation at even lower temperatures when combined with other components as in deposits. Also the system K_2O - SiO_2 has a minimum melting point at 742 °C (68% SiO_2 and 32% K_2O).

Experiments

We have performed 12 one day experiments at full load at two straw fired power plants in the towns Haslev and Slagelse. At both places the straw was received in the form of Hesston bales. Other aspects than deposition were investigated during the experiments, however, this presentation contains only work concerning the deposition properties of the straw.

Haslev: A sketch of the boiler is shown in Figure 1. The bales are continuous fed in four rows into the four burners, where the combustion takes place on the surface of the front bales. The full load fuel input was around 5500 Kg/h corresponding to 18 MW.

Slagelse: (see Figure 2) The bales are reamed and the straw are fed by 9 screws into a moving grate boiler. The full load fuel input was around 7400 Kg/h corresponding to 30 MW.

Table 1 shows the 12 straw types that were applied for the experiments. Wheat, barley and rape were used with water contents of 11 to 16 %, chloride contents of 0.06 to 0.95 % (dry matter) and a potassium contents of 0.28 to 1.97 % (dry matter).

The experimental programme included air cooled deposition probes (around 1.8 meter long and with a diameter of 38 mm) inserted near the superheaters and in the boiler chamber. The deposition probes were kept as near at 510°C as possible by the air cooling system. The fouling removal system, normally applied at the plants, in the form of the sootblowing and fonbal cleaning systems, was stopped during the experiments. After one experiment the deposition probes were withdrawn and the deposition was removed from the probes, the first fraction by a brush (loose deposit) and the second fraction by a steel brush and a knife (hard deposit). At the same position, as the deposition probes, temperature and the gaseous alkali content was measured. During all the experiments the operating conditions were monitored and the flue gas emissions were measured (HCl, CO, TOC, CO_2, O_2, NO_x and SO_2). Gaseous alkali measurements are in the developmental phase, and the results will be reported separately.

Aerosol samples were collected in the upstream of the fly ash filter. The aerosol size distribution was studied by a low-pressure cascade impactor and a scanning mobility particle seizer. It was possible to study particles from 0.01 to 2 micron.

In experiment 1 and 2 at Haslev and experiment 1,3,6,7 and 8 at Slagelse the amount of fed straw and the generated fly and bottom ash, was also measured. Detailed chemical analyses of straw, ash and deposits were performed.

Results

With respect to deposition wheat and barley were seen to behave reasonably similar, while rape was markedly different. The rape straw has a higher sulfur and calcium content but a much lower silicium content. In the following wheat and barley are discussed simultaneously while the experiment with rape is not included.

A very high amount of submicron aerosols was generated in the boilers. The mean diameter of the particles was around 0.3 micron. The particles consisted mainly of K, Cl and S. A large fraction of the alkaline in the fuel evaporate during the combustion and condensate as aerosols later in the furnace chamber. Figure 3 shows that a close correlation exists between the mass loading of submicron aerosols and the potassium contents of the straw. A detailed discussion of the aerosol formation mechanisms is given in reference 5.

In agreement with the aerosol measurements the fly ash is compared with the straw ash enriched with potassium, chloride and sulfur (see Table 2). The bottom ash has a slightly decrease in the same elements compared with the straw ash.

Table 3 shows chemical analyses of straw ash, bottom ash, fly ash and deposits from experiment 6 at Slagelse. A piece of loose deposits was analyzed with an environmental scanning electron microscope (ESEM) coupled with energy dispersive x-ray spectroscopy. The ESEM gave results as the proportion between the elements. In the table the elements are prescribed to give a total of 65%. The ESEM analysis gives information about the layer a few micron deep into the sample. Table 3 shows that compared with the fly ash the deposits are rich in silicium, this is probably caused by impaction of larger particles on the probe. This was not the case for all the experiments. The hard deposit of experiment 6 has a much higher chlorine to potassium ratio than the loose deposit. This was also observed in most of the other experiments. The ESEM analysis of the inner and the outer side of the deposit is reasonably similar and dominated strongly by potassium and chlorine. The surfaces are probably dominated by elements from the aerosols or from condensation of vapors.

During experiment number 6 two probes were inserted into the furnace chamber. Deposits at the extra probe were removed at different time intervals to study the dependency of residence time (see Table 4). It is seen that the total flux of deposition was reasonable independent of time while the fraction of hard deposit increased with the time.

The total deposition flux on the probes has been related to the potassium content in the straw. Figure 4 shows the results at the superheaters and Figure 5 the results in the furnace chamber. Similar to the aerosol generation a reasonable correlation with the water soluble potassium content in the straw is seen.

Figure 6 shows the flux of hard deposit in the furnace as a function of the chlorine content in the straw. A better correlation between the chlorine content of the straw and the hard deposits was seen than between the potassium content and the amount of hard deposits. With an increasing chloride content, the Cl to K ratio is also higher, this leads probably to condensation at a lower temperature (shown by equilibrium calculations in reference 6). With less potassium condensed prior to the probe, more potassium condensate directly on the probe surface. Also a high KCl content of the deposit gives a lowering of the deposit melting temperature.

Figure 7 shows the amount of hard deposits at the superheaters. Here, the picture is less clear. Because the temperature is lower the amount of hard deposits is lower and the
measuring error much higher. Looking at Figure 6 and 7 it is seen that an increase in local temperature and in straw chlorine content gives an increase in the amount of hard deposit.

One experiment was performed with Rape straw. Large amounts of isolating deposits were generated in a short time and the temperature in the boiler increased fast. The experiment had to be stopped after 4 hours because of problems with the ash removal system.

Conclusion

It is the first time that such detailed measurements on straw fired boilers have been performed. Deposition formation on surfaces in the boiler can occur by different mechanisms: Condensation, impaction and termoforesis[7]. We think that if the deposition has been partly melted, or if it is generated to a high degree by condensation the deposition is harder and will be more troublesome for the boiler operators.

No correlation could be seen between the traditional laboratory generated ash softening and melting temperatures and the deposition in the boilers.

The results of the experiments with respect to deposition could be summarized in the following points:

- Large amounts of potassium evaporate and later condensate as aerosols.
- A high content of water soluble potassium gives a higher amount of total deposition.
- The local amount of hard deposits on convective surfaces is dependent on whether the alkaline condense as aerosols or directly on the boiler surfaces.
- Increasing local gas temperature gives a higher amount of hard deposits.
- A high chloride content of the straw gives a higher tendency for the formation of hard deposits.

References

1. Kiørboe, L. (1990). Slaggedannelse i fyringsanlæg. Case-stories. dk-TEKNIK (In Danish).
2. Thellesen, H.Z. (1988). Halmens egenskaber til fyringsformål. Slaggedannelse. Statens Jordbrugstekniske Forsøg. Beretning Nr. 40 (In Danish).
3. Baxter, L.L., T.R. Miles, T.R. Miles Jr., B.M. Jenkins, G.H. Richards and L.L. Oden (1993). Transformations and deposition of inorganic material in biomass boilers. Sandia National Laboratories, Livermore.
4. Undersøgelse af halms kemiske sammensætning - med relation til forbrænding og forgasning. Foretaget af bioteknologisk institut for Elsam/Elkraft. December 1994 (In Danish).
5. Christensen, K.A. (1995). The formation of submicron particles from the combustion of straw. Ph.D. thesis. Department of Chemical Engineering, Technical University of Denmark.
6. Hald, P. (1994). Alkali metals at combustion and gasification. Equilibrium calculations and gas phase measurings. Ph.D. thesis. Department of Chemical Engineering, Technical University of Denmark.
7. Baxter, L.L. (1993). Ash deposition during coal and biomass combustion: A mechanistic approach. *Biomass and Bioenergy* 4(2), 85-102.

Tables

Table 1. **Straw applied for the 8 hour experiments.**

Experiment	Straw type	Water content %	Cloride % of dry straw	Potassium (water soluble) % of dry straw
Has1	Wheat	15.1	0.29	0.57
Has2	Wheat	13.5	0.52	1.27
Has3	Barley	12.0	0.56	1.93
Has4	Wheat	14.6	0.44	1.01
Sla1	Wheat	15.0	0.06	0.28
Sla2	Wheat	13.3	0.20	0.74
Sla3	Barley	11.6	0.32	1.36
Sla4	Barley	13.6	0.95	1.97
Sla5	Wheat	13.9	0.51	1.07
Sla6	Wheat	13.2	0.86	1.50
Sla7	Wheat	16.1	0.14	0.48
Sla8	Rape	14.0	0.33	1.40

Table 2. **Mean mineral composition (experiments 1 and 2 at Haslev and 1,3,6 and 7 at Slagelse) of Straw ash, bottom ash and fly ash.**

Elements (dry sample)	Si	Al	Fe	Ca	Mg	Na	K	S	P	Cl	Sum
Mean in straw ash %	23.67	0.36	0.28	7.72	0.98	0.41	21.59	1.93	0.99	6.78	64.70
Mean in flyash %	7.12	0.17	0.45	2.74	0.42	0.43	37.36	3.21	0.75	22.44	75.09
Mean in bottum ash %	24.22	0.53	0.38	7.64	1.22	0.62	18.26	0.27	1.15	4.89	59.18

Straw ash were generated at 550C

Table 3. **Mineral composition for experiment 6 at Slagelse of traw ash, bottom ash, fly ash, the furnace deposition probe and the inner and outer side of deposits (by ESEM).**

Elements (dry sample)	Si	Al	Fe	Ca	Mg	Na	K	S	P	Cl	Sum
straw ash %	24.30	0.07	0.10	5.65	0.84	0.13	29.06	1.59	0.96	11.90	74.60
Fly ash %	2.15	0.11	0.28	1.22	0.16	0.57	50.64	3.12	0.65	33.00	91.90
Bottum ash %	28.03	0.30	0.26	7.86	1.33	0.26	17.43	0.14	1.18	0.73	57.53
Hard deposit %	10.28	0.11	2.52	4.07	0.60	0.15	32.38	1.96	1.09	19.00	72.16
lose deposit %	19.16	0.21	0.29	6.43	0.96	0.22	24.08	3.77	1.31	5.40	61.83
ESEM inner side, %	1.24	0.05	0.18	0.72	0.04	0.23	30.75	1.53	0.18	30.09	65.01
ESEM outer side, %	5.56	0.09	0.22	5.77	0.29	0.11	29.37	2.93	1.46	19.20	65.00

Table 4: **Experiment 6 at Slagelse: Deposition in the furnace as a function of residence time.**

Time the probe were inserted h	0.33	0.66	1.33	2.67	7.17
Total deposit flux g/m2/h	96.1	64.2	69.2	59.6	67.4
Hard deposit flux g/m2/h	1.99	0.76	1.12	10.1	41.96

Figures

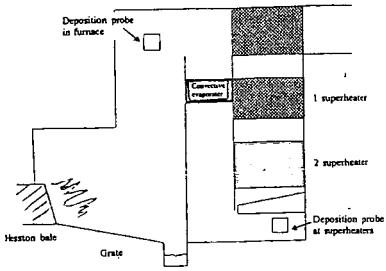

Fig. 1. Haslev straw fired boiler.

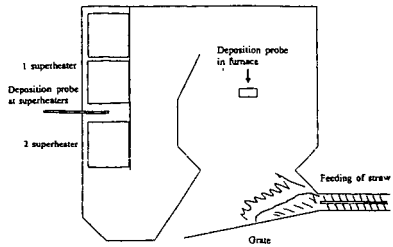

Fig. 2. Slagelse Straw fired boiler.

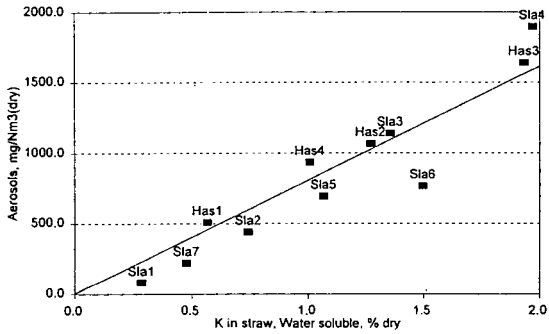

Fig. 3. Total aerosols (0.01 to 2 micron) in the flue gas as a function of water soluble K in the straw.

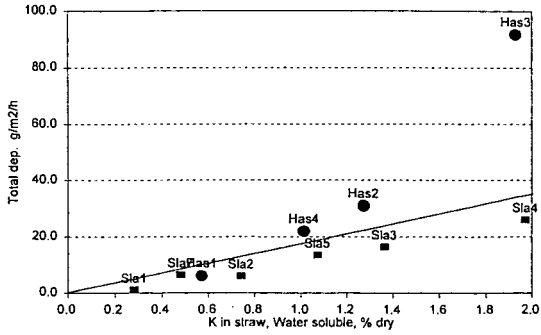

Fig. 4. Total deposition flux at the superheaters as a function of water soluble K in the straw.

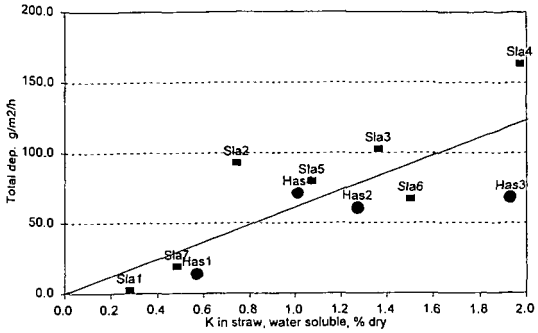

Fig. 5. Total deposition flux in the furnace as a function of water soluble K in the straw.

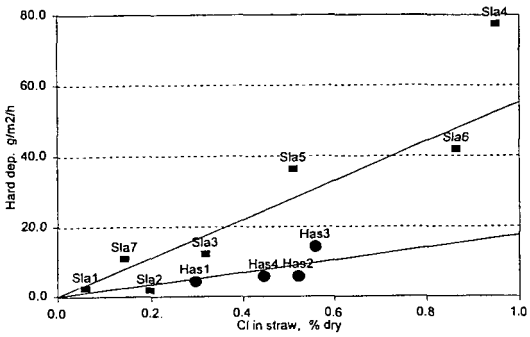

Fig. 6. Deposition flux of hard material in the furnace as a function of Cl in the straw.

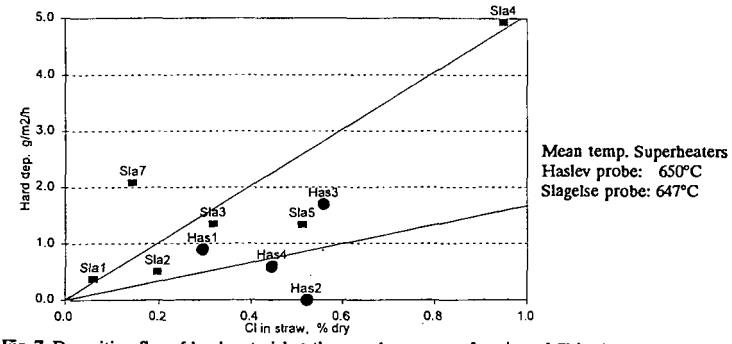

Fig. 7. Deposition flux of hard material at the superheaters as a function of Cl in the straw.

BED MATERIAL AGGLOMERATION IN PFB BIOMASS GASIFICATION

Nader Padban, Samuel Kiuru & Anders L. Hallgren
Dept. of Chem. Eng. II, P.O.B. 124 Chemical Center
University of Lund, S-221 00 Lund, Sweden

Keyword: Biomass, Bed material, Alkali induced agglomeration, Ash

1. Introduction

Small amounts of alkali compounds can drastically change the behavior of bed materials in fluidized bed gasification systems. Alkali-induced agglomeration and defluidization of the bed may cause severe operational problems and can be detrimental to the overall process. Enhanced tendency for agglomerations in the bed has been found in systems utilizing biomass or so called alternative solid fuels as feed-stock. The fuel alkali may add to the accumulation of alkali compounds in the bed. Adhesion tendencies between the particles seem to increase due to sticky layers of alkali condensations on the particle surfaces. In the present study an endeavor was made to establish a method for investigating suitable bed materials and the effect from biomass ash on the bed behavior in PFB biomass gasification. In this approach first results show that the composition of the particles in the bed, the temperature, and the mobility of the particles are of primary importance.

Agglomeration of bed material and problems caused by ash sintering in fluidized bed combustion/gasification processes has been reported frequently in the literature. According to Prabir et al [1] agglomeration of bed material can under certain conditions occur even at the temperatures below the ash fusion temperature and gas velocity higher than minimum fluidization velocity. Squire [2] and Siegill [3] describe the defluidization phenomena as a direct consequence of stickiness of bed material. This could be caused by changed properties of bed material at a certain temperature or due to liquid deposition on the surface of the particles.

Ash agglomeration in a fluidized-bed coal gasifier may be influenced by the high surface tension of mineral matter. Capillary forces may draw mineral matter from the interior of a hot carbon particle in order to be accumulated as ash on the particle surface [2].

Gerald P. Huffman et al [4] investigated the high-temperature behavior of coal ash in reducing and oxidizing atmospheres. The results from that study suggest that significant partial melting of the ashes occurs at temperatures as low as 200-400 °C below the initial deformation temperature defined by ASTM ash cone fusion test. According to their experiments ash melting is accelerated by reducing conditions. In a reducing atmosphere the ash melting will mainly be controlled by the iron-rich corner of the FeO-Al_2O_3-SiO_2 phase diagram.

B.K.Dutta et al [5] propose that the softening temperature of a coal ash is lower in mild reducing atmosphere than in oxidizing or strongly reducing atmosphere. The decreased ash fusion temperature is caused by the fluxing effect of different iron oxides. Depending on the temperature, the state of these oxides will changed and consequently even their fluxing effect. In an oxidizing atmosphere iron will be present as Fe_2O_3 and in mild reducing atmosphere as FeO, while in a strong reducing environment it tends to exist in metallic form. Ferrous oxide has the maximum fluxing effect on coal ash. Additionally, Dutta et al report that in the case of excess iron and in oxidizing atmosphere, the effect of alkali in decreasing the ash softening temperature may be very low or even insignificant.

R.G. Rizeq and F. Shadman [6] describe two different mechanisms for alkali-induced agglomeration of solid particles in coal combustors and gasifiers. In the case of low alkali concentration agglomeration is a result of formation of low-melting glassy phases on the

particle surfaces. In alkali rich conditions alkali salts will form a molten layer on the surface of particles which result in adhesion of particles. Their experiments even show that the minimum agglomeration temperature of some minerals can be decreased several hundred degrees depending on the alkali content.

In connection to the effect of alkaline compounds on ash sintering and deposit forming in peat gasification, Moilanen [7] show that there is a clear correlation between chemical composition and sintering strength of peat ashes at 800°C. According to those investigations the sintering strength of peat ashes rises by increased B/A (bas/acid) ratio in these ashes.

Up to now most research efforts considering ashes and bed materials have been concentrated to coal combustion and gasification processes. Since the bed material in these processes often differs from those used in biomass gasification there is a need for further investigations in this area. In gasification and combustion of biomass, where external bed material is used, not only the problems caused by ash melting and sintering but also problems created by reactions between bed material and ashes must be considered.

Previous work at the department of Chem. Eng.II [8] have shown that the agglomeration and cake forming phenomena in bed material in presence of alkaline compounds depend on both temperature and the kind of alkali present. The stable alkali compounds such as chlorides do not react with bed materials consisting of Al and Si at temperatures below 800°C, while unstable compounds such alkali nitrates cause agglomeration of bed materials at the temperatures as low as 550°C. Therefore the knowledge about the composition of different alkali and other fluxing materials in ashes is necessary for predication of ash effects on bed material.

In the present work ash content and chemical composition of ashes for two different biomass has been investigated. The effect of temperature on the chemical composition of these ashes has been studied. Different mixtures of ash/bed material have been treated thermally to study the agglomeration or cake forming phenomena in the bed material.

2. Experimental

2.1 The Sample preparation

To study the temperature effect on ash chemical composition two different biomasses was preliminary ashed at 550°C. The ashing procedure has taken place in presence of air and at atmospheric pressure. The produced ashes were subsequently heated at 650°C and 900°C in 1 hour. The chemical composition of the ashes obtained from the tempearture treatment was determined by **atomic absorption Spectrophotometry** (AAs) and **ion chromatography** (IC).

Mixtures of ashes (obtained in 550°C) and bed material (consisting 99.5% of SiO_2) were used in investigating the agglomeration and cake forming phenomena caused by alkali in the bed material. The bed material/ash quotes for the samples were 0, 0.25,1 and 4. In the preparation of mixtures the required bed material amount was placed as a layer on the weighted ash sample.

Samples were treated thermally in an oven to 900°C. The residence time at 900°C was one hour for all samples. **Scanning Electron Microscopy** (SEM) was then used for analyses.

2.2 Analysis procedures

Analysis for solid samples in the form of ashes, ceramics, glasses, minerals and etc. can be made in several different ways:

i. X-ray fluorescence spectroscopy (XRF) is the most simple and accurate method without need for any cumbersome digestion procedure of the sample.

ii. methods that require melting + digestion in order to transfer the solid sample into a solution before the real analysis can start. Such method may be ICP and AAS with flame and preferably with graphite furnace and IC.

For analyses, AAS with air-C_2H_2 and N_2O-C_2H_2 flame and IC were available. All elements Al, Si, Ca, Fe, Mg, Mn, K, Na, S and P can be analyzed by AAS with a graphite furnace. Since the last mentioned instrumentation was not available AAS with flame was used for all the mentioned elements except for S and P which were analyzed by isocratic IC. For phosphor a new analytical method for IC had to be developed and because sulfur cannot be analyzed on AAS, the next best way was to analyze both S and P by existing IC equipment. S and P separated in the IC column system as SO_4^{2-} and PO_4^{3-} ions. In the determining of S and P a small volume, typically 1 to 2 ml, filtered through 0.22 micron membrane filter, was introduced with a syringe or with a sample changer into a 50 μL loop. The anions of interest, SO_4^{2-} and PO_4^{3-}, were separated and measured using a isocratic system comprised of a guard column, separator column, suppressor column and conductivity detector.

For the AAS analysis, 40-70 mg fine-grounded ash sample was mixed with 1:12 parts lithium methaborate dihydrate, $LiBO_2.2H_2O$ in a graphite or platina crucible. The mixtures were then molted at 900°C in CO_2 atmosphere. The melt was dissolved in dilute nitric acid under stirring (10-15 hour). After appropriate dilutions the obtained solutions were analyzed by AAS for measuring the amount of Si, Al, Ca, K, Na, Fe, Mg and Mn in samples.

In the Scanning Electron Microscopy (SEM) studies the investigated areas were different for pure ashes and ash-bed material mixtures. In order to achieve a more general conception of the ash surfaces, in the case of pure ash the studied area was relatively large, however, for the characterization of different particles in mixtures point analyses (studied area~ $9\mu^2$) were performed.

3. Results and discussions

Heating pure ashes results in a decrease in volume and the ash particles tend stick together. However the adhesion is not strong and can easily be destroyed by finger touch.

Agglomeration of bed material particles was observed in all ash-bed material mixtures , independently on ash/bed material quote. The size of the agglomerate for EB,biomass was much smaller than for those related to Salix. Generally the agglomerate size increases by increasing ash/bed material quote.

The AAS/IC (bulk) analysis of ashes from different-temperatures shows no significant temperature-related variations in chemical composition in ash of any sort.This could indicate that the ashes, already in the lowest ashing temperature, have reached a chemical equilibrium in solid /or condensed phase.

Comparison between the results from AA/IC and SEM shows considerable differences in chemical composition for both ashes. Generally Si , Al and K content determined by SEM analysis is much lower than those determined by AA/IC. Although

SEM analysis shows the chemical composition of the outer surfaces of particles (max. penetration = 3μ), the explanation can be that most of these elements are in the inner part of the ash particles. According to this assumption the outer shell will consist of oxides, sulfates, carbonates and phosphates of Ca, Mg, Mn and K.

The stronger agglomeration tendency for Salix mixtures may depend on the higher potassium content in these samples.

Table III shows some results of SEM point analysis studies for particles in the mixtures. The particles containing high silicon represent bed material grain from the agglomerates. These results indicate that the composition of the particle surface can vary drastically from one point to another in the same sample. Applied SEM analysis method has not shown to be satisfactory for larger surface examinations.

4. Conclusions

The ashes from biomasses are not homogeneous materials, and their chemical composition differ from one particle to another. Higher alkali content in ash surfaces contribute to a stronger agglomeration tendency in ash- bed material mixtures. The agglomerates consist of bed material particles surrounded by small particles rich in Ca and with varying concentration in K, P, S and another elements. Preliminary results indicate that agglomeration may be related to a wide range of low melting compounds consisting of this elements and Si. Studies of phase diagrams [9] show that since only the compounds containing alkali can have melting points lower than 900°C, we can not exclude the importance of alkali in agglomeration phenomena.

5. Acknowledgments

This work has financially been supported by the National Board for Industrial and Technical Development (Nutek)

References

1. Pabir Basu and A. Sarka; Agglomeration of coal ash in fluidized beds; Center of Energy Studies, Technical University of Nava, Halifax, Canada B3J 2X4.
2. A. M. Squiers et al; Behaviour of mineral matter in a fluidized bed gasifying cone; the ignifluid process; Trans. Brit. Ceram Soc. 1976, 75, 85-91.
3. J. H. Siegill; Defluidization phenomena in fluidized bed of sticky particles at high temperatures, PhD dissertation, The City University of New York, (1976).
4. G. P. Huffman et al; Investigation of the high temperature behaviour of coal ash in reducing and oxidizing atmospheres; US Steel Corporation, Research Laboratory, Monroeville, Pennsylvania 15146, USA.
5. B. K. Dutta et al. A study of the fusion characteristics of coal ashes: Softening temperature of coal ashes in a mild reducing atmosphere; Planning & Development Department, Fertilizer Corporation of India Ltd, Sindri.
6. R.G. Rizeq & F. Shadman; Alkali-induced agglomeration of solid particles in coal combustors and gasifiers; Chem. Eng. Comm. 1989, Vol. 81, pp. 83-96
7. A.Moilanen; Ash behaviour in gasification; Technical Research Centre of Finland; Laboratory of Fuel Processing Technology; Espoo, Finland.
8. N. Padban; Master thesis; Dept. of Chemical Engineering II, Lund University, Sweden.
9. Levin; Ribbins; McMurdie.; Phasc diagrams for ceramists. American Ceramic Society, 1964- .

Table 1. Composition of ashes in different temperatures ; analyzed by AAS/IC

Content, %		Si	Al	Ca	K	Na	Mg	Mn	Fe	S	P
	550°C	11.7	1.8	24.9	9.1	0.9	6.4	2.3	0.8	1.1	1.2
EB,biomass	650°C	12.6	1.9	25.1	9.9	1.3	7.0	2.6	0.9	1.1	1.6
	900°C	12.0	1.9	29.4	9.4	1.5	7.4	2.9	1.0	1.5	1.6
	550°C	2.6	0.8	30.1	11.0	0.7	4.6	0.3	0.5	1.4	2.2
Salix	650°C	1.6	0.9	29.5	12.1	1.0	4.3	0.3	0.7	1.6	2.5
	900°C	2.4	0.9	33.6	12.6	0.8	5.3	0.4	0.7	1.8	3.1

Table II. Ash composition for Salix and EB,biomass ; SEM studies

Content%	Si	Al	Ca	K	Mg	Mn	S	P
EB,biomass ash	3.02	0.78	37.33	3.58	4.56	9.97	2.23	4.27
	4.21	1.07	39.23	3.23	3.59	7.06	2.93	3.41
Salix ash	0.354	0.065	43.92	6.81	3.5	0.56	0.52	9.45
	0.68	0.089	43.82	6.01	2.78	0.73	2.66	7.69

Table III. Chemical composition of some particles in agglomerates ; SEM studies

Content%	Si	Ca	K	S	P
EB,biomass;ash/BM=0.25	24.64	18.48	2.04	1.08	2.48
EB,biomass;ash/BM=0.25	5.19	39.6	0.19	2.28	4.04
EB,biomass;ash/BM=1	2.87	52.53	2.58	2.58	1.48
EB,biomass;ash/BM=4	8.4	33.64	1.04	1.4	4.26
EB,biomass;ash/BM=4	34.38	10.75	0.41	0.68	1.83
Salix,ash/BM=0.25	34.36	6.25	13.51	0.17	0.0
Salix,ash/BM=0.25	5.33	38.19	1.64	4.18	7.17
Salix,ash/BM=0.25	1.17	40.30	0.24	3.94	10.97
Salix,ash/BM=1	41.92	3.09	0.27	0.27	1.72
Salix,ash/BM=1	2.78	42.23	1.4	0.54	11.89
Salix ,ash/BM=4	0.39	24.68	23.36	1.51	11.77
Salix ,ash/BM=4	0.42	57.2	0.89	0.57	5.7

SEM-photo of quartz sand particle embedded in alkali (50X).

LABORATORY ILLUSTRATIONS OF THE TRANSFORMATIONS AND DEPOSITION OF INORGANIC MATERIAL IN BIOMASS BOILERS

Larry L. Baxter[1], and Bryan M. Jenkins[2]

[1]Combustion Research Facility
Sandia National Laboratories
Livermore, CA 94551-0969

[2]Dept. of Biological & Agricultural Eng.
University of California, Davis
Davis, CA 95616-5294

Keywords: combustion, biomass, inorganic material, ash

ABSTRACT

Boilers fired with certain woody biomass fuels have proven to be a viable, reliable means of generating electrical power. The behavior of the inorganic material in the fuels is one of the greatest challenges to burning the large variety of fuels available to biomass combustors. Unmanageable ash deposits and interactions between ash and bed material cause loss in boiler availability and significant increase in maintenance costs. The problems related to the behavior of inorganic material now exceed all other combustion-related challenges in biomass-fired boilers. This paper reviews the mechanisms of ash deposit formation, the relationship between fuel properties and ash deposit properties, and a series of laboratory tests in Sandia's Multifuel Combustor designed to illustrate how fuel type, boiler design, and boiler operating conditions impact ash deposit properties.

INTRODUCTION

Biomass-fired electric power generating stations are assuming increasingly prominent positions in energy and environmental issues in many regions of the world [Hustad and Sønju, 1992]. Such power stations typically are small (less than 50 MW_e net output), and rely on indigenous fuel supplies. Fuels for such facilities can be broadly classified into the categories of wood, agricultural residues, urban and municipal waste, and energy crops. Wood commonly represents the fuel of choice and the design fuel for biomass power stations. Wood's use is limited by availability, cost, and permitting agreements but in most cases not by fireside related problems (fouling, slagging, corrosion, etc.) in the boiler. The cost of wood fuel for such power stations in recent years was impacted by competition among the biomass power stations in some regions of the US, although such competition has waned in the last 18 months. At its peak, the cost of wood fuel in Northern California (USA) increased by over a factor of two from its baseline value prior to significant biomass combustion demand [Turnbull, 1993]. The availability of wood is beginning to decrease as a result of substantial reductions in logging associated with economic policy and wildlife protection. The probability of high fuel prices and unreliable availability motivate evaluation of new fuels for these combustors.

The motivation to develop new fuels for some power stations is driven by regulation and legal agreements more than by economics or availability. For example, under Title I of the U.S. federal Clean Air Act Amendments of 1990, states designate areas within their boundaries as attainment, non-attainment, or unclassifiable for each of six pollutants [1989]. Designations are based on either federal or state air quality standards. Operating permits for all biomass-fired power stations are based in part on their impacts on air quality. For power stations in or near non-attainment areas, permits often require a net *reduction* in the amount of pollutant (NO_x, particulate matter, etc.) generated in that area. This is accomplished by use of offset fuels, that is, fuels that would otherwise be burned in the field and produce higher levels of pollutants than what is produced if the same fuels are burned in a boiler. Agricultural byproducts generally and straw in particular represent common examples of offset fuels. Some power stations agree in their permits to consume sufficient offset fuel that they compensate for the pollutants produced from their overall operation, resulting in a net decrease in pollution as a result of operating the power plant.

Economic, long-term-planning, environmental, regulatory, and legal motivations can be strong for using offset or alternative fuels in biomass combustors. In addition, large and reasonably stable supplies of these fuels can be secured in many regions of the country. In practice, combustion of these fuels has proven difficult. Problems vary from fuels handling and storage to seasonal variations in both the amount and the quality of the supply. Arguably the most daunting issue, and the subject of this investigation, is the inorganic material in the fuel and its impact on the combustor. For example, essentially all biomass-fired power stations in

California that were designed and permitted based on using straw as an offset fuel opt to process straw by means other than combustion. These decisions are driven by the consistent experience of unmanageable bed agglomeration, slagging deposits, and convection pass fouling when burning straw. Several international studies have been completed in the general area of straw combustion [FEC Consultants Ltd., 1988; Livingston, 1991; Martindale, 1982; Martindale, 1984]. In many cases, addition of as little as 10 % straw to the boiler fuel supply for an electric power-generating facility causes an unscheduled shutdown within a few hours. Field experience with some other offset or alternative fuels (orchard prunings, nut shells or hulls, fruit pits, etc.) demonstrates borderline operation, with blend ratios limited to only 10-15 % when fired with wood [Miles, 1992; Miles and Miles, 1993; Miles, et al., 1993].

General mechanisms of ash deposition and laboratory/pilot-scale tests of bed agglomeration during straw combustion are discussed elsewhere [Baxter, 1993; Salour, et al., 1993]. The current investigation combines laboratory and field data in examining the causes of fireside problems during biomass combustion in a mechanistic way. Laboratory tests were conducted in a pilot-scale combustor and incorporated both *in situ* and *post mortem* analyses of ash deposit morphology, composition, and rate of accumulation. In separate reports, the details of an extensive series of laboratory and field tests of over a dozen biomass fuels and their ash-related combustion behaviors are discussed [Baxter, et al., 1995; Jenkins, et al., 1994; Miles, et al., 1994]. These sets of data are analyzed both separately and in comparison to demonstrate several of the most important aspects of ash behavior during straw combustion. This paper summarizes the laboratory findings during these investigations and illustrates many of the issues associated with the ash behavior of biomass fuels.

FACILITIES

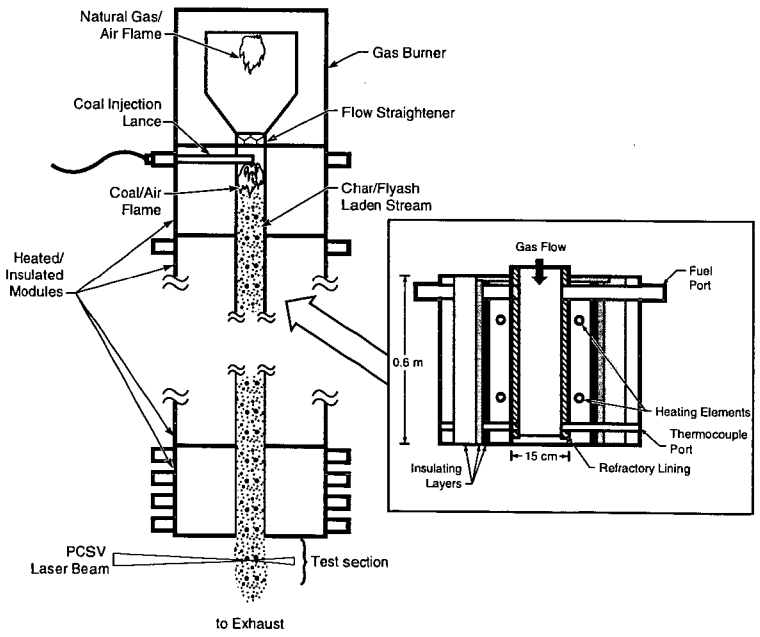

Figure 1 Schematic diagram of the Sandia Multifuel Combustor used in these combustion tests with modular guard heater inset.

The Multifuel Combustor (MFC) at Sandia was used to perform laboratory- and pilot-scale tests on ash deposition during combustion of the solid fuels indicated in Table I. The MFC is a pilot-scale (30 kW) down-fired, turbulent flow reactor that simulates the gas temperature and composition histories experienced by particles in combustion systems (Figure 1). A gas burner is used to provide a vitiated air to the remainder of the combustor. Gases from the burner flow through a series of modular sections that include guard heaters, fuel insertion ports, and thermocouple insertion ports. At the end of these modular heaters is the test section of the combustor. In this section, several air-cooled deposition surfaces that simulate waterwalls and convection pass tubes are injected in the particle-laden, vitiated flow. In the experiments described here, surface temperatures of these tubes are measured using thermocouples. Surface

temperature was held constant in each individual experiment but varied from 350 to 650°C among the several experiments performed. Further details about the MFC are available in the literature [Baxter, 1993].

Table 1 *Biomass Fuels Tested in Sandia's Multifuel Combustor*

Fuel	Moisture (% fuel)	Ash (% dry fuel)	Higher Heating Value (MJ/kg, daf)
		Herbaceous Fuels	
Rice Straw	11.22	19.17	18.74
Wheat Straw	8.39	8.08	19.31
Switch Grass	12.98	5.86	19.91
		Ligneous Fuels	
Almond Shells	7.52	2.87	19.83
Pistachio Shells	8.08	1.28	19.90
Olive Pits	6.97	1.83	21.97
Almond Hulls	8.02	5.75	20.00
Humus	12.51	34.64	12.89
		Commercial Fuels	
Urban Wood Fuel Blend	8.62	7.54	19.97
Nonrecyclable Paper	5.95	8.21	23.44
Wood/Straw Blend	9.25	7.33	20.56

The MFC was designed to simulate conditions in a coal combustor and has nominal fuel residence times of up to about four seconds. Typical fuel residence times in pulverized coal combustors are about two seconds. In the biomass tests, fuels were comminuted, typically to sizes less than 1 mm. This provided for nearly complete carbon conversion of the straws within the maximum residence time available in the combustor.

In all straw combustion tests, fuel was inserted into the MFC at a height of approximately 4.3 m (14 ft.) above the beginning of the test section. Ash deposits were collected from a simulated water wall and convection pass tube as well as from the internal ceramic liner of the MFC.

RESULTS AND DISCUSSION

Alkali metal behavior, in particular potassium, was identified at the beginning of the investigation as a concern. Traditional clean wood fuels contain little ash (< 1 %), and the ash contains relatively small amounts of potassium (5-20 %). The two commercial wood fuels indicated in Table 1 contain less clean sources of wood (urban wood waste, for example) and are blended with other, high ash fuels. The dominant ash components of clean wood include silicon and aluminum. Less traditional fuels, including essentially all of the nonprocessed herbaceous fuels and most of the nonprocessed agricultural residues, contain much more ash (Table 1) and higher potassium concentrations. Processed fuels, such as bagasse from sugar cane, often have very low alkali contents. The behavior of alkali is highlighted below (Figs. 2-4).

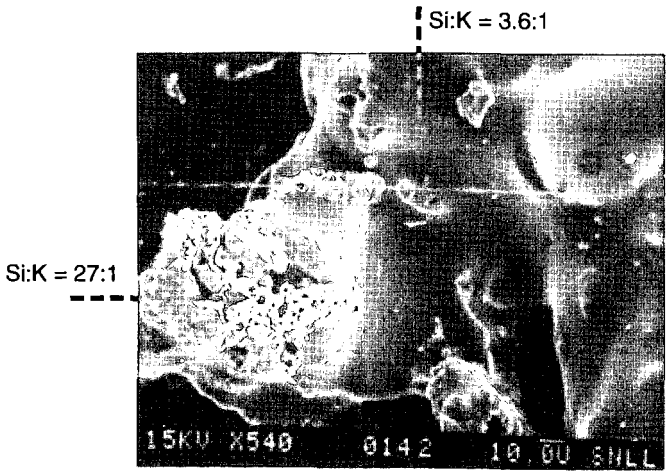

Figure 2. Elemental composition of different regions of a straw ash deposit.

Alkali materials in many forms are slightly volatile under combustion conditions. The resulting inorganic vapors react with other fuel or ash components to exaccerbate ash deposition problems by two primary mechanisms. The first mechanism is the formation of molten deposits, an example of which is seen in Fig. 2. The silicon to potassium ratio of two regions of a straw deposit are indicated. The molten region has a silicon to potassium ratio of less than 4:1, whereas the same ratio in the granular region is over 25:1. Alkali metals generally decrease the melting point of silica by formation of alkali silicates. Potassium, the primary alkali metal in biomass, is more mobile during combusiton than is common in, for example, coal. This leads to formation of soft or molten deposits for many nontraditional biomass fuels at lower temperatures than is common for coal or traditional woods.

The second mechanism of alkali metals contributing to ash deposition during biomass combustion is the formation of sulfated compounds. The low temperatures of steam tube surfaces promote the condensation of alkali vapors on surfaces. At surface temperatures, alkali sulfates are stable chemical species. The formation of an alkali sulfate layer of the deposit in intimate contact with the surface leads to the formation of a tenacious deposit. This is illustrated in Fig. 3, where the composition of an ash deposit was measured at the deposit crown, in the center of the deposit, and at the probe surface (positions A, B, and C, respectively). The concentration of sulfur monotonically increased as the measurement point approached the probe surface, with the ratio of sulfur at position C being over twice as high as at point A.

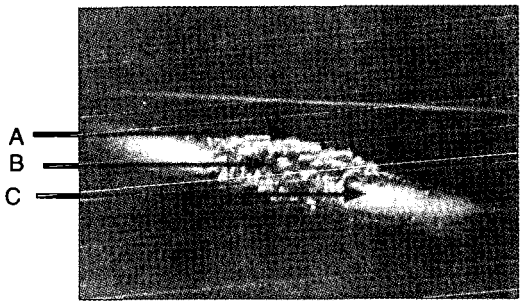

Fig. 3. Illustration of the formation of a sulfate bonding layer in a wheat straw ash deposit.

Similar behaviors are noted in the field experiments, as indicatd in Fig. 4. The analysis compares the composition of the fuel ash and a deposit collected from a furnace surface that experiences little direct impaction of particles. The amount of direct particle impaction on a surface depends primarily on boiler design. This deposit was collected from the wall opposite the furnace exit and convection pass entrance, where particles are directed away from the wall and into the convection pass. Very few impact on the boiler surface in this region. The vapors, on the other hand, are carried with the gases to the wall where they condense and react to form sulfates. As can be seen, the deposit composition is highly enriched in alkali metals and sulfur compared to the fuel ash composition. If boiler design or operating conditions change such that there is greater impact of particles in this region, the composition silica and other species associated with particles increases.

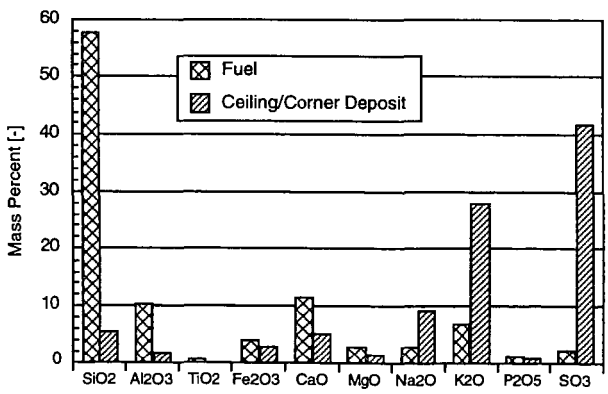

Fig. 4. Comparison between elemental composition of the fuel ash and a thin layer of reflective ash deposited on the ceiling and upper corner of the furnace. All compositions are expressed as oxides.

CONCLUSIONS

A series of laboratory and field tests illustrate the principal mechanisms of ash deposit formation during combustion of biomass fuels. Relationships among the amount and mode of occurence of inorganic material in the fuel, boiler design, and boiler operating conditions that influence the type of ash deposit formed are discussed. Specific examples of ash deposit formation during combustion of straw are used to illustrate the mechanisms.

Important attributes of ash deposits are determined by the relative rates of particle impaction on surfaces, condensation, and chemical reactions. Deposit morphology, composition, tenacity, porosity, and reflectivity are influenced by the mechanism of deposition. For a specific fuel, the dominant deposition mechanisms vary with location in the boiler and with boiler operating conditions.

Distinguishing characteristics of biomass combustion include the large amount of silica and vaporizable alkali in the ash of nontradtional fuels and the tendency of the silica and alkali to combine chemically on heat transfer surfaces. Alkali vapors condense on cool surfaces to form thin, reflective, alkali-based deposits. The alkali chemically combines with sulfur to form sulfates. In regions where silicon-based fly ash particles accumulate on surfaces, alkali combines with the silica to form silicates. These alkali-silicates have melting temperatures near or below the prevailing gas temperatures. This leads to sintering and formation of molten phases in the deposit. The rate of sintering depends on both deposit temperature and the amount of alkali in the gas phase.

REFERENCES

(1989). "Federal Register: Part III; Air Contaminants" (Final Rule No. 29 CFR Part 1910).

Baxter, L. L. (1993). "Ash Deposition During Biomass and Coal Combustion: A Mechanistic Approach." ***Biomass and Bioenergy***, ***4*** (2), 85-102.

Baxter, L. L., Jenkins, B. M., Miles, T. R., Miles Jr., T. R., Oden, L., Bryers, R., Milne, T., and Dayton, D. (1995). "Ash Behavior in Biomass Boilers" No.

FEC Consultants Ltd., O. (1988). "Straw Firing of Industrial Boilers" (Contractor Report No. ETSU B 1158). Energy Technology Support Unit: Department of Energy: United Kingdom.

Hustad, J. E., and Sønju, O. K. (1992). "Biomass Combustion in IEA Countries." ***Biomass and Bioenergy***, ***2***(1-6), 239-261.

Jenkins, B. M., Baxter, L. L., Miles, T. R., Jr., T. R. M., Oden, L. L., Bryers, R. W., and Winther, E. (1994). "Composition of Ash Deposits in Biomass Fueled Boilers: Results of Full-scale and Laboratory Simulations". In *ASAE*, (pp. Paper No. 946007). St. Joseph, MI 49085-9659: ASAE.

Livingston, W. R. (1991). "Straw Ash Characteristics" (Contractor Report No. ETSU B 1242). Energy Technology Support Unit: Department of Energy: United Kingdom.

Martindale, L. P. (1982). "The Potential for Large Scale Projects Featuring Straw as a Fuel in the UK" No. ETSU.

Martindale, L. P. (1984). "The Potential for Straw as a Fuel in the UK" No. ETSU.

Miles, T. R. (1992). "Operating Experience with Ash Deposition in Biomass Combustion Systems". In *Biomass Combustion Conference*, . Reno, NV:

Miles, T. R., and Miles, T. R., Jr. (1993). "Alkali Deposits in Biomass Power Plant Boilers". In *Biomass Power Program*, . Washington, DC:

Miles, T. R., Miles, T. R., Jr., Baxter, L. L., Jenkins, B. M., and Oden, L. L. (1993). "Alkali Slagging Problems with Biomass Fuels". In *First Biomass Conference of the Americas: Energy, Environment, Agriculture, and Industry*, 1 (pp. 406-421). Burlington, VT: National Renewable Energy Laboratory.

Miles, T. R., Thomas R. Miles, J., Baxter, L. L., Bryers, R. W., Jenkins, B. M., and Oden, L. L. (1994). "Boiler Deposits from Firing Biomass Fuels." ***Biomass & Bioenergy***, (submitted).

Salour, D., Jenkins, B. M., Vafaei, M., and Kayhanian, M. (1993). "Control of In-bed Agglomeration by Fuel Blending in a Pilot Scale Straw and Wood Fueled AFBC." ***Biomass and Bioenergy***, ***4***(2), 117-133.

Turnbull, J. H. (1993). "Use of Biomass in Electric Power Generation: The California Experience." ***Biomass and Bioenergy***, ***4***(2), 75-84.

THE BEHAVIOUR OF ALKALI METALS IN BIOMASS CONVERSION SYSTEMS

Pia Hald
Department of Combustion Research
Risoe National Laboratory
Roskilde, Denmark

Keywords: alkali metals, gas phase measuring, equilibrium

INTRODUCTION

The development towards reduced environmental impact and improved energy efficiency has in recent years lead to development of new power technology and a renewed interest in the use of biomass in the power supply.

The advantage of substituting coal by biomass are that the emission of CO_2, which contributes to the greenhouse effect, is reduced. A disadvantage of biomass is that the problems concerning alkali metals often become more severe. That is due to the difference of how the alkali metals are bound in coal and biomass.

During combustion and gasification alkali metals may contribute to slagging, deposition, corrosion and fluidized bed agglomeration. Whether or where in the system the problems appear is related to the transformations of the alkali metals and these depend on fuel and process conditions.

The alkali metal remains in the ash fractions during the process or is released as gaseous alkali metal. The gaseous alkali metal reacts with the ash fractions or condense due to saturation. The alkali metals in the ash fractions, bottom ash and fly ash, may transform during the process dependent on which components are favoured.

Studies on the alkali metal transformations are carried out in order to predict and thereby reduce the mentioned problems. Tools to study the fate of alkali metals are measuring of gas phase alkali metal, equilibrium calculations and chemical analyses of solid materials as e.g. deposits.

The problems of alkali metals are known from coal conversion. With respect to coal the problems are mainly related to sodium and with respect to biomass the problems are mainly related to potassium. Hald (1994) contains a literature survey on alkali metals in coal conversion systems and compare coal and straw concerning alkali metals. A system for measuring of gas phase alkali metals was designed and the sampling efficiency was tested. A comprehensive equilibrium study was performed and the results organized in tables as an easy access to equilibrium results. How ash components contribute to melt formation is discussed. The use of the developed tools is demonstrated for a fluidized bed combustor and a gasifier. Theoretical and experimental discussions are mainly related to straw and coal, but the results may be used in the study of other fuels. Some results from Hald (1994) are presented below, arranged in the sections alkali metals in the fuel, alkali metals at equilibrium, gas phase measuring, alkali metals in a fluidized bed combustor and alkali metals in a straw gasifier.

ALKALI METALS IN THE FUEL

Using straw as fuel the alkali metal related problems become more pronounced than with coal, even though the content of the alkali metals may be quite similar. That is due to the difference of how the alkali metals are present in the fuels which is important for their fate during the conversion process.

The alkali metal alumina silicates are the alkali metal components in fuels which are the most stable and those with the highest melting points. Because of that alumina silicates are used as getter materials to reduce the amount of gas phase alkali metals and increase the melting points.

Alkali metals in a less stable form, easier released to gas phase during a conversion process, are those present as the more simple salts, e.g. KCl, NaCl and salts of carboxylic acids. Alkali metal not present as alumina silicates are in the following denoted the soluble alkali metals. Alkali metals as chlorides, carbonates and sulphates have relatively low melting points compared to the alkali metal alumina silicates.

Alkali metal related problems using coal are primarily due to sodium, although the potassium content often is higher than that of sodium. That is due to larger amounts of sodium in a soluble form.

In contrast to coal the content of Al_2O_3 in biomass is relatively small and the most alkali metals are present in a soluble form. Another important difference between coal and biomass is that getter materials may be present within the coal and react with the soluble alkali metal to form alkali metal alumina silicates.

The amount of melt formation depends on the combination of components and temperature. Equilibrium calculations will show which components are favoured.

ALKALI METALS AT EQUILIBRIUM

Equilibrium calculations may be used in the description of which components are favoured and what influence a change in process conditions will have. Exact amounts may be determined by gas phase measurings and chemical analyses of the solid materials.

An extensive equilibrium study was performed and some general tendencies for the alkali metals were revealed. The calculations involving more equilibrium equations were performed by use of an equilibrium model (Michelsen, 1989) assuming gas phase ideality and phases immiscible.

The ideal gas phase assumption was studied and shown to be acceptable for gasification/combustion gases, the relative deviation of the volume is maximum 4 % at pressures up to 80 atm in the temperature range 300 K to 2000 K. It was shown that with ideal liquid mixtures, containing alkali metals, present the gas phase content of alkali metals will be lower than if phases were immiscible.

General tendencies about which non-silicate alkali metal components to be favoured in ash materials or at condensation, at high and low temperature and at oxidizing or reducing conditions, could be arranged relatively to the ratios alkali metals to chloride (M/Cl) and alkali metals to sulphur (M_2/S), see Table 1. S, Cl and M describe the molar content of sulphur, chlorine and soluble alkali metals in the selected equilibrium system. The system can e.g. be the global system or a sub system as e.g. the gas phase. M_2 denotes M divided by two as alkali metals and sulphur form components in the mole ratios 2 : 1.

A general difference between coal and straw can be described by the mole ratios M_2/S and M/Cl, see Table 2. The sulphur content is lowest in straw and the chloride content in straw is in about the same range as in high chlorine coals.

Alkali metals, chlorine and sulphur from coal will be in the gas phase in the same ratios as given for the pure coal in Table 2. By use of Table 1 it is seen that alkali metals condensed from gas phase at coal combustion may be present only as M_2SO_4. This agree with what is described in the literature about sodium condensation in coal combustion systems.

With all soluble alkali metal, all sulphur and all chlorine from straw present in the gas phase, the mole ratios for the gas phase are as in Table 2. At combustion conditions Table 1 shows possibility for both alkali metal sulphates, carbonates and chlorides to condense when cooling the gas.

Results from measuring of potassium, chloride and sulphur in gas phase at straw combustion (those measurements mentioned in Jensen et al. (1995)) show that the chloride content typically exceeds the potassium content (M/Cl $<$ 1). This leaves no possibility for alkali metal carbonate formation when the gaseous potassium condenses (see Table 2, M/Cl $<$ 1 and M_2/S $>$ 1). This is an example of how the equilibrium calculations and gas phase measurings may be used in the evaluation of deposition mechanisms.

Alkali metals are in the gas phase as MCl(g) and MOH(g). The distribution depends on the M/Cl ratio and the temperature. At temperatures above 800 °C no MCl will be found in solid or liquid form (see Table 1). This is true for a combustion or a gasification system using fuels with alkali metal contents similar or lower than straws. Both release of alkali metal from the fuel and the condensation of gaseous alkali metal are determined by kinetics. The equilibrium information about alkali metal chloride tells that with sufficient residence time of the fuel ash all alkali metal chlorides will be released to gas phase at temperatures above 800 °C and cooling a gas the alkali metal chlorides will not condense at temperatures above 800 °C.

Other examples of how the equilibrium calculations may be used to describe a change in the conversion system are 1) that more alkali metals will be present in gas phase with an increasing chloride to alkali metal ratio. 2) With coal as fuel, changing from reducing to oxidizing conditions, the amount of alkali metals present in gas phase may decrease due to condensation of alkali metal sulphates. With straw as fuel this change will not be as significant as straw contains much less sulphur than coal.

The tendency to melt formation will increase with increasing amounts of the alkali metal components with low melting points present. Those alkali metal components act as fluxing agents for the other ash components. Calculating freezing point depression by equation (1) it may be evaluated to which extent the ash component denoted i contributes to melt formation.

$$\Delta T = T^{*} - T = -\frac{R}{\Delta H_m} \cdot T^{*} \cdot T \ln(x_i) \qquad (1)$$

ΔT is the freezing point depression, T^{*} the melting point of the pure solid i (equals freezing point), R the gas constant, ΔH_m the molar melting enthalpy for component i and x_i the mole fraction of the component i in the mixture. At temperatures above T no solid phase of component i will be present. The freezing point curve for a component i can be described by the set of T, x_i. Freezing points of a number of components at $x_i = 0.8$ were calculated, the results are given in Table 3. A material as Al_2O_3 has a high melting point and a high melting enthalpy leading to a very small freezing point depression. A component as SiO_2 has a low melting enthalpy which give a large freezing point depression.

One important differences between coal and straw is that SiO_2 in straw is present as pure SiO_2 instead of as alumina silicates. The melting point of SiO_2 is significantly reduced by the presence of components with low melting points and may therefore contribute to melt formation also at the lower temperatures.

GAS PHASE MEASURING

A sampling system for gas phase measuring was designed in order to measure the amount of alkali metals in the gas phase. The sampling system comprises a probe and bubblers. The probe carries an alumina condenser, which is moderately inert to alkali metals.

A verification of gaseous alkali metal sampling systems has been needed as alkali metals may condense as small aerosol particles possibly evading the sampling system. Therefore a laboratory system to study the sampling efficiency was developed. The sampling efficiency was studied with KCl(g) in the range of 250 - 500 ppm(v) and with NaCl(g) in the range of 0.5 - 250 ppm(v). The results show that 94 $\pm$ 6 % of alkali metals are captured with a gas flow of 5 Nl/min.

Soluble alkali metal in particles sampled coincident with the gas phase alkali metal may contribute to the measured gas phase result and in every sampling it may be evaluated to which extent.

Sampling with filter should be investigated, this could be done with the laboratory system used for studying sampling efficiency. Different things may be taken into account, typical filter materials react with or adsorb the gaseous alkali metal and a filter cake may react with or release gaseous alkali metal until equilibrium is obtained. In the alkali metal measurings mentioned in Jensen et al. (1995) the use of a quartz filter was tested, the results will be reported later.

ALKALI METALS IN A FLUIDIZED BED COMBUSTOR

The alkali metal behaviour is described for a 80 MW Circulating Fluidized Bed Combustor (CFBC), Grenaa Denmark. The CFBC is fed with a fuel mixture of coal and straw (heating value of about 50 % of straw and coal, respectively). Limestone is added for in bed removal of sulphur. The use of coal in combination with straw decreases the tendencies of bed material agglomeration, deposition and corrosion.

Potassium and chloride contents were measured in the CFBC, after the cyclone in front of two heat exchangers. The content of potassium was in average 100 ppm(v) and of chloride in average 110 ppm(v). This is about 25 % of total soluble potassium introduced and about 60 % of the total chloride introduced.

The gas temperature at the measuring point was about 800 °C, the maximum gas temperature in the system, about 920 °C, was in the top of the cyclone. Nordin (1993) reports for a fluidized bed system that the temperature at the surface of a burning particle may be about 150 °C higher than the gas temperature. This means that the particle temperature could have been above 1000 °C.

Deposits on the two heat exchangers were analyzed and the results are given as oxides. The first heat exchanger met by the gas contained about 5 % potassium as K_2O and the second about 30 %. The analyses of the deposits and equilibrium calculations indicated condensed alkali metal sulphates not to form to the extent of equilibrium at the location of measuring. The rate of condensation is such that the potassium is found in the deposit on the second heat exchanger.

A scanning electron microscopy analysis of the first micron layer (tube side) of the deposit on the second heat exchanger showed a first layer of potassium sulphate.

The introduced fuel combination has the ratios $M_2/S < 1$ and $M/Cl > 1$. When adding limestone for the capture of sulphur it can be explained as the ratio M_2/S increases, but gas phase measurements indicated a M_2/S ratio < 1. By use of Table 1 it is seen that gaseous potassium will deposit only as potassium sulphate. This agree with the chemical analyses of the deposit.

The kind of bed material may influence on the extent of melt formation, bed materials were evaluated and the influence of addition of limestone discussed. The bed material should have a relatively high melting point together with a relatively high melting enthalpy (see equation (1)) as e.g. CaO and Al_2O_3 (see Table 3). It may be considered which components may be formed as e.g. CaO will react with sulphur to form $CaSO_4$. A material which captures the alkali metals forming compounds with higher melting points may be preferred. Addition of limestone gives a possibility for reduction of the extent of melt formation as 1) the ratio $CaSO_4$ to K_2SO_4 increases (eutecticum at 875 °C), 2) the concentration of ash in the bed material decreases and 3) CaO itself contributes only to melt formation to a minor extent (see Table 3).

ALKALI METALS IN A STRAW GASIFIER

Potassium measurings were performed in a 50 kW moving bed straw gasifier, Laboratory of Energetics, The Technical University of Denmark. The gasifier was operating 12 hours during which the ash materials were accumulated in the system. The maximum temperature was about 950 °C in the top of the reactor where the fuel was introduced. The temperature was reduced downwards in the reactor, and the produced gas left in the bottom where the gas temperature was about 750 °C.

The potassium content was measured to 450 ppm(v) in the outlet gas at a temperature of 750 °C, that is 35 % of the total potassium content in the straw. The result is in reasonable agreement with equilibrium calculations at a temperature of 750 °C. It can not be known whether the measured potassium content has been released on the way downwards in the reactor or if it is an equilibrium established due to the accumulation of ash material.

Equilibrium calculations for the total system show that potassium in condensed form will be present as chlorides and carbonates if potassium silicates are not included in the calculations. This could also be found by the use of Table 1 and Table 2. If potassium silicates are included in the calculations the carbonates will not form. This is one of the general results, the alkali metal silicates are favoured to the carbonates.

The amount of potassium in the gas phase at 750 °C is the same whether potassium silicates are included in the calculations or not. The possible potassium silicates are $K_2O \cdot (SiO)_x$, where $x=2$ below 950 °C and $x=4$ above 950 °C.

CONCLUSION

Results of equilibrium calculations combined with gas phase measurements of the alkali metals, chlorine and sulphur were demonstrated as useful tools in the investigation of the alkali metal behaviour at gasification and combustion.

REFERENCES

Barin I.: Thermochemical Data of Pure Substances, VCH (1989)

Hald P.: Alkali metals at Combustion and Gasification, Equilibrium Calculations and Gas Phase Measurings, Department of Chemical Engineering, The Technical University of Denmark, Ph.D.-thesis (1994)

Jensen P.A., Stenholm M., Hald P., Christensen K.A.: Deposition investigation in straw fired boilers, Risoe National Laboratory, Denmark (1995)

Michelsen M.L.: Calculation of multiphase ideal solution chemical equilibrium, Fluid Phase Equilibria 53, 53-80 (1989)

Nordin A.: On the chemistry of combustion and gasification of biomass fuels, peat and waste; environmental aspects, Ph.D.-thesis, University of Umeå (1993)

Weast R.C.: CRC Handbook of Chemistry and Physics, 63rd edition, CRC Press (1983)

Table 1 Mole ratios M_2/S and M/Cl describing which condensed non-silicate alkali metal components are favoured at low or high temperatures (T) and at reducing (Red.) or oxidizing (Ox.) conditions.

		$M_2/S \leq 1$ $M/Cl \leq 1$	$M_2/S \leq 1$ $M/Cl > 1$	$M_2/S > 1$ $M/Cl \leq 1$	$M_2/S > 1$ $M/Cl > 1$
Ox.	T < 800 °C	M_2SO_4	M_2SO_4	M_2SO_4 MCl	M_2SO_4 M_2CO_3 MCl
Ox.	T > 800 °C	M_2SO_4	M_2SO_4	M_2SO_4	M_2SO_4 M_2CO_3
Red.	T < 800 °C	MCl	M_2CO_3 MCl	MCl	M_2CO_3 MCl
Red.	T > 800 °C	-	M_2CO_3	-	M_2CO_3

Table 2 Mole ratios M_2/S and M/Cl in coal and straw.

	Coal	Straw
M_2/S	< 1	normally > 1
M/Cl	< 1	> 1

Table 3 Freezing points at $x_i = 0.8$ and ΔT at $x_i = 0.8$. Melting enthalpies and melting points for the pure components (T^*).

Component	ΔH_m (kJ/mol)	T^* (°C)	$T_{xi=0.8}$ (°C)	$\Delta T_{xi=0.8}$ (°C)
$K_2O\cdot(SiO_2)_4$	49.0	770	730	40
KCl	26.3	771	699	72
$CaCl_2$	28.5	772	705	67
NaCl	28.2	801	730	71
Na_2CO_3	29.6	850	776	74
$Na_2O\cdot(SiO_2)_2$	35.6	874	809	61
Na_2SO_4	23.8	884	788	96
K_2CO_3	27.6	901	815	86
$NaBO_2$	33.5	967	887	80
$K_2O\cdot(SiO_2)_2$	41.0	1045	971	74
K_2SO_4	34.4	1069	978	91
$MgSO_4$	14.6	1127	916	211
$CaSO_4$	27.6	1457	1277	180
SiO_2	9.6	1723	1167	556
Al_2O_3	111.1	2054	1967	87
CaO	79.5	2614	2432	182
MgO	77.8	2852	2635	217

ΔH_m-values are from Barin (1989) and T^* from Weast (1983).

Mechanisms of Alkali Metal Release During Biomass Combustion

David C. Dayton and Thomas A. Milne
National Renewable Energy Laboratory
Industrial Technologies Division
1617 Cole Boulevard
Golden, CO 80401-3393

Keywords: alkali release, biomass combustion, molecular beam mass spectrometry

Introduction

The conversion of biomass materials into electricity via combustion poses several technical and economic challenges. One of the more pressing technical challenges associated with biomass combustion is fouling and slagging in combustors. Accelerated fouling and slagging in current biomass combustion facilities has been linked to the alkali metal content of the fuel. Alkali metal release during biomass combustion causes significant problems in terms of severe fouling and slagging of heat transfer surfaces in boilers thus reducing efficiency, and in the worst case leads to unscheduled plant downtime[1]. Future biomass to electricity facilities that will incorporate integrated combined cycle systems that use biomass combustion gases directly to drive an aeroderivative turbine[2] will have even lower tolerances for alkali metal vapor release because accelerated erosion and corrosion of turbine blades results in shorter turbine lifetimes.

Hot gas cleanup methods are sought that reduce the amount of alkali vapor in biomass combustion gases to acceptable levels, thus minimizing fouling and slagging. This would be facilitated by a detailed understanding of the mechanisms of alkali release during biomass combustion as well as identifying these alkali vapor species and how these vapors lead to fouling and slagging. Our experimental approach to these issues is to identify the form of alkali metal vapors from directly sampled hot gases liberated from the combustion of small biomass samples in a variable temperature quartz tube reactor employing a molecular beam mass spectrometer (MBMS) system to monitor the combustion event. The baseline condition chosen for studying alkali metal release during biomass combustion was 1100°C in 20% O_2 in helium (simulated air). This temperature is approaching the maximum turbine inlet temperatures used for the next generation of direct biomass-fired turbines for power production. Under these conditions, the large excess of oxygen assured complete combustion and the furnace temperature was high enough to insure the partial volatilization of alkali metal containing species. By screening a large variety of biomass samples for alkali metal release, it may be possible to determine combustion conditions that minimize alkali metal release. These results may also be used to identify methods for reducing the alkali metal vapor content of the hot combustion gases.

Experimental

The release of alkali metal vapor species during biomass combustion was monitored and studied using a direct sampling, molecular beam mass spectrometer (MBMS) system. The MBMS system is ideally suited for studying the high temperature, ambient pressure environments encountered during the present alkali metal screening studies. The integrity of the sampled, high temperature combustion gases is preserved by the free-jet expansion because chemical reactions are effectively quenched and condensation is inhibited. The nature of the free jet expansion and the subsequent formation of a molecular beam allows reactive and condensable species, such as alkali metal containing vapors, to remain in the gas phase at temperatures far below their condensation point for long periods of time in comparison to reaction rates. The details of the apparatus and its application to studying alkali metal release during switchgrass combustion are described in the literature[3-5].

Small (20-60 mg) samples were combusted in a tubular quartz reactor that was placed in a standard two-zone, electric clam-shell furnace[5] set at either 1100°C or 800°C. Biomass samples were loaded into hemi-capsular quartz boats of such a size that approximately 40 mg of ground, loosely packed, material filled the boat, depending on the feedstock. The actual boat temperature and flame temperature were not measured, however, the hot gas temperature in the vicinity of the sample boat could be monitored with a type-K (chromel-alumel) thermocouple. A mixture of oxygen (20%, 10%, or 5%) in helium flowed through the reactor from back to front at a total gas flow rate of 4.4 standard liters per minute. Combustion gases had a residence time of about 0.1 seconds in the reactor before reaching the sampling orifice. When appropriate, steam was added to the reactor atmosphere by injecting water into the rear of the furnace through a needle fed by a syringe pump. Stainless steel shot was packed around the tip of the needle to increase the surface area for water evaporation. This provided a steady flow of 20% steam by volume.

The end of the reactor was fitted around the tip of the sampling orifice positioned at the downstream end of the quartz tube reactor to sample the high temperature, ambient pressure biomass combustion gases. The orifice protruded into the furnace to keep it at an elevated temperature and thus prevent condensation on the sampling cone. The actual temperature of the orifice was not routinely measured, however, when the furnace temperature was set at 1100°C the tip of the orifice was observed to glow orange. Sampled gases underwent a free jet expansion into the first stage of the differentially pumped vacuum system. The expanded gases were skimmed by a second conical skimmer (1 mm orifice diameter) at the entrance to the second stage forming a molecular beam that was directed into the ionization region of the mass spectrometer in the third stage of the vacuum system. Ions were formed by electron impact ionization of the sampled gases with a nominal electron energy of 25 eV. The ions were filtered by a triple quadrupole mass analyzer and detected with an off axis electron multiplier. The mass spectrometer was scanned continuously at a rate of approximately 100 amu/sec. In this configuration, a complete mass spectrum was recorded once every 1.0 to 1.5 seconds. Background subtraction from the total ion signal yielded corresponding mass spectra at a given time during the combustion event or averaged over a given phase of the combustion event.

A total of 23 different biomass feedstocks have been screened for alkali metal vapor release under four different combustion conditions. Only the results from one combustion condition, 1100°C and 20% oxygen in helium, will be discussed below. The list of feedstocks is as follows: planer shavings of lodgepole pine (*Pinus contarta*); eucalyptus (*Eucalyptus saligna Sm.*); poplar (*Populus deltoides x nigra var. Caudina*); corn stover (*Zea mays L.*); switchgrass (*Panicum virgatum L.*); wheat straw (*Triticum aestivum.*); rice straw; (Sandia) switchgrass (*Panicum virgatum L.*); pistachio shells (*Pistacia vera*); almond shells (*Prunnus amygdalus*); almond hulls (*Prunnus amygdalus*); wood waste #1; wood waste #2; waste paper; Danish wheat straws (*Triticum aestivum*) from Slagelse and Haslev (Danish power plants) (SLAG001, SLAG002, and HAS001); alfalfa stems (*medicago sativa L.*) (IGT001 and IGT002); summer switchgrass (*Panicum virgatum L.*); Dakota switchgrass (*Panicum virgatum L.*); and two willows (*Salix veminalus*, *Salix alba*, tops only). This set of feedstocks can be divided into various classes of biomass identified as woody feedstocks, herbaceous feedstocks, grasses, agricultural residues, and waste feedstocks. It will become apparent that the varying nature of the feedstocks results in unique differences in terms of alkali metal release during combustion.

Results and Discussion

The combustion of the solid biomass samples occurs in three distinct phases: the combustion phase, the char combustion phase, and the ash cooking phase[4,5]. The details of the combustion event are available in the literature[5]. Based on these studies, it became obvious that the most important information concerning the species and amount of alkali metal released during biomass combustion was contained in the mass spectra averaged over the char combustion phase. Mass spectra averaged during the char combustion phases of all 23 feedstocks screened for alkali metal release qualitatively reflected the feedstock composition as determined from the ultimate and ash analyses. Although the ultimate analysis can be used to determine the total amount of alkali metal in a given feedstock, it does not reflect how much alkali metal is released into the gas phase nor the form of the alkali metal released.

The mass spectra averaged during the char combustion phase of the woody feedstocks (pine, eucalyptus, poplar, and willow) revealed that little alkali metal was released. As an example, the char phase mass spectrum averaged during the combustion of willow is presented in Figure 1. The mass spectral results are consistent with the ultimate and ash analyses for this willow sample that indicate low alkali metal levels. The only indication of alkali metal release is the detection of K^+, however, the parent alkali metal species which yield this fragment could not be identified. Based on previous results[4], the primary mechanism for alkali metal release during the combustion of low alkali containing woody feedstocks involves the vaporization or decomposition of potassium sulfate.

In general, the straws and grasses (switchgrass, wheat straw, alfalfa stems, and rice straw) contain high levels of potassium and chlorine. The mass spectrum averaged during the char phase of rice straw combustion is shown in Figure 2. Based on the composition of rice straw (shown in the inset) determined from the ultimate and ash analysis of the sample, this feedstock has high levels of both potassium and chlorine. As a result, strong mass spectral signals are observed at m/z=74 and 76, corresponding to the KCl parent ions. In fact, the fragment ions of the KCl dimer (K_2Cl^+ at m/z = 113 and m/z = 115) were also observed. Significant intensity was also observed at m/z=39, the K^+ fragment. The intensity of these signals is a function of the amounts of potassium and chlorine available in the feedstock. For high chlorine containing feedstocks, like rice straw, it is also possible to identify HCl released during combustion. The dominant mechanism for alkali metal release during

the combustion of feedstocks with high potassium and chlorine contents is through the vaporization of potassium chloride.

The agricultural residues, pistachio shells, almond shells, and almond hulls, tend to have high potassium content but low chlorine content. In fact, the almond hulls have the highest level of potassium of all 23 feedstocks studied. The mass spectrum averaged over the char phase of almond hulls combustion is shown in Figure 3. The dominant alkali metal species observed in the char phase mass spectra averaged during almond hulls combustion were potassium hydroxide (m/z = 56) and potassium cyanate, KOCN (m/z = 81). The high nitrogen content in addition to the high potassium content of the almond hulls and the oxidizing combustion conditions contribute to the formation of KOCN. At this time it is not clear whether KOCN is directly released or KCN is released and then reacts with oxygen to form the cyanate. The relatively low chlorine level of the almond hulls forces the alkali metal release to other thermodynamically stable forms.

The waste feedstocks (wood waste #1, wood waste #2, and waste paper) are not as bad as their name implies in terms of alkali metal release. These feedstocks tend to have relatively low alkali levels, and as a result, it was difficult to identify any alkali species in the mass spectra averaged over the char combustion phases of these feedstocks. The waste feedstocks do have moderately high chlorine levels (0.13 w%). However, HCl was the only chlorine species identified in the char phase mass spectra.

Multiple alkali release mechanisms can occur simultaneously during biomass combustion depending on the feedstock composition. This is most apparent from the mass spectral results recorded during the char phase of alfalfa stems combustion shown in Figure 4. Alfalfa stems have a high potassium, chlorine, and nitrogen content. As a result, there is substantial alkali metal released in the form of KCl, KOH, and KOCN.

Once the major biomass combustion products were identified, including the major alkali metal containing species released, correlations were sought between the mass spectral data and the ultimate analysis data for the 23 feedstocks screened. The chlorine content determined in the ultimate analyses correlated well with the mass spectral intensities of identifiable chlorine containing species, HCl and KCl, monitored at m/z=36 and 74 (HCl^+ and KCl^+, respectively). Most of the available chlorine is released into the gas phase and can be accounted for during biomass combustion[6].

The potassium content of a given feedstock does not correlate as well with the parent and fragment ions (KOH^+, $KOCN^+$, KCl^+, and K^+) identified in the char phase mass spectra that result from the dominant gas phase potassium species. The overall potassium content of a given feedstock does not necessarily correspond to a high level of alkali metal vapor released during biomass combustion[6]. Almond hulls have the highest potassium content of the 23 feedstocks, yet combustion of almond hulls does not release the most potassium vapor (KCl, KOH, and/or KOCN). Rice straw has a high potassium content, however, it also has the highest chlorine content of any of the 23 feedstocks. As a result, significant alkali metal vapor is released as KCl during rice straw combustion. Alfalfa stems and switchgrass also have a high potassium and chlorine content that accounts for the above average alkali metal vapor released during combustion. It appears that those feedstocks with high potassium and the higher chlorine levels tend to release more alkali metal vapors (based on an average of the 23 feedstocks studied) than those feedstocks with high potassium and low chlorine contents.

Conclusions

The MBMS technique has proven to be a valuable and versatile tool for studying alkali vapor release during biomass combustion. The most significant parameter which affects alkali vapor release is the feedstock being combusted. While each individual feedstock appears to have it's own unique combustion properties, these feedstocks can often be grouped together into classes of feedstocks. Woody feedstocks have comparatively little alkali content and low levels of chlorine. Consequently, combustion of woody feedstocks leads to very little alkali vapor release, usually via a mechanism involving the vaporization of potassium sulfate.

Herbaceous feedstocks, grasses and straws contain very high levels of alkali and chlorine compared to the woody feedstocks. Large amounts of alkali metal, in the form of potassium chloride, are released into the gas phase during combustion of herbaceous feedstocks which results in a high fouling and slagging potential for these feedstocks. The results of these alkali screening studies implicate the chlorine content of a given feedstock as a facilitator of alkali release[6].

While chlorine content has been linked to substantial alkali vapor release, it is not essential. The agricultural residues still release significant amounts of alkali vapor during combustion, however, the

alkali is in the form of the hydroxide and potassium cyanate instead of the chloride. These studies identify a new mechanism for alkali metal release that involves the formation of potassium cyanate. This mechanism of alkali transport seems to be dominant during the combustion of feedstocks that have high potassium and nitrogen contents.

Having identified these dominant gas phase species it should be possible to identify how these alkali metal containing species contribute to fouling and slagging in industrial combustion systems. Methods can now be sought to sequester or reduce the level of these species in the gas phase if they prove to be major precursors to deposit formation. Additives to the bed material in fluid bed combustors can be sought to capture these species after they are released. Alkali getter beds or separate hot gas cleanup units can be designed knowing that the major alkali species in the gas phase have been identified based on the feedstocks screened in this study.

Acknowledgements

The authors are grateful for the support of the Solar Thermal and Biomass Power Division of the Department of Energy Office of Energy Efficiency and Renewable Energy. Special thanks go to Richard L. Bain and Ralph P. Overend for both programmatic and technical support and guidance. Mr. Gerald Cunningham of Hazen Research, Inc. is acknowledged for providing feedstocks and their analyses. We would also like to acknowledge the efforts of Thomas R. Miles, Sr. and Thomas R. Miles, Jr. of Thomas R. Miles Consulting Engineers and Dr. Larry Baxter of Sandia National Laboratories Combustion Research Facility.

References

1. Turnbull, J.H., Biomass and Bioenergy, **1993**, 4, pp. 75-84.

2. Bain, R.L. and Overend, R.P., *Advances in Solar Energy: An Annual Review of Research and Development, Volume 7.* Ed. Karl W. Boer, American Solar Energy Society. Chapter 11, **1992**.

3. Evans, R.J. and Milne, T.A., Energy and Fuels, **1987** 1, pp. 123-127.

4. French, R.J., Dayton, D.C., and Milne, T.A., "The Direct Observation of Alkali Vapor Species in Biomass Combustion and Gasification," NREL Technical Report (NREL/TP-430-5597). January 1994.

5. Dayton, D.C., French, R.J., and Milne, T.A., submitted for publication in Energy and Fuels.

6. Dayton, D.C., R.J. French, and T.A. Milne, "Identification of Gas Phase Alkali Species Released During Biomass Combustion," Proceedings of the Bioenergy '94 Conference, October 2-6, 1994, Reno, NV. p. 607.

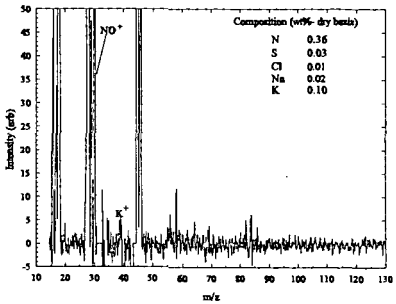

Figure 1: Mass spectrum averaged over the char phase of willow combustion at 1100°C in 20% oxygen in helium. The signals have been normalized to the $^{34}O_2^+$ signal measured before sample insertion. The composition in the inset is from the ultimate and ash analyses of the feedstock on a moisture free basis.

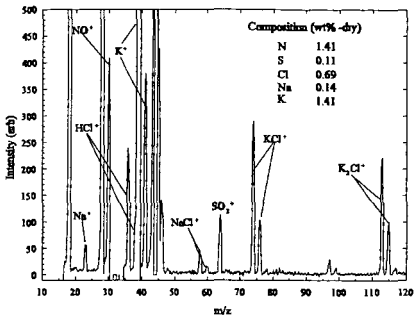

Figure 3: Mass spectrum averaged over the char phase of rice straw combustion at 1100°C in 20% oxygen in helium. The signals have been normalized to the $^{34}O_2^+$ signal measured before sample insertion. The composition in the inset is from the ultimate and ash analyses of the feedstock on a moisture free basis.

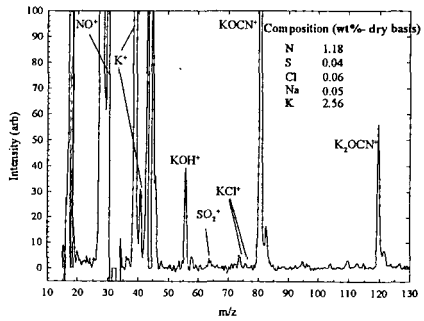

Figure 4: Mass spectrum averaged over the char phase of almond hulls combustion at 1100°C in 20% oxygen in helium. The signals have been normalized to the $^{34}O_2^+$ signal measured before sample insertion. The composition in the inset is from the ultimate and ash analyses of the feedstock on a moisture free basis.

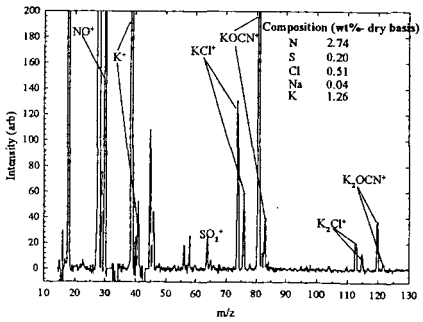

Figure 2: Mass spectrum averaged over the char phase of alfalfa stems combustion at 1100°C in 20% oxygen in helium. The signals have been normalized to the $^{34}O_2^+$ signal measured before sample insertion. The composition in the inset is from the ultimate and ash analyses of the feedstock on a moisture free basis.